On the Late Saalian glaciation (160 - 140 ka): a climate modeling study

Florence Colleoni

▶ **To cite this version:**

Florence Colleoni. On the Late Saalian glaciation (160 - 140 ka): a climate modeling study. Climatology. Université Joseph-Fourier - Grenoble I; Stockholm University, 2009. English. NNT : . tel-00418445

HAL Id: tel-00418445
https://theses.hal.science/tel-00418445

Submitted on 18 Sep 2009

HAL is a multi-disciplinary open access archive for the deposit and dissemination of scientific research documents, whether they are published or not. The documents may come from teaching and research institutions in France or abroad, or from public or private research centers.

L'archive ouverte pluridisciplinaire **HAL**, est destinée au dépôt et à la diffusion de documents scientifiques de niveau recherche, publiés ou non, émanant des établissements d'enseignement et de recherche français ou étrangers, des laboratoires publics ou privés.

LABORATOIRE DE GLACIOLOGIE ET GÉOPHYSIQUE DE
L'ENVIRONNEMENT - UMR 5183
Centre National de la Recherche Scientifique
Université Joseph Fourier
54, rue Molière - Domaine Universitaire BP 96
38402 St-Martin d'Hères Cedex (France)

DEPARTMENT OF GEOLOGY AND GEOCHEMISTRY
Stockholm University
Svante Arrhenius väg 8C
106 91 Stockholm (Sweden)

On the Late Saalian glaciation (160 - 140 ka): a climate modeling study

Florence COLLEONI

Thèse de doctorat de l'Université Joseph Fourier (Grenoble 1)

(Arrêtés ministériels du 5 juillet 1984 et 30 mars 1992)

Co-tutelle avec l'Université de Stockhom (Suède)

Spécialité: Sciences de la Terre, de l'Univers et de l'Environnement

Date de Soutenance:
14 septembre 2009

Composition du jury:

Anne-Marie BOULLIER	Examinateur
Johan NILSSON	Rapporteur
Masa KAGEYAMA	Rapporteur
Jan BACKMAN	Examinateur
Gerhard KRINNER	Directeur de thèse
Martin JAKOBSSON	Co-Directeur de thèse

Abstract

This thesis focuses on the glaciation of the Late Saalian period (160 -140 ka) over Eurasia. The *Quaternary Environment of the Eurasian North* project evidenced that during this period, the Eurasian ice sheet was substantially larger than during the entire Weichselian cycle and especially than during the Last Glacial Maximum (21 ka, LGM). The Late Saalian astronomical forcing were different, especially at 140 ka considered as the Late Saalian glacial maximum, than during the LGM while greenhouse gas concentrations (CO_2 and CH_4) were similar. However, the large Late Saalian ice sheet extended further to the West than during the LGM and consequently dammed the main Siberian rivers, creating ice-dammed lakes in front of the ice sheet's southern margins. The Late Saalian atmospheric dust content recorded in Antarctic ice cores was smaller compared to the LGM. To understand how this ice sheet could have grown so large over Eurasia during the Late Saalian, we use an Atmospherical General Circulation Model (AGCM), an AGCM coupled to an oceanic mixed layer module and a vegetation model to explore the influence of regional parameters, sea surface temperatures (SST) and orbital parameters on the surface mass balance of the Late Saalian Eurasian ice sheet.

We first perform 21-year snap-shots of the 140 ka glacial maximum to simulate the influence of proglacial lakes and dust deposition on snow on the surface mass balance of the Late Saalian Eurasian ice sheet. Proglacial lakes cools the summer climate, reducing the ablation along the southern margins of the ice sheet while dust deposition on snow slightly warm the regional climate, inducing more ablation along these margins. Combined together, the dust-induced warming enhances the cooling effect of proglacial lakes. At 140 ka, the impact of the substitution from conifera to tundra highly increases the regional albedo which causes an important regional cooling due to the development of a permanent snow cover along the entire ice sheet margins. Simulated 140 ka SST underestimate the available Late Saalian SST derived marine records and sea ice reached 40°N in both North Atlantic and North Pacific. This leads to an excessively cold Northern Hemisphere climate, completely stopping the ablation process over the ice sheet and reducing the amount of moisture coming from the Atlantic. Recent seismic campaign revealed the presence of a large grounded ice feature, a possible Canada Basin ice-shelf, that developed at the end of Marine Isotope Stage 6 (191-130 ka) in the Arctic Ocean. Simulations show that its impact on the Northern Hemisphere remains essentially constrained to the Arctic Ocean (regional cooling of several degree mainly due to the elevation and isolation from the oceanic heat fluxes) and to the lower troposphere.

According to geological evidences, the Late Saalian Eurasian ice sheet reached its maximum volume and extent before 160 ka but remains as large until Termination II (130 ka). Northern Hemisphere high latitudes summer insolation show a large insolation peak towards 150 ka and to understand how the Late Saalian Eurasian ice sheet could survive to this peak, we simulate the climate conditions (regional factors, SST and vegetation cover) for the three time-slices 160, 150 and 140 ka. The simulated 160 and 150 ka climate are milder than at the glacial maximum of 140 ka. Ablation is more important along the entire southern margin of the Eurasian ice sheet at 150 ka although the mean annual surface mass balance remains positive. This suggest that despite a larger 150 ka insolation, the Late Saalian Eurasian ice sheet, combined to proglacial lakes, to a vegetation cover and SST in agreement with the simulated climate, is large enough to generate its own cooling and to maintain over the continent. This thesis partly answers to the issue raised above. However, to understand how this ice sheet grew and to better estimate the interactions between ocean, atmosphere, continent and ice sheet, ice-ocean-atmosphere coupled simulations are necessary.

Résumé

Cette thèse est centrée sur la période glaciaire de la fin du Saalien (160 - 140 ka) en Eurasie. Les résultats du projet *Quaternary Environment of the Eurasian North* montrent clairement que la calotte Eurasienne de la fin du Saalien était nettement plus grosse que durant tout le cycle suivant du Weichselien et particulièrement durant le Dernier Maximum Glaciaire (21 ka, LGM). Les paramètres orbitaux de la fin du Saalien étaient très différents de ceux du LGM et spécialement à 140 ka, considéré comme le maximum glaciaire du Saalien. Cependant, les concentrations de gaz à effet de serre (CO_2 and CH_4) étaient semblables. La calotte Saalienne était plus étendue au Sud et à l'Est que pendant le LGM et a, en conséquence, interrompu le cours des principales rivières Sibériennes, créant des lacs proglaciaires le long des marges Sud de la calotte. Les enregistrements des carottes des glaces en Antarctique montrent que la concentration de poussières atmosphérique était plus faible au Saalien qu'au LGM. Afin de comprendre comment cette calotte a pu croître autant durant la fin du Saalien, nous avons utilisé un modèle de circulation générale de l'atmosphère (AGCM), un AGCM couplé à une couche mixte océanique et un modèle de distribution de végétation pour explorer l'influence des paramètres régionaux, des températures de surface océaniques (SST) et des paramètres orbitaux, sur le bilan de masse en surface de la calotte Eurasienne.

Nous avons simulé, à l'aide de snap-shots de 21 ans, l'influence des lacs proglaciaires et des dépôts de poussières sur la neige sur le bilan de masse de la calotte Eurasienne lors du maximum glaciaire de 140 ka,. Les lacs refroidissent le climat d'été et réduisent la fonte le long des marges sud de la calotte alors que les poussières ont l'effet opposé. En combinant les deux facteurs, le réchauffement cause par les dépôts de poussière amplifie l'effet des lacs proglaciaires. La substitution des forêts de conifères par de la tundra induit également un refroidissement important et donc une réduction de la fonte le long de marges sud à 140 ka. Les SST simulées par la couche mixte sont bien plus froides que ce que suggèrent les données géologiques et la couverture de glace de mer simulée atteint 40°N dans l'Atlantique Nord et dans le Pacifique Nord. Cela induit un refroidissement très important de tout l'hémisphère Nord, arrêtant totalement le processus d'ablation de la calotte et réduisant la quantité d'humidité advectée de l'Atlantique Nord. Les récentes campagnes de sismique marine ont révélé la présence d'un ice-shelf dans la bassin arctic du Canada à la fin du Stade Isotopique Marin 6 (191 - 130 ka). L'impact de cet ice-shelf sur le climat de l'hémisphère Nord se réduit à un refroidissement de l'Océan Arctique (dû principalement à l'altitude et à un isolement des flux de chaleur océanique plus efficace) confiné à la basse troposphère.

Selon les données géologiques, la calotte Eurasienne avait atteint ses limites maximum avant 160 ka mais semblait conserver cette taille jusqu'à la Terminaison II (130 ka). L'insolation d'été dans les hautes latitudes montre un pic d'insolation très net vers 150 ka et pour comprendre comment la calotte Eurasienne a pu survivre à cette augmentation d'insolation, nous avons simulé le climat (paramètres régionaux, SST et végétation) pour les trois périodes 160, 150 et 140 ka. Les climats simulés à 160 et 150 ka sont plus humides et plus doux qu'à 140 ka. La fonte est donc plus importante le long des marges Sud de la calotte à 150 ka bien que le bilan de masse en surface demeure positif. Cela suggère qu'en dépit d'une insolation plus importante à 150 ka, la calotte Saalienne, combinées aux lacs proglaciaires, à une végétation et à des SST en accord avec le climat simulé, est suffisamment imposante pour générer elle-même le froid nécessaire à sa stabilité sur le continent. Cette thèse répond en partie à la question posée initialement. Cependant, pour comprendre comment cette calotte a pu atteindre ces dimensions et pour mieux estimer l'interaction entre océan, atmosphère, continent et calotte de glace, des simulations avec un système couplé sont nécessaires.

Contents

Chapter 1

Kappa

1.1 Background and Scientific Motivations

Recently, new reconstructions of the Eurasian ice sheet extents of the last four major glacial maxima (Figure 1.1, Svendsen *et al.* (2004)) have been proposed by The Quaternary Environment of the Eurasian North project (QUEEN):

- the Late Saalian (180 - 140 ka)
- the Early Weichselian (100 - 80 ka)
- the Middle Weichselian (60 - 50 ka)
- the Late Weichselian (21 - 15 ka).

These extents have been determined by mapping marine and terrestrial glacial morphology. From these maps, it appears that the Late Saalian ice sheet (glacial maximum at ≈140 ka referred to as the Late Saalian over Eurasia[1]) was the largest Northern Eurasian ice sheet of the last four Quaternary glacial maxima. From various evidence (Ehlers *et al.*, 2004), it appears that this ice sheet started to grow before 160 ka (major ice advance), retreated slightly northward toward 150 ka, re-advanced at 140 ka (Late Saalian glacial maximum) and finally collapsed at Termination II (≈ 130 ka). Moreover, during the entire Weichselian glacial cycle, the ice volume has apparently been transferred Westward from an initial position centered over 70°N - 110°E at 90 ka toward a final position centered over Scandinavia during the Last Glacial Maximum (LGM, 21 ka). However, the dynamical processes of this "migration" are still poorly known and have not been discussed in depth in literature.

[1]This ice sheet existed during the Marine Isotope Stage 6 (MIS) glacial period, but, we will also henceforth use the term "Late Saalian" also when referring to the global environment at this time.

Most of the studies on glacial climate and ice dynamics focus on the LGM or the last Weichselian glacial/interglacial transition, probably because these are the best documented periods geologically (e.g., Calov *et al.*, 2005a,b; Bonelli *et al.*, 2009; Joussaume & Taylor, 1995; Braconnot *et al.*, 2007, http://pmip2.lsce.ipsl.fr). The Late Saalian period is "unusual" from many aspects compared to the LGM. Summer insolation over the Northern Hemisphere high latitudes and greenhouse gases (GHG) values were similar during both glacial maxima but the evolution of insolation and orbital configuration prior to the two glacial inceptions are different (Figure 1.2). When approaching ≈150 ka, summer insolation at 65°N rises about 50 W.m^{-2}. This is similar in magnitude to the insolation peak at the MIS 4/MIS 3 transition when the Eurasian ice sheet almost reached the same extent as during LGM (after ICE-5G Peltier, 2004). This raises the three main scientific questions that motivated this work:

- **How could the Late Saalian ice sheet grow so large over Eurasia and remain stable until ≈ 140 ka and how did it impact on climate at that time?**
- **Was the impact of the ice sheet on atmospheric processes similar to during other glaciations?**
- **How could the ice sheet survive the insolation peak occurring at ≈ 150 ka?**

This work concentrates on the exploration of the impact from the regional continental factors and global ocean surface conditions on the Late Saalian Eurasian ice sheet. In particular, my work focuses on the following:

1- the exploration of the impact of regional continental parameters: proglacial lakes, dust deposition

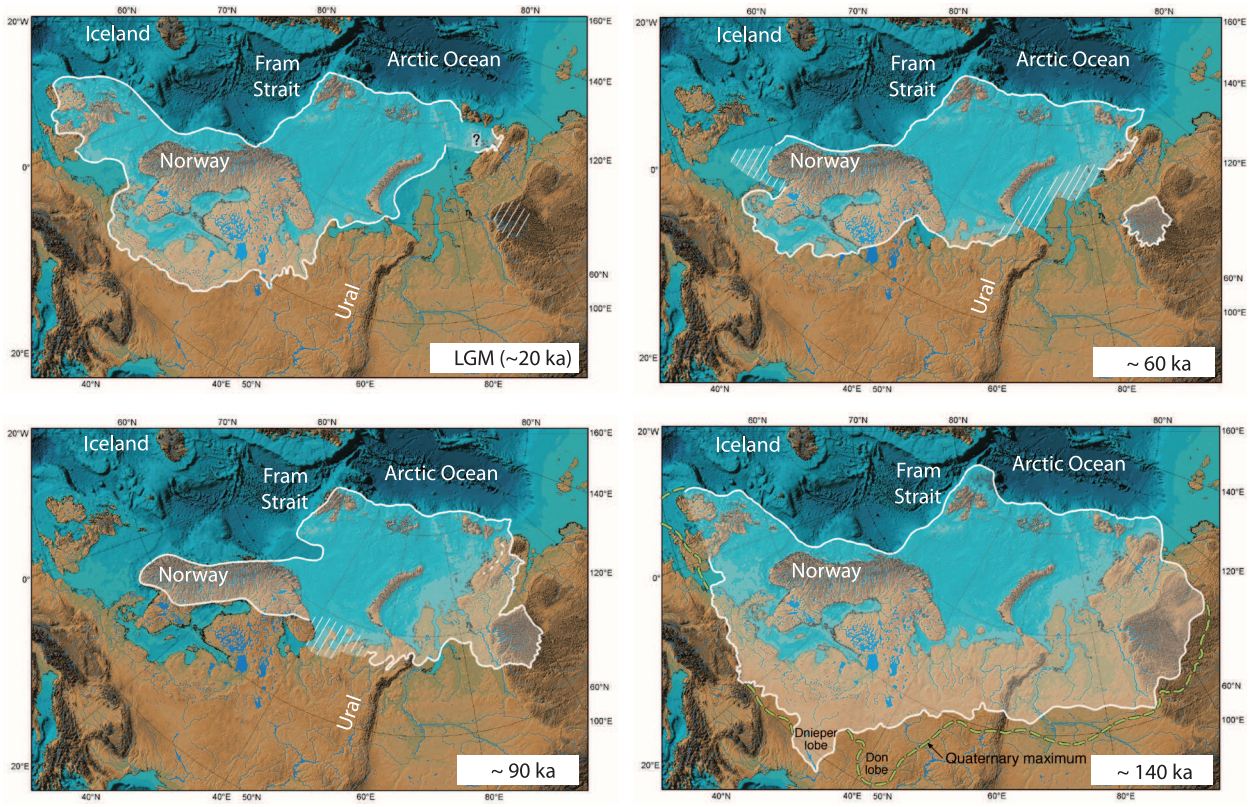

Figure 1.1: Eurasian ice sheet extents as reconstructed by the QUEEN project for the last four major glaciations. Modified from Svendsen *et al.* (2004)

2- the reconstruction of a vegetation cover in equilibrium with the Late Saalian climate

3- the simulation of Late Saalian Sea Surface Temperatures (SST) and the analysis of oceanic forcings and feedbacks

4- the impact of an Arctic Ocean ice shelf on the Northern Hemisphere climate

5- the simulation of the climate over the entire 160 - 140 ka period with a particular focus on the impact of the 150 ka Northern Hemisphere summer insolation peak on the Eurasian ice sheet

The entire work has been carried out using an Atmospheric General Circulation Model (AGCM), an AGCM mixed layer ocean model and a distributed vegetation model, to perform Late Saalian climate simulations of 21 or 31 years (Section 1.3). To allow a comparison with a well documented glaciation, most of the Late Saalian simulations presented in this thesis have also been performed for the Last Glacial Maximum (LGM).

In this introductory chapter, I first present a review of the current knowledge about the Late Saalian period (seldom discussed in literature) in term of geological evidence and orbital configuration. In this chapter, the Late Saalian is compared to the LGM, when relevant, which is generally considered as the reference glacial period. The numerical models used to simulate the Late Saalian and LGM are described with an emphasis on some particular physical features of interest in this work. Next, I present the boundary conditions used to reconstruct the Late Saalian glacial maximum. The peer-reviewed articles resulting from the study of the interactions between atmosphere, ice sheet, land and sea surface conditions feedbacks and forcings are briefly presented at the Kappa. Finally I discuss the boundary conditions used in various simulations carried out for this purpose and I conclude on the perspectives that this work opens.

1.2 The Late Eurasian Saalian period (160 ka - 130 ka)

What do we know about the Late Saalian time period?

The Saalian is the European glacial period

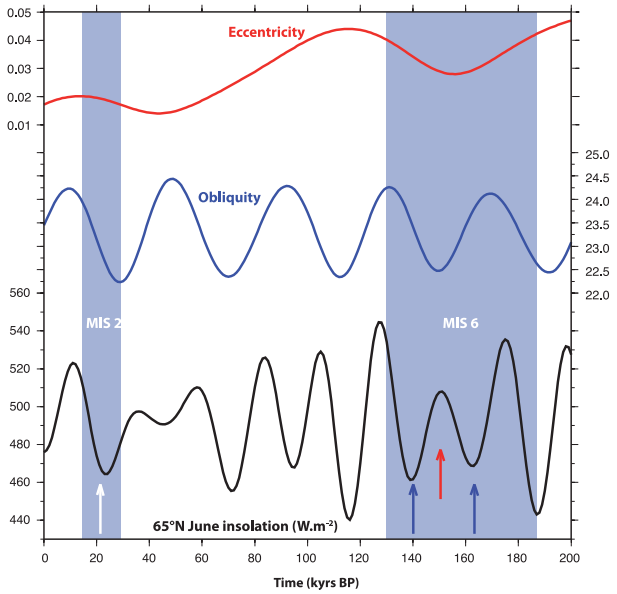

Figure 1.2: Eccentricity, obliquity and 65°N June insolation after Berger & Loutre (1991). The Last Glacial Maximum (≈21 ka), the peak Saalian (≈ 140 ka), the 150 ka insolation peak and the beginning of the Late Saalian (160 ka) are indicated by arrows (blue for stadials and red for interstadials). Orange colored fields show the entire Marine Isotope Stages 2 (MIS) and 6 respectively.

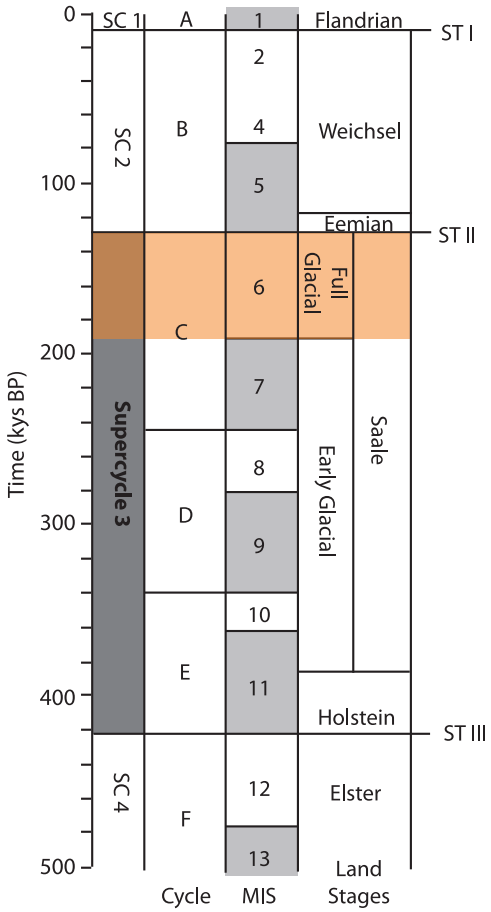

Figure 1.3: Late Quaternary glacial super-cycles after Kukla (2005). Abbreviations '*SC*' stands for *Super Cycle* and '*ST*' for *Super Termination*. Orange box indicates the Late Saalian period.

spanning ≈380 ka to ≈130 ka. It has been named after the German river "Saale", as the stratigraphical reference loess deposit for this glacial cycle is found in the vicinity of the river (Kukla & Lozek, 1961). Using the Marine Isotope Stages (MIS) from SPECMAP in combination with insolation values, Kukla (2005) divides the Late Quaternary to super-cycles (Figure 1.3). Super-cycle II consists in the entire Weichselian period (from ≈130 ka) and the onset of the Eemian interglacial while Super-cycle III is consists in by the Holsteinian and the Saalian periods taken together (≈420 ka and ≈380 ka respectively for their onsets). In this work we focus on the Late Saalian period which corresponds to the end of the "Full Glacial" phase of Super-cycle III (Figure 1.3) according to Kukla (2005) or to the end of MIS 6 (≈180 kyrs to ≈130 ka).

According to Svendsen *et al.* (2004), the ice sheet extent was substantially larger during the Late Saalian than during the LGM, especially along its southern and eastern margins in Siberia (Figure 1.1). Note that the Late Saalian ice sheet extent displayed on Figure 1.1 represents the maximum geographical extent and might not have been reached synchronously everywhere during the end of MIS 6. The green dotted line in the Late Saalian map shown on Figure 1.1 represents the maximum Quaternary extent. This implies that before the Late Saalian glacial maximum (140 ka), this Eurasian ice sheet might have extended further to south, but geological evidences of this potential larger extent are scarce and their dating still holds uncertainties at this stage.

How intense was the Late Saalian glacial period compared to the previous and following Late Quaternary glacial periods? Jouzel *et al.* (2007) estimated the temperatures based on the deuterium excess records from EPICA Dome C, East Antarctica over the last 800 ka (Figure 1.4). Masson-Delmotte *et al.* (submitted) calculated the relative intensity of each glacial and interglacial periods identified in the deuterium excess from EPICA Dome C ice cores. They use arious other proxies from EPICA Dome C were used for comparison, such as CO_2 and CH_4 atmospheric concentrations, aerosols (dust, Ca, Na) and past

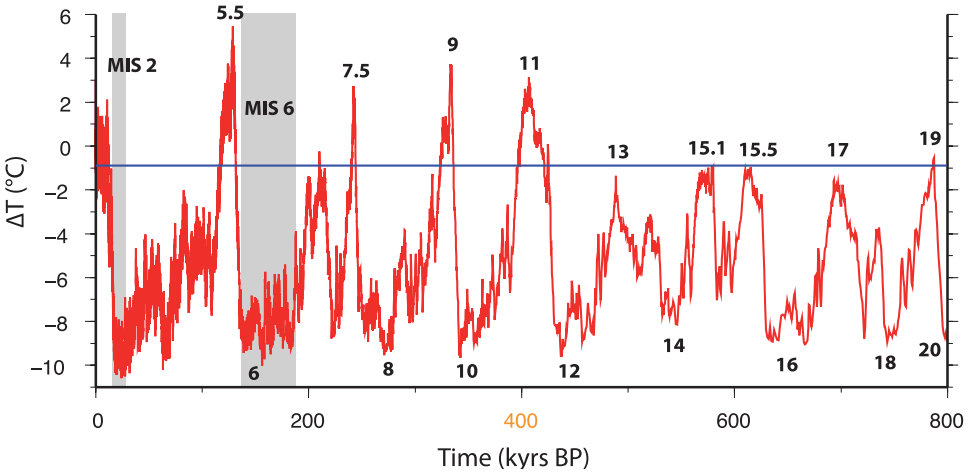

Figure 1.4: Temperature difference between the deuterium excess (δD) temperatures estimates and the average temperature of the last 1000 years (Jouzel *et al.*, 2007). Temperature are estimated from the EPICA Dome C deuterium excess from 800 ka, after correction for sea-water isotopic composition (Bintanja *et al.*, 2005) and for ice sheet elevation on EDC3 age scale (Parrenin *et al.*, 2007). Numbers indicate the various identified Marine Isotope Stages (even numbers stand for glacial periods while odd numbers correspond to interglacials). The blue line indicate the higher temperatures limit reached by the interglacials prior to 420 ka.

ice volume estimates (Bintanja *et al.*, 2005). The EPICA Dome C proxy records were centred and reduced to express their relative intensity using a specific index. From this, it appears that the two warmest interglacials are MIS 5.5 (130 ka) and MIS 11(424 ka) while the two coldest are MIS 13 (533 ka) and MIS 17 (712 ka) (Table 1a in Masson-Delmotte *et al.* (submitted)). Comparing the glacial periods reveals that the coldest periods are MIS 2 (29 ka), MIS 12 (478 ka) and MIS 16 (676 ka) while the two mildest are MIS 14 (563 ka) and MIS 6 (191 ka) (Table 1b in Masson-Delmotte *et al.* (submitted)).

The Late Saalian (MIS 6) is, according to Masson-Delmotte *et al.* (submitted), the second warmest glacial period during the last 800 ka and it precedes MIS 5.5, which likely was one of the warmest interglacials during the Quaternary period (Figure 1.4). In terms of ice volume, Bintanja *et al.* (2005) estimate that the Late Saalian only had the sixth largest global ice volume (LGM is seventh). This does not interact with the fact that the Late Saalian Eurasian ice sheet was the largest one. This only suggests that the ice distribution over the various continental ice sheets was different that at the LGM and that the Laurentide ice sheet might have been smaller than at the LGM.

1.2.1 The Late Saalian Northern Hemisphere topography

The Late Saalian is divided into three main substages: the Drenthe, Treene and Warthe (Ehlers *et al.*, 2004). The Drenthe (peak at $\approx$ 155 ka) and the Warthe (peak at $\approx$143 ka) correspond to phases of ice advance while the Treene substage is assigned to an ice retreat (occurring between the Drenthe and the Warthe substages). These ice advances have not been clearly associated with distinct moraines in Eurasia. However, the Drenthe ice sheet extent appears to be the largest of the entire Late Saalian period. In our experiments, the inferred Eurasian ice sheet does not correspond specifically to one of these three substages (Figure 1.1). Evidence of a substantial isostatic depression caused by the Late Saalian ice sheet has been found in Russia and Siberia (Astakhov, 2004). This isostatic imprint suggests that the Eurasian ice volume was larger during the Late Saalian compared to the ice volumes of the following Weichselian ice sheets. Due to the large isostatic depression, proglacial lakes probably formed southward of the ice sheet, similarly as during the Early Weichselian (Mangerud *et al.*, 2004). This is further discussed in Section 1.4.2.

The global eustatic sea level drop resulting from the Late Saalian (MIS 6) glaciation is still not constrained accurately, but seems to have been of the same order as during the LGM (Ra-

bineau *et al.*, 2006). This issue is further addressed in the Section 1.9. Consequently, the Arctic continental shelves were emerged and since these presently make up as much as ≈53% of the central Arctic Ocean area (Jakobsson, 2002), a sea level drop of 100-120 m below present level would remove more than half of the Arctic Ocean area. Furthermore, the Bering Strait was closed and the Barents Sea component of the ice sheet could have blocked the Atlantic water flux that today takes place between southern Svalbard and northern Norway (Figure 6.2).

In the Arctic Ocean, sedimentation rates and sediment composition show a dramatic change at the MIS 6/7 boundary (191 ka, e.g., Jakobsson *et al.*, 2001; Spielhagen *et al.*, 2004; O'Regan *et al.*, 2008). Prior to MIS 6, sedimentation exhibits low rates with a variability in phase with the 41 kyrs obliquity cycle while after the MIS 6/7 transition, sedimentation increases in the basin and the glacial periods are characterised by prominent coarse grain intervals (O'Regan *et al.*, 2008). There is also a change in sediment provenance. The cores covering MIS 6 from the Lomonosov Ridge in the central Arctic Ocean contains dominating components originating from the Kara and Laptev Sea area (Jakobsson *et al.*, 2001; Spielhagen *et al.*, 2004). These changes in sediment rate/composition/provenance were already discovered in earlier studies by Spielhagen *et al.* (1997), although an erroneous chronostratigraphy assigned the event in time to the MIS 16/17 boundary instead of the 6/7. The authors suggested that the observed change indicate the initiation of the first large northern Eurasian ice sheets reaching as far East as the easternmost parts of the Kara Sea.

Geophysical mapping of the central Arctic Ocean ridges and submarine extensions of the surrounding continental shelves revealed that areas generally shallower than 800-1000 m bellow the present sea level have been subjected to glacial erosion (Jakobsson, 1999; Jakobsson *et al.*, 2005, 2008a; Polyak *et al.*, 2001). The deepest and most severely glacially eroded seabed surfaces have been dated to MIS 6 (Jakobsson *et al.*, 2001, 2008b). The evidence converge toward a possible existence of an ice shelf developing in the Canada Basin and alimented by McClure Strait, Amundsen Gulf and Mackenzie ice streams coming from the Laurentide ice sheet (Polyak *et al.*, 2001; Jakobsson *et al.*, 2008b; Engels *et al.*, 2008).

The author is not aware of a complete reconstruction of the Late Illinoian Laurentide ice sheet which would be the North American equivalent to the Eurasian Late Saalian ice sheet. Since the LGM moraines in North America correspond to the most extensive identified glacial limits (Dyke *et al.*, 2002), most of the evidence of older Laurentide ice sheets has been destroyed. Consequently, we assume that the Late Illinoian ice sheet might have been close in size to the LGM or smaller. The climatic impact of a smaller Laurentide ice sheet topography is further discussed.

1.2.2 Orbital parameters and Greenhouse Gases (GHG)

Astronomical forcings at 140 ka

The principal orbital parameters are the eccentricity, determining the shape of the Earth's orbit around the Sun, the precession, modifying the length of the seasons in both hemispheres as well as the reference ellipse's position of the seasons, and the obliquity, that influences the seasonal contrasts in high latitudes.

These orbital parameters directly influence the distribution and quantity of insolation over the Northern Hemisphere high latitudes, which may in part regulate the glacial-interglacial cycles (Hays *et al.*, 1976). During a glacial period, the summer insolation is an important parameter since it determines the amount of ablation over the ice sheet (Huybers, 2006). The 65°N June insolation during the Late Saalian glacial maximum and the LGM were similar (Figure 1.2) but the extent of the Eurasian ice sheets were nevertheless substantially different during these two periods. Looking in detail at the individual values of each orbital parameter, there are however differences (Table 1.1). The Late Saalian eccentricity and obliquity are both larger than during LGM, which in fact will enhance the effect of the precession. During the Late Saalian, perihelion occurred December 6 while it occurred January 17 during LGM. Winter is consequently close to the Sun and summer is close to aphelion (Figure 1.5a). This implies that compared to the LGM:

- the effect of precession increases the contrast between the Northern and Southern

	160ka	150ka	140ka	40ka	30ka	21ka	Present-day
Eccentricity	0.028	0.029	0.033	0.014	0.017	0.019	0.017
Precession (°)	0.020	–0.028	0.031	0.000	–0.009	0.017	0.016
Obliquity (°)	23.43	22.48	23.42	23.60	22.25	22.95	23.45
Date of perihelion	Feb. 7	June 28	Dec. 6	March 31	June 18	Jan. 17	Jan. 4
CO_2 (ppm)	183	197	192	209	205	194	334
CH_4 (ppb)	383	426	401	537	481	354	1477

Table 1.1: Orbital parameters (Berger & Loutre, 1991), CO_2 (Petit *et al.*, 2001) and CH_4 (Spahni *et al.*, 2005) concentration value for the Late Saalian (160ka to 140ka), the end of MIS 3 (40ka to 30ka), the LGM (21ka) and present-day. The date of each corresponding perihelion is calculated setting the vernal equinoxe at March 21st.

Hemisphere temperatures (Raymo *et al.*, 2006) at 140 ka.

- the seasonal contrast will be more important at 140 ka due to the larger obliquity
- because summer occurs close to aphelion and spring occurs farther from the Sun than during the LGM, this will reduce the snow melting and enhances the Northern Hemisphere cooling.

These points constitute the major astronomical difference between those two glaciations.

Evolution of insolation during the end of the Late Saalian: 160 - 140 ka

According to the Milankovitch theory, the ice age cycles are generally thought to be ultimately driven by cyclical variations in the Earth's orbit (e.g., Hays *et al.*, 1976), although glacial inception per se results from a complex interaction between a suite of processes such as for example land-ice feedbacks, atmosphere-ice feedbacks, and ocean forcing (e.g. Kageyama *et al.*, 2004; Calov *et al.*, 2005a). The nature of glacial maxima also depends on the evolution of the insolation prior to the glacial maximum. Increasing obliquity causes an annual average redistribution of insolation poleward from 44°N or S from the equator, whereas precession causes insolation to change more uniformly with latitude. Raymo *et al.* (2006) show that simulated precession changes during a glaciation infer an asymmetry between the hemispheres. This antiphasing leads to a growth or decay of ice sheets out of phase between the Northern and Southern Hemisphere. The impact of precession is further considered in Paper 3 and in the Discussion of this thesis. The precession combined to changes in eccentricity also causes variations in the length of the seasons (Joussaume & Braconnot, 1997). This might an important impact especially during glacial periods, enhancing winters and shortening summers.

Before 140 ka, June insolation at high latitudes exhibits two major inflexions: a cold one, relatively to present-day June insolation, at 160 ka almost similar in amplitude to 140 ka and an insolation peak occurring around 150 ka (Figure 1.2). These variations in insolation are caused by the variations in orbital parameters.

- At 150 ka: contrary to 140 ka, perihelion occurs in early summer (June 28, Table 1.1) and consequently winter is close to aphelion (Figure 1.5b). Since summers occur when the Earth is close to the Sun, the amount of insolation at high latitudes increases by approximately 50 $W{\cdot}m^{-2}$ relatively to 140 ka (Figure 1.2). This may be the cause for the observed increase of $\approx$0.5° to 2°C in SST towards 150 ka (e.g. Calvo *et al.* (2001); Villanueva *et al.* (2002); Schaefer *et al.* (2005); Pelejero *et al.* (2006)). However, the summer duration is on the other hand shorter during 150 ka compared to 140 ka. This is the precession paradox: strong but short summers (Huybers, 2006).
- At 160 ka: the orbital configuration is similar to that of 140 ka. Perihelion occurs in late winter (February 7, Table 1.1). Obliquity is at an intermediate position in the 41 kyr cycle and is larger than at 150 ka. Compared to 140 ka, summer occurs at a shorter distance from the Sun which implies warmer summers at 160 ka.

From these three time-slices, 140 ka presents the most "glacial-friendly" orbital configuration

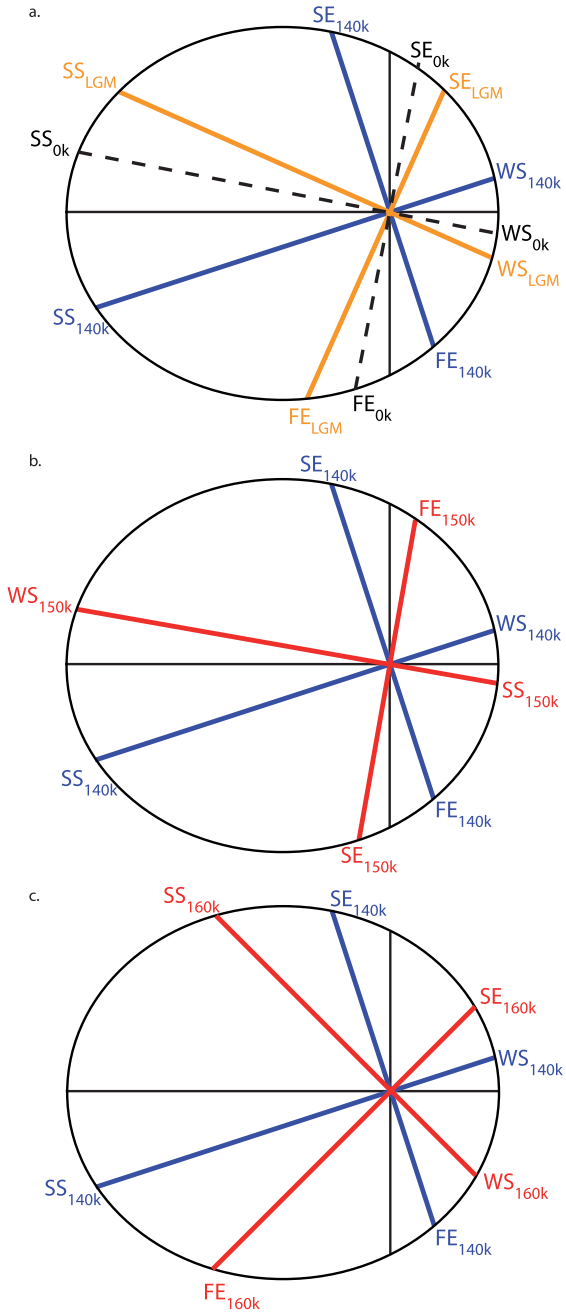

Figure 1.5: Positions of the seasons using ω values (angle from ascending node to perihelion) after Berger & Loutre (1991): ω_{0k} = 101°; ω_{21k} = 115°; ω_{140k} = 71°, ω_{150k} = –100°; ω_{160k} = 45°. a. Comparison between present-day, LGM and 140 ka; b. between 140 and 150 ka and c. between 140 and 160 ka. SE and FE stand for spring and fall equinoxes respectively while SS and WS correspond to summer and winter solstices.

in the Northern Hemisphere. This has implications for all the regional and global feedbacks further investigated in this work.

The evolution of insolation prior to the Late Saalian and the LGM appears to be significantly different: June 65° insolation is almost constant around 490 W·m^{-2} (Figure 1.2). However, Greenland ice-core analysis shows that the apparently stable climate of continental Oxygen Isotope Stage 3 (OIS) suggested by the marine oxygen isotope SPECMAP record is misleading (Meese *et al.*, 1997). High-frequency series of climate oscillations on the scale of several millennia (Dansgaard-Oeschger, DO here after Dansgaard *et al.*, 1993), not associated with fluctuations in insolation forcing, occurred during this period, and the transitions between them sometimes took less than a few decades (Wohlfarth *et al.*, 2008). The same DO events have been identified in North Atlantic Ocean cores (Bond *et al.*, 1993).

Greenhouse gas

Greenhouse gas (GHG) past atmospheric concentration can be estimated from ice cores. Various ice drilling projects have been carried out both in Antarctica and Greenland such as Vostok (Petit *et al.*, 1997, 1999), EPICA Dome C (Lorius *et al.*, 1979; Augustin *et al.*, 2004) to extract the GHG signal from ice cores and reconstruct their time evolution over the Quaternary and their link with climate changes. The debate to understand if atmospheric CO_2 acted as a forcing of the continental ice volume, implying lags of about 5000 years between the ice volume response and CO_2 forcing, or as a feedback, implying an immediate response of ice volume to CO_2, on the ice sheet surface mass balance is still open (Ruddiman, 2006). Several studies show that greenhouse gas (GHG) might be important amplifiers of the initial orbital forcing and significantly contribute to the glacial/interglacial changes (Figure 1.6 e.g. Genthon *et al.*, 1987; Raynaud *et al.*, 1993). In our work we use the concentration values from Antarctica since Greenland ice cores do not provide records old enough to reach our period of interest. During the Late Saalian, CO_2 concentration from Vostok and EPICA Dome C dropped to 192 ppm, which is similar to the LGM concentration, and CH_4 dropped to 401 ppb, which is 50 ppb higher than during the LGM (Table 1.1).

The highest estimated CH_4 concentration in the Northern Hemisphere occurs during the LGM and in the high latitudes between about 65° to 70°N because at that time, most of the Siberian plains were not glaciated (Krinner *et al.*, 2006) and accumulated 400,000 Tg of organic carbon (Zimov *et al.*, 1997). However,

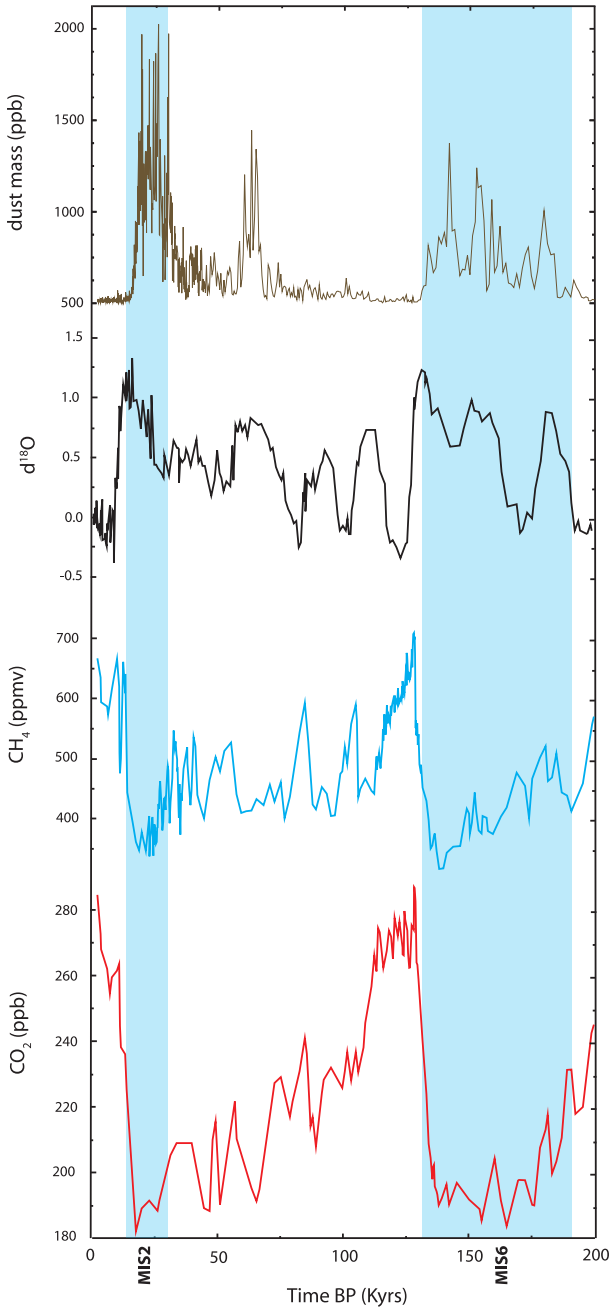

Figure 1.6: Late Quaternary greenhouse gas (GHG) values, benthic δ^{18}O and Antarctic atmospheric dust concentration. CO_2 concentration is from Vostok (Petit *et al.*, 2001), CH_4 concentration from Dome C (Spahni *et al.*, 2005), benthic δ^{18}O from (Imbrie & Duffy, 1993) and dust concentration from Dome C (Delmonte & EPICA community members, 2004).

the available space for carbon uptake within the Siberian soil also depends on the Eastern extent of the ice sheets during the glaciations. During the Late Saalian, the Eurasian ice sheet area was 56% bigger than its LGM ICE-5G counterpart (Peltier, 2004). The main difference resides in Eastern Siberia between 60° and 80°N which corresponds to the region of highest carbon uptakes and CH_4 emissions. The impact of the ice sheet extent might have contributed to the observed difference between the Late Saalian and LGM CH_4 values (Table 1.1).

1.3 Numerical models

1.3.1 LMDZ4: the atmospheric general circulation model

The LMDZ4 (Hourdin *et al.*, 2006) general circulation model is developed at the Laboratoire de Météorologie Dynamique (Paris) and is the finite-difference atmospheric component of the IPSL-CM4 coupled model. The dynamical equations are discretised on the sphere in a staggered and longitude-latitude Arakawa C-grid (e.g., Kasahara, 1977). For all our experiments, the model has been run with 96×72 grid cells horizontally and with 19 vertical layers. The horizontal resolution is irregular, varying from the highest resolution of 100 km grid cells centered over Eurasia at 65°N/60°E to 550 km outside of the zoom. However, in our Arctic experiments including a Canadian ice shelf, the horizontal resolution reaches 60 km. The impact of using a stretchable grid on climate has been discussed in Krinner & Genthon (1997) who show that in the presence of strong topographic gradients, such as on the margin of the Late Saalian ice sheet, the impact of higher spatial resolution is clearly beneficial. The LMDZ4 takes into account the climatic impact of open water surfaces and dust concentration in snow (Krinner, 2003; Krinner *et al.*, 2006) as detailed below.

Snow dust content: Krinner *et al.* (2006)

The calculation of the snow dust content is based on a two-layer snow pack model in which the maximum surface layer thickness $h_{s,max}$ is set to 8 mm (Figure 1.7). The total thickness is defined as $h = h_s + h_b$ where h_b represents the thickness of the bottom layer. The evolution of the snow pack is defined as:

- if $h < h_{s,max}$, $\Rightarrow h_b = 0$ and $h = h_s$
- if $h > h_{s,max}$, $\Rightarrow h_s = h_{s,max}$ and $h_b = h - h_s$

Dust is distributed both in the bottom and surface layers of the snow pack. The evolution of the dust content of the snow in the surface layer

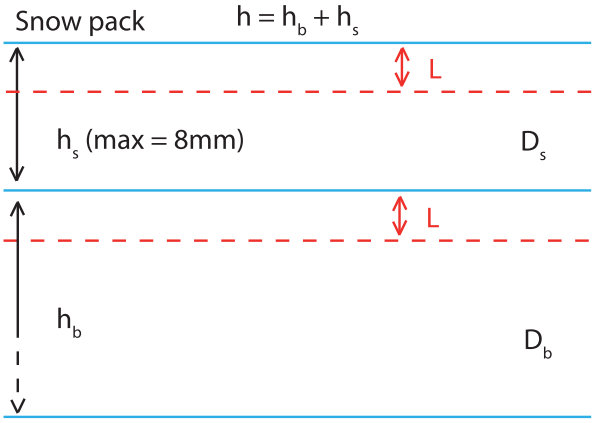

Figure 1.7: Two-layer snow pack model as implemented in LMDZ4. The surface layer h_s thickness is set at 8 mm. The bottom layer is represented by h_b while h stands for the total snow pack thickness. The dust content of the snow is distributed between the two layers: D_s for the surface layer and D_b for the bottom layer. L is the reduction in the surface layer thickness when subjected to melting or sublimation. When ablation occurs, the surface layer is automatically reset to 8 mm, reducing the bottom thickness of L. The dust content is then adjusted accounting for that coming from the bottom layer that has been readjusted (Equation 1.2).

D_s is described by:

$$\frac{dD_s}{dt} = \frac{C}{\rho h_s} \tag{1.1}$$

where C (kg.m^{-2}.day^{-1}) is a constant dust deposition rate (e.g., Mahowald *et al.*, 1999) and ρ stands for the density of snow (330 kg.m^{-3}). When melting occurs, D_s is calculated according to the readjustment of the surface layer thickness of the snow pack and of the dust content of the bottom layer D_b:

$$D_s = \frac{D'_s h'_s + min(L, h'_b) D'_b}{h_s} \tag{1.2}$$

where primes stands for the previous timestep and L represents the reduction of the snow height.

The albedo of snow is calculated accounting for the underlying albedo, the snow grain size and the dust content and averaged in the visible and near-infrared spectra.

Water surface effects: Krinner (2003)

The lake model follows that of Henderson-Sellers (1986). The model explicitly represents the penetration of sunlight into the lake and its gradual absorption; vertical eddy heat conduction as a function of friction, depth, and thermal stability; convective overturning based on vertical density gradients; water phase changes; snow accumulation on ice (the lake surface can freeze) and melt; sensible and latent turbulent surface heat fluxes; and water balance terms. In total, the lake model (comprising the underlying soil, and eventually lake ice and snow) has either $2n_l$, $3n_l$, or $4n_l$ layers, depending on whether the lake is frozen and whether snow lies on the ice.

The lake water column has a prescribed number of vertical levels (here, $n_l = 8$); below the lake, n_l layers of soil with a total thickness of 5 m insure energy conservation through total absorption of the remaining sunlight at the lake bottom and a zero flux condition at the lowermost soil layer. When the lake is frozen, n_l layers of ice are used (the same is done with snow accumulated on ice). Vertical discretization in lake and soil below lakes is calculated as a geometric series such that levels are thin at the surface and become thicker at the bottom.

Lakes lose water by two ways: evaporation and outflow. Evaporation is calculated in the AGCM surface scheme using Monin-Obukhov similarity theory. Outflow occurs with a prescribed time constant τ_{out} = 5d when the lake depth h exceeds a prescribed critical level h_c:

$$\frac{\partial h}{\partial t} = -\frac{max(h - h_c, 0)}{\tau_{out}} \tag{1.3}$$

In stand-alone simulations, h_c is set to 5 meters above the observed depth h when the real lake depth is known. Otherwise, and in AGCM simulations, initial lake depth h_i is set to 50 m and $h_c = h_i + 5$ m. Outflow from lakes is directly lost to the oceans. Tests have shown that the exact value of the timescale τ_{out} of lake outflow has very little impact on the results, as long as τ_{out} is sufficiently small to prevent lake depth from exceeding significantly the prescribed critical value h_c.

Albedo of open water is calculated as a function of solar angle. Lake albedo increases up to the prescribed background value for continental surfaces when the lake becomes shallow. When the lake is ice-covered, surface albedo is calculated like that of sea ice in the polar version of LMDZ (Krinner & Genthon, 1997).

Surface mass balance parameterizations

My entire work focuses on the Eurasian ice sheet sensitivity to regional feedbacks. This sensitivity is estimated through the calculation of the surface mass balance (SMB). Two methods have been used: the parametrization of Krinner *et al.* (2007) following Thompson & Pollard (1997) and the temperature-index method of Ohmura *et al.* (1996).

The first parametrization, first developed by Thompson & Pollard (1997), takes into account the refreezing of a part (f) of rainfall and meltwater (ranging in the interval [0;1]):

$$f = 1 - \min\left(1, \max\left(0, \frac{(\frac{M}{P_S} - 0.7)}{0.3}\right)\right) \quad (1.4)$$

where P_S is the mean annual solid precipitation, and M is the annual snow or ice melt calculated from the surface energy balance in the AGCM.

The runoff is calculated as :

$$R = (1 - f)(M + P_L) \quad (1.5)$$

where P_L is the annual liquid precipitation (rainfall). Finally the surface mass balance B is calculated as:

$$B = P_S + fP_L - E - (1 - f)M \quad (1.6)$$

with E as the annual sublimation.

The second method uses the temperature index method as proposed by Ohmura *et al.* (1996). In this method, surface ablation occurs when the mean summer surface air temperature (T_{JJA}), recalculated on a fine resolution grid with altitude-correction, exceeds a prescribed threshold of -1.8°C. The total ablation A (kg.m^{-2}.yr^{-1}) is then calculated as:

$$A = 514 \times T_{JJA} + 930 \quad (1.7)$$

where T_{JJA} is in °C. We downscale the AGCM surface air temperature on a 20-km grid by applying a 5.5°C.km^{-1} summer temperature correction to account for altitude changes (Krinner & Genthon, 1999; Abe-Ouchi *et al.*, 2007). The surface mass balance B is then calculated as:

$$B = P_S - E - A \quad (1.8)$$

with P_S and E as before.

As shown in Paper 1, the second method better captures the ablation process along the margins due to the downscaling of the prescribed climatology which increases the resolution. This leads to significantly different mean annual surface mass balance estimates. The ablation generated by the investigated feedback dominates the mean annual SMB.

Figure 1.8: Scheme of the simulations carried out using Planet Simulator (Fraedrich *et al.*, 2005) to compute Late Saalian SST and using LMDZ4 (Hourdin *et al.*, 2006) to obtain a final Late Saalian climate.

1.3.2 Planet Simulator: the AGCM mixed-layer ocean model

To simulate the Late Saalian surface ocean conditions, we use the Planet Simulator (PLASIM) general circulation model of intermediate complexity (Fraedrich *et al.*, 2005). The central part of PLASIM consists in an AGCM, which is based on the moist primitive equations representing conservation of momentum, mass and energy. The equations are solved on a Gaussian grid in the horizontal direction, corresponding to a T42 resolution (128×64), and on 10 vertical sigma levels.

Contrary to LMDZ4, PLASIM does not account for the effects of proglacial lakes and dust deposition on snow. It also includes a simplified pa-

rameterization for radiation, surface fluxes and clouds physics but its cores is a competent and comprehensive AGCM (Romanova *et al.*, 2005). The AGCM is interactively coupled to a mixed-layer ocean, in which the mixed-layer depth is set to 50 m, and to a zero-dimensional thermodynamic sea ice model. In this model, the oceanic heat transport is prescribed for every month and is parametrized according to:

$$Q_{c_2} = \rho_w c_w h_{mix} \frac{T_{mix_c} - T_{mix}}{\tau_T} \qquad (1.9)$$

where c_w is the specific heat capacity of sea water, ρ_w corresponds to the density of sea-water, h_{mix} stands for the mixed-layer depth, T_{mix} is the temperature of the mixed layer and τ_T represents the time scale at which T_{mix} is relaxed to its climatological value $T_{mix,c}$ ($\tau_T = 50$ days).

In the case of the Late Saalian, we do not dispose of any SST reconstruction for this period. We thus needed to initialise the simulation with glacial analogue SST. We chose to base the calculation on Paul & Schaefer-Neth (2003) LGM SST because this reconstruction is in closer agreement with the temperatures estimated from analysis of marine sediment cores than the LGM CLIMAP reconstruction (CLIMAP, 1981).

To calculate the monthly LGM oceanic heat fluxes and the flux correction for the sea ice, we first performed a LGM control simulation of 21 years forcing PLASIM with Paul & Schaefer-Neth (2003) LGM sea surface conditions (the first model year is discarded as spin-up). Finally to compute the Late Saalian surface oceanic conditions, PLASIM in then forced using the calculated monthly LGM ocean heat fluxes corrections but with all boundary conditions appropriate for the Late Saalian. The simulation is performed for 50 model years, sea surface equilibrium is reached after 25 model years and the last 15 years are used for analysis. The scheme of the experiments is detailed in Figure 1.8.

Since the LGM and the Late Saalian both correspond to glacial periods, it is relevant, in the absence of any Late Saalian sea surface reconstructions, to initiate the simulations using the LGM ocean heat fluxes as first approximation to equilibrate the mixed-layer with the Late Saalian climate. This method to calculate sea surface temperatures (SST) has been previously used by Romanova *et al.* (2005, 2006) to investigate the effect of ocean heat fluxes on glacial climates.

ID	Biomes
1	Tropical evergreen forest
2	Tropical semi-deciduous forest
3	Tropical deciduous forest/woodland
4	Temperate deciduous forest
5	Temperate conifer forest
6	Warm mixed forest
7	Cool mixed forest
8	Cool conifer forest
9	Cold mixed forest
10	Evegreen taiga/montane forest
11	Deciduous taiga/montane forest
12	Tropical savanna
13	Tropical xerophytic shrubland
14	Temperate xerophytic shrubland
15	Temperate sclerophyll woodland
16	Temperate broadleaved savanna
17	Open conifer woodland
18	Boreal parkland
19	Tropical grassland
20	Temperate grassland
21	Desert
22	Steppe tundra
23	Shrub tundra
24	Dwarf shrub tundra
25	Prostrate shrub tundra
27	Barren

Table 1.2: Biomes calculated by the BIOME 4 model based on the competition between the twelve defined PFTs. Gray shaded cells indicates the three high-latitude tundra biomes introduced in BIOME4 by Kaplan *et al.* (2003).

1.3.3 BIOME4: the vegetation model

BIOME4 (Kaplan *et al.*, 2003) was developed from the BIOME3 model of Haxeltine & Prentice (1996). BIOME4 is a 1-D coupled carbon and water flux model that predicts global steady state vegetation distribution, structure, and biogeochemistry. The model is driven by long-term averages of monthly mean temperatures, daily minimum temperatures, sunshine and precipitation. CO_2 concentration has to be prescribed.

BIOME4 is based on twelve plant functional types (PFTs) ranging from cushion forbs to tropical rain forest trees (Kaplan, 2001). Each PFT is assigned a small number of bioclimatic limits which determine whether it could be present in a given grid cell. The computational core of BIOME4 is a coupled carbon and water flux scheme, which determines the seasonal maximum leaf area index that maximizes the net pri-

mary production for any given PFT. To identify the biome for a given grid cell, the model ranks the tree and non-tree PFTs that were calculated for that grid cell. The resulting ranked combinations of PFTs lead to 27 different biomes (Table 1.2).

High-latitude biomes are represented by combinations of frost-tolerant PFTs. Three PFTs (cold shrub, cold graminoid or forb, and cushion forb) used to distinguish the tundra biomes have been newly defined for BIOME4. These three new tundra PFTs are shallow rooted, and are sensitive to water stress and fire. The non-tundra PFTs used by BIOME4 to simulate high-latitude vegetation types include cold and temperate broadleaved and needlers trees, xerophytic shrubs, and temperate grasses.

1.3.4 GRISLI: the ice sheet and ice shelf model

In this work, I have not really used the GRISLI ice model although, during this PhD, I have implemented a module accounting for the monthly climatology instead of mean annual climatology as usually prescribed in ice sheet models to improve the ablation calculation using the positive degree day method.

However, this thesis is based on the Late Saalian Eurasian ice sheet that has been built using GRISLI by Peyaud (2006). Consequently, I dedicate this section to the description of the main features of this ice sheet model.

GRISLI is a 3-D thermodynamical ice model that simulates the dynamics of grounded ice as well as ice shelves and ice stream regions. Inland ice deforms according to the stress balance using the shallow ice approximation (Morland, 1984; Hutter, 1983). Ice shelves and dragging ice shelves (ice streams) are described following MacAyeal (2001). This model has been developed and validated over Antarctica by Ritz *et al.* (2001) in which a comprehensive description of the model is provided. Here we list some of the recent improvements presented in Peyaud (2006) and Peyaud *et al.* (2007):

1. The thermo-mechanical coupling is extended to the ice shelves and ice streams. Ice viscosity depending on the temperature field is integrated over the thickness.

2. The basal drag τ_b under ice streams is related to ice velocity ($\tau_b = \beta$U, where U is the horizontal velocity). The factor β depends on the effective pressure N: $\beta = -cf \times N$, where cf is a constant term.

3. Basal water drainage is computed using a Darcian flow into a sediment layer. The thickness of the sediment layer is set to the ad-hoc value of 50 m. This description is too simplistic to account for the real basal processes but constitutes a siple representation of the drainage patterns.

4. Location of the ice streams is determined by the basal water head. Ice stream regions correspond to areas where the sediment layer is water saturated.

5. Ice shelf front positions are determined with a scheme in which two criteria must be fulfilled. To calv the ice from the front grid point, first, the ice thickness must decrease below 150 m. This corresponds to a general value in line with what has been observed for several of the Antarctic ice shelves. Secondly for each grid point at the front, the ice coming from the upstream points must fail to maintain a thickness above the threshold. This ability to maintain a sufficient thickness is estimated on the basis of a semi-Lagrangian scheme. Ice shelf front position changes at each timestep, and appropriate boundary conditions, adapted from Rommelaere & Ritz (1996) and Ritz *et al.* (2001), are applied for the different front configurations. Atmospheric conditions have an implicit control on ice shelves. Indeed the surface mass balance prevents the ice shelves to form in warm regions (Mercer, 1978). Simulations of West Antarctic ice shelves give front positions in agreement with observations.

To reconstruct the climate at the surface of the ice sheet, the AGCM air temperature and precipitation (ice equivalent) are adapted following Charbit *et al.* (2002). Temperature is corrected for altitude changes iteratively calculated by the ice sheet model. Vertical temperature gradients are based on classical values ranging from 5°C.km^{-1} to 8°C.km^{-1} (Krinner & Genthon, 1999; Abe-Ouchi *et al.*, 2007). Accumulation is the solid fraction of the total precipitation and ablation is calculated according to a positive degree day (PDD) method (Reeh, 1991). The precipitation P_0 (in ice equivalent) at the surface of reference is assumed to depend on the

annual temperature T with an exponential law reflecting the saturation water pressure (Charbit *et al.*, 2002):

$$P_0 = P \times e^{[0.05\times(T_0-T)]} \quad (1.10)$$

This parametrization is corrected from altitude variations. A fraction of the melting is likely to refreeze. As in the AGCM (Krinner *et al.*, 2007) this fraction increases as the amount of melting compared to snow fall decreases (Section 1.3.1).

1.4 Boundary conditions

1.4.1 On the global ice volume

Global sea level variations result from geoid[2] and solid Earth crustal height variations (Figure 1.9). Sea-level changes over long time scales are generally caused by the modification of the shape and/or the depth of the ocean floor as well as changes of the ice volume stored on the continents in the form of ice sheets and glaciers. These variations are called tectono-eustatism and glacio-eustatism respectively.

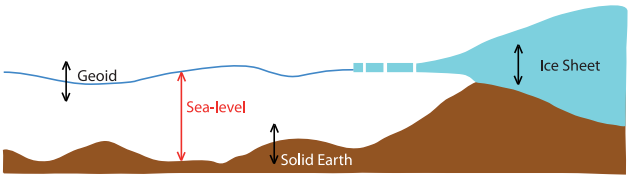

Figure 1.9: Sea-level variations according to the geoid, the solid Earth and the ice thickness variations.

During the glaciations, the growth and decay of the ice sheets over the continents affect the solid Earth. The ice load creates large deflections, affecting both the lithosphere and the mantle, that relax during and after the ice melting until reaching the isostatic equilibrium. The isostatic depression from the ice load or the following post-glacial rebound may have a direct impact on the near-field areas, i.e. areas located near or underneath the ice sheets, and consequently it may have an impact on the regional sea level in case these areas interact with the ocean. On the contrary, far-field areas, i.e. areas not directly affected by the glacio-isostatism, are assumed to only record the eustatic sea level.

[2]equipotential surface, commonly defined as the ocean surface

Eustatic sea level estimates

For the LGM, far-field areas are determined using post-glacial rebound modelling and the eustatic sea level is determined in such areas using coral measurements. Sub-surface corals represent good indicators of sea level since their growth is sensitive to water depth, and thus, to fluctuations of the surface of the ocean. But since they are attached to the continent, sea level estimates have to be corrected for local tectonics in order to extract the pure eustatic sea level (Milne & Mitrovica, 2008). In their study, Milne & Mitrovica (2008) show that Barbados, Sunda, the Bonaparte Gulf , which are usually considered as reference far-field sites [3], hold an uncertainty on the eustatic sea level estimates of ≈10 m (Figure 1.10). They suggest that sites such as Seychelles (Indian Ocean) can provide improved estimates of past eustatic sea level since they are only slightly affected by glacio-isostatic adjustment. (Figure 1.10). Other sites such as Bengazi (Mediterranean) provide well constrained glacio-isostatic adjustment signal for which, RSL can be easily corrected for to extract the eustatic sea-level.

For previous glacial periods, RSL coming from the sites described above time series are not available and a linear relationship between the δ^{18}O record derived from measurements on benthic foraminifera has been used at it is assumed to record the global continental ice volume (Shackleton, 1987; Bintanja *et al.*, 2005). Elaborate relationships using benthic foraminifera are also used as first approximation, but hold lots of uncertainties (Waelbroeck *et al.*, 2002) (Figure 1.11). Direct geological evidence of sea level positions through time, e.g. marine notches, terraces, archaeological data, beach rocks, peats or coral reef, can be collected on continental margins to calibrate the curves of local RSL. However, their spatial and temporal resolution is most often low. Indeed, sea level records from continental margins are subjected to the Earth local subsidence or uplift. Therefore, derived RSL records need to be corrected for the effects of tectonic sediment loading and compaction, glacio- and/or hydro-isostasy and gravitational potential, in order to obtain data effectively in-

[3]they provide accurate U/Th dated coral Relative Sea Level (RSL) records easily corrected from local tectonic contribution and then converted into eustatic sea level (Fairbanks, 1989; Peltier, 2002; Fairbanks *et al.*, 2005; Peltier & Fairbanks, 2006)

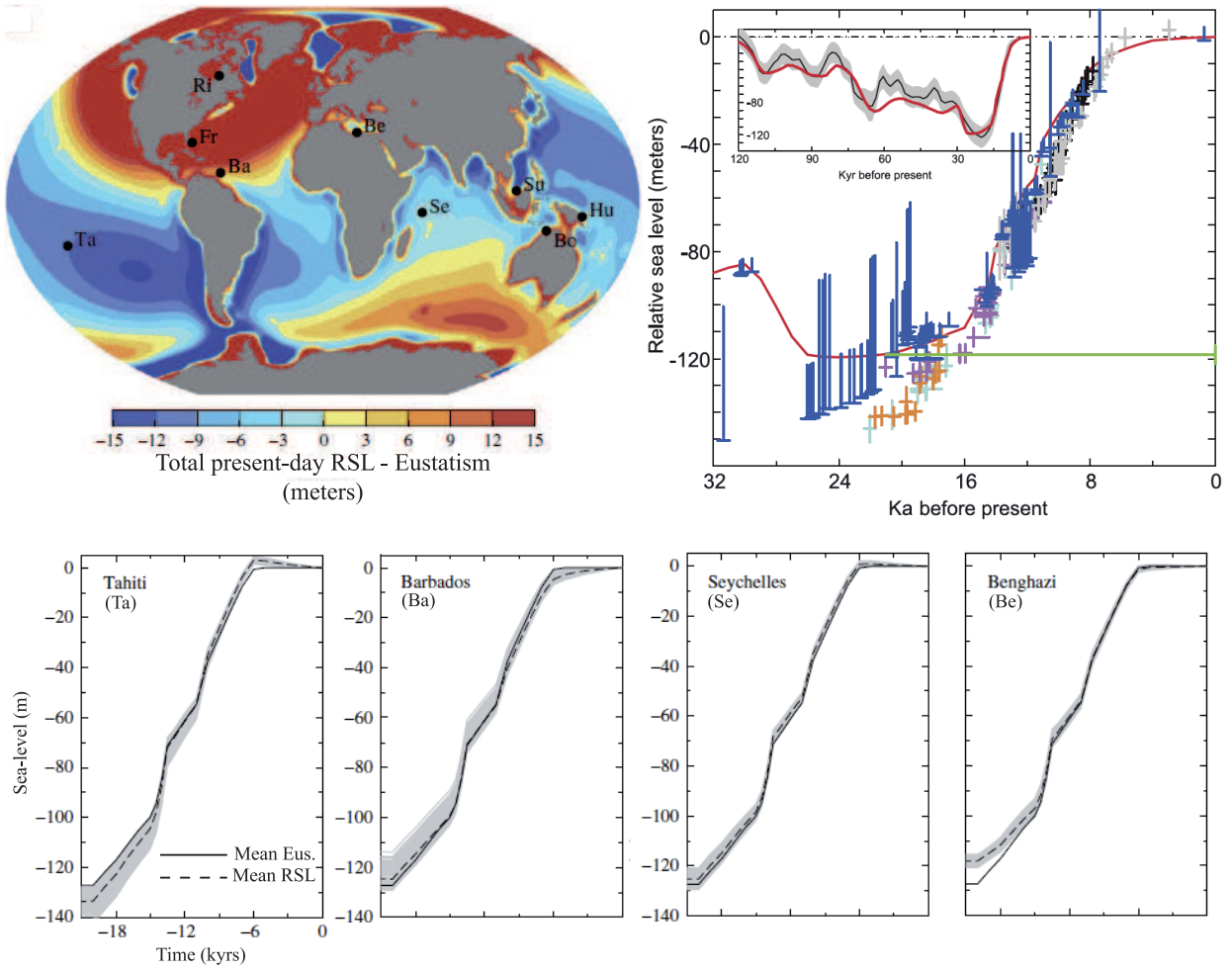

Figure 1.10: Left: Difference between present-day sea level variations and eustatic sea level due to glacial-isostatic adjustment predicted by Milne & Mitrovica (2008), using the Bassett *et al.* (2005) ice thickness scenario from LGM to present-day derived from ICE-3G (Tushingham & Peltier, 1991). Black dots indicates various location such as the Barbados (Ba), the Sunda Shelf (Su), the Bonaparte Gulf (Bo), Huon Peninsula (Hu), Freeport (Fr), Richmond Gulf (Ri), Seychelles Islands (Se), Begazi (Be) referred as reference sites for eustatic sea level estimates. Right: Figure from Peltier & Fairbanks (2006). Eustatic sea level history estimate provided by the coral-derived record from the last Barbados measurements (blue symbols from Peltier & Fairbanks (2006)), compared to measurements from Lambeck & Chappell (2001) from the Bonaparte Gulf (orange), Huon Peninsula (black), Tahiti (gray) and the Sunda Shelf (purple). The red line corresponds to the eustatic sea level predicted using the ICE-5G(VM2) model tuned for the Barbados. Inset compares the eustatic reconstruction by Waelbroeck *et al.* (2002) based upon calibrated deep sea core derived oxygen isotopic measurements to the ICE-5G (VM2) rebound prediction (red curve). Bottom: Mean RSL (dashed) and eustatic (Eus., solid) estimates from Milne & Mitrovica (2008) for the Tahiti, Barbados Seychelles and Begazi sites, using 162 Earth viscosity and lithospheric models (gray lines) and accounting for Bassett *et al.* (2005) ice model.

terpreted as eustatic sea level (Rabineau *et al.*, 2006).

The maximum eustatic sea level drop estimated for the Late Saalian glacial maximum ranges from about 92 m (Rabineau *et al.*, 2006) to 150 m below present sea level (Waelbroeck *et al.*, 2002). The estimate by Rabineau *et al.* (2006) based on measurements carried out in the Gulf of Lyon, should probably be considered on the smaller end for the Late Saalian period as their value derived from the same site for the LGM is too small due to a biased correction of the isostatic contribution. The Gulf of Lyon is located in the vicinity of the Alps that hosted large glaciers during glacial periods. Spada *et al.* (2009) have shown that the Alps have a significant influence on Mediterranean sea level records from the LGM until today. I have not find any additional data that shed new lights on the maximum estimate of -150 m by Waelbroeck

et al. (2002). However, the Late Saalian RSL was recorded to range between 90 m to more than 150 m below present level in Eurasia (see Lambeck *et al.* (2006) for the review of available RSL data). These values are however not corrected for the isostatic component and do not represent eustatic values. Therefore in all our Late Saalian experiments we set the sea level to -110 m (Astakhov, 2004) and to -130 m (Peltier, 2004) for our LGM simulations.

From sea level to ice volume

From the previous section, it is evident that global estimates of the Late Quaternary sea level fluctuations are still far from well constrained. One could argue that all the LGM (MIS 2) values converge towards -130 m $\pm$10 m and that Late Saalian (MIS 6) oxygen isotopes fluctuations exhibit similar values to that of LGM. But the problem is more complex because the global equivalent sea level ice volume has to be spatially distributed between the individual ice sheets that developed during the various ice ages. If we consider that each eustatic value derived from corals or oxygen isotopes hold an error of about 10%, the maximum estimate for the Late Saalian has an uncertainty of 15m while the minimum has 9 m. Assuming this uncertainty, it is evident that the uncertainty amounts to at least half of the equivalent sea level (ESL) volume attributed to the Eurasian ice sheet in ICE-5G during the LGM ($\approx$17 m).

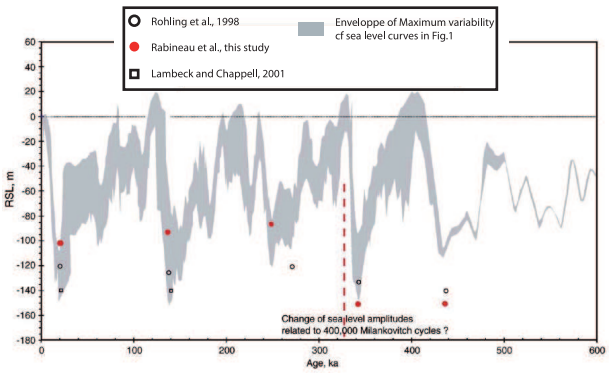

Figure 1.11: Figure from Rabineau *et al.* (2006). Relative sea level curve envelope including the minimum and maximum RSL estimates for the last 600 ka.

ESL values attributed to the various ice sheets have changed substantially since the first ice model ICE-1 of Andrews (1976). In the model version ICE-5G (Peltier, 2004), the ESL attributed to the volume of the Laurentide ice sheet has increased by 20 m compared to the previous versions, the Eurasian ice sheet volume has decreased by 7 m ESL and that of Antarctica has decreased by 10 m (Table 1.3). The ESL contribution of the latter seems still to be overestimated and recently Ivins & James (2005) proposed new estimates for the Antarctic ice sheet's volume variations since LGM, based on a synthesis of the current constraints on past ice history and present-day mass balance, which suggest an ESL contribution well below what have been suggested by other publicly available ice models (Table 1.3).

ESL (m)	**Tot.**	**L**	**E**	**A**	**G**	**O**
ICE-1	77	58	16	/	3	/
ICE-3G	115	55	24	26	6	4
ICE-4G	104	59	21	17	6	1
ICE-5G	126	74	17	17	2	2
ANU05	134	86	16	28	3	1
IJ05	/	/	/	8	/	/

Table 1.3: Equivalent eustatic sea levels (m, ESL) corresponding to the contribution of the various ice sheets since the LGM (21 ka) according to ICE1 (Andrews, 1976), ICE-3G (Tushingham & Peltier, 1991), ICE-4G (Peltier, 1994), ICE-5G (Peltier, 2004), ANU05 (Lambeck *et al.*, 2003) and IJ05 (Ivins & James, 2005) ice models. L corresponds to the Laurentide ice sheet, E to the Eurasian ice sheet, A to Antarctica. O stands for the remaining small ice caps over Pantagonia, New-Zealand and the Island. Calculation have been performed using SELEN (Spada & Stocchi, 2007) at harmonics degree L=72 and using a pixel resolution R=18 (4718 pixels over the entire Earth).

Distributing ice volume between the various ice sheets is not easy. Two approaches are classically used: the first one consists of using a glacio-isostatic adjustment model in which initial ice ESL is prescribed through the imposed ice growth and melting chronology, as well as mantle viscosity and lithospheric elastic thickness, and then adjusting the ice volume combining ice mechanics equations to RSL field observations and δ^{18}O-derived sea levels (Lambeck & Chappell, 2001; Waelbroeck *et al.*, 2002, e.g.); the second one involves using a dynamic ice model coupled to a simplified isostatic module, forced with a prescribed climatology, and let the model run until the ice sheet reaches equilibrium ($\approx$200 kyrs, e.g., Siegert, 2001; S.J. *et al.*, 2000).

The Late Saalian Eurasian ice sheet

For the Late Saalian glacial maximum, two recent model reconstructions of the Eurasian ice sheet have been performed: the isostatic reconstruction of Lambeck *et al.* (2006) and the dynamical ice sheet of Peyaud (2006). The reconstruction by Lambeck *et al.* (2006) is based on the following various assumptions and settings:

1- The lithospheric thickness and viscosity are set to 80 km and 10^{25} Pa.s (infinite) respectively

2- The Earth's mantle is divided into two layers with a viscosity 3×10^{20} Pa·s for the upper mantle and 5×10^{21} Pa·s for the lower mantle

3- The elastic moduli and density of the Earth's layers are taken from the PREM (Dziewonski & Anderson, 1981) and mantle rheology is described by a simplified Maxwell viscoelasticity

4- the initial geometry of the ice sheet is fixed, a priori, with two main domes: one over Scandinavia and one over the Kara coastlines

5- Late Saalian eustatic sea level is taken from Lambeck & Chappell (2001) and equals to 140 m

6- Finally, the ice mechanics equations of Paterson (1994) and the isostatic radial rebound calculation are used to estimates the ice thickness of the initial Late Saalian topography

The final reconstruction yields a mean ice elevation of approximately 3000 m (≈4000 m ice thickness) with a local deflection of ≈ 1000 m (Figure 1.12). The total ice volume is about 60 m ESL. This reconstruction links the British Isles ice cap to the huge Eurasian ice sheet. The QUEEN Late Saalian ice sheet is not extended over the southern part of the British Isles as the field data from this area are not conclusive (Svendsen *et al.*, 2004).

The reconstruction of Peyaud (2006) has been computed using the GRISLI ice model based on the shallow ice approximation (Section 1.3.4). Temperature gradient and precipitation are prescribed so that the ice sheet morphology grows

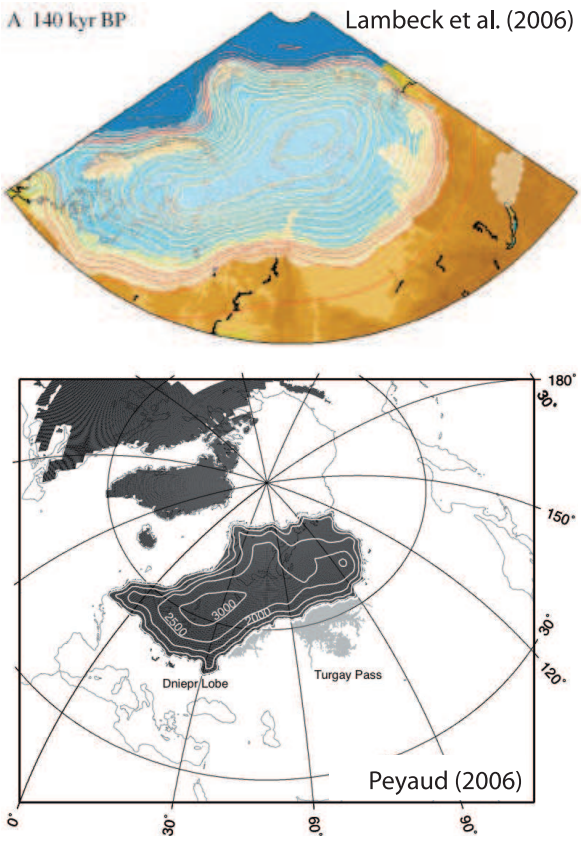

Figure 1.12: Top: Figure from Lambeck *et al.* (2006); Bottom: ice sheet topography from Peyaud (2006) and associated (see the following Section) proglacial lakes.

to fit the QUEEN limits (Figure 1.1). In the experiment, eustatic sea level was set to -110 m below present (Astakhov, 2004) and GRISLI ran for 200 kyrs in order to reach the ice sheet equilibrium. The GRISLI model Late Saalian ice sheet has a shape rather similar to that of Lambeck *et al.* (2006). The mean elevation is also about 3000 m, domes are located almost at the same place and ice volume is ≈ 61 m ESL. The lithospheric deflection allows proglacial lakes to develop in both Lambeck *et al.* (2006) and Peyaud (2006) scenarii, especially in the Siberian Plains.

In all the contributing peer-reviewed articles presented below, we used Peyaud (2006) Eurasian ice topography. The Laurentide, the Greenland and the Antarctic ice sheets were prescribed according to the LGM ICE-5G ice topography since there are no direct evidence to contrain their topography during the Late Saalian.

1.4.2 Ice-dammed lakes

Due to the Eurasian ice sheet growing large and extending far into the Russian and West Siberian Plains during the last glacial cycle, the conti-

nental rivers Yenissei and Ob became dammed several times (Grosswald, 1980; Svendsen *et al.*, 2004). This damming caused the rivers to change their directions and flow towards the Aral Lake and the Caspian and the Black seas and large ice-dammed lakes were formed in front of the ice sheet in the North (Mangerud *et al.*, 2001). Three main ice-dammed lake systems have been distinguished: West Siberian plains, Lake Komi (formed West of the Ural mountain range) and the White Sea basin (Figure 1.12 and 6.1). Paleo-shorelines and other related deposits from these lakes have been dated to the Early and Mid-Weichselian at about 90 ka and 60 ka respectively (Mangerud *et al.*, 2004). The configuration of the Eurasian ice sheet during LGM did apparently not allow larger ice-dammed lakes to form (Svendsen *et al.*, 1999; Mangerud *et al.*, 2004). Table 1.4 summarises geometrical properties estimated for the Weichselian paleo-lakes by Mangerud *et al.* (2001).

	Level (m a.s.l.)	Area (10^3 km^2)	Vol. (10^3 km^3)
White Sea	90 - 110	76	2.4
Lake Komi	100	218	15
WS Plain	60	613	15

Table 1.4: Early Weichselian ice-dammed lakes geographical parameters as estimated by Mangerud *et al.* (2001). WS corresponds to the West Siberian plains. Lakes level is expressed relatively to present sea level.

Ice-dammed lakes constitute an important regional factor in a climate context. As shown by Krinner *et al.* (2004) for the Early Weichselian glaciation, their main effect is to cool the local climate during summer because of their large heat capacity. This reduced the summer ablation along the ice sheet margins, thus, the lakes directly contributed to the maintenance of the continental ice sheet. Similarly, Lake Agassiz, located along the Southern margin of the Laurentide ice sheet, produced a negative temperature anomaly of about -5°C in July and reduced precipitations by about 50% (Hostetler *et al.*, 2000), different from reduced rainfall obtained by (Krinner *et al.*, 2004).

Although no geological evidence of ice-dammed lakes have been found from the Late Saalian, we assumed that, given the large southward and eastward extent of the Eurasian ice sheet and the resulting lithospheric deflection, proglacial lakes should have formed in the Russian and Siberian plains similarly as during the Early and Middle Weichselian glaciations. However, the Late Saalian ice-dammed lakes must have been located further to the South (Figure 6.1). During the Late Saalian, the important damming of the river network should also have led to a flow into the Aral Lake and Caspian Sea through the Turgay pass (Figure 6.1). The lakes were reconstructed by filling the topographic basins located South of the Eurasian ice sheet and accounting for the isostatic depression until reaching the Turgay pass threshold. The reconstructed Late Saalian Siberian ice-dammed lakes (Figure 6.1) looks similar to the Mansi Lake that was proposed to have formed during the LGM by Grosswald (1980).

1.4.3 Dust sources

LMDZ4 does not simulate the atmospheric transport of dust. The radiative forcing induced by the presence of dust in the atmosphere is still not well constrained since it requires a coupling between a three-dimensional dust transportation model and an AGCM. Harvey (1988) and Crowley & North (1991) show that dust radiative impact can cause an atmospheric cooling of 1°C to 3°C in high latitudes and Claquin *et al.* (2003) show that north of 45°N, the radiative effect is between about -0.3 and -0.9 W·m^{-2}.

Dust deposition on snow during glacial periods has been addressed in several studies. Peltier & Marshall (1995) suggest that dust deposition in the ablation zone of an ice sheet may lower the albedo enough to help triggering glacial terminations which cannot be triggered by orbital forcing alone. Similarly, Calov *et al.* (2005b) show that using present-day dust concentration rates, which are substantially lower than during glacial periods, in coupled-climate ice-sheet simulations leads to a rapid expansion of ice sheet both in Eurasia and in North America whereas using glacial rates leads to a larger melting in the ablation zone. Finally, Krinner *et al.* (2006), prescribed Mahowald *et al.* (1999) LGM dust concentration rates in simulations using LMDZ4. The striking result is that Siberia remains ice-free during the LGM due the high dust deposition in this region.

The analysis of Antarctic ice cores have revealed that fluctuations of dust concentration over time are strongly correlated to glacial and interglacial periods. Compared to interglacials, ice ages present high dust concentration (Figure 1.13 top) due to the colder and more arid

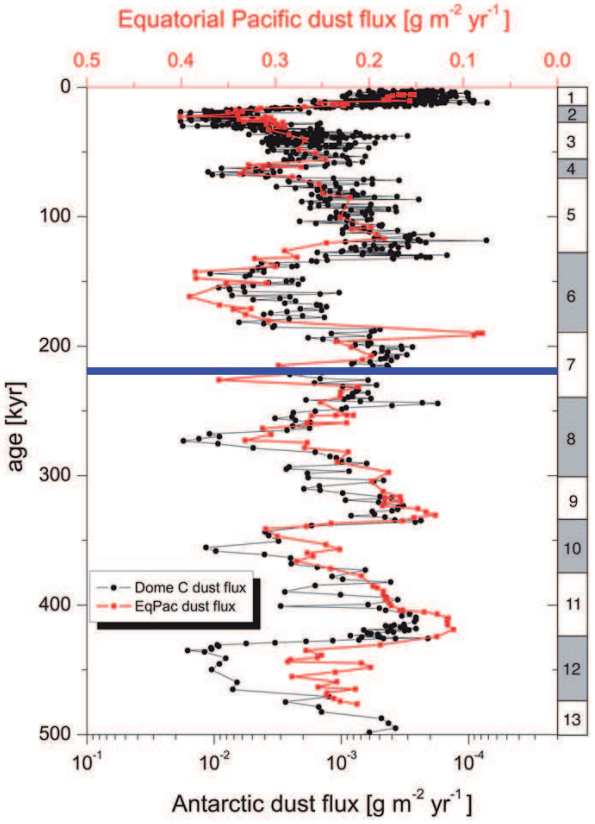

Figure 1.13: Dust concentration in ppb from EPICA Dome C, Antartica (Delmonte & EPICA community members, 2004) (top) and correlation between Equatorial Pacific and Antarctica dust fluxes after Winckler *et al.* (2008) (bottom). The thick blue line separates the upper part of the highly correlated dust fluxes from both regions (MIS 7 to MIS 1) from the lower part showing uncorrelated fluxes.

climate causing strong erosion of desert soils. In analogy to most of the boundary conditions required to simulate the Late Saalian, dust deposition rates have only been simulated for the LGM (Mahowald *et al.*, 1999; Claquin *et al.*, 2003). The Antarctic dust concentration recorded at EPICA Dome C shows that the Late Saalian dust deposition rates were ≈40% lower than at the LGM (Delmonte & EPICA community members, 2004). The Antarctic dust concentration has been linked to that of the Northern Hemisphere by Winckler *et al.* (2008) who highlight a strong correlation between the Antarctic and the Equatorial Pacific dust fluxes for the last five glaciations (Figure 1.13). Since the Equatorial Pacific is fed by Asian dust, they conclude that Northern and Southern Hemipsheres dust fluxes are similarly affected by the global climate fluctuations. Moreover, the analysis of Central Siberian loess deposits supports the 40% difference observed in EPICA Dome C ice-core records between the LGM and the Late Saalian glaciations (Chlachula, 2003).

At the time of the first paleoclimate runs for this thesis, the updated dust deposition rates from Mahowald *et al.* (2006) were not yet published. Therefore, the previous dust estimates by Mahowald *et al.* (1999) for the LGM were used. These rates were adapted to the Late Saalian as described below. The difference between the Mahowald *et al.* (2006) and Mahowald *et al.* (1999) LGM dust deposition maps is shown in Figure 1.14.

The global MIS6 dust deposition rates D_{MIS6} have been obtained by applying an homogeneous factor of 60% to the LGM deposition rates D_{LGM} given by Mahowald *et al.* (1999), assuming that ice accumulation and dust sources were similar during the LGM and the MIS6 glacial maximum (see Paper 1).

The LGM dust deposition rates (Figure 1.14a) have been multiplied by the ratio described above. But the LGM dust deposition distribution overlaps the Eastern part of the Late Saalian Eurasian ice sheet and consequently may enhance the positive feedback from a reduction in the albedo value by ≈20%. The Eurasian LGM ice sheet used by Mahowald *et al.* (1999) to reconstruct the LGM dust deposition fluxes is smaller and thinner than the Late Saalian ice sheet. In our Late Saalian simulations, this would lead to excessive dust deposition in the regions which are ice-covered in our experiments set up, because dust deposition is generally higher in low-lying areas than over the dry ice sheet. To avoid unrealistically high dust concentrations on the ice, we have reduced the amount of dust deposition over the Eastern part of the Eurasian ice sheet (Figure 1.14c) by multiplying all the dust deposition rates greater than 2.5 $g{\cdot}m^2{\cdot}yr^{-1}$ over the ice sheet with 0.025. Some dust still accumulates on the ice sheet but in more reasonable concentrations. We did not redistribute the excess of dust removed by this operation since the quantity can be considered minor (Figure 1.14c).

1.4.4 LGM vegetation cover

Some previous studies have addressed the climatic impact from vegetation changes during glacial periods. The main effect results from the snow-albedo feedback since changing from taiga to tundra increases the local albedo, which cools the local atmosphere in turn inducing larger

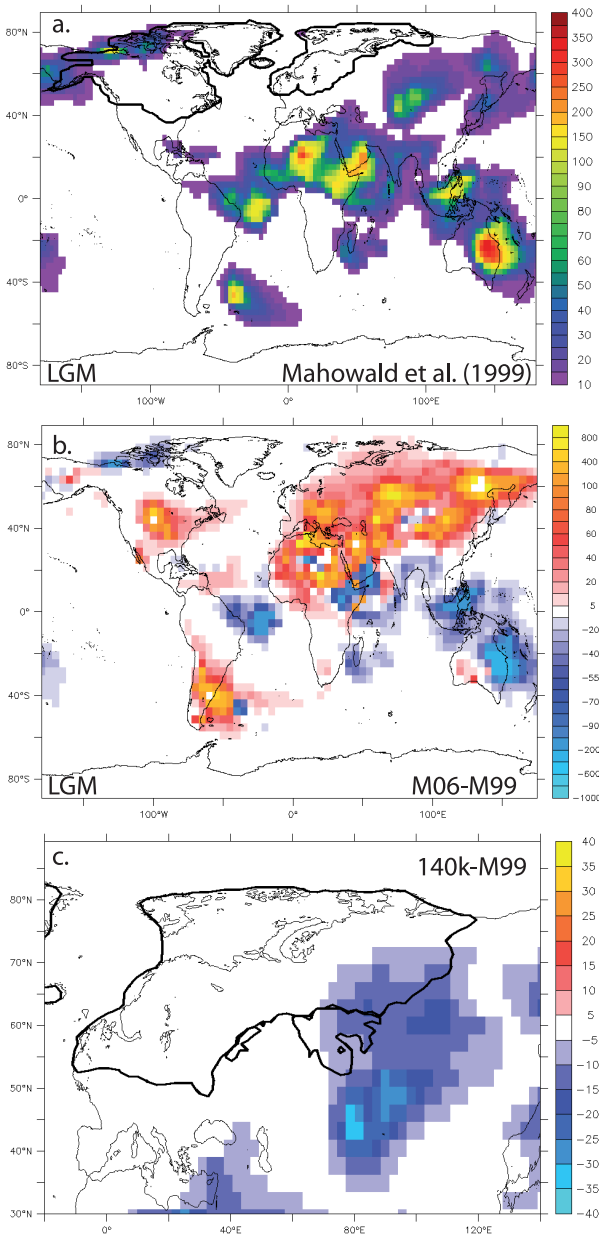

Figure 1.14: a. LGM Mahowald *et al.* (1999) dust deposition rate ($g{\cdot}m^2{\cdot}yr^{-1}$), b. difference in dust deposition rate between Mahowald *et al.* (2006) and Mahowald *et al.* (1999) (M06 - M99), c. difference between Mahowald *et al.* (1999) and the modified 140k dust deposition rates over Eurasia (140k - M99). Black thick lines correspond to the ice sheet margins and proglacial lakes.

snow accumulation. Two methodologies regarding numerical model setup are classically used to investigate this impact: vegetation-AGCM coupled models or asynchronously coupled models. de Noblet *et al.* (1996) followed the second methodology and after five iterations, starting from the potential present-day vegetation, arrived at a summer cooling of 5°C over Siberia due to the replacement of coniferous forest by tundra. Similarly, using land-atmosphere coupled models, Crowley & Baum (1997); Kubatzki & Claussen (1998); Levis *et al.* (1999) and Crucifix & Hewitt (2005) reported that glacial vegetation with small forest extent over the boreal regions caused a regional cooling of 2°C to 4°C in western Europe and Siberia in LGM atmospheric general circulation model (AGCM) simulations.

It is worth noting here that the strongest climatic impacts from LGM vegetation were found in studies using the present-day potential vegetation in LGM control runs. The present-day potential vegetation corresponds to the vegetation as it would be without any anthropogenic interventions such as for example agriculture. The potential vegetation implies larger forested areas in Eurasia compared to what exists today and this decreases the local albedo. The LGM vegetation, on the contrary, is characterized by large tundra areas over Eurasia due to the cold and arid climate, increasing the local albedo. Consequently, the observed climatic anomaly resulting from the comparison between the present-day potential vegetation and the LGM vegetation shows a larger amplitude than if the LGM vegetation were compared directly to the real present-day vegetation accounting for agricultural soils.

Vegetation is an important regional factor that indirectly impacts on temperature through changes in land albedo. However, few LGM reconstructions based directly on palynological data are available (e.g. Adams *et al.*, 1990; Crowley, 1995). For the Late Saalian period, even less pollen data exist (e.g. de Beaulieu *et al.*, 2001) and consequently we had to force all our experiments with LGM vegetation as a first approximation. However Crowley (1995) shows that during MIS 6, the carbon storage signal (derived from deep-sea $\delta^{13}C$) exhibits an excess of $approx$ 50% compared to the present-day value which is much higher than the difference between LGM and current values. This may to indicate a weaker continental carbon uptake caused by more arid global climatic conditions. But, as previously described, MIS 6 atmospheric dust concentration is at least 40% lower than during the LGM (Delmonte & EPICA community members, 2004) which is opposite to the idea of a more arid MIS 6 climate compared to the LGM. This may indicate that, although the MIS 6 vegetation was mostly of tundra and desert similarly to that of the LGM, the erosion on the emerged continental shelves due to the lower sea level

was somewhat reduced. In the following, two LGM reconstructions based on the collection of palynological data are described.

Adams *et al.* (1990) LGM vegetation map

This LGM reconstruction is based on a collection of palynological, pedological and sedimentolgical evidence (sources listed in Adams *et al.* (1990)). The various types of vegetation have been separated according to the classification of Olson *et al.* (1983). The LGM reconstruction assumes a drop in sea level of 130 m as boundary for the expansion of vegetation. Most of Eurasia is classified as desert or semi-desert areas. On the contrary Western Europe is covered by temperate grasslands (Figure 1.15a). This implies a particularly arid LGM climate.

Crowley (1995) LGM vegetation map

In our experiment, we prescribed the LGM vegetation map from Crowley (1995) (Figure 1.15b). This LGM vegetation has been reconstructed using 214 sites from the COHMAP pollen database (Webb & al., 1995). The data from these sites were grouped into 12 biomes categories and used in the GENESIS general circulation model that incorporates a land-surface-transfer scheme (Pollard & Thompson, 1995). Vegetation was subsequently calculated using ICE-4G LGM ice topography and an eustatic sea level of -110 m (Peltier, 1994). The results show the main part of Siberia covered by tundra while the Russian and Siberian Plains are covered by conifers. Western Europe hosts temperate grasslands. Compared to the LGM map by Adams *et al.* (1990) the map produced by Crowley (1995) show less arid vegetation because Siberia is covered by tundra and conifera exists in the Russian Plains, contrary to Adams *et al.* (1990).

In all the simulations (except those including BIOME 4 iterations) the Late Saalian climate has been forced using Crowley (1995) vegetation map since it was the most recent global palynological LGM reconstruction and since no vegetation map exists for 140 ka time period. In addition, we have used BIOME 4 to compute a vegetation in better agreement with the simulated climate. Usually, LMDZ4 is coupled to ORCHIDEE (Krinner *et al.*, 2005), a dynamical vegetation model, but this latter does not include high latitude biomes essential for the simulation

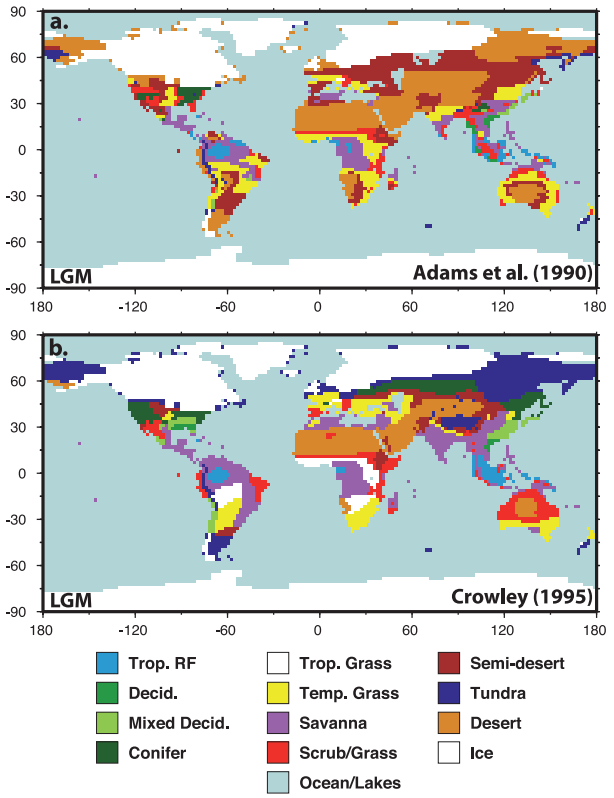

Figure 1.15: LGM vegetation maps from a. Adams *et al.* (1990) and b. Crowley (1995).

of glacial climates, which is why BIOME 4 is used here.

1.4.5 Sea surface conditions

Within the framework of the Paleoclimate Modeling Intercomparison Projects (PMIP) I (Joussaume & Braconnot, 1997, http://pmip.lsce.ipsl.fr) and II (Braconnot *et al.*, 2007, http://pmip2.lsce.ipsl.fr), Kageyama *et al.* (1999, 2006) showed that the use of different prescribed and simulated sea surface temperatures (SST) in AGCM experiments leads to different climate-related (mostly snow fall and temperatures) oceanic and continental climate anomaly patterns of various amplitudes over the North Atlantic and Eurasia. These discrepancies can be explained by both the use of different models. Moreover Kageyama *et al.* (1999) found that compared to less extended sea ice covers in the North Atlantic, the CLIMAP reconstruction shifts the stormtrack activity eastward. Both Ruddiman & McIntyre (1979) and Hebbeln *et al.* (1994) show independently that seasonally open waters in the North Atlantic, such as suggested by the recent MARGO LGM SST reconstructions (Kucera *et al.*, 2005a),

during the LGM significantly influence the mass balance of the Northern Hemisphere ice sheets (Pollard *et al.*, 2000).

In this work we use three different sea surface temperature reconstructions: the CLIMAP LGM reconstruction (CLIMAP, 1981) is used in Papers 1 and 3, Paul & Schaefer-Neth (2003) LGM reconstruction in Papers 2, 3, 4 and Chapter 6 and finally a simulated SST in Paper 3 and Chapter 6 to which temperature estimates for 140 ka from marine sediment core data are compared. These reconstructions exhibit discrepancies due to the different proxy methods applied to derive SST from those proxies, improvement of dating methods and numerical models interpolation. For example, the applied proxy reconstruction methods by different authors include: micropaleontological transfer functions, oxygen isotopes in biogenic skeletons, unsaturated ratio $U_{37}^{K'}$ (alkenone) and trace elements in biological carbonates (Sr/Ca, Mg/Ca, U/Ca). Bard (2001) and Mix *et al.* (2001) show the need to perform multiproxy SST reconstructions in order to get an idea of the performance of the various methods and estimate upper and lower bounds of uncertainties of the resulting SST values. This was done within the recent MARGO Project (Waelbroeck *et al.*, 2009)

To illustrate the differences between the various SST reconstructions used in this work, we present the temperature anomalies between the reconstructed paleo-temperatures and the present-day observations from the Hadley Centre (referred as HadISST) averaged between 1970 to 1999 (Rayner *et al.*, 2003).

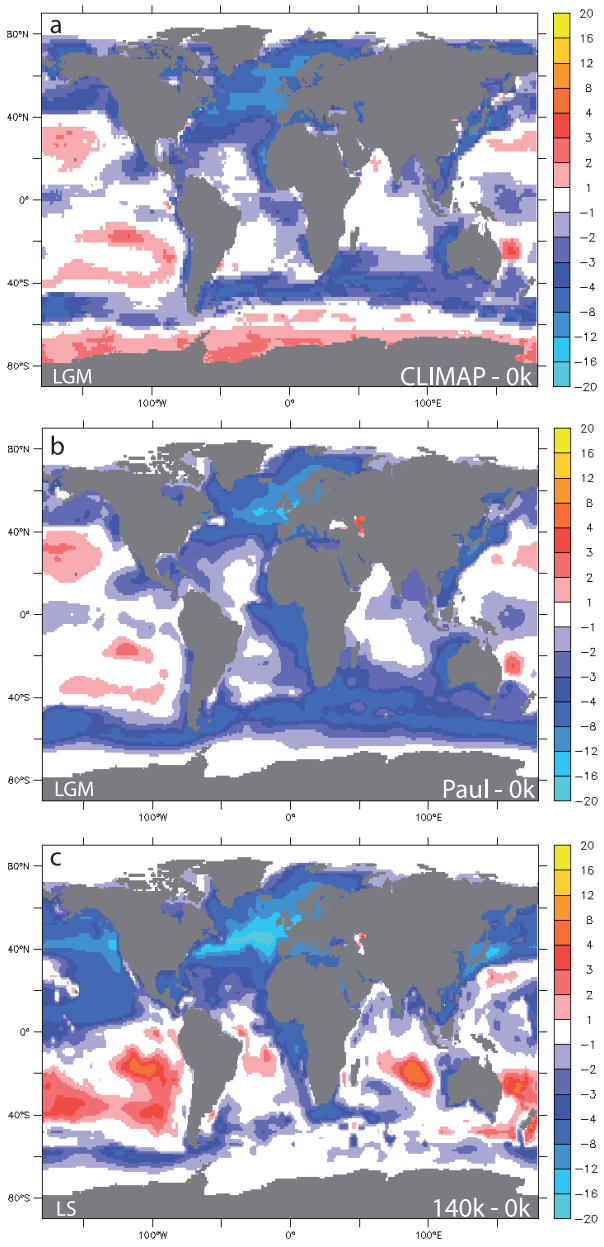

Figure 1.16: Difference in mean annual sea surface temperature (°C) between: a. LGM CLIMAP (1981) and present-day, b. LGM Paul & Schaefer-Neth (2003) and present-day, c. simulated 140k and present-day.

CLIMAP LGM

The Climate, Long-Range Investigation, Mapping and Prediction (CLIMAP) focused on the last glacial ocean with the main objective to evaluate the oceanic changes resulting from the shift into and out of the last interglacial period The project used a very large number of marine sediments cores with a maximum coverage in the North and South Atlantic. Winter and summer SST were estimated using regional transfer functions derived from the species composition of foraminifera, radiolaria and coccoliths. The uncertainty of the SST estimates is about 1° to 2°C. Sea-ice cover was defined where SST was cooler than the sea water freezing temperature (–1.8°C). Compared to HadlSST, the CLIMAP LGM reconstruction shows a mean annual cooling of about 12°C in the North Atlantic and of about 4°C in the Bering Sea region due to the LGM sea ice cover extending in these regions (Figure 1.16a). The LGM South Oceans also exhibits cooler temperatures by about 4°C. Finally the subtropical Pacific Ocean was warmer ≈2°C warmer during LGM compared to present-day according to CLIMAP.

Paul & Schaefer-Neth (2003) LGM SST

This more recent reconstruction is based on several available datasets:

- Atlantic Ocean: Pflaumann *et al.* (2003) sea surface temperature isotherms extrapolated to the West.
- North Atlantic: de Vernal *et al.* (2000) August and February estimates
- South Atlantic: Niebler *et al.* (2003) annual mean SST and seasonality; Gersonde *et al.* (2003)
- Pacific and Indian Oceans: CLIMAP (1981)

The sea ice extent has been determined in the Northern Hemisphere by extending Pflaumann *et al.* (2003) sea ice cover to the west using de Vernal *et al.* (2000) February and August estimates. Around Antarctica, SST reconstruction is based on Gersonde *et al.* (2003).

Compared to HadISST, this mean annual LGM reconstruction is cooler by about 9°C in the North Atlantic and by about 4°C in the Bering Sea region (Figure 1.16b). However, in this LGM reconstruction, sea ice is less extended to South compared to CLIMAP in the North Atlantic. The mean annual LGM World south oceans also exhibits cooler temperatures by about 4°C. Finally the Pacific Ocean is warmer by about 2°C during LGM.

The MARGO Project (Waelbroeck et al.*, 2009): a LGM multiproxy reconstruction*

The MARGO project (Waelbroeck *et al.*, 2009) is based on a multiproxy approach with the argument that no particular proxy method provides better estimates of past SST than another (Bard, 2001; Mix *et al.*, 2001). This project uses SST estimates from 696 available marine sediment records. The data coverage is rather dense in the North Atlantic, the Southern Ocean and in the Tropics (Figure 1.17).

The resulting SST reconstruction shows that during LGM, there were large East-West gradients in the Tropics and North Atlantic (Figure 1.17). These gradients are still not captured by existing coupled Atmosphere-Ocean GCM LGM simulations and may reflect critical discrepancies between the simulated LGM and present-day atmosphere-ocean system. One important result is that on contrary to CLIMAP, all proxies converge toward ice-free conditions in the Nordic seas during the glacial summer (Figure 1.17). Moreover, the tropical cooling visible in the CLIMAP reconstruction is more extended in MARGO and the subtropics Pacific is less warm than in CLIMAP.

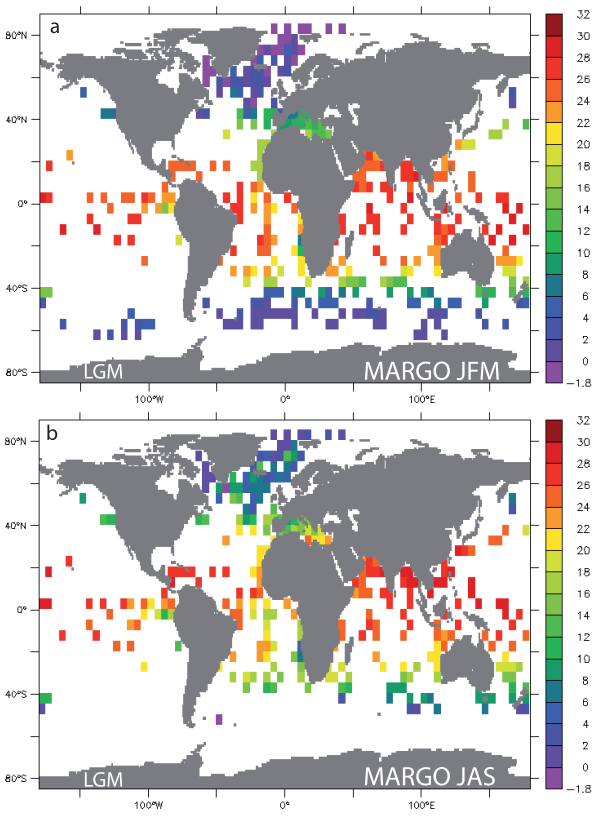

Figure 1.17: MARGO Project (Waelbroeck *et al.*, 2009) LGM reconstruction for winter January-February-March (a) and summer July-August-September (b). Pixels correspond to marine sediment cores-derived SST (°C) and sea ice limit is indicated by pixels whose temperature is lower than -1.8°C

These results illustrate the necessity to use more recent LGM reconstructions than CLIMAP which holds temperature biases in critical areas. In our work, we compare the impact of CLIMAP sea surface conditions on the climate simulated by LMDZ4 to that of Paul & Schaefer-Neth (2003) in several simulations. The more realistic LGM simulations are carried out using the Paul & Schaefer-Neth (2003) reconstruction which is more in agreement with the summer open-water in the Nordic Sea and with a stronger tropical cooling as proposed in the MARGO reconstruction.

The Late Saalian glacial maximum surface ocean (140 ka)

The methods used to simulate the Late Saalian sea surface conditions are detailed in Section 1.3.2. Compared to HadISST, the calculated Late Saalian SST present a large cooling

of -18°C in the North Atlantic and North Pacific (Figure 1.16c). This is due to the larger southward sea ice cover reaching Spain and Canada in the Late Saalian reconstruction. In the Southern Ocean, cooling is small (-2°C). On the contrary, the South Pacific is approximately 5°C warmer than in HadISST. This Late Saalian reconstruction is colder than both the LGM CLIMAP (1981) and Paul & Schaefer-Neth (2003) SST. Globally, the Northern Hemisphere is cooler than HadlSST while the Southern Hemisphere is warmer than HadISST. This is due to the larger eccentricity enhancing the effect of precession compared to Late Saalian than during present-day (Section 1.2.2). This enhances the asymmetry between the two hemispheres (Raymo *et al.*, 2006). This point is further discussed in Paper 3 and Chapter 6.

1.4.6 The Arctic Ocean ice shelf

The Arctic Ocean North of the Fram Strait and the northern Canadian Arctic Archipelago is nearly landlocked and has an area of $\approx 9.5 \times 10^6$ km^2 of which ≈53% is constituted of shallow continental shelves (Jakobsson, 2002) (Figure 6.2). The mean depths of the shallow seas, including the continental shelf, ranges from less than 50 m to slightly more than 300 m while large areas of the deep central basins exceed 4000 m water depth (Jakobsson *et al.*, 2008b). During the LGM as as during the Late Saalian, the only open gateway between the Arctic Ocean and the World Ocean was the Fram Strait located between Northeastern Greenland and Svalbard. Currently, the depth of Fram Strait threshold is 2550 m (Klenke & Schenke, 2002) and the closest distance between Greenland and Svalbard across the strait is 440 km (Jakobsson *et al.*, 2007). This distance was certainly reduced by more than 20% during LGM and the Late Saalian when large parts of continental shelves on both sides of the strait were either exposed due to a lower sea level or covered by ice sheets. Recent estimates show that the present sea ice export through the Fram Strait is about 2200 m^3·yr^{-1} (Kwok *et al.*, 2004).

During the Arctic Ocean 96 expedition with Swedish icebreaker Oden, large-scale erosion of the seabed was discovered from chirp sonar mapping of the crest of the Lomonosov Ridge in the central Arctic Ocean approximately 1000 m below the present sea level (Jakobsson, 1999). Further geophysical mapping during the Scientific Ice Expeditions (SCICEX) 1999 with nuclear submarine USS Hawkbill revealed that the erosional features on the Lomonosov Ridge were caused by glacier ice grounding (Polyak *et al.*, 2001). Icebreaker surveys of the Chukchi Borderland together with the USS Hawkbill data from the Alaskan northern margin provided data that suggested the existence of an ice rise on the Chukchi Borderland acting as a local ice sheet and large floating ice shelves in the Canadian part of the Arctic Ocean (Jakobsson *et al.*, 2005, 2008b; Engels *et al.*, 2008). In addition to the geophysical data, sediment cores were acquired from these glacial features during the icebreaker expeditions. These cores made it possible to date some of the mapped glaciogenic bedforms and the results converge to the end of MIS 6 (≈160 -140 ka) while no evidence of deep ice grounding has been found for the LGM (Jakobsson *et al.*, 2008b; Polyak *et al.*, 2007). Recent mapping data providing information on the Arctic Ocean glacial history were acquired during the Lomonosov Ridge off Greenland Ex-

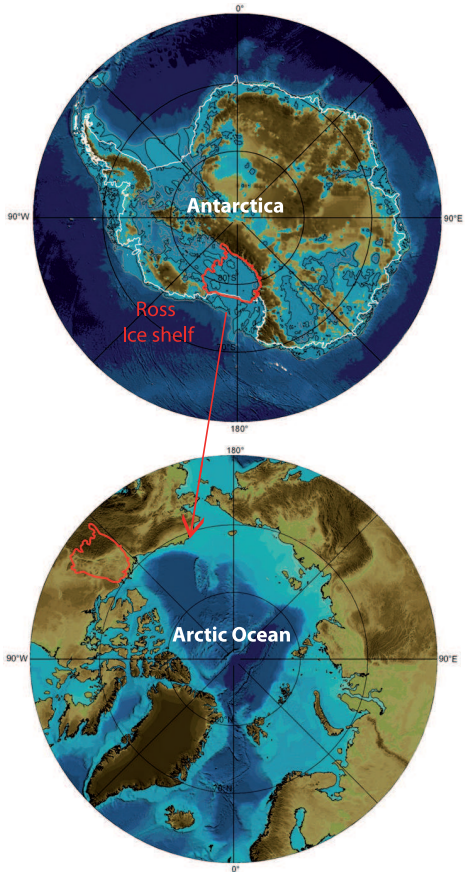

Figure 1.18: Comparison between the Antarctic Ross ice shelf size (red contours in top frame) and the Canadian Arcti basin (bottom frame, see Figure 6.1). Courtesy M. Jakobsson

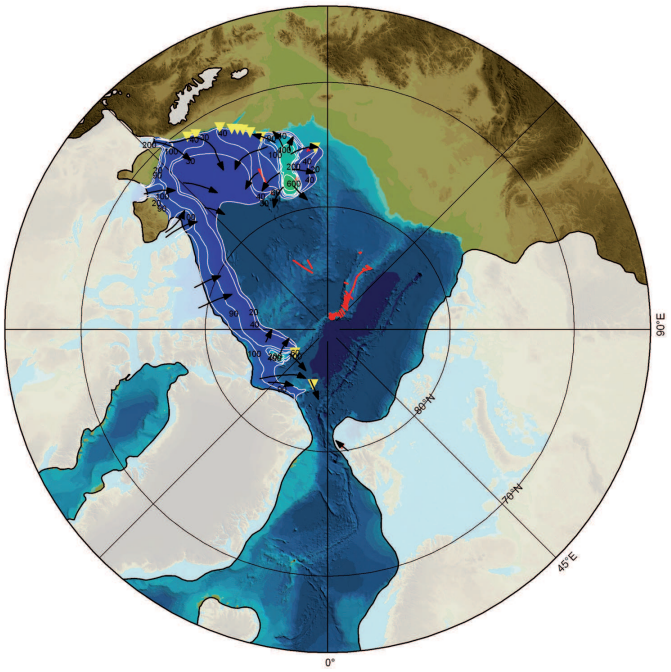

Figure 1.19: MIS 6 Canadian ice shelf reconstruction (dark blue). Yellow triangles indicates places where glacial erosion marks have been evidenced, converging toward the existence of a large floating ice feature in the Arctic Ocean. Black arrows indicate hypothetical ice flow directions partly based on the marine seismic profiles. Red lines indicate the seismic profiles carried out over the Lomonosov ridge. Courtesy M. Jakobsson.

pedition (LOMROG) 2007 (Jakobsson & co authors, 2009). These data show that a MIS 6 ice shelf did not extend over the entire Arctic Ocean, as suggested by Hughes *et al.* (1977) for the LGM (see below), since the Morris Jesup Rise, which is extending the continental shelf of Northern Greenland, only has been subjected to ice grounding of singular deep icebergs and not larger floating ice masses (Jakobsson pers. comm.). In other words, the accumulation of existing geophysical mapping and geological coring data do not support the existence of a single dynamic ice shelf over the MIS 6 Arctic Ocean but a large ice shelf with associated ice rises acting as local ice sheets in the Amerasian Basin.

The Arctic ice shelf in literature

During the last decades, the idea that the Arctic Ocean might have been completely covered by a 1-km thick ice shelf during the Quaternary glaciations has been discussed in terms of ice dynamics but the impact upon climate of such a glacial feature has never been explored. Mercer (1970) was the first to develop the idea of the existence of a Quaternary based ice sheet in the Arctic Ocean with an ice shelf forming a critical component. He did not precisely outline but he proposed that it should first have developed in the Amerasian part as it there would be less susceptible to the influx of warm water from the Atlantic through Fram Strait. He suggested that the ice shelf developed in a glacial period prior to the LGM since the cold climate then did not last long enough to produce an extended and thick floating ice shelf. Hughes *et al.* (1977) and Grosswald & Hughes (1999) developed Mercer's idea and proposed a 1-km thick ice shelf covering the entire Arctic Ocean during LGM. In part, their LGM reconstruction was supported by geological evidence, such as glaciogenic morphological features recorded on the continental shelves and the transportation of erratics for example along the coasts of Northern Greenland. However, the evidence they used was mostly not well constrained in time. Finally, they assumed that without a thick Arctic Ocean ice shelf, the Eurasian and Laurentide ice sheets could not have remained stable. They developed the concept of a multi-component interconnected ice aggregate (continental ice sheets, 'marine' ice sheets, ice streams and ice shelves) dynamically active.

The ice shelf reconstruction topography

In order to test if a large floating ice shelf in the Arctic Ocean could had an impact on the climate during the Late Saalian glacial maximum, a reconstruction of the MIS 6 ice shelf extent and topography is required. Probably the best way to evaluate where an ice shelf could have existed in the Arctic Ocean, is to compare the geographical setting with Antarctica as well as the glaciogenic seafloor morphology that have been mapped in both arctic and Antarctic regions. This work is presently being carried out in detail by Jakobsson et al., (in prep), although for the climate modelling experiments in Chapter 5 of this thesis, it is enough to roughly outline the ice shelf extent and topography as the AGCM LMDZ4 was not set up to work with a high-resolution grid (see 1.3). Furthermore, the AGCM simulations in Chapter 5 are designed to generally evaluate if there is a difference in climate impact from a limited ice shelf in the Amerasian Arctic Ocean versus a completely ice shelf filled ocean as proposed by Hughes *et al.* (1977). Therefore, the first draft of the ice shelf extent by Jakobsson et al., (in prep) is used for the climate simulations.

The Ross (487 000 km^2 and 750 m thick (mean)) and the Filchner-Ronne ice shelves (430,000 km^2 and 600 m thick (mean)) are the largest Antarctic ice shelves. To allow for comparison with the Arctic, the outline of the Ross Ice Shelf is placed near the Canada Basin of the Arctic Ocean (Figure 1.18). This shows that the spatial dimension of the Canada Basin is not too far from the Ross Ice Shelf.

The usual mean observed thickness at the front of the large present Antarctic ice shelves is about 200 m, which means that $\approx$ 20 m are emerged above sea level. However, some of the shelves have portions that are significantly thicker and the final thickness at the front from where icebergs are calved depends on how far the ice shelf flowed from the grounding line as well as basal accretion or melting etc. As discussed above, scours marks have been observed in the Arctic Ocean down to water depth of $\approx$ 1000 m bellow present sea level implying that thick icebergs drafting around 890 m at minimum (with a 110 m lower sea level than present) flowed in the MIS 6 Arctic Ocean (e.g. Jakobsson, 1999; Jakobsson *et al.*, 2008b; Polyak *et al.*, 2001). However, the presently available data do not suggest that the MIS 6 ice shelves were this thick in general; most of the deepest scours are from singular icebergs.

To reconstruct a generalised ice shelf in the Canada Basin of the Arctic Ocean for the modelling experiments, the extent was taken from the preliminary version of Jakobsson et al. (in prep) where the thickness was inferred by assuming a general gradient from an ice thickness of 1000 m at the grounding line at about the continental shelf break. From this point where the ice becomes afloat, the ice shelf is thinned by 5 m/km until it reaches a thickness of 200 m which then defines the ice shelf front. Some manual adjustment to make the hypothesised ice shelf conform to collected geophysical and geological data has been done by Jakobsson et al (in prep). The 200 m thick front is the classical calving limit used in thermodynamical ice models such as GRISLI (Peyaud, 2006; Peyaud *et al.*, 2007). In the Canada Basin, we assume that the ice shelf results from the merging between the ice flowing from the Chukchi Borderland and that from the three ice streams draining the Laurentide continental ice lobes (McClure Strait, Amundsen Gulf and Mackenzie ice streams) evident in ICE-5G (Figure 1.19, Peltier, 2004).

1.5 Summary of the peer reviewed articles

This thesis was carried out following a specific logic of investigation: the regional continental factors such as dust deposition on snow and proglacial lakes were first studied in a climate context and constitute the main topic of Paper 1. This was followed by an effort to compute vegetation in agreement with the Late Saalian climate in Paper 2 and the outcome was compared to the LGM vegetation. From Paper 2, it became evident that it was needed to simulate SST to better understand the Late Saalian glacial maximum climate. Thus SST became the main topic of Paper 3 in which we also explored the sensitivity of the LGM Eurasian ice sheet. New data from the Lomonosov Ridge off Greenland (LOMROG) 2007 expedition made it possible to better constrain the extent of a MIS 6 floating ice-shelf in the Arctic Ocean. Since this ice shelf seem to be a special feature of the Late Saalian (MIS 6), its effect on the Late Saalian Arctic climate is investigated in Paper 4. Finally, to better understand the climate dynamics of the entire Late Saalian period (160 - 140 ka) snap-shots were

performed at 140 ka, 150 ka and 160 ka combining all the reconstructed Late Saalian boundary conditions and using all the methods developed in Papers 1-4. This is the subject of Paper 5 which is included as a manuscript in this thesis.

Paper 1: Regional factors

The article entitled "Influence of regional parameters on the surface mass balance of the Eurasian ice sheet during the peak Saalian (140 kya)" constitutes the basis for this entire thesis work. The article addresses the hypothesis that the large Late Saalian Eurasian ice sheet extent and volume result from feedbacks between regional continental parameters and climate processes (Section 1.1). In this study, we mainly evaluate the influence of dust deposition on snow and proglacial lakes on the surface mass balance (SMB) of the Late Saalian Eurasian ice sheet. However, a part of Paper 1 is also focused on the impact of small vegetation changes such as replacing the conifera by tundra and the climate difference induced by two prescribed LGM SST reconstructions. The influence of vegetation and SST are further studied in Paper 2 and 3.

To simulate the Late Saalian climate and to address the problem of regional factors, we use LMDZ4 (Section 1.3.1, Hourdin *et al.*, 2006). Seven model simulations of 21 years each have been carried out: a present-day control run (REF0), a reference Late Saalian simulation (REF140), DUST140 and LAKES 140 accounting for dust deposition on snow and proglacial lakes respectively, FULL140 including both dust and proglacial lakes, VEG140 in which forest has been removed and finally SST140 forced with Paul & Schaefer-Neth (2003) SST reconstruction (the other runs were forced using CLIMAP (CLIMAP, 1981)).

In DUST140, dust deposition locally warms the Eurasian climate during spring by $\approx 1°C$ in particular along the southern margins of the Eurasian ice sheet. However, this is not enough to decrease the ice sheet's mean annual SMB. In LAKES140, proglacial lakes cool the summer climate locally by $\approx 14°C$ and over Eurasia by $\approx 2°C$. This reduces surface melt along the southern margin of the Eurasian ice sheet by about 200 to 2000 mm·yr^{-1}. Consequently the mean annual SMB over the entire ice sheet is significantly increased by ≈ 28 mm·yr^{-1}, compared to the REF140 mean annual value, due to a decrease in mean annual ablation of the same amount. The results from simulation FULL140, where both proglacial lakes and dust deposition are included, are interesting since the presence of the former parameter reduces the impact of the latter, particularly during summer. Consequently, summer temperature is decreased by about 1°C to 2°C over Eurasia compared to REF140 and proglacial lakes still cause a local cooling of $\approx 14°C$. The final result is that when both proglacial lakes an dust are included in simulation FULL140, the net effect for the mean annual SMB of the Eurasian ice sheet is nearly similar as when only proglacial lakes are included. SMB is increased by ≈ 23 mm·yr^{-1} due to a decrease in ablation by ≈ 25 mm·yr^{-1} during summer. In VEG140 where dust and proglacial lakes are included, a switch from needle-leaf to tundra vegetation affects the regional climate but not enough to significantly influence the SMB of the nearby ice margin. Finally, changing the SST boundary conditions used in the simulation experiments from CLIMAP to Paul & Schaefer-Neth (2003) LGM reconstructions broadly affects the regional climate with significant consequences for the SMB (–24 mm·yr^{-1} when Paul & Schaefer-Neth (2003) LGM SST are used).

In summary, this paper shows that the regional parameters significantly influence the Eurasian climate during the Late Saalian. This has important consequences for the surface mass balance of the Late Saalian Eurasian ice sheet particularly along the margins which are affected by ablation during summers.

The method used to estimate the SMB of the Eurasian ice sheet is indeed critical for the analysis of the simulation experiments. Two methods have been used: the energy surface mass balance (Thompson & Pollard, 1997) and the positive degree day (PDD, Ohmura *et al.* (1996)) which includes a downscaling onto a finer grid. The energy surface mass balance gives negative values for all the simulations while the PDD method provides positive values for all of them. This results from the higher grid resolution in the PDD method which is able to fully account for the ablation along the margins of the ice sheet. This PDD method substantially reduces the ablation at the margins and will be used in the following papers instead of the energy balance method.

Paper 2: Vegetation feedbacks

Following Paper 1, the article "Sensitivity of the Late Saalian (140 ka) and LGM (21 ka) Eurasian ice sheet surface mass balance to vegetation feedbacks" proposes a computed reconstruction of the Late Saalian vegetation cover. Similarly to Paper 1, the AGCM LMDZ4 is used, but this time asynchronously coupled to the equilibrium vegetation model BIOME4 (Kaplan *et al.*, 2003). The SMB of the Eurasian ice sheet is also in this work the main indicative parameter used to analyze the results from different simulations and this SMB is calculated using the PDD method described in Ohmura *et al.* (1996). To better understand the impact of vegetation feedbacks on the Late Saalian Eurasian ice sheet, similar simulations were carried out for the LGM Eurasian ice sheet and climate.

Since no vegetation map had been compiled for the Late Saalian time period prior to this work, the LGM (C21) and the Late Saalian (C140) climate snapshots (21 years) were initially simulated by forcing LMDZ4 with the existing LGM vegetation map by Crowley (1995). New vegetation maps were subsequently computed by forcing BIOME4 with the monthly mean and minimum daily temperatures, the monthly mean precipitation and the cloud cover fraction obtained from the two C21 and C140 AGCM simulations. Then this vegetation is given as a new boundary condition to the AGCM. Steady state vegetation was obtained after three iterations and the final AGCM runs, using the derived LGM and Saalian vegetation maps are referred to as B21 and B140 respectively.

BIOME4 computes a continuous East-West taiga and mixed-forest belt over Eurasia, both for LGM and Late Saalian periods. This is different from the vegetation distribution portrayed on the LGM map by Crowley (1995). However, the net primary production of this forest-type vegetation is lower than 350 $gC{\cdot}m^{-2}$. This suggests that the computed forest has a low density and is not particularly productive compared to the present-day Eurasian forests (> 460 $gC{\cdot}m^{-2}$). During the Late Saalian, vegetation changes induce a large increase in albedo (more than 30%) as a result of the accumulation of a permanent snow cover in the three climate iterations. This causes a regional cooling over Eurasia of about 15°C. During the LGM, the replacement of conifera (Crowley, 1995) by tundra in the Russian plains increases the albedo by 15%. The regional climate is cooled by approximately 2.5°C due to this albedo change. On the contrary, over Europe, the development of taiga and mixed forest reduces the albedo with approximately 20% which causes a slight regional warming (≈ 2°C). As a result of the vegetation changes, ablation along the margins of the Late Saalian ice sheet is significantly reduced by about 56 $mm{\cdot}yr^{-1}$, leading to an increased SMB of about 67 $mm{\cdot}yr^{-1}$, while there are no significant SMB changes observed from vegetation feedbacks at the LGM.

In summary, this work shows that using a computed Late Saalian vegetation map in the climate simulations with LMDZ4 leads to a different climate state than when using the initial LGM Crowley (1995) vegetation reconstruction. This directly affects the SMB of the ice sheet, in particular along the southern margins. Moreover although a simulated LGM vegetation distribution should be good as first approximation to model previous ice ages, this study highlights the need to simulate vegetation using interactive coupled atmosphere-vegetation models to account for the climatic feedbacks.

Paper 3: Late Saalian SST

This article entitled "The Late Saalian surface ocean (140 ka): sensitivity of the Late Saalian Eurasian ice sheet to sea surface conditions" forms a continuation of Paper 1 in which it became clear that SST is a critical parameter of climatic importance that needs to be further addressed. The paper focuses on the sensitivity of the Late Saalian Eurasian ice sheet to various prescribed and simulated sea surface temperatures (SST). Since no Late Saalian SST global reconstruction exists, we prescribed as a first approximation, LGM SST from CLIMAP (CLIMAP, 1981) and from Paul & Schaefer-Neth (2003). Numerical experiments are carried out both for the LGM and the Late Saalian in order to make comparisons possible. The Late Saalian surface ocean is simulated using the Planet Simulator AGCM coupled to a mixed layer ocean model (Fraedrich *et al.*, 2005) in order to derive SST for this time period. The simulated SST are then used to force LMDZ4.

In total five snap-shots of 21 years each are carried out using the LMDZ4: $CLIM_{140}$ and $CLIM_{21}$ forced using CLIMAP LGM SST, $P03_{140}$ and $P03_{21}$ forced using Paul & Schaefer-Neth (2003) LGM SST (referred to as P03) and fi-

nally $FULL_{140}$ forced using the simulated SST for the Late Saalian time period. The main difference between P03 and CLIMAP sea surface conditions in the Northern Hemisphere resides in the larger sea ice extent reaching as far south as 45°N during winter and 50°N during summer in the North Atlantic in the CLIMAP reconstruction. The CLIMAP SST reconstruction tends to cool the mean annual temperature by approximately 15°C over the North Atlantic and weakens the Icelandic depression when it is used for simulation of the LGM and Late Saalian. Evaporation and precipitation are reduced over the North Atlantic by more than 80%. However, during the Late Saalian, the cold temperature anomaly remains confined to Arctic Ocean while it spreads further over Eurasia during the LGM. This is due to the difference in ice elevation which is almost doubled during the Late Saalian compared to the LGM. Surface mass balance (SMB) present values of the same order for all simulations (from 208 to 248 $kg{\cdot}m^{-2}{\cdot}yr^{-1}$) but for the Late Saalian, the difference between CLIMAP and P03 is not as large as for the LGM (14 $kg{\cdot}m^{-2}{\cdot}yr^{-1}$ and 40 $kg{\cdot}m^{-2}{\cdot}yr^{-1}$ respectively).

Late Saalian SST (referred to as PS140) that have been simulated using the monthly LGM ocean heat fluxes calculated from Paul & Schaefer-Neth (2003) are further compared to P03. PS140 is completely different from P03 and exhibits a large asymmetry between the two hemispheres. Indeed, the Northern Hemisphere shows a 9°C cooler mean annual temperature while the Southern Hemisphere is warmer by about 2°C to 6°C. This effect seems at a first glance comparable to the "seesaw" effect that has been attributed to results from thermohaline variations in the Atlantic Ocean and which causes a heat transfer from one of the two hemisphere to the other (Stocker, 1998). However Planet Simulator does not simulate deep ocean circulation and the same meridional heat flux is prescribed in both experiments. Consequently, the asymmetry seen in SST cannot result from such a "seesaw" effect. Instead, the asymmetry may be explained by the larger eccentricity enhancing the precessional effect during the Late Saalian compared to the LGM. This orbital configuration may be the key to the large sea ice cover reaching 40°N in both North Atlantic and North Pacific during both winter and summer as seen for the last glacial inception by Khodri *et al.* (2005).

The main consequence, when prescribing PS140 in the LMDZ4 simulations, for the Northern Hemisphere climate is a mean annual cooling of about 10°C compared to P03. As for CLIMAP, the larger sea ice extent weakens the Icelandic depression and reduces evaporation over the North Atlantic. However, since this colder climate persists during the entire year, moisture fluxes coming from the Atlantic and from the North Pacific and advected over Eurasia are almost cancelled. Although the Eurasian ice sheet is not subjected to ablation anymore even during summer, the mean annual SMB is reduced by approximately 26 $kg{\cdot}m^{-2}{\cdot}yr^{-1}$ compared to that of $P03_{140}$ due a lack of accumulation.

In this paper, we have shown that the Eurasian ice sheet is sensitive to any prescribed or simulated SST reconstruction, but that the amplitude of this sensitivity significantly depends on the initial imposed ice topography. The Late Saalian Eurasian ice sheet is less sensitive than the LGM because of its higher elevation and more southward extent. This large topography compensates for variations in SMB along the Atlantic margin exposed to the moisture fluxes.

Our simulated Late Saalian SST appears to be in good agreement with marine sediment core data in the tropical and equatorial regions whereas in the higher latitudes the simulated SST appears to be underestimated both in the North Atlantic and North Pacific. This means that the sea ice cover derived from the simulated SST may extend too far towards lower latitudes. However, Crowley (1981) did suggest that during the Late Saalian, the polar front migrated much further southward compared to its LGM position.

Paper 4: the Arctic ice shelf

In this study, we focus on a particular MIS 6 oceanic glacial feature: an Arctic ice shelf and its impact on the Northern Hemisphere climate. During the last decade of Arctic icebreaker and nuclear submarine expeditions, large-scale glacial erosion and glaciogenic bedforms have been mapped on the central Arctic Ocean seafloor in water depths down to approximately 1000 m below present sea level. Some of the mapped glaciogenic features on the Lomonosov Ridge, Chukchi Borderland and along the Northern Alaskan margin indicate that the glacial Arctic Ocean hosted large Antarctic-

style ice shelves (e.g. Jakobsson, 1999; Polyak *et al.*, 2001; Jakobsson *et al.*, 2005, 2008b; Engels *et al.*, 2008). Furthermore, dating of sediment cores collected from glacially eroded areas of the Lomonosov Ridge indicate that the most extensive and deepest ice grounding occurred during MIS 6 and not during LGM (Jakobsson *et al.*, 2001). This implies that the largest ice shelves in the Arctic Ocean coexisted with the largest extension of the Eurasian continental ice sheet.

Several decades before this geophysical evidence emerged, Mercer (1970) proposed that there may have existed Antarctic style ice shelves in the Arctic Ocean during the Pleistocene glacial periods. His idea was further developed by Hughes *et al.* (1977) who suggested a 1-km thick ice shelf covering the entire Arctic Ocean and forming a critical part of a huge ice sheet, including the Laurentide and Eurasian ice sheets, that behaved as one dynamic system during the Last Glacial Maximum (LGM).

If an Antarctic-style ice shelf was present in the Arctic Ocean during MIS 6, how did it influence the MIS 6 Northern Hemisphere climate? Could it have impacted on the surface mass balance (SMB) of the MIS 6 Eurasian ice sheet and contribute to its large southward extent?

From the recent geophysical evidence collected in the Arctic Ocean, Jakobsson et al., (in prep.) reconstructed a $\approx$ 800 m thick ice shelf covering the Canada Basin (a size comparable size to that of the Ross ice shelf in Antarctica) and extending along the North American margin to Greenland. We use LMDZ4 to investigate the climatic impacts of both a limited MIS 6 ice shelf covering portions of the Canada Basin and a fully ice shelf covered Arctic Ocean. Three snapshots of 21 years each have been performed accounting for the boundary conditions of 140 ka: REF5m, which accounts for a 5 m thick sea ice cover over the entire Arctic Ocean, SHELF, accounting for the Canada Basin ice shelf and GH, accounting for a 1-km thick ice shelf covering the entire Arctic Ocean.

Results show that both ice shelves causes a temperature cooling of about 3°C over the Arctic Ocean mainly due to the combined effect of ice elevation and a very efficient insulation from the underlying ocean heat fluxes stopping the snow cover from melting during summer. In REF5m, the Archimedes effect limits the snow mass accumulating over the sea ice. When the sea ice sinks into the ocean under the snow weight, part of the snow transforms into sea ice and part of the remaining snow melts during summer. The Archimedes effect is negligible in SHELF and GH since the ice shelves are $\approx$ 1-km thick, stopping snow from melting during summer. This cooling extends up to 2000 m of altitude in the atmosphere. However, in both cases, the impact of the shelves is not strong enough to influence the large scale circulation.

The SMB of the ice shelves is positive, $\approx$ 93 kg·m^{-2}·yr^{-1} for the Canada Basin ice shelf and $\approx$ 46 kg·m^{-2}·yr^{-1} for the large Arctic ice shelf. This suggests that both ice shelves are probably in equilibrium with the MIS 6 climate. The cooling caused by these ice shelves only affects the Arctic margins of the continental ice sheets that exhibits a positive surface mass balance and particularly the Greenland margins. However, this cooling is not strong enough to significantly influence the surface mass balance of the entire MIS 6 Eurasian ice sheet.

The ice front horizontal velocity of the Canada ice shelf is estimated at $\approx$ 1 km.yr^{-1} which is comparable to the recent measurements carried out over the Ross ice shelf (Antarctica). The existence of large ice shelf covering the entire Arctic Ocean would imply a mean annual velocity of icebergs of $\approx$ 12 km.yr^{-1} through the Fram Strait. These estimates, assuming the equilibrium of the ice shelves, are based on their total mass balance, the input ice flux from the Laurentide and Eurasian ice sheets and on the basal melting flux from the Ross ice shelf adjusted to the area of each ice shelf (our simulations do not include any realistic marine processes involving the ice shelf). These estimates are realistic and show that both ice shelf configurations could occur under the MIS 6 climatic conditions.

Paper 5: The Late Saalian climate dynamics (in preparation)

In this last study the evolution of climate is considered throughout the entire Late Saalian period by simulating the 140, 150 and 160 ka timeslices in order to understand the relative stability of the Eurasian ice sheet. Paper 5 is, in a sense, a synthesis paper where the methods used in Papers 1-4 are applied to reconstruct for each considered time-slice the dust deposition on snow distribution (Colleoni *et al.*, 2009a), to simulate the vegetation cover (Colleoni *et al.*, 2009d) and the surface ocean conditions (Colleoni *et al.*,

2009b, , submitted). We use LMDZ4 (Hourdin *et al.*, 2006), Planet Simulator (Fraedrich *et al.*, 2005) and BIOME4 (Kaplan *et al.*, 2003).

As in Paper 3, we simulate the 140, 150 and 160 ka SST by prescribing the oceanic flux corrections obtained from a 21 year long LGM run (forced by Paul & Schaefer-Neth (2003) SST) using Planet Simulator and adjusting the orbital parameters and the CO_2 to each time-slice. Equilibrium is reached after 50 model years. The derived SST are thereafter used to force LMDZ4 to simulate the Late Saalian climate over 21 model years. Subsequently, three asynchronous iterations between LMDZ4 and BIOME4 are performed to compute vegetation in agreement with the regional climate. The last LMDZ4 iteration of each time-slice (FULL140, FULL150 and FULL160) is further used for analysis and the last BIOME4 iteration (B3) is compared to the first one (B1) to address the evolution of the vegetation cover.

At 160 ka (perihelion in late boreal winter), the simulated SST in the Northern (Southern) Hemisphere are much warmer (colder) than at 140 ka (Paper 3) and the sea ice cover does not extend as far south and is quite similar to the CLIMAP sea ice extent during both winter and summer. Vegetation is mainly constituted by tundra along the entire margins of the Eurasian ice sheet and in Siberia. However, Northern Siberia also presents some barren soil areas due to the accumulation of a permanent snow cover. BIOME4 also allows taiga and mixed forest to develop in Europe and Central Eurasia. The Northern Hemisphere climate 160 ka is warmer and generally milder than at 140 ka due to the lower eccentricity combined to a different precession effect generating warmer surface ocean conditions and warmer atmospheric conditions. Consequently the mean annual SMB is slightly affected by main ablation along the Russian and western European margins but is positive and in fact larger than at 140 ka.

At 150 ka (perihelion in early boreal summer), the simulated SST in the Northern (Southern) Hemisphere are also much warmer (colder) than at 140 ka. SST are warmer than at 160 ka during fall due to the delayed response of the ocean to the larger high latitude summer insolation. Likely because of this, sea ice cover 150 ka is the least extended for the entire Late Saalian period during both winter and summer. During summer, the Eastern Norwegian Sea is open similarly to the Paul & Schaefer-Neth (2003) LGM reconstruction. Tundra is less extensive than at 160 ka especially in Europe and in the Russian Plains and the barren soil area is decreased compared to 160 ka. On the contrary, taiga and mixed forest develop farther to North in these regions. The Northern Hemisphere climate is warmer and milder compared to 160 ka and 140 ka most likely as a consequence from the effect of precession. The mean annual SMB is strongly influenced by increased ablation along the entire southern margins of the Eurasian ice sheet. However, compared to 160 ka and 140 ka, the larger precipitation rate induces a larger SMB over the entire ice sheet which compensates for the ablation increase along the southern margins. Consequently, the SMB is positive and comparable to that calculated for 160 ka.

Finally at 140 ka (perihelion in early boreal winter), the large eccentricity enhances the effect of precession and causes a major cooling of the surface ocean. As a result, the sea ice cover reaches as far south as 40°N in both the North Atlantic and the North Pacific during winter and summer. This reduced seasonality is due to cool spring and summer which reduce the sea ice melting. Tundra is more extended compared to than at 150 ka and 160 ka but the barren soil area has increased due to a larger permanent snow cover. As a consequence, the taiga and mixed forest northern limits are shifted southward. The 140 ka Northern Hemisphere climate is the coldest during of the entire Late Saalian period. The mean annual SMB is not affected by ablation, not even during summer due to the large snow accumulation along the margins positively contributing to the SMB through the snow-albedo feedback. However, the large sea ice cover prevents most of the evaporation and moisture fluxes over the North Atlantic which represents the main moisture source for the Eurasian ice sheet. Therefore, accumulation over the ice sheet is reduced compared to 150 ka and 160 ka and the SMB, although positive, is the smallest during the entire Late Saalian period.

Our simulations clearly match the Late Saalian Eurasian ice sheet chronology: a large ice sheet at 160 ka, a retreat 150 ka and a readvance 140 ka but not enough in order to become as large again as 160 ka. The retreat at 150 ka is expressed through the negative SMB along the entire southern margins, and the readvance during

the Late Saalian glacial maximum is manifested by the very cold simulated Northern Hemisphere climate despite the fact that our simulations does not account for the deep ocean circulation. From our experiments, we therefore propose that the Late Saalian climate and ice sheet evolution during this period is mainly driven by orbital forcings. However, to better assess the climate and ice sheet dynamics, it is necessary to performed Atmosphere-Ocean coupled simulations as well as ice sheet dynamics simulations.

Discussion

This work focuses on the Late Saalian glacial period spanning 160-140 ka coinciding with MIS 6, and preceding the last interglacial commonly referred to as the Eemian or MIS 5.5. The three scientific questions for this thesis outlined in the introduction originated from the ice sheet extension maps produced by the QUEEN project (Svendsen *et al.*, 2004) which showed that the Late Saalian Eurasian ice sheet extended further to south and east over Eurasia than the Early, Middle and Late Weichselian ice sheets. In this section, I will further discuss the results from the simulation experiments of Chapters 2-6 and the three formulated scientific questions on the nature of the Late Saalian ice sheet and its interaction with the contemporary climate. The critical boundary conditions are further explored by a set of new simulations designed to test scenarios that were omitted in the published articles.

The Late Saalian glacial maximum appears to have taken place around 140 ka. This time presents a larger precession effect compared to the LGM (Table 1.1). In fact, the entire Late Saalian exhibits larger eccentricities than during the 40-21 ka period while obliquity shows a similar evolution. In turn, a larger eccentricity causes the effects from precession to become enhanced. Despite that there are clear differences between orbital parameters, greenhouse gas concentrations seem to have been nearly equal during the Late Saalian and the LGM (Table 1.1).

To address the ice sheet and climate dynamics through simulations primarily with the AGCM LMDZ4, we first needed to reconstruct some of the critical 160-140 ka boundary conditions such as dust, proglacial lakes, vegetation cover, and sea-surface temperature (SST). An Arctic Ocean large floating ice shelf was also investigated as existing geological evidences indicate that such feature existed during the MIS 6 (e.g. Jakobsson *et al.*, 2008b). In summary, this is the logic order for the reconstructions of the boundary conditions used in the simulations:

1- dust deposition on snow was reconstructed for 140 ka using information from the Antarctic ice cores.

2- proglacial lakes have been outlined for 140 ka and such large bodies of water have been shown to affect the local temperature along the ice sheet margins with consequences for SMB (Krinner *et al.*, 2004).

3- the 140 ka vegetation cover was simulated in agreement with the boundary conditions specified in 1 and 2. SST at 140 ka were first simulated independently prescribing a LGM vegetation map, but using dust deposition on snow and proglacial lakes adapted to the Late Saalian (points 1 and 2).

4- we then computed SST in agreement with the Late Saalian climate for the three timeslices 140 ka, 150 ka and 160 ka adapting all the boundary conditions following the methods used in the articles presented in Chapters 2 - 4.

5- Finally we calculated a vegetation cover in agreement with the climate of each snapshot for 140, 150 and 160 ka to obtain an overview of the climate dynamics of the entire Late Saalian glacial period.

On the Late Saalian boundary conditions

Dust deposition on snow

The main feedback caused by dust deposited on snow is to melt the snow cover during spring through a decrease in local albedo. We did not explore the impact from a larger dust deposition rate, in line with what has been estimated for the LGM, during the Late Saalian in any of the experiments included in the articles. Therefore, I performed two Late Saalian 21 years snapshots: DUST21 using the LGM dust deposition map (Mahowald *et al.*, 1999) and REF without any dust deposition on snow.

As described in Paper 1, the LGM Antarctic atmospheric dust content recorded in ice cores

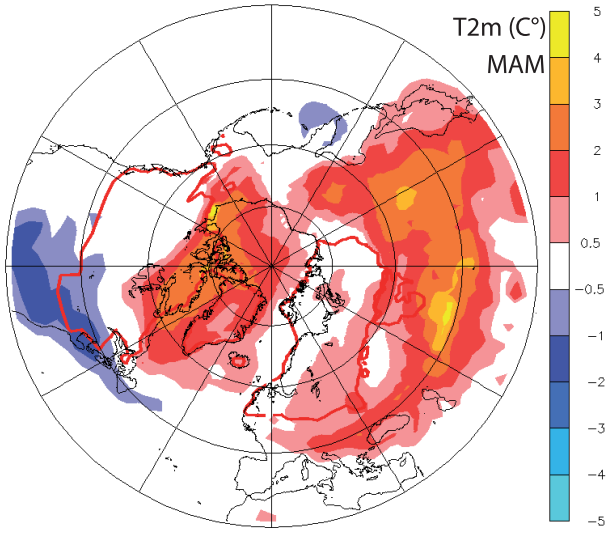

	REF	DUST21
Tot. precip.	296	302
Snow	282	285
Evap.	49	53
Abl.	8	14
SMB	225	218

Figure 1.20: Spring temperature anomaly between DUST21 and REF (°C). Mean annual surface mass balance (kg.m^{-2}.yr^{-1}) and its components for the two simulations DUST21 and REF.

is about 40% larger than the Late Saalian. In DUST21 we thus account for a 40% larger dust deposition rates than in the adapted map in Paper 1. Note also that contrary to the Late Saalian map in which we artificially removed some dust overlapping the Eastern part of the Eurasian ice sheet, DUST21 accounts for the original Mahowald *et al.* (1999) LGM map without any modifications.

During spring, the dust deposition on snow in DUST21 causes a warming of 3°C over the entire Eurasia (Figure 1.20). This anomaly reaches the southern part of the Eurasian ice sheet. Consequently, the SMB is characterized by a larger ablation in DUST21 but compared to REF, the difference is not statistically significant. Finally the mean annual SMB is lower in DUST21 (218 kg.m^{-2}.yr^{-1}) than in REF (225 kg.m^{-2}.yr^{-1}) but again, this difference is not significant. This shows that even if our Late Saalian dust deposition map, presented in Paper 1 and used for all the 140 ka simulations, is an adaptation of the LGM (Mahowald *et al.*, 1999) reconstruction, increasing dust deposition rates in Eurasia (even over the Eastern part of the ice sheet) does not influence the mean annual SMB of the Eurasian ice sheet significantly.

Proglacial lakes

In Paper 1, we showed that ice-dammed lakes cool the summer climate due to their low thermal inertia and this significantly reduced ablation along the southern margin of the Late Saalian Eurasian ice sheet. However, there are no direct geological evidence of huge Late Saalian Siberian ice-dammed lakes, such as for examples dated paleo-shorelines or other lake deposits. On the other hand, the paleotopography with the ice sheet in place strongly suggests that ice-dammed lakes should have formed in front of the ice sheet's southern margin.

	REF	**LAKE100m**	**LAKE235m**
Total precip.	351	336	341
Snow	313	303	310
Evap	68	65	65
Ablation	89	74	61
SMB	156	164	184

Table 1.5: Mean annual surface mass balance (SMB) values and components for simulations REF, LAKE235m (see Paper 1) and LAKE100m in kg.m^{-2}.yr^{-1}. "Total precip." stands for Total precipitation

Therefore, we followed the approach of Mangerud *et al.* (2004) and assumed that lakes developed and drained into the Caspian Sea via the Turgay Pass (Figure 1.21a). The reconstructed Late Saalian ice-dammed lakes in Siberia reached a size of 1.86×10^6 km^2, but since we do not have any geological evidence to support this reconstruction, I test the impact of a different lake morphology. Instead of filling with water up to a level of 235 m above present sea level as in Paper 1, the topography is filled only up to 100 m (Figure 1.21b). Lakes are then confined to the Southern ice sheet margin exclusively.

The effect from these much less extensive ice-dammed lakes is that during summer, the temperature cooling is of the order of ≈8°C over the lakes (Figure 1.21c). However, contrary to the

cooling generated by the large proglacial lake in Paper 1, this cooling does not impact on the temperature over the southern margin of the Late Saalian ice sheet. The lake is not large enough to cause an anomaly extending in altitude; the cooling is blocked by the ice sheet's steep topography. The cooling induced by the lakes only spreads southward, where topography is flat enough to not stop the atmospheric circulation. The amplitude of the summer cooling over the lake is comparable to that simulated in Paper 1. In summary, changing the sizes of the ice-dammed lakes does not impact on the amplitude of the temperature anomalies, but the spatial extent of the cooling effect is smaller.

Although the regional climate is not strongly affected by the presence of the Siberian proglacial lake, the SMB of the nearby ice sheet shows differences (Table 1.5). Ablation and evaporation are reduced compared to REF as well as precipitation. The reduction in precipitation is less important than the reduction in ablation and evaporation. The mean annual SMB of the ice sheet is thus larger in LAKE100m (164 kg.m^{-2}.yr^{-1}) than in REF (156 kg.m^{-2}.yr^{-1}). However, compared to REF, the difference in SMB is statistically significant based on the Student t-test as explained in Paper 1. In Paper 1, the decrease in SMB is significant and larger than that caused by the small Siberian proglacial lake.

To conclude, the variation of the size of proglacial lakes induce significant changes of the SMB of the Eurasian ice sheet's southern margin even if the spatial extent of the induced cooling is substantially different. However, changes in SMB are not proportional to the prescribed proglacial lake size (see also Paper 1). Since the Late Saalian Eurasian ice sheet is sensitive to changes in regional parameters nearby its southern margin, the reconstruction of proglacial lakes requires attention.

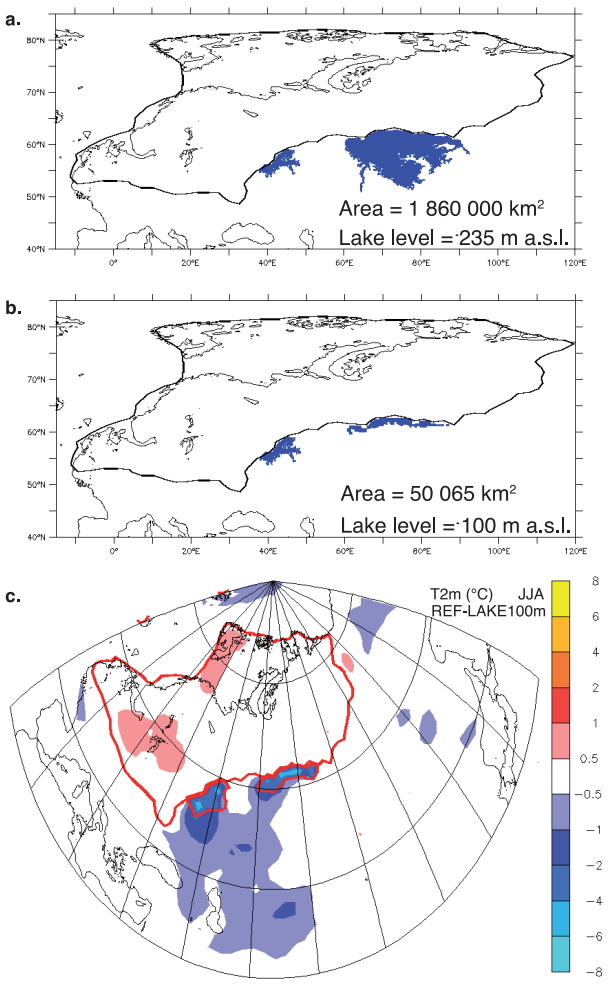

Figure 1.21: In simulation LAKE100m, we only reduced the Siberian lake compared to that used in Paper 1. a. Proglacial lakes used in Paper 1, the lake have been fill until the topographic level 235 m. b. Proglacial lakes used in LAKE100m. We fill the Siberian deflection south to the ice sheet until the topographic level 100 m above the Late Saalian sea level. c. Difference in summer temperature (°C) between simulations LAKE100m and REF (with no proglacial lakes). Area of the lakes in both case is indicated in the figure (Mediterranean area is ≈2 510 000 km^2).

Vegetation

To compute vegetation cover in equilibrium with our Late Saalian simulated climates, we used BIOME 4 (Kaplan *et al.*, 2003). We simulated both LGM and Late Saalian vegetation cover using an asynchronous coupling between this model and the LMDZ4, similarly to de Noblet *et al.* (1996). Our computed vegetation has a large band of taiga and mixed forest towards 40°N (Paper 2), even in the coldest climatic conditions of the Late Saalian simulation forced with the simulated SST at 140 ka (Chapter 6).

The debate concerning the growth of trees in Eastern and Western Europe during the LGM glacial maximum is still ongoing. The emerging vision of the LGM vegetation is that refugials allowed trees to grow under glacial conditions. This is supported by pollen evidences (e.g. Willis & van Andel, 2004; Tarasov *et al.*, 2000, 2007). But in our reconstructions, BIOME 4 allows a continuous East-West belt of forest to develop for which the northern limit corresponds to the

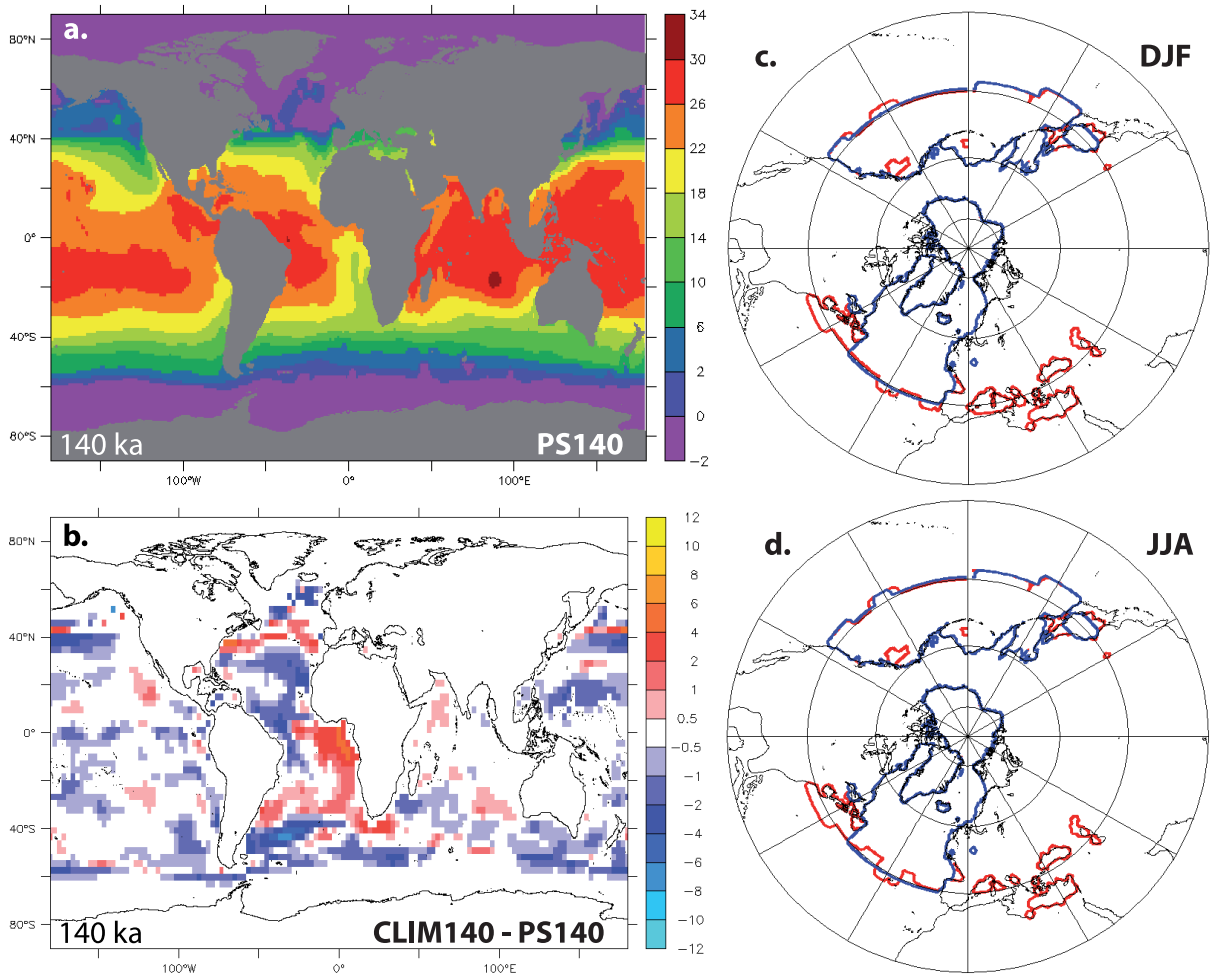

Figure 1.22: Comparison between the simulated 140 ka sea surface temperatures PS140 and CLIM140 obtained prescribing ocean heat fluxes based on LGM Paul & Schaefer-Neth (2003) and LGM CLIMAP (1981) SST respectively (Section 1.3). a. Simulated 140 ka SST based on LGM Paul & Schaefer-Neth (2003) ocean heat fluxes; b. difference between simulated CLIM140 and PS140 SST; c. and d. 140 ka simulated sea ice cover for winter (DJF) and summer (JJA) for the two SST reconstructions: CLIM140 (blue), PS140 (red).

10°C summer isotherm. The reason why an extended forest area is derived by BIOME 4 even under severe glacial conditions may be that the model does not account for the effects of permafrost.

Alfano *et al.* (2003) simulated the vegetation cover during the 60 - 20 ka time period using BIOME 3.5 to test the sensitivity of various factors such as temperatures and permafrost. The results show that BIOME 3.5 fails to compute a permafrost extent southward that conforms with the geological evidence. This will stop tundra from developing much southward at the expense of other biomes, which may partly be the explanation of our simulated forest belt, in disagreement with the LGM refugial hypothesis supported by pollen data. This bias might have also been propagated in the Late Saalian experiments.

Late Saalian surface ocean

In Paper 3, we simulated the Late Saalian sea surface temperatures (SST) using Planet Simulator (Section 1.3, Fraedrich *et al.*, 2005). We obtained very cold sea surface temperature and a sea ice cover reaching 40°N in both the North Atlantic and the North Pacific (Figure 1.22a). However, as discussed in Paper 3, the fact that Planet Simulator does not model the deep circulation enhances the impact of orbital forcings on the surface ocean and in our case results in the strongly asymmetric temperature change between the Northern and Southern Hemisphere.

For the reconstruction of Paper 3 we used Paul & Schaefer-Neth (2003) SST to get LGM ocean heat fluxes corrections. But how would the scenario look like regarding the Late Saalian SST if we used another SST reconstruction, such

as CLIMAP (1981) SST to compute LGM ocean heat fluxes corrections? In order to test this, I followed the methods described in Paper 3 and carried out one more Late Saalian simulation (CLIM140) using CLIMAP LGM ocean heat fluxes for the interest of this discussion. To facilitate reading, simulated Late Saalian SST derived from Paul & Schaefer-Neth (2003) LGM ocean heat fluxes is called PS140 (same as PS140 in Paper 3).

When using CLIM140 to force the Late Saalian climate, this leads to colder SST than when using PS140 (Figures 1.22c and d). The difference in SST generated by the discrepancy between CLIM140 and PS140 is not large since CLIMAP and Paul & Schaefer-Neth (2003) are both LGM SST reconstructions. However, the 140 ka SST using CLIM140 are warmer in the tropic and toward 40°N by 4°C than when using CLIM140. On the contrary, the equatorial, South Atlantic and North Pacific are colder by about 2°C. Sea-ice cover extends similarly to 40°N in the two simulations during both winter and summer.

Whichever of the tested sets of LGM SST is used to compute ocean heat fluxes, the simulations of the 140 ka glacial maximum using these heat fluxes will yield similar SST. The sea ice cover seems not to be sensitive to the prescribed ocean heat transport since the extensions are similar in the two simulations. On the other hand, the simulations seem to respond strongly to the 140 ka orbital forcings. Khodri *et al.* (2005) showed that precession at 115 - 120 ka ("friendly-glacial configuration") reduced the sea ice cover spring melting leading to a reduced seasonality. Moreover, precession influences surface ocean shifting the polar front southward in the North Atlantic with consequences for the position of the subpolar and subtropical gyres. This may explain why the sea ice cover in our 140 ka experiments extends farther to the South compared to what is observed for the LGM limit.

Since we focus on a glacial period, it seems more appropriate to use glacial ocean heat transport to force the Late Saalian climate as we did in Paper 3. However, as also discussed in Paper 3, the 140 ka SST forced by the LGM Paul & Schaefer-Neth (2003) ocean heat fluxes are colder in the North Atlantic and in the North Pacific than the marine sediment cores SST records show while they are in good agreement in the tropics. Our simulated Late Saalian SST only account for the orbital forcings and do not redistribute the excess of heat over high latitudes. This leads to an underestimate of the Northern Hemisphere SST compared to the marine sediment cores data.

Ice topography: mass conservation

In all our experiments, we prescribed the North American and Antarctica LGM ice sheets from ICE-5G (Peltier, 2004). The author is not aware of literature addressing the Late Saalian Laurentide ice sheet geological extent as well as its dynamics. Since in North America the LGM moraines are the more extensive than for the other previous glacial periods, it appears probable that the Late Saalian Laurentide ice sheet was of comparable size or smaller than during the LGM. Previously, we indicated that the global Late Saalian ice volume ranges between 92 m and 150 m equivalent sea level (ESL) and that we choose to prescribe a -110 m sea level (Astakhov, 2004) in our experiment. What are the implications of this choice?

- **ESL is $\approx$ 92 m below present-day sea level**: the Eurasian ice sheet equals to 61 m ESL, the ICE-5G Laurentide is 84 m ESL and Antarctica contributes 17 m ESL. This leads to a large excess in ice volume of about 70 m ESL! Consequently, the contribution of the Laurentide and Antarctica has to be largely reduced to equilibrate the eustatic sea level. This means that in any case, Laurentide is much smaller than in ICE-5G.

- **ESL is $\approx$ 150 m below present-day sea level**: since the total contribution of all ice sheet is of $\approx$ 162 m ESL, this leads to an excess of 12 m, easily removable from the Laurentide ice sheet and/or Antarctica. Consequently, Laurentide ice sheet will be slightly lower than in ICE-5G.

- **ESL is $\approx$ 110 m below present-day sea level**: The excess is of 52 m ESL. This requires at least a 50% reduction of the thickness of the LGM Laurentide.

The reduction of the Laurentide ice volume results in a reduction in elevation and should have consequences on the atmospheric circulation (Kageyama & Valdes, 2000) which might influence the surface mass balance of the Eurasian ice sheet.

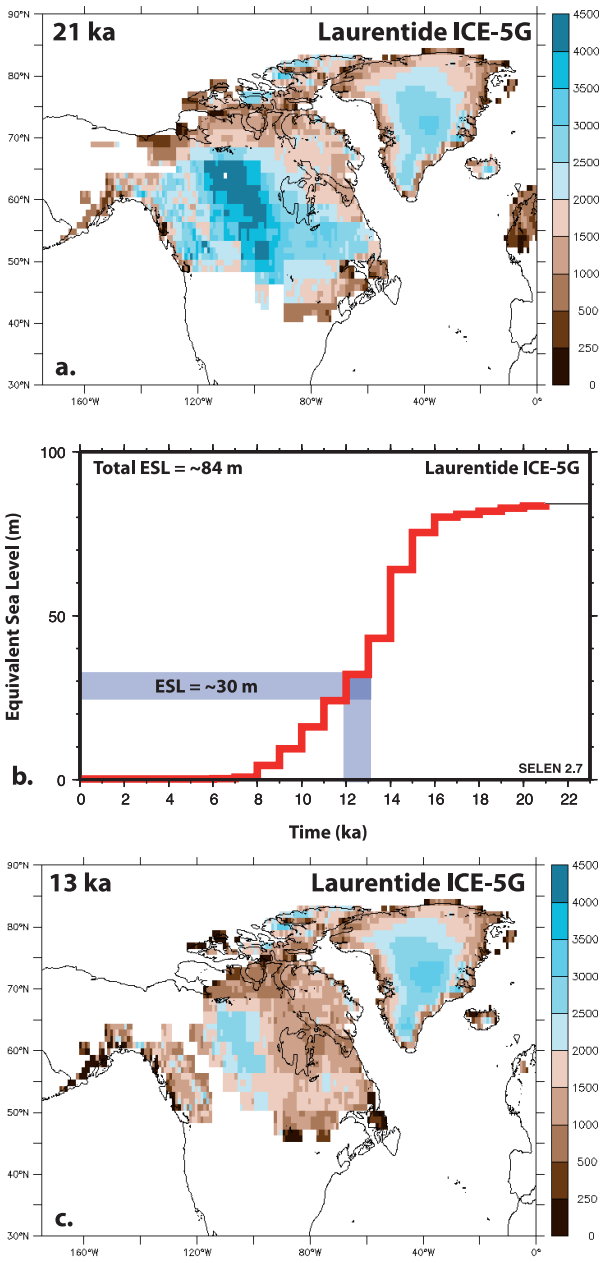

Figure 1.23: Impact of a reduced Laurentide on Late Saalian climate in the Northern Hemisphere. a. ICE-5G Laurentide ice topography at LGM (Peltier, 2004), b. Equivalent Sea-level deglaciation chronology of the ICE-5G Laurentide from LGM to present-day using SELEN isostatic model (Spada & Stocchi, 2007). Since the LGM, Laurentide contributed 84 meters to sea level rise. For our experiment, we use the Laurentide ICE-5G snap-shot corresponding to about 30 m ESL (occurring at 13 ka), coherent with the total Late Saalian eustatic sea level. c. ICE-5G Laurentide ice topography at 13 ka.

However, Kageyama & Valdes (2000) investigated the effect for the LGM during which the Eurasian ice sheet was substantially lower than during the Late Saalian. To test whether a significant reduction of the ice volume of the Laurentide ice sheet significantly influences the surface mass balance of the Late Saalian Eurasian ice sheet, we performed two 140 ka snap-shots using LMDZ4: one Late Saalian reference simulation with the LGM Laurentide topography (Lau21) and one using a smaller Laurentide topography (Lau13). In Lau13, the total eustatic sea level implies at least a reduction of the Laurentide ice volume from $\approx$ 84 m ESL to 30 m ESL (Figure 1.23a and c). We thus assume that the remaining 22 m ESL are removed from Antarctica). Since we do not have any Laurentide reconstruction, we used the snap-shot of ICE-5G in which the Laurentide ESL equals $\approx$ 30 m. This occurs toward 13 ka (Figure 1.23b). Boundary conditions are set for both experiments using Paul & Schaefer-Neth (2003) LGM SST, dust deposition and proglacial lakes adapted as detailed in Section 1.4.3 and 1.4.2, Crowley (1995)'s LGM vegetation map, and GHG and orbital forcing for 140 ka and a sea level of -110 m a.s.l.

	Lau13	Lau21
Total precipitation	284	303
Snow	271	288
Evap	50	51
Ablation	12	11
SMB	208	221

Table 1.6: Surface mass balance (SMB) values and components for both simulations Lau13 and Lau21 in kg.m^{-2}.yr^{-1}.

Compared to the LGM Laurentide, the elevation at 13 ka is reduced by 50%. The ice sheet does not reach Alaska and does not extend to the South as much as during the LGM. This induces a large positive temperature anomaly of $\approx$ 8° to 12°C over North America (Figure 1.24a). The different ice topographies impact on the large scale circulation of the Northern Hemisphere. Several studies have shown that during the Northern Hemisphere glacial winter the jet stream splits into two main branches (e.g. Kutzbach & Wright, 1985; Rind, 1987; Bromwich *et al.*, 2004) (Figure 1.24c). The northern branch of the split jet maintains strong cold air advection over eastern Canada and the North Atlantic, while cyclones developing along the southern branch are responsible for enhanced precipitation along the southeastern Laurentide Ice Sheet margin. In Lau13,

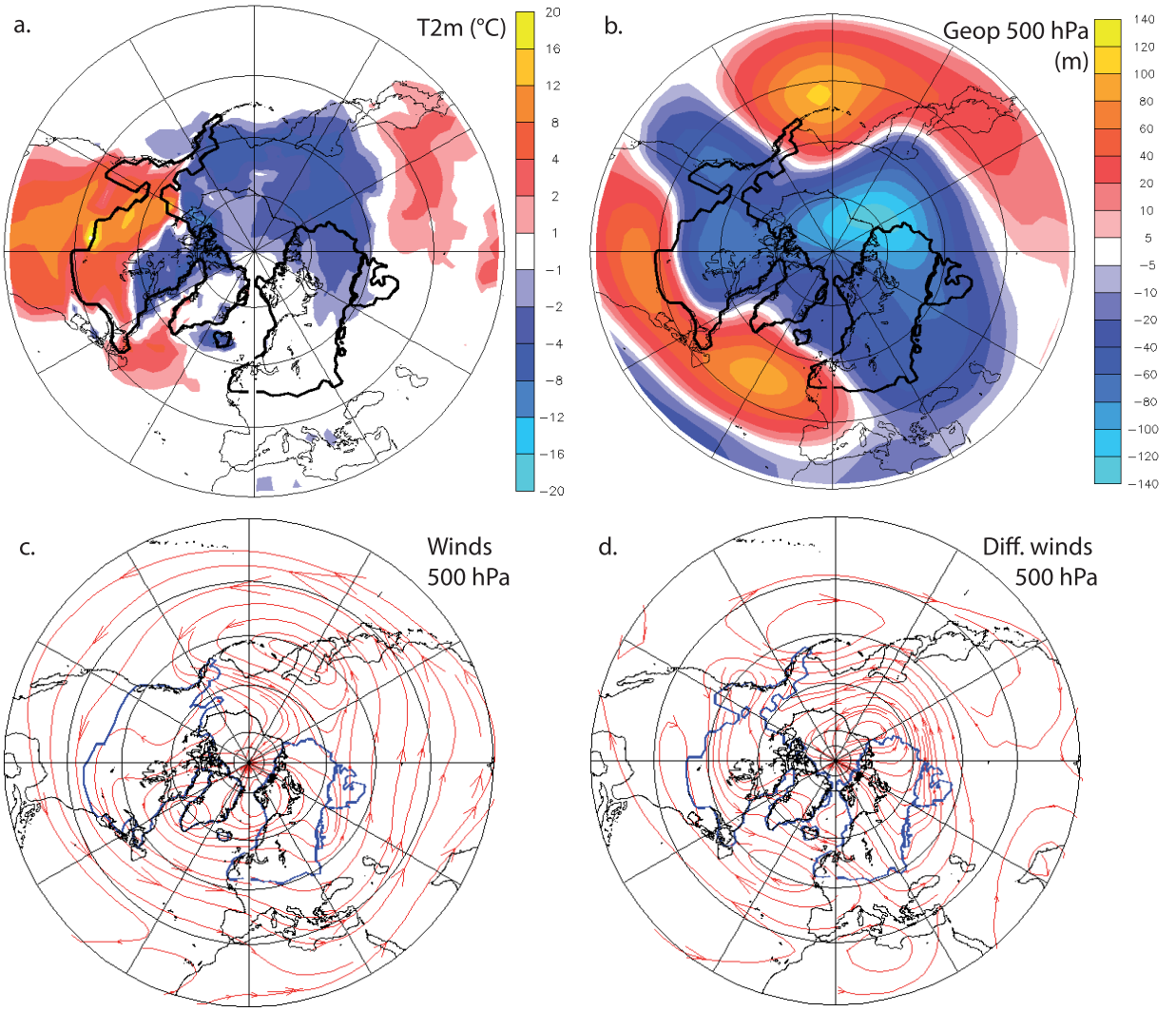

Figure 1.24: Impact of a reduced Laurentide on the January Late Saalian climate in the Northern Hemisphere. a. difference (Lau13 - Lau21) in surface air temperature (m), b. difference (Lau13 - Lau21) of the height of the 500 hPa geopotential (m), c. 500 hPa winds flowlines for simulation Lau21. Split jets are clearly visible over the Laurentide ice sheet, d. Difference in 500 hPa winds between Lau13 and Lau21.

the lower elevation causes a reduction in the January jet streams intensity and slightly modifies their direction. This increases the anticyclonic activity over Eastern Siberia inducing a negative anomaly of about -4°C (Figure 1.24a). This cooling also affects the eastern margin of the Eurasian ice sheet (≈ -2° to -4°C). The changes in elevation also influence the mid-tropospheric circulation patterns causing a large positive anomaly in 500 hPa geopotential height along the southern margin of the Laurentide ice sheet while a large negative anomaly develops over the Canadian Arctic and the entire Eurasia reflecting modifications in the jet stream intensity and direction.

Mean annual surface mass balance of the Eurasian ice sheet is significantly affected by the lower Laurentide and induced-changes in large scale circulation (a bilateral student t-test was performed with a probability threshold $<$ 0.05%). Compared to Lau21, precipitation is decreased significantly by 20 kg·m^{-2}·yr^{-1} due to the decrease in temperature over the Eastern part of the ice sheet (Figure 1.24 and Table 1.6). On the contrary, ablation is similar in both simulations since no melting is observed in the reference run Lau21. Mean annual surface mass balance is consequently lower in Lau13 than in Lau21 due to a reduction in precipitation over the Eastern part of the ice sheet.

To conclude, a lower Laurentide, matching the total Late Saalian eustatic equivalent sea level used in this work, induces changes in the surface mass balance through decrease in local pre-

cipitation (caused by changes in circulation) but does not induce more ablation. We prescribed the LGM Laurentide as first approximation. Here that a smaller Laurentide significantly reduces the SMB of the Eurasian ice sheet although this does not represent a major impact. However, the impact over Eurasia is important since it causes a mean annual cooling of about 4°C over the Eastern Siberia (not shown) with a similar spatial pattern to that occurring in January (Figure 1.24a) reducing the snow melting during spring in this area. This might increase the stability of the Siberian part of the ice sheet which is an area that remained unglaciated during the following glaciations of the Weichselian cycle.

Orbital forcings

During the Late Saalian, eccentricity (enhancing the effect of precession) and obliquity were larger than during the LGM. In this work we never tested the impact of orbital parameters on the Northern Hemisphere climate and on the surface mass balance of the Late Saalian Eurasian ice sheet compared to the LGM. We thus performed one 21-years snap-shot using LMDZ4 and including all the 140 ka boundary conditions but accounting for the LGM orbital parameters (referred as ORBIT$_{21k}$. The reference simulation refers to as ORBIT$_{140k}$) (Table 1.1).

The difference in orbital forcings results in anomalies of the shortwave downward radiation at the top of the atmosphere: in ORBIT$_{140k}$, during the end of winter, spring and half of the summer, the Earth receives less radiation inducing a reduction of about 20 W·m^{-2}·yr^{-1} in the high latitudes between 50° and 70°N. On the contrary, the amount of solar radiation during fall is increased by about 40 W·m^{-2}·yr^{-1} at the same latitudes (Figure 1.25). This is also reflected by the paleo-climatic season length (Table 1.7). When using the LGM orbital parameters (ORBIT$_{21k}$), winter and fall are longer than during the Late Saalian (ORBIT$_{140k}$) whereas spring and summer are shorter. The main difference in season length occurs in spring which is particularly long during the Late Saalian due the large eccentricity. This contributes to keep a relatively important snow cover until summer, inducing cooler spring and summer temperatures at high latitudes during the Late Saalian.

Consequently during the Late Saalian summer, winter temperature are increased by 4°C over the Arctic Ocean, over Siberia and over the eastern part of the ice sheet (Figure 1.25a). On the contrary, summer is colder by about 4°C over the entire Eurasia and over the ice sheet when using the Late Saalian astronomical parameters (Figure 1.25b). This is of the same order than the temperature anomaly induced by orbital variations during the LGM discussed in Abe-Ouchi *et al.* (2007). This increases snow fall over Siberia especially during summer (Figure 1.25c and d). During winter, snow fall is increased by 40% in ORBIT$_{140k}$ over the ice sheet due to the warmer temperature induced by the orbital parameters while during summer, the global cooling causes a reduction in snow fall by about 40% over the ice sheet (Figure 1.25c and d).

	ORBIT$_{21k}$	**ORBIT$_{140k}$**
Winter	93	90
Spring	89	97
Summer	90	92
Fall	94	86
Tot. pre.	312	303
Snow	295	288
Evap	57	51
Abl.	17	11
SMB	221	221

Table 1.7: Length (in days) of the paleo-climatic seasons at 21 ka and 140 ka following the method of Berger & Loutre (1991). Surface mass balance (SMB) values and components for both simulations ORBIT$_{21k}$ and ORBIT$_{140k}$ in kg·m^{-2}·yr^{-1}. "Abl." stands for Ablation whereas "Tot. pre." corresponds to Total precipitation.

The surface mass balance (SMB) of the Eurasian ice sheet is not influenced significantly by the orbital forcings since even if ablation is slightly larger than during the full Late Saalian climate, precipitation are also increased since summer in ORBIT$_{21k}$ are warmer. Mean annual SMB also present equals values due to spatial compensation over the ice sheet.

The Late Saalian orbital configuration at 140 ka presents large eccentricity and obliquity values. This impacts on the seasons, highly cooling spring and summer and influencing the snow accumulation over continent (Khodri *et al.*, 2005), especially in Siberia which a particularly sensitive region. However, changes in orbital variations do not significantly influence the mean an-

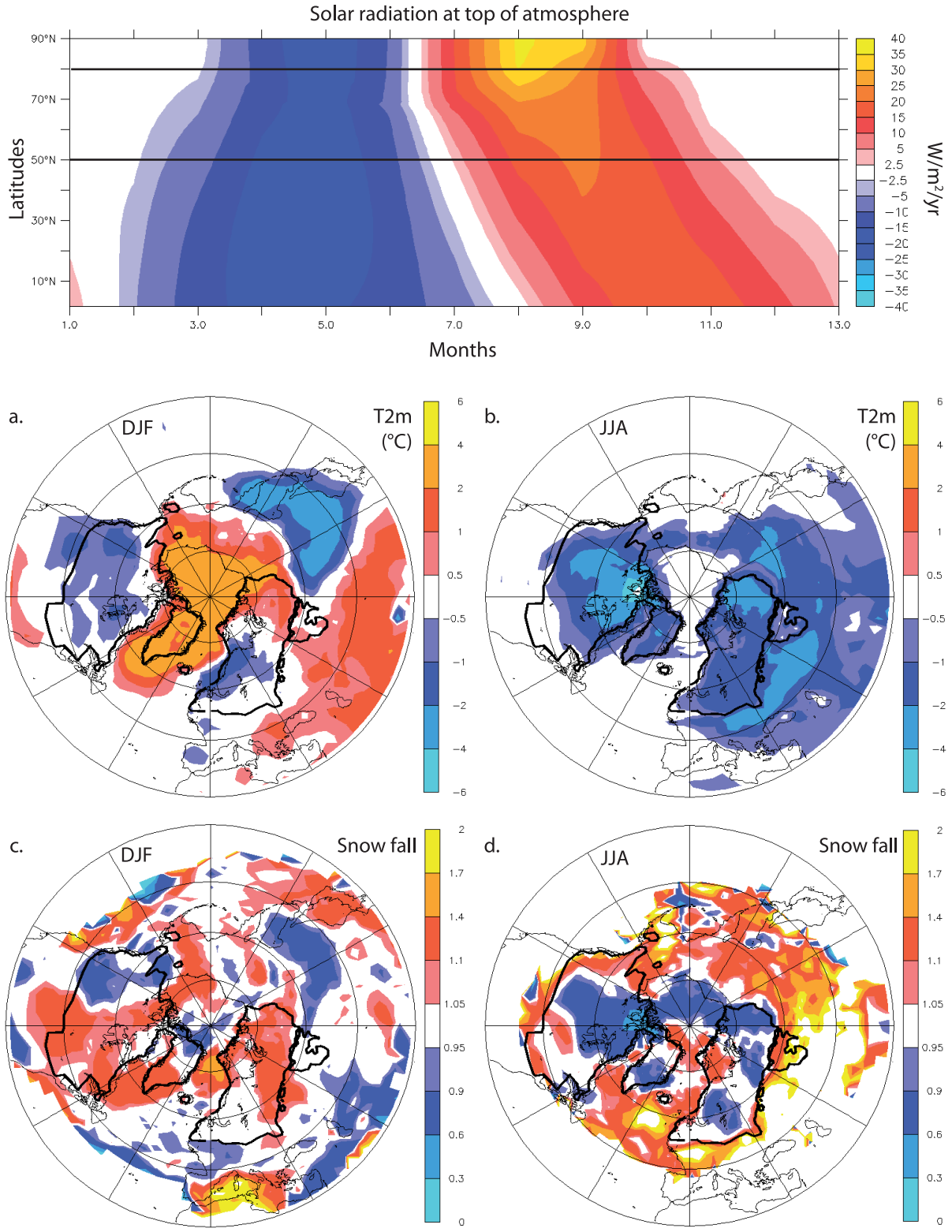

Figure 1.25: Monthly difference ($ORBIT_{140k}$ - $ORBIT_{21k}$) in shortwave downward radiation at top of atmosphere in the Northern Hemisphere in $W.m^{-2}.yr^{-1}$. Black line indicate the band in high latitudes of interest in this work (50° - 70°N). Climatic anomalies are expressed as the difference ($ORBIT_{140k}$ - $ORBIT_{21k}$): a. and b. temperature anomalies for winter (DJF) and summer (JJA), c. and d. mean annual snow fall anomaly (%)

nual surface mass balance. But the combination between this large eccentricity and precession might have had a great importance during the re-advance stage following the ice retreat of 150 ka, strengthening the ice sheet toward 140 ka.

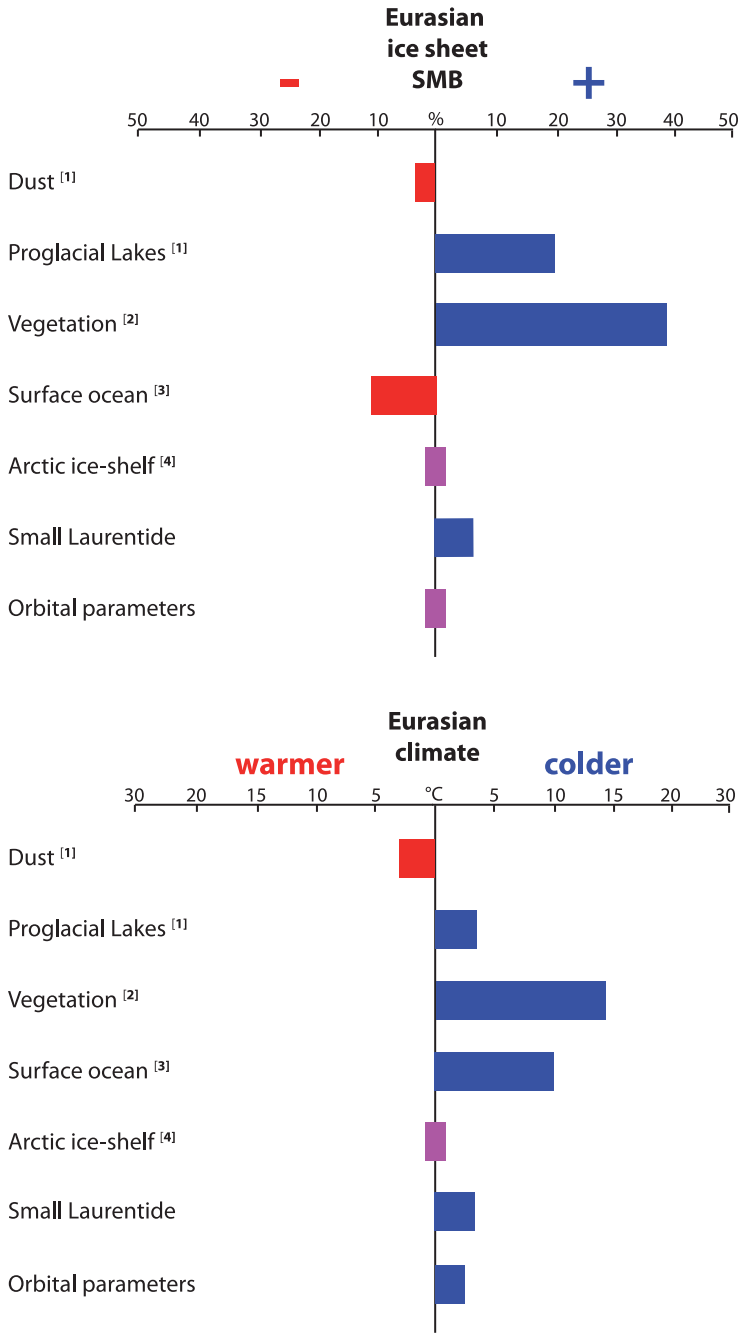

Figure 1.26: Synthesis of all the climatic contribution of the factors investigated in this thesis. Top: positive or negative contributions to the surface mass balance of the Late Saalian Eurasian ice sheet. Purple bars in the top frame indicate a negligible contribution to the surface mass balance. Bottom: influence on the Late Saalian Eurasian climate. Numbers in brackets refer to the published or submitted articles presented in this thesis.

Main conclusions

1- How could the Late Saalian ice sheet grow so large over Eurasia and remain stable until ≈ 140 ka and how did it impact on climate at that time?

Since the Late Saalian Eurasian ice sheet was unusually large and extended much more southward than during the LGM, its southern margin was sensitive to any changes in regional parameters.

In this work I have explored, in collaboration with my co-authors of the included articles, various regional and global factors that may have an impact on the Late Saalian Eurasian ice sheet's existence. We have shown that dust deposition on snow tends to warm the climate and increases melting during spring and sum-

mer. Proglacial lakes have an opposite effect and instead tend to cool the local climate. Since their surface remains frozen during spring and open during summer, their low thermal inertia causes a decrease in temperature which locally reduces the ablation along the margins. Simulated SST in agreement with the boundary conditions, dust, proglacial lakes and vegetation as well as the Late Saalian climate are significantly colder than the LGM SST used as first approximation to force the AGCM simulations. With the simulated SST, sea-ice cover reaches 40°N in both North Atlantic and North Pacific. This generates a mean annual Northern Hemisphere cooling of about 10°C. Reducing the Laurentide elevation leads to a regional cooling over Eastern Eurasia due to the northward migration of the Siberian high during winter which occurs simultaneously to a lower intensity of the split jets. All these effects, except that of dust, mainly influence the amount of snow fall and the melting season of the continental snow cover which in turn increases the albedo, cooling the atmosphere (Figure 1.26).

However, the main climatic impact comes from the orbital forcing through the combination of a large eccentricity and a favourable precession angle (Figure 1.25). The 140 ka astronomical configuration decreases the amount of insolation received by the Earth in the high latitudes, especially during spring and consequently, substantially reduces the snow cover melting. Compared to LGM one, the orbital configuration of 140 ka should result in cooler springs and summers which are the two seasons during which the ice sheet is more subject to ablation. However, fall occurs at perihelion leading to higher insolation at this time of the year. Our simulated SST reacted directly to astronomical forcings and as discussed in Paper 3, Khodri *et al.* (2005) show that favourable precession induces a migration of the polar front to South and reduces the melting of the sea ice cover during spring.

From the experiments in this thesis I suggest that the large Late Saalian ice sheet 140 ka results mainly from the orbital configuration that stopped snow from melting during spring. This seems to be the main factor that allowed the Eurasian ice sheet to grow further southward than during LGM. The regional parameters (proglacial lakes and vegetation) help to this relative stability since they all cool the Eurasian climate (Figure 1.26), but they have a more weaker impact on the growth of the ice sheet than the orbital forcings. However, once the Late Saalian Eurasian ice sheet reached its maximum extent, we show that its surface mass balance decreases due to the lack of accumulation caused by the orbitally-driven global Northern Hemisphere cooling.

2- Was the impact of the ice sheet on atmospheric processes similar to during other glaciations?

In Paper 2 and Paper 3, we compared the impact of the simulated vegetation and prescribed sea surface conditions on the LGM climate and Eurasian ice sheet. Krinner *et al.* (2006) have shown that dust deposition on snow stopped the Eurasian ice sheet from growing over Siberia at the LGM. We have shown that changes in the vegetation cover affected the Late Saalian ice sheet more than the LGM. This is because the Late Saalian ice sheet extended further to the South and consequently was more sensitive to any variations in the regional parameters along the southern margin (more subject to ablation). On the contrary, the LGM Eurasian ice sheet had a limited southward extent and consequently was not as sensitive as the Late Saalian to changes occurring over Central Eurasia.

However, in Paper 3, we show that the LGM Eurasian ice sheet is sensitive to modifications in the prescribed North Atlantic sea surface conditions since most of its volume is concentrated along the Atlantic and Arctic Eurasian margins. The Late Saalian ice sheet is not as sensitive to the North Atlantic oceanic conditions since most of its volume is concentrated further eastward in the Russian and Siberian plains and compensates for the climatic fluctuations occurring northward.

Finally, during the LGM, eccentricity was less important than during the glacial maximum of the Late Saalian but obliquity was quite similar. The lower LGM Eurasian topography presented less obstacles to the atmospheric circulation over Eurasia. During the Late Saalian, most of the westward large-scale circulation coming towards Eurasia was confined to the Arctic region while that originating in the North Pacific was limited to Eastern Siberia.

How could the ice sheet survive the insolation peak at ≈ 150 ka?

In Chapter 6, we have explored the entire Late Saalian period simulating the 140, 150 and 160 ka time-slices. From geological evidences, we know that the Late Saalian was subdivided into three substages: two stadials, one before ≈160 ka, one interstadial ≈155 ka and the glacial maximum ≈143 ka (140 ka is used in the text). It seems that despite an orbital configuration that induces a warmer climate in the Northern Hemisphere, only the southern margin of the Late Saalian Eurasian ice sheet was affected by summer ablation at 150 ka. Moreover, since the Northern Hemisphere climate was warmer, precipitation was larger than at 140 ka and 160 ka and the surface ocean showed open water conditions during summer. As a result, accumulation was larger at 150 ka over the entire Eurasian ice sheet and this compensated for the strong ablation along the southern margins. Consequently, it seems that the large Eurasian ice sheet was able to survive the 150 ka interstadial because of its large volume and high topography that autogenerated a regional cooling and because of the large precipitation rates indirectly caused by the astronomical forcing.

Following the geological evidence and the results from Chapter 6, I suggest that the ice sheet retreat at 150 ka might have been therefore limited and when orbital forcings turned into a more glacial configuration at 140 ka, the ice sheet might have re-advanced a last time but not until its previous position of 160 ka. In particular, this re-advance might have been limited by the lower precipitation rates and moisture fluxes cancelled by the large southward sea ice cover resulting from the orbital forcings. However, although lower than at 160 ka, the simulated surface mass balance still remains positive.

Perspectives

With this study I address half of the problem with my co-authors: the relative maintenance of the large Eurasian ice sheet during the entire Late Saalian period. However, we do not investigate how the sheet grew before reaching its maximum extent at 160 ka. The exploration of the period prior to 160 ka corresponding to the beginning of MIS 6 is critical in order to further understand why the Late Saalian ice sheet become so large.

All the simulations have been carried out using LMDZ4. It would be interesting to perform key simulations with different AGCM to evaluate the dependence of the results to the type of model used.

To investigate the climate processes that contributed to the growth of this large Late Saalian Eurasian ice sheet in depth, it is necessary to use a fully coupled Atmosphere-Ocean GCM to better estimate oceanic conditions that may have played an important role on the maintenance and growth of this ice sheet and especially the ocean heat transport over high latitudes.

It is also necessary to use a thermo-dynamical ice model such as GRISLI to perform transient simulations in order to study the dynamics of the Eurasian ice sheet: from where it started to grow, how much time is needed to built the ice sheet, how much time is needed to melt it completely. It is also necessary to build a Laurentide ice sheet associated with the simulated climate to understand if it may have been as large as during the LGM. These perspectives will be the object of further investigations in the future.

Acknowledgments

I owe Gerhard and Martin this great adventure. It has been full of surprises all the time. I met a lot of really wonderful people and I discovered really amazing fields. When I started the Ph.D., I already knew that I wanted to carry on with research. And, now that this experience is over, I am more convinced than at the beginning that research and science are amazing! I would like to thank, from the bottom of my heart Gerhard and Martin that supervised me in the best way it could have been for me: a lot of independence, a lot of support, lots of shared experiences and lots of interactive discussions. Despite the fact that the first one is a physicist and the second one a geologist, their common point is, without any doubt, their deep love for science and chocolate...

Part of this work could not have been done if I would not have met Johan Liakka during the Karthaus ice modeling summer school in 2007. He performed numerous numerical experiments for me and we had a really interactive work even when I left Stockholm. We even shared a combined seminar at Stockholm University that was very complementary. I sincerely hope that we will carry on this collaborative work in the future.

I had a lot of discussions with a part of the "Get 'n Co" group and especially Vincent Peyaud and Catherine Ritz. Thanks to Vincent's PhD (2006) during which he reconstructed the Saalian ice sheet, I could developed mine. He also taught me GRISLI and helped me to modify some routines with the great help of Catherine who even visited me during my stay in Stockholm.

This bring me to the LGGE. I have been really impressed by the great research dynamics that rules the LGGE and the broad range of topics from present-day to remote periods, from ice to atmosphere. I would like to thank each person of this institute and particularly the administration department and Michel Fily.

At the beginning of the Ph.D, this joint-supervision was not planned and it has been motivated by Gerhard's stay in Potsdam Alfred Wegener Institute and by the broad range of topics required to developed this Ph.D. Naturally, we asked Martin Jakobsson and the Department of Marine Geoscience of Stockholm University. Joint-supervision was a new concept for them. I have been welcomed very cheerfully at Stockholm University and I have been really impressed and attracted by the Swedish research system that is particularly efficient and dynamic. I would like to specially thank Aladstair, Eve, Jan and many others from the Geoscience department.

I would like now to dedicate some lines to Giorgio Spada. In parallel to this Ph.D, I carried on with the topics I studied during my master thesis in Italy: post-glacial rebound and sea level variations. These topics have always attracted me a lot and I strongly thank Giorgio to have accepted me in his group and strengthened our friendship. He always included me in all his projects to which I directly contributed during the last four years. I think that we will still closely work together in the future.

I would like to thank all my "office-mates" from both LGGE and Stockholm University, Ludovic, Catherine, Jean-Charles, Hélène, Benjamin, Theodora, Cécile, Daniella and Emma, Giuliat and Aurélien (thanks for playing the piano with me). A special dedicate to Anne-Morwenn because without her "special teaching" I would not have been able to follow my own way to carry out research.

This bring me this time to the source, the old CLDG of the University of La Rochelle. Everything starting there. I have been fully supported by everybody there even while I just started courses. I specially thanks Hervé that offered to me two wonderful summers to cartography amazing and mysterious geological fields wherever in France. I am grateful to Mikhail to have show me the way of post-glacial rebound. To finish, I dedicate part of this work to Jean-Claude, colleague and dear friend, who gave me so much time and friendship, from which I learned all the basis of university research.

Finally I thank from the bottom of my heart my entire family that supported me during all these years and that helped me to fulfill my dream.

References

Abe-Ouchi, A., Segawa, T., & Saito, F. 2007. Climatic Conditions for modelling the Northern Hemisphere ice sheets throughout the ice age cycle. *Clim. Past*, **3**, 423–438.

Adams, J.M., Faure, H., Faure-Denard, L., McGlade, J.M., & Woodward, F.I. 1990. Increases in terrestrial carbon storage from the Last Glacial Maximum to the present. *Nature*, **348**(6303), 711–714.

Alfano, M.J., Barron, E.J., Pollard, D., Huntley, B., & Allen, J.R.M. 2003. Comparison of climate model results with European vegetation and permafrost during oxygen isotope stage three. *Quaternary Research*, **59**, 97–107.

Andrews, W.R. Peltierand J.T. 1976. Glacial Isostatic Adjustment I: the Forward Problem. *Geophys. J. Roy astr. Soc.*, **46**, 605–646.

Astakhov, V.I. 2004. Middle Pleistocene glaciations of the Russian North. *Quaternary Sci. Rev.*, **23**(11-13), 1285–1311.

Augustin, L., Barbante, C., Barnes, P.R.F., Barnola, J.-M., Bigler, M., Castellano, E., Cattani, O., Chappellaz, J., Dahl-Jensen, D., Delmonte, B., Dreyfus, G., Durand, G., Falourd, S., Fischer, H., Flückiger, J., Hansson, M.E., Huybrechts, P., Jugie, G., Johnsen, S.J., Jouzel, J., Kaufmann, P., Kipfstuhl, J., Lambert, F., Lipenkov, V.Y., Littot, G.C., Longinelli, A., Lorrain, R., Maggi, V., Masson-Delmotte, V., Miller, H., Mulvaney, R., Oerlemans, J., Oerter, H., Orombelli, G., Parrenin, F., Peel, D.A., Petit, J.-R., Raynaud, D., Ritz, C., Ruth, U., Schwander, J., Siegenthaler, U., Souchez, R., Stauffer, B., Steffensen, J. Peder, Stenni, B., Stocker, T.F., Tabacco, I.E., Udisti, R., van de Wal, R.S.W., van den Broeke, M., Weiss, J., Wilhelms, F., Winther, J-G., Wolff, E.W., & Zucchelli, M. 2004. Middle Pleistocene glaciations of the Russian NorthEight glacial cycles from an Antarctic ice core. *Nature*, **429**, 623–628.

Bard, E. 2001. Comparison of alkenones estimates with other paleotemperature proxies. *Goechem. Geophy. Geosy.*, **2**(1), 1002.

Bassett, S.E., Milne, G.A., Mitrovica, J.X., & Clark, P.U. 2005. Ice Sheet and Solid Earth Influences on Far-Field Sea-Level Histories. *Science*, **309**, 925–928.

Berger, A., & Loutre, M.F. 1991. Insolation values for the climate of the last 10 millions years. *Quaternary Sci. Rev.*, **10**(4), 297–317.

Bintanja, R., van de Wal, R.S.W., & Oerlemans, J. 2005. Modelled atmospheric temperatures and global sea levels over the past million years. *Nature*, **437**, 125–128.

Bond, G., Broecker, W., Johnsen, S., McManus, J., Labeyrie, L., Jouzel, J., & Bonani, G. 1993. Correlations between climate records from North Atlantic sediments and Greenland ice. *Nature*, **365**, 143–147.

Bonelli, S., Charbit, S., Kageyama, M., Woillez, M.-N., Ramstein, G., Dumas, C., & Quiquet, A. 2009. Investigating the evolution of major Northern Hemisphere ice sheets during the last glacial-interglacial cycle. *Clim. Past Discuss.*, **5**, 1013–1053.

Braconnot, P., Otto-Bliesner, B., Harrison, S., Joussaume, S., Peterchmitt, J.-Y., Abe-Ouchi, A., Crucifix, M., Driesschaert, E., Fichefet, Th., Hewitt, C.D., Kageyama, M., Kitoh, A., Lan, A., Loutre, M.-F., Marti, O., Merkel, U., Ramstein, G., Valdes, P., Weber, S.L., Yu, Y., & Zhao, Y. 2007. Results of PMIP2 coupled simulations of the Mid-Holocene and Last Glacial Maximum - Part 1: experiments and large-scale features. *Clim. Past*, **3**(2), 261–277.

Bromwich, D.H., Toracinta, R. E., Wei, H., Oglesby, R.J., Fastook, J.L., & Hughes, T.J. 2004. Polar MM5 Simulations of the Winter Climate of the Laurentide Ice Sheet at the LGM. *J. Clim.*, **17**(17), 3415–3433.

Calov, R., Ganopolski, A., Claussen, M., Petoukhov, V., & Greve, R. 2005a. Transient simulation of the last glacial inception. Part I: glacial inception as a bifurcation in the climate system. *Clim. Dynam.*, **24**(6), 545–561.

Calov, R., Ganopolski, A., Petoukhov, V., Claussen, M., Brovkin, V., & Kubatzki, C. 2005b. Transient simulation of the last glacial inception. Part II: sensitivity and feedback analysis. *Clim. Dynam.*, **24**(6), 563–576.

Calvo, E., Villanueva, J., Grimalt, J.O., Boelaert, A., & Labeyrie, L. 2001. New insights into the glacial latitudinal temperature gradients in the North Atlantic. Results from UK?37 sea surface temperatures and terrigenous inputs. *Earth Planet. Sc. Lett.*, **188**(3-4), 509–519.

Charbit, S., Ritz, C., & Ramstein, G. 2002. Simulations of northern hemisphere ice-sheet retreat: sensitivity to physical mechanisms involved during the Last Deglaciation. *Quaternary Sci. Rev.*, **21**, 243–265.

Chlachula, J. 2003. The Siberian loess record and its signicance for reconstruction of Pleistocene climate change in north-central Asia. *Quaternary Sci. Rev.*, **22**, 1879–1906.

Claquin, T., Roelandt, C., Kohfeld, K., Harrison, S., Tegen, I., Prentice, I., Balkanski, Y., Bergametti, G., Hansson, M., Mahowald, N., Rodhe, H., & Schulz, M. 2003. Radiative forcing of climate by ice-age atmospheric dust. *Clim. Dyn.*, **20**(2-3), 193–202.

CLIMAP. 1981. The last interglacial ocean. *Quaternary Res.*, **21**, 123–224.

Colleoni, F., Krinner, G., Jakobsson, M., Peyaud, V., & Ritz, C. 2009a. Influence of regional factors on the surface mass balance of the large Eurasian ice sheet during the peak Saalian (140 kyrs BP). *Global Planet. Change*, **HOTRAX special issue**.

Colleoni, F., Liakka, J., Krinner, G., Jakobsson, M., Masina, S., & Peyaud, V. 2009b. The Late Saalian surface ocean (140 kyrs BP): sensitivity of the Late Saalian Eurasian ice sheet to sea surface conditions. *Clim. Dynam.*, submitted.

Colleoni, F., Krinner, G., & Jakobsson, M. 2009d. Sensitivity of the Late Saalian (140 kyrs BP) and LGM (21 kyrs BP) Eurasian ice sheet surface mass balance to vegetation feedbacks. *Geophs. Res. Lett.*, **36**, L08704.

Crowley, T.J. 1981. Temperature and circulation changes in the eastern North Atlantic during the last 150,000 years: Evidence from the planktonic foraminiferal record. *Mar. Micropaleontol.*, **6**(2), 97–129.

Crowley, T.J. 1995. Ice age terrestrial carbon changes revisited. *Global Biogeochem. Cycles*, **9**(3), 377–389.

Crowley, T.J., & Baum, S.K. 1997. Effect of vegetation on an ice-age climate model simulation. *J. Geophys. Res.*, **102**(D14), 16463–16480.

Crowley, T.J., & North, G.R. 1991. *Paleoclimatology*. Oxford University Press. Clarendon Press. New York. Oxford. US.

Crucifix, M., & Hewitt, C.D. 2005. Impact of vegetation changes on the dynamics of the atmosphere at the Last Glacial Maximum. *Clim. Dynam.*, **25**(5), 447–459.

Dansgaard, W., Johnsen, S.J., Clausen, H.B., Dahl-Jensen, D., Gundestrup, N.S., Hammer, C.U., Hvidberg, C.S., Steffensen, J.P., Sveinbjornsdottir, A.E., & Jouzel, J. 1993. Evidence for general instability of past climate from a 250-kyr ice-core record. *Nature*, **364**(6434), 218–220.

de Beaulieu, J-L., Andrieu-Ponel, V., Reille, M., Grger, E., Tzedakis, C., & Svobodova, H. 2001. An attempt at correlation between the Velay pollen sequence and the Middle Pleistocene stratigraphy from central Europe. *Quaternary Sci. Rev.*, **20**, 1593–1602.

de Noblet, N.I., Prentice, I. C., Jousseaume, S., Texier, D., Botta, A., & Haxeltine, A. 1996. Possible role of atmosphere-biosphere interactions in triggering the last glaciation. *Geophysical Research Letters*, **23**(22), 3191–3194.

de Vernal, A., Hillaire-Marcel, C., Turon, J.L., & Matthiesen, J. 2000. Reconstruction of sea-surface temperature, salinity and sea-ice cover in the northern North Atlantic during the Last Glacial Maximum based on dynocyst assemblages. *Can. J. Earth Sci.*, **37**, 725–750.

Delmonte, B., & EPICA community members. 2004. *EPICA Dome C Ice Cores Insoluble Dust Data, IGBP PAGES/World Data Center for Paleoclimatology Data Contribution Series, NOAA/NGDC Paleoclimatology Program, Boulder CO, USA*.

Dyke, A.S., Andrews, J.T., Clark, P.U., England, J.H., Miller, G.H., Shaw, J., & Veillette, J.J. 2002. The Laurentide and Innuitian ice sheets during the Last Glacial Maximum. *Quaternary Sci. Rev.*, **21**, 9–31.

Dziewonski, A.M., & Anderson, D.L. 1981. Preliminary reference Earth model. *Phys. Earth Planet. In.*, **25**, 297–356.

Ehlers, J., Eissmann, L., Lippstreu, L., Stephan, H.J., & Wansa, S. 2004. *Pleistocene glaciations of North Germany. In: Ehlers, J., Gibbard, P.L. (Eds.), Quaternary GlaciationsExtent and Chronology. Vol. 1. Europe*. Elsevier, Amsterdam.

Engels, J.L., Edwards, M.H., Polyak, L., & Johnson, P.D. 2008. Seaoor evidence for ice shelf ow across the AlaskaBeaufort margin of the Arctic Ocean. *Earth Surf. Proc. Land.*, **33**, 1047–1063.

Fairbanks, R. G., Mortlock, R.A., Chiu, T-C., Cao, L., Kaplan, A., Guilderson, T.P., Fairbanks, T.W., Bloom, A.L., Grootes, P.M., & Nadeau, M-J. 2005. Radiocarbon calibration curve spanning 0 to 50,000 years BP based on paired ^{230}Th/ ^{234}U/ ^{238}U and ^{14}C dates on pristine corals. *Quaternary Sci. Rev.*, **24**, 1781–1796.

Fairbanks, R.G. 1989. A 17,000 year glacial eustatic sea level record: influence og glacial meltng rates in the Younger Dryas event and deep ocean circulation. *Nature*, **342**, 637–641.

Fraedrich, K., Jansen, H., Kirk, E., Luksch, U., & Lunkeit, F. 2005. The Planet Simulator: Towards a user friendly model. *Meteorol. Z.*, **14**, 299–304.

Genthon, C., Barnola, J-M., Raynaud, D., Lorius, C., Jouzel, J., Barkov, N.I, Korotkevich, Y.S., & Kotlyakov, V.M. 1987. Vostok ice core: climatic response to CO_2 and orbital forcing changes over the last climatic cycle. *Nature*, **329**(1), 414–418.

Gersonde, R., Abelmann, A., Brathauer, U., Becquey, S., Bianchi, C., Cortese, G., Grobe, H., Kuhn, G., Niebler, H-S., Segl, M., Sieger, R., Zielinski, U., & Ftterer, D.K. 2003. Last glacial sea surface temperatures and sea-ice extent in the Southern Ocean (Atlantic-Indian sector): A multiproxy approach. *Paleoceanography*, **18**(3), 1060.

Grosswald, M.G. 1980. Late Weishcelian Ice Sheets of Northern Eurasia. *Quaternary Res.*, **13**(1), 1–32.

Grosswald, M.G., & Hughes, T.J. 1999. The case for an ice shelf in the Pleistocene Arctic ocean. *Polar Geogr.*, **23**(1), 23–54.

Harvey, L.D.D. 1988. Climatic impact of ice-age aerosols. *Nature*, **334**, 333–335.

Haxeltine, A., & Prentice, I.C. 1996. BIOME3: An equilibrium terrestrial biosphere model based on ecophysiological constraints, resource availability, and competition among plant functional types. *Global Biogeochem. Cy.*, **10**(4), 693–710.

Hays, J.D., Imbrie, J., & Shackleton, N.J. 1976. Variations in the Earth's orbit: Pacemaker of the Ice Ages. *Science*, **196**, 1121–1132.

Hebbeln, D., Dokken, T., Andersen, E.S., Hald, M;, & Elverhoi, A. 1994. Moisture supply for northern ice-sheet growth during the Last Glacial Maximum. *Nature,* **370**, 357–360.

Henderson-Sellers, A. 1986. Calculating the surface energy balance for lake and reservoir modeling: A review. *Rev. Geophys.*, **24**, 625–649.

Hostetler, S., Bartlein, P.J., Clark, P.U., Small, E.E., & Solomon, A.M. 2000. Simulated influences of Lake Agassiz on the climate of central North America 11,000 years ago. *Nature*, **405**, 334–337.

Hourdin, F., Musat, I., Bony, S., Braconnot, P., Codron, F., Dufresne, J-L., Fairhead, L., Filiberti, M-A., Frieflingstein, P., Grandpeix, J-Y., Krinner, G., Levan, P., Li, Z-X., & Lott, F. 2006. The LMDZ4 general circulation model : climate performance and sensitivity to parametrized physics with emphasis on tropical convection. *Clim. Dynam.*, **27**(7-8), 787–813.

Hughes, T., Denton, G.H., & Grosswald, M.G. 1977. Was there a late-Wurm Arctic Ice Sheet? *Nature*, **266**, 596–602.

Hutter, K. 1983. *Theoretical Glaciology - Material Science of Ice and the Mechanics of Glaciers and Ice Sheets*. Mathematical Approaches to Geophysics, vol. 1. TERRAPUB/KTK, Japan and Reidel, Japan - Springer.

Huybers, P. 2006. Early Pleistocene Glacial Cycles and the Integrated Summer Insolation Forcing. *Science*, **313**, 508–511.

Imbrie, J., & Duffy, A. 1993. *SPECMAP Archive 4*.

Ivins, E.R., & James, T.S. 2005. Antarctic glacial isostatic adjustment: a new assessment. *Antarct. Sci.*, **17**(4), 541–553.

Jakobsson, M. 1999. First high-resolution chirp sonar profiles from the central Arctic Ocean reveal erosion of Lomonosov Ridge sediments. *Mar. Geol.*, **154**, 111–123.

Jakobsson, M. 2002. Hypsometry and volume of the Arctic Ocean and its constituent seas. *Geochem. Geophy. Geosy.*, **3**(5), 1–18.

Jakobsson, M., & co authors. 2009. *Lomonosov Ridge Off Greenland 2007 (LOMROG) - Cruise Report, Cruise report, Geological Survey of Denmark and Greenland, Copenhagen, 122 pp.*

Jakobsson, M., Lovlie, R., Arnold, E. M., Backman, J., Polyak, L., Knutsen, J. O., & Musatov, E. 2001. Pleistocene stratigraphy and paleoenvironmental variation from Lomonosov Ridge sediments, central Arctic Ocean. *Global Planet. Change*, **31**(1-4), 1–22.

Jakobsson, M., Gardner, J.V., Vogt, P., Mayer, L.A., Armstrong, A., Backman, J., Brennan, R., Calder, B., Hall, J.K., & Kraft, B. 2005. Multibeam bathymetric and sediment profiler evidence for ice grounding on the Chukchi Borderland, Arctic Ocean. *Quaternary Res.*, **63**, 150–160.

Jakobsson, M., Backman, J., Rudels, B., Nycander, J., Frank, M., Mayer, L., Jokat, W., Sangiorgi, F., ORegan, M., Brinkhuis, H., King, J., & Moran, K. 2007. The Early Miocene Onset of a Ventilated Circulation Regime in the Arctic Ocean. *Nature*, **447**(21), 986–990.

Jakobsson, M., Polyak, L., Edwards, M., Kleman, J., & Coakley, B. 2008a. Glacial geomorphology of the Central Arctic Ocean: the Chukchi Borderland and the Lomonosov Ridge. *Earth Surf. Proc. Land.*, **33**(4), 526–545.

Jakobsson, M., Macnab, R., Mayer, L., Anderson, R., Edwards, M., Hatzky, J., Schenke, H. W., , & Johnson, P. 2008b. An improved bathymetric portrayal of the Arctic Ocean: Implications for ocean modeling and geological, geophysical and oceanographic analyses. *Geophys. Res. Lett.*, **35**(7), L07602.

Joussaume, S., & Taylor, K.E. 1995. Status of the Paleoclimate Modeling Intercomparison Project (PMIP). *Pages 425–430 of: Proceedings of the rst international AMIP scientic conference*.

Joussaume, Sylvie, & Braconnot, Pascale. 1997. Sensitivity of paleoclimate simulation results to season definitions. *J. Geophys. Res.*, **102**(D2), 1943–1956.

Jouzel, J., Masson-Delmotte, V., Cattani, O., Dreyfus, G., Falourd, S., Hoffmann, G., Minster, B., Nouet, J., Barnola, J.M., Chappellaz, J., Fischer, H., Gallet, J.C., Johnsen, S., Leuenberger, M., Loulergue, L., Luethi, D., Oerter, H., Parrenin, F., Raisbeck, G., Raynaud, D., Schilt, A., Schwander, J., Selmo, E., Souchez, R., Spahni, R., Stauffer, B., Steffensen, J.P., Stenni, B., Stocker, T.F., Tison, J.L., Werner, M., & Wolff, E.W. 2007. *EPICA Dome C Ice Core 800KYr Deuterium Data and Temperature Estimates*.

Kageyama, M., & Valdes, P.J. 2000. Impact of the North American ice-sheet orography on the Last Glacial Maximum eddies and snowfall. *Geophysical Research Letters*, **27**(10), 1515.

Kageyama, M., Valdes, P. J., Ramstein, G., Hewitt, C., & Wyputta, U. 1999. Northern Hemisphere Storm Tracks in Present Day and Last Glacial Maximum Climate Simulations: A Comparison of the European PMIP Models. *J. Climate*, **12**, 742–760.

Kageyama, M., Charbit, S., Ritz, C., Khodri, M., & Ramstein, G. 2004. Quantifying ice-sheet feedbacks during the last glacial inception. *Geophys. Res. Lett.*, **31**, L24203.

Kageyama, M., Laîne, A., Abe-Ouchi, A., Braconnot, P., Cortijo, E., Crucix, M., de Vernal, A., Guiot, J., Hewitt, C.D., Kitoh, A., Kucera, M., Marti, O., Ohgaito, R., Otto-Bliesner, B., Peltier, W.R., Rosell-Mele, A., Vettoretti, G., Weber, S.L., Yum, Y., & Members, MARGO Project. 2006. Last Glacial Maximum

temperatures over the North Atlantic, Europe and western Siberia: a comparison between PMIP models, MARGO seasurface temperatures and pollen-based reconstructions. *Quaternary Sci. Rev.*, **25**, 2082–2102.

Kaplan, J.O. 2001. *Geophysical applications of vegetation modeling*. Ph.D. thesis, Lund University, Lund, Sweden.

Kaplan, J.O., Bigelow, N.H., Prentice, I.C., Harrison, S.P., Bartlein, P.J., Christensen, T.R., Cramer, W., Matveyeva, N.V., McGuire, A.D., Murray, D.F., Razzhivin, V.Y., Smith, B., Walker, D.A., Anderson, P.M., Andreev, A.A., Brubaker, L.B., Edwards, M.E., & Lozhkin, A.V. 2003. Climate change and Arctic ecosystems: 2. Modeling, paleodata-model comparisons, and future projections. *J. Geophys. Res.*, **102**(D19), ALT12.1–ALT12.17.

Kasahara, A. 1977. Computational aspects of numerical models for weather prediction and climate simulation, in Methods in computational physics. *J. Chang.*, **17**, 1–66.

Khodri, M., Cane, M. A., Kukla, G., Gavin, J., & Braconnot, P. 2005. The impact of precession changes on the Arctic climate during the last interglacial–glacial transition. *Earth Planet Sc. Lett.*, **236**, 285–304.

Klenke, M., & Schenke, H.W. 2002. A new bathymetric model for the central Fram Strait. *Mar. Geophys. Res.*, **23**, 367–378.

Krinner, G. 2003. Impact of lakes and wetlands on boreal climate. *J. Geophy. Res.*, **108**(D16), 4520.

Krinner, G., & Genthon, C. 1997. The Antarctic surface mass balance in a stretched grid general circulation model. *Ann. Glaciol.*, **25**, 73–78.

Krinner, G., & Genthon, C. 1999. Altitude dependence of the ice sheet surface climate. *Geophys. Res. Lett.*, **26**, 2227–2230.

Krinner, G., Mangerud, J., Jakobsson, M., Crucifix, M., Ritz, C., & Svendsen, J.I. 2004. Enhanced ice sheet growth in Eurasia owing to adjacent ice-dammed lakes. *Nature*, **427**, 429–432.

Krinner, G., Viovy, N., de Noblet-Ducoudre, N., Ogee, J., Polcher, J., Friedlingstein, P., Ciais, P., Sitch, S., & Prentice, I. C. 2005. A dynamic global vegetation model for studies of the coupled atmosphere-biosphere system. *Global Biogeochem. Cy.*, **19**, GB1015.

Krinner, G., Boucher, O., & Balkanski, Y. 2006. Ice-free glacial northern Asia due to dust deposition on snow. *Clim. Dynam.*, **27**(6), 613–625.

Krinner, G., Magand, O., Simmonds, I., Genthon, C., & Dufresne, J.L. 2007. Simulated Antarctic precipitation and surface mass balance at the end of the twentieth and twenty-first centuries. *Clim. Dynam.*, **28**, 215–230.

Kubatzki, C., & Claussen, M. 1998. Simulation of the global bio-geophysical interactions during the Last Glacial Maximum. *Clim. Dynam.*, **14**, 461–471.

Kucera, M., Rosell-Mele, A., Schneider, R., Waelbroeck, C., & Weinelt, M. 2005a. Multiproxy approach for the reconstruction of the glacial ocean surface (MARGO). *Quaternary Sci. Rev.*, **24**, 813–819.

Kukla, G. 2005. Saalian supercycle, Mindel/Riss interglacial and Milankovitchs dating. *Quaternary Sci. Rev.*, **24**, 1573–1583.

Kukla, G., & Lozek, V. 1961. *Loesses and related deposits, Survey of Czechoslovak Quaternary*.

Kutzbach, J.E., & Wright, H.E. 1985. Simulation of the climate of 18,000 yr BP: Results for the North American North Atlantic European sector. *Quaternary Sci. Rev.*, **4**, 147–187.

Kwok, R., Cunningham, G.F., & Pang, S.S. 2004. Fram Strait sea ice outflow. *J. Geophys. Res.*, **109**, C01009.

Lambeck, K., & Chappell, J. 2001. Sea Level Change Through the Last Glacial Cycle. *Science*, **292**, 679–686.

Lambeck, K., Purcell, A., Johnston, P., Nakada, M., & Yokoyama, Y. 2003. Water-load definition in the glacio-hydro-isostatic sea-level equation. *Quaternary Sci. Rev.*, **22**, 309–318.

Lambeck, K., Purcell, A., Funder, S., Kjaer, K.H., Larsen, E., & Moller, P. 2006. Constraints on the Late Saalian to early Middle Weichselian ice sheet of Eurasia from field data and rebound modelling. *Boreas*, **35**, 539–575.

Levis, S., Foley, J.A., & Pollard, D. 1999. CO_2, climate, and vegetation feedbacks at the Last Glacial Maximum. *J. Geophys. Res.*, **104**(D24), 31435–31669.

Lorius, C., Merlivat, L., Jouzel, J., & Pourchet, M. 1979. A 30,000 yr isotope climatic record from Antarctic ice. *Nature*, **280**, 644–648.

MacAyeal, D.R. 2001. Large Scale ice ow over a vicous basal Sediment: Theory and Application to Ice Stream B, Antarctica. *J. Geophys. Res.*, **94**, 4071–4087.

Mahowald, N., Kohfeld, K., Hansson, M., Balanski, Y., Harrisson, S., Prentice, J., Schulz, M., & Rodhe, H. 1999. Dusts sources and deposition during the last glacial maximum and current climate: a comparison of model results with paleodata from ice cores and marine sediments. *J. Geophys. Res.*, **104**(D13).

Mahowald, N.M., Muhs, D.R., Levis, S., Rasch, P.J., Yoshioka, M., Zender, C.S., & Luo, C. 2006. Change in atmospheric mineral aerosols in response to climate: Last glacial period, preindustrial, modern, and doubled carbon dioxide climates. *J. Geophys. Res.*, **111**(D10202).

Mangerud, J., Astakhov, V., Jakobsson, M., & Svendsen, J.I. 2001. Huge ice-age lakes in Russia. *J. Quaternary. Sci.*, **16**(8), 773–777.

Mangerud, J., Jakobsson, M., Alexanderson, H., Astakhov, V., Clarke, G.K.C., Henriksen, M., Hjort, Christian, Krinner, G., Lunkka, J-P., Moller, P., Murray, A., Nikolskaya, Olga, Saarnisto, M., & Svendsen, J.I. 2004. Ice-dammed lakes and rerouting of the drainage of northern Eurasia during the Last Glaciation. *Quaternary Sci. Rev.*, **23**, 1313–1322.

Masson-Delmotte, V., Stenni, B., Pol, K., Braconnot, P., Cattani, O., Falourd, S., Kageyama, M., Jouzel, J., Landais, A., Minster, B., Krinner, G., Johnsen, S., Rthlisberger, R., Chappellaz, J., Hansen, J., Mikolajewicz, U., & Otto-Bliesner, B. submitted. EPICA Dome C record of glacial and interglacial intensities. *Quaternary Sci. Rev.*

Meese, D.A., Gow, A.J., Alley, R.B., Zielinski, G.A., Grootes, P.M., Ram, M., Taylor, K.C., Mayewski, P.A., & Bolzan, J.F. 1997. The Greenland ice-sheet Project 2 depth-age scale: Methods and results. *J. Geophys. Res.*, **102**, 26411–26423.

Mercer, J.H. 1970. A former ice sheet in the Arctic Ocean. *Palaeogeogr. Palaeocl.*, **8**, 19–27.

Mercer, J.H. 1978. West Antarctic Ice Sheet and CO2 greenhouse effect: a threat of disaster. *Nature*, 321–325.

Milne, G.A., & Mitrovica, J.X. 2008. Searching for eustasy in deglacial sea-level histories. *Quaternary Sci. Rev.*, **27**, 2292–2302.

Mix, A., Bard, E., & Shneider, R.R. 2001. Environmental processes of the Ice Age: Land, Oceans, Glaciers (EPILOG). *Quaternary Sci. Rev.*, **20**(4), 627–657.

Morland, L. 1984. Thermo-mechanical balances of ice sheet ow. *Geophys. Astrophys. Fluid Dyn.*, **29**, 237–266.

Niebler, H.-S., Arz, H. W., Donner, B., Mulitza, S., Patzold, J., & Wefer, G. 2003. Sea surface temperatures in the equatorial and South Atlantic Ocean during the Last Glacial Maximum, (23-19 ka). *Paleoceanography*, **18**(3), 1069.

Ohmura, A., Wild, M., & Bengtsson, L. 1996. A possible change in mass balance of Greenland and Antarctic ice sheets in the coming century. *J. Glaciol.*, **9**(9), 2124–2135.

Olson, J.S., Watt, J.A., & Allinson, L.J. 1983. *Carbon in Live Vegetation in Major Ecosystems*.

O'Regan, M., King, J., Backman, J., Jakobsson, M., PŁlike, H., Moran, K., Heil, C., Sakamoto, T., Cronin, T.M., & Jordan, R.W. 2008. Constraints on the Pleistocene chronology of sediments from the Lomonosov Ridge. *Paleoceanography*, **23**.

Parrenin, F., Barnola, J.-M., Beer, J., Blunier, T., Castellano, E., Chappellaz, J., Dreyfus, G., Fischer, H., Fujita, S., Jouzel, J., Kawamura, K., Lemieux-Dudon, B., Loulergue, L., Masson-Delmotte, V., Narcisi, B., Petit, J.-R., Raisbeck, G., Raynaud, D., Ruth, U., Schwander, J., Severi, M., Spahni, R., Steffensen, J. P., Svensson, A., Udisti, R., Waelbroeck, C., , & Wolff, E. 2007. The EDC3 chronology for the EPICA Dome C ice core. *Clim. Past*, **3**, 485–497.

Paterson, W.S.B. 1994. *The Physics of Glaciers*. Pergamon, New York.

Paul, A., & Schaefer-Neth, C. 2003. Modeling the water masses of the Atlantic Ocean at the Last Glacial Maximum. *Paleoceanography*, **18**(3).

Pelejero, C., E.Calvo, Barrows, T.T., Logan, G.A., & Deckker, P. 2006. South Tasman Sea alkenone palaeothermometry over the last four glacial/interglacial cycles. *Mar. Geol.*, **230**(1-2), 73–86.

Peltier, W.R. 1994. Ice Age Paleotopography. *Science*, **265**, 195–201.

Peltier, W.R. 2002. On eustatic sea level history: Last Glacial Maximum to Holocene. *Quaternary Sci. Rev.*, **21**, 377–396.

Peltier, W.R. 2004. Global glacial isostasy and the surface of the ice-age Earth: The REF140-5G (VM2) Model and GRACE. *Annu. Rev. Earth Pla. Sci.*, **32**, 111–149.

Peltier, W.R., & Fairbanks, R.G. 2006. Global glacial ice volume and Last Glacial Maximum duration from an extended Barbados sea level record. *Quaternary Sci. Rev.*, **25**, 3322–3337.

Peltier, W.R., & Marshall, S. 1995. Coupled energy-balance/ice-sheet model simulations of the glacial cycle: A possible connection between terminations and terrigenous dust. *J. Geophys. Res.*, **100**(D7), 14269–14290.

Petit, J.R., Basile, I., Leruyuet, A., Raynaud, D., Lorius, C., Jouzel, J., Stievenard, M., Lipenkov, V.Y., Barkov, N.I., Kudryashov, B.B., Davis, M., Saltzman, E., & Kotlyakov, V. 1997. Four climate cycles in Vostok ice core. *Nature*, **387**, 359–360.

Petit, J.R., Jouzel, J., Raynaud, D., Barkov, N.I., Barnola, J.-M., Basile, I., Benders, M., Chappellaz, J., Davis, M., Delayque, G., Delmotte, M., Kotlyakov, V.M., Legrand, M., Lipenkov, V.Y., Lorius, C., Ppin, L., Ritz, C., Saltzman, E., & Stievenard, M. 1999. Climate and atmospheric history of the past 420,000 years from the Vostok ice core, Antarctica. *Nature*, **399**, 429–436.

Petit, J.R., Jouzel, J., Raynaud, D., Barkov, N., Barnola, J., Basile, I., Bender, M., Chapellaz, J., Davis, J., Delaygue, G., Delmotte, M., Kotlyakov, V., Legrand, M., Lipenkov, V., Lorius, C., Ppin, L., Ritz, C., Saltzman, E., & Stievenard, M. 2001. *Ice core data for 420,000 year, IGBP PAGES/World Data Center for Paleoclimatology Data Contribution Series, NOAA/NGDC Paleoclimatology Program, Boulder CO, USA*.

Peyaud, V. 2006. *Role of the Ice Sheet Dynamics in major climate changes*. Ph.D. thesis, Laboratoire de Glaciologie et de Géophysique de l'Environnement, Université Grenoble I.

Peyaud, V., Ritz, C., & Krinner, G. 2007. Modeling the Early Weichselian Eurasian Ice Sheets: role of ice shelves and influence of ice-dammed lakes. *Clim. Past*, **3**, 375–386.

Pflaumann, U., Sarnthein, M., Chapman, M., d'Abreu, L., Funnell, B., Huels, M., Kiefer, T., Maslin, M., Schulz, H., Swallow, J., van Kreveld, S., Vautravers, M., Vogelsang, E., & Weinelt, M. 2003. Glacial North Atlantic: Sea-surface conditions reconstructed by GLAMAP 2000. *Paleoceanography*, **18**(3), 10–21.

Pollard, D., & Thompson, S.L. 1995. Use of a land-surface-transfer scheme (LSX) in a global climate model: the response to doubling stomatal resistance. *Global Planet. Change*, **10**(1-4), 129–161.

Pollard, D., PMIP, Participating, & Group. 2000. Comparisons of ice-sheet surface mass budgets from Paleoclimate Modeling Intercomparison Project (PMIP) simulations. *Global Planet. Change*, **24**, 79–106.

Polyak, L., Edward, M.H., Coakley, B.J., & Jakobsson, M. 2001. Ice shelves in the Pleistocene Arctic Ocean inferred from glaciogenic deep-sea bedforms. *Nature*, **410**, 453–457.

Polyak, L., Bischof, D. Darby J., & Jakobsson, M. 2007. Stratigraphic constraints on late Pleistocene glacial erosion and deglaciation of the Chukchi margin, Arctic Ocean. *Quaternary Res.*, **67**, 234–245.

Rabineau, M., Berne, S., Olivet, J.L., Aslanian, D., Guillocheau, F., & Joseph, P. 2006. Paleo sea levels reconsidered from direct observation of paleoshore-line position during glacial maxima (for the last 500,000 yr). *Earth Planet. Sc. Lett.*, **252**, 119–137.

Raymo, M.E., Lisiecki, L.E., & Nisancioglu, K.H. 2006. Plio-Pleistocene Ice Volume, Antarctic Climate, and the Global $\delta^{18}O$ Record. *Science*, **313**, 492–495.

Raynaud, D., Jouzel, J., Barnola, J-M., Chapellaz, J., Delmas, R.J., & Lorius, C. 1993. The ice record of Greenhouse Gases. *Science*, **259**, 926–934.

Rayner, N.A., Parker, D.E., Horton, E.B., Folland, C.K., Alexander, L.V., Rowell, D.P., Kent, E.C., & Kaplan, A. 2003. Global analyses of sea surface temperature, sea ice, and night marine air temperature since the late nineteenth century. *J. Geophys. Res.*, **108**(D14), 4407.

Rind, D. 1987. Components of the ice age circulation. *J. Geophys. Res.*, **92**, 4142–4281.

Ritz, C., Rommalaere, V., & Dumas, C. 2001. Modeling the evolution of Antarctic ice sheet over the last 420,000 years: Implications for altitude changes in the Vostok region. *J. Geophys. Res.*, **106**(D23), 31943–31964.

Romanova, V., Lohmann, G., & Grosfeld, K. 2005. Effect of land albedo, CO2, orography, and oceanic heat transport on extreme climates. *Clim. Past*, **92**, 4241–4281.

Romanova, V., Lohmann, G., Grosfeld, K., & Butzin, M. 2006. Effect of land albedo, CO2, orography, and oceanic heat transport on extreme climates. *Quaternary Sci. Rev.*, **25**, 832–845.

Rommelaere, V., & Ritz, C. 1996. A thermomechanical model of ice-shelf ow. *Ann. Glaciol.*, **23**, 13–20.

Ruddiman, W.F. 2006. Ice-driven CO_2 feedback on ice volume. *Clim. Past*, **2**, 43–55.

Ruddiman, W.F., & McIntyre, A. 1979. Warmth of the subpolar North Atlantic Ocean during Northern Hemisphere ice-sheet growth. *Science*, **204**, 173–175.

Schaefer, G., Rodger, J.S., Hayward, B.W., Kennett, J.P., Sabaa, A.T., & Scott, G.H. 2005. Planktic foraminiferal and sea surface temperature record during the last 1 Myr across the Subtropical Front, Southwest Pacific. *Mar. Micropaleontol.*, **54**(3-4), 191–212.

Shackleton, N. 1987. Oxygen isotopes, ice volume and sea-level. *Quaternary Sci. Rev.*, **6**, 183–190.

Siegert, M. 2001. Modelling the Eurasian Ice Sheet through a full (Weichselian) glacial cycle. *Global and Planetary Change*, **31**(1-4), 367–385.

S.J., Marshall, Tarasov, L., Clarke, G.K.C., & Peltier, W.R. 2000. Glaciological reconstruction of the Laurentide Ice Sheet: physical processes and modelling challenges. *Can. J. Earth Sci.*, **37**(5), 769–793.

Spada, G., & Stocchi, P. 2007. SELEN: a Fortran 90 program for solving the "Sea Level Equation". *Comput. and Geosci.*, **33**(4), 538–562.

Spada, G., Stocchi, P., & Colleoni, F. 2009. Glacio-isostatic adjustment in the Po plain and in the northern Adriatic region. *Pure and Applied Geophysics*, **in press**.

Spahni, R., Chappellaz, J., Stocker, T., Loulergue, L., Hausammann, G., Kyawamura, G., Flckiger, J., Schwander, J., Raynaud, D., Masson-Delmotte, V., & Jouzel, J. 2005. *Epica Dome C CH4 data to 650 kya BP*.

Spielhagen, R.F., Bonani, G., Eisenhauer, A., Frank, M., Frederichs, T., Kassens, H., Kubik, P., Mangini, A., Pedersen, N. Nogaard, Nowaczyk, N.R., SchŁper, S., Stein, R., Thiede, J., Tiedemann, R., & Wahsner, M. 1997. Arctic Ocean evidence for late Quaternary initiation of northern Eurasian ice sheets. *Geology*, **25**, 783–786.

Spielhagen, R.F., Baumann, K.-H, Erlenkeuser, H., Nowaczyk, N.R., Norgaard-Pedersen, N., Vogt, C., & Weiel, D. 2004. Arctic Ocean deep-sea record of northern Eurasian ice sheet history. *Quaternary Sci. Rev.*, **23**(11-13), 1455–1483.

Stocker, T.F. 1998. The seesaw effect. *Science*, **282**, 61–62.

Svendsen, J.I., Astakhov, V.I., Bolshiyanov, D.Y., Demidov, I., Dowdeswell, J.A., Gataullin, V., Hjort, C., Hubberten, H.W., Larsen, E., Mangerud, J., Melles, M., Moumlller, P., Saarnisto, M., & Siegert, M.J. 1999. Maximum extent of the Eurasian ice sheets in the Barents and Kara Sea region during the Weichselian. *Boreas*, **28**(1), 234–242.

Svendsen, J.I., Alexanderson, H., Astakhov, V.I., Demidov, I., Julian, A.D., Funder, S., Gataulling, V., Henriksen, M., Hjort, J., Houmark-Nielsen, M., Hubberten, H.W., Ingulfsson, O., Jakobsson, M., Kjer, K.H., Larsen, E., Lokrantz, H., Lunkka, J.P., Lys, A., Mangerud, J., Matiouchkov, A., Murray, A., Muller, P., Niessen, F., Nikolskaya, O., Polyak,

L., Saarnisto, M., Siegert, C., Siegert, M.J., Spielhagen, R.W., & Ruedige, S. 2004. Late Quaternary ice sheet history of Northern Eurasia. *Quaternary Sci. Rev.*, **23**, 1229–1271.

Tarasov, P., Williams, J.W., Andreev, A., Nakagawa, T., Bezrukova, E., Herzschuh, U., Igarashi, Y., Muller, S., Werner, K., & Zheng, Z. 2007. Satellite-and pollen-based quantitative woody cover reconstructions for northern Asia: Verification and application to late-Quaternary pollen data. *Earth Planet. Sci. Lett.*, **264**, 284–298.

Tarasov, P.E., Volkova, V.S., Webb, T., Guiot, J., Andreev, A.A., Bezusko, L.G., Bezusko, T.V., Bykova, G.V., Dorofeyuk, N.I., Kvavadze, E.V., Osipova, I.M., Panova, N.K., & Sevastyanov, D.V. 2000. Last glacial maximum biomes reconstructed from pollen and plant macrofossil data from northern Eurasia. *J. Biogeogr.*, **27**(3), 609–620.

Thompson, S.L., & Pollard, D. 1997. Greenland and Antarctic mass balances for present and doubled atmospheric CO2 from the GENESIS Version-2 Global Climate Model. *J. Climate*, **10**, 871–900.

Tushingham, A.M., & Peltier, W.R. 1991. ICE-3G: A New Global Model of Late Pleistocene Deglaciation Based Upon Geophysical Predictions of Post-Glacial Relative Sea Level Change. *J. Geophys. Res.*, **96**, 4497–4523.

Villanueva, J., Flores, J.A., & Grimalt, J.O. 2002. A detailed comparison of the Uk?37 and coccolith records over the past 290 kyears: implications to the alkenone paleotemperature method. *Org. Geochem.*, **33**(8), 897–905.

Waelbroeck, C., Labeyrie, L., Michel, E., Duplessy, J.C., McManus, J.F., Lambeck, K., Balbon, E., & Labracherie, M. 2002. Sea-level and deep water temperature changes derived from benthic foraminifera isotopic records. *Quaternary Sci. Rev.*, **21**(1-3), 295–305.

Waelbroeck, C., Paul, A., Kucera, M., Rosell-Melé, A., Weinelt, M., Schneider, R., Mix, A. C., Abelmann, A., Armand, L., Bard, E., Barker, S., Barrows, T. T., Benway, H., Cacho, I., Chen, M.-T., Cortijo, E., Crosta, X., de Vernal, A., Dokken, T., Duprat, J., Eldereld, H., Eynaud, F., Gersonde, R., Hayes, A., Henry, M., Hillaire-Marcel, C., Huang, C.-C., Jansen, E., Juggins, S., Kallel, N., Kiefer, T., Kienast, M., Labeyrie, L., Leclaire, H., Londeix, L., Mangin, S., Matthiessen, J., Marret, F., Meland, M., Morey, A. E., Mulitza, S., Pfaumann, U., Pisias, N. G., Radi, T., Rochon, A., Rohling, E. J., Sbaf, L., SchŁfer-Neth, C., Solignac, S., Spero, H., Tachikawa, K., & Turon, J.-L. 2009. Constraints on the magnitude and patterns of ocean cooling at the Last Glacial Maximum, MARGO Project Members. *Nature Geoscience*, **2**, 127–332.

Webb, R., & al. 1995. *Bibliography and inventory of sites with information for constructing digital global aps of vegetation distribution 18,000 yr. B.P.*

Willis, K.J., & van Andel, T.H. 2004. Trees or no trees? The environments of central and eastern Europe during the Last Glaciation. *Quaternary Sci. Rev.*, **23**, 2369–2387.

Winckler, G., Anderson, R.F., Fleisher, M.Q., McGee, D., & Mahowald, N. 2008. Covariant Glacial-Interglacial Dust Fluxes in the Equatorial Pacific and Antarctica. *Science*, **320**, 93–96.

Wohlfarth, B., Veres, D., Ampel, L., Lacourse, T., Blaauw, M., Preusser, F., Andrieu-Ponel, V., Kravis, D., Lallier-Vergs, E., Bjrck, S., Davies, S., de Beaulieu, J.-L., Risberg, J., Hormes, A., Kasper, H.U., Possnert, G., Reille, M., Thouveny, N., A., & Zander. 2008. Rapid ecosystem response to abrupt climate changes during the last glacial period in western Europe, 40-16 ka. *Geology*, **36**, 407–410.

Zimov, S.A., Voropaev, Y.V., Semiletov, I.P., Davidov, S.P., Prosiannikov, S.F., Chapin, F.S., Chapin, M. C., Trumbore, S., & Tyler, S. 1997. North Siberian Lakes: A Methane Source Fueled by Pleistocene Carbon. *Science*, **277**, 800–802.

Manuscript 1

Colleoni F., Krinner G., Jakobsson M., Peyaud V. and C. Ritz, Influence of regional factors on the surface mass balance of the large Eurasian ice sheet during the peak Saalian (140 kyrs BP), *Global and Planetary Change*, HOTRAX spe. issue, in press.

Contribution:

- Implementing dust deposition on snow and open water surface modules in the atmospheric general circulation model LMDZ4, model evaluation
- Designing and running the experiments using LMDZ4 and the vegetation model BIOME4
- Analyzing the results
- Main part of the writing

Résumé
Les récentes reconstructions de la calotte de glace Eurasiatique, basées sur des données géologiques, montrent qu'au maximum glaciaire du Saalien ($\approx$ 140 ka), la calotte de glace était plus volumineuse que lors du Dernier Maximum Glaciaire (LGM, 21 ka). Afin de comprendre l'origine de cette différence, nous avons utilisé le modèle de circulation générale atmosphérique (AGCM) LMDZ4 pour évaluer l'impact des lacs proglaciaires, des dépôts de poussières sur la neige, de la végétation et des température de surface océanique, sur le bilan de masse en surface de la calotte Eurasiatique à 140 ka. Les données géologiques suggèrent que ces facteurs régionaux étaient différents au LGM et pouvaient donc en partie contribuer à l'importante extension vers le Sud de la calotte Saalienne. Au total, sept simulations ont été réalisées. Les dépôts de poussière sur la neige réduisent le bilan de masse moyen annuel par le biais d'une fonte plus importante au printemps et en été. Au contraire, les lacs proglaciaires refroidissent le climat d'été et diminuent la fonte de la calotte le long des marges Sud. En combinant ces deux facteurs, la fonte de la calotte est également réduite en été à cause du refroidissement causé par les lacs qui compense largement le réchauffement local induit par les dépôts de poussières. La substitution des conifères par de la tundra affecte également le climat régional, mais pas suffisamment pour influencer le bilan de masse de la calotte. Cependant, afin de mieux évaluer l'impact des changements de végétation sur le bilan de masse et afin d'améliorer les conditions aux limites pour la période du Saalien, la simulation d'une végétation en équilibre avec le climat est nécessaire. Pour finir, les changements de température de surface océanique affectent de manière significative le climat régional et le bilan de masse de la calotte Eurasiatique.

Global and Planetary Change xxx (2009) xxx–xxx

Contents lists available at ScienceDirect

Global and Planetary Change

journal homepage: www.elsevier.com/locate/gloplacha

Influence of regional parameters on the surface mass balance of the Eurasian ice sheet during the peak Saalian (140 kya)

F. Colleoni [a,*], G. Krinner [a], M. Jakobsson [b], V. Peyaud [a], C. Ritz [a]

[a] Laboratoire de Glaciologie et Géophysique de l'Environnement, UJF, CNRS, France
[b] Department of Geology and Geochemistry, Stockholm University, 10691 Stockholm, Sweden

ARTICLE INFO

Article history:
Received 3 June 2008
Accepted 28 March 2009
Available online xxxx

Keywords:
surface mass balance
Eurasian ice sheet
Saalian
proglacial lakes
dust
SST
vegetation

ABSTRACT

Recent geologically-based reconstructions of the Eurasian ice sheet show that during the peak Saalian (≈140 kya) the ice sheet was larger over Eurasia than during the Last Glacial Maximum (LGM) at ≈21 kya. To address this problem we use the LMDZ4 atmospheric general circulation model to evaluate the impact on the Saalian ice sheet's surface mass balance (SMB) from proglacial lakes, dust deposition on snow, vegetation and sea surface temperatures (SST) since geological records suggest that these environmental parameters were different during the two glacial periods. Seven model simulations have been carried out. Dust deposition decreases the mean SMB by intensifying surface melt during summer while proglacial lakes cool the summer climate and reduce surface melt on the ice sheet. A simulation including both proglacial lakes and dust shows that the presence of the former parameter reduces the impact of the latter, in particular, during summer. A switch from needle-leaf to tundra vegetation affects the regional climate but not enough to significantly influence the SMB of the nearby ice margin. However, a steady-state vegetation in equilibrium with the climate should be computed to improve the boundary conditions for further evaluations of the vegetation impact on the ice sheet's SMB. Finally, changes of the SST broadly affect the regional climate with significant consequences for the SMB.

© 2009 Elsevier B.V. All rights reserved.

1. Introduction

During the Quaternary Period, Northern Eurasia has been affected by several major glaciations. The Quaternary Environment of the Eurasian North (QUEEN) project reconstructed the Eurasian maximum extension for the last four major glaciations (Svendsen et al., 2004): The Late Saalian (180–140 kya), the Early Weichselian (100–80 kya), the Middle Weichselian (60–50 kya), and the Late Weichselian (21–15 kya). The maximum extents of these ice sheets have been determined by mapping marine and terrestrial glacial morphology. From these studies, it appears that the Late Saalian ice sheet (maximum at c. 140 kya referred to as the Late Saalian over Eurasia[1]) was the largest Northern Eurasian ice sheet of the Late Quaternary.

The Late Saalian ice sheet extended further east and southeast over Eurasia than at the (LGM) and it appears to have been as much as approximately 56% larger during its maximum extent (Fig. 1). This suggests that the ice volume was also larger at 140 kya over Eurasia, which is confirmed by a large lithospheric depression due to continental ice loading inferred from mapped paleo-lakes levels and raised shorelines dated to this time (Astakhov, 2004). However, the eustatic sea level is not sufficiantly constrained to conclude that significant differences existed between the global ice volume during the time periods for the LGM and the Late Saalian ice sheet. The review by Rabineau et al. (2006) shows that eustatic sea level estimations range from ≈120 m (Peltier and Fairbanks, 2006) to 163 m (CLIMAP, 1984) below the present sea level during the LGM and from 120 m (Shackleton, 1987; Rohling et al., 1998) to more than 130 m (Ferland et al., 1995) during the Late Saalian.

The main global forcings determining climate and build-up of ice sheets, such as orbital insolation and concentration of greenhouse gases, appear to have been similar for the Late Saalian and the LGM (Fig. 1). But the peak Saalian (140 kya) is also the consequence of a different evolution of the global insolation prior to its glacial maximum than that before the LGM. Moreover, it is clear that the Milankovitch theory alone cannot explain the variations in ice sheet volume and extent during the peak of the Quaternary glacial periods and the initial insolation forcing has to be increased by global and regional feedbacks (e.g. Krinner et al. (2004)). We focus this study on the potential impact of regional parameters such as proglacial lakes, dust deposition on snow, vegetation cover and sea surface temperatures on the regional climate and on the surface mass balance (SMB) of the Late Saalian Eurasian ice sheet. More specifically:

(1) We test the impact of dust deposition on the ice sheet's SMB since Calov et al. (2005) showed that dust deposition on snow

* Corresponding author.
E-mail address: flocolleoni@gmail.com (F. Colleoni).

[1] This ice sheet existed during the MIS6 glacial period, although we will henceforth use the term "Late Saalian" also when referring to the global environment at this time.

0921-8181/$ – see front matter © 2009 Elsevier B.V. All rights reserved.
doi:10.1016/j.gloplacha.2009.03.021

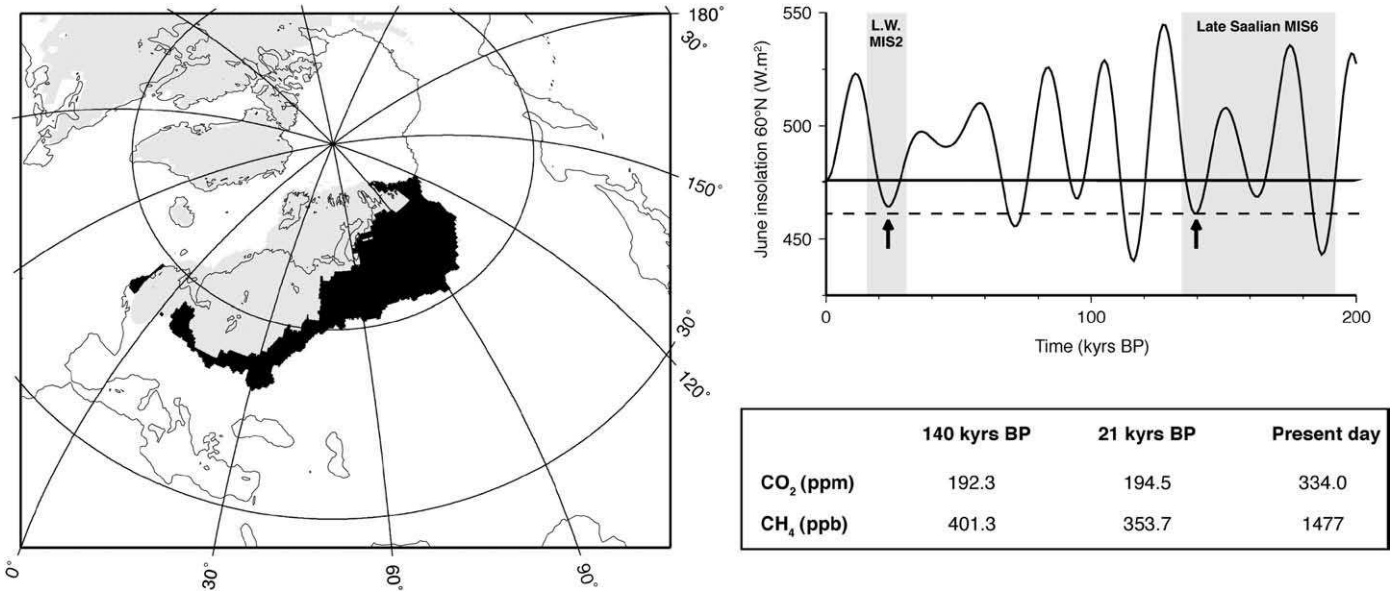

	140 kyrs BP	21 kyrs BP	Present day
CO_2 (ppm)	192.3	194.5	334.0
CH_4 (ppb)	401.3	353.7	1477

Fig. 1. Summary of the main differences between the LGM and the Late Saalian glacial maximum. Left: difference in ice extent between the LGM (gray) and the Late Saalian (black). The ice sheet extends further southward and eastward during the Late Saalian compared to LGM. Top right: June insolation at 60°N (Berger and Loutre, 1991), arrows point the Late Saalian glacial maximum (140 kya) and Late Weichselian (L.W.) glacial maximum (21 kya). The thick black line indicates the present-day insolation at 60°N. Note that the insolation was similar during both the LGM and Late Saalian glacial maximum. Bottom right: concentration of greenhouses gases measured in the Vostok and EPICA Dome C (Petit et al., 2001; Spahni et al., 2005) for the Late Saalian, the LGM and present-day.

reduced the albedo value by 10% to 30% and Krinner et al. (2006) showed that dust deposition on snow during the LGM can help explain the absence of ice sheets in Eastern Siberia. Considering that the downward solar radiation is about 100 $W \cdot m^{-2}$ at Northern latitudes and ice and snow albedo are of about 60% to 80%, the dust content of the snow induces an increase of 6 $W \cdot m^{-2}$ to 8 $W \cdot m^{-2}$, which is significantly higher than the effect produced by the atmospheric dust content.

(2) Since the LGM ice sheet extent was smaller than during the Late Saalian, the major northern Russian and Western Siberian rivers could still flow to the Arctic Ocean and no significant proglacial lakes seem to have formed in Siberia (Mangerud et al., 2004). On the contrary, the Late Saalian ice sheet blocked these rivers and large proglacial lakes could have formed in a similar way as during the Early Weichselian (Mangerud et al., 2001, 2004). Proglacial lakes can have a different influence on the regional climate depending on the regional settings. Krinner et al. (2004) showed that the large Early Weichselian ice-dammed lakes had a strong climatic impact as they cooled the near-surface summer climate due to their high thermal inertia. On the contrary, Hostetler et al. (2000) showed that at 11 kya in North America, the cooling induced by Lake Agassiz reduced the amount of moisture spreading over the Laurentide ice sheet, contributing to its retreat. Therefore, the impact of the proglacial lakes south of the Saalian ice sheet margin cannot be easily predicted and must be evaluated in GCM simulations.

(3) Vegetation plays an important role in the climate system as it modifies heat exchange and water vapor content of the atmosphere (Crowley and Baum, 1997). Simulations by Crowley and Baum (1997) showed that the replacement of conifer forest by tundra in Eurasia during the LGM cooled the regional climate.

(4) Sea surface conditions (sea-ice extent, thickness and concentration, sea surface temperatures) are an obvious climatic forcing on the adjacent continents. However, SST has been suggested to play a key role in the climate system. For example Smith et al. (2003) prescribed various sea-ice cover extents (SIC) to test the impact on the LGM and Holocene climate inducing large precipitation changes over Eurasia. Ruddiman and McIntyre (1979) as well as Hebbeln et al. (1994) showed that by introducing seasonally open water conditions in the North Atlantic during the LGM, mass balance of the Northern Hemisphere ice sheets was largely affected. Because there are no global- or even regional-scale reconstructions of the Late Saalian sea surface conditions, we test two different LGM reconstructions as possible surrogates.

The relative importance of these regional-scale forcings for the SMB of the Late Saalian Eurasian ice sheet is assessed in this study using an atmospheric general circulation model.

The relative importance of these regional-scale forcings for the SMB of the Late Saalian Eurasian ice sheet is assessed in this study using an atmospheric general circulation model. Our model exercise complements the HOTRAX sediment core studies by addressing the paleoenvironment during the Marine Isotope Stage 6 (MIS 6; when the Late Saalian Eurasian ice sheet existed), which is manifested in sedimentary features indicative of a very large glaciation at the Arctic margins (Adler et al., 2009-this issue).

2. Methods

We use the LMDZ4 AGCM (Hourdin et al., 2006) which takes into account the climatic impact of open water surfaces and dust concentration in snow (Krinner, 2003; Krinner et al., 2006). The model has been run with 96×72 grid cells horizontally and with 19 vertical layers. The horizontal resolution is irregular, varying from the highest resolution of 100 km grid cells centered over Eurasia at 65°N/60°E to 550 km elsewhere. The impact of using a stretchable grid on climate as been discussed in Krinner and Genthon (1997) who show that in the presence of strong topographic gradients, such as on the margin of the Late Saalian ice sheet, the impact of higher spatial resolution is clearly beneficial.

2.1. Modeling parameters

Except for the Eurasian region, we used the LGM global ice topography ICE-5G (Peltier, 2004), assuming that the differences between the real Late Saalian glacial maximum and LGM far from our region of interest are small enough to not critically influence our results. The Eurasian Late Saalian maximum topography (Fig. 2) was

Please cite this article as: Colleoni, F., et al., Influence of regional parameters on the surface mass balance of the Eurasian ice sheet during the peak Saalian (140 kya), Glob. Planet. Change (2009), doi:10.1016/j.gloplacha.2009.03.021

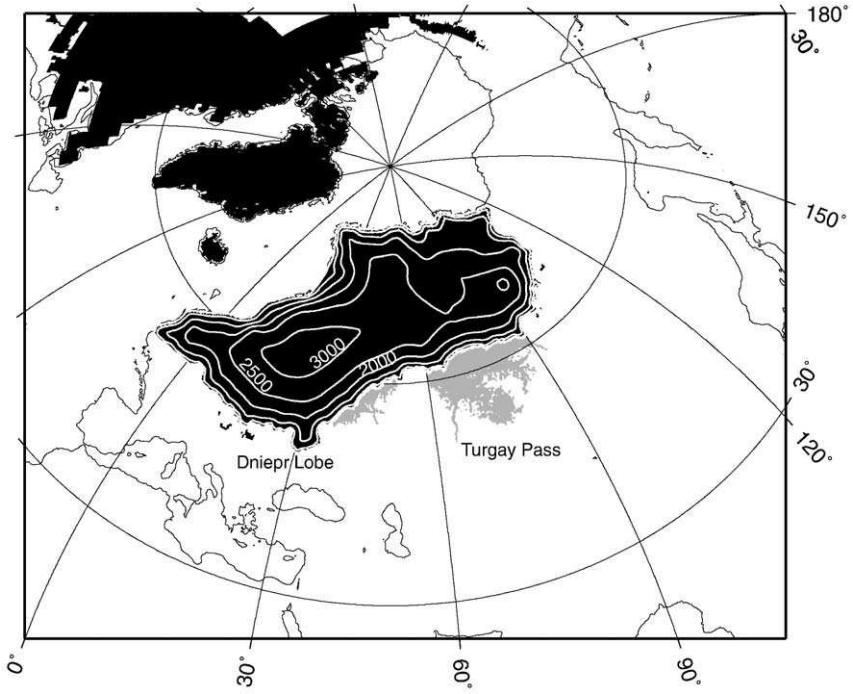

Fig. 2. Late Saalian glacial maximum topography (140 kya) and reconstructed proglacial lakes (gray). Maximum elevation for the Eurasian ice sheet is ≈3200 m which corresponds to ≈4300 m of ice thickness.

computed in previous work (Peyaud, 2006) using the GRISLI ice-model (Ritz et al., 2001) forced by a glacial index based on insolation values and the QUEEN reconstructed ice sheet extent (Svendsen et al., 2004). For more details about the ice modeling methods see Peyaud et al. (2007). We are aware of the fact that it is possible that the ice sheet did not reach its maximum extent everywhere at 140 kya. However, this is not possible to account for a more accurate extent due to lack of datable constraining field data (Svendsen et al., 2004). The modelled ice thickness of Eurasia reaches about ≈4300 m over Scandinavia, which corresponds to a ≈3200 m ice elevation (lithospheric deflection has been taken into account). These values are of the same order as those of Lambeck et al. (2006) who, using a rebound model, computed a mean ice thickness of about ≈4200 m over Eurasia corresponding to ≈3200 m of ice elevation.

Due to the isostatic depression caused by the Late Saalian ice sheet, large ice-dammed lakes probably existed along the southern margin, similar to those that existed during the Early Weichselian (Mangerud et al., 2001, 2004). In this study, ice-dammed lakes have been reconstructed according to the methods of Mangerud et al. (2001) (Fig. 3).

The distribution of dust deposition during MIS 6 has neither been determined from geological data nor modelled in previous work. We have therefore adapted the LGM spatial distribution modelled by Mahowald et al. (1999) by using the EPICA Dome C ice core dust concentration records (Delmonte and coauthors, 2004) for the LGM and the Late Saalian time periods (Fig. 3). Winckler et al. (2008) recently showed that during the late-Pleistocene glacial cycles, dust fluxes in both hemispheres had a common response to global climate change. During the LGM, dust concentration recorded at EPICA Dome C was approximately $C_{DC,LGM} \approx 1370$ ppm whereas during the Late Saalian glacial maximum it was $C_{DC,MIS6} \approx 830$ ppm. The global MIS 6 dust deposition rates D_{MIS6} have therefore been obtained by applying a homogeneous factor to the LGM deposition rates D_{LGM} given by Mahowald et al. (1999), assuming that ice accumulation and dust sources were similar during the LGM and the MIS6 glacial maximum:

$$D_{MIS6} = D_{LGM} \times \frac{C_{DC,MIS6}}{C_{DC,LGM}} = D_{LGM} \times 0.60 \quad (1)$$

Dust deposition fluxes are presented in Fig. 4 for the LGM (Mahowald et al., 1999) as well as the difference in dust distribution between the LGM and the Late Saalian obtained after modifications. First, the dust deposition rates have been multiplied by the ratio described above. However the LGM dust deposition distribution overlaps the eastern part of the Eurasian ice sheet (Fig. 4) and consequently induces a reduction in the albedo value by about 20%. The Eurasian LGM ice sheet used by Mahowald et al. (1999) to reconstruct the LGM dust deposition fluxes is smaller and thinner than the Late Saalian ice sheet. In our Late Saalian simulations, this would lead to excessive dust deposition in the regions which are ice-covered, because dust deposition is generally higher in low-lying areas than over the dry ice sheet (Fig. 6). To avoid unrealistically high dust concentrations on the ice, we reduced the amount of dust deposition over the Eastern part of the Eurasian ice sheet (Fig. 4b). All the dust deposition rates greater than 2.5 $g \cdot m^{-2} \cdot yr^{-1}$ over the ice sheet have been multiplied by 0.025 and some dust still accumulates on the ice sheet but in reasonable concentration. We did not redistribute the excess of dust removed by this operation since the quantity can be

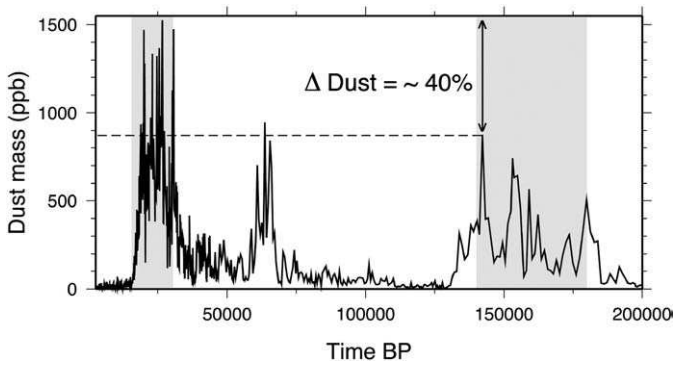

Fig. 3. Dust concentration (ppb) inferred from EPICA Dome C ice cores (Delmonte and coauthors, 2004). Gray shadows indicate the time period of the Late Saalian and the Late Weichselian ice sheets. There is about 40% difference in dust concentration between these two time periods.

Please cite this article as: Colleoni, F., et al., Influence of regional parameters on the surface mass balance of the Eurasian ice sheet during the peak Saalian (140 kya), Glob. Planet. Change (2009), doi:10.1016/j.gloplacha.2009.03.021

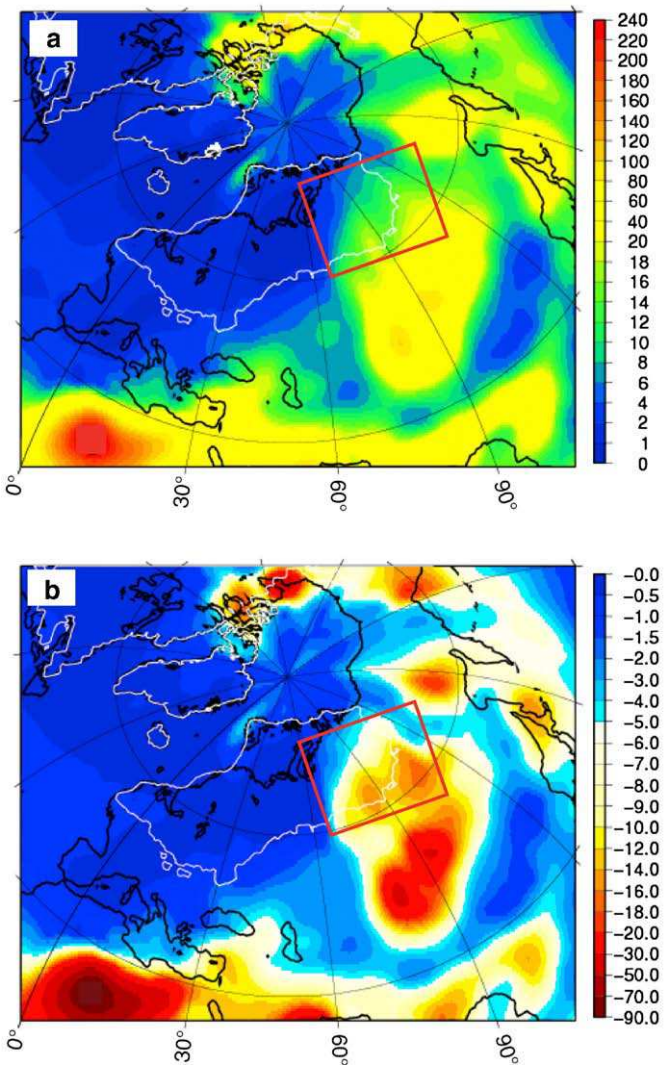

Fig. 4. Top: LGM dust deposition fluxes after Mahowald et al. (1999). Bottom: Difference between the LGM and the Late Saalian adaptation (Section 2). Unit: g m^{-2} yr^{-1}. White contours correspond to the Late Saalian ice margins. Red boxes focus on the part of the ice sheet where we artificially removed more dust (Section 2).

considered minor (see Fig. 4). The dust content of the snow, and the resulting snow albedo are calculated according to the model of Krinner et al. (2006). The LMDZ4 model does not take into account the radiative forcing induced by the atmospheric dust content but only the dust content of the snow, because the radiative effect of the surface albedo decreases over highly reflective areas and outweighs the reflective effect of dust as an atmospheric aerosol (Claquin et al., 2003; Krinner et al., 2006).

Since no consistent Late Saalian global vegetation exists, we use the LGM vegetation map from Crowley (1995) as a first approximation (Fig. 5). In this map, tundra covers all Siberia and needle-leaf trees are present in the Russian plains. To test the sensitivity of the Late Saalian Eurasian ice sheet to vegetation changes, we replaced the needle-leaf trees area by tundra. The seasonal leaf phenology is calculated using the parametrization of Jolly et al. (2005).

Similarly, there is no SST reconstruction available for the Late Saalian period. Therefore, LGM SST compiled in the CLIMAP project (CLIMAP, 1984) was prescribed as first order of approximation. The influence of SST forcings on the ice sheet's SMB is explored using an alternative SST dataset (Fig. 6) from Paul and Schaefer-Neth (2003) (referred to as Paul).

Finally, orbital parameters have been set according to Berger and Loutre (1991) and greenhouse gas concentrations (GHG) have been specified (Fig. 1) according to Vostok and EPICA Dome C ice core concentration records (Petit et al., 2001; Spahni et al., 2005).

2.2. Parametrization of surface mass balance

We test two methods for the computation of the ice sheet surface mass balance. The first follows Krinner et al. (2007). This parametrization, first developed by Thompson and Pollard (1997), takes into account the refreezing of a part (f) of rainfall and melt-water (ranging in the interval [0;1]):

$$f = 1 - \min\left(1, \max\left(0, \frac{\left(\frac{M}{P_S} - 0.7\right)}{0.3}\right)\right) \quad (2)$$

where P_S is the annual mean solid precipitation, and M is the annual snow or ice melt calculated from the surface energy balance in the AGCM.

The runoff is calculated as:

$$R = (1 - f)(M + P_L) \quad (3)$$

where P_L is the annual liquid precipitation (rainfall). Finally the surface mass balance B is calculated as:

$$B = P_S + fP_L - E - (1 - f)M \quad (4)$$

with E as the annual sublimation.

The second method uses the temperature index method as proposed by Ohmura et al. (1996). In this method, surface ablation is diagnosed when the mean summer surface air temperature (T_{JJA}), recalculated on a fine resolution grid with altitude-correction, exceeds a prescribed threshold of −1.8 °C. The total ablation A (in kg m^{-2} yr^{-1}) is then calculated as:

$$A = 514^{\circ}C^{-1} \times T_{JJA} + 930 \quad (5)$$

where T_{JJA} is in °C. We downscale the AGCM surface air temperature to a 20-km grid by applying a 5.5 °C km^{-1} summer temperature

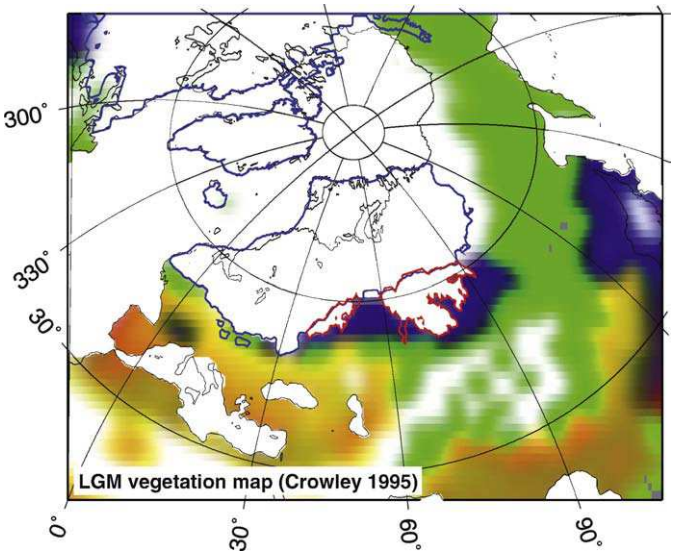

Fig. 5. RGB prescribed LGM vegetation map (Crowley, 1995). Three main biomes are displayed: tundra (green), needle-leaf trees (dark blue) and broad-leaved trees (red). Mixed forest is consequently in purple and mixed tundra–broad-leaved trees forests range in orange–brown color interval.

Please cite this article as: Colleoni, F., et al., Influence of regional parameters on the surface mass balance of the Eurasian ice sheet during the peak Saalian (140 kya), Glob. Planet. Change (2009), doi:10.1016/j.gloplacha.2009.03.021

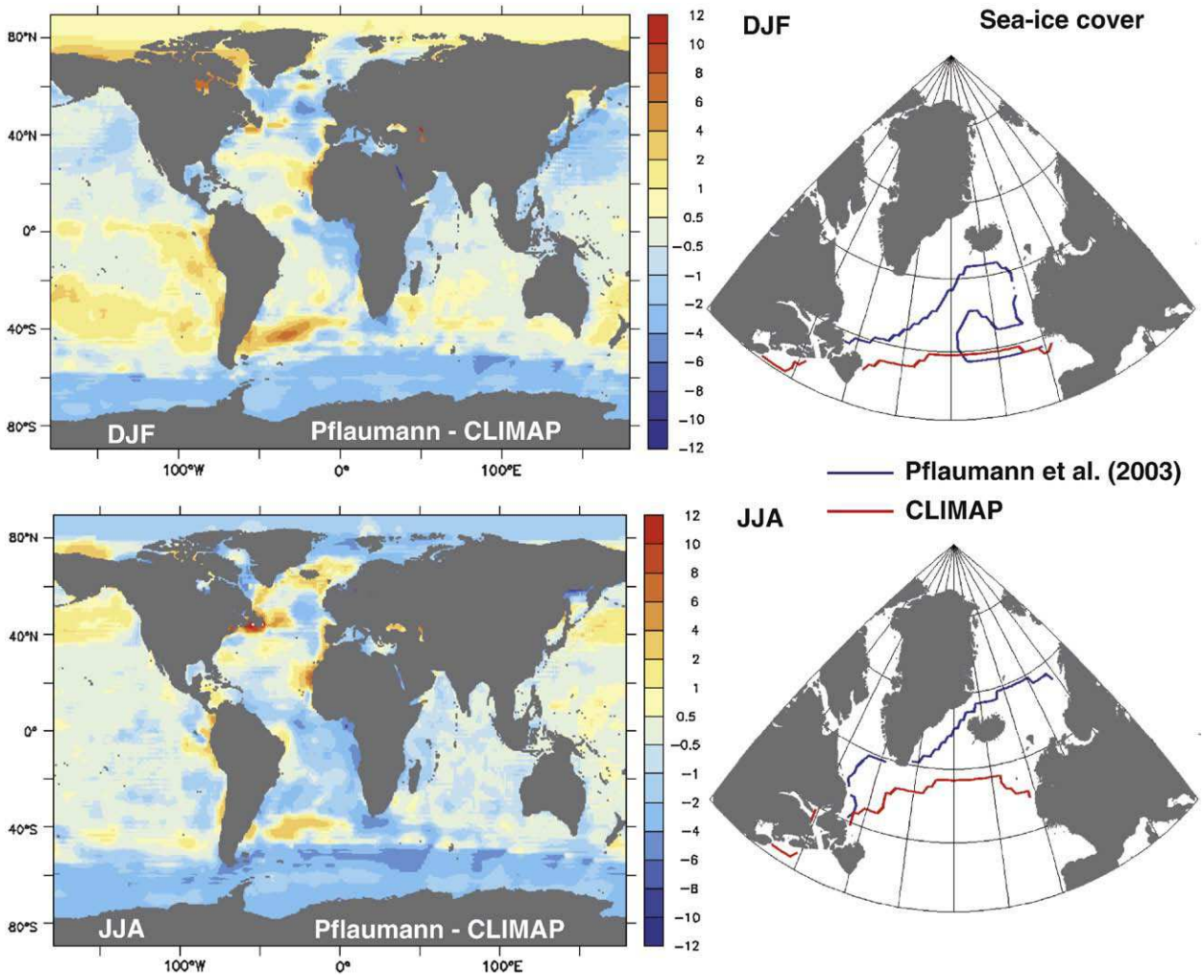

Fig. 6. LGM sea surface temperature anomalies between CLIMAP SST (CLIMAP, 1984) and Paul and Schaefer-Neth (2003) SST for winter (DJF) and summer (JJA). Sea-ice extent (SIC) are derived directly from the two SST datasets following the −1.8 °C isotherm. The dark blue line stands for Paul and Schaefer-Neth (2003) SIC while the red line stands for CLIMAP SIC.

correction to account for altitude changes (Krinner and Genthon, 1999; Abe-Ouchi et al., 2007). The surface mass balance B is then calculated as:

$$B = P_S - E - A \tag{6}$$

with P_S and E as before.

2.3. AGCM experiments

Altogether, seven simulations of 21 years (snapshots) were carried out, the first year being discarded as spin-up. The settings are summarized in Table 1. Our simulations include a present-day control run (simulation REF0: present-day with modern dust deposition) which was forced by AMIP II average 1979–1993 sea surface conditions (Taylor et al., 2000). The Late Saalian paleoclimate simulations were carried out to test the individual and combined impacts of proglacial lakes, dust deposition on snow, vegetation feedbacks and SST forcings. Simulation REF140, which does not take into account lakes or dust deposition, will be considered as the "reference" Saalian simulation. Simulation LAKES140 takes into account the effect of proglacial lakes, simulation DUST140 involves the impact of dust deposition only while simulation FULL140 includes the combined effects of proglacial lakes and dust deposition on snow. Finally VEG140 and SST140 take into account both proglacial lakes and dust deposition as well as vegetation feedbacks and SST forcings respectively. To address the impact of regional input parameters, DUST140, LAKES140 and FULL140 are compared to simulation REF140 while VEG140 and SST140 are compared to FULL140. Air temperature, albedo and sea-level pressure (SLP) anomalies are calculated as a difference while precipitation anomalies are presented as a ratio.

To evaluate if the observed differences between the calculated SMB values and their components for both methods can be interpreted as an effect of the investigated regional factors, student t-tests have been performed between REF140 and LAKES140, DUST140, FULL140 and

Table 1
Simulations carried out in this work. AMIPII refers to the present-day sea surface temperatures (SST) from Taylor et al. (2000) while CLIMAP and Paul and Shaefer-Neth (2003) stand for LGM SST. "Crowley modif." corresponds to the LGM vegetation map (Crowley, 1995) in which conifera have been replaced by tundra.

ID	Time period (kya)	Lakes	Dust	SST	Veget.
REF0	0	No	Yes	AMIPII	Present-day
REF140	140	No	No	CLIMAP	Crowley
LAKES140	140	Yes	No	CLIMAP	Crowley
DUST140	140	No	Yes	CLIMAP	Crowley
FULL140	140	Yes	Yes	CLIMAP	Crowley
VEG140	140	Yes	Yes	CLIMAP	Crowley modif.
SST140	140	Yes	Yes	Paul and Schaefer-Neth (2003)	Crowley

Please cite this article as: Colleoni, F., et al., Influence of regional parameters on the surface mass balance of the Eurasian ice sheet during the peak Saalian (140 kya), Glob. Planet. Change (2009), doi:10.1016/j.gloplacha.2009.03.021

Table 2
Mean annual surface mass balance (SMB) and its components (averaged over the Eurasian ice sheet, in kg m^{-2} yr^{-1}). The upper part of the table contains the components used or valid for both SMB parametrization methods, the second part those used for the Ohmura et al. (1996) method, and the third part those used for calculating the SMB following Thompson and Pollard (1997). LAKES140, DUST140 and FULL140 are compared to REF140 while VEG140 and SST140 are compared to FULL140. Significant differences (according to a two-sided student t-test) are represented by an asterisk near the SMB value.

(kg m^{-2} yr^{-1})	REF140	DUST140	LAKES140	FULL140	VEG140	SST140
Tot. precip.	361	361	351	357	359	353
Snow	320	320	317	320	323	318
Evap	72	73	70*	70*	70	73*
Ablation	108	112	77*	80*	81	94*
SMB (Ohmura et al., 1996)	140	135	170*	170*	172	150*
Melt	744	768	590*	612*	606	557*
Runoff	779	803	619*	642*	636	587*

between FULL140 and VEG140, SST140. Since the simulated datasets are available for 20 years each, the number of degrees of freedom is $N1+N2-2=38$. The null hypothesis H_0 is defined as $\sigma_1 \neq \sigma_2$ and we will be accepted if probability is lower than 5%. Significant differences are indicated in Table 2 by a solid star nearby the values.

3. Results

3.1. Present-day control run

The simulated present-day surface climate (REF0) is here compared with observations compiled by the Climatic Research Unit (CRU, New et al. (1999)) and by the European Centre for Medium-Range Weather Forecast (ECMWF, Uppala et al. (2005)). REF0 takes into account the effect of dust deposition on snow, but due to the low present-day dust deposition rates (Mahowald et al., 1999), this effect is small, as reported previously by Krinner et al. (2006). The simulated winter surface air temperature is overestimated by more than 10 °C in the Eastern Siberian mountains (Fig. 7a). This is probably due to the low AGCM resolution which is unable to correctly represent the complex topography which in turn impacts on the balance between the drag and lift forces affecting the planetary wave scheme (Lott, 1997). However, it should be noted that these mountain ranges comprise extremely data-sparse regions making also the observational records uncertain. This warm winter bias appears to lead to an overestimate (by 50% to 100%) of the precipitation in the same region. The simulated surface air temperature in summer exhibits a mean warm bias of about 2 °C to 3 °C over a large part of Eurasia (Fig. 7). Further west, the simulated winter climate is colder than the observations. Surface air temperatures are underestimated by about 8 °C. Winter precipitation is overestimated by about 30% over Scandinavia and underestimated by about 50% over the Russian and Siberian plains. During summer, precipitation is overestimated by 50% to 100% over Eastern Siberia and Scandinavia which confirms that this overestimation of precipitation might be linked to the mentioned temperature error. However, the underestimation of precipitation seems not to be linked to the temperature bias but to circulation anomalies. 500 hPa geopotential height, both for winter and summer, exhibits positive anomalies over Siberia and Alaska linked to the warm temperature bias (Fig. 7). The incorrect representation of planetary waves in these regions impact on the atmospheric circulation, creating a cyclonic anomaly over Europe during winter, inducing reduced precipitations over Eurasia. During summer, REF0 is warmer than the CRU records. However, the mean annual temperature bias over Eurasia (−15°W to 150°E; 40°N to 85°N) is negligible and similar to that previously described in Krinner et al. (2006). REF0 overestimates the mean annual precipitation over Eurasia by about 30% compared to the observations. This is again similar to the results reported by Krinner et al. (2006).

3.2. Reference Late Saalian simulation: no lakes and no dust

Model run REF140 was carried out to simulate the full glacial conditions of the Late Saalian, including the proper orbital forcing, greenhouse gas concentrations, the reconstructed ice sheet extent and topography, sea surface conditions and vegetation cover. This simulation does, however, not take into account proglacial lakes or dust deposition on snow and it is seen here as our reference simulation because these latter parameters are usually not taken into account in AGCM simulations.

The results show that during summer, the 0 °C isotherm is clearly constrained by the presence of the Eurasian ice sheet (Fig. 8a). Winter temperatures over the center of the ice sheet are below −50 °C whereas in ice-free regions mean temperature reaches ≈−30 °C. During summer, the temperature over the ice sheet does not exceed −20 °C. Southward of the ice sheet, temperatures reach 20 °C. Mean air surface temperature compared to simulated present-day climate exhibit negative anomalies of about −30 °C during winter over the ice sheet and −15 °C over the ice-free region (not shown in the figures). Over the Eurasian ice sheet, the mean annual cooling induced by the presence of ice is about −24 °C. Compared to simulation REF0, mean annual precipitation is reduced by about 68% over ice-free parts of Eurasia. Precipitation over the northern part of the ice sheet reaches a minimum of about 32 $kg \cdot m^{-2} \cdot yr^{-1}$ (Fig. 8c). Maximum precipitation over the ice sheet occurs off the British Isles, ≈1600 $kg \cdot m^{-2} \cdot yr^{-1}$ and along the southern Russian limit, ≈1000 $kg \cdot m^{-2} \cdot yr^{-1}$. The precipitation and temperature cycles appear to be tightly linked to the variations of the moisture holding capacity of the air, which depends on temperature (Robin, 1977). The simulated Late Saalian sea-level pressure (SLP) over the North Atlantic (not shown) does not exhibit an Icelandic low, probably because of the extended sea-ice cover, while a strong winter depression is developing over the North Pacific with SLP values down to 990 hPa. Convergence of the moisture fluxes shows that possible moisture sources for the Eurasian ice sheet can be located over the Southeastern margin of the Laurentide ice sheet and over the North Atlantic (Fig. 8d). Moisture flux direction is similar in all the following simulations.

The two methods used to calculate the surface mass balance yield largely different results. Table 2 provides quantitative values of some of the components of the SMB. Total precipitation comprises rain and snowfall. In all cases, the temperature index method results in a positive surface mass balance, while the method based on the approach by Thompson and Pollard (1997) yields extremely negative estimates of the SMB. For reasons given in the discussion later in this paper, we think that in this study, the Ohmura et al. (1996) temperature index method is to be preferred. In the following, only results obtained with this method will be analysed in detail.

The mean ice sheet surface mass balance is 140 $kg \cdot m^{-2} \cdot yr^{-1}$ shows that Negative surface mass balance occurs along the southern ice sheet margins as well as locally on the western margin (Fig. 9a).

3.3. Impact of proglacial lakes on the surface mass balance

A comparison between simulation REF140 and LAKES140 shows that negative temperature anomalies develop over the lakes (≈−4 °C) and over the western part of the Eurasian ice sheet (≈−2°; Fig. 10). This appears to be linked to the presence of proglacial lakes which are frozen and cool the above atmosphere. Proglacial lakes remain frozen during winter, spring and fall (except the southern part for the latter season) while they are totally open during summer. Winter precipitation anomalies regionally differ: the northern part of the ice sheet undergoes a 60% precipitation decrease while the southern and western parts exhibit an increase of about 20%. This winter precipitation pattern in the South is sustained by the southern ice sheet margin which constitutes a moisture source in itself as shown by the convergence map (Fig. 10f).

Please cite this article as: Colleoni, F., et al., Influence of regional parameters on the surface mass balance of the Eurasian ice sheet during the peak Saalian (140 kya), Glob. Planet. Change (2009), doi:10.1016/j.gloplacha.2009.03.021

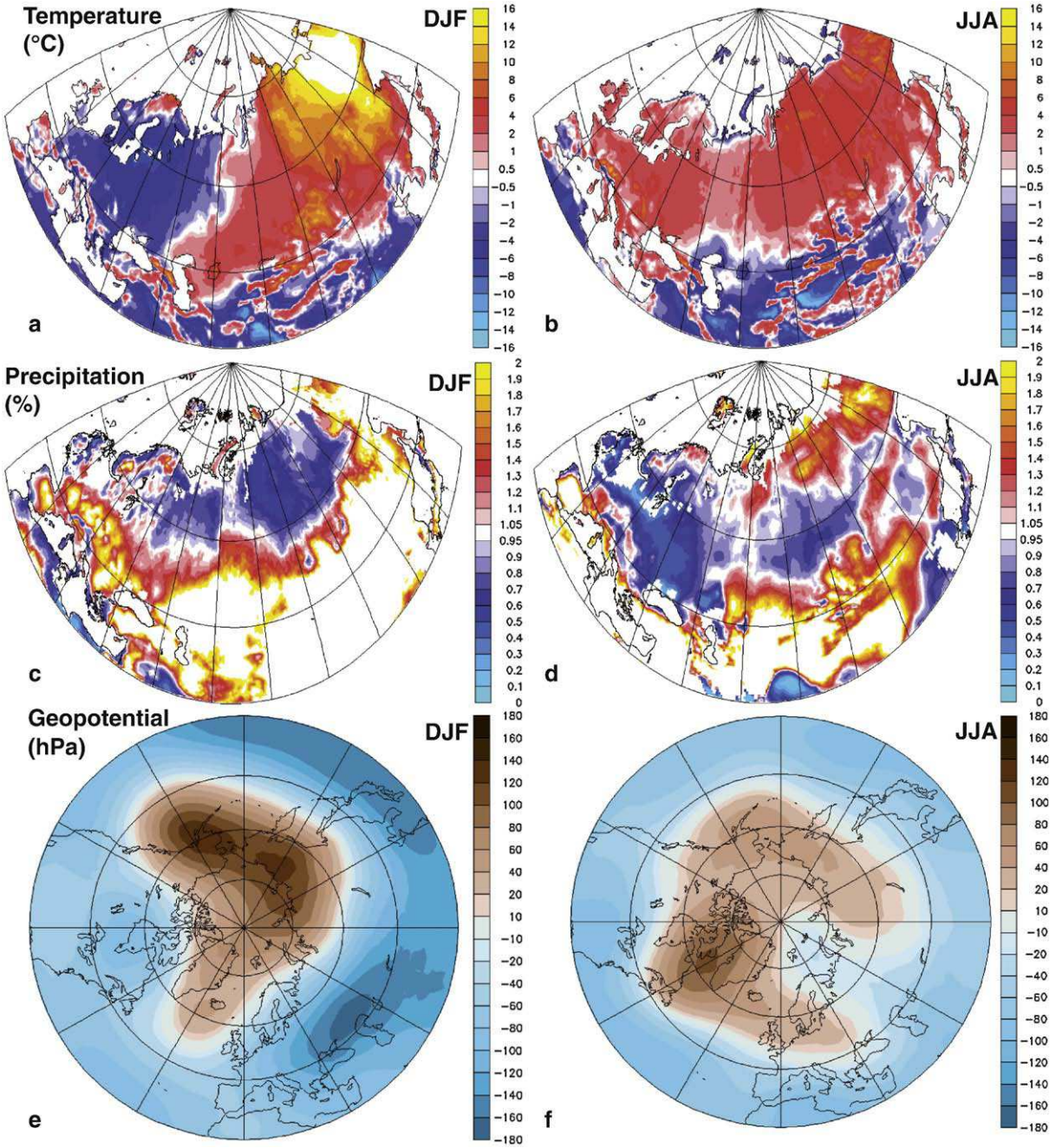

Fig. 7. Present-day control run (REF0) climate compared to Climatic Research Unit temperatures and precipitations (New et al., 1999) and to European Centre for Medium-Range Weather Forecasts geopotential height 500 hPa (Uppala et al., 2005). Winter (DJF) and summer (JJA) surface air temperature anomalies are calculated as $T2m_{REF0} - T2m_{CRU}$, in °C. Winter (DJF) and summer (JJA) precipitation anomalies are calculated as $precip_{REF0} / precip_{CRU}$. Finally, geopotential height anomalies are expressed as for T2m anomalies.

During summer, a strong negative temperature anomaly is visible over the lakes (about −14 °C). This anomaly spreads all over the south-eastern part of the ice sheet, and cools the air temperature by 1 °C to 2 °C. This leads to reduced precipitation rates over the south-eastern part of the ice sheet of about 20%, implying that the proglacial lakes during the Late Saalian had an even greater effect on climate than estimate by Krinner et al. (2004) in the same region during the Early Weichselian (90 kya). A positive precipitation anomaly (≈30%) appears along the Central European margins and over the German and Scandinavian parts of the ice sheet (≈10%).

The strong summer cooling induced by the proglacial lakes leads to reduced surface melt on the adjacent ice margins and further to the west (Fig. 10c). The ice-sheet-wide average ablation decreases from 108 $kg \cdot m^{-2} \cdot yr^{-1}$ in REF140 to 77 $kg \cdot m^{-2} \cdot yr^{-1}$ in LAKES140 (Table 2). The most striking difference is linked to a modified accumulation pattern. The lake-induced summer cooling leads to reduced summer precipitation over a large part of the ice sheet (Fig. 10d), and therefore to a reduced surface mass balance in the interior. However, this is compensated for by increased moisture disposal over the southwestern part of the ice sheet. Total precipitation is therefore similar in REF140 (361 $kg \cdot m^{-2} \cdot yr^{-1}$) and LAKES140 (351 $kg \cdot m^{-2} \cdot yr^{-1}$), and the solid precipitation, which preferentially falls during the cold season on the southern margin, is almost identical (320 and 317 $kg \cdot m^{-2} \cdot yr^{-1}$, respectively).

3.4. Impact of dust deposition on the surface mass balance

In simulation DUST140, dust-induced net-warming of about 1 °C to 2 °C lasts all the year due to the decreased albedo caused by dust deposition on snow (not shown here). The warming is specially

Please cite this article as: Colleoni, F., et al., Influence of regional parameters on the surface mass balance of the Eurasian ice sheet during the peak Saalian (140 kya), Glob. Planet. Change (2009), doi:10.1016/j.gloplacha.2009.03.021

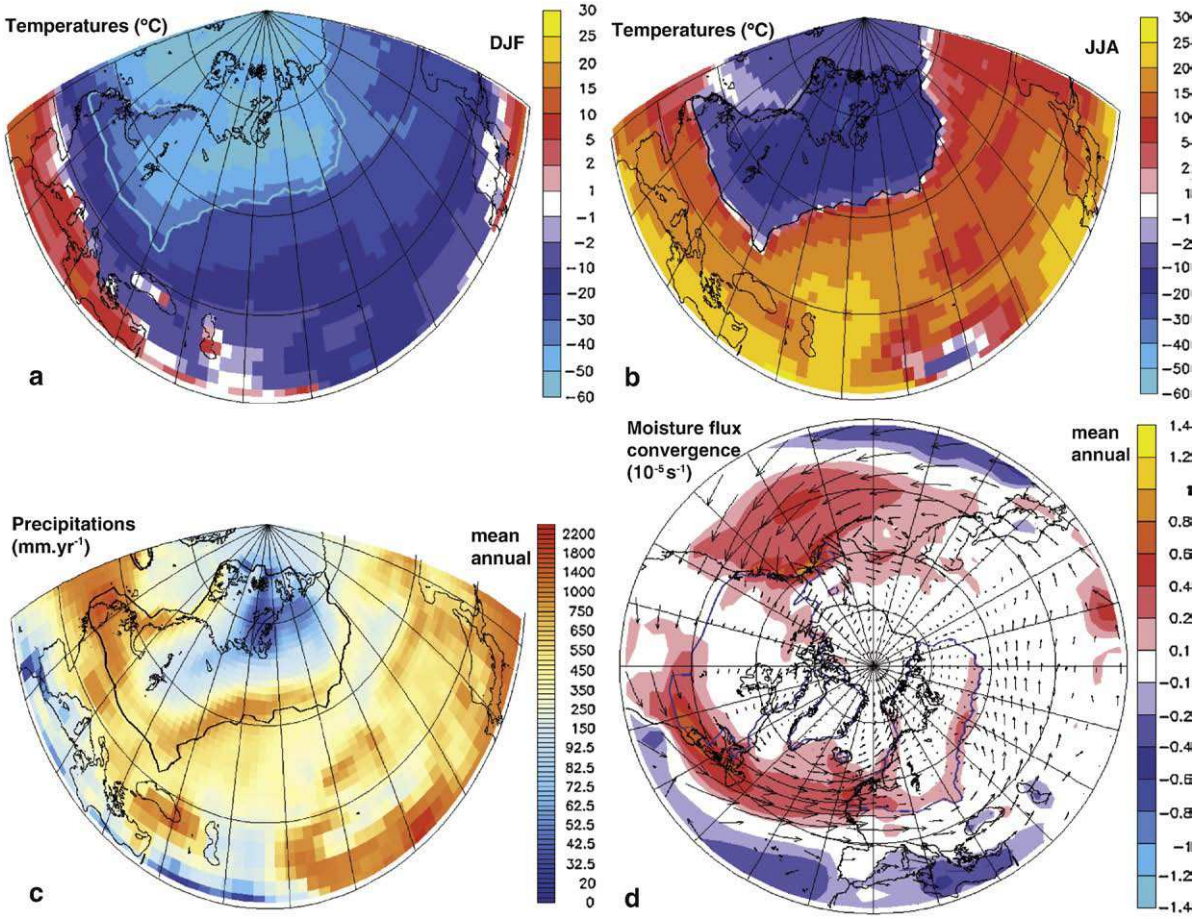

Fig. 8. Late Saalian surface air temperature (in °C) for simulation REF140. (a): winter (DJF); (b): summer (JJA); (c): mean annual precipitation (in kg m^{-2} yr^{-1}) and (d) convergence of the moisture fluxes in 10^{-5} s^{-1} (black arrows represent moisture fluxes). The black thick contour indicates the margins of the Late Saalian Eurasian ice sheet.

extended during spring. The winter (DJF) and summer (JJA) temperatures, precipitation and melt anomalies with respect to simulation REF140 are presented in Fig. 11. During winter, air surface temperatures over the ice sheet are similar to that of REF140 whereas in the ice-free region (Europe and East Siberia), dust-induced temperature changes are positive (1° to 2 °C). Precipitation is increased by 10% to 30% over the south-eastern margins of the ice sheet due to the moisture fluxes that exhibit the same pattern over the ice sheet. Since during summer, no significant anomaly occurs, spring anomalies, which are much more developed, are displayed in Fig. 11. Temperatures are approximately 1 °C to 2 °C higher on the central and western part of the Eurasian ice sheet (Fig. 11a). Consequently precipitation globally increases over the eastern part of the ice sheet by about 30% to 70%.

Since the warming is not strongest in summer, the diagnosed snow melt increases only slightly from 108 $kg \cdot m^{-2} \cdot yr^{-1}$ in REF140 to 112 $kg \cdot m^{-2} \cdot yr^{-1}$ in DUST140 (Table 2). Because the ice-sheet solid precipitation is identical in both simulations, the calculated SMB is very similar (135 $kg \cdot m^{-2} \cdot yr^{-1}$ in DUST140 compared to 140 $kg \cdot m^{-2} \cdot yr^{-1}$ in REF140), and the mean difference over the ice sheet is statistically insignificant. However, the local significance is displayed in Fig. 15a and discussed in Section 4.

3.5. Full glacial simulation: impact of lakes and dust on the surface mass balance

Simulation FULL140 takes into account both the effect of lakes and dust. This simulation is intended to be closer to the full glacial conditions that existed during the peak Saalian in Eurasia than the simulations presented before. The winter, temperatures are 2 °C lower over the western part of the Eurasian ice sheet compared to REF140 (Fig. 12). A negative temperature anomaly exists over the lakes (≈ −4 °C) and is similar to that shown on Fig. 10 for the simulation LAKES140. Precipitation rates generally match the temperature pattern. During summer, similarly to simulation LAKES140, a strong negative temperature anomaly of ≈ −14 °C develops over the lakes and spreads southward (≈1° to 2 °C) and over the eastern part of the ice sheet (Fig. 13). Compared to the simulation LAKES140, this summer negative anomaly is much more spatially extended. Consequently, precipitation is decreased by 50% to 80% over the lakes and on the eastern part of the ice sheet. A positive precipitation anomaly is observed on the westernmost part of the ice sheet, due to an increase of the moisture flux intensity (≈30% to 60%, not shown here).

The average accumulation, ablation and resulting SMB in FULL140 (250, 80, and 170 $kg \cdot m^{-2} \cdot yr^{-1}$, respectively) are very similar to LAKES140 (247, 77, and 170 $kg \cdot m^{-2} \cdot yr^{-1}$, respectively).

3.6. Full glacial simulation: vegetation feedbacks

Simulation VEG140 includes the modified LGM vegetation map in which needle-leaf trees have been replaced by tundra (Fig. 5) and also takes into account proglacial lakes and dust deposition impact.

VEG140 is compared to FULL140 and anomalies are reported in Fig. 13. The switch from needle-leaf trees to tundra causes a positive albedo anomaly of about 3 to 10% near the proglacial lakes which can be correlated to the negative temperature anomaly of about 1 °C spreading over the Eastern part of the ice sheet. The albedo anomaly is strengthened by a more frequent snow cover along the southern margins of the ice sheet (Fig. 13). The small positive temperature

Please cite this article as: Colleoni, F., et al., Influence of regional parameters on the surface mass balance of the Eurasian ice sheet during the peak Saalian (140 kya), Glob. Planet. Change (2009), doi:10.1016/j.gloplacha.2009.03.021

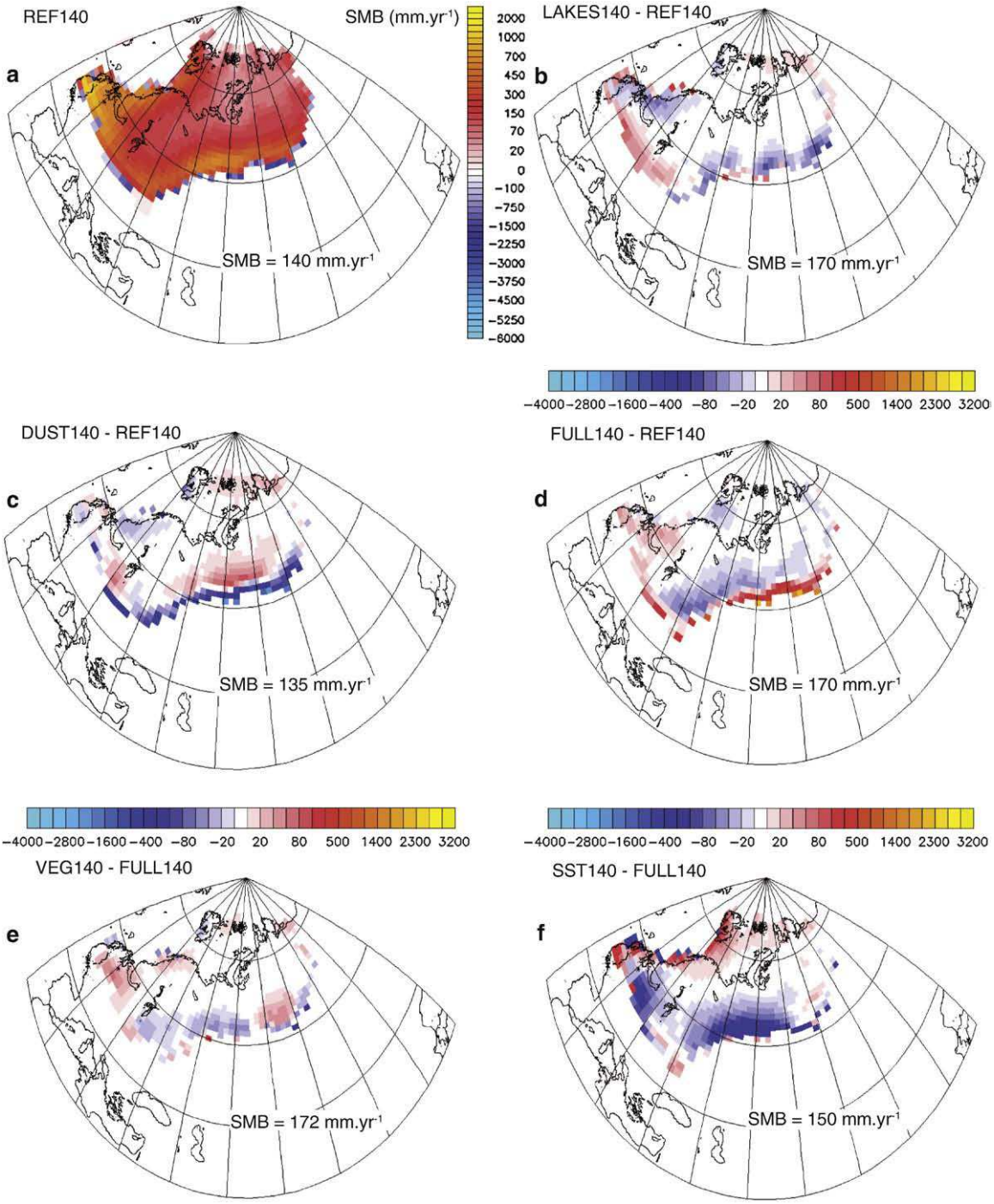

Fig. 9. (a): Simulated mean annual surface mass balance (SMB) of the Eurasian ice sheet (in mm yr^{-1}) for REF140; differences between the SMB values of REF140 and (b) LAKES140, (c) DUST140, (d) FULL140. (e) and (f) show the difference between simulation FULL140 and VEG140 and SST140 respectively. Indicated SMB value corresponds to the mean SMB over the entire ice sheet (Table 3).

anomaly developing over the Arctic and the North Atlantic spreads along the European margins of the ice sheet reducing the snow cover in the ice-free regions. Diagnosed changes in melt intensity are of course directly linked to the simulated summer surface air temperature changes. Because these are relatively weak, and because the diagnosed melt rates in FULL140 are also moderate, the vegetation changes have almost no impact on the average ice sheet surface mass balance.

3.7. Full glacial simulation: sensitivity to sea surface conditions

In SST140 we prescribed Paul and Schaefer-Neth (2003) sea surface conditions to test the sensitivity of the SMB to different SST forcings. CLIMAP and Paul and Schaefer-Neth (2003) SST reconstructions are to some extent different as seen in Fig. 6. During winter (DJF), the southern hemisphere is cooler by ≈4 °C in Paul and Schaefer-Neth (2003) while the northern hemisphere is warmer by ≈2 °C except in the Northern Atlantic where SST are cooler by about 2 °C. During summer, the Paul reconstruction is globally cooler than CLIMAP. These SST differences lead to different sea-ice cover (SIC) in the North Atlantic (Fig. 6). During winter, the North Atlantic south of Iceland is essentially open in Paul and Schaefer-Neth (2003) while ice-covered in CLIMAP. During summer, the Norwegian Sea is open in Paul and Schaefer-Neth (2003) while CLIMAP suggests a sea-ice cover almost similar to winter. The following results are compared to those of FULL140.

Please cite this article as: Colleoni, F., et al., Influence of regional parameters on the surface mass balance of the Eurasian ice sheet during the peak Saalian (140 kya), Glob. Planet. Change (2009), doi:10.1016/j.gloplacha.2009.03.021

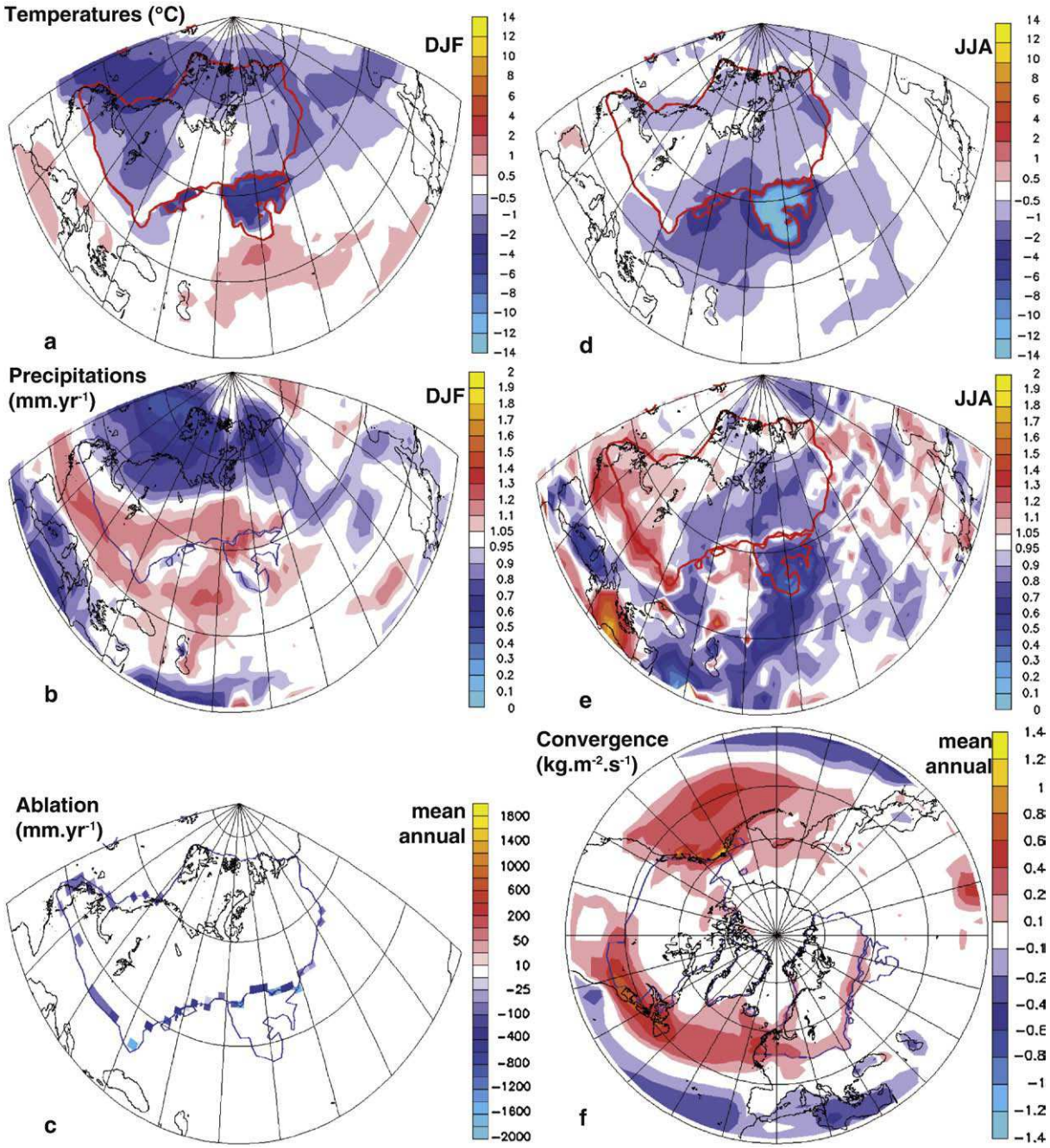

Fig. 10. (a, d) Seasonal air temperature (in °C), (b, e) precipitation (ratio) anomalies for LAKES140 (with respect to REF140) during winter (DJF) and summer (JJA). (c) Mean annual melt anomalies and (f) moisture fluxes convergence. Blue contours indicate the ice sheet margins and lake shorelines.

A positive temperature anomaly of about 5 °C develops during winter time over the Western part of the ice sheet due to the difference in sea-ice extent between CLIMAP and Paul and Schaefer-Neth (2003) (Fig. 14a). This anomaly warms Eurasia by about 2.5 °C. A negative anomaly of about 2.5 °C develops over the Eastern part of the ice sheet due to an increase in snowfall by about 20% (Fig. 14e) along the eastern margin. During summer, a positive anomaly of about 2.5 °C develops over the North Atlantic due the difference in SIC. However, because of the summer air surface temperature, the warm anomaly caused by the difference in SIC is less visible. Rainfall is increased by more than 100% over the southwestern part of the ice sheet, over the North Atlantic (due to the reduced sea-ice cover) and over Central Eurasia. It is evident that snowfall increases over the ice-free regions by 20%, especially over Siberia, and decreases by 30% over the Russian part of the ice sheet due to the warm temperature anomaly developing during winter (Fig. 14a). Furthermore, the reduced SIC causes a stronger cyclonic activity over the North Atlantic (Fig. 14c).

Over the ice sheet, melt increases along the entire margin as a consequence of a warmer ocean (compared to FULL140). On average ice sheet ablation is 94 $kg \cdot m^{-2} yr^{-1}$ (compared to 80 $kg \cdot m^{-2} yr^{-1}$ in FULL 140). As a consequence, the average SMB of the ice sheet attains 150 $kg \cdot m^{-2} \cdot yr^{-1}$.

4. Discussion

The six Late Saalian simulations carried out here (REF140, LAKES140, DUST140, FULL140, VEG140, SST140) aim to evaluate the impact from dust deposition, proglacial lakes, vegetation and sea surface temperatures on the surface mass balance (SMB) of the large Late Saalian Eurasian ice sheet. The main goal is to understand if these

Please cite this article as: Colleoni, F., et al., Influence of regional parameters on the surface mass balance of the Eurasian ice sheet during the peak Saalian (140 kya), Glob. Planet. Change (2009), doi:10.1016/j.gloplacha.2009.03.021

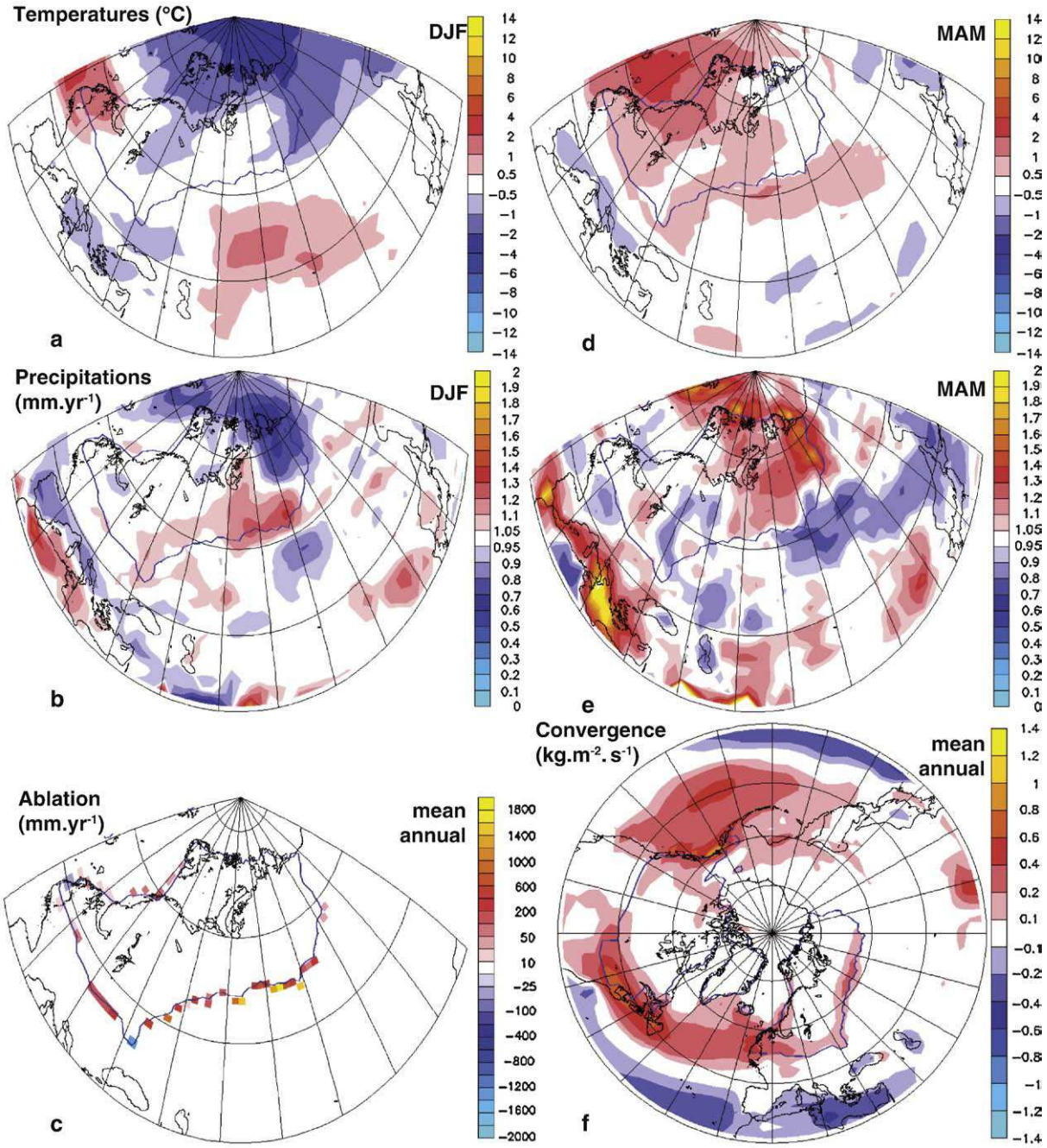

Fig. 11. (a, d) Seasonal air temperature (in °C), (b, e) precipitation (ratio) anomalies for DUST140 (with respect to REF140) during winter (DJF) and spring (MAM). (c) Mean annual melt anomalies and (f) moisture fluxes convergence. Blue contours indicate the ice sheet margins.

parameters could have contributed significantly to the maintenance of this ice sheet during the glacial maximum.

Table 2 shows that the surface mass balance calculated using the two different methods tested here (following Ohmura et al. (1996) and Thompson and Pollard (1997), respectively) yield very different results. In the method suggested by Thompson and Pollard (1997), snow and ice melt, and therefore also runoff, are calculated using the surface energy balance directly from the AGCM plus a refreezing parameterization. This leads to extremely high ablation. The reason for this is twofold. First, the horizontal resolution of the model in the region of interest, although relatively good compared to other global models, is not sufficient to correctly resolve the ablation zone. Second, and more importantly, the AGCM land surface model is a mosaic scheme in which a grid point can be partially land, open ocean, sea ice and continental ice sheet. At the ice sheet margin, this leads to spuriously high ablation values because the fraction of the grid point which is partially land (and not ice sheet) skews the energy balance. When the Ohmura et al. (1996) method is used, this problem can be avoided. Therefore, this diagnostic method is preferred here. In studies of the Antarctic surface mass balance with the same AGCM (Krinner et al., 2007, 2008), the problem of calculating SMB did not occur because ice sheet grid points were not fractional, spatial resolution was higher (60 km), and melt along the ice sheet margin is small anyway. Note that the basic results of the tests carried out here would be similar with the Thompson and Pollard (1997) method. For example, in both cases, dust deposition on the ice sheet increases ablation, while the proglacial lakes reduce it.

Although the horizontal resolution of our GCM in the region of interest is comparatively good, it is clear that simulations at even higher spatial resolution might yield different results concerning the

Please cite this article as: Colleoni, F., et al., Influence of regional parameters on the surface mass balance of the Eurasian ice sheet during the peak Saalian (140 kya), Glob. Planet. Change (2009), doi:10.1016/j.gloplacha.2009.03.021

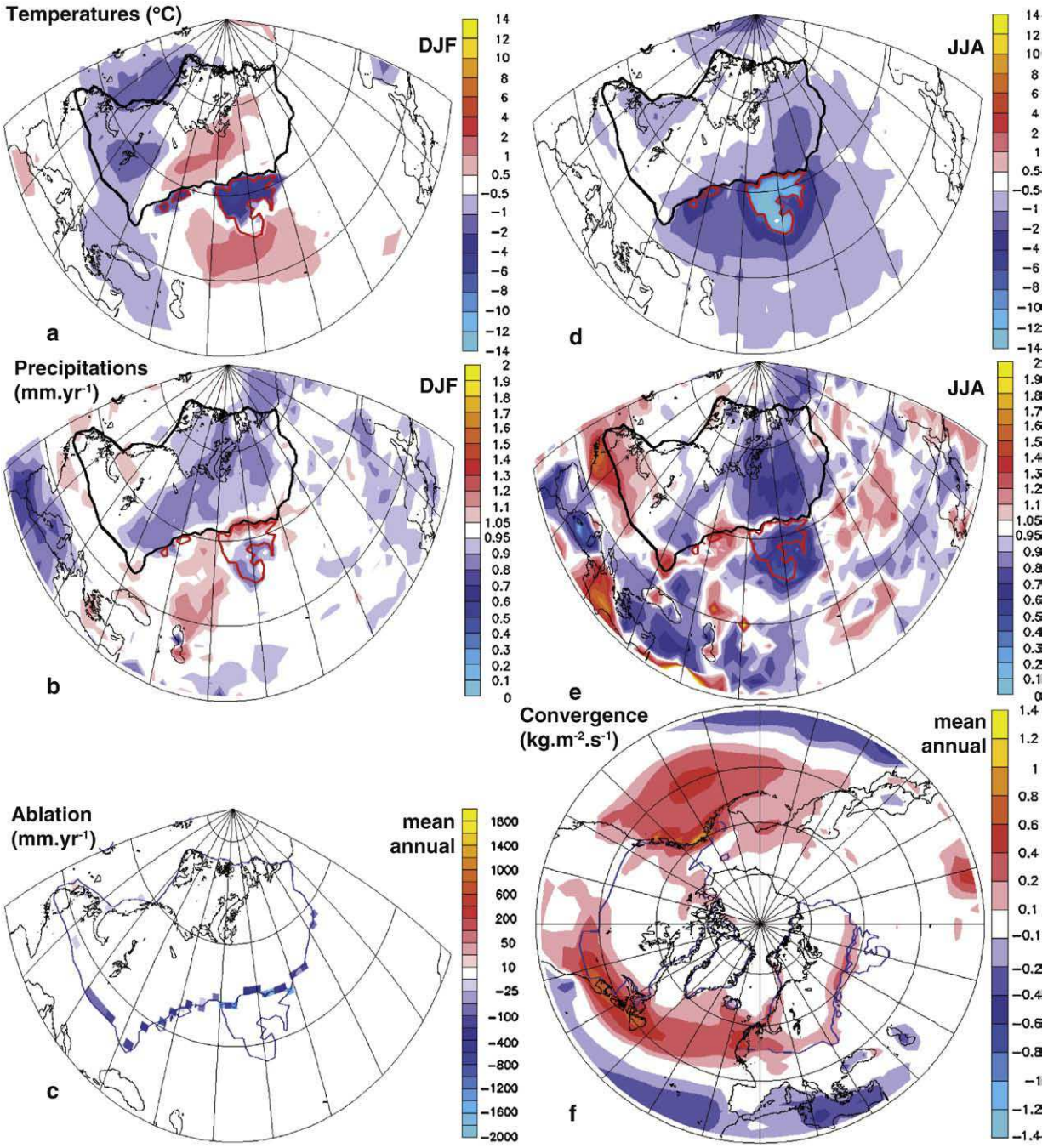

Fig. 12. (a, d) Seasonal air temperature (in °C), (b, e) precipitation (ratio) anomalies for FULL140 (with respect to REF140) during winter (DJF) and summer (JJA). (c) Mean annual melt anomalies and (f) moisture fluxes convergence. Blue contours indicate the ice sheet margins and lake shorelines.

different terms of the SMB. The marginal regions of ice sheets are commonly characterized by strong topographic gradients and therefore, the representation in a GCM is there particularly sensitive regarding the horizontal resolution. These regions have the highest precipitation as well as surface melt. For example, Krinner et al. (2007) have shown in the case of Antarctica that estimates of future SMB changes that ice sheet strongly depend on the model resolution. Therefore the absolute values of the simulated surface mass balances are subject to large uncertainties. However, the relative impacts of the various phenomena (proglacial lakes on one hand and dust deposition on the snow on the other hand) on the SMB appear trustworthy in our study.

Locally, the results may not be homogeneous and Fig. 15 displays a maps of the student t-test performed over the ice sheet with two levels of probability (95% and 90%). For LAKES140, FULL140 and SST140, significant SMB changes occur at the ice sheet margin(linked to reduced ablation) and in the interior (linked to modified precipitation patterns: Fig. 14e).

For all the simulations, the length of the melting season is equal but the amplitude of the melting is different (not shown here). Consequently, the difference between all the SMB values depends on the maximum melting.

In the ice sheet reconstruction used in our simulations, the Dniepr Lobe has been taken into account. The Dniepr Lobe is located on the

Please cite this article as: Colleoni, F., et al., Influence of regional parameters on the surface mass balance of the Eurasian ice sheet during the peak Saalian (140 kya), Glob. Planet. Change (2009), doi:10.1016/j.gloplacha.2009.03.021

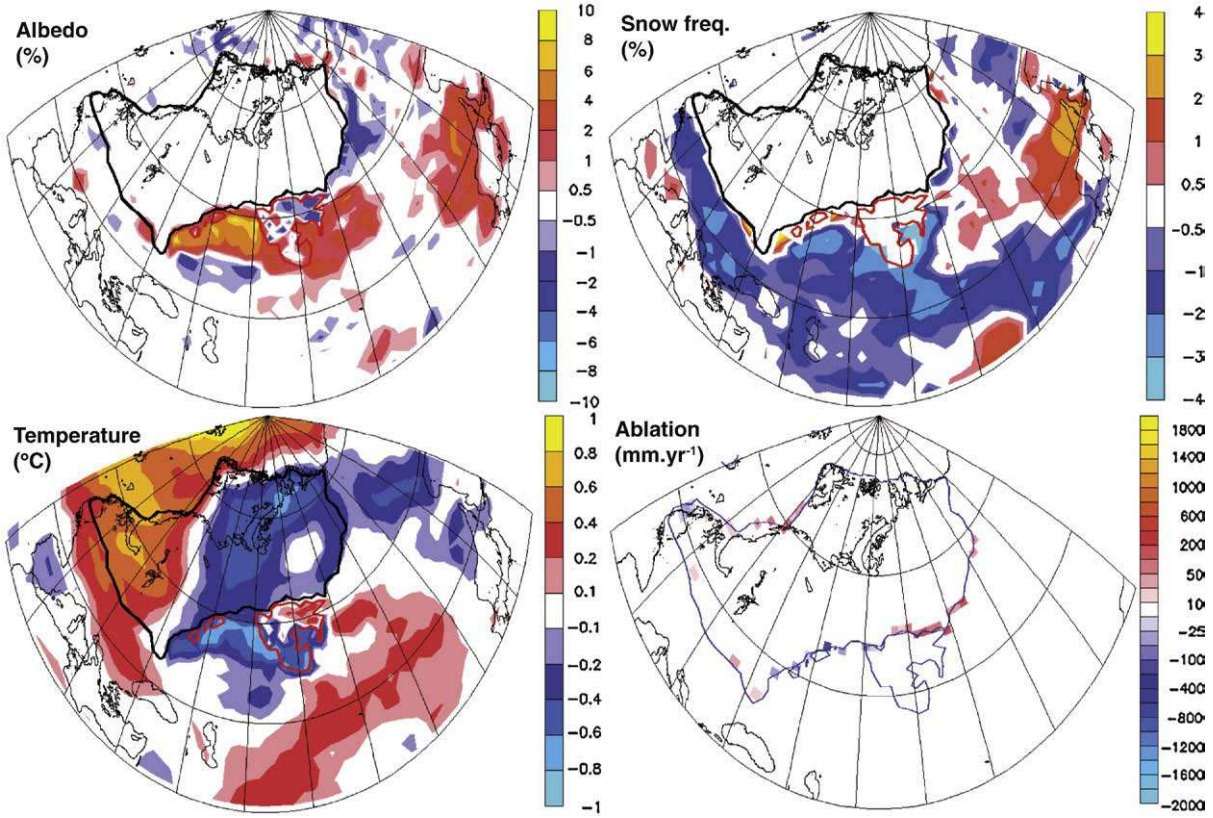

Fig. 13. Mean annual albedo, temperature (in °C), snow frequency and melt anomalies for simulation VEG140 with respect to simulation FULL140. Blue contours indicate the ice sheet margins and lake shorelines.

southwestern limit of the Eurasian ice sheet, directly North of the Black Sea (Fig. 2). This lobe is comparable to the North American Des Moines lobe, which formed a part of the Laurentide ice sheet between 20 kya and 14 kya (Dyke et al., 2002). There is no available information in the Western literature about how long time the Dniepr Lobe may have existed. However, the extent outlined by Svendsen et al. (2004) suggests that the ice lobe probably was dynamically decoupled from the rest of the ice sheet. In all our simulations, the Dniepr lobe exhibits the largest negative surface mass balance values up to $-5000\ kg\cdot m^{-2}\cdot yr^{-1}$ (Fig. 9). Due to these extreme values, the Dniepr Lobe skews the average ice sheet SMB values. Since the existence of this lobe was probably very short compared to that of the ice sheet, we recalculated the SMB of the ice sheet without the Dniepr Lobe for our simulations (Table 3). The ice-sheet mean melt values are slightly modified by the exclusion of the Dniepr lobe. Student t-tests have been performed as for the previous SMB values including the Dniepr Lobe and the results are similar (Table 3): differences are significant for all the simulations except for DUST140′ and VEG140′ (the symbol ′ indicates the simulations that exclude the Dniepr lobe for the SMB calculation).

The total precipitation over the Late Saalian ice sheet in FULL140 is to 357 $kg\cdot m^{-2}\cdot yr^{-1}$ and the SMB to 170 $kg\cdot m^{-2}\cdot yr^{-1}$ Table 2. These values are broadly similar to those of the present-day Greenland ice sheet. For example, regional model simulations by Fettweis (2007) of the Greenland ice sheet over the last two decades yield an average precipitation of 363 kg $m^{-2}\cdot yr^{-1}$ and a SMB of 191 $kg\cdot m^{-2}\cdot yr^{-1}$. The LMDZ AGCM therefore simulates a Late Saalian West Eurasian ice sheet in an approximate but probably precarious equilibrium in spite of its large southward extent.

We performed a LGM simulation (≈21 kya), using ICE-5G orography (Peltier, 2004), CLIMAP LGM sea surface temperatures (CLIMAP, 1984), LGM dust concentration from Mahowald et al. (1999) and the vegetation map from Crowley (1995) to estimate the impact of our SMB calculations on a spatially restricted ice sheet. Model resolution is similar to that used in this work and simulation length is 20 years. Using the temperature index method from Ohmura et al. (1996), the simulated SMB is positive (210 $kg\cdot m^{-2}\cdot yr^{-1}$) and similar to that of FULL140. In other words, the large southward extent of the Late Saalian ice sheet certainly leads to a reduced overall surface mass balance (compared to that of the LGM ice sheet). This implies that the large extent of this ice sheet must be a result of long-term glacial dynamics and not of a short advance during a short glacial maximum period.

In REF140 and DUST140, melt rate values are larger than in the two other simulations (Table 2) and a negative surface mass balance prevails along the southern margin (Fig. 9). Strong surface melt is induced by the advection of heat toward the continent and in the case of DUST140, this is slightly enhanced by the positive feedback of the albedo due to the presence of dust on the ice sheet. Since the climate described in REF140 benefits from high moisture fluxes and large heat advection toward the continent, it is a relatively "warm" glacial climate. Consequently, the dust-induced warming effect is minimized because of this initial "warmer" climate. In LAKES140, proglacial lakes have been inserted into the relatively "warm" climate of REF140. They tend to reduce summer snow melt by cooling the regional climate in their vicinity. In FULL140, melt distribution is close to that of LAKES140 (Fig. 9) and the Russian and Siberian ice margins have positive SMB values of the same order as LAKES140. That is, when dust deposition and proglacial lakes are combined, lakes still strongly influence the ice sheet, reducing the melting over the southern margins and increasing the spatial average SMB. This effect is illustrated by the difference in melt values between DUST140 and FULL140 (Table 2) and by the distribution of precipitation in FULL140 (Fig. 13).

A student t-tests shows that the difference in the mean SMB value induced by the switch in vegetation from conifera to tundra in VEG140 is not significant compared to FULL140. However, locally this vegetation change induces a strong albedo feedback and cools the surrounding

Please cite this article as: Colleoni, F., et al., Influence of regional parameters on the surface mass balance of the Eurasian ice sheet during the peak Saalian (140 kya), Glob. Planet. Change (2009), doi:10.1016/j.gloplacha.2009.03.021

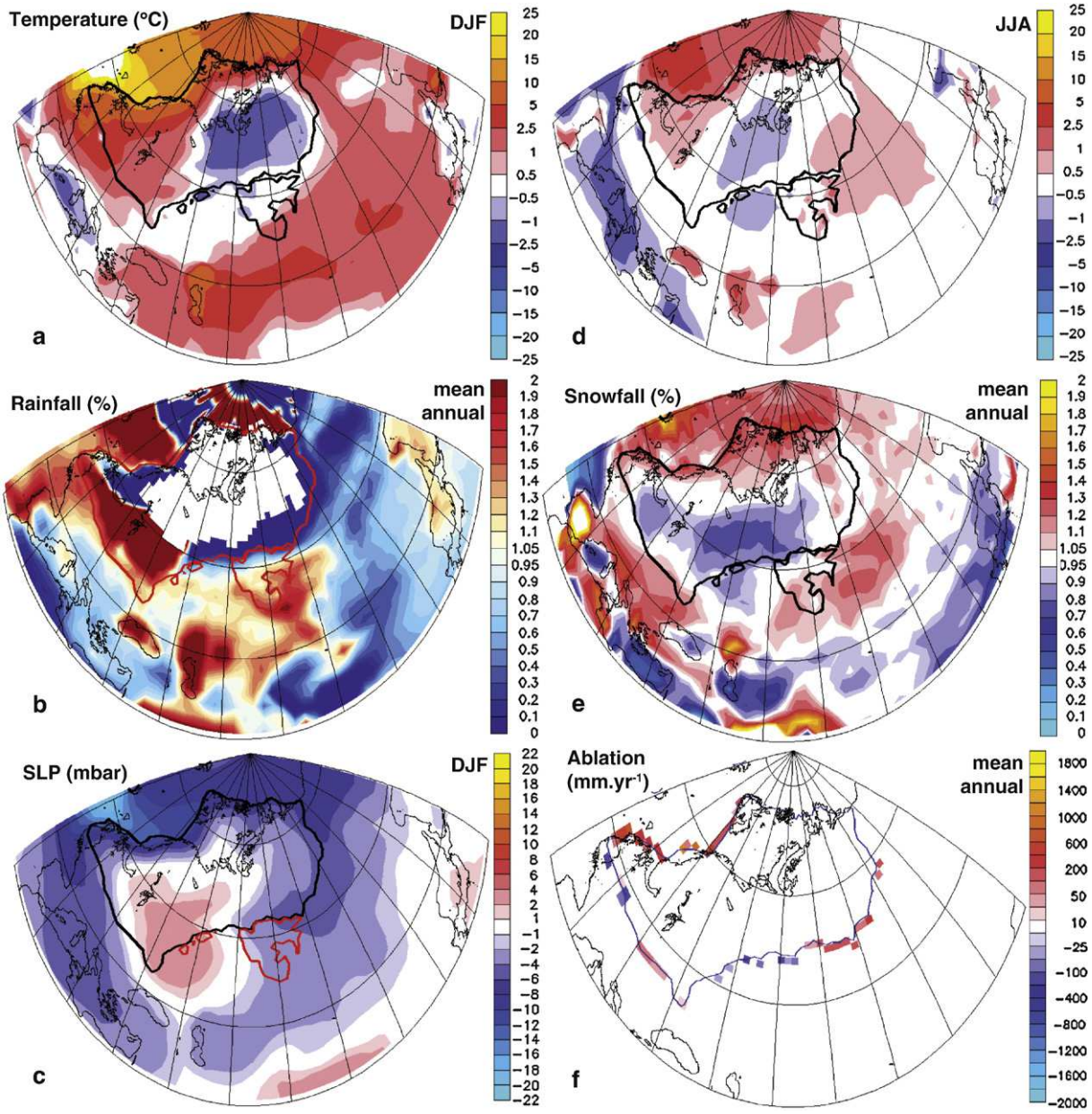

Fig. 14. Temperature anomalies (a, d) for winter (DJF) and summer (JJA), mean annual rainfall anomaly (b), mean annual snowfall anomaly (d), winter sea-level pressure (c) and mean annual melt (f) anomalies for simulation SST140 with respect to FULL140. Blue contours indicate the ice sheet margins and lake shorelines.

climate. Finally, forcing the AGCM with different sea surface conditions in SST140 leads to a strong feedback of the climate system. Compared to CLIMAP SST, Paul and Schaefer-Neth (2003) SST are cooler in the tropic and present a more reduced sea-ice cover in the North Altantic. This difference induces a large precipitation increase along the Atlantic margins and over Eurasia due to a global warming of these regions. Consequently, melting is increased along the Russian and Atlantic margins.

As stated before, the wet bias of the LMDZ AGCM in Eastern Siberia appears to be linked to a warm winter bias. Further west, the model exhibits a cold bias during the same season. Could these biases influence our results? It is however not sure that the AGCM will exhibit the same biases in another climate. This is unfortunately impossible to assess as long as there are no reliable surface air temperature reconstructions for the Late Saalian. In any case, the Eurasian summer climate is quite well reproduced by the model, and it is the summer temperature which critically influence the SMB of an ice sheet by determining melt rates. This is, for example, the main basis of the Milankovich theory of orbital glacial cycles (e.g. Hays et al. (1976)). Therefore, we may suppose that the temperature errors produced by LMDZ4 for the present climate do not critically deteriorate our results.

Another problem is linked to the ice sheet topography, which was obtained from previous studies (Peyaud, 2006) using the GRISLI ice-sheet model forced by a glacial index based on insolation. Recently a similar reconstruction of the Late Saalian Eurasian ice sheet was obtained using paleo-sea-level data and rebound modelling Lambeck et al. (2006). This ice sheet presents very similar ice thickness (≈4200 m) and ice surface elevation (≈3200 m) to that of Peyaud (2006). We are aware that both methods present some limitations but both converged toward a satisfying similar ice topography at the limit of all the existing knowledge about this period. Another important point is that of the global ice topography. In our study we assumed an eustatic sea level of about 110 m lower than present-day sea level. The Laurentide ice sheet contributes ≈74 m while the Antarctic ice sheet contributes ≈20 m. Our Late Saalian Eurasian ice sheet contributes ≈60 m ESL (comparable to that of Lambeck et al., 2006), which leaves ≈50 m to share between the Laurentide and the

Please cite this article as: Colleoni, F., et al., Influence of regional parameters on the surface mass balance of the Eurasian ice sheet during the peak Saalian (140 kya), Glob. Planet. Change (2009), doi:10.1016/j.gloplacha.2009.03.021

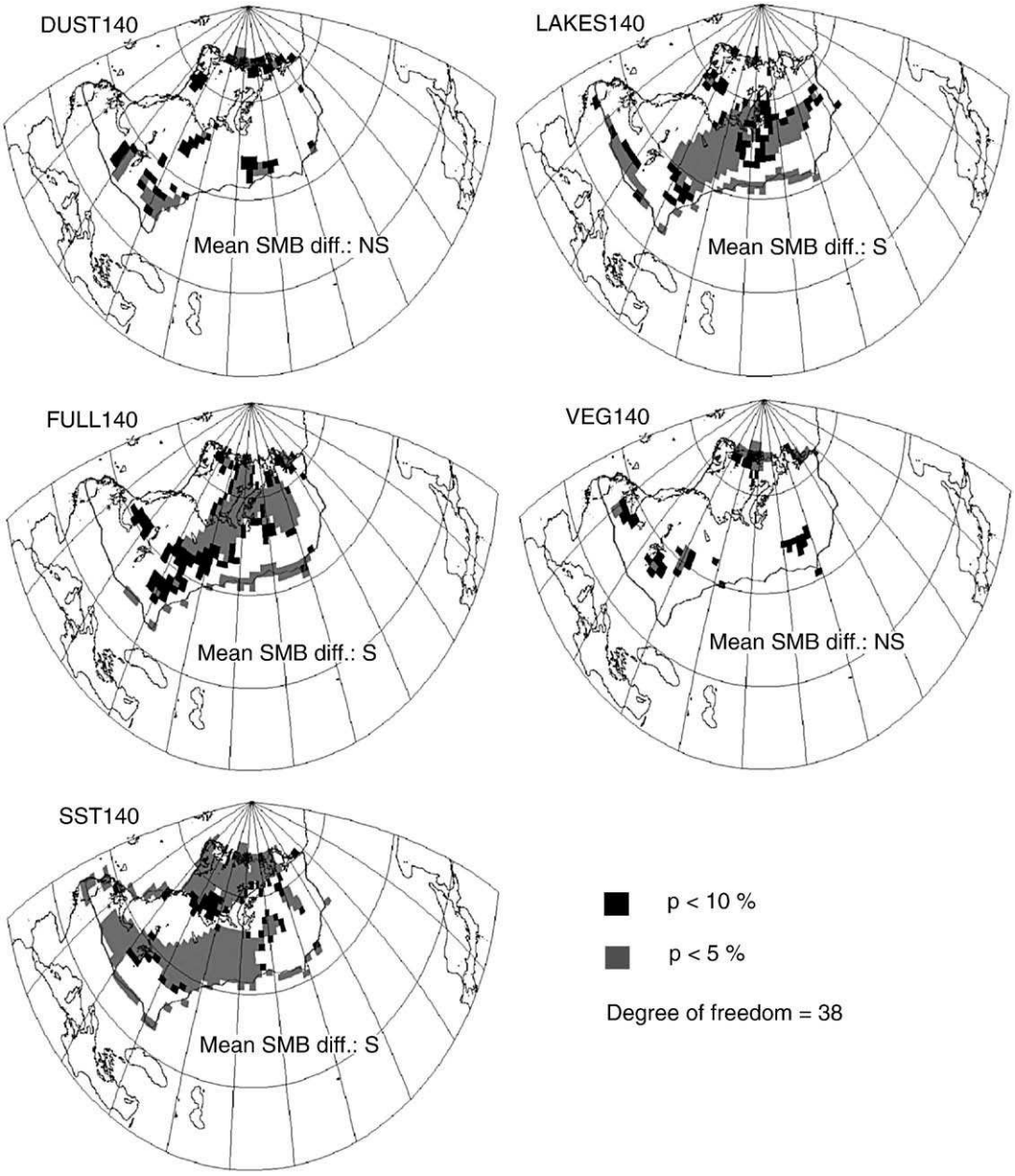

Fig. 15. Map of the Student t-test performed over the Eurasian ice sheet. Student t-test has been performed using 38 degrees of freedom with two levels of confidence: $p \leq 10\%$ (black pixels) and $p \leq 5\%$ (gray pixels). Note that gray pixels automatically overlap most of black pixels. The significance of the mean Student test over the ice sheet is indicated by NS (non significant) and S (significant). DUST140, LAKES140 and FULL140 are compared to REF140 while VEG140 and SST140 are compared to FULL140.

Antarctic ice sheets. Whatever the distribution of the ice over these two ice sheets, the Laurentide has to be reduced to equilibrate the eustatic sea level. This may have some consequences on the atmospheric circulation (Kageyama and Valdes, 2000).

Finally a last word of caution concerns the imposed spatial pattern of dust deposition on the surface. Here we imposed a spatial pattern obtained by Mahowald et al. (1999) in simulations of the Last Glacial Maximum (21 kya) climate. Of course both the spatial pattern and the overall magnitude of dust deposition at the LGM is not necessarily correctly depicted by the model used by Mahowald et al. (1999), and it is equally uncertain that the ratio between the peak Saalian and LGM dust deposition rates in Siberia is the same as that obtained from ice cores in central east Antarctica, as supposed in the present study (although Winckler et al. (2008) suggest that orbital-scale dust flux variability is coherent on very large spatial scales). Another uncertainty comes from the fact that we artificially reduced the Mahowald et al. (1999) dust deposition rates in regions that were ice-covered during the peak Saalian, but not during the LGM, in order to obtain values more usual for ice marginal areas. However, there is currently no better way to prescribe peak Saalian dust deposition rates.

Table 3
As Table 2, but excluding the Dniepr lobe. Significant differences (according to a two-sided student test) are represented by a star near the SMB value.

($kg\ m^{-2}\ yr^{-1}$)	REF140′	DUST140′	LAKES140′	FULL140′	VEG140′	SST140′
Tot. precip.	351	352	341	346	349	343
Snow	313	314	310	314	317	317
Evap	68	69	65*	66*	66	70*
Ablation	89	93	61*	64*	64	77*
SMB (Ohmura et al., 1996)	156	152	184*	184*	187	164*
Melt	411	430	314*	325*	323	307
Runoff	436	455	333*	344*	343	325
SMB (Thompson and Pollard, 1997)	−155	−174	−60*	−67*	−64	−58*

Please cite this article as: Colleoni, F., et al., Influence of regional parameters on the surface mass balance of the Eurasian ice sheet during the peak Saalian (140 kya), Glob. Planet. Change (2009), doi:10.1016/j.gloplacha.2009.03.021

5. Conclusions

To summarize, the main results and conclusions of this work about the Late Saalian period are the following:

(1) In a "warm" glacial climate, the effect of proglacial lakes on climate and surface mass balance is enhanced and the effect of dust deposition on snow is reduced;
(2) Dust deposition on the ice sheet and on the surrounding continental ice-free regions leads to increased surface melt;
(3) Combined with dust deposition, that is, in a "warm" background climate with higher melt rates, proglacial lakes on the southern margin Late Saalian Eurasian ice sheet reduce surface melt and thus increase the SMB of the ice sheet;
(4) Compared to a simulation without dust deposition and proglacial lakes, their combined effects decrease melting. The total increase of the ice sheet SMB is stronger than the sum of their individual effects;
(5) Switch from conifera to tundra in the vicinity of the ice sheet induces a regional cooling and locally affects the SMB by reducing the snow melt. But the mean effect over the ice sheet is not significant with this type of vegetation;
(6) Forcing the atmospheric model with different sea surface conditions presenting a reduced sea-ice cover leads to a global warming, increasing melting and contributing to a less positive SMB;
(7) If the Dniepr lobe is excluded, the simulated SMB for all the simulations is slightly more positive.

This study clarifies which regional factors influence most strongly the surface mass balance of the ice sheet during the peak Saalian (140 kya). The ice sheet's huge topography directly controls the moisture fluxes directions, inducing precipitation and limiting melting along its south margins. This can help to explain the large southward extent. In this context, it is worth noting that an even larger Eurasian ice sheet, extending over almost the entire boreal Eurasia, has recently been suggested as a major feature of a postulated future stable state of the climate system with permanent continental ice cover of similar extent in both hemispheres (Crowley and Hyde, 2008). In that study, the extremely large Eurasian ice sheet favoured its own existence through feedbacks in the climate system, similar to processes shown here.

A new study aiming at improving the vegetation map by using a dynamic vegetation model is in progress as well as more detailed tests on the sensitivity of this ice sheet to various SST datasets. Another step will be to study the origin of the huge ice volume of this Late Saalian Eurasian ice sheet by asynchronous coupling with a dynamic ice sheet model (Peyaud et al., 2007) over at least one precessional cycle preceding the Late Saalian glacial maximum.

Acknowledgments

The authors particularly thank Lev Tarasov and Masa Kageyama for their very constructive suggestions. We would like to thank Xavier Fettweis for his personal communications and G. Spada for his helpful comments. The authors wish to acknowledge the use of the Ferret program for analysis and graphics in this paper. Ferret is a product of NOAA's Pacific Marine Environmental Laboratory (Information is available at http://ferret.pmel.noaa.gov/Ferret/). The authors acknowledge support by the Agence Nationale de laRecherche (projects IDEGLACE and PICC), the Région Rhône Alpes (programme Explora'Doc) and the Ministère des Affaires Étrangères Français for their support. The climate simulations were carried out at IDRIS/CNRS and on the Mirage scientific computing plateform in Grenoble (France).

References

Abe-Ouchi, A., Segawa, T., Saito, F., 2007. Climatic conditions for modelling the northern hemisphere ice sheets throughout the ice age cycle. Clim. Past 3, 423–438.
Adler, R.E., Polyak, L., Ortiz, J.D., Kaufman, D.S., Channell, J.E.T., Xuan, C., Grottoli, A.G., Sellén, E., Crawford, K.A., 2009-this issue. Sediment record from the western Arctic Ocean with an improved Late Quaternary age resolution: HOTRAX core HLY0503-8JPC, Mendeleev Ridge. Glob. Planet. Change. doi:10.1016/j.gloplacha.2009.03.026.
Astakhov, V., 2004. Middle Pleistocene glaciations of the Russian north. Quat. Sci. Rev. 23 (11–13), 1285–1311.
Berger, A., Loutre, M., 1991. Insolation values for the climate of the last 10 million years. Quat. Sci. Rev. 10 (4), 297–317.
Calov, R., Ganopolski, A., Petoukhov, V., Claussen, M., Brovkin, V., Kubatzki, C., 2005. Transient simulation of the last glacial inception. Part II: sensitivity and feedback analysis. Clim. Dyn. 24 (6), 563–576.
Claquin, T., Roelandt, C., Kohfeld, K., Harrison, S., Tegen, I., Prentice, I., Balkanski, Y., Bergametti, G., Hansson, M., Mahowald, N., Rodhe, H., Schulz, M., 2003. Radiative forcing of climate by ice-age atmospheric dust. Clim. Dyn. 20 (2–3), 193–202.
CLIMAP, 1984. The last interglacial ocean. Quat. Res. 21, 123–224.
Crowley, T., 1995. Ice age terrestrial carbon changes revisited. Global Biogeochem. Cycles 9, 377–389.
Crowley, T., Baum, S., 1997. Effect of vegetation on an ice-age climate model simulation. J. Geophys. Res. 102 (D14), 16463–16480.
Crowley, T., Hyde, W., 2008. Transient nature of late Pleistocene climate variability. Nature 465, 226–230.
Delmonte, B., coauthors, 2004. Epica Dome C Ice Cores Insoluble Dust Data.
Dyke, A., Andrews, J., Clark, P., England, J., Miller, G., Shaw, J., Veillette, J., 2002. The Laurentide and Innuitian ice sheets during the last glacial maximum. Quat. Sci. Rev. 21 (1–3), 9–31.
Ferland, M., Roy, P., Murray-Wallace, C., 1995. Glacial lowstand deposits on the outer continental shelf of southeastern Australia. Quat. Res. 44 (2), 294–299.
Fettweis, X., 2007. Reconstruction of the 1979–2006 Greenland ice sheet surface mass balance using the regional climate model MAR. Cryosphere 1, 21–40.
Hays, J., Imbrie, J., Shackleton, N., 1976. Variations in the Earth's orbit: pacemaker of the ice ages. Science 196, 1121–1132.
Hebbeln, D., Dokken, T., Andersen, E., Hald, M., Elverhoi, A., 1994. Moisture supply for northern ice-sheet growth during the last glacial maximum. Nature 370 (6488), 357–360.
Hostetler, S., Bartlein, P., Clark, P., Small, E., Solomon, A., 2000. Simulated influence of the Lake Agassiz on the climate of the central North America 11,000 years ago. Nature 405, 334–337.
Hourdin, F., Musat, I., Bony, S., Braconnot, P., Cordon, F., Dufresne, J., Fairhead, L., Filiberti, M., Friedlingstein, P., Grandpeix, J., Krinner, G., LeVan, P., Li, Z., Lott, F., 2006. The LMDZ4 general circulation model: climate performance and sensitivity to parametrized physics with emphasis on tropical convection. Clim. Dyn. 27 (7–8), 783–813.
Jolly, W., Ramakrishna, N., Running, S., 2005. A generalized, bioclimatic index to predict foliar phenology in response to climate. Glob. Chang. Biol. 11, 619–632.
Kageyama, M., Valdes, P., 2000. Impact of the North American ice-sheet orography on the last glacial maximum eddies and snowfall. Geophys. Res. Lett. 27 (10), 1515.
Krinner, G., Genthon, C., 1997. The Antarctic surface mass balance in a stretched grid general circulation model. Ann. Glaciol. 25, 73–78.
Krinner, G., Genthon, C., 1999. Altitude dependence of the ice sheet surface climate. Geophys. Res. Lett. 26, 2227–2230.
Krinner, G., 2003. Impact of lakes and wetlands on boreal climate. J. Geophys. Res. 108, 4520.
Krinner, G., Mangerud, J., Jakobsson, M., Crucifix, M., Ritz, C., Svendsen, J., 2004. Enhanced ice sheet growth in Eurasia owing to adjacent ice-dammed lakes. Nature 427 (6973), 429–432.
Krinner, G., Boucher, O., Balkanski, Y., 2006. Ice-free glacial northern Asia due to dust deposition on snow. Clim. Dyn. 27 (6), 613–625.
Krinner, G., Magand, O., Simmonds, I., Genthon, C., Dufresne, J., 2007. Simulated Antarctic precipitation and surface mass balance at the end of the twentieth and twenty-first centuries. Clim. Dyn. 28, 215–230.
Krinner, G., Guicherd, B., Ox, K., Genthon, C., Magand, O., 2008. Influence of oceanic boundary conditions in simulations of Antarctic climate and surface mass balance change during the coming century. J. Climate 21, 938–962.
Lambeck, K., Purcell, A., Funder, S., Kjaer, K., Larsen, E., ans Möller, P., 2006. Constraints on the Late Saalian to early Middle Weichselian ice sheet of Eurasia from field data and rebound modelling. Boreas 35, 539–575.
Lott, F., 1997. Alleviation of stationary biases in a GCM through a mountain drag parameterization scheme and a simple representation of mountain lift forces. Mon. Weather Rev. 127 (5), 788–801.
Mahowald, N., Kohfeld, K., Hansson, M., Balanski, Y., Harrisson, S., Prentice, J., Schulz, M., Rodhe, H., 1999. Dusts sources and deposition during the last glacial maximum and current climate: a comparison of model results with paleodata from ice cores and marine sediments. J. Geophys. Res. 104 (D13).
Mangerud, J., Astakhov, V., Jakobsson, M., Svendsen, J., 2001. Huge ice-age lakes in Russia. J. Quat. Sci. 16 (8), 773–777.
Mangerud, J., Jakobsson, M., Alexanderson, H., Astakhov, V., Clarke, G., Henriksen, M., Hjort, C., Krinner, G., Lunkka, J.-P., Moller, P., Murray, A., Nikolskaya, O., Saarnisto, M., Svendsen, J., 2004. Ice-dammed lakes and rerouting of the drainage of northern Eurasia during the last glaciation. Quat. Sci. Rev. 23, 1313–1322.
New, M., Hulme, M., Jones, P., 1999. Representing twentieth century space–time climate variability. Part 1: development of a 1961–90 mean monthly terrestrial climatology. J. Climate 12, 829–856.

Please cite this article as: Colleoni, F., et al., Influence of regional parameters on the surface mass balance of the Eurasian ice sheet during the peak Saalian (140 kya), Glob. Planet. Change (2009), doi:10.1016/j.gloplacha.2009.03.021

Ohmura, A., Wild, M., Bengtsson, L., 1996. A possible change in mass balance of Greenland and Antarctic ice sheets in the coming century. J. Glaciol. 9 (9), 2124–2135.
Paul, A., Schaefer-Neth, C., 2003. Modeling the water masses of the Atlantic Ocean at the last glacial maximum. Paleoceanography 18 (3). doi:10.1029/2002PA000783.
Peltier, W., 2004. Global glacial isostasy and the surface of the ice-age Earth: the ICE-5G (VM2) model and grace. Annu. Rev. Earth Planet. Sci. 32, 111–149.
Peltier, W., Fairbanks, R., 2006. Global glacial ice volume and last glacial maximum duration from an extended Barbados sea level record. Quat. Sci. Rev. 25, 3322–3337.
Petit, J., Jouzel, J., Raynaud, D., Barkov, N., Barnola, J., Basile, I., Bender, M., Chapellaz, J., Davis, J., Delaygue, G., Delmotte, M., Kotlyakov, V., Legrand, M., Lipenkov, V., Lorius, C., Ppin, L., Ritz, C., Saltzman, E., Stievenard, M., 2001. Ice core data for 420,000 year.
Peyaud, V., 2006. Role of the ice sheet dynamics in major climate changes. Ph.D. thesis, Laboratoire de Glaciologie et de Géophysique de l'Environnement, Université Grenoble I.
Peyaud, V., Ritz, C., Krinner, G., 2007. Modeling the early Weichselian Eurasian ice sheets: role of ice shelves and influence of ice-dammed lakes. Clim. Past 3, 375–386.
Rabineau, M., Berne, S., Olivet, J., Aslanian, D., Guillocheau, F., Joseph, P., 2006. Paleo sea levels reconsidered from direct observation of paleoshore-line position during glacial maxima (for the last 500,000 yr). Earth Planet. Sci. Lett. 252, 119–137.
Ritz, C., Rommalaere, V., Dumas, C., 2001. Modeling the evolution of Antarctic ice sheet over the last 420,000 years: implications for altitude changes in the Vostok region. J. Geophys. Res. 106 (D23), 31943–31964.
Robin, G., 1977. Ice cores and climatic changes. Philos. Trans. R. Soc. 280, 143–168.
Rohling, E., Fenton, M., Bertrand, F., Ganssen, G., Caulet, J., 1998. Magnitudes of sea level lowstands of past 500,000 years. Nature 394, 162–165.
Ruddiman, W., McIntyre, A., 1979. Warmth of the subpolar North Atlantic Ocean during northern hemisphere ice-sheet growth. Science 204, 173–175.
Shackleton, N., 1987. Oxygen isotopes, ice volume and sea level. Quat. Sci. Rev. 6, 183–190.
Smith, L., Miller, G., Otto-Bliesner, B., Shin, S.-I., 2003. Sensitivity of the northern hemisphere climate system to extreme changes in Holocene Arctic sea ice. Quat. Sci. Rev. 22 (5–7), 645–658.
Uppala, S.M., Kllberg, P., Simmons, A., Andrae, U., da Costa Bechtold, V., Fiorino, M., Gibson, J., Haseler, J., Hernandez, A., Kelly, G., Li, X., Onogi, K., Saarinen, S., Sokka, N., Allan, R., Andersson, E., Arpe, K., Balmaseda, M., Beljaars, A., van de Berg, L., Bidlot, J., an S. Caires, N.B., Chevallier, F., Dethof, A., Dragosavac, M., Fisher, M., Fuentes, M., Hagemann, S., Hlm, E., Hoskins, B., Isaksen, L., Janssen, P., Jenne, R., McNally, A., Mahfouf, J., Morcrette, J., Rayner, N., Saunders, R., Simon, P., Sterl, A., Trenberth, K., Untch, A., Vasiljevic, D., Viterbo, P., Woollen, J., 2005. The era-40 re-analysis. Q. J. R. Meteorol. Soc. 131, 2961–3012.
Spahni, R., Chappellaz, J., Stocker, T., Loulergue, L., Hausammann, G., Kyawamura, G., Flckiger, J., Schwander, J., Raynaud, D., Masson-Delmotte, V., Jouzel, J., 2005. Epica Dome C CH4 Data to 650 kya bp.
Svendsen, J., Alexanderson, H., Astakhov, V., Demidov, I., Dowdeswell, J., Funder, S., Gataullin, V., Henriksen, M., Hjort, C., Houmark-Nielsen, M., Hubberten, H., Ingolfsson, O., Jakobsson, M., Kjaer, K., Larsen, E., Lokrantz, H., Lunkka, J., Lysa, A., Mangerud, J., Matiouchkov, A., Murray, A., Moller, P., Niessen, F., Nikolskaya, O., Polyak, L., Saarnisto, M., Siegert, C., Siegert, M., Spielhagen, R., Stein, R., 2004. Late Quaternary ice sheet history of northern Eurasia. Quat. Sci. Rev. 23 (11–13), 1229–1271.
Taylor, K., Williamson, D., Zwiers, F., 2000. The sea surface temperature and sea-ice concentration boundary conditions for AMIP II simulations, program for climate model diagnosis and intercomparison, Lawrence Livermore National Laboratory.
Thompson, S., Pollard, D., 1997. Greenland and Antarctic mass balances for present and doubled atmospheric CO2 from the GENESIS version-2 global climate model. J. Climate 10, 871–900.
Winckler, G., Anderson, R., Fleisher, M., McGee, D., Mahowald, N., 2008. Covariant glacial–interglacial dust fluxes in the equatorial Pacific and Antarctica. Science 320, 93–96.

Please cite this article as: Colleoni, F., et al., Influence of regional parameters on the surface mass balance of the Eurasian ice sheet during the peak Saalian (140 kya), Glob. Planet. Change (2009), doi:10.1016/j.gloplacha.2009.03.021

Manuscript 2

Colleoni F., Krinner G. and Jakobsson M. 2009. Sensitivity of the Late Saalian (140 kyrs BP) and LGM (21 kyrs BP) Eurasian ice sheet surface mass balance to vegetation feedbacks, *Geophys. Res. Lett.*, **36**, L08704

Contribution:

- Designing and running experiments using LMDZ4 and BIOME4 models
- Analyzing the results
- Main part of the writing

Résumé
Dans cet article, un modèle de circulation générale atmosphérique est couplé de manière asynchrone à un model de végétation afin d'évaluer si les rétroactions causées par les changements de végétation pourraient expliquer pourquoi la calotte de glace Eurasiatique de la fin du Saalien (140 ka) était plus étendue et plus grande qu'au Dernier Maximum Glaciaire (LGM, 21 ka). Les changements de végétation simulés provoquent un refroidissement régional du climat en Eurasie à 140 ka alors qu'ils réchauffent légèrement le climat au LGM. En conséquence, l'ablation le long des marges sud de la calotte est significativement réduit à 140 ka, ce qui entraine une augmentation du bilan de masse en surface à 140 ka alors qu'aucun changement notable n'est observé pour le LGM.

GEOPHYSICAL RESEARCH LETTERS, VOL. 36, L08704, doi:10.1029/2009GL037200, 2009

Click Here for Full Article

Sensitivity of the Late Saalian (140 kyrs BP) and LGM (21 kyrs BP) Eurasian ice sheet surface mass balance to vegetation feedbacks

F. Colleoni,[1] G. Krinner,[1] and M. Jakobsson[2]

Received 7 January 2009; revised 7 March 2009; accepted 23 March 2009; published 24 April 2009.

[1] This work uses an atmospheric general circulation model (AGCM) asynchronously coupled to an equilibrium vegetation model to investigate whether vegetation feedbacks could be one of the reasons why the Late Saalian ice sheet (140 kyrs BP) in Eurasia was substantially larger than the Last Glacial Maximum (LGM, 21 kyrs BP) Eurasian ice sheet. The modeled vegetation changes induce a regional cooling for the Late Saalian while they cause a slight regional warming for LGM. As a result, ablation along the margins of the Late Saalian ice sheet is significantly reduced, leading to an increased surface mass balance, while there are no significant mass balance changes observed from vegetation feedbacks at LGM. **Citation:** Colleoni, F., G. Krinner, and M. Jakobsson (2009), Sensitivity of the Late Saalian (140 kyrs BP) and LGM (21 kyrs BP) Eurasian ice sheet surface mass balance to vegetation feedbacks, *Geophys. Res. Lett.*, *36*, L08704, doi:10.1029/2009GL037200.

1. Introduction

[2] Numerous studies have shown that vegetation influences the regional and global climate through changes in albedo and modifications to the hydrological cycle [*Charney*, 1975; *Kleidon et al.*, 2000; *Brovkin et al.*, 2003]. At high latitudes, a strong feedback is caused by the higher albedo of tundra-type vegetation compared to boreal forest, in particular when a snow cover is present. The transition from taiga to tundra at a given place thus induces a regional cooling. Similarly, *Crowley and Baum* [1997] reported that glacial vegetation with its reduced forest extent over the boreal regions caused a regional cooling of 2°C to 4°C in western Europe and Siberia in LGM atmospheric general circulation model (AGCM) simulations [*Kubatzki and Claussen*, 1998; *Levis et al.*, 1999; *Crucifix and Hewitt*, 2005]. It is worth noting that the strongest impacts of LGM vegetation were found in studies using the present-day potential vegetation in LGM control runs. The present-day vegetation distribution is more similar to LGM biogeography because agricultural surfaces are more similar to steppes than forests.

[3] Here we focus on the sensitivity of the Late Saalian (140 kyrs BP) Eurasian ice sheet to different prescribed and modeled vegetation distributions. The West Eurasian ice sheet was significantly larger during the Late Saalian than the ice sheet in this region during LGM [*Svendsen et al.*, 2004]. We address the question of whether vegetation feedbacks on the Late Saalian ice sheet's surface mass balance contributed to this difference. We use the LMDZ4 atmospheric general circulation model [*Hourdin et al.*, 2006] asynchronously coupled with the BIOME4 vegetation model [*Kaplan et al.*, 2003]. Similar experiments are carried out for the LGM allowing a comparison between the results. The impacts of other environmental factors on regional climate, such as dust deposition on snow and proglacial lakes during the Late Saalian, the Early Weichselian and LGM investigated by *Colleoni et al.* [2009] and *Krinner et al.* [2004, 2006].

2. Methods

[4] The LMDZ4 atmospheric general circulation model [*Hourdin et al.*, 2006] and the BIOME4 equilibrium vegetation model [*Kaplan et al.*, 2003] were asynchronously coupled. Since no vegetation map is compiled for the Late Saalian, the LGM and Late Saalian climates were initially obtained by forcing the LMDZ4 model with the existing LGM vegetation map by *Crowley* [1995] (runs C21 and C140, Figure 1). New vegetation maps were subsequently computed by forcing BIOME4 with the monthly mean and minimum daily temperatures, the monthly mean precipitation and the cloud cover fraction obtained from the two previous C21 and C140 AGCM simulations. Steady state was obtained after three iterations. The final AGCM runs, using LGM and Saalian vegetation maps shown in Figures 1b and 1c, are referred to as B21 for the LGM and B140 for the Late Saalian.

[5] All AGCM simulations are 21 years long. The first year is discarded in the analyses as spinup. All simulations take into account the effect of proglacial lakes and dust deposition on snow. Since we prescribed the initial LGM vegetation, the simulations are considered as control runs. The surface mass balance is calculated after the temperature-index method of *Ohmura et al.* [1996]. Simulations were forced using LGM sea surface temperatures from *Paul and Schäfer-Neth* [2003]. Boundary conditions are set using the modelled LGM dust deposition rates from *Mahowald et al.* [1999], orbital parameters from *Berger and Loutre* [1991] and greenhouse gases from *Petit et al.* [2001] and *Spahni et al.* [2005]. Late Saalian ice topography is obtained from *Peyaud* [2006] while LGM is modeled using ICE-5G [*Peltier*, 2004]. The equations and details on the Late Saalian boundary conditions are given in the auxiliary material and discussed by *Colleoni et al.* [2009].[1]

3. Results

3.1. LGM and Late Saalian Vegetation Maps

[6] The annual maximum foliage projected cover (see auxiliary material) used for simulations C21 (and C140) is

[1]Laboratoire de Glaciologie et Géophysique de l'Environnement, UJF, CNRS, France.
[2]Department of Geology and Geochemistry, Stockholm University, Stockholm, Sweden.

Copyright 2009 by the American Geophysical Union.
0094-8276/09/2009GL037200$05.00

[1]Auxiliary materials are available in the HTML. doi:10.1029/2009GL037200.

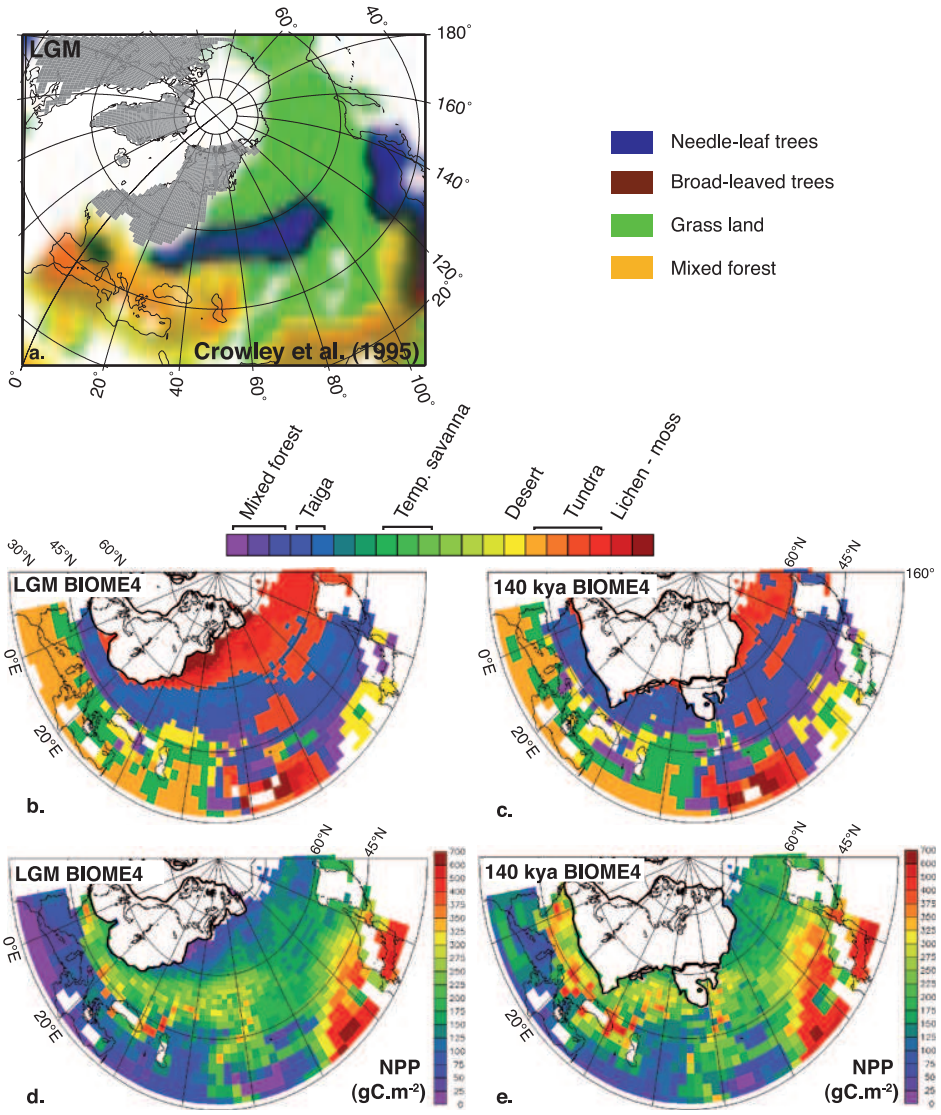

Figure 1. Annual foliage projected cover (dimensionless, see auxiliary material) for: (a) C21 and C140 using the paleobiogeography from *Crowley* (1995), (b) the computed Late Saalian vegetation cover (B140), (c) the corresponding net primary production (in gC/m^2), (d and e) same as Figures 1b and 1c but for the LGM (B21). The types of vegetation are described on the figure. Thick lines indicate the LGM, the Late Saalian Eurasian ice sheet maximum extents and proglacial lakes (see auxiliary material).

displayed in Figure 1a. The biome distributions computed for B21 and B140 are shown on Figures 1b and 1c, respectively, together with their associated net primary productions (Figures 1d and 1e). The main differences to the *Crowley* [1995] vegetation map reside in the taiga distribution: both for the LGM and the Late Saalian, BIOME4 simulates a continuous boreal forest belt across the entire Eurasian land mass (Figures 1b and 1c).

[7] The mean annual net primary production of the forest (mixed and taiga) in Europe, Russia and Siberia ranges between 100 and 350 gC.m^{-2} during both periods, while it ranges from ≈460 to ≈630 gC.m^{-2} for the present [*Schulze et al.*, 1999; *Gower et al.*, 2001]. This suggests that the computed forest has a low density and is not productive (see discussion).

[8] The vegetation computed by the BIOME4 model for the LGM clearly differs from that of *Crowley* [1995]. The differences can result from either the use of different vegetation and AGCM models or from different LGM ice topographies: ICE-4G [*Peltier*, 1994] was used by *Crowley* [1995] and ICE-5G in the present work. In ICE-4G the Eurasian ice sheet extends into West Siberia whereas this is not the case in ICE-5G.

3.2. Impact on the Ice Sheet Surface Mass Balance

[9] For the Late Saalian, near the proglacial lakes, in European Russia and Siberia, albedo is about 30% to 50% higher in B140 than in C140 (Figure 2e) as a consequence of the perennial snow cover (not shown here). This leads to a regional cooling of −5°C to −15°C (Figure 2f) caused by the progressive disappearance of needle-leaf vegetation and

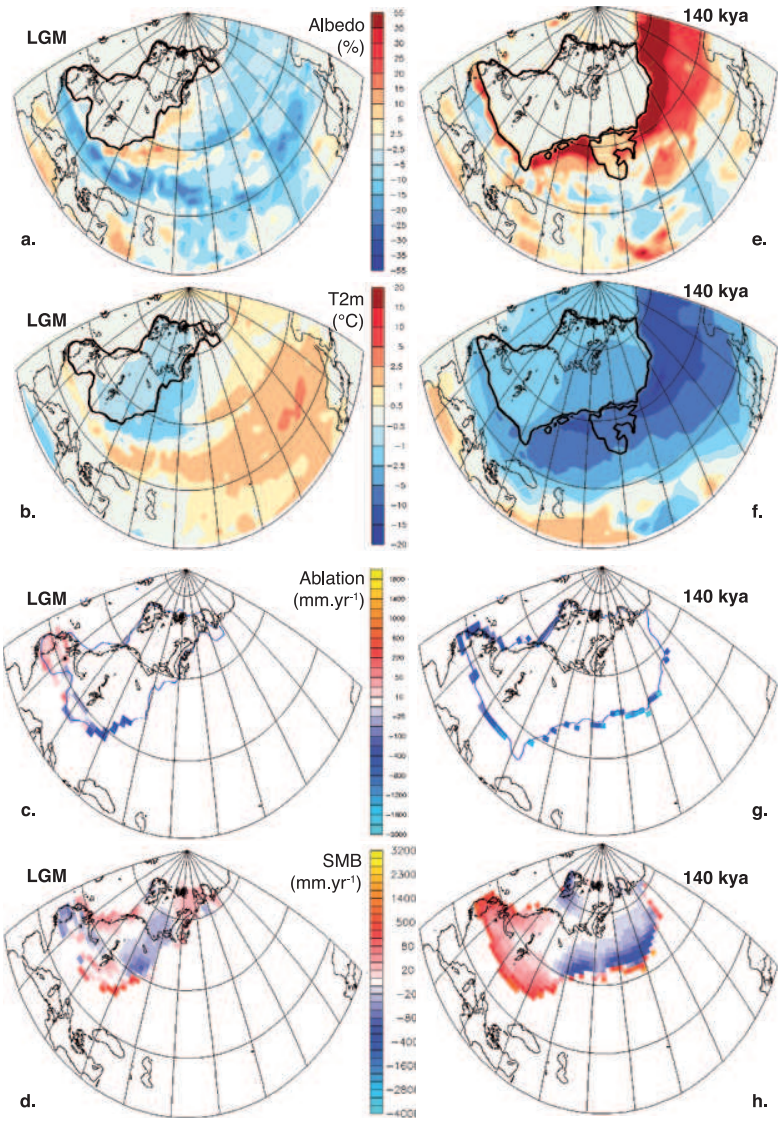

Figure 2. (a–d)Simulated climate anomalies due to vegetation changes for the LGM (B21-C21) and (e–h) the Late Saalian (B140-C140). All the climatic components are represented as annual mean anomalies between the first iteration (vegetation as on Figure 1a) and the third iteration (vegetation as on Figures 1b and 1c): albedo (Figures 2a and 2e), air surface temperature (Figures 2b and 2f), surface melt (Figures 2c and 2g) and surface mass balance (Figures 2d and 2h).

the reduction of tundra in the vicinity of the ice sheet during the three vegetation iterations (Figure 1a and 1c). This regional cooling spreads along the ice margins and southward.

[10] For the LGM, the effect of vegetation change is the opposite. The development of needle-leaf vegetation mainly over Eurasia causes a regional decrease in albedo of about 20%. This leads to a warming of 1°C to 2.5 °C in annual mean air temperature (Figures 2a and 2b). On the south-eastern margin of the ice sheet, a regional cooling of about 1°C is associated with a slight reduction of the local tree cover.

[11] The surface mass balance (SMB) of the ice sheets is reported in Table 1. The average SMB over the entire ice sheet for the Late Saalian simulations, C140 and B140, is 164 $kg.m^{-2}.yr^{-1}$ and 231 $kg.m^{-2}.yr^{-1}$ respectively. For the LGM, the simulated SMB is 210 $kg.m^{-2}.yr^{-1}$ (C21) and

Table 1. Values of the Main Components of the Surface Mass Balance of the LGM and Late Saalian Eurasian Ice Sheets[a]

($kg.m^2.yr^{-1}$)	C21	B21	C140	B140
SMB[b]	210	213	164	231*
Ablation	118	115	77	21
Tot. precip.	488	484	330	327
Snow	430	425	317	307
Evap	104	99	66	55

[a]Using Crowley's vegetation (C21 and C140 respectively), and using the BIOME4 vegetation (B21 and B140 respectively). Student t-tests have been performed to determine whether the differences observed between the results of these simulations are significant (solid star near the SMB values) or not with a probability of 5%.

[b]SMB, surface mass balance.

213 $kg.m^{-2}.yr^{-1}$ (B21). These differences, displayed on Figures 2d and 2h, are mainly a consequence of ablation changes (Figures 2c and 2g), while precipitation and evaporation remain essentially unchanged (Table 1).

4. Discussion and Conclusions

[12] In our simulations the SMB of the Late Saalian ice sheet increases when the prescribed vegetation distribution is changed from the *Crowley* [1995] LGM vegetation map to the one simulated with a global biogeography model forced by a Saalian GCM climate. This SMB increase is significant at 95%, as shown by a Student t-test (Table 1), while we do not find a significant difference in SMB due to vegetation in the LGM simulations.

[13] In the Late Saalian simulations, the lower density of vegetation in East Siberia and along the ice margins causes a regional cooling of about −10°C, spreading westward and southward. In this region, SMB becomes positive due to reduced ablation (Figure 2g and Table 1). The local cooling also induces a perennial snow cover, which contributes to a more positive SMB through the higher albedo (Figure 2a). The effect of the vegetation distribution change is not the same for LGM simulations because the positive SMB value simulated in Russia is balanced by the negative SMB caused by the replacement of grass with taiga in Western Europe.

[14] During the LGM, contrary to ICE-4G used by *Crowley* [1995], Siberia is entirely ice-free in ICE-5G. Consequently, vegetation changes in this area cannot affect the SMB of the ICE-5G ice sheet as much as for the Late Saalian. Indeed, the large Late Saalian ice volume and extent cause an initial cooling that is reinforced by vegetation feedbacks.

[15] Compared to *Crowley* [1995] our LGM simulated climate allows for the growth of a low density mixed forest over Europe. This agrees with the review of *Willis and van Andel* [2004] who show that some refugial for forest-type vegetation existed in Central and Eastern Europe during the LGM. According to *Tarasov et al.* [2000] taiga developed in European Russia and in Siberia but slightly southward of their present-day limits. Cool mixed forest also developed in Mongolia and on the eastern part of the Black Sea, which is consistent with our reconstruction. However, our reconstructions allow for more mixed forest near the LGM ice sheet margins than observed in the pollen data.

[16] The influence fluctuations in SST have on vegetation in our AGCM experiments must be considered with caution, particularly concerning the Late Saalian simulation experiments as these are forced by LGM SST. This will be the object of further studies. In any case, the most important result of this work is that, although a simulated LGM vegetation distribution should be a valid approximation to model previous ice ages, it appears that using an iteratively calculated Late Saalian vegetation map leads to a significantly different simulation of the climate for that period and directly impacts ice sheet dynamics through the consequent variations of surface mass balance. This highlights the need to compute vegetation using fully coupled atmosphere-vegetation models that can capture these dynamics interactions.

[17] **Acknowledgments.** The authors acknowledge support by the Agence Nationale de la Recherche (project IDEGLACE), the Région Rhône Alpes (programme Explora'Doc) and the Ministère des Affaires Étrangères Français for their support. This is a contribution from the Bert Bolin Centre for Climate Research, Stockholm University. The climate simulations were carried out at IDRIS/CNRS and on the Mirage scientific computing plateform in Grenoble (FRANCE).

References

Berger, A., and M. Loutre (1991), Insolation values for the climate of the last 10 millions years, *Quat. Sci. Rev.*, *10*(4), 297–317.

Brovkin, V., S. Levis, M.-F. Loutre, M. Crucifix, M. Caussen, A. Ganopolski, C. Kubatzi, and V. Petoukhov (2003), Stability analysis of the climate-vegetation system in the northern high latitudes, *Clim. Change*, *57*(1–2), 119–138.

Charney, J. (1975), Dynamics of deserts and drought in the Sahel, *Q. J. R. Meteorol. Soc.*, *101*(428), 193–202.

Colleoni, F., G. Krinner, M. Jakobsson, V. Peyaud, and C. Ritz (2009), Influence of regional parameters on the surface mass balance of the Eurasian ice sheet during the peak Saalian (140 kya), *Polar Res.*, in press.

Crowley, T. (1995), Ice age terrestrial carbon changes revisited, *Global Biogeochem. Cycles*, *9*(3), 377–389.

Crowley, T., and S. Baum (1997), Effect of vegetation on an ice-age climate model simulation, *J. Geophys. Res.*, *102*(D14), 16,463–16,480.

Crucifix, M., and C. Hewitt (2005), Impact of vegetation changes on the dynamics of the atmosphere at the Last Glacial Maximum, *Clim. Dyn.*, *25*(5), 447–459.

Gower, S., O. Krankina, R. Olson, M. Apps, S. Linder, and C. Wang (2001), Net primary production and carbon allocation patterns of boreal forest ecosystems, *Ecol. Appl.*, *11*(5), 1395–1411.

Hourdin, F., et al. (2006), The LMDZ4 general circulation model: Climate performance and sensitivity to parametrized physics with emphasis on tropical convection, *Clim. Dyn.*, *27*(7–8), 787–813.

Kaplan, J. O., et al. (2003), Climate change and Arctic ecosystems: 2. Modeling, paleodata-model comparisons, and future projections, *J. Geophys. Res.*, *108*(D19), 8171, doi:10.1029/2002JD002559.

Kleidon, A., K. Fraedrich, and A. Heimann (2000), A green planet versus a desert world: Estimating the maximum effect of vegetation on the land surface climate, *Clim. Change*, *44*(4), 471–493.

Krinner, G., J. Mangerud, M. Jakobsson, M. Crucifix, C. Ritz, and J. Svendsen (2004), Enhanced ice sheet growth in Eurasia owing to adjacent ice-dammed lakes, *Nature*, *427*(6973), 429–432.

Krinner, G., O. Boucher, and Y. Balkanski (2006), Ice-free glacial northern Asia due to dust deposition on snow, *Clim. Dyn.*, *27*(6), 613–625.

Kubatzki, C., and M. Claussen (1998), Simulation of the global biogeophysical interactions during the Last Glacial Maximum, *Clim. Dyn.*, *14*(7–8), 461–471.

Levis, S., J. Foley, and D. Pollard (1999), Co_2, climate, and vegetation feedbacks at the Last Glacial Maximum, *J. Geophys. Res.*, *104*(D24), 31,435–31,669.

Mahowald, N., K. Kohfeld, M. Hansson, Y. Balkanski, S. P. Harrison, I. C. Prentice, M. Schulz, and H. Rodhe (1999), Dust sources and deposition during the Last Glacial Maximum and current climate: A comparison of model results with paleodata from ice cores and marine sediments, *J. Geophys. Res.*, *104*(D13), 15,895–15,916.

Ohmura, A., M. Wild, and L. Bengtsson (1996), A possible change in mass balance of Greenland and Antarctic ice sheets in the coming century, *J. Glaciol.*, *9*(9), 2124–2135.

Paul, A., and C. Schäfer-Neth (2003), Modeling the water masses of the Atlantic Ocean at the Last Glacial Maximum, *Paleoceanography*, *18*(3), 1058, doi:10.1029/2002PA000783.

Peltier, W. (1994), Ice age paleotopography, *Science*, *265*(5169), 195–201.

Peltier, W. (2004), Global glacial isostasy and the surface of the ice-age Earth: The ICE-5G (VM2) model and GRACE, *Annu. Rev. Earth Planet. Sci.*, *32*, 111–149.

Petit, J. R., et al. (2001), Vostok ice core data for 420000 years, http://users.aims.ac.za/irina/dustVostok.txt, World Data Cent. Paleoclimatology, Boulder, Colo.

Peyaud, V. (2006), Role of the ice sheet dynamics in major climate changes, Ph.D. thesis, Lab. de Glaciol. et de Geophys. de l'Environ., Univ. Grenoble I, Grenoble, France.

Schulze, E., et al. (1999), Productivity of forests in the Eurosiberian boreal region and their potential to act as a carbon sink—A synthesis, *Glob. Change Biol.*, *5*(6), 703–722.

Spahni, R., et al. (2005), EPICA Dome C CH_4 Data to 650KYrBP, ftp://ftp.ncdc.noaa.gov/pub/data/paleo/icecore/antarctica/epica_domec/edc-ch4-2005-650k.txt, World Data Cent. Paleoclimatology, Boulder, Colo.

Svendsen, J., et al. (2004), Late Quaternary ice sheet history of northern Eurasia, *Quat. Sci. Rev.*, *23*(11–13), 1229–1271.

Tarasov, P., et al. (2000), Last Glacial Maximum biomes reconstructed from pollen and plant macrofossil data from northern Eurasia, *J. Biogeogr.*, *27*(3), 609–620.

Willis, K., and T. van Andel (2004), Trees or no trees? The environments of central and eastern Europe during the last glaciation, *Quat. Sci. Rev.*, *23*(23–24), 2369–2387.

F. Colleoni and G. Krinner, Laboratoire de Glaciologie et Géophysique de l'Environnement, 54 rue Molière BP96, F-38402 St-Martin-d'Hères CEDEX, France. (flocolleoni@gmail.com; krinner@lgge.obs.ujf-grenoble.fr)

M. Jakobsson, Department of Geology and Geochemistry, Stockholm University, SE-106 91 Stockholm, Sweden. (martin.jakobsson@geo.su.se)

Manuscript 3

Colleoni F., Liakka J., Krinner G., Jakobsson M., Masina S. and Peyaud V., The Late Saalian surface ocean (140 ka): sensitivity of the Late Saalian Eurasian ice sheet to sea surface conditions, *Climate Dynamics*, submitted.

Contribution:

- Designing and running the experiments using LMDZ4
- Adapting LMDZ4 outputs to Planet Simulator (PLASIM) and partly designing the PLASIM experiments
- Analyzing the results
- Main part of the writing

Résumé
Ce travail analyse la sensibilité du bilan de masse en surface (SMB) de la calotte Eurasiatique aux changements de température de surface océaniques (SST) durant le Dernier Maximum Glaciaire (21 ka , LGM) et le maximum glaciaire du Saalien (140 ka). Puisque qu'aucune reconstruction de SST à 140 ka n'a jamais été réalisée, nous avons testé la sensibilité du climat à 140 ka en utilisant un modèle de circulation générale atmosphérique (AGCM) forcé par deux reconstructions prè-existantes de SST LGM. Par la suite, un essai de reconstruction des SST à 140 ka est réalisé à l'aide d'un AGCM couplé à une couche mixte océanique. Les SST simulées à 140 ka sont plus froides dans l'hémisphère Nord et plus chaudes dans l'hémisphère Sud que les SST du LGM. La glace de mer s'étend très au Sud jusqu'à 40°N aussi bien dans l'Atlantique Nord que dans le Pacifique Nord. Les changements de SST affectent le SMB de la calotte Eurasienne aussi bien à 21 ka qu'à 140 ka bien que la calotte Eurasiatique à 140 ka soit bien moins sensible aux changements de SST que durant le LGM.

The Late Saalian surface ocean (140 ka): sensitivity of the Late Saalian Eurasian ice sheet to sea surface conditions.

F. Colleoni[1,2] **. J. Liakka**[3] **. G. Krinner**[1] **. M. Jakobsson**[2] **. S. Masina**[4] **. V. Peyaud**[1]

[1]Laboratoire de Glaciologie et Géophysique de l'Environnement, UJF, CNRS, France

[2]Department of Geology and Geochemistry, Stockholm University, 106 91 Stockhlom, Sweden

[3]Department of Meteorology, Stockholm University, 106 91 Stockholm, Sweden

[4]Centro Euro-Mediterraneo per i Cambiamenti Climatici, and Istituto Nazionale di Geofisica e Vulcanologia, Bologna, Italy

Abstract

This work focuses on the Late Saalian (140 ka) and LGM (21 ka) Eurasian ice sheets surface mass balance (SMB) sensitivity to changes in sea surface temperatures (SST). Since no global Late Saalian SST compilations exist, we test the sensitivity of the Late Saalian climate using an AGCM forced with two data-based LGM SST reconstructions. Furthermore, an attempt to reconstruct the Late Saalian SST is performed using an AGCM coupled to a mixed-layer ocean. The resulting Late Saalian SST are cooler than the LGM SST in the Northern Hemisphere and warmer in the Southern. The winter sea ice extends to 40°N in both North Atlantic and Pacific oceans. Changes in SST affect the SMB of the Eurasian ice sheet during both glaciations although the Late Saalian ice sheet is less sensitive to the prescribed SST changes than the LGM.

Sea surface conditions, Late Saalian, Eurasian ice sheet, Climate modelling, Quaternary

Introduction

During the Quaternary, the Northern Hemisphere continents have to a large extent been covered by ice sheets that formed during the Late Quaternary ice ages. Particularly, during the Late Saalian glaciation, with its maximum at about 140 ka, the Eurasian ice sheet[4] covered more than 11×10^6 km^2 and extended further southward and eastward than during the Last Glacial Maximum (LGM, 21 ka) (Svendsen *et al.*, 2004). The Late Saalian Eurasian ice sheet was ≈54 percent larger in area and twice as thick as the LGM one (Peyaud, 2006; Peltier, 2004). How such a large ice sheet could develop over Eurasia? To better understand the climatic processes that could lead to this ice topography, previous studies numerically addressing the impact of regional factors (dust deposition on snow and proglacial lakes, Colleoni *et al.* (2009a)) and vegetation feedbacks (Colleoni *et al.*, 2009d) on the surface mass balance of the Late Saalian Eurasian ice sheet have been carried out. However, the Late Saalian simulations were forced with LGM sea surface temperatures (SST) reconstructions as a first approximation since no global maps of the Late Saalian SST exist. Consequently, this work addresses the sensitivity of the Late Saalian Eurasian ice sheet's surface mass balance to the state of the oceanic surface.

The ice age cycles are generally thought to be ultimately driven by cyclical variations in the Earth's orbit (e.g. Hays et al., 1976), although glacial inception per se results from a complex interaction between a suite of processes such as for example land-ice feedbacks, atmosphere-ice feedbacks, and ocean forcing. In comparison to the LGM, the Late Saalian period presents a larger eccentricity of the Earth's orbit (Berger & Loutre, 1991) enhancing the impact of variations in precession. This leads to cooler and longer summers and shorter and warmer winters (perihelion occurs at December 6th) in the Northern Hemisphere high latitudes while greenhouse gas concentrations seems to have been similar during these two periods (Petit *et al.*, 2001; Spahni *et al.*, 2005) (Figure 4.1). The nature of glacial maxima also depends on the evolution of the solar insolation, as a function of the Earth's orbital parameters, prior to the glacial inception and this evolution was markedly different between the Late Saalian and the LGM (Figure 4.1). Although it is possible to point out differences in orbital forcing between the Late Saalian and the LGM glacial periods, the question of why the Eurasian ice sheet could extend so much further to the east and south during the Late Saalian remain unaddressed.

[4]This ice sheet existed during the MIS6 glacial period, although, we will henceforth use the term "Late Saalian" also when referring to the global environment at this time.

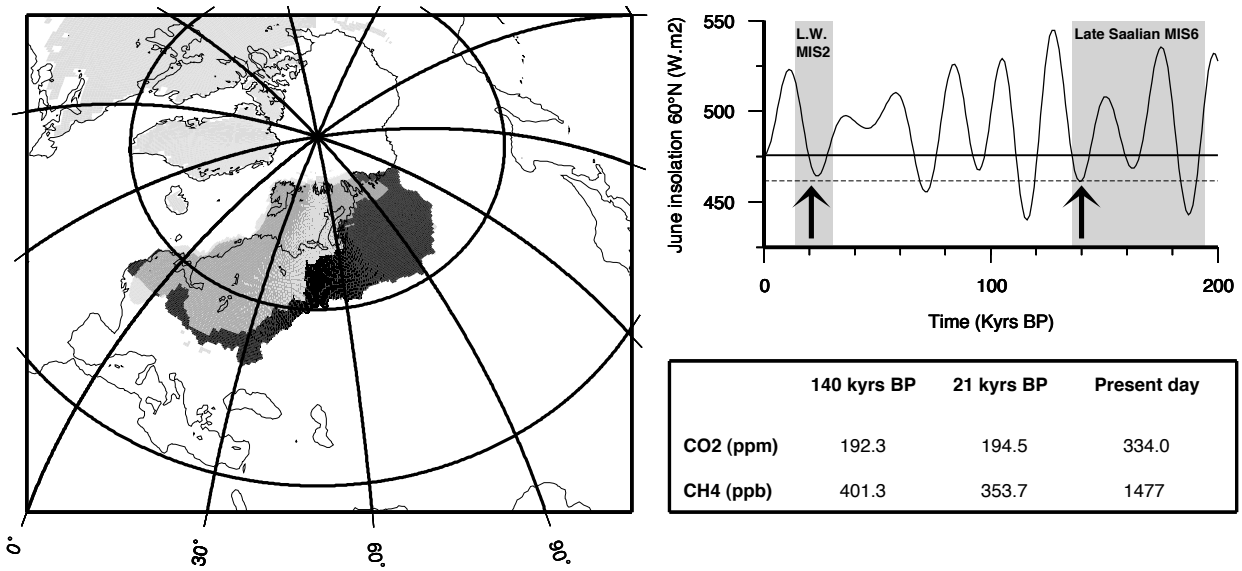

	140 kyrs BP	21 kyrs BP	Present day
CO2 (ppm)	192.3	194.5	334.0
CH4 (ppb)	401.3	353.7	1477

Figure 4.1: Summary of the main differences between the LGM and the Late Saalian glacial maximum. Left: difference in ice extent between the LGM (gray) and the Late Saalian (black). Ice extent is much more important during the Late Saalian southward and eastward. Top right: June insolation at 60°N (Berger & Loutre, 1991), arrows point the Late Saalian glacial maximum (140 kya BP) and Late Weichselian (L.W.) glacial maximum (21 kya BP). Thick black line indicates the present-day insolation value at 60°N. Insolation values are similar for the LGM and the Late Saalian. Bottom right: greenhouses gases concentration values from Vostok and Dome C (Petit *et al.*, 2001; Spahni *et al.*, 2005) for the Late Saalian, the LGM and present day. Values between the LGM and the Late Saalian show no significant differences.

In previous studies we have shown, however, that the presence of large ice dammed lakes and reduced dust deposition on snow directly contributed to the relative stability of the Eurasian ice sheet during the Late Saalian (Colleoni *et al.*, 2009a) and that the Late Saalian steady-state modeled vegetation significantly influenced the ice sheet's surface mass balance (Colleoni *et al.*, 2009d). In these studies, we forced an Atmospheric General Circulation Model (AGCM) with CLIMAP LGM sea surface temperatures (CLIMAP, 1984; Paul & Schaefer-Neth, 2003) since no SST reconstructions exist for the Late Saalian. This limits the interpretation of the other regional feedbacks whose amplitude and intensity can be different depending on the climatic context and the ice sheet extent over continents (Kageyama *et al.*, 2006).

Most of the previous modeling studies addressing the influence of SST and sea ice cover on the ice age climate focused on the LGM since there is a considerably large number of continental and marine geological records available for further comparison with numerical simulations. Some of these studies force AGCM with prescribed LGM SST reconstructions (e.g. Kageyama *et al.* (1999)) to which a regional temperature perturbation is eventually applied to explore the impacts of North Atlantic or tropic SST on the Northern Hemisphere climate (e.g. Rind (2006); Toracinta *et al.* (2004)). In other studies, SST are computed using a coupled Atmosphere-Ocean General Circulation model (e. g. Ramstein & Joussaume (1995); Dong & Valdes (1998)). Within the framework of the Paleo Model Intercomparison Projects (PMIP) I and II, Kageyama *et al.* (1999, 2006) show that the use of prescribed and simulated SST in AGCM experiments leads to different climate-related (mostly snow fall and temperatures) oceanic and continental climate anomaly patterns of various amplitude over the North Atlantic and Eurasia when compared to the palynologic databases available for Eurasia. These discrepancies are explained by the use of different models whose computed climate depends on the physics of each model. Ruddiman & McIntyre (1979) and Hebbeln *et al.* (1994) show that seasonally open waters in the North Atlantic, such as suggested by the recent MARGO LGM SST reconstructions (Kucera *et al.*, 2005a), during the LGM significantly influence the mass balance of the Northern Hemisphere ice sheets.

These studies clearly show that SST strongly influence the atmosphere by the means of oceanic heat exchange variations. The differ-

Table 4.1: Measured SST from various sources for both LGM (21 ka) and Late Saalian (140 ka): [1]Calvo *et al.* (2001), [2]Schneider *et al.* (1995), [3]Schneider *et al.* (1996), [4]Schneider (1999), [5]Pelejero *et al.* (2006), [6]Kirst *et al.* (1999), [7]Villanueva *et al.* (2002), [8]Pahnke & Sachs (2006), [9]Mashiotta T.A (1999), [10]Lea *et al.* (2000), [11]Nurnberg & Groeneveld (2006), [12]Wei *et al.* (2007), [13]Hippler *et al.* (2006), [14]Abreu *et al.* (2003), [15]Kandiano *et al.* (2004), [16]Chapman *et al.* (2000), [17],Chen *et al.* (2003) [18]Schaefer *et al.* (2005), [19]Chen *et al.* (2002). Data are classified according to annual values (Annu.), summer values (Sum.) and winter values (Win.). Data have been measured and interpreted according different methods: alkenone (Alk.), Mg/Ca ratio, foraminifera.

Ocean	SST(°C) -21k	SST(°C) -140k	Season	Method	Ref.
Atl.	12.5	13.8	Annu.	Alk.	[1]
Atl.	21.5	21.5	”	Alk.	[2]
Atl.	18.0	18.0	”	Alk.	[4]
Atl.	9.8	11.5	”	Alk.	[5]
Atl.	10.2	9.2	”	Alk.	[5]
Atl.	16.5	17.0	”	Alk.	[2]
Atl.	23.0	24.0	”	Alk.	[3]
Atl.	14.5	14.25	”	Alk.	[6]
Atl.	8,8	14.0	”	Alk.	[7]
Atl.	13.0	16.0	”	Alk.	[8]
Pacif.	22.5	22.5	”	Mg/Ca	[10]
Pacif.	26.0	26.0	”	Mg/Ca	[10]
Pacif.	19.0	19.0	”	Mg/Ca	[11]
Pacif.	22.0	21.25	”	Mg/Ca	[12]
Pacif.	21.0	22.0	”	44Ca/40Ca	[13]
Pacif.	9.8	9.0	”	Alk.	[8]
Ant.	6.6	7.0	”	Mg/Ca	[9]
Atl.	5.0	8.0	Sum.	foram	[14]
Atl.	3.5	3.0	”	Mg/Ca	[15]
Atl.	11.75	12.5	”	mod. ana.	[16]
Pacif.	27.4	28	”	planc. trans.	[17]
Pacif.	12.5	11	”	mod. ana.	[18]
Pacif.	4.0	3.5	”	mod. ana.	[18]
Pacif.	23.0	23.0	Win.	planc. trans.	[17]
Pacif.	9.0	8.0	”	mod. ana.	[18]
Atl.	11.0	13.0	”	planc. trans.	[19]
Atl.	0.0	0.0	”	Mg/Ca	[15]

ent SST forcings (prescribed or calculated) also modulate the simulated climate feedbacks. Consequently it is of importance to determine how different prescribed SST reconstructions can influence the surface-atmosphere interactions during the Late Saalian. Here we focus on the Late Saalian climate to investigate the reasons of the ice sheet's stability under various oceanic conditions. Were the Late Saalian (MIS 6) SST different from the LGM (MIS 2)? There are only few SST estimates for MIS 6 based on marine sediment cores. Some of them are listed in Table 4.1 together with the LGM SST estimates allowing a direct comparison for each coring site. To understand how SST could have influenced the Late Saalian climate and the surface mass balance of the Eurasian ice sheet, we use both the approaches described above. We first test the effect on the Late Saalian climate of forcing an AGCM model with two different prescribed LGM SST reconstructions and the Late Saalian continental and orbital boundary conditions. To allow for comparison, the same runs using the two LGM SST reconstructions are performed for the LGM time period. Finally, since from the data (Table 4.1) it is not clear whether the Late Saalian and the LGM surface oceans were different, we try to estimate a new SST through a modeling experiment. We use a simplified AGCM coupled to an ocean mixed-layer model to understand whether or not simulated Late Saalian SST lead to highly different temperatures than for LGM SST reconstructions used as first approximation in atmosphere only GCM experiments and if these new surface oceanic conditions lead to a different Late Saalian climate state.

Methods and settings

This work is divided into two distinct parts:

1- the study of the sensitivity of the Late Saalian ice sheet to two prescribed LGM SST reconstructions.

2- the simulation of SST in agreement with the Late Saalian boundary conditions and their impact on the Late Saalian climate.

In the first part, the Late Saalian and the LGM climates are explored performing 21 years snap-shots using LMDZ4 AGCM (see description below, Hourdin *et al.* (2006)). In the second part, Late Saalian SST are computed using the Planet Simulator AGCM mixed-layer model (Fraedrich *et al.*, 2005). To allow for comparison with the Late Saalian climate simulated in the first part, a 20 years snap-shot is performed forcing LMDZ4 with the simulated Late Saalian SST. The outline of the simulations performed in the second part is presented in Figure 4.2.

Late Saalian atmospheric simulations

Twenty-one-year long snap-shots are performed using the LMDZ4 atmospheric general circulation model (Hourdin *et al.*, 2006) which takes into account the climatic impact of open water

Figure 4.2: Scheme of the simulations carried out using Planet Simulator (Fraedrich *et al.*, 2005) to compute Late Saalian SST and using the LMDZ4 (Hourdin *et al.*, 2006) to obtain a final Late Saalian climate. Methods and boundary conditions for each stage are detailed in the Methods section.

surfaces and dust concentration in snow (Krinner, 2003; Krinner *et al.*, 2006). The LMDZ4 model only takes into account the dust content of snow because its radiative effect prevails on that induced by the atmospheric dust content in snow-covered regions. The inferred dust content of the snow and the resulting snow albedo are calculated following Krinner *et al.* (2006). The model is run with 96×72 grid cells and with 19 vertical layers. The horizontal resolution is irregular, varying from 100 km in Eurasia (at 65°N/60°E) to 550 km at the antipodes of this point.

Simulating the Late Saalian SST

In order to compute the Late Saalian surface ocean conditions, we use the Planet Simulator (PLASIM) general circulation model of intermediate complexity (radiative scheme of intermediate complexity) (Fraedrich *et al.*, 2005). The central part of PLASIM consist in an AGCM, which is based on the moist primitive equations representing conservation of momentum, mass and energy. The equations are solved on a Gaussian grid in the horizontal direction, corresponding to a T42 resolution (128×64) in the horizontal direction, and on 10 vertical sigma levels.

Differently from the LMDZ4, PLASIM does not account for the effects of proglacial lakes and dust deposition on snow. The AGCM is interactively coupled to a mixed-layer ocean (the mixed-layer depth is set to 50 m) and to a zero-dimensional thermodynamic sea ice model. In this model, the oceanic heat transport is prescribed for every month and is parametrized according to:

$$Q_{c_2} = \rho_w c_w h_{mix} \frac{T_{mix_c} - T_{mix}}{\tau_T} \qquad (1.11)$$

where c_w is the specific heat capacity of sea water, ρ_w corresponds to the density of sea-water, h_{mix} stands for the mixed-layer, T_{mix} is the temperature of the mixed layer and τ_T represents the time scale at which T_{mix} is relaxed to its climatological value $T_{mix,c}$ ($\tau_T = 50$ days). This method to calculate SST has been previously used by Romanova *et al.* (2005, 2006) to investigate the effect of ocean heat fluxes on glacial climates. In the absence of any Late Saalian sea surface reconstructions, the oceanic heat transports are calculated using LGM SST reconstructions. Thus we performed a LGM control simulation of 21 years forcing PLASIM with Paul & Schaefer-Neth (2003) LGM sea surface conditions (the first model year is discarded as spin-up). We choose to base the calculation on Paul & Schaefer-Neth (2003) LGM SST because this reconstruction is in closer agreement with the temperatures estimated from analysis of marine sediment cores than the LGM CLIMAP reconstruction (CLIMAP, 1984). In this LGM control run, we use ICE-5G ice topography (Peltier, 2004), vegetation is prescribed as the fraction of forest extracted from Crowley (1995) LGM vegetation map, the CO_2 concentration is set to 194 ppm and the orbital parameters are calculated for 21 ka according to Berger & Loutre (1991).

To simulate the Late Saalian surface oceanic conditions, PLASIM in then forced using the calculated monthly LGM ocean flux corrections. Orbital parameters are adjusted to 140ka, CO_2

Table 4.2: Summary of the various sea surface conditions used in the AGCM simulations: [1] Paul & Schaefer-Neth (2003) (referred to as P03 in the text), [2] (CLIMAP, 1984) (refers to as CLIMAP) LGM reconstructions and PS140 for the computed Late Saalian surface ocean (this study). The Late Saalian and the LGM time periods are referred to as 140k and 21k respectively.

ID	21k	140k
P03	[1]	
CLIMAP	[2]	
PS140		PLASIM sim.

concentration is set to 192.3 ppm and vegetation is prescribed similarly to that of the LGM control run. The simulation is performed for 50 model years, sea surface equilibrium is reached after 25 model years and the last 15 years are used for analysis. The various SST reconstructions used in this work are summarised in Table 4.2.

Boundary conditions

LGM boundary conditions

In the LGM experiments, we use ICE-5G (Peltier, 2004), LGM dust deposition map from Mahowald *et al.* (1999) and LGM vegetation map from Crowley (1995). Eustatic sea-level is set at -130 m a.s.l. and corresponds to the LGM ice equivalent sea-level of ICE-5G. Orbital parameters have been set according to Berger & Loutre (1991) and greenhouse gas (GHG) concentrations (Figure 4.1) have been specified according to Dome C ice core concentration records (Petit *et al.*, 2001; Spahni *et al.*, 2005). Contrary to the Late Saalian, proglacial lakes seem not to have formed during the LGM. Consequently our LGM global geography does not include reconstructions of proglacial lakes.

Late Saalian boundary conditions

Except in the Eurasian region, we used the LGM global ice topography and ice sheet extents provided by Peltier (2004), assuming that the differences between the Late Saalian glacial maximum and LGM geographies far from our region of interest are sufficiently small to not critically influence our results. The Eurasian Late Saalian maximum topography was computed with the GRISLI ice model (Ritz *et al.*, 2001; Peyaud, 2006; Peyaud *et al.*, 2007) using the reconstructed ice limits from Svendsen *et al.* (2004) and taking into account lithospheric deflection (Figure 4.1). Eustatic sea-level is set at -110 m a.s.l according to Astakhov (2004).

Ice dammed lakes, created from a blocking of the Yenissei and Ob rivers by the Saalian ice sheet and by its melt water, have been reconstructed according to the methods of Mangerud *et al.* (2001). More details are given in Colleoni *et al.* (2009a).

Dust concentrations recorded in the ice core retrieved from EPICA Dome C, East Antarctica, suggest that dust deposition was 40% lower during MIS 6 compared to the LGM (Delmonte & coauthors, 2004). Winckler *et al.* (2008) recently showed that during the late-Pleistocene glacial cycles, dust fluxes in both the Northern and Southern hemispheres had a common response to global climate change. The MIS 6 spatial distribution of dust deposition is therefore mapped by applying a 40% reduction to the LGM distribution modeled by Mahowald *et al.* (1999). More details on the reconstruction of the spatial dust deposition at 140 ka are given in Colleoni *et al.* (2009a).

Since no vegetation compilation for 140 ka exists, we use the Crowley (1995) LGM vegetation map as a first order approximation. The climatic feedbacks from a modeled vegetation distribution for the Late Saalian have been explored in Colleoni *et al.* (2009d). The results show that vegetation significantly affects regional temperature by several degrees and consequently impacts on the surface mass balance of the Eurasian ice sheet through the snow-vegetation-albedo feedback.

Finally, orbital parameters have been set according to Berger & Loutre (1991) and greenhouse gas (GHG) concentrations (Figure 4.1) have been specified according to EPICA Dome C ice core concentration records (Petit *et al.*, 2001; Spahni *et al.*, 2005).

AGCM Simulations

In total, five LMDZ4 snap-shots of 21 years each have been carried out. $P03_{140}$ and $CLIM_{140}$ (140 here refers to the Late Saalian) have been forced using Paul & Schaefer-Neth (2003) (P03) and CLIMAP (1984) (CLIMAP) LGM sea surface conditions (Table 4.3 and 4.2). To allow for comparison, similar experiments have been per-

Table 4.3: Summary of the LMDZ4 21 years snap-shots performed in this work and their boundary conditions. Simulations ran for the Late Saalian period (140ka) and the LGM (21ka). *cf.* Table 4.2 for the SST reconstructions. As described in the Methods, we use ICE-5G (Peltier, 2004) ice topography for both simulated time periods. For the Late Saalian, the Eurasian component (referred to as Euras140k in this table) is from Peyaud (2006). Dust deposition map are from Mahowald *et al.* (1999) LGM reconstructions and are adapted to the Late Saalian according to the method described in the Methods. "Lakes" correspond to the proglacial lakes that were present during the Late Saalian only and we prescribed LGM vegetation (Crowley, 1995) for all the simulations.

	Time period	SST	Ice topo.	Dust	Lakes	Vegetation
FULL$_{140}$	140ka	PS140	ICE-5G+Euras140k	adapted from [1]	Yes	LGM
P03$_{140}$	140ka	P03	"	"	Yes	LGM
CLIM$_{140}$	140ka	CLIMAP	"	"	Yes	LGM
P03$_{21}$	21ka	P03	ICE-5G	[1]	No	LGM
CLIM$_{21}$	21ka	CLIMAP	ICE-5G	[1]	No	LGM

formed for the LGM period (P03$_{21}$ and CLIM$_{21}$). Since the Paul & Schaefer-Neth (2003) reconstruction is better in agreement with geological evidence than CLIMAP, P03$_{140}$ and P03$_{21}$ will be considered as the reference simulations and all impacts will be expressed as anomalies (differences or ratio). The mean annual SMB is calculated for each simulation using the components listed in Table 4.4. Finally a last Late Saalian snap-shot (FULL$_{140}$) was carried out using the LMDZ4 forced by the simulated Late Saalian SST (PS140, Section) from this study. Since these Late Saalian simulated SST have been generated using the computed ocean heat fluxes from the LGM Paul & Schaefer-Neth (2003) reconstruction, FULL$_{140}$ is further compared to P03$_{140}$.

The annual surface mass balance of the ice sheet is evaluated according to the temperature index method of Ohmura *et al.* (1996). In this method, surface ablation is diagnosed when mean summer surface air temperature (T_{JJA}), recalculated on a fine resolution grid with altitude-correction, exceeds a prescribed threshold of -1.8°C. The total ablation (in kg.m^{-2}.year^{-1}) is then calculated as:

$$A = 514°C^{-1} \times T_{JJA} + 930 \qquad (1.12)$$

where T_{JJA} is in °C. We downscale the GCM surface air temperature to a 20-km grid by applying a 5.5°C.km^{-1} summer temperature correction to account for altitude changes (Krinner & Genthon, 1999; Abe-Ouchi *et al.*, 2007). The surface mass balance B is then calculated as:

$$B = P_S - E - A \qquad (1.13)$$

where P_S and E represent solid precipitation and evaporation respectively.

To evaluate whether the observed differences between the various climate variables can be interpreted as an effect of the investigated sea surface conditions, student tests have been performed between P03 and CLIM, and P03 and FULL140. Since the simulated datasets are available for 20 years each, the degree of freedom is 38 calculated from (N1 + N2 - 2). The null hypothesis H_0 is defined as $\sigma_1 \neq \sigma_2$ and results will be accepted if probability is lower than 5%.

Results

In this section we compare the sensitivity to prescribed SST P03 and CLIMAP by analyzing their climatic impacts during the Late Saalian (CLIM$_{140}$ - P03$_{140}$) and then during the LGM (CLIM$_{21}$ - P03$_{21}$). Following this analysis we present the simulated surface ocean reconstruction PS140 and evaluate its impact on the Late Saalian Eurasian climate by comparing simulations FULL$_{140}$ and P03$_{140}$.

CLIMAP versus Paul & Schaefer-Neth (2003)

The LGM sea surface temperatures by Paul & Schaefer-Neth (2003) (referred to as P03) and CLIMAP (CLIMAP, 1984) are similar except for in the North Atlantic and in the tropical and equatorial regions. During winter (December, January, February, DJF), the CLIMAP reconstruction suggests about 2°C colder temperatures than P03 in the Southern Hemisphere, while it

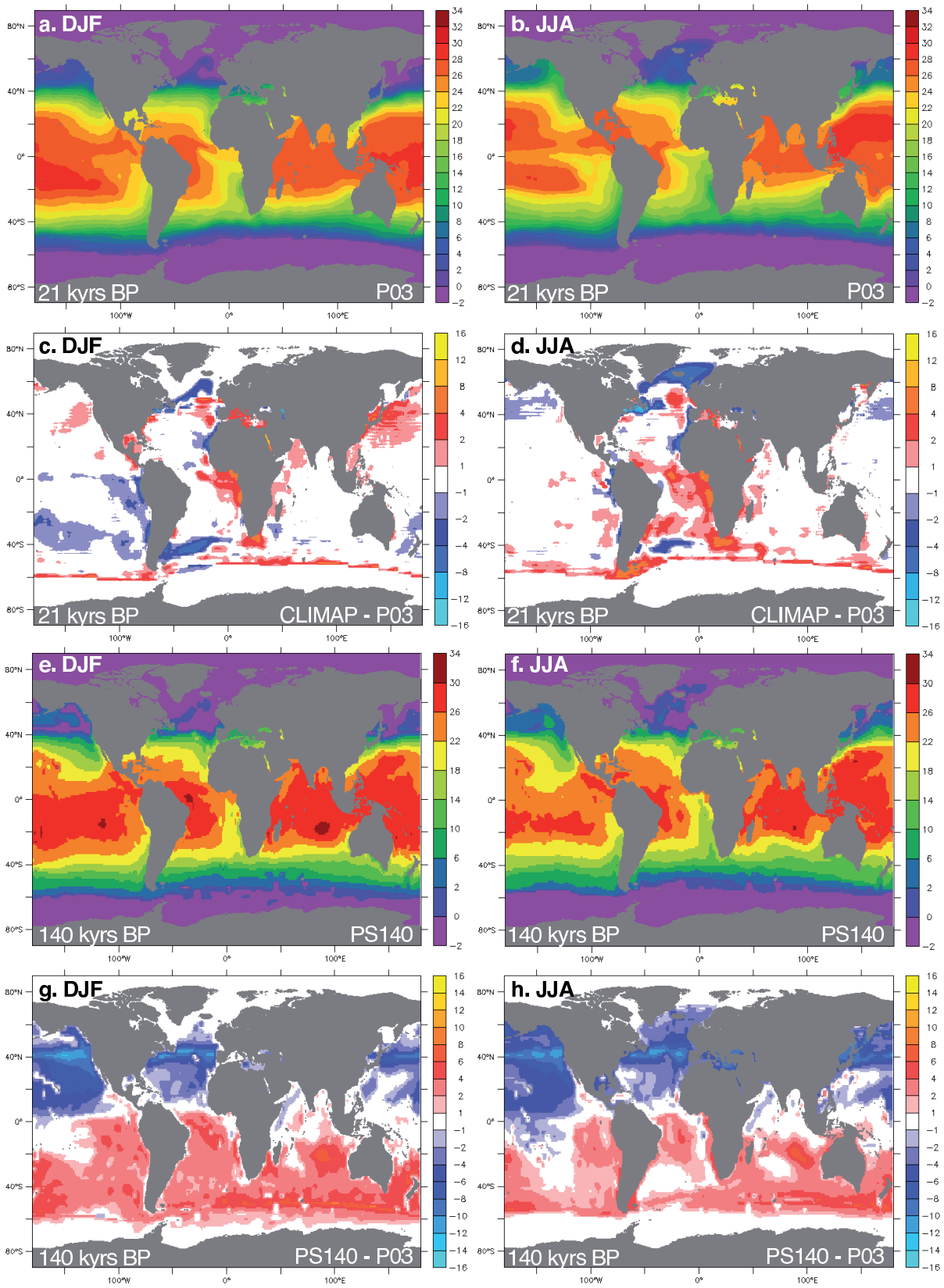

Figure 4.3: Prescribed and simulated SST conditions: a. Winter (December - January - February, DJF) from Paul & Schaefer-Neth (2003) (referred as P03), b. same as a. but for summer (June - July - August, JJA); LGM SST anomalies between CLIMAP (1984) and P03 during winter (c) and summer (d); Simulated Late Saalian SST (referred as PS140) for winter (e) and summer (f) and SST anomalies between PS140 and P03 for both seasons (g and h).

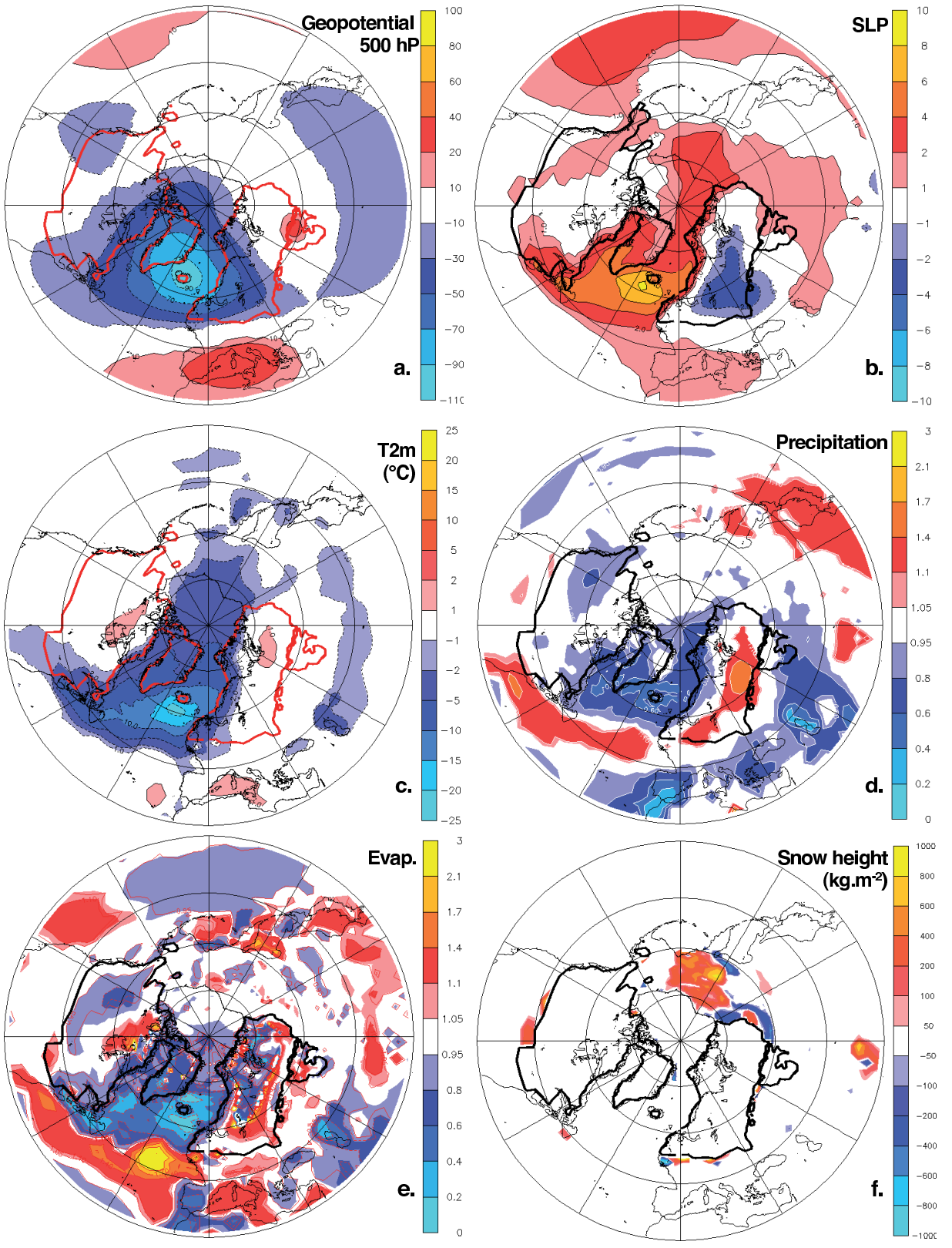

Figure 4.5: Late Saalian mean annual climate anomalies between CLIMAP (simulation $CLIM_{140}$) and P03 (simulation $P03_{140}$) over the Northern hemisphere (30°-90°N). Difference are calculated as ($CLIM_{140}$ - $P03_{140}$) for: a. geopotential height at 500 hPa (m), b. sea-level pressure (SLP in mbar), c. air temperature at 2 meters (t2m in °C); d. ,e. precipitation and evaporation anomalies expressed as the ratio ($CLIM_{140}/P03_{140}$) and f. continental snow height (m). Refer to Table 4.3 for details about the settings of the simulations.

Table 4.4: Mean annual surface mass balance (SMB) and its components (average over the Eurasian ice sheet, in kg$\cdot yr \cdot^{-1} \cdot m^2$). Significant difference from the Student test (CLIM - P03 and PS - P03) are indicated by a solid start nearby the values.

$(kg.m^2.yr^{-1})$	**FULL$_{140}$**	**P03$_{140}$**	**CLIM$_{140}$**	**P03$_{21}$**	**CLIM$_{21}$**
Tot. precip	238*	303	308	488	445*
Snow	236*	288	294*	430	401*
Evap.	37*	51	48*	104	86*
Ablation	0*	11	7*	118	67*
SMB PDD	199*	**225**	**239***	**208**	**248***

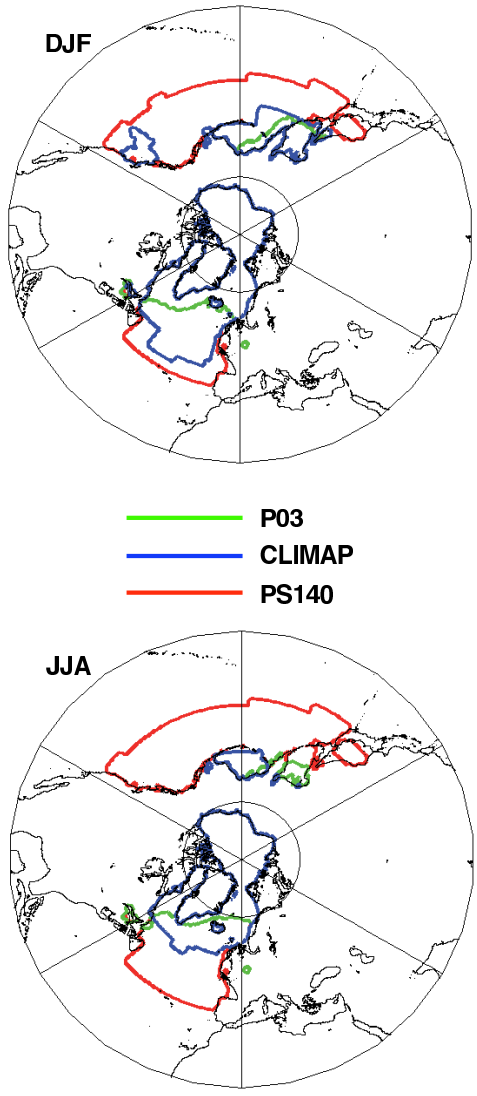

Figure 4.4: Northern Hemisphere sea ice extent for the three SST reconstructions used in the present study (Figure 4.3): P03 (green), CLIMAP (blue) and PS140 (red) for winter (DJF) and summer (JJA).

is about 2°C to 4°C warmer in the Asian North Pacific. During summer (June, July, August, JJA), the CLIMAP North Pacific is ≈ 1°C to 2°C colder than P03. Along the tropical and equatorial African shorelines large differences of ≈ 4°C to 8°C between the two reconstructions can be observed during both winter and summer (Figure 4.3c and d). Finally, in the North Atlantic high latitudes, the large CLIMAP sea ice cover induces a cooling of ≈2°C to 5°C during both winter and summer. During winter, the CLIMAP sea ice covers the entire North Atlantic from 45°N Northward, while the sea ice is open in P03 southward of Iceland in the East and from 60°N in the West (Figure 4.4). The CLIMAP sea ice limit retreats northward in summer but still covers a large part of the North Atlantic while in P03, the southern portion of the Norwegian Sea becomes open. In the North Pacific, sea ice remains confined to the Bering Sea and its extent is similar during both winter and summer in P03 while in CLIMAP, the annual cycle of sea ice extent is stronger (Figure 4.4).

The Late Saalian glacial maximum: comparing CLIM$_{140}$ and P03$_{140}$

Compared to P03, the most extensive CLIMAP sea ice extent induces a large negative temperature anomaly of about 20°C to 25°C in the North Atlantic south of Iceland (Figure 4.5c). This affects the 500 hPa geopotential which exhibits a strong negative anomaly of ≈50 to 110 meters over this area (Figure 4.5a). In CLIMAP, sea ice extends much more southward than in P03. Storm tracks are generally stronger where the meridional gradients of surface temperatures are the strongest. In CLIM$_{140}$, storm tracks are consequently strengthened at the sea ice edge (≈45°N) which tends to reduce the Icelandic depression located further to the North and causes an increase in sea-level pressure (SLP) by about 8 mbars (Figure 4.5b). This effect has

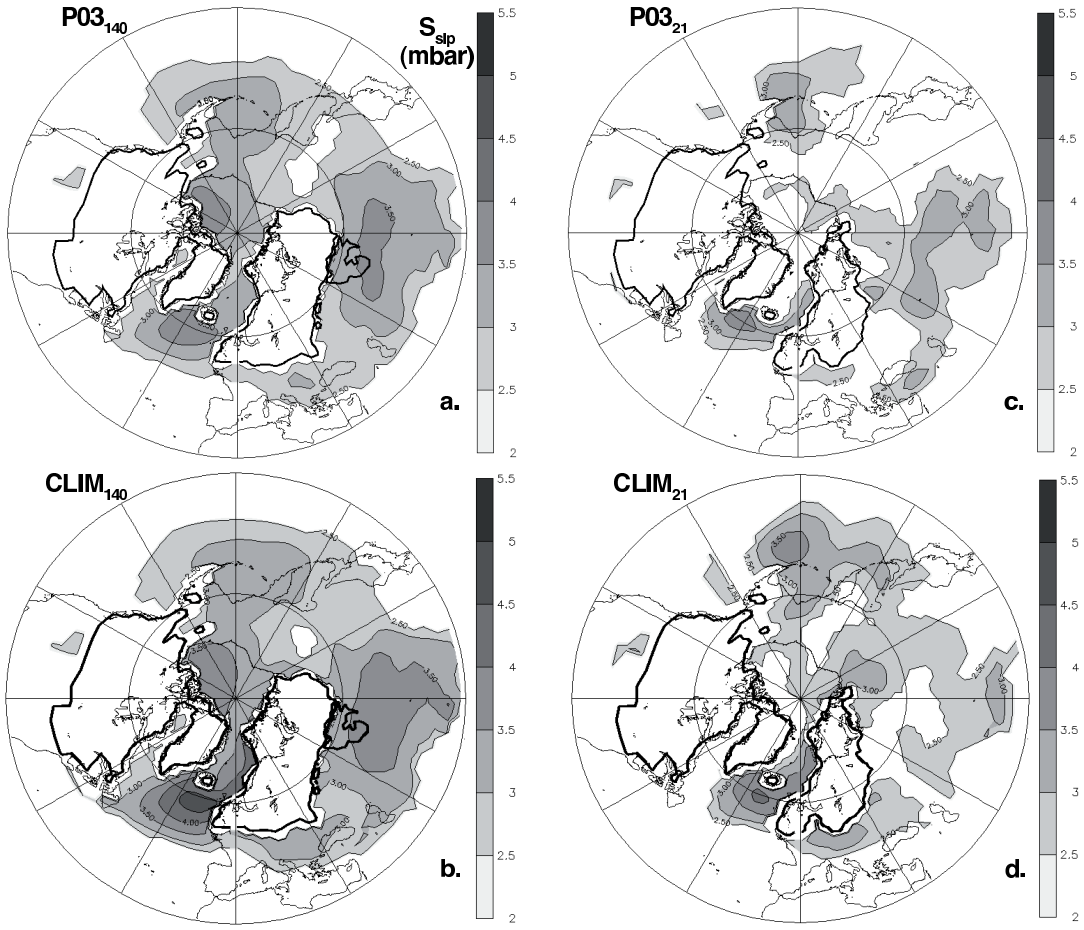

Figure 4.6: Northern hemisphere variance of band pass filtered (3:7) winter sea-level pressure (mbar) following Kageyama *et al.* (1999) for the Late Saalian (a, b) and the LGM (c, d) for simulations forced with CLIMAP (b, d) and Paul & Schaefer-Neth (2003) SST (a, c). Black thick lines stand for the ice sheet contours of both periods.

been documented by Simmonds & Wu (1993) in the present-day Southern Hemisphere who show that cyclones become weaker over the sea ice area. In this region, evaporation almost ceases (Figure 4.5c) which decreases precipitation by approximately 40% to 60% over the North Atlantic. Since the CLIMAP sea ice reaches further south, evaporation and precipitation are concentrated at the sea ice edge (Figure 4.5c and e). Storm track activity is intensified and shifted further to East (Figure 4.6a and b) compared to $P03_{140}$. This has been shown by Kageyama *et al.* (1999) in which the LGM extentive sea ice (compared to present-day sea ice cover) pulls the storm track eastward. As a result of the regional cooling caused by the CLIMAP sea ice cover (Figure 4.5c), precipitation is decreased by about 50% over Central Eurasia. However, the sea ice increase leads to a larger snow mass in Siberia in $CLIM_{140}$ (Figure 4.5f).

Surface mass balance (SMB) is more positive along the southern ice sheet margins of the Eurasian ice sheet (300 mm·yr^{-1}) when CLIMAP SST are prescribed (Figure 4.7b) due to an increase in precipitation by about 30% to 70% over these areas (Figure 4.5e). On the contrary, the Atlantic margin exhibits negative SMB values (≈-200 mm·yr^{-1}) due to a reduction in precipitation over the Arctic Ocean also affecting this margin (Figure 4.5e.). The mean annual SMB is positive in both the $CLIM_{140}$ and the $P03_{140}$ simulations due to a small ablation and evaporation (Table 4.4). The difference between $CLIM_{140}$ (239 mm·yr^{-1}) and $P03_{140}$ (225 mm·yr^{-1}) is statistically significant at 5% but not very strong.

The Last Glacial Maximum: comparing $CLIM_{21}$ and $P03_{21}$

During the LGM, the climatic impact caused by the CLIMAP sea ice cover shows a pattern similar to the Late Saalian. Compared to $P03_{21}$, $CLIM_{21}$

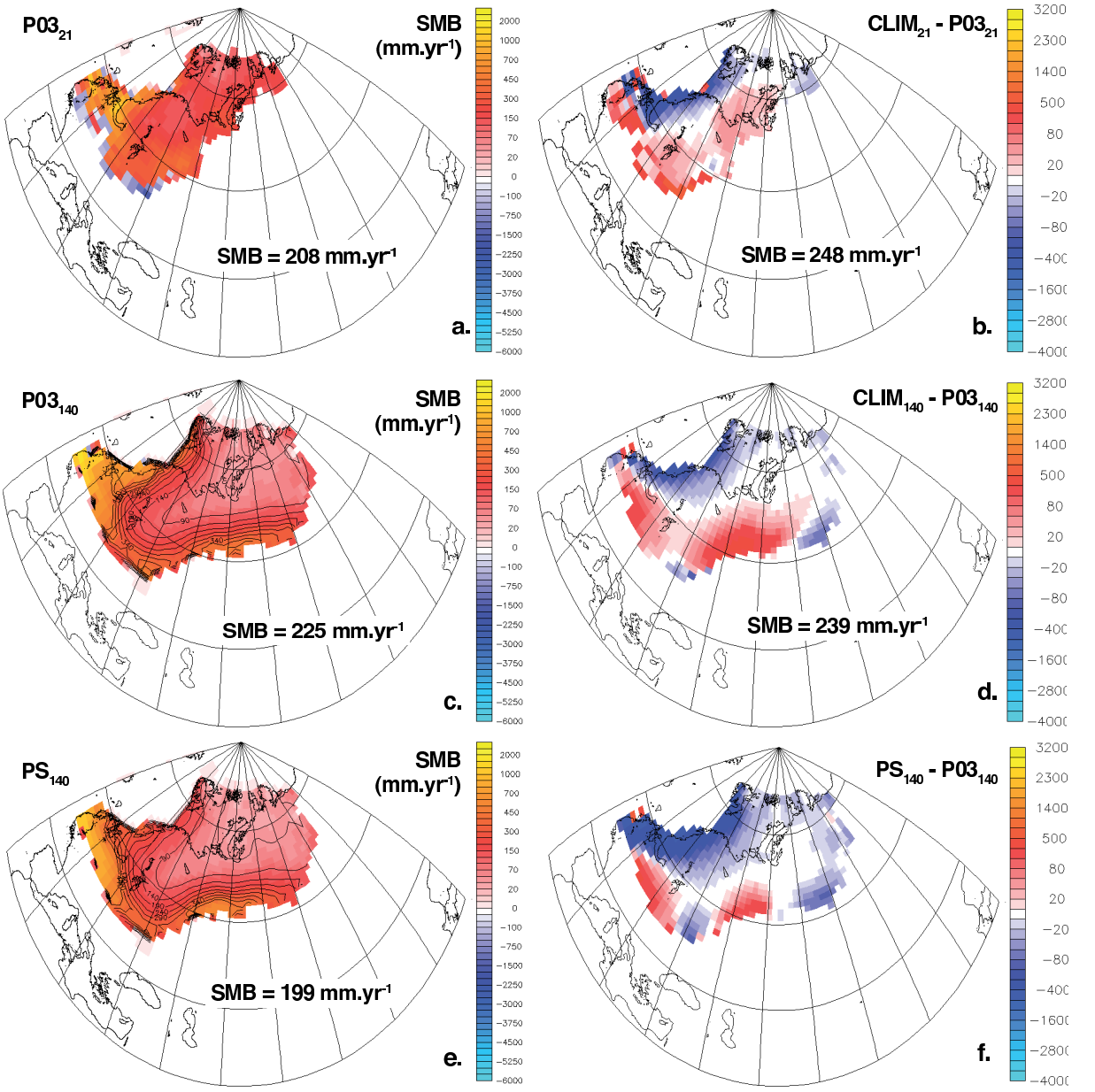

Figure 4.7: Surface mass balance (SMB) of the Eurasian ice sheet reference simulations P03$_{21}$ (a), P03$_{140}$ (c) and SMB anomalies between the reference simulations and CLIM$_{21}$ (b) and CLIM$_{140}$ (d) ; e same as for c. but for simulation PS$_{140}$ (with simulated SST) and f. corresponds SMB anomalies between PS$_{140}$ and the reference Late Saalian simulation P03$_{140}$. Values indicated on the figures correspond to the mean annual surface mass balance of each simulations summarized in Table 4.4.

presents a negative anomaly of about 5°C to 25°C over the North Atlantic. However this negative temperature anomaly spreads over Eurasia and causes a cooling of ≈5°C (Figure 4.8c). This in turn influences the 500 hPa geopotential height which exhibits a negative anomaly of about 60 meters over this region. As explained in the previous paragraph, storm tracks are generally stronger where the meridional gradients of surface temperatures are the strongest. Similarly to CLIM$_{140}$, in CLIM$_{21}$, storm tracks are consequently strengthened at the sea ice edge (≈45°N) which tends to reduce the Icelandic depression located northward and causes an increase in SLP by about 8 mbars (Figure 4.8b). Large sea ice cover almost stops evaporation and consequently decreases precipitation by ≈60% over the North Atlantic (Figure 4.8c and e). As for CLIM$_{140}$, evaporation and precipitation are increased at the sea ice edge in CLIM$_{21}$ and storm track activity is intensified and shifted southward (Figure 4.6c and d.). Contrary to the Late Saalian, the LGM Siberian snow height is almost similar in both CLIM$_{21}$ and P03$_{21}$ simula-

tions (Figure 4.8f).

The higher SMB values along the southern margin in $CLIM_{21}$ results from the fact that cooler temperatures are spreading over Eurasia especially over Europe (Figure 4.7b.). As for the Late Saalian, the Atlantic margins show more negative SMB in $CLIM_{21}$ than in $P03_{21}$ due to the CLIMAP sea ice cooling effect. However, this negative SMB anomaly extends farther into the ice sheet during the LGM. This contributes to strongly reduce evaporation from the ice sheet. The LGM mean SMB ($kg.m^{-2}.yr^{-1}$) in $CLIM_{21}$ (248 $kg.m^{-2}.yr^{-1}$) is significantly higher than that of $P03_{21}$ (208 $kg.m^{-2}.yr^{-1}$, Table 4.4).

The Late Saalian surface ocean

In the previous section, we have shown that the Late Saalian Eurasian ice sheet is less sensitive to changes in SST than its LGM counterpart. The much higher Late Saalian ice sheet confines most of the circulation anomalies caused by the variation in the sea ice extent into the North Atlantic and the Arctic Ocean while they spread over Eurasia during the LGM. Since the simulations with the two ice topographies react differently to SST forcing, there clearly is a need to simulate the Late Saalian surface ocean in equilibrium with the associated ice sheet topography. In the following section, we present the results from the numerical experiment carried out using an AGCM coupled to a mixed layer ocean module. The experiment setup is previously described in the Methods.

Simulated sea surface conditions

The simulated Late Saalian SST (referred as PS140) are shown in Figure 4.3. The difference between P03 and PS140 presents a pronounced asymmetric temperature distribution between the Northern and the Southern hemisphere during both winter (DJF) and summer (JJA) (Figure 4.3g and h). The equilibrium state of PS140 is globally warmer than P03 by about 4°C in the Southern hemisphere and cooler by about 4°C in the Northern Hemisphere. A zonal band of 16°C anomaly appears in the North Atlantic and in the North Pacific at 40°N. This anomaly is a consequence of the different positions of the sea ice edges in PS140 and P03. In P03, the North Atlantic is open during both winter and summer while this is not the case in PS140, where North Atlantic remains covered during both seasons (Figure 4.3). In PS140, the sea ice limit reaches the south of Spain (≈40°N), which is the southernmost sea ice edge that we use in this study since CLIMAP sea ice cover stops in Brittany during winter and off Ireland during summer (Figure 4.3). During summer, the negative anomaly observed in the North Atlantic between PS140 and P03 spreads northward in the Norwegian Sea due to the open ocean conditions in P03 (Figure 4.3h) . This induces a cooling of about 4°C in this region. In the North Pacific, the cooling is caused by the development of sea ice cover South to the North of Japan for the Asian part and to the South of Canada for the American part in PS140. In P03, the Pacific sea ice extent is small and confined to the Bering Sea. Due to the similar sea ice extent in winter and in summer, seasonality is strongly reduced in PS140 compared to P03.

The simulated Late Saalian surface ocean PS140 shows not a good agreement with the mean annual marine sediment data reported in Table 4.1. Comparison is displayed on Figure 4.9. In the tropical and equatorial Atlantic, PS140 matches Late Saalian data well. In the Southern Atlantic and in Southern Tasmania, data suggest that our reconstruction overestimates temperatures. In this study, the North Atlantic and Pacific constitute key areas for the impacts generated on the Late Saalian ice sheets. In these regions, our reconstruction is colder than data and sea ice edge reaches the North of Spain in the Atlantic and South Canada in the Pacific. However, the Late Saalian geological marine evidence indicates that the polar front was shifted much more southward than during the LGM (Crowley, 1981). On the contrary, in the Northern Pacific, no references can confirm the large sea ice extent simulated in our reconstruction. This suggests that PLASIM underestimates sea surface temperature in this region and that slightly more open conditions over the Northern Hemisphere are required to match the reconstruction.

Impact of the simulated SST on the Late Saalian climate

The simulated SST described in the previous section have been used to generate a new Late Saalian snap-shot simulation using the LMDZ4 model. The aim of this simulation is to test the impact of these new oceanic boundary condi-

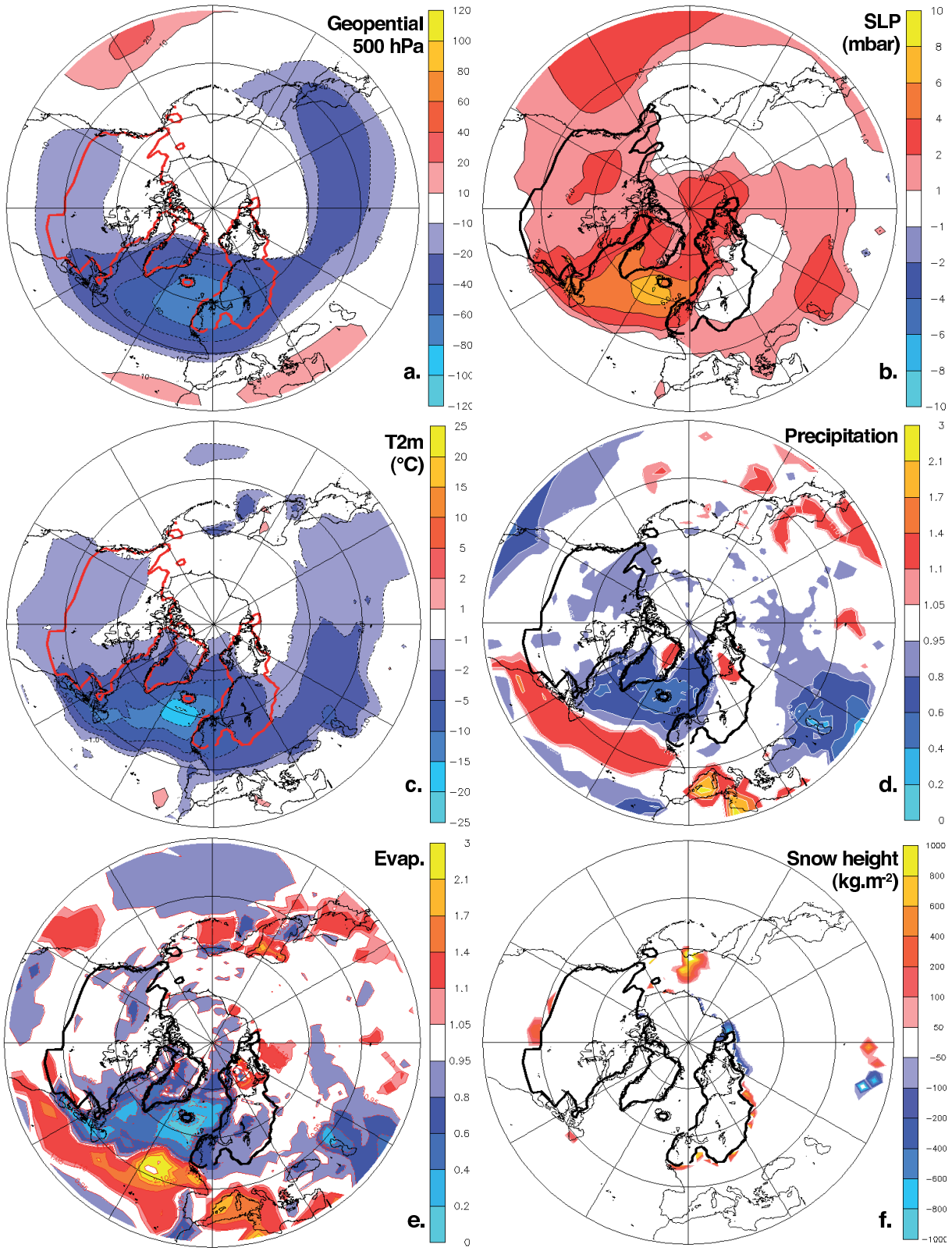

Figure 4.8: Same as for Figure 4.5 but for the LGM period: $CLIM_{21}$ - $P03_{21}$ (see Table 4.3)

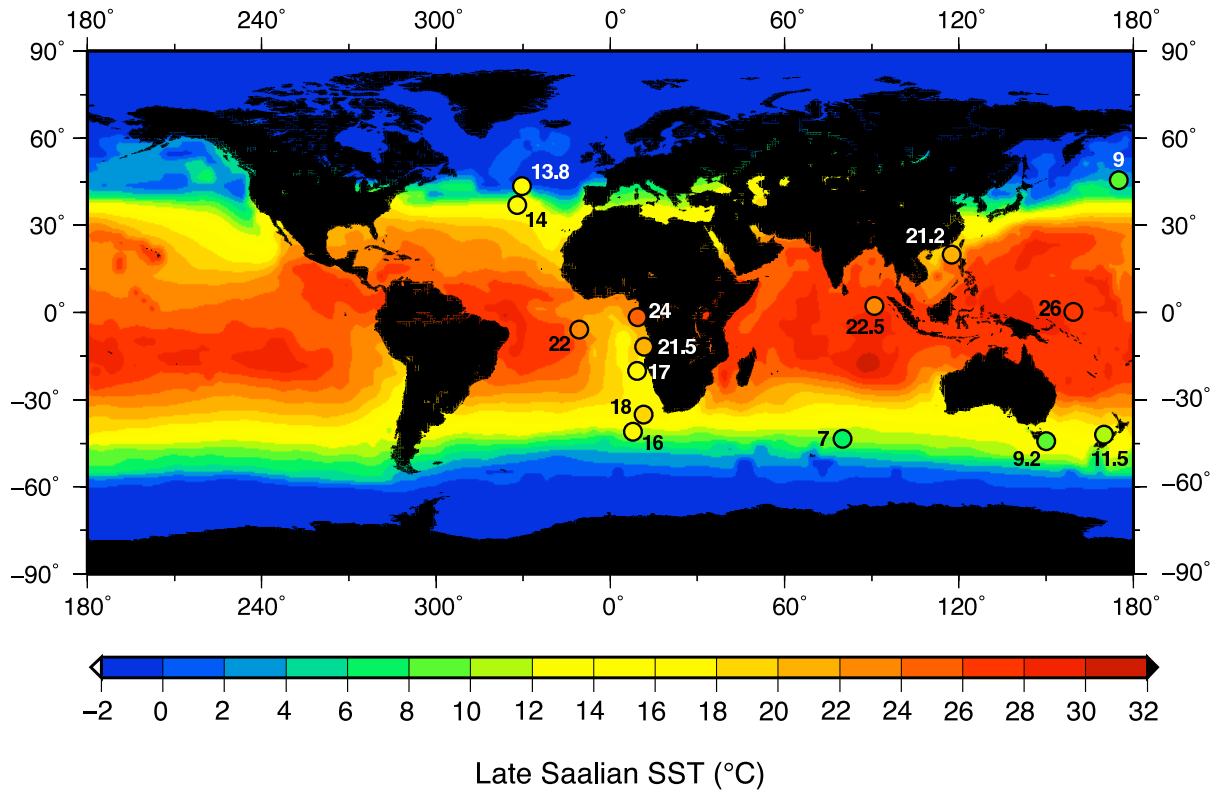

Figure 4.9: Comparison between computed mean annual sea surface temperatures PS140 (°C) and 140 ka marine sediment cores data (dots and associated numbers) summarised in Table 4.3.

tions on the Eurasian climate and more precisely on the surface mass balance of the Eurasian ice sheet.

The cooling of the ocean surface causes an annual drop in air temperature of about ≈10°C over the entire Northern Hemisphere. This large decrease in temperature induces global more anticyclonic conditions over the Northern Hemisphere during both seasons (Figure 4.10b. and 4.11b.).

During winter (DJF, December - January - February), in both the North Atlantic and the North Pacific, the large southward sea ice extent (Figure 4.4) causes a negative temperature anomaly of ≈20°C to 45°C (Figure 4.10c.). This increases sea level pressure (SLP) by ≈20 mbars over the North Atlantic and the North Pacific where sea ice is more extended. This anticyclonic activity, combined to a larer cooling and to a larger sea-ice extent, contributes to the large reduction (or cancellation) of precipitation and evaporation over these area by more than 90% (Figure 4.10d and f). The large sea ice extent also globally affects the 500 hPa geopotential over the Northern hemisphere (≈-120 m anomaly) and large negative anomalies of ≈200 meters are located over the North Atlantic and the Bering Sea. Those circulation changes intensify the stormtrack activity whose North Atlantic center is shifted eastward compared to $CLIM_{140}$ and $P03_{140}$ (Figure 4.10e). During summer (JJA, June - July - August), the cooling is less important than during winter and temperatures over the entire hemisphere are homogeneous (Figure 4.11c.). SLP anomalies still indicate more anticyclonic conditions mainly over the North Pacific due to the presence of sea ice in $FULL_{140}$. As for winter, geopotential is affected by the sea ice cover in the North Atlantic and exhibits a stronger negative anomaly (Figure 4.11a.). Its amplitude is nevertheless reduced compared to that occuring during winter because summer temperatures are more than 30°C warmer than winter temperature in this area.

Over Siberia, winter temperature is decreased by about 5°C which leads to a decrease in precipitation of about 20 to 40% and mostly cancels evaporation over the entire Siberia. This results from the presence of a permanent snow cover in $FULL_{140}$ which is more extended than in $P03_{140}$ (Figure 4.12a and b). In $FULL_{140}$, moisture fluxes over Siberia normally coming from the North Pacific are reduced compared to those

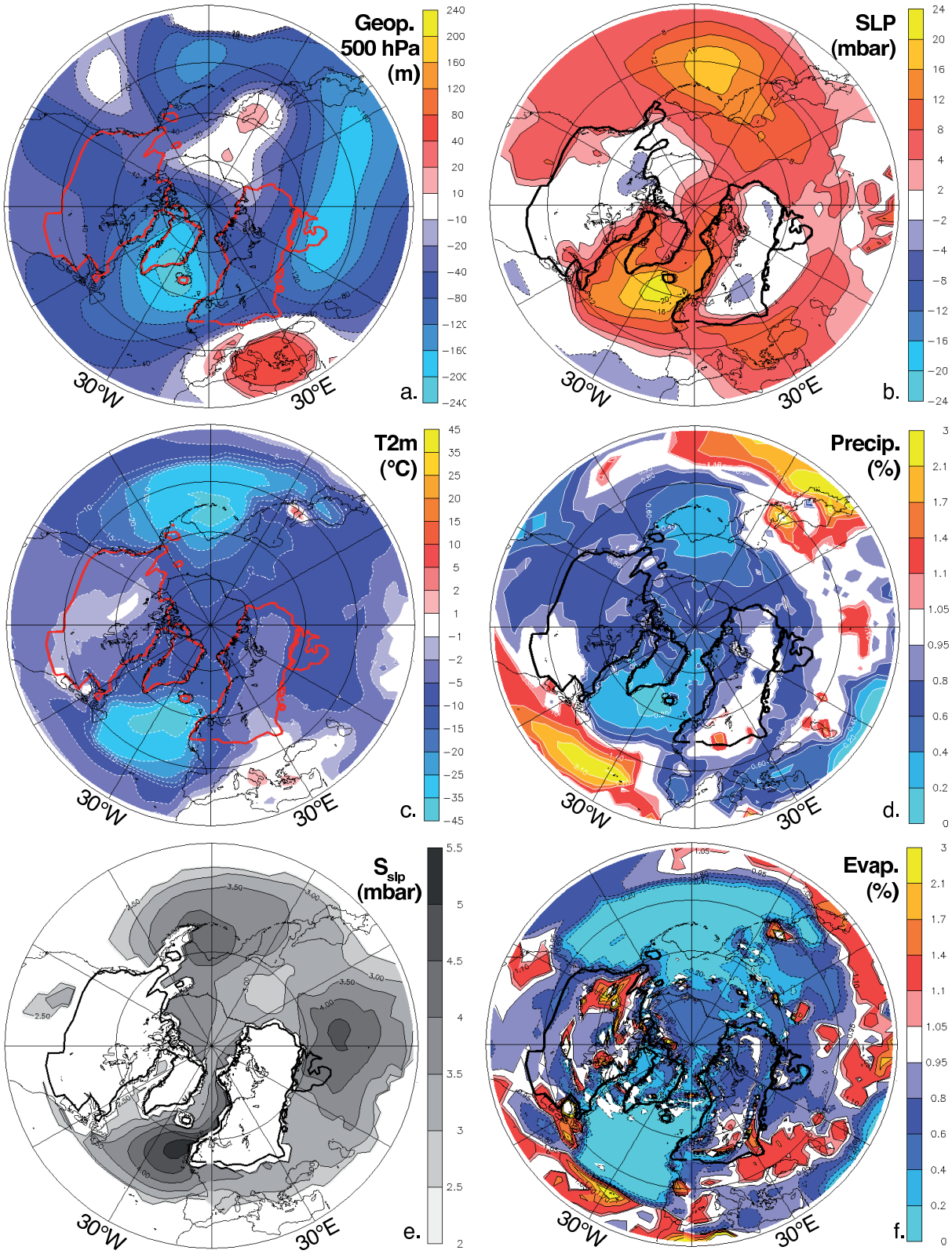

Figure 4.10: Late Saalian winter climate anomalies between PS140 (simulation PS_{140}) and P03 (simulation $P03_{140}$) over the Northern hemisphere (30°-90°N). Differences are calculated as (PS_{140} - $P03_{140}$) for: a. geopotential height at 500 hPa (m), b. sea-level pressure (SLP in mbar), c. air temperature at 2 meters (t2m in °C); d. and f. precipitation and evaporation anomalies expressed as the ratio ($CLIM_{140}/P03_{140}$) and f. winter storm-track activity (as for Figure 4.6). Refer to Table 4.3) for details about the settings of the simulations.

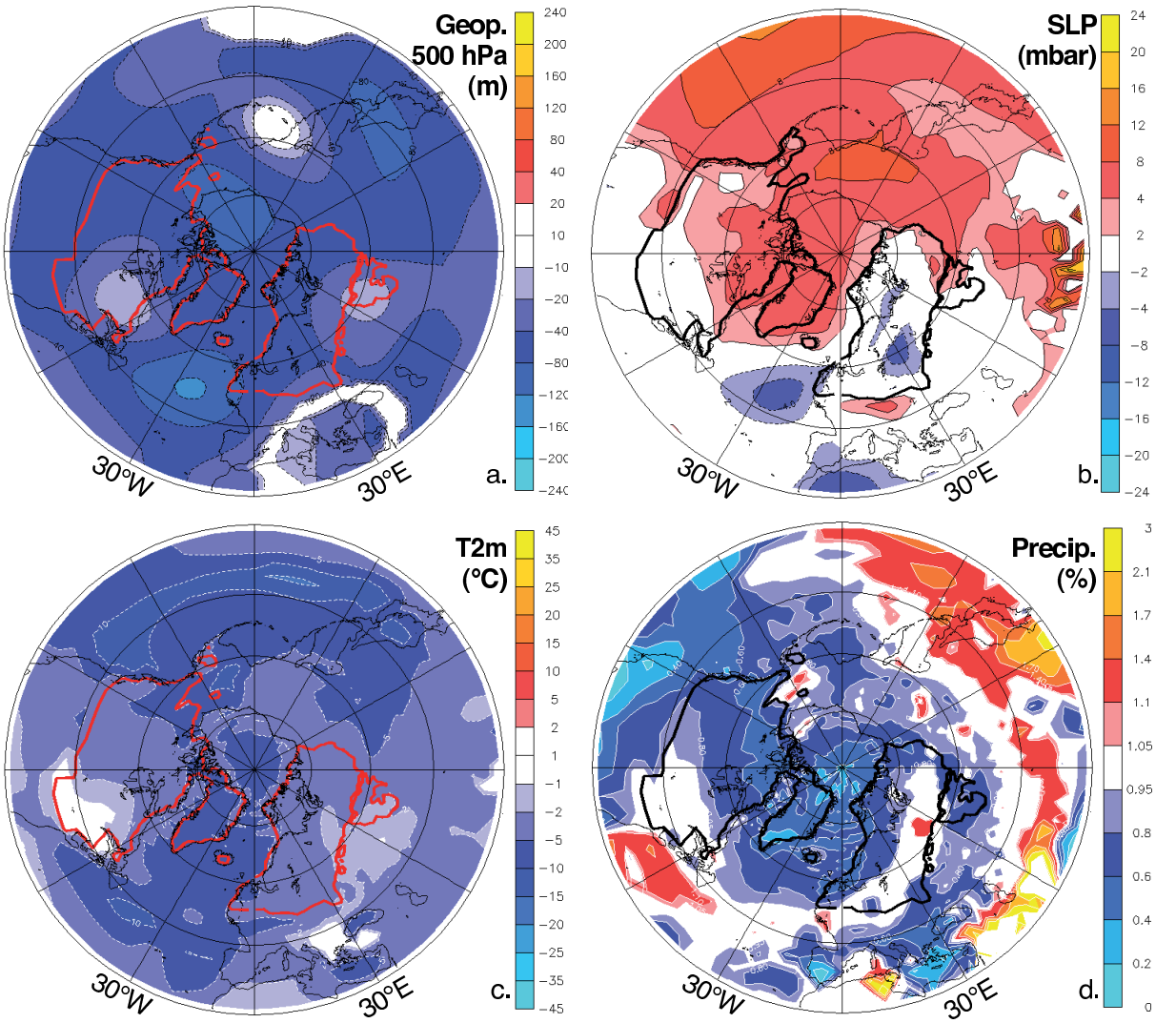

Figure 4.11: Same as for Figure 4.10 (a-d), but for summer.

of $P03_{140}$ (Figure 4.12c and d) due the larger sea ice cover that develops in the North Pacific in PS140 (Figure 4.4). Therefore, the larger snow cover in $FULL_{140}$ cannot result from larger moisture fluxes but from the global cooling generated by the simulated SST which reduces the melting of the snow during spring and summer months.

Because of the global cooling, especially during summer, there is no more ablation over the ice sheet (Figure 4.7e.). The surface mass balance (SMB) is more positive over the Western part of the ice sheet since the global cooling reduces the ablation caused by the moisture fluxes coming from the East Atlantic (Figure 4.7f.). On the contrary, due to the strong negative temperature dramatically reducing precipitation over Siberia, the Eastern part of the ice exhibits a far more negative SMB compared to $P03_{140}$. Similarly, the Atlantic margin exhibits a more negative SMB value because moisture fluxes are strongly reduced and cannot provide this area with precipitation as in $P03_{140}$ (Figure 4.12e and f). Mean annual surface mass balance is about 199 $mm{\cdot}yr^{-1}$ (Table 4.4). Compared to $P03_{140}$, evaporation has been reduced by 14 $mm{\cdot}yr^{-1}$ and snow fall by 52 $mm{\cdot}yr^{-1}$. In the case of $FULL_{140}$, the lack of accumulation prevails on the absence of ablation and decreases SMB.

Discussion

The few marine sediment cores where SST reconstructions are available both for the LGM and for the Late Saalian periods suggest quite similar temperatures (Table4.1). However, these few estimates from the vast World Ocean do not rule out that SST nevertheless could play a critical role in explaining why the Late Saalian and the LGM Eurasian ice sheets differed largely in both

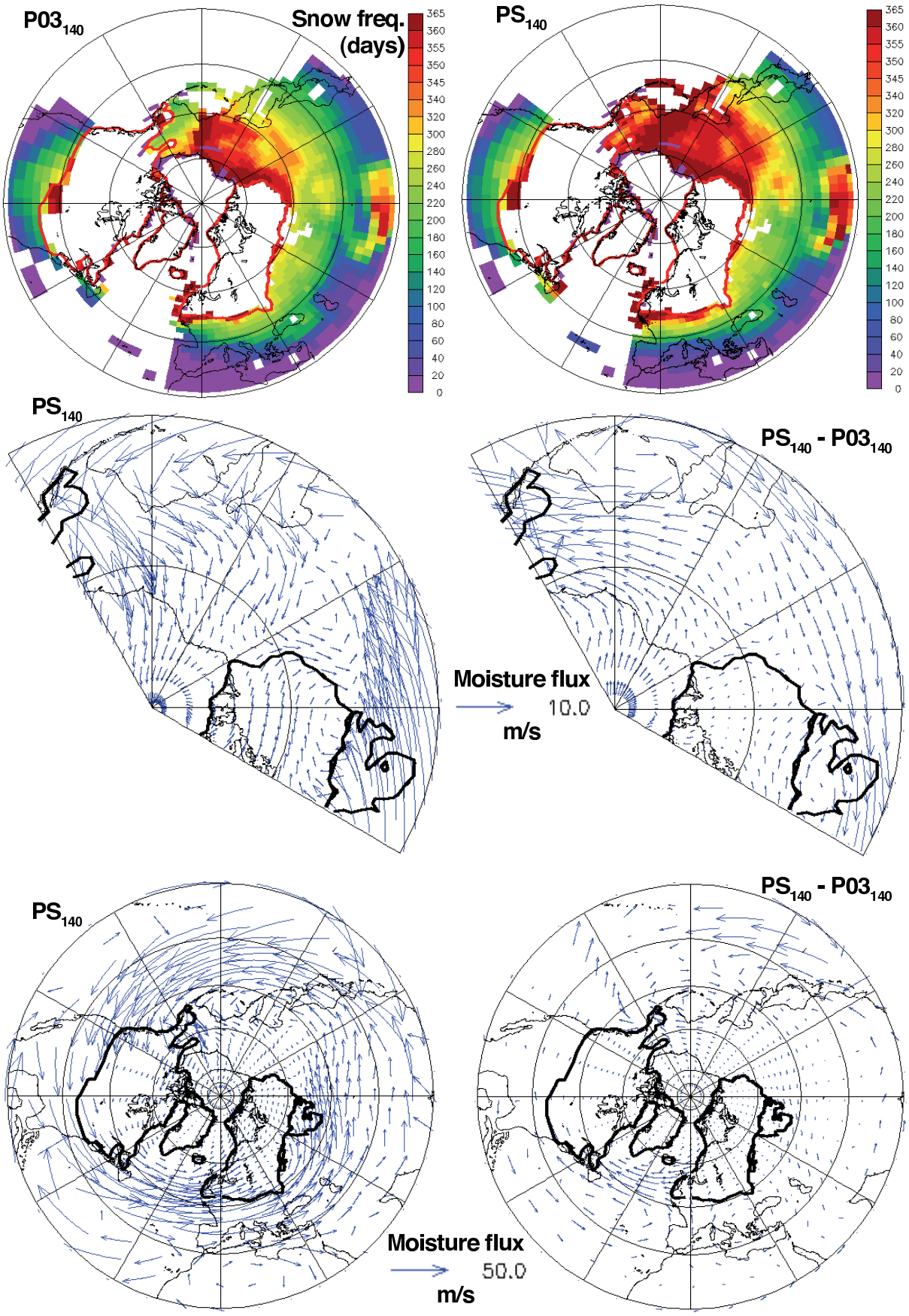

Figure 4.12: Late Saalian snow frequency (days) of simulations $P03_{140}$ and PS_{140} (top frames); Moisture fluxes over Siberia for PS_{140} and flux differences between PS_{140} and $P03_{140}$ (middle frames); bottom frames same as for middle frames but over the Northern hemisphere.

volume and extent. The large size of the Saalian ice sheet initially motivated this work and we specifically address whether the global sea surface conditions may have been different during its existence compared to during the LGM and if the climate forcing from SST could have been different during these two glacial periods. Ultimately we address the impacts from SST on the surface mass balance of the Eurasian ice sheet.

We have thus performed three sets of experiments:

- Prescribing LGM Paul & Schaefer-Neth (2003) SST for both glacial periods.
- Prescribing LGM CLIMAP (1984) SST for both glacial periods.
- Simulating the 140 ka (peak of the Late Saalian) SST using a simplified AGCM coupled to a mixed-layer ocean model.

CLIMAP versus Paul & Schaefer-Neth (2003)

Changing sea surface conditions towards colder SST causes large negative geopotential anomalies during both Late Saalian and LGM over the North Atlantic. This is mainly due to an increased sea ice extent. Compared to P03, the CLIMAP SST generates a Northern Hemisphere cooling leading to reduced ablation along the southern margins of the Eurasian ice sheet and thus to a more positive SMB. However, the amplitude and the intensity of the climate anomalies over the North Atlantic and Eurasia are strongly dependent on the Eurasian ice sheet topography. In all the Late Saalian simulations, its high orography blocks climatic impact from changing SST and sea ice over the North Atlantic and the Arctic Ocean from spreading over Eurasia. This strengthens the contrast between ocean and continent, and also intensifies the North Atlantic storm tracks during the Late Saalian time period (Figure 4.6). During the LGM, the lower ice topography allows for an open circulation over Eurasia and over the ice sheet itself.

The SMB values between the two simulations of the LGM simulations present larger differences than for the Late Saalian simulations: 40 $mm{\cdot}yr^{-1}$ and 14 $mm{\cdot}yr^{-1}$ in difference between the mean annual SMB respectively (Table 4.4). For both time periods, the Atlantic and the Arctic margins are very sensitive to any changes in SST or sea ice extent (Figure 4.7). However since the LGM ice sheet is lower and less extended over Eurasia than the Late Saalian, its SMB is more sensitive to the climatic conditions along the North Atlantic margins. On the contrary, since the Late Saalian ice sheet is higher and larger, although responding in a similar way to the LGM ice sheet along the oceanic margins, its SMB is less sensitive because the higher elevation and the larger extent compensate for temperature fluctuations and consequently reduce the effect on ablation and sublimation (Table 4.4).

The differences between the mean annual SMB values are statistically significant for both glacial periods as shown by the Student T-test at 5% (Table 4.4). Note that for the Late Saalian simulations, total precipitation and snow fall over the ice sheet are of the same order and differences are mainly caused by ablation and evaporation variations. This is not the case for the LGM simulations which show significant differences between all the components. The CLIMAP SST lead to a more positive SMB for both glacial periods. Consequently, we can conclude that seasonally open North Atlantic induces more heat advection toward the continent and this directly affects the ablation of the ice sheet. Similarly to Dong & Valdes (1998), we show that smaller sea ice cover or cooler SST do not impact significantly on precipitation but only on ablation and evaporation when using the CLIMAP and Paul & Schaefer-Neth (2003) LGM SST, regardless of the ice topography (Table 4.4, solid stars).

The Late Saalian surface ocean

Simulated oceanic conditions

We show that the Late Saalian simulated SST are colder than the temperatures derived from the marine records, particularly in the North Atlantic. This suggests that more open water conditions may have prevailed in the Northern Hemisphere than simulated in this work. The experiment using ocean heat fluxes calculated with the prescribed CLIMAP SST to compute the Late Saalian surface ocean leads to similar sea ice extent and sea surface temperature as when using Paul & Schaefer-Neth (2003)-derived ocean heat fluxes. However, is it possible to develop such a large and southward extending sea ice cover in both North Atlantic and North Pacific as our simulated Late Saalian SST suggest (Figure 4.4)?

The Late Saalian orbital configuration is characterised by a large eccentricity, a perihelion occurring at early December (referring the vernal equinox to March 21st) implying summers near the aphelion, and an intermediate obliquity of 23.42° (41 kyrs cycle). This typical glacial orbital configuration causes relatively long but cold summers and cooler springs reducing the melting of snow accumulated during winter. The effect of precession is strengthened by the large eccentricity. During the LGM, on the contrary, the eccentricity is smaller compared to the Late Saalian which leads to a less dominant precession effect. The eccentricity is smaller as well as the obliquity (22.95°, close to minimum in the 41 kyrs cycle) and perihelion occurs in mid January. Consequently, the effect of precession during the LGM is reduced compared to the Late Saalian. This leads to a reduction in the incoming solar radiation at the top of the atmosphere in the [30° - 70°] latitudes band of ≈20 W.m^{-2} during the Late Saalian spring and summer compared to the LGM and to an increase of ≈20 W.m^{-2} during fall.

Several studies have investigated the impact of precession and obliquity on the Arctic climate using coupled atmosphere-ocean GCMs. Khodri *et al.* (2005) and Jackson & Broccoli (2003) show that typical glacial orbital configurations (perihelion in boreal winter) contribute to extend the sea ice cover southward, mainly due to a large reduction of the sea ice melting during spring and a less pronounced seasonality, and contribute to the migration of the polar front southward. This corresponds to the SST pattern simulated in this study and may explain why our sea ice extends southward compared to its LGM position.

Differences between Paul & Schaefer-Neth (2003) and the simulated Late Saalian SST result in a pronounced inter-hemispheric temperature asymmetry (Figure 4.3g and h). In our reconstruction, the Northern Hemisphere is colder by about 2°C to 6°C relatively to Paul & Schaefer-Neth (2003) while the Southern Hemisphere is warmer by about 2°C to 6°C. At a first glance it seems like this asymmetry could be associated with a "seesaw" effect (Broecker, 1998; Stocker, 1998; Ganopolski & Rahmstorf, 2001; Clark *et al.*, 2002) resulting from thermohaline variations in the Atlantic Ocean in turn causing heat release from one of the two hemispheres out of phase with the other. However, Planet Simulator does not simulate deep circulation and consequently, this inter-hemispheric asymmetry cannot result from such a "seesaw" effect. Since PLASIM does not simulate deep circulation, the model is not able to re-equilibrate excess or lack of oceanic heat caused by the asymmetric astronomical forcings. In other words, the observed asymmetry in our results cannot be caused by deep ocean circulation changes. Indeed, during the Late Saalian, the large eccentricity enhances the precession effect, increasing the asymmetry between the two hemispheres (Raymo *et al.*, 2006). This results in cooler SST in the Northern Hemisphere and warmer in the Southern Hemisphere than during the LGM (Figure 4.3e and f).

However, it should be noted when interpreting our results that the simulation experiments also account for all the regional factors feedbacks. These include the fact that the Late Saalian Eurasian ice sheet was significantly larger than the LGM one which contributes to a regional cooling over Eurasia in our simulations. In addition, the prescribed vegetation is mainly comprised of tundra and steppe, enhancing the albedo effect due to a larger snow accumulation (Colleoni *et al.*, 2009d). The dammed lakes in front of the southern Late Saalian ice sheet margin cool the summer climate and consequently reduce the ablation along the ice sheet's margins (Krinner *et al.*, 2004; Colleoni *et al.*, 2009a). Finally, the dust deposition on snow covered ground is less during the Late Saalian than during the LGM and dust deposition on snow (Krinner *et al.*, 2006; Colleoni *et al.*, 2009a). These environmental factors contribute to cool the regional climate in addition to the effect of cooler SST.

Related climate anomalies

To better understand the SST impact on the variability of different climate components, we have briefly looked at the role of the Arctic Oscillation (AO) in the Northern Hemisphere climate. The AO has been defined as the first empirical orthogonal function (EOF) of the winter geopotential at 500 hPa (December-March, DJFM) from 20°-90°N over the 20 model years (Thompson & Wallace, 1998). The first EOF shows that the AO is the dominant pattern of variations of geopotential at 500 hPa in the Northern Hemisphere with 60% of variance for the Late Saalian (140k, simulation FULL$_{140}$), 49% of variance for the

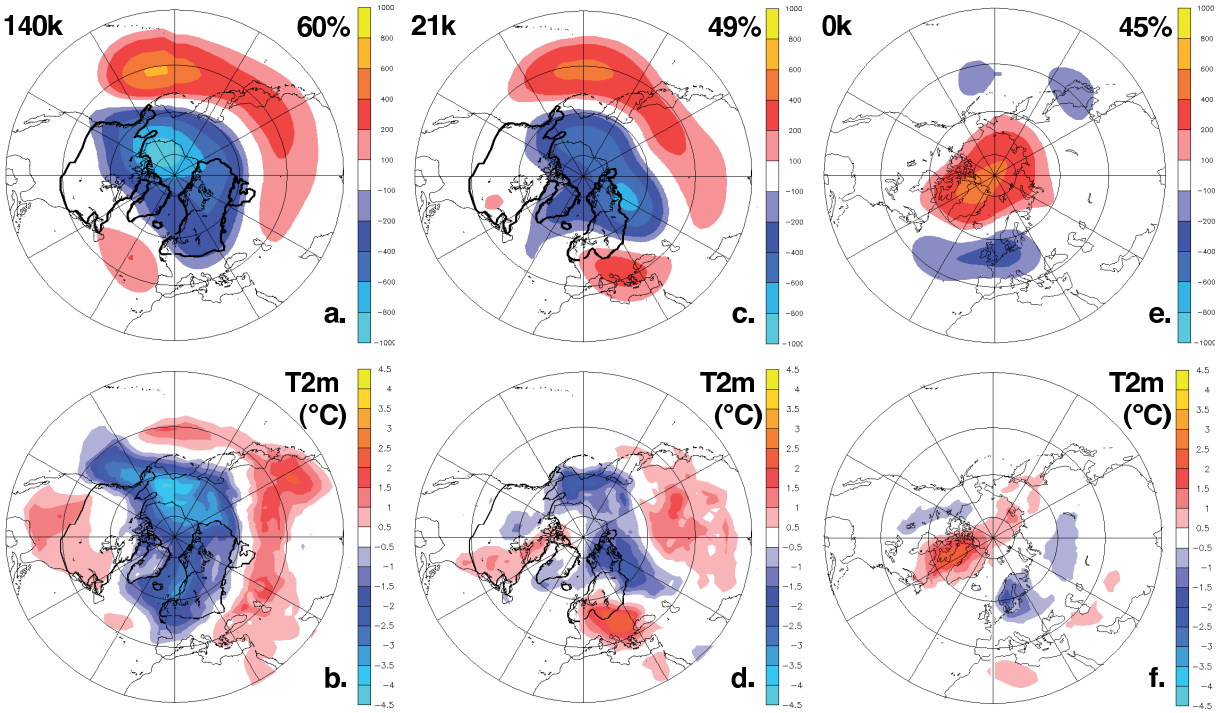

Figure 4.13: Arctic Oscillation (AO) based on the method of Thompson & Wallace (1998). a, c and e corresponds to the first empirical orthogonal function calculated over the leading mode (December-March) of the geopotential height 500 mbars for the Late Saalian PS_{140} simulation (140k), the LGM $P03_{21}$ simulation (21k) and present-day (0k). Percentages above figures indicate the contribution of the AO to the nonseasonal variance of the Northern Hemisphere climate for the three time periods. b, d, and f corresponds to the regression of winter air temperatures (T2m, °C) on the leading mode of the geopotential height. Other climate variables present weak regression and are not displayed.

LGM (21k, simulation $P03_{21}$) and 45% of variance for present-day (Figure 4.13a, c and e). The present-day control run has been performed using the LMDZ4, with boundary conditions adjusted to modern vegetation, dust, SST, greenhouse gases and orbital forcings (more details in Colleoni *et al.* (2009a)). The AO presents two main centers of opposite sign during the Late Saalian and the LGM periods that are located over the North Pacific and over the Arctic Ocean (Figure 4.13a and c).

Surface air temperature has been regressed on the geopotential leading principal component and are displayed in Figure 4.13b, d and f. Temperatures are in phase with the Arctic Oscillation for all time periods and over Siberia, the associated temperature anomaly is larger during the Late Saalian, by -4.5°C (Figure 4.13b), than during the LGM, by -1°C to -2°C (Figure 4.13d). Correlation over Siberia between temperature and the AO is stronger during the Late Saalian (r^2= 0.75) than during the LGM (0.4) and present-day (0.1). This shows that during the Late Saalian period, temperature over Siberia is particularly sensitive to the AO while this is less the case in the LGM and present-day simulations.

If we compare the climatic implications from the large PS140 sea ice cover with the implications from the smaller sea ice cover resulting from CLIMAP SST during the Late Saalian, the role of the North Pacific is particularly important. Indeed, the PS140 sea ice cover is extensive over this region while this is not the case in CLIMAP. On the contrary, the sea ice extents are broadly similar between the two datasets in the North Atlantic (Figure 4.4). In $FULL_{140}$ the simulated surface ocean causes a global cooling of 10°C of the entire Northern hemisphere. This is probably due to the presence of sea ice in the North Pacific extending further to South from the Bering Sea in PS140. However, if the ocean is open (as it is the case in CLIMAP and Paul & Schaefer-Neth (2003) North Pacific), the LMDZ4 cannot simulate temperature and this consequently induces a biased inter-annual variability in this region.

There are some caveats that should be considered when evaluating our study on the sensitivity of the Late Saalian Eurasian ice sheet to

SST. First, we test the impacts from two SST reconstructions that were published prior to the undertaking *Multiproxy approach for the Reconstruction of the Global Ocean surface* MARGO (Kucera *et al.*, 2005a). Thus, the evaluated SST datasets may hold biases compared to the more recent MARGO reconstructions leading to a different regional climate interpretation (Kageyama *et al.*, 1999, 2006). However, Waelbroeck *et al.* (2009) suggest that the Paul & Schaefer-Neth (2003) LGM SST reconstruction is the best available LGM reconstruction to date for the LGM North Atlantic. The second caveat concerns the simulated Late Saalian surface ocean. This has been carried out using a simplified AGCM coupled to mixed-layer ocean module. In the simulation, Crowley (1995) LGM vegetation map has been prescribed and is kept constant during the entire experiment. As shown in Colleoni *et al.* (2009d), vegetation feedbacks for the Late Saalian dramatically influence the regional climate more than during the LGM. The use of a coupled Land-Atmosphere-Ocean general circulation model should lead to a different Late Saalian surface ocean and this may in fact influence the maximum sea ice extent.

In our experiments, we assume an eustatic sea level of about -110 m below present-day sea level. The Laurentide ice sheet contributes ≈74 m, Antarctica contributes ≈20 m and our Late Saalian Eurasian ice sheet contributes ≈60 m ESL (comparable to that of Lambeck *et al.* (2006)). This leads to an ice volume in excess relatively to the eustatic sea-level. Assuming that the Antarctic ice volume did not vary significantly, as during the LGM, the Laurentide should be reduced to equilibrate the eustatic sea level. This may have some consequences on the atmospheric circulation (Kageyama & Valdes, 2000) and on the distribution of the geopotential anomalies even over Eurasia.

Finally, a word of caution regarding the Late Saalian Eurasian ice sheet reconstruction used in our simulations. We have shown in this study that the huge Eurasian ice sheet extending far into Eastern Siberia with a high surface elevation, significantly modifies circulation, cools temperatures and reduces precipitation. This Eurasian Late Saalian ice configuration (Svendsen *et al.*, 2004) represents the maximum MIS 6 geographic extent and some limits may not have been reached at the same time during MIS 6. Nevertheless, geological evidence suggests that the Late Saalian ice sheet reached a much larger extent than the LGM (Svendsen *et al.*, 2004) and also marine records from the central Arctic Ocean suggest a much more extensive glaciation during MIS 6 than during MIS 2 (Polyak *et al.*, 2001; Jakobsson *et al.*, 2005, 2008).

Conclusions

In this work, we test the sensitivity of the Late Saalian Eurasian ice sheet to different prescribed LGM sea surface conditions. We show that the choice of the prescribed SST can impact significantly and differently on the surface mass balance depending on the ice volume and extent. The Late Saalian Eurasian ice sheet is less sensitive to oceanic changes since its huge topography compensates for regional climatic changes more than the LGM ice sheet.

An attempt of Late Saalian reconstruction has been carried out using a mixed-layer ocean model. The Late Saalian reconstruction is mostly in agreement with the marine core sediment data except in the North Atlantic and Pacific where sea ice cover extends too much southward. Compared to the LGM SST reconstructions, the simulated SST present a large inter-hemispheric asymmetry caused by the Late Saalian orbital forcings. This leads to cooler (warmer) SST in the Northern (Southern) Hemisphere. During the Late Saalian, the large eccentricity enhances the effect of precession over the high latitudes contrary to the LGM and reduces the amount of incoming solar radiations over the high latitudes at top of atmosphere by 20 $W.m^{-2}$ during both spring and summer. This results in a Northern Hemisphere atmospheric cooling enhanced by the continental feedbacks (ice sheet topography and the reduction in snow melting). The large simulated sea ice extent, reducing the moisture fluxes, combined to the Northern Hemisphere cooling causes a reduction of the surface mass balance entirely due to the reduction of accumulation.

A word of caution should be addressed about the choice of boundary conditions and about the fact that the LGM climate response cannot be directly applied to other ice ages, especially when ice distribution over continents is very different. One perspective is to compute ocean circulation in equilibrium with climate using a Ocean-Atmosphere general circulation model to simu-

late the Late Saalian deep and surface circulation, to investigate the effect of such a large ice sheet on thermohaline circulation. One other perspective is to model surface ocean conditions for the entire Late Saalian periods (160 - 140 ka) which includes one important insolation peak toward 150 ka to understand the evolution of climate prior to the last glacial maximum of the Late Saalian.

Acknowledgements

We would like to thanks Antje Voelker for her contributions and Catherine Ritz and Thomas Crowley for their useful discussions. The authors acknowledge support by the Agence Nationale de la Recherche (project IDEGLACE), the Région Rhône Alpes (programme Explora'Doc) and the Ministère des Affaires Étrangères Français and The Bert Bolin Centre for Climate Research (Stockholm University) for their support. The climate simulations were carried out at IDRIS/CNRS and on the Mirage scientific computing plateform in Grenoble (France).

References

Abe-Ouchi, A., Segawa, T., & Saito, F. 2007. Climatic conditions for modelling the Northern Hemisphere ice sheets throughout the ice age cycle. *Clim. Past*, **3**, 423–438.

Abreu, L., Shackleton, N.J., Schonfeld, J., Hall, M., & Chapman, M. 2003. Millennial-scale oceanic climate variability off the Western Iberian margin during the last two glacial periods. *Mar. Geol.*, **196**(1), 1–20.

Astakhov, V.I. 2004. Middle Pleistocene glaciations of the Russian North. *Quaternary Sci. Rev.*, **23**(11-13), 1285–1311.

Berger, A., & Loutre, M.F. 1991. Insolation values for the climate of the last 10 millions years. *Quaternary Sci. Rev.*, **10**(4), 297–317.

Broecker, W.S. 1998. Paleocean circulation during the last deglaciation: A bipolar seesaw? *Paleoceanography*, **13**(2), 119–121.

Calvo, E., Villanueva, J., Grimalt, J.O., Boelaert, A., & Labeyrie, L. 2001. New insights into the glacial latitudinal temperature gradients in the North Atlantic. Results from UK?37 sea surface temperatures and terrigenous inputs. *Earth Planet. Sc. Lett.*, **188**(3-4), 509–519.

Chapman, M.R., Shackleton, N.J., & Duplessy, J.C. 2000. Sea surface temperature variability during the last glacial-interglacial cycle: assessing the magnitude and pattern of climate change in the North Atlantic. *Palaeogeogr. Palaeocl.*, **157**(1), 1–25.

Chen, M.T., Chang, Y.P., Chang, C.C., Wang, L.W., Wang, C.H., & Yu, E.F. 2002. Late Quaternary sea-surface temperature variations in the southeast Atlantic: a planktic foraminifer faunal record of the past 600 000 yr (IMAGES II MD962085). *Mar. Geol.*, **180**(1-4), 163–181.

Chen, M.T., Shiau, L.J., Yu, P.S., Chiu, T.C., Chen, Y.G., & Wei, K.Y. 2003. 500 000-Year records of carbonate, organic carbon, and foraminiferal sea-surface temperature from the southeastern South China Sea (near Palawan Island). *Palaeogeogr. Palaeocl.*

Clark, P.U., Pisias, N.G., Stocker, T.F., & Weaver, A.J. 2002. The role of the thermohaline circulation in abrupt climate change. *Nature*, **415**, 863–869.

CLIMAP. 1984. The last interglacial ocean. *Quaternary Res.*, **21**, 123–224.

Colleoni, F., Krinner, G., & Jakobsson, M. 2009. Sensitivity of the Late Saalian (140 kyrs BP) and LGM (21 kyrs BP) Eurasian ice sheet surface mass balance to vegetation feedbacks. *Geophs. Res. Lett.*, **36**, L08704.

Colleoni, F., Krinner, G., Jakobsson, M., Peyaud, V., & Ritz, C. in press. Influence of dust deposition and proglacial lakes on the surface mass balance of the large Eurasian ice sheet during the peak Saalian (140 kyrs BP). *Global Planet. Change*.

Crowley, T.J. 1981. Temperature and circulation changes in the eastern North Atlantic during the last 150,000 years: Evidence from the planktonic foraminiferal record. *Mar. Micropaleontol.*, **6**(2), 97–129.

Crowley, T.J. 1995. Ice age terrestrial carbon changes revisited. *Global Biogeochem. Cycles*, **9**(3), 377–389.

Delmonte, B., & coauthors. 2004. *EPICA Dome C Ice Cores Insoluble Dust Data*.

Dong, B., & Valdes, P.J. 1998. Simulations of the Last Glacial Maximum climates using a generalcirculation model: prescribed versus computed sea surface temperatures. *Clim. Dynam.*, **14**, 571–591.

Fraedrich, K., Jansen, H., Kirk, E., Luksch, U., & Lunkeit, F. 2005. The Planet Simulator: Towards a user friendly model. *Meteorol. Z.*, **14**, 299–304.

Ganopolski, A., & Rahmstorf, S. 2001. Rapid changes of glacial climate simulated in a coupled climate model. *Nature*, **409**, 153–158.

Hebbeln, D., Dokken, T., Andersen, E.S., Hald, M;, & Elverhoi, A. 1994. Moisture supply for northern ice-sheet growth during the Last Glacial Maximum. *Nature*, **370**, 357–360.

Hippler, D., Eisenhauer, A., & Nagler, T.F. 2006. Tropical Atlantic SST history inferred from Ca isotope thermometry over the last 140ka. *Geochim. Cosmochim. Ac.*, **70**(1), 90–100.

Hourdin, F., Musat, I., Bony, S., Braconnot, P., Codron, F., Dufresne, J-L., Fairhead, L., Filiberti, M-A., Frieflingstein, P., Grandpeix, J-Y., Krinner, G., Levan, P., Li, Z-X., & Lott, F. 2006. The LMDZ4 general circulation model : climate performance and sensitivity to parametrized physics with emphasis on tropical convection. *Clim. Dynam.*, **27**(7-8), 787–813.

Jackson, C.S., & Broccoli, A.J. 2003. Orbital forcing of Arctic climate: mechanisms of climate response and implications for continental glaciation. *Clim. Dynam.*, **21**, 539–557.

Jakobsson, M., Gardner, J.V., Vogt, P.R., Mayer, L.A., Armstrong, A., Backman, J., Brennan, R., Calder, B., Hall, J.K., & Kraft, B. 2005. Multibeam bathymetric and sediment profiler evidence for ice grounding on the Chukchi Borderland, Arctic Ocean. *Quaternary Res.*, **63**, 150–160.

Jakobsson, M., Polyak, L., Edwards, M., Kleman, J., & Coakley, B. 2008. Glacial geomorphology of the Central Arctic Ocean: the Chukchi Borderland and the Lomonosov Ridge. *Earth Surf. Proc. Land.*, **33**(4), 526–545.

Kageyama, M., & Valdes, P.J. 2000. Impact of the North American ice-sheet orography on the Last Glacial Maximum eddies and snowfall. *Geophys. Res. Lett.*, **27**(10), 1515.

Kageyama, M., Valdes, P. J., Ramstein, G., Hewitt, C., & Wyputta, U. 1999. Northern Hemisphere Storm Tracks in Present Day and Last Glacial Maximum Climate Simulations: A Comparison of the European PMIP Models. *J. Climate*, **12**, 742–760.

Kageyama, M., Lane, A., Abe-Ouchi, A., Braconnot, P., Cortijo, E., Crucix, M., de Vernal, A., Guiot, J., Hewitt, C.D., Kitoh, A., Kucera, M., Marti, O., Ohgaito, R., Otto-Bliesner, B., Peltier, W.R., Rosell-Mele, A., Vettoretti, G., Weber, S.L., Yum, Y., & Members, MARGO Project. 2006. Last Glacial Maximum temperatures over the North Atlantic, Europe and western Siberia: a comparison between PMIP models, MARGO seasurface temperatures and pollen-based reconstructions. *Quaternary Sci. Rev.*, **25**, 2082–2102.

Kandiano, E.S., Bauch, H.A., & Muller, A. 2004. Sea surface temperature variability in the North Atlantic during the last two glacialinterglacial cycles: comparison of faunal, oxygen isotopic, and Mg/Ca-derived records. *Palaeogeogr. Palaeoclim.*, **204**(1-2), 145–164.

Khodri, M., Cane, M. A., Kukla, G., Gavin, J., & Braconnot, P. 2005. The impact of precession changes on the Arctic climate during the last interglacialglacial transition. *Earth Planet Sc. Lett.*, **236**, 285–304.

Kirst, J.G., Schneider, R.R., Muller, P.J., von Storch, I., & Wefer, G. 1999. Late Quaternary Temperature Variability in the Benguela Current System Derived from Alkenones. *Quaternary Res.*, **52**(1), 92–103.

Krinner, G. 2003. Impact of lakes and wetlands on boreal climate. *J. Geophy. Res.*, **108**(D16), 4520.

Krinner, G., & Genthon, C. 1999. Altitude dependence of the ice sheet surface climate. *Geophys. Res. Lett.*, **26**, 2227–2230.

Krinner, G., Mangerud, J., Jakobsson, M., Crucifix, M., Ritz, C., & Svendsen, J.I. 2004. Enhanced ice sheet growth in Eurasia owing to adjacent ice-dammed lakes. *Nature*, **427**, 429–432.

Krinner, G., Boucher, O., & Balanski, Y. 2006. Ice-free glacial northern Asia due to dust deposition on snow. *Clim. Dynam.*, **27**(6), 773–777.

Kucera, M., Rosell-Mele, A., Schneider, R., Waelbroeck, C., & Weinelt, M. 2005a. Multiproxy approach for the reconstruction of the glacial ocean surface (MARGO). *Quaternary Sci. Rev.*, **24**, 813–819.

Lambeck, K., Purcell, A., Funder, S., Kjaer, K.H., Larsen, E., & ans Möller, P. 2006. Constraints on the Late Saalian to early Middle Weichselian ice sheet of Eurasia from field data and rebound modelling. *Boreas*, **35**, 539–575.

Lea, D.W., Pak, D.K., & Spero, H.J. 2000. Climate Impact of Late Quaternary Equatorial Pacific Sea Surface Temperature Variations. *Science*, **289**(5485), 1719–1724.

Mahowald, N., Kohfeld, K., Hansson, M., Balanski, Y., Harrisson, S., Prentice, J., Schulz, M., & Rodhe, H. 1999. Dusts sources and deposition during the last glacial maximum and current climate: a comparison of model results with paleodata from ice cores and marine sediments. *J. Geophys. Res.*, **104**(D13).

Mangerud, J., Astakhov, V., Jakobsson, M., & Svendsen, J.I. 2001. Huge ice-age lakes in Russia. *J. Quaternary. Sci.*, **16**(8), 773–777.

Mashiotta T.A, Lea D.W, Spero H.J. 1999. Glacial interglacial changes in Subantarctic sea surface temperature and d18O-water using foraminiferal Mg. *Earth. Planet. Sc. Lett.*, **170**(4), 417–432.

Nurnberg, D., & Groeneveld, J. 2006. Pleistocene variability of the Subtropical Convergence at East Tasman Plateau: Evidence from planktonic foraminiferal Mg/Ca (ODP Site 1172A). *Geochem. Geophy. Geosy.*, **7**, doi:10.1029/2005GC000984.

Ohmura, A., & Reeh, N. 1996. New precipitation and accumulation maps for Greenland. *J. Glaciol.*, **125**(37), 140–148.

Pahnke, K., & Sachs, J.P. 2006. Sea surface temperatures of southern midlatitudes 0160 kyr B.P. *Paleoceanography*, **21**, doi:10.1029/2005PA001191.

Paul, A., & Schaefer-Neth, C. 2003. Modeling the water masses of the Atlantic Ocean at the Last Glacial Maximum. *Paleoceanography*, **18**(3), doi:10.1029/2002PA000783.

Pelejero, C., E.Calvo, Barrows, T.T., Logan, G.A., & Deckker, P. De. 2006. South Tasman Sea alkenone palaeothermometry over the last four glacial/interglacial cycles. *Mar. Geol.*, **230**(1-2), 73–86.

Peltier, W.R. 2004. Global glacial isostasy and the surface of the ice-age Earth: The REF140-5G (VM2) Model and GRACE. *Annu. Rev. Earth Pla. Sci.*, **32**, 111–149.

Petit, J.R., Jouzel, J., Raynaud, D., Barkov, N., Barnola, J., Basile, I., Bender, M., Chapellaz, J., Davis, J., Delaygue, G., Delmotte, M., Kotlyakov, V., Legrand, M., Lipenkov, V., Lorius, C., Ppin, L., Ritz, C., Saltzman, E., & Stievenard, M. 2001. *Ice core data for 420,000 year*.

Peyaud, V. 2006. *Role of the Ice Sheet Dynamics in major climate changes*. Ph.D. thesis, Laboratoire de Glaciologie et de Géophysique de l'Environnement, Université Grenoble I.

Peyaud, V., Ritz, C., & Krinner, G. 2007. Modeling the Early Weichselian Eurasian Ice Sheets: role of ice shelves and influence of ice-dammed lakes. *Clim. Past*, **3**, 375–386.

Polyak, L., Edward, M.H., Coakley, B.J., & Jakobsson, M. 2001. Ice shelves in the Pleistocene Arctic Ocean inferred from glaciogenic deep-sea bedforms. *Nature*, **410**, 453–457.

Ramstein, G., & Joussaume, S. 1995. Sensitivity experiments to sea surface temperatures, sea-ice extent and ice-sheet reconstruction for the Last Glacial Maximum. *Ann. Glaciol.*, **21**, 343–347.

Raymo, M.E., Lisiecki, L.E., & Nisancioglu, H.K. 2006. Plio-Pleistocene Ice Volume, Antarctic Climate, and the Global δ18O Record. *Science*, **313**(5786), 492–495.

Rind, D. 2006. Components of the ice age circulation. *J. Geophys. Res.*, **2**, 31–42.

Ritz, C., Rommalaere, V., & Dumas, C. 2001. Modeling the evolution of Antarctic ice sheet over the last 420,000 years: Implications for altitude changes in the Vostok region. *J. Geophys. Res.*, **106**(D23), 31943–31964.

Romanova, V., Lohmann, G., & Grosfeld, K. 2005. Effect of land albedo, CO2, orography, and oceanic heat transport on extreme climates. *Clim. Past*, **92**, 4241–4281.

Romanova, V., Lohmann, G., Grosfeld, K., & Butzin, M. 2006. Effect of land albedo, CO2, orography, and oceanic heat transport on extreme climates. *Quaternary Sci. Rev.*, **25**, 832–845.

Ruddiman, W.F., & McIntyre, A. 1979. Warmth of the subpolar North Atlantic Ocean during Northern Hemisphere ice-sheet growth. *Science*, **204**, 173–175.

Schaefer, G., Rodger, J.S., Hayward, B.W., Kennett, J.P., Sabaa, A.T., & Scott, G.H. 2005. Planktic foraminiferal and sea surface temperature record during the last 1 Myr across the Subtropical Front, Southwest Pacific. *Mar. Micropaleontol.*

Schneider, R.R. 1999. *Atlantic Alkenone sea-surface temperature records, In: Reconstructing Ocean History: A window into the future, De Abrantes F and Mix A.C. Eds.* Heidelberg edn. Berlin: Springer.

Schneider, R.R., Muller, P.J., & Ruhland, G. 1995. Late Quaternary Surface Circulation in the East Equatorial South Atlantic: Evidence from Alkenone Sea Surface Temperatures. *Paleoceanography*, **10**(2), 197–219.

Schneider, R.R., Muller, P.J., Ruhland, G., Meinecke, G., Schmidt, H., & Wefer, G. 1996. *Late Quaternary Surface temperatures and productivity in the East Equatorial South Atlantic: Response to changes in trade/monsoon wind forcing and surface water advection. In: Wefer G. et al. (eds) The South-Atlantic: Present and Past circulation*. Heidelberg edn. Berlin: Springer.

Simmonds, I., & Wu, X. 1993. Cyclone behaviour response to changes in winter Southern Hemisphere sea-ice concentration. *J. Climate*, **119**, 1121–1148.

Spahni, R., Chappellaz, J., Stocker, T., Loulergue, L., Hausammann, G., Kyawamura, G., Flckiger, J., Schwander, J., Raynaud, D., Masson-Delmotte, V., & Jouzel, J. 2005. *Epica Dome C CH4 data to 650 kya BP*.

Stocker, T.F. 1998. The seesaw effect. *Science*, **282**, 61–62.

Svendsen, J.I., Alexanderson, H., Astakhov, V.I., Demidov, I., Dowdeswell, J.A., Funder, S., Gataullin, V., Henriksen, M., Hjort, C., Houmark-Nielsen, M., Hubberten, H.W., Ingolfsson, O., Jakobsson, M., Kjaer, K.H., Larsen, E., Lokrantz, H., Lunkka, J.P., Lysa, A., Mangerud, J., Matiouchkov, A., Murray, A., Moller, P., Niessen, F., Nikolskaya, O., Polyak, L., Saarnisto, M., Siegert, C., Siegert, M.J., Spielhagen, R.F., & Stein, R. 2004. Late Quaternary ice sheet history of northern Eurasia. *Quaternary Sci. Rev.*, **23**(11-13), 1229–1271.

Thompson, D.W.J., & Wallace, J.M. 1998. The Arctic Oscillation signature in the wintertime geopotential height and temperature fields. *Geophys. Res. Lett.*, **25**(9), 1297–1300.

Toracinta, R.E., Oglesby, R.J., & Bromwitch, D.H. 2004. Atmospheric Response to Modified CLIMAP Ocean Boundary Conditions during the Last Glacial Maximum. *J. Climate*.

Villanueva, J., Flores, J.A., & Grimalt, J.O. 2002. A detailed comparison of the Uk?37 and coccolith records over the past 290 kyears: implications to the alkenone paleotemperature method. *Org. Geochem.*, **33**(8), 897–905.

Waelbroeck, C., Paul, A., Kucera, M., Rosell-Melé, A., Weinelt, M., Schneider, R., Mix, A. C., Abelmann, A., Armand, L., Bard, E., Barker, S., Barrows, T. T., Benway, H., Cacho, I., Chen, M.-T., Cortijo, E., Crosta, X., de Vernal, A., Dokken, T., Duprat, J., Eldereld, H., Eynaud, F., Gersonde, R., Hayes, A., Henry, M., Hillaire-Marcel, C., Huang, C.-C., Jansen, E., Juggins, S., Kallel, N., Kiefer, T., Kienast, M., Labeyrie, L., Leclaire, H., Londeix, L., Mangin, S., Matthiessen, J., Marret, F., Meland, M., Morey, A. E., Mulitza, S., Pfaumann, U., Pisias, N. G., Radi, T., Rochon, A., Rohling, E. J., Sbaf, L., Schaefer-Neth, C., Solignac, S., Spero, H., Tachikawa, K., & Turon, J.-L. 2009. Constraints on the magnitude and patterns of ocean cooling at the Last Glacial Maximum, MARGO Project Members. *Nature Geoscience*, **2**, 127–332.

Wei, G., Deng, W., Liu, Y., & Li, X. 2007. High-resolution sea surface temperature records derived from foraminiferal Mg/Ca ratios during the last 260 ka in the northern South China Sea. *Palaeogeogr. Palaeoclim.*, **250**(1-4), 126–138.

Winckler, G., Anderson, R.F., Fleisher, M.Q., McGee, D., & Mahowald, N. 2008. Covariant Glacial-Interglacial Dust Fluxes in the Equato-

rial Pacific and Antarctica. *Science*, **320**, 93–96.

Manuscript 4

Colleoni F., Jakobsson M., Krinner G., The role of an Arctic ice shelf in the climate of the last glacial maximum of MIS 6 (140 ka), *Quaternary Sci. Rev.*, submitted.

Contribution:

- Adjusting the ice shelf topography into the LMDZ4 boundary conditions
- Designing the experiments using LMDZ4
- Analyzing the results
- Half part of the writing

Résumé
Durant les dernières décennies, les expéditions Arctiques ont mis en lumière des traces d'érosion glaciaire datant du Pleistocène sur la Ride Lomonosov, l'ile de Chukchi et le long de la marge Nord Alaska. Ces traces montrent que l'Océan Arctique a abrité de grands ice shelves de type Antarctique. Les sédiments prélevés sur la Ride Lomonosov indiquent que les marques les plus profondes et les plus étendues laissées sur le fond océanique lors du passage de larges masses de glace datent du Stade Isotopique Marin 6 (MIS 6). L'extention précise de ces ice shelves Pléistocène n'est pas connue mais leur taille semble cependant comparable à celle des ice shelves exitant actuellement en Antarctique. Si un ice shelf de type Antarctique s'était développé dans l'Océan Arctique pendant le MIS 6, de quelle manière aurait-t-il influencé le climat de l'Hémisphère Nord? A-t-il- pu influencer le bilan de masse en surface (SMB) de l'énorme calotte Eurasienne du MIS 6 et ainsi contribuer à son extention vers le Sud? Nous utilisons ici un modèle de circulation générale atmosphérique afin d'étudier l'impact climatique d'un ice shelf remplissant le bassin du Canada et d'un ice shelf recouvrant tout l'Arctique. Les résultats montrent que les deux configurations d'ice shelf produisent un refroidissement d'environ 3°C au-dessus de l'Arctique dû principalement à l'effet combiné de l'altitude et de l'isolation plus efficaces des flux de chaleur provenant de l'océan sous-jacent, empêchant ainsi la couverture neigeuse de fondre pendant l'été. Le SMB moyen annuel des ice shelves est positif. La vitesse horizontale du front de l'ice shelf remplissant le bassin du Canada est estimée à $\approx$ 1 km.yr^{-1}. Cette vitesse est comparable à celle mesurée récemment au front de l'ice shelf Ross, en Antarctique. L'existence d'un ice shelf recouvrant tout l'Océan Arctique impliquerait une vitesse moyenne annuelle d'icebergs $\approx$ 18 km.yr^{-1} à travers le détroit de Fram. Ces estimations montrent que les deux configurations testées dans ce travail pourraient subsister sous les conditions climatiques du MIS 6. Cependant, le refroidissement provoqué par les ice shelves affecte uniquement les calottes continentales le long des marges Arctiques et n'est passez fort pour influencer de manière significative le bilan de masse global de la calotte Eurasienne du MIS 6.

The role of an Arctic ice shelf in the climate of the last glacial maximum of MIS 6 (140 kyrs BP)

F. Colleoni[1,2] **. M. Jakobsson**[2] **. G. Krinner**[1]

[1]Laboratoire de Glaciologie et Géophysique de l'Environnement, UJF, CNRS, France

[2]Department of Geology and Geochemistry, Stockholm University, 106 91 Stockhlom, Sweden

Abstract

During the last decade, Arctic icebreaker and nuclear submarine expeditions have revealed large-scale Pleistocene glacial erosion on the Lomonosov Ridge, Chukchi Borderland and along the Northern Alaskan margin indicating that the glacial Arctic Ocean hosted large Antarctic-style ice shelves. Dating of sediment cores indicate that the most extensive and deepest ice grounding occurred during Marine Isotope Stage (MIS) 6. The precise extensions of Pleistocene ice shelves in the Arctic Ocean are unknown but seem comparable to present existing Antarctic ice shelves. How would an Antarctic-style ice shelf in the MIS 6 Arctic Ocean influence the Northern Hemisphere climate? Could it have impacted on the surface mass balance (SMB) of the MIS 6 Eurasian ice sheet and contribute to its large southward extent? We use an Atmospheric General Circulation Model to investigate the climatic impacts of both a limited MIS 6 ice shelf covering portions of the Canada Basin and a fully ice shelf covered Arctic Ocean. Results show that both ice shelves cause a temperature cooling of about 3°C over the Arctic Ocean mainly due to the combined effect of ice elevation and insulation from the underlying ocean heat fluxes which stop the snow cover from melting during summer. The calculated The SMB of the ice shelves are positive. The ice front horizontal velocity of the Canada Basin ice shelf is estimated to ≈1 km.yr^{-1} which is comparable to the recent measurements of the Ross ice shelf, Antarctica. The existence of large continous ice shelf covering the entire Arctic Ocean would imply a mean annual velocity of icebergs of ≈12 km.yr^{-1} through the Fram Strait. Our modeling results show that both ice shelf configurations could be viable under the MIS 6 climatic conditions. However, the cooling caused by these ice shelves only affects the Arctic margins of the continental ice sheets and is not strong enough to significantly influence the surface mass balance of the entire MIS 6 Eurasian ice sheet. *Keywords: Arctic ice shelf, Marine Isotope Stage 6, atmospheric modeling,climate*

Introduction

The Antarctic continent is covered by a complex system of glacier ice masses grounded both above and below sea level. This continental ice sheet system flows into the ocean at several places to form large floating ice shelves. The largest of these are the Ross and Ronne-Filchner Ice Shelves that together cover more than 900,000 km^2 and bound the marine-based West Antarctic Ice Sheet (British Antarctic Survey, 2005). The Arctic Ocean, on the other hand, hosts no similar ice shelves today, only relatively small and thin ice shelves along the Northern Ellesmere Island exist (Jeffries, 1992, 2002). However, during the last decade of Arctic icebreaker and nuclear submarine expeditions, large-scale glacial erosion and glaciogenic bedforms have been mapped on the central Arctic Ocean seafloor in water depths down to approximately 1000 m below present sea level (e.g. Jakobsson, 1999; Polyak *et al.*, 2001). Some of the mapped glaciogenic features on the Lomonosov Ridge, Chukchi Borderland and along the Northern Alaskan margin indicate that the glacial Arctic Ocean hosted large Antarctic-style ice shelves (Polyak *et al.*, 2001; Jakobsson *et al.*, 2005, 2008; Engels *et al.*, 2008). Several decades before this geophysical evidence emerged, Mercer (1970) proposed that there may have existed Antarctic style ice shelves in the Arctic Ocean during the Pleistocene glacial periods. His idea was further developed by Hughes *et al.* (1977) who suggested a 1-km thick ice shelf covering the entire Arctic Ocean and forming a critical part of a huge ice sheet, including the Laurentide and Eurasian ice sheets, that behaved as one dynamic system during the Last Glacial Maximum (LGM).

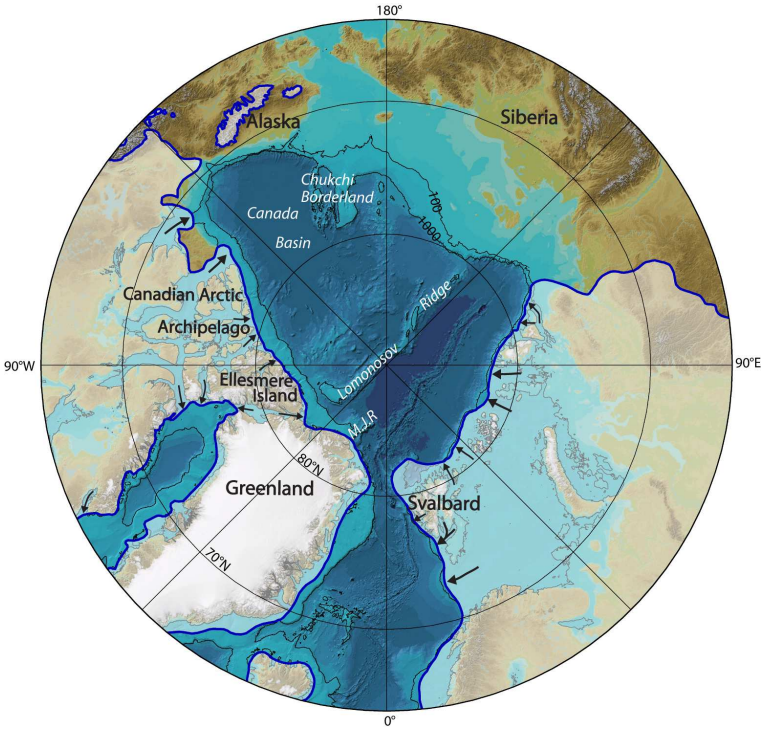

Figure 5.1: Arctic Ocean IBCAO bathymetry (Jakobsson *et al.*, 2008a). "M.J.R." stands for the Morris Jesup Rise. White shadow and blue thick lines delimit the North American and Eurasian continental ice sheets as reconstructed at 140 ka. Arrows indicate possible ice flows direction.

The precise extension of ice shelves in the Arctic Ocean is unknown, although the geophysical data collected from icebreakers and submarines suggest a more limited extension than that proposed by Hughes *et al.* (1977) for the LGM. Furthermore, dating of sediment cores collected from glacially eroded areas of the Lomonosov Ridge indicate that the most extensive and deepest ice grounding occurred during Marine Isotope Stage (MIS) 6 and not during LGM (Jakobsson *et al.*, 2001). This implies that the largest ice shelves in the Arctic Ocean coexisted with the largest extension of the Eurasian continental ice sheet, referred to as the Late Saalian with its peak at 140 ka (Svendsen *et al.*, 2004). If an Antarctic-style ice shelf was present in the Arctic Ocean during MIS 6, the question of how it influenced the atmospheric circulation and regional climate arises. Also, could it have impacted on the Surface Mass Balance (SMB) of the Eurasian Late Saalian ice sheet and, thus, play a role in explaining why it grew so large? In order to answer this question we use an Atmospheric General Circulation Model (AGCM) to investigate the climatic impacts of both a limited MIS 6 ice shelf covering portions of the Canada Basin as the recent geophysical mapping indicate (Jakobsson et al., in prep) and a fully ice shelf covered Arctic Ocean as proposed by Hughes *et al.* (1977).

Methods

We have adopted the ice shelf extension in the Canada Basin for our simulation experiments from the ongoing work by Jakobsson et al., (in prep.) involving the compilation of all available geophysical and geological data that constrain the spatial extensions of the Pleistocene Arctic Ocean glaciations. However, the precise MIS 6 ice shelf extension in the Canada Basin is not critical for our AGCM experiments as we are generally addressing the potential influence on the atmospheric circulation from an Antarctic-sized (Ross and Ronne-Filchner ice shelves) ice shelf and from one fully covering the entire Arctic Ocean as proposed by Hughes *et al.* (1977). The ice shelf extension in the Canada Basin is reconstructed from the assumption that the MIS 6 Laurentide ice sheet (the thickness retrieved from LGM ICE-5G, Peltier, 2004) extended to the continental shelf break of the Canadian Arctic Archipelago from where an ice shelf extended into the Arctic Ocean (Figure 5.1) (Polyak *et al.*, 2001; Jakobsson *et al.*, 2008). The ice shelf thickness has been inferred by applying a thin-

ning following a gradient of -5 m/km (Martin Siegert pers. comm.) from the grounding line, located at the shelf break. The maximum extension has been defined as the location to where the ice shelf had thinned to obtain a thickness of 200 m (Figure 5.2a). The mean elevation of the Canada Basin ice shelf is 80 meters. The Chukchi Borderland is covered by a local marine ice sheet reaching an elevation of 800 meters above the MIS 6 sea level (-110 m a. m.s.l., Astakhov, 2004) and a smaller ice rise is formed over the southern Lomonosov Ridge. To investigate the Hughes *et al.* (1977) hypothesis, the entire Arctic Ocean has been filled with a 1-km thick ice shelf extending down to 80°N in the Fram Strait (Figure 5.4).

To test the potential climatic impact of a Canada Basin ice shelf as the impact of a larger ice shelf following Hughes *et al.* (1977), we performed three AGCM snapshots of 21 years (Table 5.3). Climate simulations are performed using the LMDZ4 atmospheric general circulation model (Hourdin *et al.*, 2006; Krinner, 2003; Krinner *et al.*, 2006). The model was run with 144×109 grid cells and with 19 vertical layers. The first year is discarded in the analyses as spin-up.

Since the Arctic Ocean sea ice cover might have been thicker during glacial periods than during interglacials, sea ice (prescribed from Paul & Schaefer-Neth (2003)) thickness is uniformly set to 5 meters following Otto-Bliesner *et al.* (2006). The Surface Mass Balance (SMB) is calculated after the temperature-index method of Ohmura *et al.* (1996). In this method, surface ablation is diagnosed when mean summer surface air temperature (T_{JJA}), recalculated on a fine resolution grid with altitude-correction, exceed a prescribed threshold of -1.8°C.

Simulation REF5m does not account for the impact of an Arctic ice shelf and will be considered as the "reference" MIS 6 simulation. Simulation SHELF includes the Canada ice shelf (Jakobsson, 2009, in prep.). The parts of the Arctic Ocean not occupied by this ice shelf are filled with a 5 m thick sea ice cover, which also extends into the North Atlantic as far south as proposed by Paul & Schaefer-Neth (2003) for the LGM. Simulation GH accounts for the uniform 1-km thick ice shelf covering the entire Arctic Ocean. The remaining open North Atlantic is filled with sea ice as far south as in the SHELF simulation.

Table 5.1: Simulations carried out in this work. "Ca. IS" corresponds to the Canada Basin Ice Shelf, "GH" stands for Hughes *et al.* (1977) large Arctic ice shelf and SIC stands for sea ice cover.

	Ca. IS	**GH**	**SIC thick.**	**period (ka)**
REF5m			5 m	140
SHELF	X		5 m	140
GH		X	5 m	140

MIS 6 boundary conditions are set using Mahowald *et al.* (1999) dust deposition adapted to 140 ka, the 140 ka orbital values (Berger & Loutre, 1991) and greenhouse gas concentrations from Petit *et al.* (2001) and Spahni *et al.* (2005). Late Saalian Eurasian ice topography is obtained from Peyaud (2006) while the Laurentide and Antarctic ice sheets are from ICE-5G LGM reconstruction (Peltier, 2004). The Late Saalian ice topography reaches a thickness of 4200 m, corresponding to a surface altitude of 3200 m above seal-level. Proglacial lakes are defined according to the methods of Mangerud *et al.* (2001) and sea level is set to 110 meters below present-day sea-level (Astakhov, 2004) for defining the coastlines. Simulations have been forced using LGM sea surface temperatures from Paul & Schaefer-Neth (2003). The equations and details on the Late Saalian boundary conditions are discussed in Colleoni *et al.* (2009d).

Results

The Canada ice shelf

The ice shelf occupying the area north of the Canadian Arctic Archipelago and along the Northern Alaskan margin causes a mean annual negative air temperature anomaly of about 3°C directly over its surface (Figure 5.2d). This anomaly is mainly confined to the lower part of the troposphere. It culminates at approximately -1°C around 2000 m (Figure 5.2c). Compared to the recent work by Krinner *et al.* (2009) in which the temperature anomaly induced by sea-ice thickness variations is constrained by the winter inversion in the boundary layer, the anomaly observed in SHELF extends higher in the atmosphere because of the high elevation of the ≈1-km thick ice-shelf. The local cooling effect from the ice shelf is caused by three main factors: the

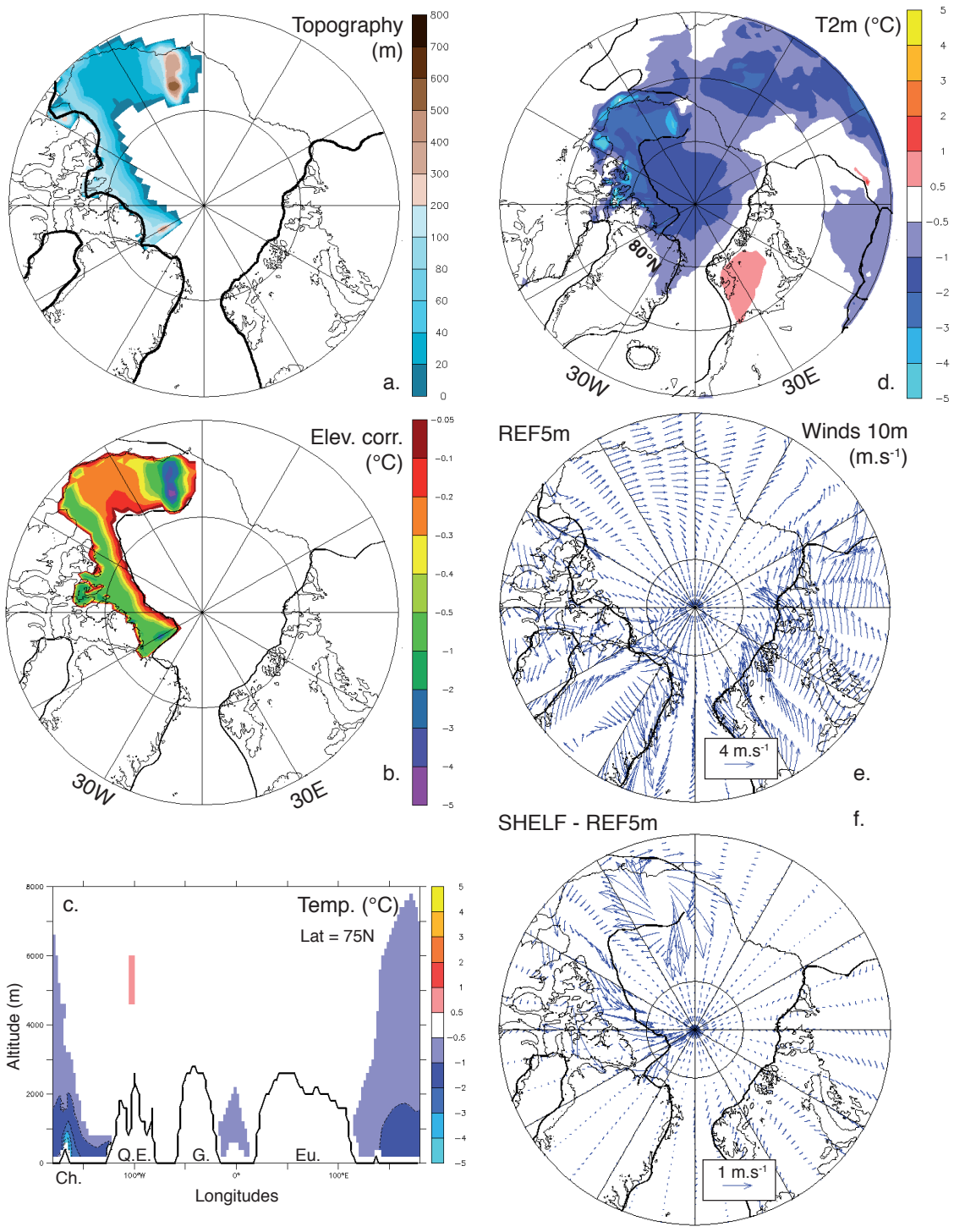

Figure 5.2: Mean annual climatic anomalies (SHELF - REF5m): a. Canada Basin ice shelf topography (m); b. Altitude correction using a lapse rate of 8°C/km; c. temperature profile at 75°N, main topographic features are indicated: Chukchi Island (Ch.), Queen Elisabeth Archipelago (Q.E.), Greenland (G.) and the Arctic margin of the Eurasian ice sheet (Eu.). The profile runs along the entire ice shelf along the 75°N parallel; d. surface air temperature (°C); e. Surface winds for simulation REF5m ($m \cdot s^{-1}$); f. surface winds anomalies (SHELF - REF5m) in $m \cdot s^{-1}$.

altitude of the shelf ice, its thickness (which isolates the atmosphere from the underlying ocean) and possible feedbacks. Under present-day conditions, the sensitivity of surface air temperature to changes in surface topography in the coastal regions (between 0 m and 1000 m) of Greenland and Antarctica is about 5°C/km (Krinner & Genthon, 1999). However, the glacial high Arctic atmosphere was most likely as dry and cold as the atmosphere above the central part of the Antarctic and Greenland ice sheets. We therefore use a lapse rate of 8°C/km which is typical for these

Table 5.2: Back-of-the-envelope heat flux calculation settings. Ice and snow thermal conductivities are 2.2 W·m^{-1}K^{-1} and 0.3 W·m^{-1}K^{-1} respectively. T_S stands for the surface temperature. For the simulation SHELF, values are given only for the Canada Basin (200 meters thick) since the thickness along North America equals that of the thick ice shelf in GH. REF3m refers to a simulation similar to REF5m but prescribing a uniform sea ice thickness of 3 meters.

	Flux (W·m^{-2})	**Ice thick.** (m)	**Snow** (m)	**T_S** (°C)
REF5m	**11**	5	0	-25
	6	5	0.5	-25
REF3m	**18**	3	0	-25
	12	3	0.2	-25
SHELF	**0.25**	200	0	-22
	0.25	200	0.2	-22
GH	**0**	1000	10	-22

Table 5.3: Mean annual surface mass balance (SMB) for the Arctic margins of the Laurentide ice sheet (Lau), of the Greenland ice sheet (Green), for both (N.A.) and of the Eurasian ice sheet (Euras.).

$(kg \cdot m^2 \cdot yr^{-1})$	**Lau.**	**Green.**	**N.A.**	**Euras.**
REF5m	158	222	180	108
SHELF	153	200	163	116
SHELF-REF5m	5	22	17	8
GH	147	193	160	108
GH-REF5m	11	30	20	0

regions today (Krinner & Genthon, 1999). The reconstructed Canada Basin ice shelf mean elevation is between 20 and 100 m above sea level along the coast of Greenland and North America and between 20 and 40 m in the Canada Basin. Consequently the elevation alone induces a cooling of ≈0.5° to 1°C along Greenland and North America, 0.25°C over the Canada Basin and as much as 5°C over the local ice sheet on the Chukchi Borderland (Figure 5.2b). This temperature signal caused by elevation changes represents one third of the total simulated temperature cooling over the ice shelf.

The ice shelf thickness represents one of the other factors causing a cooling. Sea ice, as well as an ice shelf, insulates the atmosphere from the ocean and, thus, prevents a great part of the heat exchange. This isolation can be estimated using a back-of-the-envelope calculation for each simulation. In REF5m, heat flux from the ocean through the 5 m thick sea ice alone would be about 11 W·m^{-2}, and about 6 W·m^{-2} when accounting for a 0.5 m snow cover (Table 5.2). In SHELF, the shelf ice is thinner over the Canada Basin (≈200 m) than along the coast of North America and Greenland (≈1000 m, Figure 5.1). This is negligible compared to the surface thermal radiation (≈160 W·m^{-2}) which is the largest single component of the surface energy balance (Huwald *et al.*, 2005). Over the Canada Basin, fluxes would be negligible. In addition, snow accumulated on top of the sea ice enhances the isolation effect and snow on the ice shelf also contributes to the regional cooling by raising its albedo during summer. In SHELF, the higher elevation combined to more efficient ocean heat fluxes isolation reduce summer snow melting and consequently increases snow height. The maximum snow height on sea ice is shelf regulated due to Archimedes principle. The sea ice sinks into the ocean under the weight of the snow, which subsequently transforms into ice when coming in contact with the water and, thus, the sea ice thickness is increased and the maximum snow height regulated. The remaining snow melts during summer.

The atmospheric cooling generated by the ice shelf spreads across the Arctic Ocean and causes a general decrease in air temperature of 2°C (Figure 5.2d). The temperature decrease is particularly evident during spring and summer. This is due to the presence of snow on the ice shelf that did not melt during spring and consequently increases the local summer albedo by 20% (not shown). The anomaly also extends to Eastern Siberia where temperatures are ≈ -1.5°C lower than without the ice shelf (Figure 5.2d). The colder temperatures contribute to increase the continental snow cover in Eastern Siberia. The cooling induced by the ice shelf is not large enough to modify the large scale circulation significantly but it influences the surface winds (winds at an altitude of 10 m, Figure 5.2e). The winds coming from the Laurentide ice sheet are redirected Eastward along the coast of Greenland, especially during summer, due to the cooling generated by the ice shelf and its snow cover (Figure 5.2e and f). The relatively small ice cap on the Chukchi Borderland generates katabatic winds (Figure 5.2f).

Since the effect of the ice shelf on the atmosphere is limited in altitude, the SMB of the surrounding ice sheets is only affected along the Arctic margins (Table 5.3 and Figure 5.3b). The cooling from the ice shelf has the most promi-

nent effect on SMB along the Greenland margin (-22 kg·m^{-2} ·yr^{-1} in SHELF) since the surface winds in that region have been greatly influenced (Figure 5.2f). The mean annual SMB of the ice shelf is ≈93 kg·m^{-2} ·yr^{-1} (Figure 5.3a). The total mass balance of the ice shelf, including calving, basal melting and feeding for the adjacent continental ice sheets, is addressed in the discussion.

A 1-km thick Arctic Ocean ice shelf

In simulation GH, we test the impact of a 1-km thick ice shelf fully covering the Arctic Ocean as hypothesized by Hughes *et al.* (1977). Such an ice shelf causes a negative temperature anomaly of about -3.5°C over the entire Arctic Ocean (Figure 5.4a). The temperature anomaly remains constrained to the lower 2000 m of the atmosphere (Figure 5.4b). In GH, the altitude correction of surface air temperature is 0.8°C over the entire ice shelf. This implies that the height of the ice shelf contributes one quarter of the total temperature signal derived from our simulation. When this altitude effect is removed (not performed on the figures), the cooling from a continuous 1-km thick ice shelf is about -2.7°C (Figure 5.4a). The isolation between the ocean and atmosphere caused by the 1-km ice shelf is as strong as in simulation SHELF, no heat flux from the ocean would be perceptible (Table 5.2). Similarly to SHELF, the higher elevation in GH increases the snow height but on a larger spatial scale because of the larger exent of the ice shelf. The regional cooling spreads over Eastern Siberia and decreases surface air temperatures by about -2°C (Figure 5.4a.). As for SHELF, the cooling does not modify the large scale circulation significantly. However compared to REF5m, the surface winds are strengthened along all the Arctic margins probably due to stronger thermal gradients except along the Eurasian margins (Figure 5.4c).

The surface mass balances of the large ice sheets around the Arctic Ocean are affected along their northernmost Arctic margin when the 1-km thick ice shelf is present, but the difference compared to our reference simulation is of the same order as for SHELF (Table 5.3). The more sensitive Greenland margin actually experiences a SMB reduction of 29 kg·m^{-2} ·yr^{-1} due to lower precipitation compared to when a limited ice shelf is present in the Arctic Ocean (Figure 5.3d). The other continental ice sheets are not so sensitive to the fully shelf ice covered Arctic Ocean since the temperature signal does not reach the top of their high elevation and since melting of their Arctic margins is small. The SMB of the continuous Arctic Ocean ice shelf is ≈46 kg·m^{-2} ·yr^{-1} implying that the ice shelf is probably in equilibrium with the MIS 6 climate since its thickness and snow cover provides an efficient isolation from ocean heat fluxes (Figure 5.3c). In both simulations SHELF and GH, precipitation is decreased by 30% over the entire Arctic resulting from the cooling generated by the presence of the ice shelves, which cause a reduction of evaporation over the ice-shelf. No significant zonal change of atmospheric energy transport across the 70°N meridian is observed in our simulations. This was noted by Krinner *et al.* (2009) in simulations with variable present-day and future Arctic sea ice thicknesses.

Discussion

We have addressed the potential climatic impacts of a floating ice shelf in the Canada Basin of the Arctic Ocean because recent marine geophysical and geological data suggest that such an ice shelf existed some time during MIS 6 (Jakobsson, in prep.). Some decades before chirp sonar profiles first revealed extensive ice grounding as deep as 1000 m below present sea level at about 87°N on the Lomonosov Ridge (Jakobsson, 1999), the hypothesis of a 1-km thick ice shelf covering the entire Arctic Ocean was put forward by Hughes *et al.* (1977), a theory inspired by Mercer (1970). Even if the new mapping data now suggest a more limited ice shelf than proposed by Hughes *et al.* (1977), we found it relevant to also test the climatic impact from such a huge feature in the glacial Arctic.

Both tested ice shelves cause a distinct cooling of 3 to 5°C confined in altitude to the lower 2000 m of the troposphere (Figures 5.2c and 5.4b). This cooling is mainly due to that a thick ice shelf prevents ocean heat fluxes from reaching the lower atmosphere. When we remove the cooling effect caused by the ice shelf elevation, this temperature anomaly is still significant and ranges between 2 and 4°C. Despite generally lower precipitation over the Arctic Ocean, the higher elevation and isolation of ice shelves compared to sea ice increases the amount of snow accumulating on the ice. This results in a higher sum-

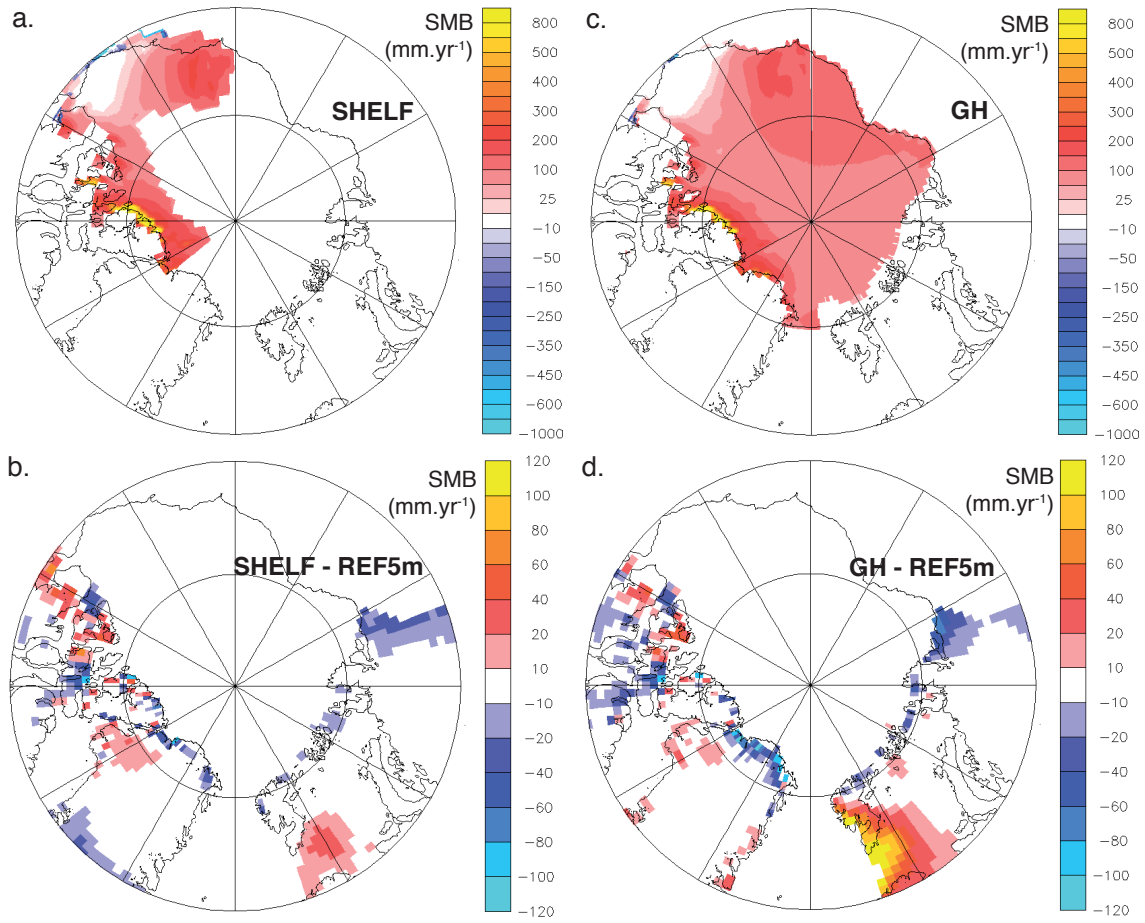

Figure 5.3: Mean annual Surface Mass Balance (SMB). a. Canada ice shelf surface mass balance (SHELF); b. SMB difference between SHELF and REF5m along the Arctic margins of the Eurasian and the Laurentide ice sheets; c. Hughes *et al.* (1977) Arctic ice shelf (GH); d. same as b. but between GH and REF5m.

mer albedo that, in turn, further enhances the regional cooling. However, the cooling is not strong enough to affect the large scale circulation and the surface mass balance of the northernmost parts of the Arctic MIS 6 ice sheets.

In the simulations we prescribed a 5 m thick sea ice assuming that it generally was thicker during a glacial maxima than at present interglacial conditions (Otto-Bliesner *et al.*, 2006) when the average sea ice thickness is around 3 m or less (Spreen *et al.*, 2006). To test the sensitivity of our simulations regarding sea ice thickness, we carried out all the experiments also using a thickness of 3 m (Krinner *et al.*, 2009). The results from these simulations show that the temperature cooling caused by the presence of a large or a small ice shelf, when the elevation effect is removed, is of the order of 1.5°C. This signal is about 50% weaker than when considering a 5 m thick sea ice cover (SHELF and GH). In simulation SHELF, the permanent snow cover, not affected by the Archimedes effect contrary to simulation REF5m, enhances the cooling also in the vicinity of the ice shelf due to a stronger summer albedo effect. As shown by Krinner *et al.* (2009), sea ice thickness is not the most critical parameter but as it influences processes in the lower troposphere to some extent, the temperature over the entire Arctic area is affected.

We have shown that the surface mass balance of a limited Canada Basin ice shelf as well as a continuous the large Arctic Ocean 1-km thick ice shelf covering the entire Arctic Ocean were positive under the simulated MIS 6 climate conditions. But are the ice fluxes coming from the North American and Eurasian ice sheets enough to allow such ice shelves to develop in the Arctic Ocean? Bigg & Wadley (2001) estimated the flux of icebergs during the LGM using both CLIMAP (1981) and ICE4G (Peltier, 1994) ice sheet reconstructions. In their estimates, ice fluxes into the Amerasian part of the Arctic Ocean from the northern Laurentide ice sheet amount to ≈528 $km^3 \cdot yr^{-1}$ using CLIMAP and ≈445 $km^3 \cdot yr^{-1}$ using ICE4G while fluxes from the Northern Greenland ice sheet are estimated

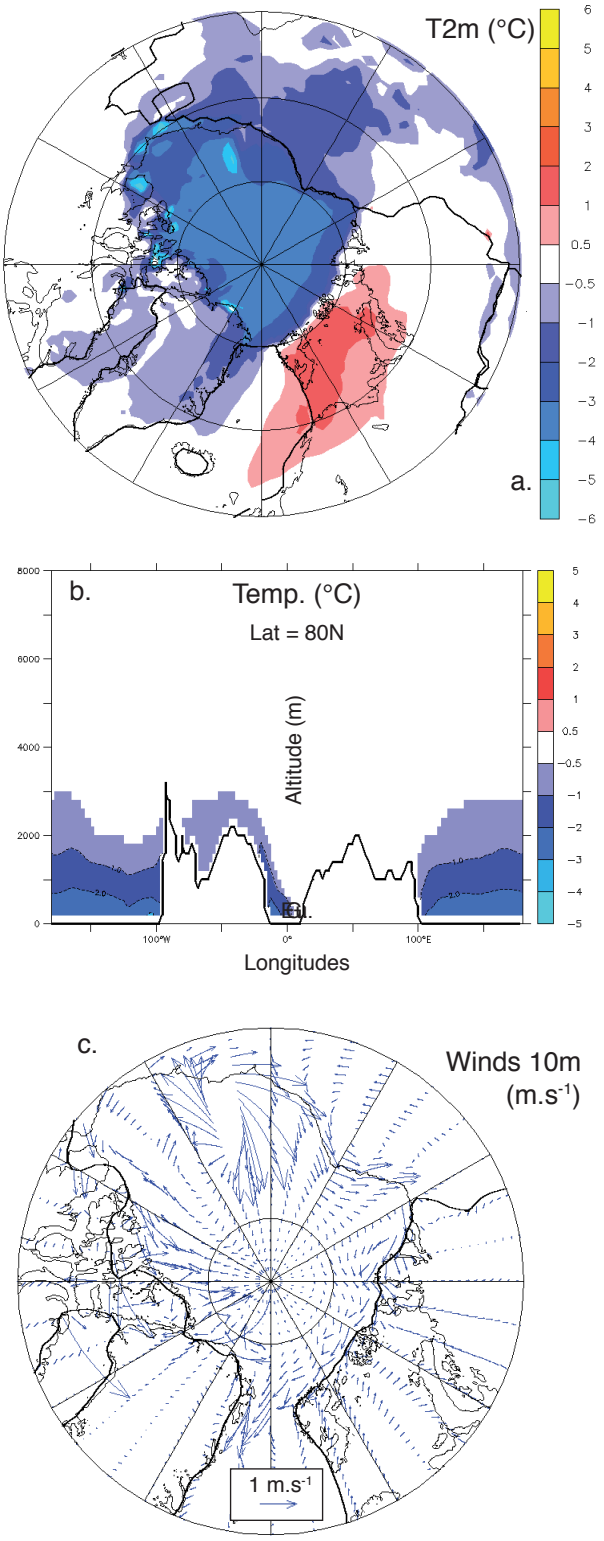

Figure 5.4: Mean annual climatic anomalies (GH - REF5m): a. surface air temperature (°C); b. temperature profile at 80°N, main topographic features are indicated. the profile runs along the entire ice shelf along the 80°N parallel: Greenland (G.) and the Arctic margin of the Eurasian ice sheet (Eu.); c. 10 m winds speed difference between GH and REF5m ($m.s^{-1}$).

to ≈25 $km^3 \cdot yr^{-1}$ (CLIMAP) and ≈40 $km^3 \cdot yr^{-1}$ (ICE-4G). The total surface mass balance of the Canada Basin ice shelf is ≈$1.83 \cdot 10^{14}$ $kg \cdot yr^{-1}$, corresponding to approximately 200 $km^3 \cdot yr^{-1}$ (ice density = 931 $kg \cdot m^{-3}$). Supposing equilibrium, accounting for the input from the Laurentide ice sheet from Bigg & Wadley (2001) and assuming a basal melting bellow the ice shelf of ≈259 $km^3.yr^{-1}$ (Jacobs *et al.*, 1992) (based on the Ross estimates of 86 $km^3.yr^{-1}$ and adjusted to the large ice shelf area), leads to an estimated calving rate of 494 $km^3.yr^{-1}$. Given a northern edge length of ≈ 2300 km and 0.2 km thick, this yields a mean annual flow velocity at the ice shelf front of about 1.1 $km.yr^{-1}$. This velocity is close to the recent satellite measurements showing a horizontal velocity of the Ross ice shelf front of about 1 $km.yr^{-1}$ (Rignot *et al.*, 2008).

The large ice shelf covering the entire Arctic Ocean has a SMB of ≈$1.61\ 10^{14}$ $kg \cdot yr^{-1}$ corresponding to 1720 $km^3 \cdot yr^{-1}$. Summing all the LGM contributions to the Arctic Ocean estimated by Bigg & Wadley (2001) yields 1290 and 943 $km^3 \cdot yr^{-1}$ using CLIMAP and ICE-4G respectively. However, the Eurasian Ice Sheet is smaller in both CLIMAP and ICE-4G LGM reconstructions than the Late Saalian adopted from Svendsen *et al.* (2004) and used in our study. Therefore, the flux from the Eurasian Ice Sheet as estimated by Bigg & Wadley (2001) will likely have to be doubled in order to conform to the large Late Saalian Ice Sheet. Assigning this doubling and summing the fluxes by Bigg & Wadley (2001), 2027 $km^3.yr^{-1}$ ice is estimated to flow into the Arctic Ocean. A total of 1772 $km^3.yr^{-1}$ ice would be available or calving from a continuous Arctic Ocean ice shelf if the basal melting of 993 $km^3.yr^{-1}$ (see the Canada Basin ice shelf example above) is up-scaled to its area and the calculated SMB for the continuous Arctic Ocean ice shelf is applied. How would the Fram Strait look like when the ice from this huge ice shelf is exiting the Arctic Ocean? If the continuous Arctic Ocean ice shelf is on the order of 1-km thick, as proposed by Hughes *et al.* (1977), the width of the Fram Strait where this ice anc flow through is approximately 146 km. This width is derived by measuring between the 1000 m isobaths in the Fram Strait; a depth chosen since a 1-km thick ice shelf would draft approximately 900 m below sea level, which, in turn, can be estimated to some 100 m lower than present during MIS 6. This yield an ice flow velocity through the Fram Strait of approximately 12 $km.yr^{-1}$.

However, our experiments and mass balance estimations do not include any realistic marine processes involving the ice shelf. Studies of the Antarctic ice shelves show that melting beneath their deeper parts as well as basal accretion constitute a significant mass balance component (Fricker *et al.*, 2001; Jacobs *et al.*, 1992). It is for this reason not possible to draw firm conclusions from our calculations whether or not the ice shelves in focus for our study were viable.

This paper is part of a suite of studies on the climatic feedbacks from global and regional factors with the potential of influencing the SMB of the Eurasian ice sheet during the later part of MIS 6, i.e. the late Saalian Ice Sheet 140 ka (Colleoni *et al.*, 2009a,d,b). The main scientific question in focus is why the Late Saalian Ice Sheet grew so much larger than the Weichselian ice sheets. In this present work we have addressed how an ice shelf limited to the Canada Basin would have interacted with the MIS 6 climate and compared this with the interaction from a continuous 1-km thick ice shelf covering the entire Arctic Ocean as hypothesized by Hughes et al (1977). Our main conclusion is that both ice shelves cause a regional cooling, but not large enough to impact the large scale atmospheric circulation and, thus, the cooling does not spread much further than the margins surrounding the Arctic Ocean. Therefore, we suggest that floating ice shelves in the Arctic Ocean may have played a role during MIS 6 to stabilize the circum Arctic ice sheets, but the climatic impact, even from an ice shelf covering the entire Arctic Ocean, would not have been large enough to serve as an explanation for the size of the Eurasian Late Saalian Ice Sheet.

Acknowledgments

The authors acknowledge support by the Agence Nationale de la Recherche (project IDEGLACE), the Région Rhône Alpes (programme Explora'Doc), the Ministère des Affaires Étrangères Français and The Bert Bolin Centre for Climate Research (Stockholm University) for their support The climate simulations were carried out at IDRIS/CNRS, on the Mirage scientific computing plateform in Grenoble (France) and on the computing plateform at AWI (Germany).

References

A. Abe-Ouchi and T. Segawa and F. Saito. 2007. Climatic Conditions for modelling the Northern Hemisphere ice sheets throughout the ice age cycle. *Clim. Past*, **3**, 423–438.

Astakhov, V.I. 2004. Middle Pleistocene glaciations of the Russian North. *Quaternary Sci. Rev.*, **23**, 1229–1271.

Berger, A., & Loutre, M.F. 1991. Insolation values for the climate of the last 10 million years. *Quaternary Sci. Rev.*, **10**(4), 297–317.

Bigg, G.R., & Wadley, R. 2001. The origin and flux of icebergs released into the Last Glacial Maximum Northern Hemisphere oceans: the impact of ice-sheet topography. *J. Quaternary Sci.*, **16**, 565–573.

British Antarctic Survey. 2005. *Antarctic Factsheet Geographical Statistics, British Antarctic Survey, http://www.antarctica.ac.uk/*.

CLIMAP. 1981. *Seasonal reconstruction at the Earth's surface at the Last Glacial Maximum, Map Chart Series MC-36, Geological Society of America, Boulder CO, USA*.

Colleoni, F., Krinner, G., Jakobsson, M., Peyaud, V., & Ritz, C. 2009a. Influence of dust deposition and proglacial lakes on the surface mass balance of the large Eurasian ice sheet during the peak Saalian (140 kyrs BP), in press. *Global Planet. Change*.

Colleoni, F., Krinner, G., & Jakobsson, M. 2009b. Sensitivity of the Late Saalian (140 kyrs BP) and LGM (21 kyrs BP) Eurasian ice sheet surface mass balance to vegetation feedbacks, accepted. *Geophys. Res. Lett.*

Colleoni, F., Liakka, J., Krinner, G., Jakobsson, M., Masina, S., & Peyaud, V. submitted. The Late Saalian surface ocean (140 kyrs BP): sensitivity of the Late Saalian Eurasian ice sheet to sea surface conditions. *Clim. Dynam.*

Crowley, T.J. 1995. Ice age terrestrial carbon changes revisited. *Global Biogeochem. Cycles*, **9**(3), 377–389.

Delmonte, B., & coauthors. 2004. *EPICA Dome C Ice Cores Insoluble Dust Data, IGBP PAGES/World Data Center for Paleoclimatology Data Contribution Series, NOAA/NGDC Paleoclimatology Program, Boulder CO, USA*.

Engels, J.L., Edwards, M.H., Polyak, L., & Johnson, P.D. 2008. Sea floor evidence for ice shelf flow across the Alaska-Beaufort margin of the Arctic Ocean. *Earth Surf. Proc. Land.*, **33**, 1047–1063.

Fricker, H.A., Popov, S., Allison, I., & Young, N. 2001. Distribution of marine ice beneath the Amery Ice Shelf. *Geophysical Research Letters*, **28**(11), 2241–2244.

Hourdin, F., Musat, I., Bony, S., Braconnot, P., Codron, F., Dufresne, J-L., Fairhead, L., Filiberti, M-A., Frieflingstein, P., Grandpeix, J-Y., Krinner, G., Levan, P., Li, Z-X., & Lott, F. 2006. The LMDZ4 general circulation model : climate performance and sensitivity to parametrized physics with emphasis on tropical convection. *Clim. Dynam.*, **27**(7-8), 787–813.

Hughes, T., Denton, G.H., & Grosswald, M.G. 1977. Was there a late-Wurm Arctic Ice Sheet? *Nature*, **266**, 596–602.

Huwald, H., Tremblay, L-B., & Blatter, H. 2005. Reconciling different observational data sets from Surface Heat Budget of the Arctic Ocean (SHEBA) for model validation purposes. *Journal of Geophysical Research*, **110**(C5), C05009.

Jacobs, S.S., Helmer, H.H., Doake, C.S.M., Jenkins, A., & Frolich, R.M. 1992. Melting of the ice shelves and the mass balance of Antarctica. *Journal of Glaciology*, **130**(38), 375–387.

Jakobsson, M. 1999. First high-resolution chirp sonar profiles from the central Arctic Ocean reveal erosion of Lomonosov Ridge sediments. *Mar. Geol.*, **154**, 111–123.

Jakobsson, M., Lovlie, R., Arnold, E.M., Backman, J., Polyak, L., Knutsen, J.O., & Musatov, E. 2001. Pleistocene stratigraphy and paleoenvironmental variation from Lomonosov Ridge sediments, central Arctic Ocean. *Global Planet. Change*, **31**(1-4), 1–21.

Jakobsson, M., Gardner, J.V., Vogt, P., Mayer, L.A., Armstrong, A., Backman, J., Brennan, R., Calder, B., Hall, J.K., & Kraft, B. 2005. Multibeam bathymetric and sediment profiler evidence for ice grounding on the Chukchi Borderland, Arctic Ocean. *Quaternary Res.*, **63**, 150–160.

Jakobsson, M., Macnab, R., Mayer, L., Anderson, R., Edwards, M., Hatzky, J., Schenke, H. W., & Johnson, P. 2008a. An improved bathymetric portrayal of the Arctic Ocean: Implications for ocean modeling and geological, geophysical and oceanographic analyses. *Geophys. Res. Lett.*, **35**(7), L07602.

Jakobsson, M., Polyak, L., Edwards, M., Kleman, J., & Coakley, B. 2008b. Glacial geomorphology of the Central Arctic Ocean: the Chukchi Borderland and the Lomonosov Ridge. *Earth Surf. Proc. Land.*, **33**(4), 526–545.

Jeffries, M.O. 1992. Arctic Ice Shelves and Ice Islands: Origin, Growth and Disintegration, Physical Characteristics, Structural-Stratigraphic Variability, and Dynamics. *Rev. Geophys.*, **30**(3), 245–267.

Jeffries, M.O. 2002. *in R.S. Williams, J.G. Ferrigno (Eds), Satellite Image Atlas of Glaciers of the World: Glaciers of North America*. United States Geological Survey, Washington, USA.

Krinner, G. 2003. Impact of lakes and wetlands on boreal climate. *J. Geophy. Res.*, **108**(D16), 4520.

Krinner, G., & Genthon, C. 1999. Altitude dependence of the ice sheet surface climate. *Geophys. Res. Lett.*, **26**, 2227–2230.

Krinner, G., Boucher, O., & Balkanski, Y. 2006. Ice-free glacial northern Asia due to dust deposition on snow. *Clim. Dynam.*, **27**(6), 613–625.

Krinner, G., Rinke, A., Dethloff, K., & Gorodetskaya, I. 2009. Impact of prescribed Arctic sea ice thickness in simulations of the present and future climate. *Clim. Dynam.*, **in press**.

Mahowald, N., Kohfeld, K., Hansson, M., Balanski, Y., Harrisson, S., Prentice, J., Schulz, M., & Rodhe, H. 1999. Dusts sources and deposition during the last glacial maximum and current climate: a comparison of model results with paleodata from ice cores and marine sediments. *J. Geophys. Res.*, **104**(D13).

Mangerud, J., Astakhov, V., Jakobsson, M., & Svendsen, J.I. 2001. Huge ice-age lakes in Russia. *J. Quaternary. Sci.*, **16**(8), 773–777.

Mercer, J.H. 1970. A former ice sheet in the Arctic Ocean. *Palaeogeogr. Palaeocl.*, **8**, 19–27.

Ohmura, A., Wild, M., & Bengtsson, L. 1996. A possible change in mass balance of Greenland and Antarctic ice sheets in the coming century. *J. Glaciol.*, **9**(9), 2124–2135.

Otto-Bliesner, B.L., Brady, E.C., Clauzet, G., Tomas, R., Levis, S., & Kothavala, Z. 2006. Last Glacial Maximum and Holocene Climate in CCSM3. *J. Climate*, **19**(11), 2526.

Paul, A., & Schaefer-Neth, C. 2003. Modeling the water masses of the Atlantic Ocean at the Last Glacial Maximum. *Paleoceanography*, **18**(3), doi:10.1029/2002PA000783.

Peltier, W.R. 1994. Ice age paleotopography. *Science*, **265**, 195–201.

Peltier, W.R. 2004. Global glacial isostasy and the surface of the ice-age Earth: The ICE-5G (VM2) Model and GRACE. *Annu. Rev. Earth Pla. Sci.*, **32**, 111–149.

Petit, J.R., Jouzel, J., Raynaud, D., Barkov, N., Barnola, J., Basile, I., Bender, M., Chapellaz, J., Davis, J., Delaygue, G., Delmotte, M., Kotlyakov, V., Legrand, M., Lipenkov, V., Lorius, C., Ppin, L., Ritz, C., Saltzman, E., & Stievenard, M. 2001. *Ice core data for 420,000 year, IGBP PAGES/World Data Center for Paleoclimatology Data Contribution Series, NOAA/NGDC Paleoclimatology Program, Boulder CO, USA*.

Peyaud, V. 2006. *Role of the Ice Sheet Dynamics in major climate changes*. Ph.D. thesis, Laboratoire de Glaciologie et de Géophysique de l'Environnement, Université Grenoble I.

Peyaud, V., Ritz, C., & Krinner, G. 2007. Modeling the Early Weichselian Eurasian Ice Sheets: role of ice shelves and influence of ice-dammed lakes. *Clim. Past*, **3**, 375–386.

Polyak, L., Edward, M.H., Coakley, B.J., & Jakobsson, M. 2001. Ice shelves in the Pleistocene Arctic Ocean inferred from glaciogenic deep-sea bedforms. *Nature*, **410**, 453–457.

Rignot, E., Bamber, J.L., van den Broeke, M.R., Davis, C., Li, Y., van de Berg, W. Jan, & van Meijgaard, E. 2008. Recent Antarctic ice mass loss from radar interferometry and regional climate modelling. *Nature Geoscience*, **1**, 106–110.

Ritz, C., Rommalaere, V., & Dumas, C. 2001. Modeling the evolution of Antarctic ice sheet over the last 420,000 years: Implications for altitude changes in the Vostok region. *J. Geophys. Res.*, **106**(D23), 31943–31964.

Spahni, R., Chappellaz, J., Stocker, T., Loulergue, L., Hausammann, G., Kyawamura, G., Flckiger, J., Schwander, J., Raynaud, D., Masson-Delmotte, V., & Jouzel, J. 2005. *Epica Dome C CH4 data to 650 kya BP, IGBP PAGES/World Data Center for Paleoclimatology Data Contribution Series, NOAA/NGDC Paleoclimatology Program, Boulder CO, USA*.

Spreen, G., Kern, S., Stammer, D., Forsberg, R., & Haarpainter, J. 2006. Satellite-based estimates of sea-ice volume flux through Fram Strait. *Annals of Glaciology*, **44**, 321–328.

Svendsen, J.I., Alexanderson, H., Astakhov, V.I., Demidov, I., Dowdeswell, J.A., Funder, S., Gataullin, V., Henriksen, M., Hjort, C., Houmark-Nielsen, M., Hubberten, H.W., Ingolfsson, O., Jakobsson, M., Kjaer, K.H., Larsen, E., Lokrantz, H., Lunkka, J.P., Lysa, A., Mangerud, J., Matiouchkov, A., Murray, A., Moller, P., Niessen, F., Nikolskaya, O., Polyak, L., Saarnisto, M., Siegert, C., Siegert, M.J., Spielhagen, R.F., & Stein, R. 2004. Late Quaternary ice sheet history of northern Eurasia. *Quaternary Sci. Rev.*, **23**(11-13), 1229–1271.

Winckler, G., Anderson, R.F., Fleisher, M.Q., McGee, D., & Mahowald, N. 2008. Covariant Glacial-Interglacial Dust Fluxes in the Equatorial Pacific and Antarctica. *Science*, **320**, 93–96.

Manuscript 5

Colleoni F., Liakka J., Krinner G., Jakobsson M., The Late Saalian period (160 - 140 ka): insight on an unusual glaciation, unpublished.

Contribution:

- Designing the experiments
- Reconstructing the boundary conditions for the 160 ka, the 150 ka and the 140 ka time-slices
- Running the BIOME 4 model
- Analysing the results
- Main part of the writting

Résumé
A la différence des articles présentés précédement qui se concentrent uniquement sur le maximum glaciaire de 140 ka, ce chapitre analyse l'évolution climatique de la fin du Saalien de 160 à 140 ka. A cette période, la calotte Eurasienne était plus large et plus haute que pendant le Dernier Maximum Glaciaire (LGM, 21 ka). L'insolation du mois de Juin dans les hautes latitudes se caractérise par deux extrema glaciaires de 140 et 160 ka, et une augmentation d'insolation très net à 150 ka. Selon la chronologie de la calotte Eurasienne, celle-ci aurait atteint son extension maximum vers 160 ka et survécu jusqu'à 140 ka. Afin de comprendre comment cette calotte a pu survivre au pic d'insolation de 150 ka, nous avons utilisé plusieurs modèles pour simuler l'évolution de la végétation, de la température de l'océan et pour finir, du climat de la fin du Saalien sur les trois snap shots 140, 150 et 160 ka. Les résultats montrent que cette période est principalement dominée par les variations des paramètres orbitaux et répond à la forte excentricité, qui accentuent l'effet de la précession, qui caractérise la fin du Saalien, surtout à 140 ka. De 160 à 150 ka, l'Atlantique Nord reste libre en été alors qu'il en est complètement couvert jusqu'à 40°N à 140 ka. Le climat avant 140 ka est donc plus humide, ce qui contribue à un bilan de masse en surface de la calotte Eurasienne plus élevé qu'à 140 ka. A l'opposé, l'important refroidissement causé par les paramètres astronomiques de 140 ka induit un climat froid et sec dans tout l'hémisphère Nord qui stoppe totalement la fonte de la calotte mais qui réduit également l'accumulation et donc son bilan de masse en surface.

The Late Saalian period (160 - 140 ka): insight on an unusual glaciation

F. Colleoni[1,2] **. J. Liakka**[3] **. G. Krinner**[1] **. M. Jakobsson**[2]

[1]Laboratoire de Glaciologie et Géophysique de l'Environnement, UJF, CNRS, France

[2]Department of Geology and Geochemistry, Stockholm University, 106 91 Stockhlom, Sweden

[3]Department of Meteorology, Stockholm University, 106 91 Stockholm, Sweden

Abstract This work focuses on the climate evolution over the Late Saalian period (160 - 140 ka) over Eurasia. At this time, the Eurasian ice sheet was larger and higher than during the Last Glacial Maximum. June insolation over the high latitudes presents a large fluctuation over this period: two glacial minima toward 160 and 140 ka and a large insolation peak toward 150 ka. From the geological evidence chronology, it seems clear that the large Eurasian ice sheet already reached its maximum extent at 160 ka. To understand how this ice sheet could survive the 150 ka June insolation maximum, we use several numerical models to simulate the evolution of the vegetation cover, the surface ocean temperatures and finally the evolution of the Late Saalian climate over the three time slices 140, 150 and 160 ka. Results show that the Late Saalian climate variations are dominated by orbital forcings, responding to a large eccentricity enhancing the precession effect especially at 140 ka. From 160 to 150 ka, the surface ocean exhibits open water conditions in the North Atlantic during summer while sea surface temperature at 140 ka are clearly colder with a large sea ice extent reaching 40°N in both the North Atlantic and the North Pacific. This corresponds to a milder climate before 140 ka inducing a larger positive surface mass balance despite the 150 ka insolation peak because of larger precipitation rates. On the contrary, the drastic cooling caused by the astronomical forcing at 140 ka leads to a drier climate cancelling ablation and reducing the accumulation over the ice sheet.

Introduction

Recent reconstructions of the Late Quaternary Eurasian ice sheets extent by the Quaternary Environment of the Eurasian North project (QUEEN, Svendsen *et al.*, 2004) suggest that during the Late Saalian (160 - 140 ka), the Eurasian ice sheet extended more southward and eastward than during the entire Weichselian cycle (130 - 14 ka). Compared to the Last Glacial Maximum (≈ 21 ka, LGM), the ice volume over Eurasia was twice bigger implying a higher and larger Late Saalian ice sheet while the global sea level fall recorded for both periods was similar (Waelbroeck *et al.*, 2002; Rabineau *et al.*, 2006). How could such a big ice sheet develop over Eurasia?

In previous studies presented in this thesis, we investigated the impact of the proglacial lakes, dust deposition on snow (Colleoni *et al.*, 2009a), vegetation cover (Colleoni *et al.*, 2009d), sea surface temperature (Colleoni *et al.*, 2009b) and the Canada Basin Arctic ice shelf (Colleoni *et al.*, 2009c) on the Northern Hemisphere climate and on the surface mass balance of the Late Saalian glacial maximum Eurasian ice sheet (140 ka). However these studies only focus on the Late Saalian glacial maximum and only consider the impact of regional factor on the relative stability of this ice sheet during this glacial maximum. In those studies, the Late Saalian Eurasian ice sheet surface mass balance is often unsensitive to regional changes except to vegetation changes and proglacial lakes impact when located the vicinity of the ice margins. A close examination of the evolution of the June summer insolation at high latitudes (Figure 6.1) and the assumption that this ice sheet reached its maximum extent before 140 ka as suggested by Svendsen *et al.* (2004), rises a new question: how could this large ice sheet survive the 150 ka insolation peak? In this study, we investigate the climate evolution over the entire Late Saalian period.

In the glacial chronology, the first glacial maximum of the Late Saalian is the Denthre substage (max ≈155 ka) during which the Eurasian ice sheet reached its maximum extent. This stage is followed by the Treene substage marked by a retreat of the ice sheet northward from its largest extent. Finally, the ice sheet extended again dur-

ing the Warthe substage whose maximum occurred toward 143 ka (Ehlers *et al.*, 2004). The Bering Strait is closed and the Arctic continental shelves are emerged due to the low sea level (≈ -110 to -150 m a.s.l.). The only remaining open strait is the deep but narrow Fram Strait. During this period, an Arctic ice shelf also developed in the Canada Basin (Jakobsson, in prep.; Colleoni *et al.*, 2009c).

The nature and amplitude of a glacial maximum of the ice sheet configuration at a given time depends on the evolution of climate prior to the glaciation. It is therefore important to account for the climate state before the Late Saalian glacial maximum (140 ka). Compared to the LGM (and to the 20 kyrs preceding the glacial maximum), greenhouse gases are almost similar but astronomical parameters are different (Table 6.1 and Figure 6.1). Before the LGM, the summer insolation in high latitudes at 40 ka is larger than at 160 ka while the summer insolation at 30 ka is similar to that at 150 ka (Figure 6.1). This results from the precession cycle (≈23 kyrs) and larger eccentricity. The summer insolation, during the 20 kyrs prior to the LGM, is almost constant and larger than that preceding the Late Saalian and the eccentricity is weaker which reduces the effect of the precession during the 40-21 ka time period. This influences the ice sheet growth (Imbrie *et al.*, 1993; D., 1998).

Compared to the LGM, the Late Saalian period is characterised by a high eccentricity that enhanced the effect of precession and a high obliquity increasing the seasonal contrasts (Table 6.1). 160 ka and 140 ka represent the two glacial substages of the Late Saalian period. The perihelion occurs during the boreal winter for both periods respectively (Table 6.1). However, the eccentricity at 160 ka is smaller than at 140 ka and the difference in precession influences the length of the seasons (Table 6.2). At 150 ka, summer insolation in the high latitudes is stronger than at 140 ka (Figure 6.1). At 150 ka, similarly to 160 ka, eccentricity is reduced compared to that of 140 ka and obliquity presents the smallest value of the entire period. Perihelion occurs close to summer solstice contrary to the two other time-slices (Table 6.1).

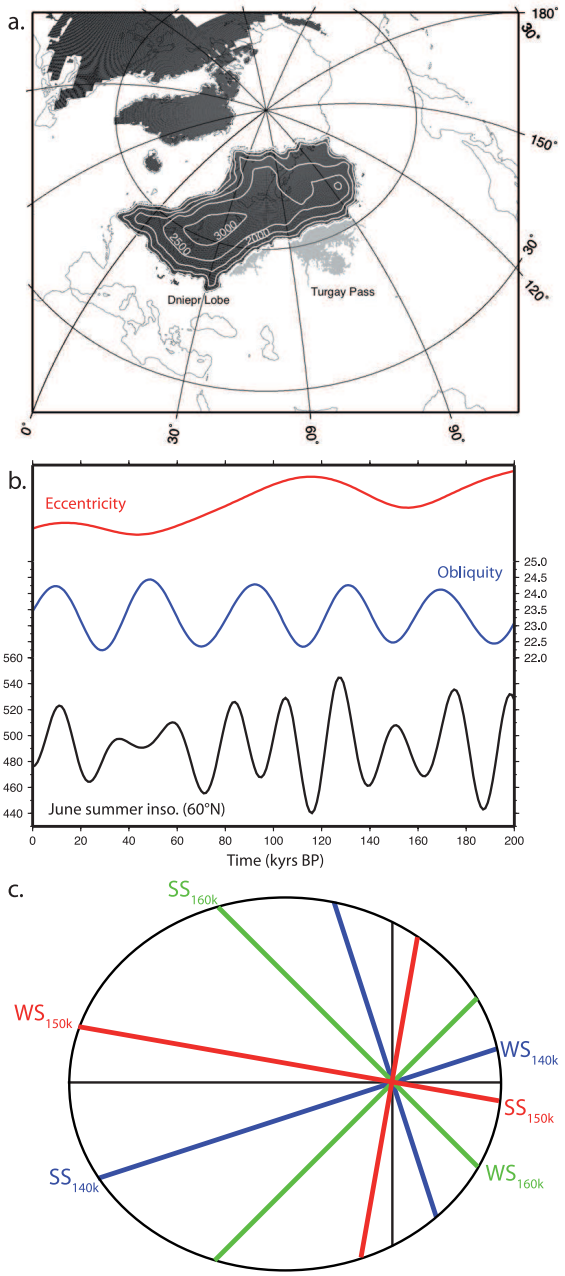

Figure 6.1: a. Late Saalian Eurasian ice topography. Ice sheets are in black while proglacial lakes are in gray (reconstructed from Mangerud *et al.* (2001) and filled up to the Turgay Pass). b. Orbital parameters from Berger & Loutre (1991). Summer insolation at 60°N is in W.m^{-2}. We present the 41 kyrs obliquity cycles (blue) and the 400 kyrs eccentricity cycles (red). c. Positions of the seasons for 140, 150 and 160 ka along the Earth revolution around the Sun, SS and WS stand for Summer and Winter Solstice respectively. Spring equinox has been fixed at March 21st.

At 160 ka, summer and fall are the longest seasons with a larger downward solar radiation at top of the atmosphere of about 30 W.m^{-2} in the high latitudes (Figure 6.2c), as a consequence of the perihelion occurring at the middle of winter (Table 6.2). However, the season lengths are similar to the LGM since for this latter period, perihelion occurs after the winter solstice (Table 6.1). At 150 ka, contrary to 140

	-160 ka	-150 ka	-140 ka	-40k	-30k	-21k	Present-day
Eccentricity	0.028	0.029	0.033	0.014	0.017	0.019	0.017
Obliquity	23.43	22.48	23.42	23.60	22.25	22.95	23.45
Date of perihelion	Feb. 7	June 28	Dec. 6	March 31	June 18	Jan. 17	Jan. 4
CO_2 (ppm)	183	197	192	209	205	194	334
CH_4 (ppb)	383	426	401	537	481	354	1477

Table 6.1: Orbital parameters (Berger & Loutre, 1991), CO_2 (Petit *et al.*, 2001) and CH_4 (Spahni *et al.*, 2005) concentration value for the Late Saalian (-160 k to -140 ka), the end of MIS 3 (-40k to -30k), the LGM (-21k) and present-day.

ka, summers is close to the perihelion causing shorter but warmer springs and summers and a larger solar radiation by about 40 W.m^{-2} in the 50 - 70°N band (Figure 6.2b). At 140 ka, summer is close to the aphelion inducing longer and colder springs and summers.

Comparison between LGM and 140 ka shows that during the boreal spring and summer, solar radiation at the top of the atmosphere is weaker at 140 ka due to the larger eccentricity strengthening the precession impact (summer occurs at aphelion in both cases) (Figure 6.2d). Furthermore, during boreal fall and winter, solar radiation is stronger at 140 ka. Compared to LGM, 150 ka presents stronger spring and summers because the 150 ka summer occurs at perihelion while it occurs near the aphelion during the LGM (Figure 6.2e). Consequently, fall and winter are also stronger at 150 ka. Finally, at 160 ka, the orbital effect is similar to 150 ka because summer occurs closer to the Sun while winter occur farther than at the LGM (Figure 6.2f).

To summarise, at 140 ka, the larger eccentricity may cause cooler and longer spring and summer (perihelion occurring at December 6). At 150 ka, summer occurs at perihelion which might explain the warmer but shorter spring and summers (perihelion occurring at June 28). Finally at 160 ka, spring and summers are warmer and shorter than at 140 ka because the distance to the sun is smaller (perihelion occurring at February 7).

In the following, we address the climatic impact of simulated sea surface temperatures, simulated vegetation cover and orbital forcings over the entire Late Saalian period 160 -140 ka, using the LMDZ4 (Hourdin *et al.*, 2006) Atmospheric General Circulation Model (AGCM), the simplified coupled GCM Planet Simulator (Fraedrich *et al.*, 2005) and the equilibrium vegetation model BIOME 4 (Kaplan *et al.*, 2003). We numerically equilibrate all the boundary conditions in agreement with the Late Saalian climate. We then propose a synthesis of all the results and discuss in depth the orbital parameters which are certainly the key factors of the large ice volume over Eurasia during this period. Finally we propose some perspective to carry on with the study of the Late Saalian glaciation.

Methods and settings

In this work, we combine the approaches used in the previous studies to compute the effect of dust deposition, open water surfaces, vegetation and oceanic surface conditions, insolation, the dynamics of vegetation cover and the surface ocean temperatures (Colleoni *et al.*, 2009a,d,b, submitted). Since our interest focuses on the entire Late Saalian time period (160 -140 ka), we performed snapshots corresponding to the three summer insolation minima and maxima respectively observed in Figure 6.1 : 140, 150 and 160 ka.

Numerical models

Late Saalian atmospheric simulations

Climate simulations are performed using the LMDZ4 atmospheric general circulation model (Hourdin *et al.*, 2006; Krinner, 2003; Krinner *et al.*, 2006). The model was run with 96×72 grid cells and with 19 vertical layers. The horizontal resolution is irregular, varying from 100 km in Eurasia (at 65°N/60°E) to 550 km at the antipodes of this point. As far as dust is concerned, LMDZ4 only takes into account the dust content of snow whose radiative effect prevails on that induced by the atmospheric dust content over snow. The inferred dust content of the

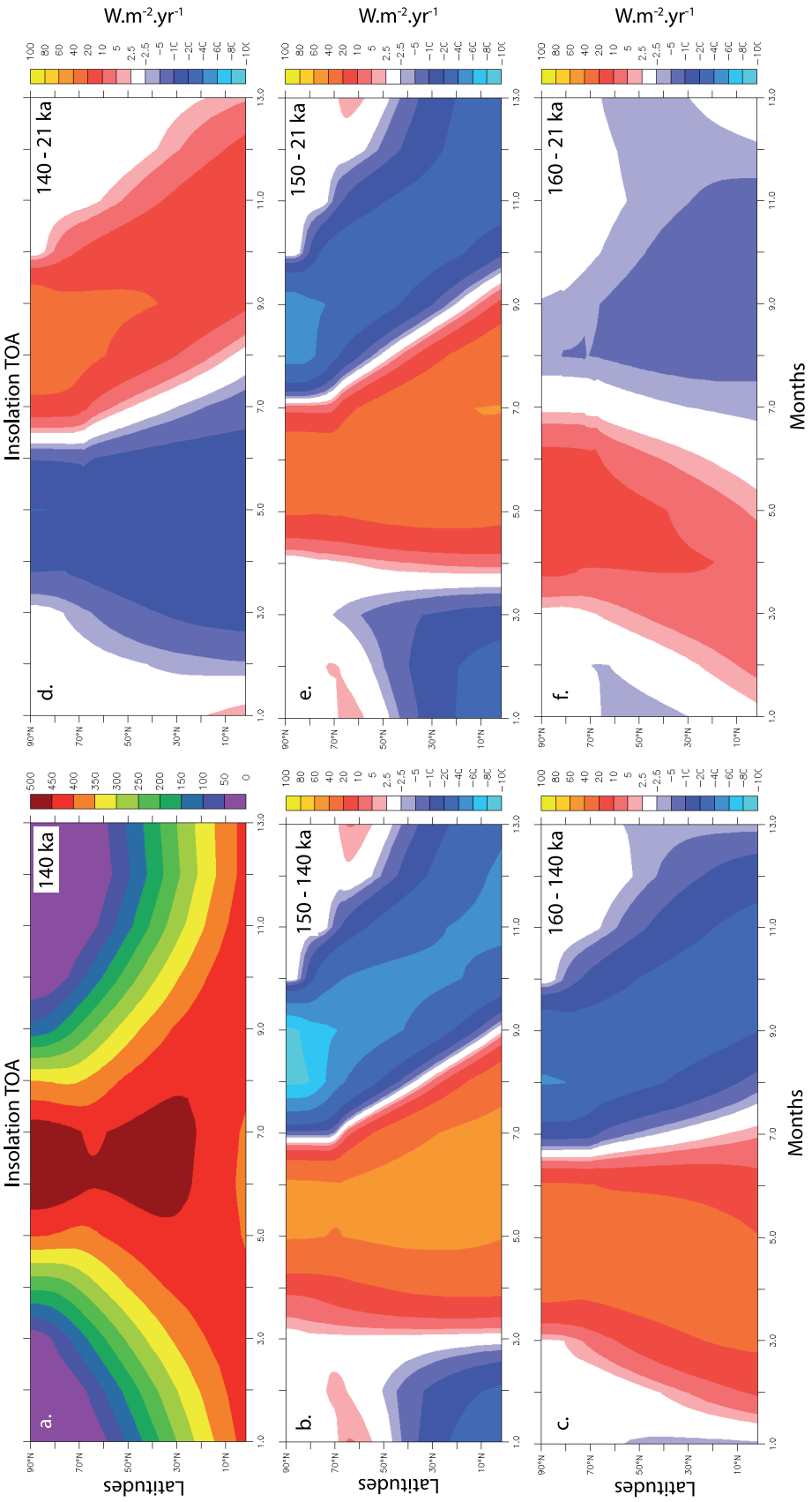

Figure 6.2: Annual insolation cycle at the top of the atmosphere ($W.m^{-2}$) in the Northern Hemisphere. a. for the 140 ka; b. and c. difference between 150 ka and 140 ka, 160 ka and 140 ka respectively; d. e. and f. difference between the three time periods and the LGM (21 ka).

snow, and the resulting snow albedo are calculated following Krinner *et al.* (2006).

	LGM	140 ka	150 ka	160 ka
Winter	93	90	91	89
Spring	89	97	96	88
Summer	90	92	92	93
Fall	94	86	87	94

Table 6.2: Length (in days) of the paleo-climatic seasons at LGM, 140, 150 and 160 ka following the method of Berger & Loutre (1991).

Simulating the Late Saalian SST

To compute the Late Saalian surface ocean, we use the Planet Simulator (PLASIM) general circulation model of intermediate complexity (Fraedrich *et al.*, 2005). The central part of PLASIM consist in an atmospheric GCM, which is based on the moist primitive equations representing conservation of momentum, mass and energy. The equations are solved on a Gaussian grid, in the horizontal direction, corresponding to a T42 resolution (128×64), and on 10 vertical sigma levels. Differently from the LMDZ4, PLASIM does not account for the effects of proglacial lakes and dust deposition on snow. PLASIM is interactively coupled to a mixed-layer ocean (mixed-layer set to 50 m) and to a zero-dimensional thermodynamic sea ice model. In our experiments, the mixed layer is forced by prescribed values of the oceanic heat transport parametrized as a flux correction as follows:

$$Q_{c_2} = \rho_w c_w h_{mix} \frac{T_{mix_c} - T_{mix}}{\tau_T} \qquad (1.14)$$

where c_w is the specific heat of sea water, ρ_w corresponds to the density of sea-water, h_{mix} stands for the mixed-layer, T_{mix} is the temperature of the mixed-layer and the time scale τ_T equals 50 days. This method to predict SST has been previously used by Romanova *et al.* (2006, 2005) to investigate the effect of ocean heat fluxes on glacial climates. In the present study, we assume that the mixed layer is influenced in a comparable way during the LGM and the Late Saalian periods and that the flux corrections calculated for the LGM can be applied to the Late Saalian surface ocean.

To calculate the oceanic heat fluxes and the flux correction for the sea ice, we thus performed

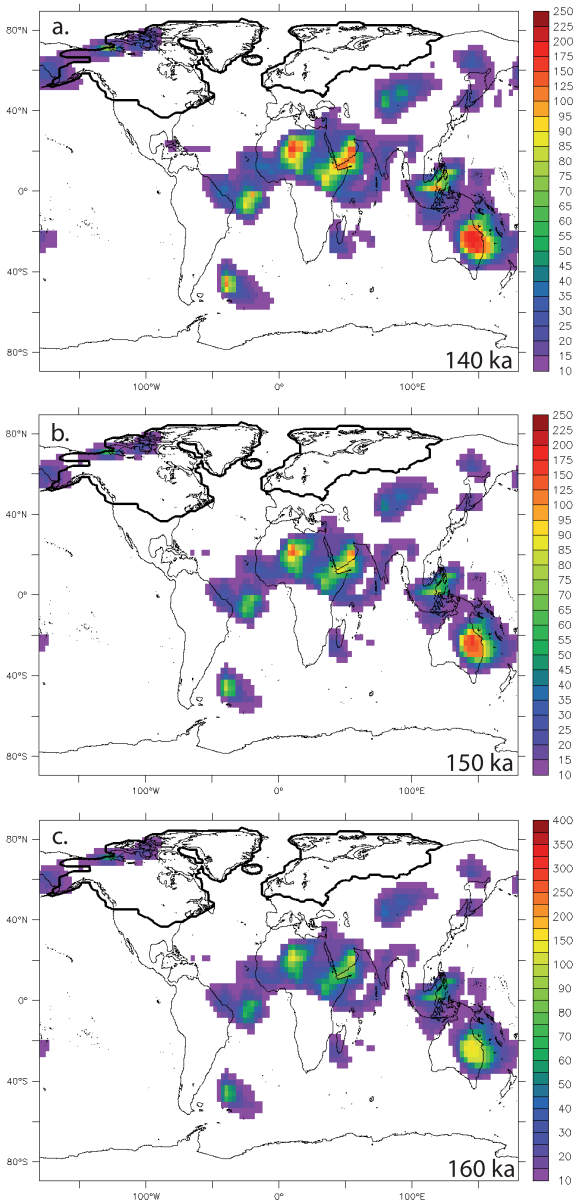

Figure 6.3: Dust deposition map (g.m^{-2}.yr^{-1}) for a. 140 ka, b. 150 ka and c. 160 ka adapted from Mahowald *et al.* (1999) LGM dust deposition map following the procedure described in the methods.

an LGM control simulation with prescribed sea surface conditions of Paul & Schaefer-Neth (2003). We choose to base the calculation on Paul & Schaefer-Neth (2003) SST since this global reconstruction is in better agreement with the overall recent marine sediment cores analysis than that of CLIMAP (1984). In the LGM control run, we use ICE-5G topography and coastlines (Peltier, 2004). Vegetation is prescribed as the fraction of forest extracted from the LGM vegetation map of Crowley (1995), the CO_2 concentration is set to 194 ppm (Petit *et al.*, 2001) and the orbital parameters are calculated for 21

ka according to Berger & Loutre (1991). The control simulation is performed for 21 model years and the first model year is discarded as spin-up. The 20 years monthly averaged surface heat fluxes are assumed to equal the oceanic heat fluxes. The sea ice flux correction corresponds to the heat flux required to relax the height of the ice-surface to its climatological value, on a time-scale given by a relaxation constant set to 1350 years.

The fluxes calculated for the LGM control run are thereafter used to simulate the Late Saalian climate conditions with the ocean and sea ice modules switched on. Orbital parameters are adjusted to 140 ka, CO_2 concentration is set to 192.3 ppm and vegetation is prescribed similarly to that of the LGM control run. The simulation is performed for 50 model years. Sea surface equilibrium is reached after 25 model years and the last 15 years are used for analysis.

Calculation of a steady-state vegetation cover

New vegetation maps are computed with BIOME4 (Kaplan *et al.*, 2003). BIOME4 is a coupled carbon water flux model that predicts the global equilibrium vegetation distribution, structure and biogeochemistry and determines the seasonal maximum leaf area index. It is particularly adapted for simulating "cold" vegetation types. In BIOME4, twelve plant functional types have been implemented and correspond to thirty physiologically distinct classes of vegetation ranging from cushion forbs to tropical rain forest (Kaplan *et al.*, 2003).

LMDZ4 and BIOME4 were asynchronously coupled. We first forced LMDZ4 using the existing LGM vegetation map by Crowley (1995) to obtain an initial Late Saalian climate separately for 140, 150 and 160 ka. Following the method in Colleoni *et al.* (2009d), new vegetation maps were subsequently computed by forcing BIOME4 with the monthly mean and minimum daily temperatures, the monthly mean precipitation and the cloud cover fraction obtained from the previous LMDZ4 simulations. Steady state was obtained after three iterations.

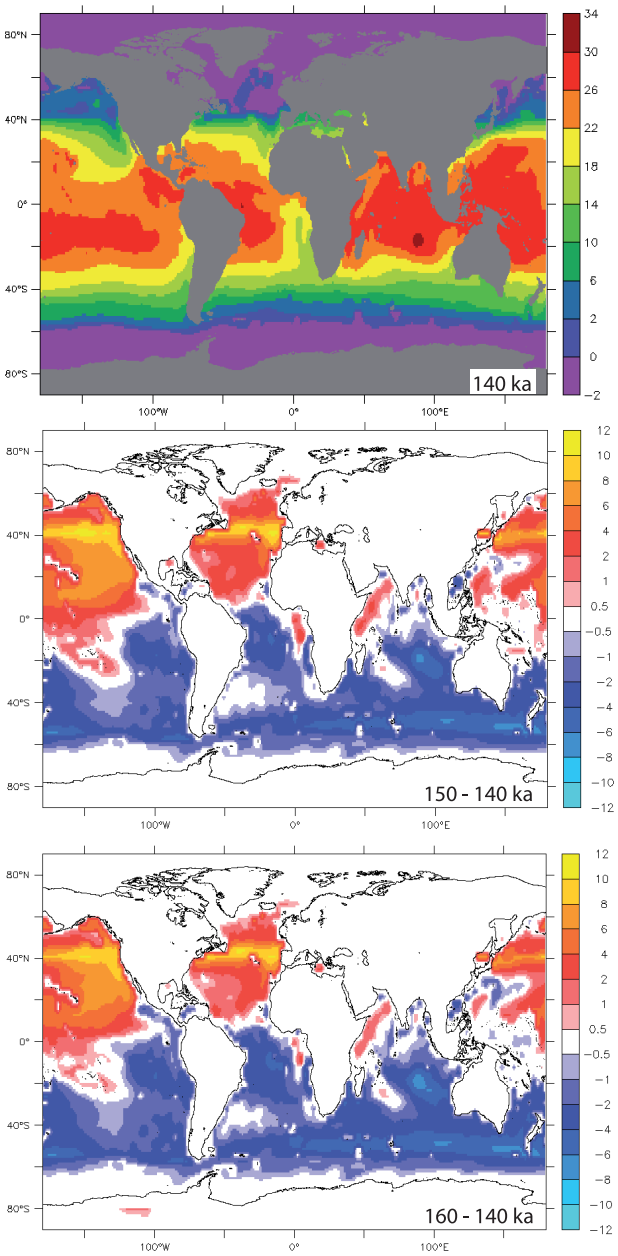

Figure 6.4: Simulated mean annual sea surface temperatures (°C): a. for simulations FULL140 (140 ka, after Colleoni *et al.* (2009b, submitted)); b. difference between FULL150 (150 ka) and FULL140 (this study); c. difference between FULL160 (160 ka) and FULL140 (this study).

Late Saalian boundary conditions

Except for the Eurasian region, we used the LGM global ice topography and ice sheet extents provided by Peltier (2004), since no global reconstructions exist for the Late Saalian and assuming that the differences between the Late Saalian glacial maximum and LGM geographies far from our region of interest are sufficiently small to not critically influence our results. The Eurasian Late Saalian maximum topography was computed with the GRISLI ice model (Ritz *et al.*, 2001; Peyaud, 2006; Peyaud *et al.*, 2007) using the reconstructed ice limits from Svendsen *et al.* (2004) and taking into account lithospheric deflection (Figure 6.1). Ice dammed lakes, created

from a blocking of the Yenissei and Ob rivers by the Saalian ice sheet and by the melt water from the ice sheet, have been reconstructed according to the methods of Mangerud *et al.* (2001).

In the previous studies presented in this thesis, the ice topography and proglacial lakes were attributed to the peak Saalian, 140 ka. Here, we did not re-adapt the ice topography to the 150 and 160 ka time-slices. Similarly, we did not remove proglacial lakes since the ice sheet was already built at 160 ka and did probably not retreat totally during the insolation peak of 150 ka.

	Time (ka)	Vegetation
REF140	140	Crowley
REF150	150	Crowley
REF160	160	Crowley
FULL140	140	BIOME4
FULL150	150	BIOME4
FULL160	160	BIOME4

Table 6.3: Summary of the LMDZ4 simulations carried out in this work. "Crowley" refers to the Crowley (1995) LGM vegetation map used to force the reference simulations, while BIOME4 refers to as the new simulated vegetation cover using the BIOME 4 vegetation model (Kaplan *et al.*, 2003). All the simulations presented in this table include the effect of proglacial lakes and dust deposition on snow and were forced using the new Late Saalian SST calculated with Planet Simulator (Fraedrich *et al.*, 2005).

Following the method to adapt dust deposition on snow at 140 ka, (Colleoni *et al.*, 2009a), we reconstructed dust deposition for 150 and 160 ka. Since no Late Saalian dust reconstruction have been simulated, we use the Mahowald *et al.* (1999) LGM dust deposition map. We then apply a ratio of ≈70% at 150 ka and ≈50% at 160 ka based on the EPICA Dome C, East Antarctica ice core dust concentration (Delmonte & coauthors, 2004) to the LGM dust deposition map. Winckler *et al.* (2008) recently showed that during the late-Pleistocene glacial cycles, dust fluxes in both hemisphere had a common response to global climate change since MIS 7. Dust distribution for the three snap-shots are displayed in Figure 6.3.

Finally, orbital parameters have been set according to Berger & Loutre (1991) and greenhouse gas (GHG) concentrations have been specified according to Vostok (Petit *et al.*, 2001) and EPICA Dome C (Spahni *et al.*, 2005) ice core concentration records.

AGCM Simulations

For each time-slice at 140, 150 and 160 ka, one 21 years LMDZ4 snap-shot forced by the simulated SST has been performed, the first year being discarded as spin-up. Simulations REF140, REF150 and REF160 have been carried out to get a reference Late Saalian climate in agreement with SST and orbital parameters. Those reference climates were then used to force

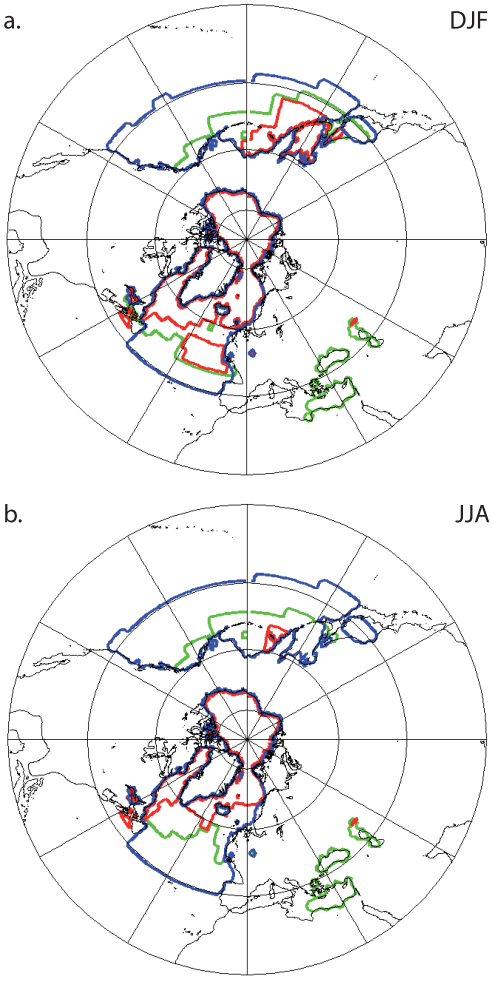

Figure 6.5: Simulated winter (DJF) and summer (JJA) sea ice cover for 140 ka (blue), 150 ka (red) and 160 ka (green).

BIOME 4 to get new vegetation maps that in turn have been finally used for a second 21-year run with LMDZ4. In total, three iterations of 21 years each have been carried out for each time period, the first year being discarded as spin-up. Finally the last climate states FULL140, FULL150 and FULL160 result from the new simulated SST

and the steady-state Late Saalian vegetation (Table 6.3).

The annual surface mass balance of the ice sheet is evaluated according the temperature index method of Ohmura *et al.* (1996). In this method, surface ablation is diagnosed when mean summer surface air temperature (T_{JJA}), recalculated on a fine resolution grid with altitude-correction, exceeds a prescribed threshold of -1.8°C. The total ablation (in kg.m^{-2}.yr^{-1}) is then calculated as:

$$A = 514°C^{-1} \times T_{JJA} + 930 \qquad (1.15)$$

where T_{JJA} is in °C. We downscale the GCM surface air temperature to a 20-km grid by applying a 5.5°C.km^{-1} summer temperature correction to account for altitude changes (Krinner & Genthon, 1999; Abe-Ouchi *et al.*, 2007). The surface mass balance B is then calculated as:

$$B = P_S - E - A \qquad (1.16)$$

with P_S and E as solid precipitation and evaporation respectively.

Results: synthesis over the 160 - 140 ka time period

Simulated Sea Surface Temperatures

Sea surface temperatures (SST) for both 150 ka and 160 ka have been simulated following Colleoni *et al.* (2009b, submitted). Simulated SST at 140 ka exhibit cold mean annual temperatures in the high latitudes, negative as far South as Spain (Figure 6.4a). The 140 ka SST present a larger inter-hemispheric asymmetry than at 150 ka and 160 ka due to the effect of the precession enhanced by the large eccentricity (Raymo *et al.*, 2006). As shown by Khodri *et al.* (2005), this contributes to the expansion of the sea ice cover southward and to the migration of the Polar front and the subtropical gyre further to South (Figure 6.5). On the contrary, due to a weaker orbital effect and to a more favourable precession configuration, the 150 ka and 160 ka surface ocean in the Northern Hemisphere are warmer by about 8°C than at 140 ka because the sea-ice cover does not extend as much southward as at 140 ka.

The 150 ka sea ice cover is almost similar to that of the LGM (Paul & Schaefer-Neth, 2003).

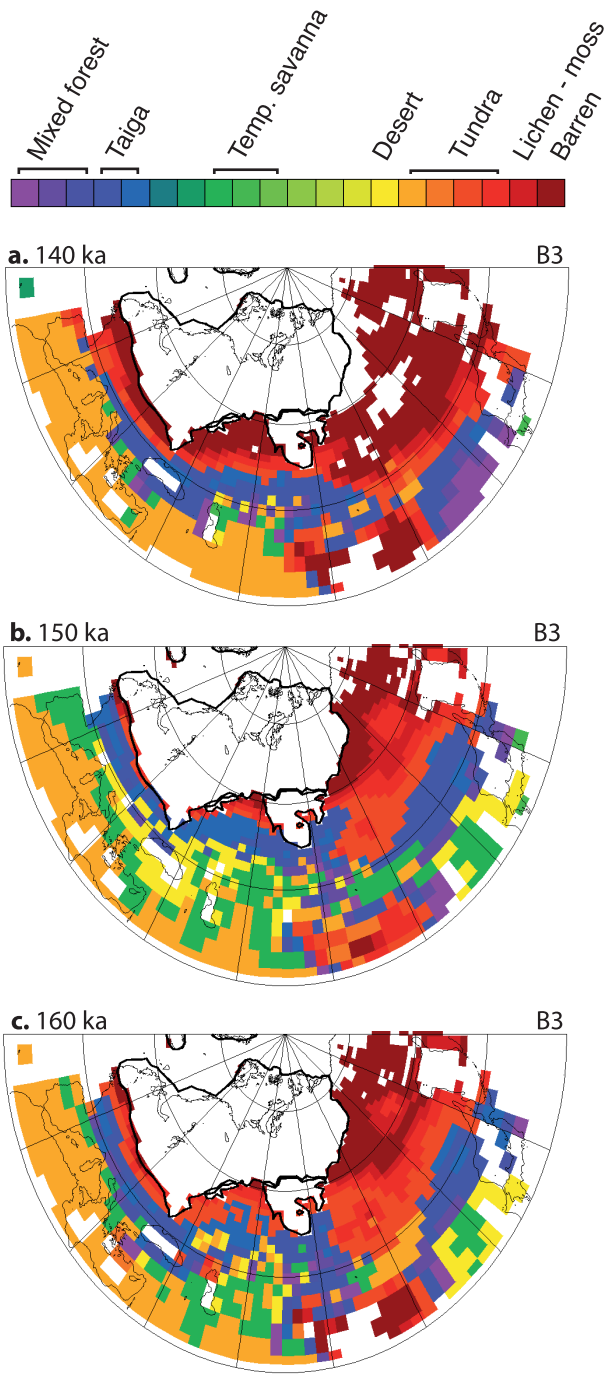

Figure 6.6: Simulated vegetation cover using the BIOME4 model (Kaplan *et al.*, 2003) for the entire Late Saalian period (140, 150 and 160 ka). Frames correspond to the third and final BIOME 4 iteration (B3). White areas over North-Eastern Siberia represent permanent snow covered regions.

At 160 ka, which corresponds to a glacial substage, the sea ice cover edge is intermediate between that of 140 ka and 160 ka during both winter and summer (Figure 6.5).

Differences in SST between 150 ka and 160 ka are small because even if the perihelion occurs at June 28 at 150 ka, the obliquity is at its

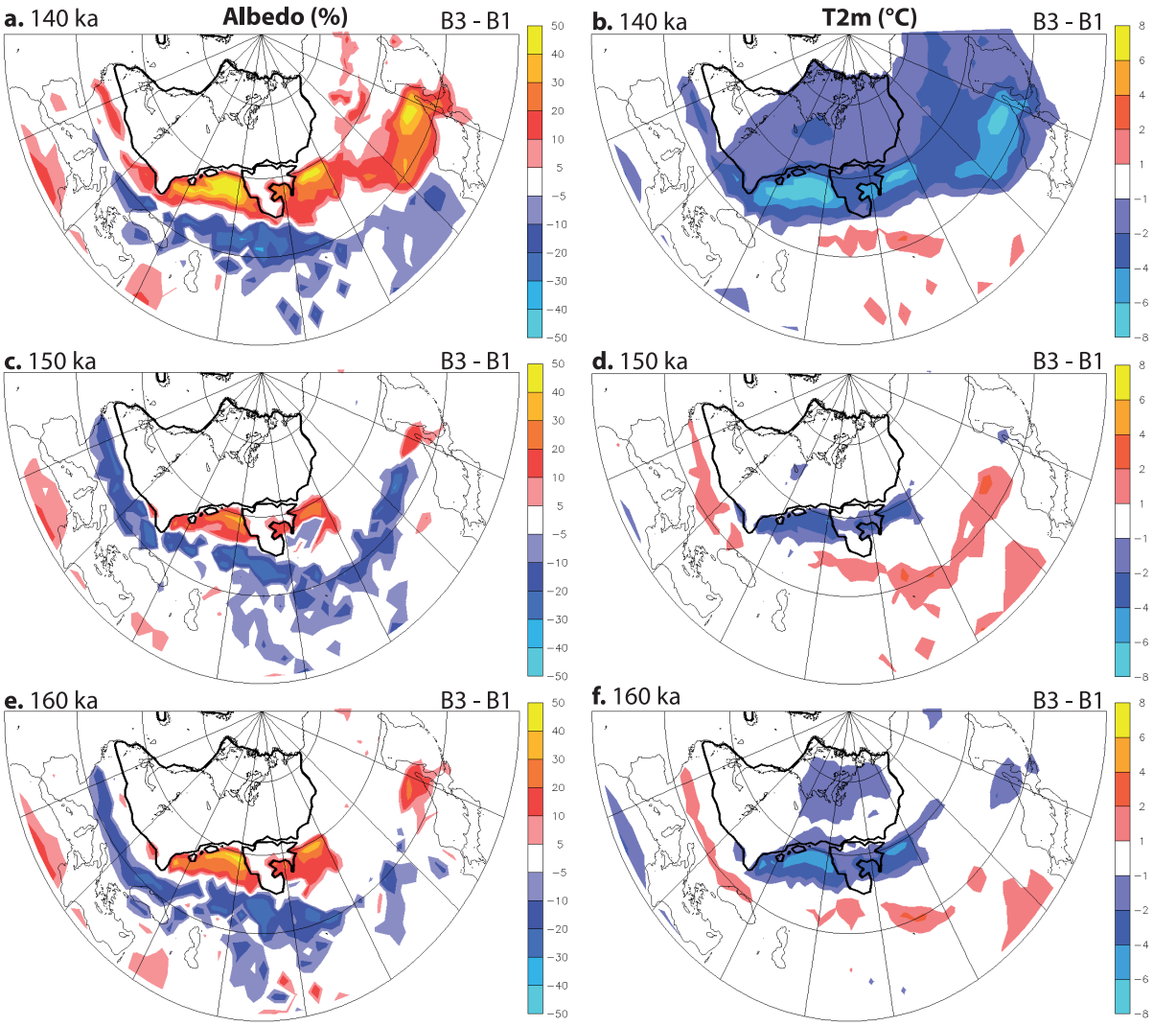

Figure 6.7: Differences in simulated mean annual albedo (a,c,e) and air surface temperature at 2 meters (T2m, b,d,f) for the entire Late Saalian period between the first and the last LMDZ4 iterations (corresponding to vegetation iterations B1 and B3 respectively, Figure 6.6).

minimum in the cycle, which reduces the effect of precession. On the contrary, at 160 ka, the obliquity is at an intermediate position, which enhances summer relatively to 150 ka even if perihelion occurs at February 7. The larger difference is observed during fall, when the 150 ka SST are warmer by 2°C. In the Pacific, the sea ice cover remains essentially confined to the Bering and Okhotsk Seas during both 150 ka and 160 ka. This is not the case at 140 ka since the sea ice cover extends until 40°N.

Vegetation cover

Following Colleoni *et al.* (2009d), a steady-state vegetation cover in agreement with the boundary conditions of each time-slice has been computed. In total three vegetation iterations have been performed for each snap-shot and only the difference between the first and the third BIOME 4 iterations are further discussed (Figure 6.6 and 6.7). The evolution of vegetation between the first and the last iteration is larger at 140 ka since the orbital configuration is more extreme than at 150 ka and 160 ka. For the two latter periods, vegetation is almost in equilibrium with LMDZ4 climate at the first BIOME 4 iteration.

At 140 ka, the barren soils extend over the various iterations due the continuously accumulating snow over Siberia and Eurasia. In the last iteration, almost all Siberia and the main part of the Russian plains are constituted by barren soils. Tundra retreated southward while the tree line of the taiga and the mixed forest remains identical (Figure 6.6a and b).

At 150 ka, barren soils are confined to the

Northern and Eastern Siberia. Tundra is limited to Siberia and to the ice sheet margins. However, taiga is more developed than at 160 ka and 140 ka and almost reaches the ice sheet margins in Western Europe and in Russia due to the warmer summer shifting northward the 10°C isotherm of importance for the growth of trees (Korner, 1998). Desert and temperate savanna are also more developed around the Black Sea and the Caspian Sea.

At 160 ka, barren soils constitute the main part of Eastern Siberia. Tundra is more developed in the Russian Plains and in Western Europe than at 150 ka since the climate is slightly colder. Taiga and mixed-forest are less developed in Western Europe and in the Russian Plains than at 150 ka and compared to 140 ka, it is quite similar.

Between the first and the last (B3) iteration, the largest climatic anomaly observed occurs at 140 ka and 160 ka due to the progression of barren soils. This increases the albedo up to 50% in the Russian plain, and up to 30% in southern Siberia (Figure 6.7a and f). The albedo causes a regional cooling (also due to an increase of snow accumulation) over these regions by about 8°C spreading over the entire Siberia and over the ice sheet (2°C). This effect has been previously reported in Colleoni *et al.* (2009d) and is weaker during the warmer 150 ka interstadial (Figure 6.7c).

Insight on the climate of the Late Saalian

In this section, since 140 ka is the coldest period of the entire Late Saalian and since all the previous studies Colleoni *et al.* (2009a), Colleoni *et al.* (2009d), Colleoni *et al.* (2009b) and Colleoni *et al.* (2009c) focus on this peak, we will consider the 140 ka climate (simulation FULL140, Table 6.3) as the reference for comparison with the climate state at 150 ka and 160 ka (simulations FULL150 and FULL160 respectively) in the Northern Hemisphere. We thus first present the 140 ka main climate variables. Then we describe the evolution of the climate over the entire Late Saalian period chronologically from 160 ka to 150 ka.

The peak Late Saalian glacial maximum climate (140 ka)

During winter (DJF), the Northern Hemisphere 30 - 90°N mean temperature is ≈ -50°C and down to ≈ -60°C over the Arctic and the Eurasian ice sheet (Figure 6.8a). Over these regions precipitation is weak (less than 200 mm.yr^{-1}) whereas over the Eastern North Atlantic and the North Pacific it exceeds 1800 mm.yr^{-1} (Figure 6.8b). During summer, temperature is -30°C over the Arctic regions, warms up to -10°C over Siberia and reaches 20°C over Southern Eurasia (Figure 6.8d). Compared to winter precipitation, summer precipitation are stronger over the ice sheets but less intense over the North Atlantic and the North Pacific oceans (Figure 6.8e).

	FULL140	**FULL150**	**FULL160**
Tot. pre.	226	329	289
Snow	226	310	282
Evap	33	53	44
Abl.	0	15	5
SMB	**193**	**243**	**233**

Table 6.4: Mean annual surface mass balance (SMB) values and components for simulations FULL140, FULL150 and FULL160, in kg.m^{-2}.yr^{-1}. "Abl." stands for Ablation whereas "Tot. pre." corresponds to Total precipitation.

The mean annual surface mass balance (SMB) over the Eurasian ice sheet at 140 ka is everywhere positive (193 kg.m^{-2}.yr^{-1}) and there is no net ablation, even during summer (Table 6.4). The main areas of accumulation are located all along ice sheet margins with SMB larger than 500 mm.yr^{-1} up to 2000 mm.yr^{-1}. This is due to the moisture fluxes coming from the Atlantic that represents the main moisture source for the Eurasian ice sheet (Figure 6.8c and f). The central part exhibits an SMB lower than 70 mm.yr^{-1} because of low precipitation rates.

Prior to the 140 ka glacial maximum: the 160 ka and 150 ka climate snap-shots

At 150 ka, perihelion occurs in summer and consequently insolation over high latitudes is stronger than at 140 ka. This results in large positive temperature anomalies over the Northern Hemisphere (Figure 6.10b). Warming is about 5°C over the Arctic Ocean, about 15°C over Siberia and about 6°C over Eurasia and the Eurasian ice sheet. The difference in sea ice cover, which is less extended at 150 ka than at

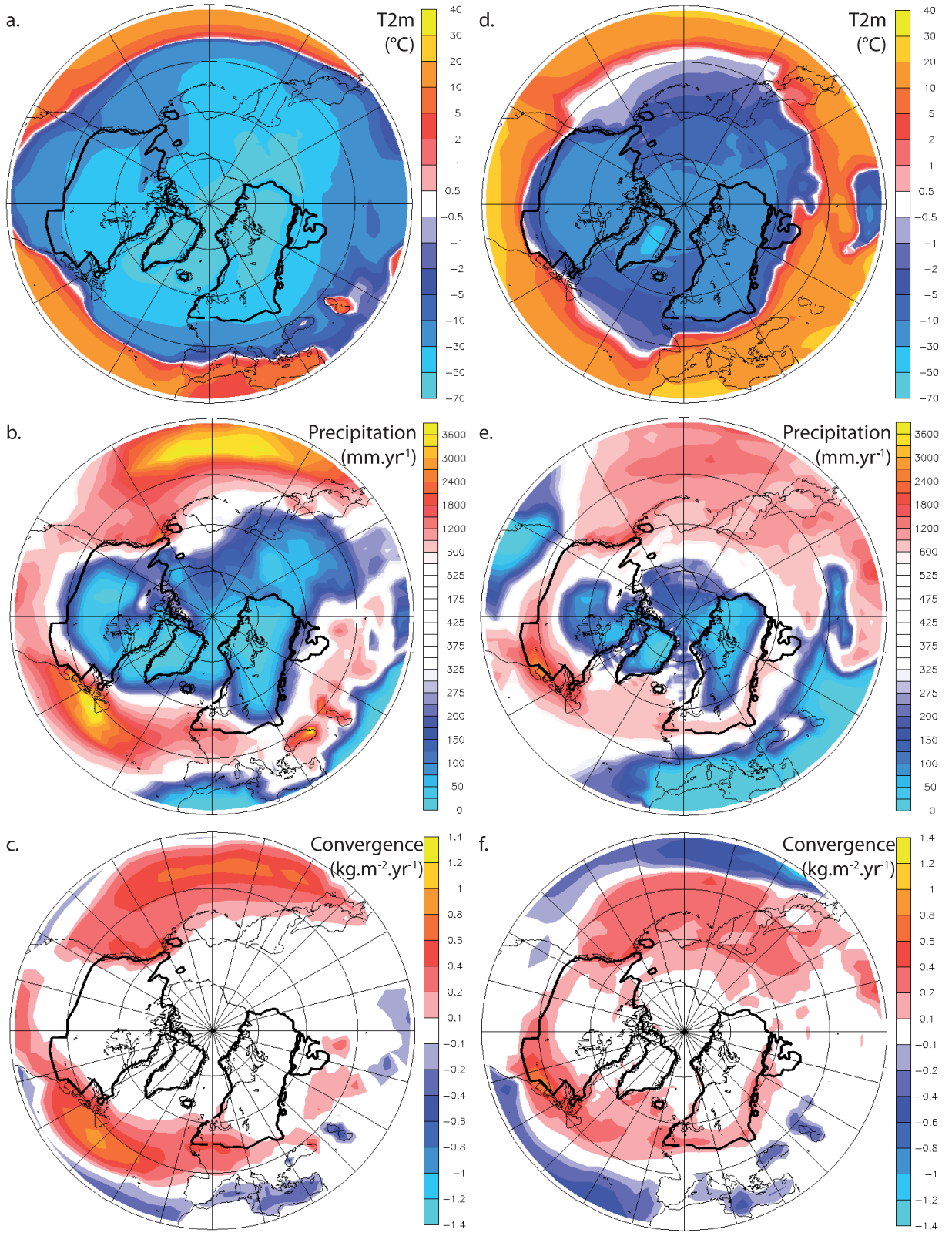

Figure 6.8: Late Saalian glacial maximum climate (140 ka). Winter climate (DJF): a. air surface temperature (T2m), b. total precipitation (mm.yr^{-1}) and c. convergence of the moisture fluxes (kg.m^{-2}.yr^{-1}). d e, and f same as a,b,and c but for summer (JJA).

140 ka (Figure 6.5) causes a regional warming of 30°C over the North Atlantic and in the North Pacific. However, despite this large difference in temperature over the Arctic region, mean annual values are still negative at 150 ka (-10°C) The Northern Hemisphere warming affects the

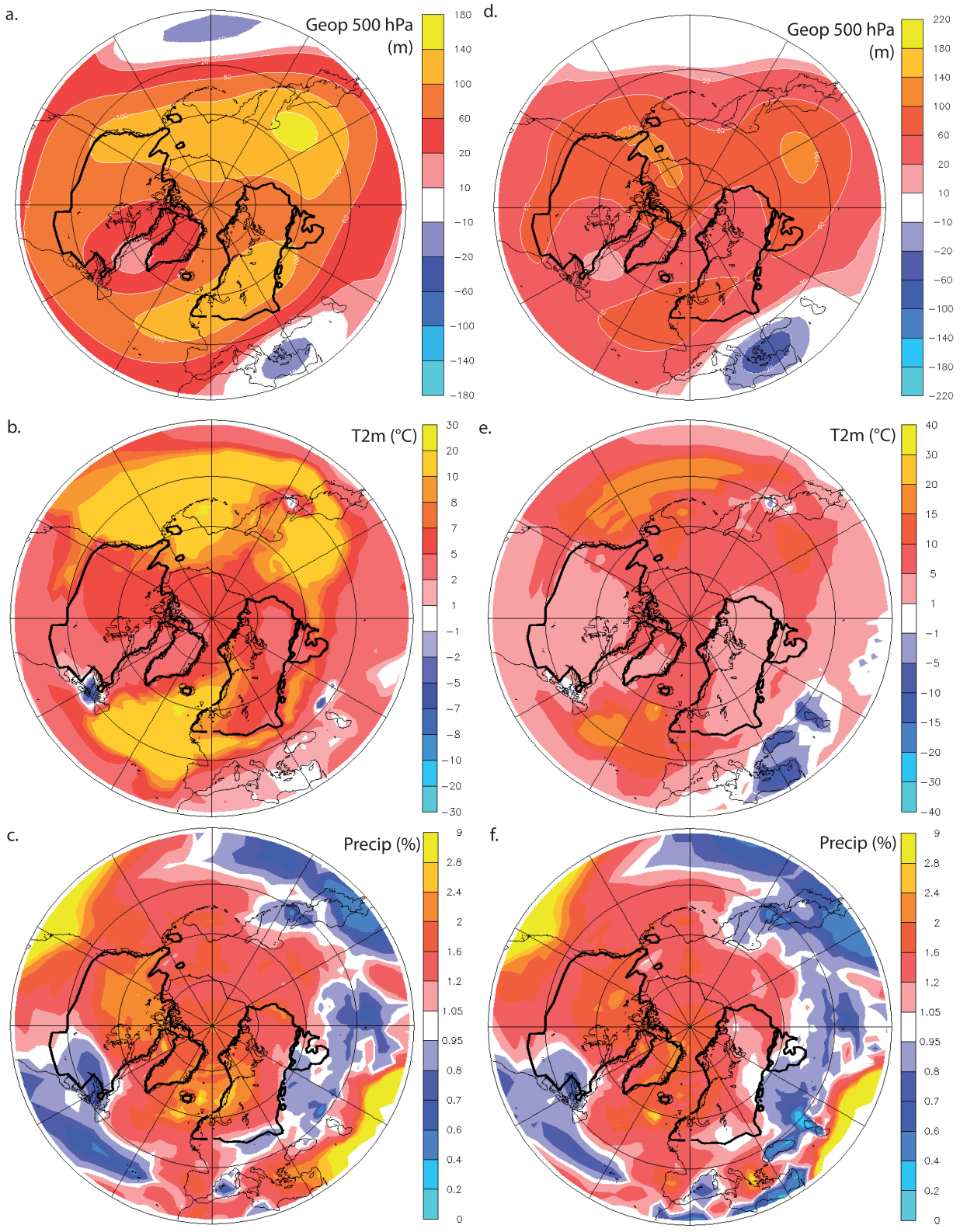

Figure 6.10: Difference in mean annual 500 hPa geopotential height (m), air temperature (°C) and precipitation ratio (%) between FULL150 and FULL140 (a., b., c.) and between FULL160 and FULL140 (d., e., f.).

large scale circulation by increasing the geopotential height at 500 hPa of 100 m over Eurasia and North America (Figure 6.10a). South of Greenland, the positive geopotential anomaly is caused by the difference in sea ice cover between FULL150 and FULL140 because during summer, this region is open at 150 ka and covered all the year at 140 ka which increases the cyclonic ac-

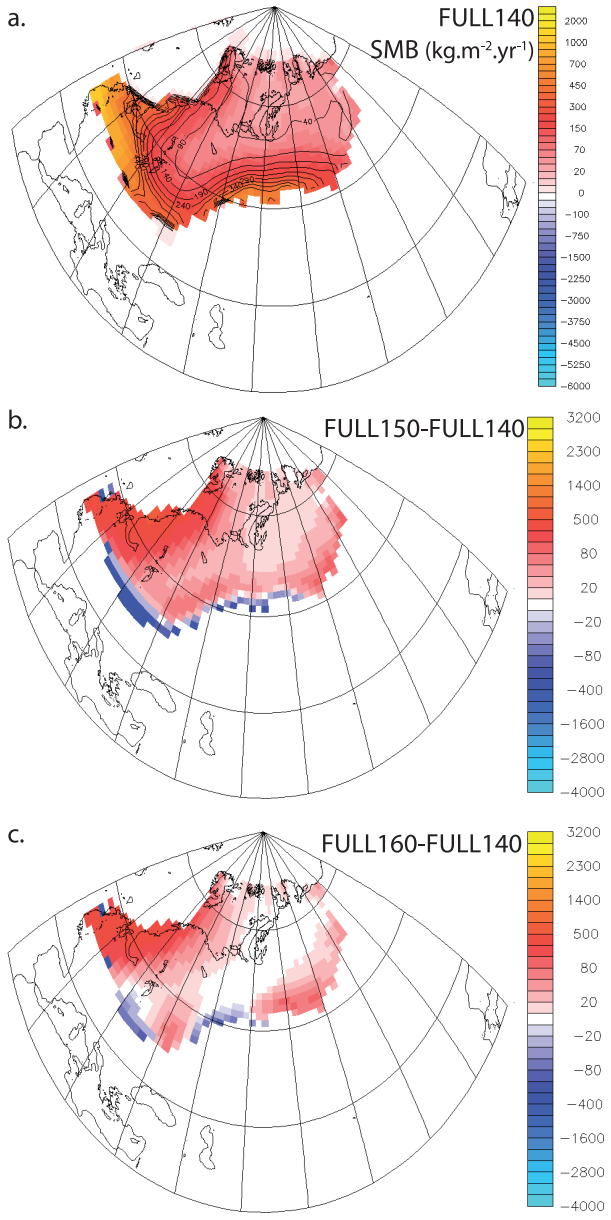

Figure 6.9: Late Saalian mean annual surface mass balance in kg.m^{-2}.yr^{-1} for a. simulation FULL140, b. difference between FULL150 and FULL140 and c. difference between FULL160 and FULL140.

tivity. The warming causes an increase in precipitation by 50% over Northern Eurasia, North America and over the ice sheets (Figure 6.10c).

Compared to 140 ka, the mean annual surface mass balance (SMB) over the Eurasian ice sheet at 150 ka is negative along the entire southern margins while it is more positive by about 500 kg.m^{-2}.yr^{-1} along the Atlantic and Arctic margins and by about 100 kg.m^{-2}.yr^{-1} over the central and eastern part of the ice sheet (Figure 6.9b). As a result of the large regional warming, precipitation over the ice sheet is larger at 150 ka than at 140 ka by about 100 kg.m^{-2}.yr^{-1} (Table 6.4). Despite the warmer 150 ka temperature that generates ablation along the southern margin, the amount of melting is small (15 kg.m^{-2}.yr^{-1}). Finally, the mean annual SMB is positive (243 kg.m^{-2}.yr^{-1}) and larger than at 140 ka (Table 6.4).

At 160 ka, as discussed previously, eccentricity is smaller and summer is warmer than at 140 ka although 160 ka corresponds to the first glacial substage of the Late Saalian. This causes a mean annual warming of about 5°C over the entire Northern Hemisphere and of 10°C over the North Atlantic, the Arctic Ocean, the North Pacific and Siberia (Figure 6.10e). This warming is caused by the sea ice cover which is less extended at 160 ka than at 140 ka (Figure 6.5). This affects the 500 hPa geopotential height which exhibits a mean positive anomaly of about 100 m (Figure 6.10d). As a consequence of the Northern Hemisphere warming, precipitation is larger at 160 ka by about 60% over the Arctic regions (Figure 6.10f).

Compared to 140 ka, the mean annual SMB is more negative along the Russian and western European margins as a consequence of the warmer 160 ka regional climate (Figure 6.9c). On the contrary, due to the larger precipitation over the North Atlantic and Arctic regions, SMB is larger by about 400 kg.m^{-2}.yr^{-1} as well as along the Eastern margins where snow height is larger and induce a positive feedback over the ice sheet. Contrary to 150 ka, the central part of the ice sheet is not affected by the 160 ka climate warming. However the mean annual ablation over the ice sheet is small but evaporation is larger than at 140 ka as well as snow fall (282 kg.m^{-2}.yr^{-1}, Table 6.4). Consequently, the mean annual SMB of the Eurasian ice sheet is larger (233 kg.m^{-2}.yr^{-1}) than at 140 ka.

Discussion

In this work we consider the climate of the entire Late Saalian period to address the question of the large ice topography of the Late Saalian Eurasian ice sheet. We therefore simulated the sea surface ocean temperatures and the vegetation cover in equilibrium with the climate of each time-slice. To simulate the Late Saalian sea surface conditions (sea surface temperatures (SST) and sea ice cover (SIC)), we used Planet Simulator, an AGCM coupled to a mixed-layer ocean module, forced using LGM ocean heat

fluxes. We then used these simulated SST and SIC to force the LMDZ4 AGCM model asynchronously coupled to the BIOME4 vegetation model to compute the climate and the vegetation cover of each time-slice.

The exclusive focus on the Late Saalian period comes from the recently published Eurasian ice sheet extents from the Late Saalian to the Last Glacial Maximum in the framework of the Quaternary Environment of the Eurasian North project (QUEEN, Svendsen *et al.* (2004)). However, while the ice sheet geographical maximum extent was reconstructed, it does not mean that these margins were reached simultaneously. This is further discussed. Up to now, this period has not really been a center of interest. Lot of the numerical experiments focus on the exceptional Eemian interglacial (MIS 5.5) corresponding to the Termination of the Late Saalian glaciation and on the Last Glacial Maximum and Holocene. Little geological evidence is available for the Late Saalian period to reconstruct the boundary conditions needed to constrain numerical experiments (Colleoni *et al.*, 2009a),(Colleoni *et al.*, 2009d), (Colleoni *et al.*, 2009b, submitted) and (Colleoni *et al.*, 2009c, submitted).

The Late Saalian period is exceptional in many aspects. First of all, the large Eurasian ice sheet covered most of Northern Eurasia (including large parts of the Eurasian Arctic continental shelf) and extended further to the South and to East than during the LGM. Building such a large ice sheet requires time to accumulate ice over the continents. In this context, it is worth noting that an even larger Eurasian ice sheet, extending over almost the entire boreal Eurasia thanks to the snow-ice albedo feedback along the southern margins, has recently been suggested as a major feature of a postulated future stable state of the climate system with permanent continental ice cover of similar extent in both hemispheres age cycle (Crowley & Hyde, 2008). During the 140 - 160 ka time period, the orbital configuration fluctuated from a moderate eccentricity at the 160 ka stadial (perihelion at the end of winter), via an interstadial period at 150 ka (perihelion in the early summer), to a full glacial maximum at 140 ka corresponding to the larger eccentricity of the entire Late Saalian period (perihelion in early winter) (Figure 6.1c). Our results clearly show that the Late Saalian period was driven by precession more than the large obliquity.

Synthesis of the main results

As a response of the orbital forcings, the Late Saalian Northern Hemisphere sea surface conditions are colder than the LGM reconstructions considered in the previous studies. The 160 ka oceanic surface is warmer than at 140 ka and the derived sea ice cover presents open-water conditions in the North Atlantic during summer. However 160 ka still corresponds to a glacial substage of the Late Saalian and the simulated vegetation is mostly constituted by tundra in the vicinity of the ice sheet margins and in Siberia (Northern Siberia is free of vegetation) and by some taiga and mixed-forest in Central Eurasia. Through the snow-albedo feedback, this vegetation cover contributes to the stability of the southern margins (Colleoni *et al.*, 2009d).

Then, at 150 ka, summer occurs at perihelion which consequently warms the surface ocean and opens the Eastern Norwegian sea during summer, similarly to the Paul & Schaefer-Neth (2003) LGM reconstruction. This broadly increases precipitations over the Northern Hemisphere. Due to the warmer and milder climate, we observe a retreat of the tundra mostly in Europe and in the Russian plains at the expense of the taiga and mixed forest whose northern limit is shifted northward close to the southern ice sheet margins (shift northward of the 10°C summer isotherm). As a consequence of a larger snow melting in Northern and Eastern Siberia, barren soils are covered with tundra.

Finally, the extreme 140 ka orbital configuration (perihelion occurs in early winter) mostly reduces snow melting during spring and summer, which occur farther from the sun than at the previous glacial substage (160 ka). As a consequence, the surface ocean is colder than at 160 ka with a large sea ice cover reaching 40°N during both winter and summer and preventing the moisture fluxes from reaching this region. Compared to LGM reconstructions, the surface ocean also exhibits an asymmetry with a cooler Northern Hemisphere and a warmer Southern Hemisphere. This pattern is not present at 160 ka and 150 ka since their orbital configuration is not as extreme as for 140 ka. As a consequence of a drier and colder climate, the simulated vegetation presents larger tundra areas and larger barren soils area in Eastern Siberia than at 160 ka and 150 ka.

The surface mass balance (SMB) of the Late Saalian ice sheet strongly responds to the vari-

ations in insolation. At 160 ka, the mean annual SMB is of 233 kg.m^{-2}.yr^{-1}. At 150 ka, the SMB is not significantly different than at 160 ka but precipitation over the ice sheet is much larger than at 160 ka and is compensated for by a larger evaporation and ablation only affecting the southern margins (Figure 6.9). At 140 ka, the colder and drier Northern Hemisphere climate reduces the moisture delivery to the ice sheet. As a result, the SMB is 193 kg.m^{-2}.yr^{-1} and is the lowest SMB value of the entire Late Saalian period.

One caveat should be considered to evaluate the impact of this study. It is about the Late Saalian ice sheet topography. In our simulations, we kept the ice sheet topography fixed to its maximum geographic extent. According to the Late Saalian ice sheet chronology over Eurasia, its extent was maximum at 160 ka and still large at 140 ka. Following the geological evidence in Germany, the southern margin may have retreated northward during the Treene substage and re-advance during the glacial maximum toward 140 ka but not until its original southward position (Svendsen *et al.*, 2004). However, without a precise geological mapping and dating, it is impossible to asses the retreat of the southern margin at 150 ka. This retreat might also have migrated the proglacial lakes northward from their assumed position in this study. This could have influenced the vegetation cover as well as the regional atmospheric circulation and thus the ice sheet surface mass balance.

One other caveat concerns the Laurentide topography. As far as we know, there is no literature addressing the Late Saalian Laurentide ice sheet topography since the most extensive glaciation over North America seems to have occurred at the LGM (Dyke *et al.*, 2002) and consequently has destroyed most of the geological evidence of previous periods. In this study we have prescribed the ICE-5G LGM Laurentide topography. Changing the ice sheet topography would impact on the Eurasian climate (Kageyama & Valdes, 2000).

As discussed in Colleoni *et al.* (2009b, submitted), Planet Simulator does not simulate deep circulation and consequently, the simulated inter-hemispheric asymmetry cannot result from a "seesaw" effect (thermohaline origin, Stocker (1998)). Since PLASIM does not simulate deep circulation, the model is not able to re-equilibrate excess or lack of oceanic heat caused by the asymmetric astronomical forcings. This results in surface ocean temperatures particularly cold or warm when enhanced by astronomical forcing. The 140 ka reconstruction is discussed in Colleoni *et al.* (2009b, submitted) relatively to marine cores data and the comparison shows that the simulation underestimates temperatures in the North Atlantic and North Pacific high latitudes.

Conclusions: the Late Saalian Eurasian ice sheet topography

How could the Late Saalian Eurasian ice sheet develop so far southward and remain large until the 140 ka glacial maximum?

Part of the question concerning the initial growth of the ice sheet has not been investigated and would require deeper work on the period prior to 160 ka. Indeed, the Late Saalian Eurasian ice sheet was already at its maximum extent at 160 ka and benefited from a relatively warm and mild glacial climate. Masson-Delmotte *et al.* (submitted) performed a multi-proxy study to estimate the intensity of the various glacial and interglacial periods since 800 ka in Central Antarctica. It appears that the MIS 6 is the fourth smallest glaciation of the Late Quaternary in terms of sea-level, greenhouse gas and dust. This has implication for the distribution of the ice volume over the various continental Late Saalian ice sheets. Despite the fact that the ice volume was not the largest of the Late Quaternary, the Late Saalian Eurasian ice sheet was the largest one from the last four major cycles. This also imply that the Late Illinoian (Late Saalian equivalent in North America) Laurentide ice sheet was much smaller than during the LGM if we equilibrate the eustatic sea-level.

The second part of the question concerns the relative stability of this large Eurasian ice volume through the entire Late Saalian period and particularly through the 150 ka interstadial. We have shown in this study that at 160 ka, the mean annual surface mass balance was positive and that the Eurasian ice sheet was subject to little ablation. Then at 150 ka, the summer insolation at the top of the atmosphere is more important during summer and fall due to the perihelion occurring during at early summer. This strongly affects the southern margin of the ice sheet which is subject to a larger summer ablation than at 160 ka. This can be asso-

ciated to the geologically suggested northward retreat of the ice sheet during the Treene substage as described by Ehlers *et al.* (2004) and Svendsen *et al.* (2004). However, although our simulations suggest increased melt rates along the southern margins, precipitation over the ice sheet is also much larger (due to the warmer climate and to the open-water conditions during both winter and summer in the North Atlantic) than at 160 ka and so compensates for ablation and evaporation. This results in a positive mean annual SMB close to that of 160 ka suggesting that even if the summer insolation is larger at 150 ka, the Eurasian ice sheet might have generated its own cooling strong enough to survive to this insolation peak. This can be tested performing transient coupled ice-atmosphere simulations. Finally, the larger 140 ka eccentricity enhances the effect of precession during the Late Saalian glacial maximum. This results in a reduced snow melting during spring and summer compared to the previous 150 ka and 160 ka time-slices and in colder surface ocean temperatures associated with a large sea ice expansion southward in both North Atlantic and North Pacific. Consequently, the ice sheet is no longer subject to ablation along the southern margin. But due to the large sea ice extent reducing the moisture fluxes transport over Eurasia, accumulation is also reduced. This leads to a smaller mean annual SMB, the smallest of the entire Late Saalian period.

Despite the 150 ka favourable precession effect increasing snow and ice melting, it seems that the large Eurasian ice sheet is able to survive through the Late Saalian period. We have shown that the surface mass balance responds to the orbital forcings which may play a larger role during the Late Saalian period than greenhouse gas variations (quite similar over the entire period) and than regional feedbacks caused by proglacial lakes, vegetation and dust deposition on snow, although they contribute to reduce the ablation along the southern margin of the Eurasian ice sheet. This may also explain why the LGM Eurasian ice sheet was so small compared to the Late Saalian one combined to the fact that the climate prior to the LGM was warm and consequently was not favourable to the growth of the ice sheet. During the LGM, eccentricity was reduced compared to the Late Saalian and consequently did not enhance the effect of precession as much as at 140 ka. At 140 ka, the combination of eccentricity and precession reduced the effect of the large obliquity. During the LGM, the effect of obliquity might have been larger and might have strengthened the effect of regional parameters on climate such as dust deposition on snow (Krinner *et al.*, 2006) that stopped the ice sheet from expanding in Siberia and more southward in Eurasia.

To investigate in more detail the climate processes that contributed to the growth of this large Late Saalian Eurasian ice sheet, it is necessary to use a full Atmosphere-Ocean model to better estimate oceanic conditions that may have played an important role on the maintenance and growth of this ice sheet and especially the ocean heat transport over latitudes. It is also necessary to use a thermo-dynamical ice model as GRISLI (which is able to simulate shelf plateforms of importance for the Late Saalian since a third of the ice sheet covers the Arctic continental shelf) to perform transient simulations in order to study the dynamics of the ice sheet (from where it started to growth, how much time is needed to built the ice sheet, how much time is needed to melt it completely). It is also necessary to build a Laurentide ice sheet associated with the simulated climate to understand if it may have been as large as during the LGM.

Acknowledgments

The author acknowledges support by the Agence Nationale de la Recherche (project IDEGLACE), the Région Rhône Alpes (programme Explora'Doc) and the Ministère des Affaires Étrangères Français and The Bert Bolin Centre for Climate Research (Stockholm University) for their support. The climate simulations were carried out at IDRIS/CNRS and on the Mirage scientific computing plateform in Grenoble (France).

References

Abe-Ouchi, A., Segawa, T., & Saito, F. 2007. Climatic Conditions for modelling the Northern Hemisphere ice sheets throughout the ice age cycle. *Clim. Past*, **3**, 423–438.

Berger, A., & Loutre, M.F. 1991. Insolation values for the climate of the last 10 millions years. *Quaternary Sci. Rev.*, **10**(4), 297–317.

Colleoni, F., Krinner, G., Jakobsson, M., Peyaud, V., & Ritz, C. 2009a. Influence of regional fac-

tors on the surface mass balance of the large Eurasian ice sheet during the peak Saalian (140 kyrs BP). *Global Planet. Change*, **HOTRAX special issue**.

Colleoni, F., Liakka, J., Krinner, G., Jakobsson, M., Masina, S., & Peyaud, V. 2009b. The Late Saalian surface ocean (140 kyrs BP): sensitivity of the Late Saalian Eurasian ice sheet to sea surface conditions. *Clim. Dynam.*, submitted.

Colleoni, F., Krinner, G., & Jakobsson, M. 2009c. The role of the Late Saalian Arctic ice-shelf in the climate of the last glacial maximum of MIS 6 (140 kyrs BP). *Quaternary Sci. Rev.*, submitted.

Colleoni, F., Krinner, G., & Jakobsson, M. 2009d. Sensitivity of the Late Saalian (140 kyrs BP) and LGM (21 kyrs BP) Eurasian ice sheet surface mass balance to vegetation feedbacks. *Geophs. Res. Lett.*, **36**, L08704.

Crowley, T.J. 1995. Ice age terrestrial carbon changes revisited. *Global Biogeochem. Cycles*, **9**(3), 377–389.

Crowley, T.J., & Hyde, W.T. 2008. Transient nature of late Pleistocene climate variability. *Nature*, **465**, 226–230.

D., Paillard. 1998. The timing of Pleistocene glaciations from a simple multiple-state climate model. *Nature*, **391**(6665), 378–381.

Delmonte, B., & coauthors. 2004. *EPICA Dome C Ice Cores Insoluble Dust Data, IGBP PAGES/World Data Center for Paleoclimatology Data Contribution Series, NOAA/NGDC Paleoclimatology Program, Boulder CO, USA*.

Dyke, A.S., Andrews, J.T., Clark, P.U., England, J.H., Miller, G.H., Shaw, J., & Veillette, J.J. 2002. The Laurentide and Innuitian ice sheets during the Last Glacial Maximum. *Quaternary Sci. Rev.*, **21**, 9–31.

Ehlers, J., Eissmann, L., Lippstreu, L., Stephan, H.J., & Wansa, S. 2004. *Pleistocene glaciations of North Germany. In: Ehlers, J., Gibbard, P.L. (Eds.), Quaternary GlaciationsExtent and Chronology. Vol. 1. Europe*. Elsevier, Amsterdam.

Farrell, W.E., & Clark, J.A. 1976. On postglacial sea-level. *Geophys. J. Roy. Astr. S.*, **46**, 647–667.

Fraedrich, K., Jansen, H., Kirk, E., Luksch, U., & Lunkeit, F. 2005. The Planet Simulator: Towards a user friendly model. *Meteorol. Z.*, **14**, 299–304.

Hourdin, F., Musat, I., Bony, S., Braconnot, P., Codron, F., Dufresne, J-L., Fairhead, L., Filiberti, M-A., Frieflingstein, P., Grandpeix, J-Y., Krinner, G., Levan, P., Li, Z-X., & Lott, F. 2006. The LMDZ4 general circulation model : climate performance and sensitivity to parametrized physics with emphasis on tropical convection. *Clim. Dynam.*, **27**(7-8), 787–813.

Imbrie, J., Berger, A., Boyle, E.A., Clemens, S.C., Duffy, A., Howard, W.R., Kukla, G., Kutzbach, J., Martinson, D.G., Mcintyre, A., Mix, A.C., Molfino, B., Morley, J.J., Peterson, L.C., Pisias, N.G., Prell, W. L., Raymo, M.E., Shackleton, N.J., & Toggweil, J. R. 1993. On the structure and origin of major glaciation cycles. 2. hte 100,000-year cycle. *Paleoceanography*, **8**(5), 699–735.

Jakobsson, M. in prep.. *Nature Geoscience*.

Jakobsson, M., Macnab, R., Mayer, L., Anderson, R., Edwards, M., Hatzky, J., Schenke, H. W., , & Johnson, P. 2008. An improved bathymetric portrayal of the Arctic Ocean: Implications for ocean modeling and geological, geophysical and oceanographic analyses. *Geophys. Res. Lett.*, **35**(7), L07602.

Kageyama, M., & Valdes, P.J. 2000. Impact of the North American ice-sheet orography on the Last Glacial Maximum eddies and snowfall. *Geophysical Research Letters*, **27**(10), 1515.

Kaplan, J.O., Bigelow, N.H., Prentice, I.C., Harrison, S.P., Bartlein, P.J., Christensen, T.R., Cramer, W., Matveyeva, N.V., McGuire, A.D., Murray, D.F., Razzhivin, V.Y., Smith, B., Walker, D.A., Anderson, P.M., Andreev, A.A., Brubaker, L.B., Edwards, M.E., & Lozhkin, A.V. 2003. Climate change and Arctic ecosystems: 2. Modeling, paleodata-model comparisons, and future projections. *J. Geophys. Res.*, **102**(D19), 12.1–12.17.

Khodri, M., Cane, M. A., Kukla, G., Gavin, J., & Braconnot, P. 2005. The impact of precession changes on the Arctic climate during the last interglacialglacial transition. *Earth Planet Sc. Lett.*, **236**, 285–304.

Korner, C. 1998. A re-assessment of high elevation treeline positions and their explanation. *Oecologia*, **115**(4), 445–459.

Krinner, G. 2003. Impact of lakes and wetlands on boreal climate. *J. Geophy. Res.*, **108**(D16), 4520.

Krinner, G., & Genthon, C. 1999. Altitude dependence of the ice sheet surface climate. *Geophys. Res. Lett.*, **26**, 2227–2230.

Krinner, G., Boucher, O., & Balkanski, Y. 2006. Ice-free glacial northern Asia due to dust deposition on snow. *Clim. Dynam.*, **27**(6), 613–625.

Mahowald, N., Kohfeld, K., Hansson, M., Balanski, Y., Harrisson, S., Prentice, J., Schulz, M., & Rodhe, H. 1999. Dusts sources and deposition during the last glacial maximum and current climate: a comparison of model results with paleodata from ice cores and marine sediments. *J. Geophys. Res.*, **104**(D13).

Mangerud, J., Astakhov, V., Jakobsson, M., & Svendsen, J.I. 2001. Huge ice-age lakes in Russia. *J. Quaternary. Sci.*, **16**(8), 773–777.

Masson-Delmotte, V., Stenni, B., Pol, K., Braconnot, P., Cattani, O., Falourd, S., Kageyama, M., Jouzel, J., Landais, A., Minster, B., Krinner, G., Johnsen, S., Rthlisberger, R., Chappellaz, J., Hansen, J., Mikolajewicz, U., & Otto-Bliesner, B. submitted. EPICA Dome C record of glacial and interglacial intensities. *Quaternary Sci. Rev.*

Ohmura, A., Wild, M., & Bengtsson, L. 1996. A possible change in mass balance of Greenland and Antarctic ice sheets in the coming century. *J. Glaciol.*, **9**(9), 2124–2135.

Paul, A., & Schaefer-Neth, C. 2003. Modeling the water masses of the Atlantic Ocean at the Last Glacial Maximum. *Paleoceanography*, **18**(3).

Peltier, W.R. 2004. Global glacial isostasy and the surface of the ice-age Earth: The REF140-5G (VM2) Model and GRACE. *Annu. Rev. Earth Pla. Sci.*, **32**, 111–149.

Petit, J.R., Jouzel, J., Raynaud, D., Barkov, N., Barnola, J., Basile, I., Bender, M., Chapellaz, J., Davis, J., Delaygue, G., Delmotte, M., Kotlyakov, V., Legrand, M., Lipenkov, V., Lorius, C., Ppin, L., Ritz, C., Saltzman, E., & Stievenard, M. 2001. *Ice core data for 420,000 year, IGBP PAGES/World Data Center for Paleoclimatology Data Contribution Series, NOAA/NGDC Paleoclimatology Program, Boulder CO, USA*.

Peyaud, V. 2006. *Role of the Ice Sheet Dynamics in major climate changes*. Ph.D. thesis, Laboratoire de Glaciologie et de Géophysique de l'Environnement, Université Grenoble I.

Peyaud, V., Ritz, C., & Krinner, G. 2007. Modeling the Early Weichselian Eurasian Ice Sheets: role of ice shelves and influence of ice-dammed lakes. *Clim. Past*, **3**, 375–386.

Rabineau, M., Berne, S., Olivet, J.L., Aslanian, D., Guillocheau, F., & Joseph, P. 2006. Paleo sea levels reconsidered from direct observation of paleoshore-line position during glacial maxima (for the last 500,000 yr). *Earth Planet. Sc. Lett.*, **252**, 119–137.

Raymo, M.E., Lisiecki, L.E., & Nisancioglu, K.H. 2006. Plio-Pleistocene Ice Volume, Antarctic Climate, and the Global $\delta^{18}O$ Record. *Science*, **313**, 492–495.

Ritz, C., Rommalaere, V., & Dumas, C. 2001. Modeling the evolution of Antarctic ice sheet over the last 420,000 years: Implications for altitude changes in the Vostok region. *J. Geophys. Res.*, **106**(D23), 31943–31964.

Romanova, V., Lohmann, G., & Grosfeld, K. 2005. Effect of land albedo, CO2, orography, and oceanic heat transport on extreme climates. *Clim. Past*, **92**, 4241–4281.

Romanova, V., Lohmann, G., Grosfeld, K., & Butzin, M. 2006. Effect of land albedo, CO2, orography, and oceanic heat transport on extreme climates. *Quaternary Sci. Rev.*, **25**, 832–845.

Simmonds, I., & Wu, X. 1993. Cyclone behaviour response to changes in winter Southern Hemisphere sea-ice concentration. *J. Climate*, **119**, 1121–1148.

Spada, G. 2003. *The theory behind TABOO - a posT glAcial reBOund calculatOr*. Samizdat Press, Golden, White River Junction.

Spada, G. 2008. ALMA, a Fortran program for computing the visco-elastic Love numbers of a spherically symmetric planet. *Comput. and Geosci.*, **34**(6), 667–687.

Spada, G., & Stocchi, P. 2007. SELEN: a Fortran 90 program for solving the "Sea Level Equation". *Comput. and Geosci.*, **33**(4), 538–562.

Spahni, R., Chappellaz, J., Stocker, T., Loulergue, L., Hausammann, G., Kyawamura, G., Flckiger, J., Schwander, J., Raynaud, D., Masson-Delmotte, V., & Jouzel, J. 2005. *Epica Dome C CH4 data to 650 kya BP, IGBP PAGES/World Data Center for Paleoclimatology Data Contribution Series, NOAA/NGDC Paleoclimatology Program, Boulder CO, USA*.

Stocker, T.F. 1998. The seesaw effect. *Science*, **282**, 61–62.

Svendsen, J.I., Alexanderson, H., Astakhov, V.I., Demidov, I., Julian, A.D., Funder, S., Gataulling, V., Henriksen, M., Hjort, J., Houmark-Nielsen, M., Hubberten, H.W., Ingulfsson, O., Jakobsson, M., Kjer, K.H., Larsen, E., Lokrantz, H., Lunkka, J.P., Lys, A., Mangerud, J., Matiouchkov, A., Murray, A., Muller, P., Niessen, F., Nikolskaya, O., Polyak, L., Saarnisto, M., Siegert, C., Siegert, M.J., Spielhagen, R.W., & Ruedige, S. 2004. Late Quaternary ice sheet history of Northern Eurasia. *Quaternary Sci. Rev.*, **23**, 1229–1271.

Waelbroeck, C., Labeyrie, L., Michel, E., Duplessy, J.C., McManus, J.F., Lambeck, K., Balbon, E., & Labracherie, M. 2002. Sea-level and deep water temperature changes derived from benthic foraminifera isotopic records. *Quaternary Sci. Rev.*, **21**(1-3), 295–305.

Winckler, G., Anderson, R.F., Fleisher, M.Q., McGee, D., & Mahowald, N. 2008. Covariant Glacial-Interglacial Dust Fluxes in the Equatorial Pacific and Antarctica. *Science*, **320**, 93–96.

Appendix A

Eurasian topography and Arctic IBCAO bathymetry

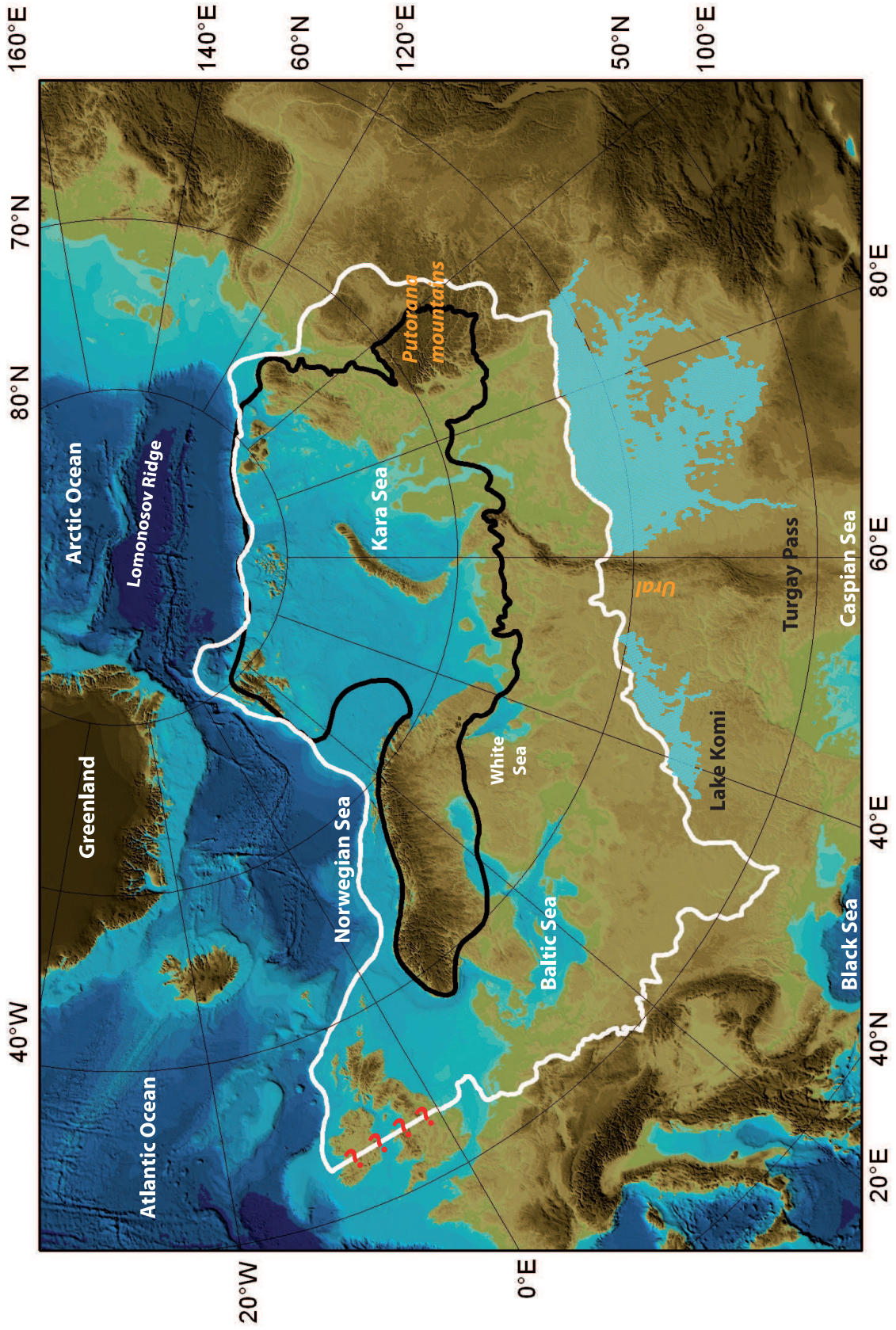

Figure 6.1: Map of Northern Eurasia. Courtesy Martin Jakobsson

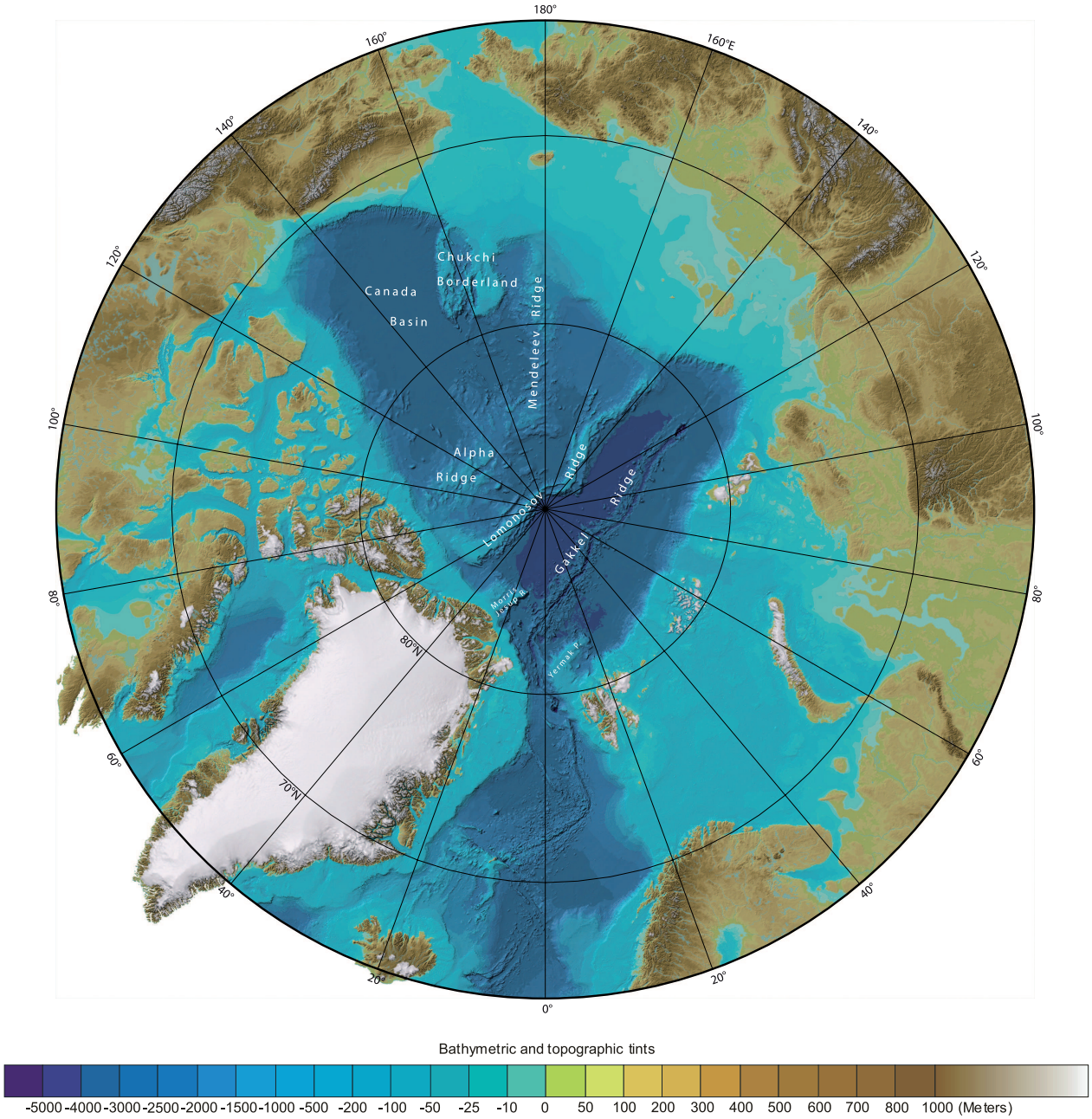

Figure 6.2: International Bathymetric Chart of the Arctic Ocean v2.23 Jakobsson *et al.* (2008)

Appendix B

Post-glacial rebound and sea level variations

Post-glacial rebound and the subsequent sea level variations have always been a very attractive topic since the theory of glacio-and hydro-isostatic sea level variations was first developed by Farrell & Clark (1976). This is now considered as a key field to estimate the future global sea level rise due to the melting of the Greenland and Antarctic ice sheets and the small continental glaciers. Post-glacial rebound represents an interface between the inner Earth processes and the external processes. Indeed, as described in the Section 1.4.1, during a glacial inception, ice sheets grow and load continents. This affects the lithosphere and the Earth mantle whose response is commonly described by two mechanical behaviours: an elastic (immediate) and a viscous (several thousands years) responses. Both responses can be expressed using visco-elastic laws, such as the simplified Maxwell rheology whose mechanical analog correspond to a dashpot and a spring, or more complex transient rheologies associating various couplings of dashpots and springs in serial and/or in parallel.

I first started to work on post-glacial rebound and sea level variations during for the Master thesis (2006), with Giorgio Spada, at the University of Urbino (Italy). At this time, this group had already developed several softwares: TABOO was already published (Spada, 2003), SELEN first version was about to be submitted (Spada & Stocchi, 2007) and ALMA code was under development (Spada, 2008). Those three open-source code correspond to specific needs in Solid Earth:

- **TABOO** (a pos**T** gl**A**cial re**BO**und calculat**O**r), 2003. TABOO solves the GIA problem for a spherically symmetric Earth model with Maxwell rheology, assuming an eustatic (i. e., spatially uniform) ocean load. It can be used for computing Love numbers for simple load time-histories and the response to surface loads of various degrees of complexity.

- **SELEN** (a **SE**a **L**evel **E**quatio**N** solver), 2007. SELEN is a Fortran 90 code for solving the Sea level Equation (SLE) associated to Glacial Isostatic Adjustment (GIA) problems. A tarball of SELEN 2.0 is available upon request to GS (email: giorgio.spada AT gmail.com). A dedicated web page (http://flocolleoni.free.fr/SELEN.html) is now available.

- **ALMA** (2008) is a program for computing the "Love numbers" of loading or tidal type of a spherically symmetric Earth. ALMA is an application of the Post-Widder formula of Laplace inversion to multi-stratified spherical models characterized by general linear visco-elastic rheologies (Hooke, Newton, Maxwell, Kelvin-Voigt, Burgers, Maxwell-Wiechert, ...).

In this ongoing collaboration (research carried out in parallel of this Ph.D.), I participated to the elaboration of three peer-reviewed articles and to a large part of the development of SELEN software more recent versions. A fourth paper about the impact of the Maxwell general law on the Earth's mantle rheology is in preparation and corresponds to an invited contribution for a special issue of Tectonophysics to be submitted by June 30. The three peer-reviewed articles presented below are included in the Project **PRIN 2006** (MINISTERO DELL'ISTRUZIONE, DELL'UNIVERSITA E DELLA RICERCA): *"The role of glacial isostatic adjustment in global and Mediterranean sea level variations: new geophysical, geological and archaeological constraints"*. This project ended in February

2009. These contributions correspond to a specific need of the Italian government to assess scientific, economical and social consequences induced by present-day and future sea level rise along the Italian coasts and especially along the Adriatic coastlines whose elevation almost corresponds to present sea level and are subjected to subsidence due to glacio-isostatic adjustment and anthropic activities.

I will actively carry on this collaboration in Solid Earth within Giorgio Spada's group and future contributions will be included into the FP7 European project **ICE2SEA** (http://www.ice2sea.eu/).

Published manuscripts:

1- P. Stocchi, F. Colleoni and G. Spada, 2009. Bounds on the Timehistory and Holocene Mass Budget of Antarctica from Sea level Records in SE Tunisia, *Pure Appl. Geophys.*, **166**, 123, doi:10.1007/s00024-009-0488-z.

2- G. Spada, P. Stocchi and F. Colleoni, 2009. Glacioisostatic Adjustment in the Po Plain and in the Northern Adriatic Region, *Pure Appl. Geophys.*, **166**, 1-16, doi:10.1007/s00024-004-0498-9.

3- P. Stocchi, L. Girometti, G. Spada, M. Anzidei and F. Colleoni, 2009. Post-glacial readjustment, sea level variations, subsidence and erosion along Italian coasts, *Bollettino di Geofisica Teorica ed Applicata*, **50** (2), 129-144.

Pure appl. geophys. 166 (2009) 1–23
DOI 10.1007/s00024-009-0488-z

© Birkhäuser Verlag, Basel, 2009

Pure and Applied Geophysics

Bounds on the Time–history and Holocene Mass Budget of Antarctica from Sea–level Records in SE Tunisia

P. STOCCHI,[1] F. COLLEONI,[2] and G. SPADA[3]

Abstract—Solving the sea–level equation for a Maxwell Earth, we analyze the sensitivity of Holocene sea–level records in SE Tunisia to the time–history of remote ice sheets. Assuming that mantle viscosity increases moderately with depth, we find that in this region the sea–level variations driven by the Northern Hemisphere ice sheets cancel, so that the late–Holocene sea–level high–stand suggested by the geological record merely reflects the melting history of Antarctica. New insight into the history of this ice sheet is obtained analyzing the information contained in a revised set of relative sea–level observations for sites across the Mediterranean covering the last 8 kyrs. From a trial–and–error misfit analysis, it holds true that in this region the match between model predictions and observations improves when the volume of water released from Antarctica is well below the value imposed by the ICE3G chronology and when a sudden meltwater pulse is allowed between 8 and 7 kyrs before present, corresponding to the epoch of the catastrophic rise event known as CRE3.

Key words: Catastrophic rise events, glacio–isostatic adjustment, Holocene sea–level changes, mantle viscosity, South east Tunisia.

1. Introduction

Geological evidence, reviewed in Section 3.2 below, indicates that in SE Tunisia sea–level was continuously falling during the mid– to late–Holocene and that a peak of ~2 m above the present datum was reached between 6 and 7 kilo years (kyr) before present (BP).[1] Since no significant tectonic activity has been reported in this area during the last ~130 kyrs (see MORHANGE and PIRAZZOLI, 2005; GUIDOBONI and COMASTRI, 2005), the observed relative sea–level (RSL) variations must be the result of glacio– and hydro–isostasy.

[1] Delft University of Technology, Delft, The Netherlands.
[2] Laboratoire de Glaciologie et Geophysique de l'Environment, Grenoble, France.
[3] Istituto di Fisica, Università di Urbino "Carlo Bo", Via Santa Chiara n. 27, I–61029 Urbino (PU), Italy. E-mail: giorgio.spada@gmail.com

[1] In the following, unless differently stated, we will use only the calendar age time scale. Some of the RSL data published in the literature have been converted from ^{14}C to calendar time scale using the radiocarbon calibration program by FAIRBANKS *et al.* (2005) (see http://radiocarbon.ldeo.columbia.edu/research/radcarbcal.htm).

Journal : **24** Dispatch : **1-4-2009** Pages : **23**
Article No. : **0488** ☐ LE ☐ TYPESET
MS Code : **0488** ☑ CP ☑ DISK

In a recent study, STOCCHI and SPADA (2007) have noticed that the observed late–Holocene sharp high–stand in SE Tunisia (∼5 kyrs BP) mostly reflects the history of melting of the Antarctic ice sheet, since the two major northern hemisphere ice sheets (Laurentide and Fennoscandia) at this time had completely melted and their contributions to relative sea–level have opposite signs and almost cancel.

Starting from the evidence in SE Tunisia, we carry out tests of the sensitivity of RSL data to various time–histories of the Antarctic ice-sheet in an attempt to constrain the melting history of Antarctica from available RSL observations. We find that to explain the amplitude and time of the SE Tunisia sea–level high–stand, the total equivalent sea–level (*ESL*, see Equation (2) below) for Antarctica must be reduced approximately by a factor of two relative to the deglaciation model ICE3G of TUSHINGHAM and PELTIER (1991), provided that melting occurs catastrophically between 7 and 8 kyrs BP. The revised *ESL* and melting history of Antarctica is compatible with studies of the deglaciation history of Antarctica (BENTLEY, 1999) and, as shown here for the first time, with RSL observations ranging from global to Mediterranean scale.

This scenario is at variance with the Shepard school of thought (SHEPARD, 1963), which suggests a nearly continuous (monotonous) sea–level rise since 18 kyrs BP (see also KIDSON, 1982). Rather, it agrees with the Fairbridge school that favors a more episodic sea–level rise (FAIRBRIDGE, 1961). Along these lines, RUDDIMAN (1987) proposed and compared three different deglaciation models: *i)* the "smooth deglaciation model''; *ii)* the "French two–step" deglaciaton model, with maximum rates from 14,000 to 12,000 and from 10,000 to 7,000 radiocarbon years BP; and *iii)* the "younger Dryas'' deglaciation model, which differs from *ii)* by a mid–deglacial reversal with significant ice growth 11,000–10,000 radiocarbon years BP. Evidence in support of two surges in meltwater at about 14,000 (referred to as MPW–1A) and 11,000 (MPW–1B) radiocarbon years BP came from the fundamental work of FAIRBANKS (1989), who extended the coral–reef sea–level curve for Barbados to the Last Glacial Maximum. FAIRBANKS *et al*. (1992) and BLANCHON and SHAW (1995) argued that MWP–1A and MWP–2A may relate to a two–step collapse of the Laurentide ice sheet. While, according to BASSETT *et al*. (2005), a sudden melting of the Antarctic ice sheet could be the "prime mover" of MWP–1A, PELTIER (2005) rejected a significant role of this ice sheet. Prior to the work of BASSETT *et al*. (2005), support for a Southern Hemisphere scenario came from sedimentological studies (see KANFOUSH, *et al*., 2000), glacio–geological and paleoceanographic analyses (CLARK *et al*., 1996), glacio–isostatic adjustment modelling (CLARK *et al*., 2002) and climatological modelling (WEAVER *et al*., 2003).

Sea–level records from drowned *Acropora palmata* in the Caribbean analyzed by BLANCHON and SHAW (1995) document three other possible catastrophic rise events (CREs): *i)* CRE1 (with an amplitude of 13.5 m, 14.2 kyrs BP), *ii)* CRE2 (7.5 m, 11.5 kyrs BP) and *iii)* CRE3 (6.5 m, 7,6 kyrs BP). CRE1 and CRE2 are synchronous to the two collapse events possibly experienced by the Laurentide ice sheet during deglaciation (BOND *et al*., 1992, 1993), and their timing coincides with that of MWP–1A and MWP–1B (see Table 1 of BENTLEY, 1999). More specifically, on the basis of terrestrial

Journal : 24 Dispatch : 1-4-2009 Pages : 23
Article No. : 0488 ☐ LE ☐ TYPESET
MS Code : 0488 ☑ CP ☑ DISK

Table 1

Earth model parameters

Layer	Range [km]	Density [kg m^{-3}]	Rigidity [GPa]	Viscosity [$\times 10^{21}$ Pa s]	
				VP1	VP2
Lithosphere	6251 − 6371	4120	73	∞	∞
Upper mantle	5951 − 6251	4120	95	1	0.5
Transition zone	5701 − 5951	4220	110	1	0.5
Lower mantle	3480 − 5701	4508	200	2	40
Core	0 − 3480	10925	0	0	0

and submerged diamictons, KAUFMAN *et al*. (1993) indicated the possibility of collapses of the Labrador Dome at 14 and 11.5 kyrs BP, which further supports a North American origin for CRE1 and CRE2. As pointed out by BLANCHON and SHAW (1995), due to the small volume of ice remaining on the Northern Hemisphere at the epoch of CRE3, its origin can be explained by invoking a role of the Antarctic ice sheet. In this study, we show that an Antarctic origin of CRE3 is compatible with RSL records in the Mediterranean during the last 8 kyrs. The monotonously melting ICE3G is unable to simultaneously account for RSL observations in SE Tunisia and in the northern Mediterranean. As discussed in the following, the melting scenario proposed here also constitutes an improvement, in the Mediterranean region, compared to models characterized by a delayed melting phase (NAKADA and LAMBECK, 1988) or by an ice re–advance during the late Holocene (GOODWIN, 1998).

Evidence supporting the sudden melting hypothesis for Antarctica comes from the continental shelf where, at the Last Glacial Maximum, the ice masses were grounded at the shelf edge and their subsequent retreat was rapid and episodic (ANDERSON and THOMAS, 1991). These authors emphasize the primary control of the sea–level on the ice sheet stability and suggest, as a consequence of global sea–level rise, the marine ice sheet decoupling mechanism, which consists in an ice shelf decoupling from the sea floor and a rapid collapse, followed by a pull-down of the ice sheet. It is reasonable that this mechanism caused a eustatic sea–level rise of a few meters within a few hundreds years, which, in turn, had a global impact on the evolution of coasts and estuaries. On the basis of the past episodic eustatic rises and given the present-day climate-related global sea–level rise (CAZENAVE and NEREM, 2004; CHURCH and WHITE, 2006), it is reasonable to consider the effects of a possible pull-down of current marine glaciers on the global coastal stability.

The manuscript is organized as follows. After a brief illustration of the methods, we will present predictions and observations of RSL curves for North Africa. In the ensuing discussion section we will extend our study to a global and a regional scale, and in particular we will test the reliability of a CRE3 meltwater episode on the basis of RSL observations in the Mediterranean. Finally, some conclusions will be presented.

Journal : 24 Dispatch : 1-4-2009 Pages : 23
Article No. : 0488 ☐ LE ☐ TYPESET
MS Code : 0488 ✔ CP ✔ DISK

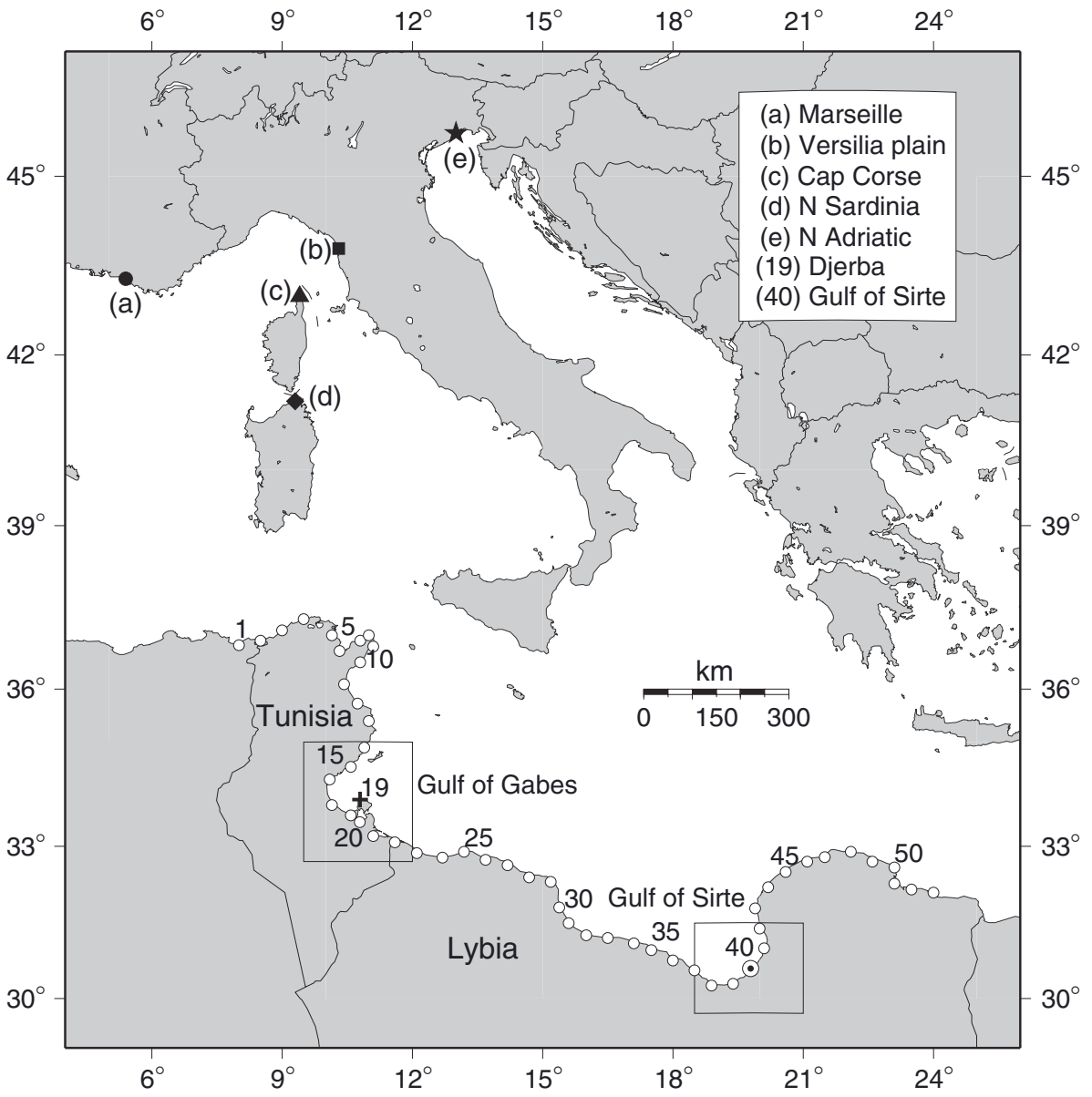

Figure 1
Map of the study region showing the RSL sites of Djerba (19, cross) and Gulf of Sirte (40, filled circle), as well as a number of other equidistant "test sites" (open circles). Also shown are the northern Mediterranean RSL sites considered in the analyses of Figures 9 and 10.

2. *Methods*

All computations were performed using the public domain program SELEN[2] by SPADA and STOCCHI (2007), which solves the sea–level equation (SLE) for a spherically symmetric Maxwell Earth. The SLE, which accounts for the effects of glacio– and hydro–isostasy, is solved by the "pseudo–spectral" method of MITROVICA and PELTIER (1991), assuming a

[2] SELEN, which comes with a GPL license, can be requested from GS (giorgio.spada@gmail.com). See web page http://flocolleoni.free.fr/SELEN.htm.

Journal : 24 Dispatch : 1-4-2009 Pages : 23
Article No. : 0488 ☐ LE ☐ TYPESET
MS Code : 0488 ☑ CP ☑ DISK

constant ocean function (i.e., fixed shorelines) and neglecting rotational feedbacks, according to the theory of FARRELL and CLARK (1976). This implies a spatio–temporal discretization in which the distribution of ice sheets varies step–wise and the basic unknowns (i.e., sea–level change S, surface displacement, and geoid height change) are decomposed in series of spherical harmonics. Details of the method were reviewed by MITROVICA and MILNE (2003) and SPADA and STOCCHI (2007). Once S is solved for, synthetic RSL curves at a site of colatitude θ and longitude λ are obtained computing

$$RSL(\theta, \lambda, t_{BP}) = S(\theta, \lambda, t_p) - S(\theta, \lambda, t_{BP}), \tag{1}$$

where t_p and t_{BP} are present time and some epoch before present, respectively. Relevant RSL sites of the study region are shown in Figure 1.

Table 1 gives the physical and rheological parameters of the incompressible five–layer Earth model used to compute the load–deformation coefficients that enter into the SLE (e.g., SPADA and STOCCHI, 2007). In this work, we have adopted the philosophy of keeping fixed the viscosity of mantle layers to *a priori* values consistent with previous studies of post–glacial adjustment and to focus on the role of the surface ice loads. In particular, the moderate viscosity increase across the transition zone and the lower mantle (a factor of 2) is in accord with that implicit in the deglaciation chronology ICE3G of TUSHINGHAM and PELTIER (1991). Such a viscosity profile is referred to as VP1 in Table 1. We note that the ensuing results are altered by a different *a priori* viscosity profile; this point will be addressed at the end of Section 4 using viscosity profile VP2, based on the work by BASSETT *et al*. (2005).

Figure 2 shows *ESL* as a function of time for the two global ice distributions considered in this study: ICE1 (PELTIER and ANDREWS, 1976) and ICE3G (TUSHINGHAM and PELTIER, 1991). Here and in the following equivalent sea–level is defined as

$$ESL = \frac{\rho_i}{\rho_w} \frac{V}{A_o}, \tag{2}$$

where ρ_i and ρ_w are the density of ice and water, respectively, V is the ice volume at a given time, and A_o is the area of the surface of the oceans (e.g., NAKADA and LAMBECK, 1988). In the two ice models, the Laurentide ice sheet (dashed) has a similar melting history and *ESL* variation ($\sim$55 m). However, in ICE3G the Fennoscandian ice sheet (dash–dotted) is associated with a significantly smaller *ESL* variation than in ICE1, and its melting terminates at 8 kyrs BP, considerably later than in ICE1 (10 kyrs BP). Differently from ICE3G, ICE1 assumes that the mass of the Antarctic ice sheet (A3 in Fig. 2) does not vary during the Holocene. It causes a total *ESL* variation of $\sim$28 m and its melting history is characterized by a stationary phase until 10 kyrs BP followed by a melting at a constant rate terminating 5 kyrs BP. During the last $\sim$8 kyrs BP, after the deglaciation of Fennoscandia and North America, A3 provides the largest contribution to the total mass budget of ICE3G. Due to the late melting of the ice masses in Antarctica and Fennoscandia in ICE3G, the *ESL* curves for the two ice models (solid lines) terminate at distinctly different

Journal : 24 Dispatch : 1-4-2009 Pages : 23
Article No. : 0488 ☐ LE ☐ TYPESET
MS Code : 0488 ☑ CP ☑ DISK

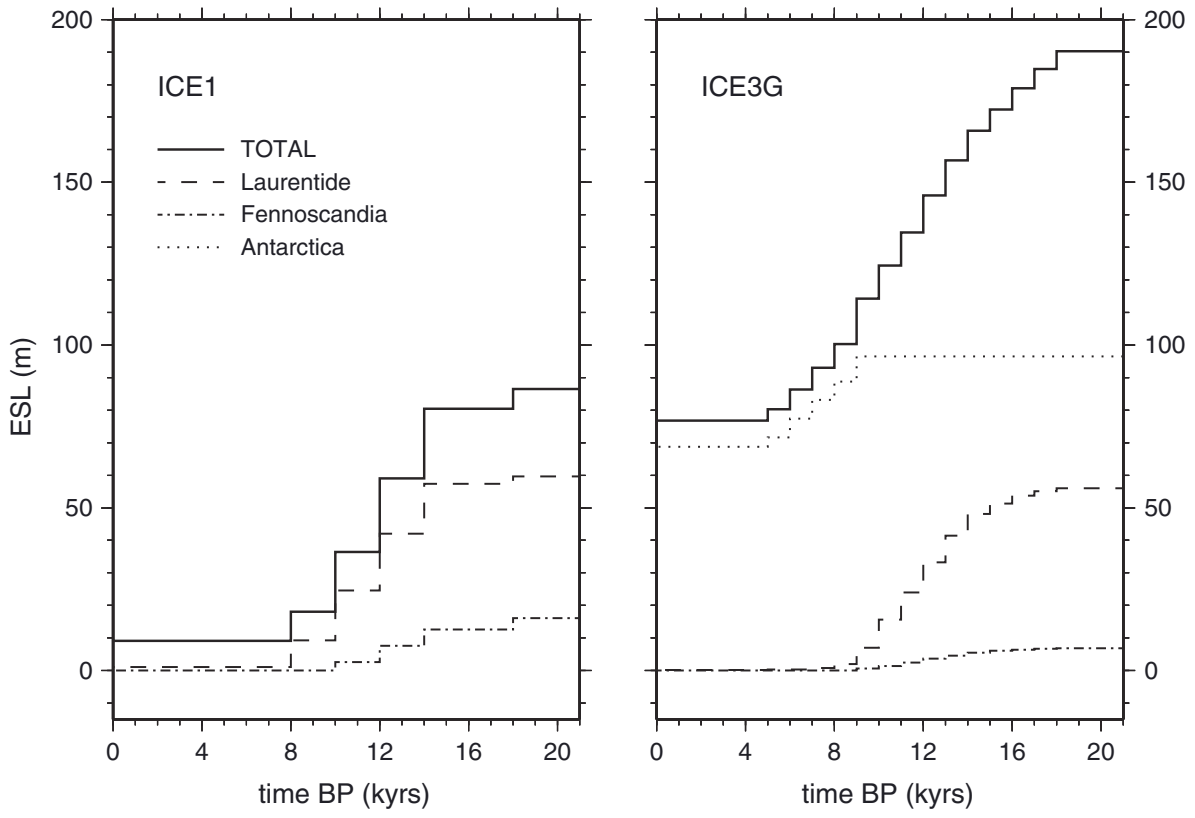

Figure 2
ESL for ice models ICE1 (left) and ICE3G (right) and individual ice sheets: Fennoscandia, Laurentide, and Antarctica (A3). Contributions from other minor components of ICE1 and ICE3G are not shown. *ESL* is defined by Equation (2).

epochs. Figure 2 only accounts for *ESL*; ice thickness distributions according to ICE1 and ICE3G can be visualized using program SELEN (SPADA and STOCCHI, 2007).

3. RSL Curves for North Africa

3.1. Model Predictions

Since the Gulf of Gabes and the Gulf of Sirte have similar shapes and latitudes and are located at comparable distances from the former ice sheets (see Fig. 1), we expect that solving the SLE for these regions provides similar patterns of sea–level change. These facts are crucial in determining the trend of postglacial RSL curves since they tune the amplitude of the "continental levering" effect (MITROVICA and MILNE, 2002), a process that significantly contributes to RSL variations in the Mediterranean (STOCCHI and SPADA, 2007). This is confirmed in Figure 3 (top), where we show RSL curves predicted for Djerba (representative of the Gulf of Gabes), and for the Gulf of Sirte using the ICE3G chronology and the rheological model VP1 (the two sites are marked by a cross and a black dot in Figure 1, respectively). The major feature of the solid curves is a sharp

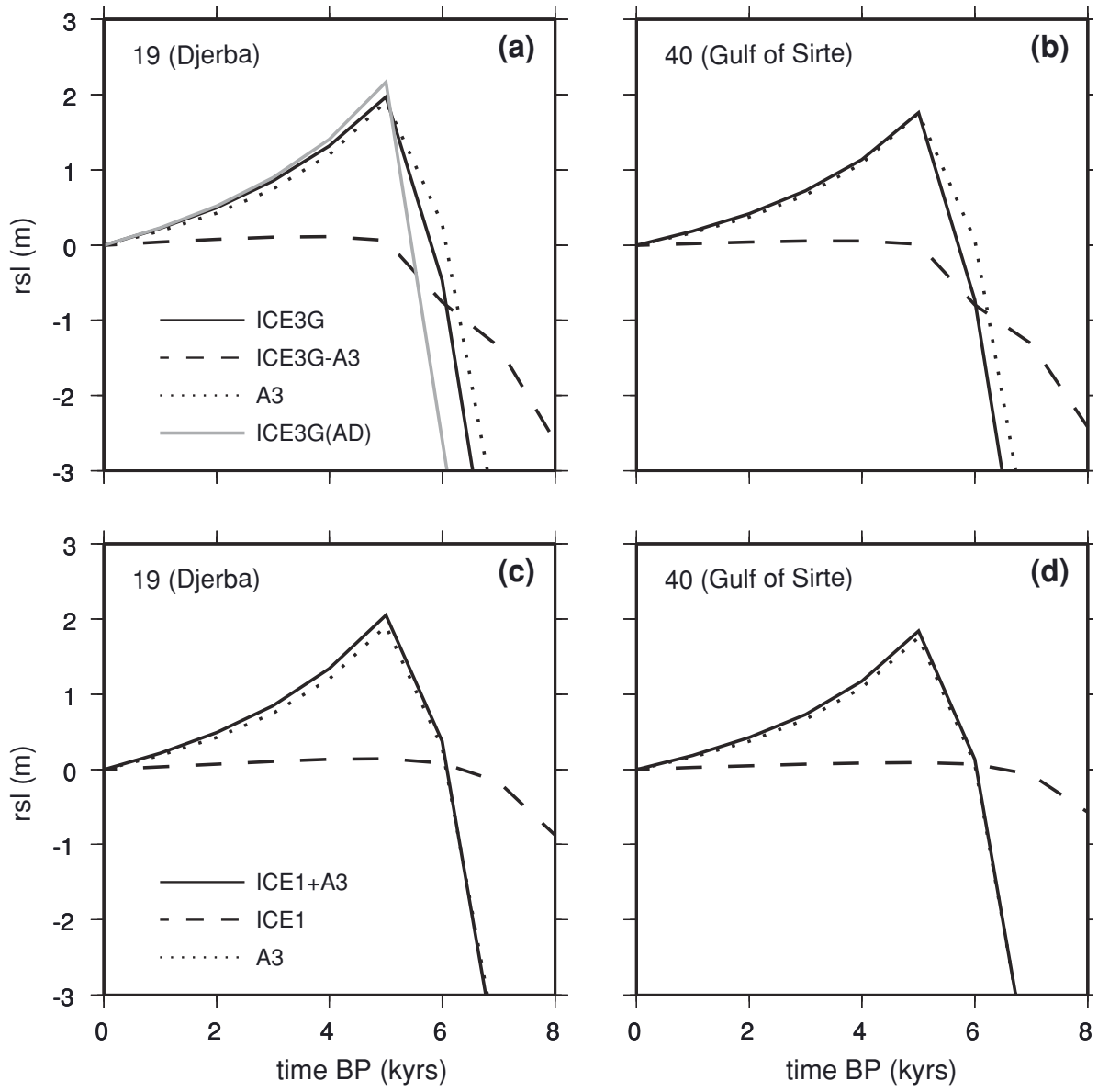

Figure 3
RSL histories predicted at Djerba (left) and Gulf of Sirte (right). In top frames, we use the ICE3G ice sheets chronology of Tushingham and Peltier (1991), ICE3G–A3 (i.e., ICE3G deprived of its Antarctic component A3), and A3. In bottom frames, we employ the old ICE1 model of Peltier and Andrews (1976), ICE1+A3, and again A3. A marked high–stand at 5 kyrs BP is visible if A3 is accounted for. The grey curve in frame (a) applies to the simplified AD model for Antarctica introduced in Section 3.3.

high–stand of $\sim$2 m at the end of deglaciation. The dashed curves show that for model ICE3G–A3, in which ICE3G is deprived of its Antarctic component, no significant RSL variations are expected during the last $\sim$6 kyrs. Thus, at these North African sites during the mid– to late–Holocene, sea–level has evolved *as if* Antarctica had the only active ice sheet (dotted curves). Frames (c) and (d) apply to model ICE1. Since ICE1+A3 essentially reproduces ICE3G (top), at these sites RSL is largely insensitive to the history of deglaciation of the Northern Hemisphere ice sheets, in spite of significant differences

Journal : 24 Dispatch : 1-4-2009 Pages : 23
Article No. : 0488 ☐ LE ☐ TYPESET
MS Code : 0488 ☑ CP ☑ DISK

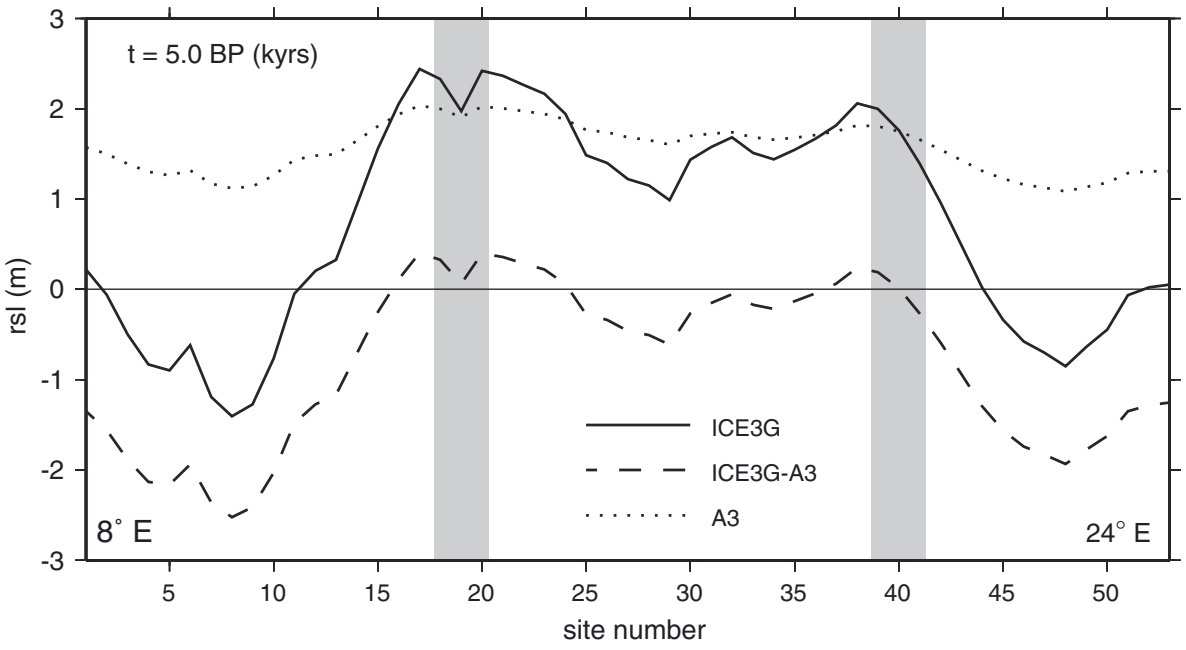

Figure 4
RSL at time $t = 5$ kyrs BP in Tunisia and Libya for longitudes between 8° and 24°E. The horizontal axis shows the RSL "test sites" of Figure 1. Ice models are the same as in Figure 3 (top). Djerba (19) and Gulf of Sirte (49) fall within the regions evidenced by shaded vertical bars.

between the Fennoscandian components of ICE1 and ICE3G (see Fig. 2). As discussed by Stocchi and Spada (2007), this also holds when the recent deglaciation chronology ICE5G (Peltier, 2004) is used. Compared to ICE1, the dashed curves show no RSL change during the last 5 kyrs, similarly to ICE3G–A3 (top).

The peculiarity of the two sites considered in Figure 3 can be better appreciated in Figure 4, showing the high–stand amplitude at $t = 5$ kyrs BP for all North African test sites marked by open circles in Figure 1. For model ICE3G (solid), the high–stand region ranges between longitudes of $\sim$10° and $\sim$22°E, corresponding to sites from 12 to 44, respectively. By further computations, we have verified that beyond these limits the RSL curves show no high–stands, but rather a monotonous sea–level rise with a kink at the time corresponding to the end of deglaciation (see also Stocchi and Spada, 2007). Where the dashed curve (ICE3G–A3) crosses the horizontal axis, RSL change only originates from the contribution of Antarctica (dotted). Djerba is close to one of these points, and another is found at the center of the Gulf of Sirte (site 40 in Fig. 1), consistent with the observation that "continental levering" is magnified in deep inlets (Mitrovica and Milne, 2002).

3.2. RSL Observations

From the analysis of the previous section, the presence of a late–Holocene high–stand is expected to be a stable feature along a significant portion of the coasts of Tunisia and

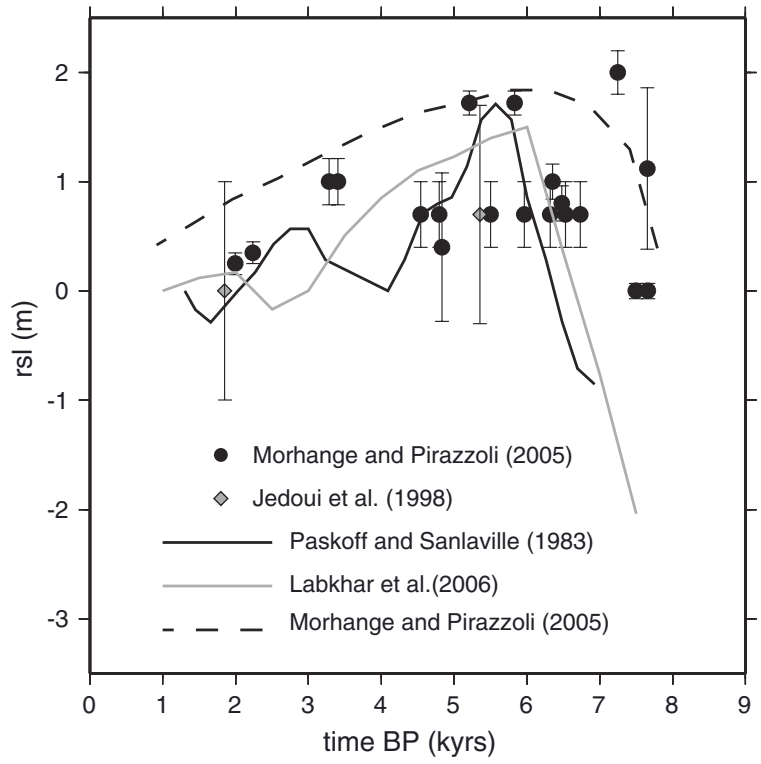

Figure 5
RSL data and trends for SE Tunisia according to various authors. All sources indicate the presence of a late–Holocene high–stand in this region, with an amplitude between 1 and 2 m. The dashed curve is obtained converting to calendar years the tentative RSL history suggested by MORHANGE and PIRAZZOLI (2005).

Lybia. This is confirmed by the field observations for the Gulf of Gabes shown in Figure 5 (to our knowledge no RSL observations are currently available for the Gulf of Sirte). As pointed out by SAMMARI *et al.* (2006), the relatively large error bars characterizing some of the SE Tunisia RSL data can be attributed to the considerable tidal excursions ($\sim$1 m) in this region.

The tentative RSL curve of PASKOFF and SANLAVILLE (1983) (solid) indicates a transgression between 6.4 and 4.3 kyrs BP with a maximum high–stand of $\sim$1.7 m and a subsequent sea–level fall following an erratic curve. Evidence from two fossilized bioclastic beaches (JEDOUI *et al.*, 1998, diamonds) also suggests the existence of a late–Holocene high–stand, but the amplitude of emergence is only weakly constrained due to the large error bars. From a review of previous evidence and new indicators along the coast of the Gulf of Gabes, MORHANGE and PIRAZZOLI (2005) have recently published a detailed RSL history for Tunisia for the last 8 kyrs, reproduced by solid circles in Figure 5. Their observations, of improved precision compared to PASKOFF and SANLAVILLE (1983) and JEDOUI *et al.* (1998), clearly indicate a late–Holocene high–stand and a subsequent irregular sea–level fall. The best–fitting RSL history suggested by Morhange and Pirazzoli, reproduced here by a dashed curve, suggests a peak high–stand of $\sim$2 m at 6 kyrs BP. Finally, the recent study by LAKHDAR *et al.* (2006) based on sedimentary records (grey curve in Fig. 5) also indicates the existence of a late–Holocene high–stand

Journal : 24 Dispatch : 1-4-2009 Pages : 23
Article No. : 0488 ☐ LE ☐ TYPESET
MS Code : 0488 ☑ CP ☑ DISK

and provides a further tentative RSL curve for SE Tunisia, consistent with that of PASKOFF and SANLAVILLE (1983).

In summary, all available data in the region of the Gulf of Gabes suggest, albeit sometimes weakly, a late–Holocene high–stand of 1–2 m between 5 and 7 kyrs BP. In the following subsection, we will study how the time and amplitude of the high–stand can be used to constrain the melting history of Antarctica.

3.3. Sensitivity Analysis

Since the Gulf of Gabes is in the far–field of the Antarctic ice sheet, it is appropriate to model it by a simple disc of constant thickness and radius. Its time–history reproduces the main features of ice model A3 (the Antarctic portion of ICE3G), i.e., a steady state until time $t = t_i$ kyrs BP followed by a deglaciation at a constant rate until time $t = t_f$ kyrs BP. We are aware that this may represent an oversimplified time–history for Antarctica, but more complex stepwise parametrizations, such as those in model ICE5G (PELTIER, 2004), are not justified by available data in the far–field and especially in SE Tunisia (see Fig. 5). For ice model A3, $t_i \sim 10$, $t_f \sim 5$ kyrs BP and $ESL \sim 28$ m, comparable to the value of 24 m proposed by DENTON and HUGHES (1981) (see left frame of Fig. 2). The simplified Antarctic ice model proposed here will hence forth be referred to as AD model, while RAD will indicate a disc model with an *ESL* variation reduced by a factor of 2 (~ 14 m). The equivalence between ICE3G and ICE3G(AD) can be appreciated by inspection of the grey curve in Figure 3a.

The contour lines in Figure 6 show the high–stand peak amplitude $HS_{\max}$ predicted at Djerba (site 19 in Fig. 1) for $0 \leq t_f \leq t_i$, while shades of grey in the background indicate computed values of the high–stand epoch t_{HS} (see caption on top). Insets show the time–history of AD (left) and RAD (right), which represent the Antarctic components of the global time–histories of deglaciation ICE3G (top) and ICE1 (bottom). A high–stand is always predicted at Djerba ($HS_{\max} > 0$). However, its maximum amplitude is very sensitive to the values of t_i and t_f and increases until $t_i = t_f$, corresponding to a sudden melting of the Antarctic ice sheet. In particular, for ICE3G(AD), a value $HS_{\max} \sim 4.3$ m is obtained for $t_i = 6$ and $t_f = 5$ kyrs BP (not shown in figure). A qualitatively similar pattern is observed for ICE1+AD (c), with $HS_{\max} \sim 4.5$ m and a slightly earlier melting ($t_i = 7$, $t_f = 6$ kyrs BP). Differences between frames (a) and (c) are only due to the different time–histories of the Northern Hemisphere ice sheets in ICE1 and ICE3G.

Circles and diamonds in Figure 6 indicate $HS_{\max}$ and t_{HS} values that match the qualitative curve of MORHANGE and PIRAZZOLI (2005) (MP05) and the observations of PASKOFF and SANLAVILLE (1983) (PS83), respectively (see Fig. 5). Peak amplitudes of the PS83 and MP05 high–stands differ by ~ 30 cm, with the former delayed by ~ 1 kyr relative to the latter. From frame (a) we observe that to explain the PS83 high–stand using the Antarctic model AD, melting must begin earlier by ~ 1 kyr with respect to A3 (triangle), while t_f must not be significantly modified. An opposite trend is observed for the MP05 high–stand, which requires a ~ 2 kyrs earlier termination of melting, implying

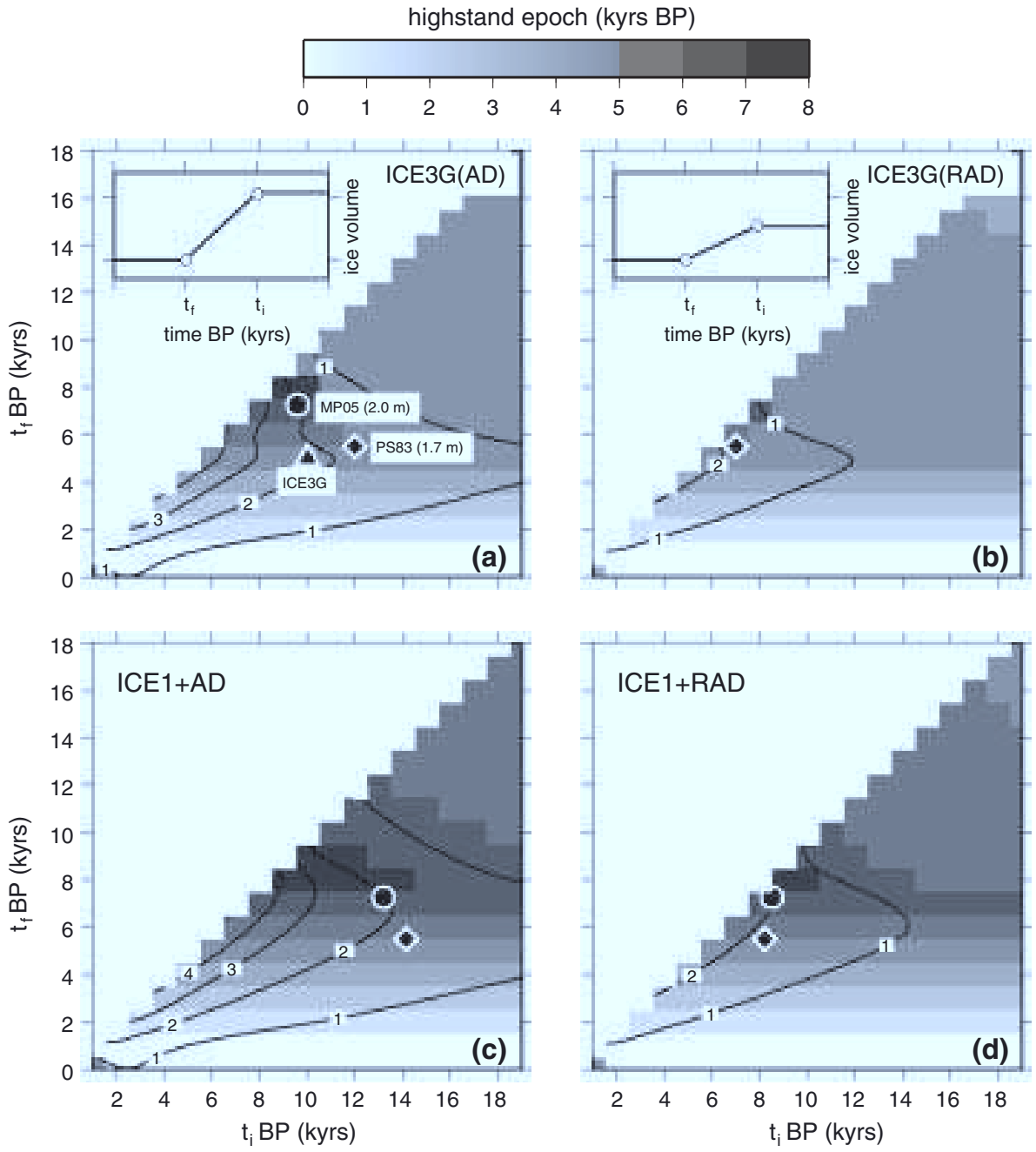

Figure 6

High–stand amplitude $HS_{\max}$ (contour lines, in meters) and high–stand epoch t_{HS} (shades of grey, in kyrs BP) predicted at Djerba for different values of parameters t_i and t_f describing the simplified time–history of Antarctica. Left and right frames apply to the geometrically simplified ice models AD and RAD for Antarctica (their time–histories are shown in the insets). In top and bottom frames the chronologies of the Northern Hemisphere ice sheets follow ICE3G and ICE1, respectively. Circles and diamonds show $HS_{\max}$ and t_{HS} according to observations of MP05 and PS83, respectively (see text).

a significant shortening of the melting phase in Antarctica. To fit the MP05 high–stand using model ICE1+AD (c), the beginning and end of melting must be shifted backwards by $\sim$3 kyrs and $\sim$2 kyrs with respect to A3, respectively. By a suitable adjustment of the

Journal : 24 Dispatch : 1-4-2009 Pages : 23
Article No. : 0488 ☐ LE ☐ TYPESET
MS Code : 0488 ☑ CP ☑ DISK

free parameters t_i and t_f, it is also possible to fit the PS83 high–stand (diamond). Thus, from frames (a) and (c) of Figure 6 it is apparent that by our simplified representation of A3, the $HS_{\max}$ and t_{HS} values suggested by the RSL curves of PS83 and MP05 can always be fitted satisfactorily. As the geometry of the contour lines and of the shaded regions indicates, the temporal parameters of the time–history can simultaneously be constrained only by knowledge of both $HS_{\max}$ and t_{HS} for a given high–stand (i.e., MP05 or PS83).

The sensitivity of North African RSL observations to the time–history of the Antarctic ice sheet, already addressed in Figure 3, motivates the analysis shown in frames (b) and (d) of Figure 6, where we use the RAD model of Antarctica with *ESL* (RAD) = *ESL* (AD)/2 (see inset). Evidence in support of RAD drives from a wide spectrum of observations ranging from paleo–climatology to thermo–mechanical modeling of ice sheets (see e.g., BENTLEY, 1999 and DENTON and HUGHES, 2002). When RAD is employed (b), $HS_{\max}$ is reduced by approximately a factor of 2 with respect to AD (a), confirming that RSL at Djerba is only affected by the melting in Antarctica. While ICE3G(RAD) can only account for the PS83 high–stand (diamond), ICE1 + RAD can also explain MP05 (circle). It is, however, clear from these diagrams that, for ICE1+RAD it is necessary to allow for $\sim$1 kyr long melting phase for Antarctica to explain the observed high–stand. Due to the coarse time discretization and the low time resolution of RSL data employed here, the duration of this possible melting episode cannot be constrained more precisely.

4. Results

The study above suggests that a drastic reduction of the *ESL* associated with Antarctica to $\sim$14 m may be reconciled with RSL observations in the Gulf of Gabes, choosing appropriate t_i and t_f values. Also, on the basis of the mentioned supporting evidence from Antarctic studies, this finding motivates us to test whether such a revised melting history may improve the agreement with other RSL observations on a regional or global scale. Here we consider separately two facets of the problem, i.e., (i) the determination of an optimum *ESL* for Antarctica and (ii) the plausibility of a catastrophic rise episode that is suggested in Figures 6b and 6d.

The first issue is addressed in Figure 7, where we consider the χ^2 misfit between data and predictions relative to various data sets, as computed in SPADA *et al.* (2006). Since a complete statistical study is not our purpose here, we proceed heuristically, leaving more rigorous analyses to future work. The misfit is shown as a function of the scaling factor F (%) modulating the *ESL* for model A3. The C curves in Figure 7 refer to computations in which the *ESL* reduction related to Antarctica is compensated by a uniform rescaling of the volumes of the other components of ICE3G to preserve its total *ESL* of $\sim$113.5 m. We show results obtained for the RSL 392 observations of the TUSHINGHAM and PELTIER (1993) RSL database (hereafter ''TP database'', solid), and potentially interesting groups of data as well. In particular, we separately consider a set

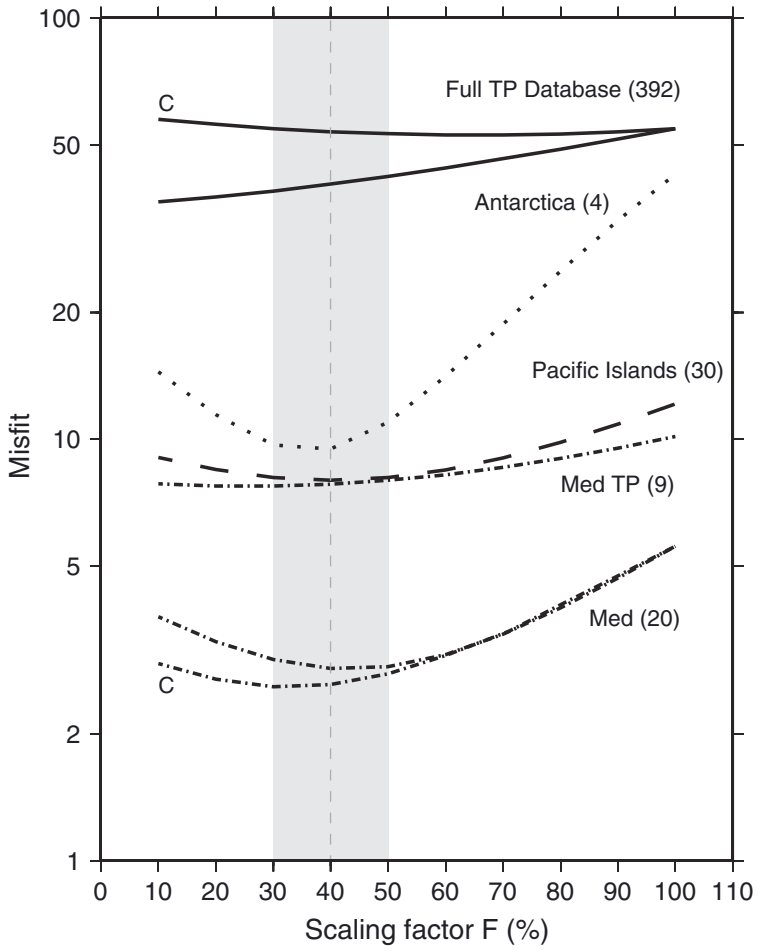

Figure 7

Effect of varying the *ESL* of ice model A3 for Antarctica on the misfit between observations and predictions on global, (solid line) and regional scales (other lines). The preferred value of the scaling factor $F \sim 40\%$ is indicated by the shaded region. The two curves labeled by C refer to the case in which the *ESL* reduction for Antarctica is compensated by an equal, opposite and uniform *ESL* increase for the other ICE3G ice sheets. Note that the misfit scale is logarithmic.

of TP sites located along the coast of Antarctica (dotted, four sites) and in the Pacific Islands region (dashed, 30 sites). In addition, we employ two data sets pertaining to the Mediterranean Sea (dash-dotted). The first includes nine of the eleven TP observations for this region (the sites of Algiers and Beirut are excluded because of their tectonic instability, see MEGHRAOUI *et al.*, 2004; MORHANGE et al., 2006), while the second collects independent RSL observations taken mostly from LAMBECK *et al.* (2004) and recently scrutinized by STOCCHI and SPADA (2007), to which the reader is referred for more information about the original sources.

The solid curve in Figure 7 indicates that the agreement with the global TP observations improves with decreasing F, with the minimum misfit obtained when Antarctica is assumed to be stationary during the Holocene $(F \mapsto 0)$, as in the ICE1 model of PELTIER and ANDREWS (1976). As expected, the maximum sensitivity to variations of F is observed for sites located along the coast of Antarctica (dotted),

Journal : 24 Dispatch : 1-4-2009 Pages : 23
Article No. : 0488 ☐ LE ☐ TYPESET
MS Code : 0488 ☑ CP ☑ DISK

suggesting a $\sim$60% *ESL* reduction with respect to the ICE3G value of $\sim$28 m. Qualitatively similar results are obtained for the other regional curves, showing a minimum for $F \sim 40\%$. It is clear that when the global database is considered (solid), the sensitivity to modifications of the *ESL* variation of Antarctica is less pronounced than for the regional datasets. This can be explained by the significant weight, in the full TP database, of sites belonging to Clark zones I and II (CLARK and LINGLE, 1979), which are most strongly influenced by the effects of near–field glaciers. It is interesting to note that regardless of the F value, the revised Mediterranean set implies misfit values considerably smaller than for Med TP, which may indicate an improved coherence of these RSL observations. The new data set also shows an improved sensitivity to *ESL* variations, with the optimum value comparable with that inferred from the Antarctic records (dotted). This confirms findings by STOCCHI and SPADA (2007), who explained the value of improved Mediterranean RSL observations in constraining the ice volume of far–field ice sheets, and particularly of Antarctica.

Inspection of the C curve relative to the full TP database in Figure 7 reveals that a uniform scaling of the *ESL* of ice sheets ICE3G components compensating for the *ESL* reduction of Antarctica deteriorates the misfit relative to the previous computations (solid). As we have directly verified, the reason is that an increase of the volumes of the Laurentide and Fennoscandian ice sheets does not help to better reproduce the RSL observations in these regions. As shown, the C curve is found to be basically insensitive to variations of the scaling factor F. Regarding the Med dataset, imposing the eustatic constraint of ICE3G slightly alters the misft curve, now showing a minimum for $F \sim 30\%$. This possibly indicates that the revised Mediterranean observations can benefit from a simultaneous reduction of the *ESL* for Antarctica and a modification of the ICE3G chronology for the nearby Fennoscandian ice sheet. The need for a revised chronology of Fennoscandia is also consistent with the findings of LAMBECK *et al.* (2004) and STOCCHI *et al.* (2005). Since mass conservation can be obtained in various manners, in the computations of this section we have chosen not to compensate for the *ESL* reduction associated with Antarctica, also following BASSETT *et al.* (2005). Possible solutions to the "missing water problem'', discussed by BENTLEY (1999), support the idea that at least some of the estimates of ice sheets volumes are not correct.

The second issue, i.e., the details of the melting history of the Antarctic ice sheet, is addressed in Figure 8 by a misfit study aimed to constrain the t_i and t_f parameters of model RAD (see inset of Fig. 6b). Here, RSL sites from the TP database and the Pacific Islands are considered in frames (a) and (b), respectively. In both cases we employ model ICE3G(RAD), in which the *ESL* for Antarctica is reduced from the reference value of 14 m used to date, to the best–fitting value of 11.2 m which is consistent with the value $F = 40\%$ suggested by the analysis of Figure 7. Using the full data set (a), the minimum misfit is reached for $t_i = 15$ and $t_f = 14$ kyrs BP. These epochs approximately bound the rapid melting event known as meltwater pulse 1 (MWP–1A) first described by FAIRBANKS (1989). This result supports a scenario in which Antarctica has been the main cause of the water pulse consistent with the recent

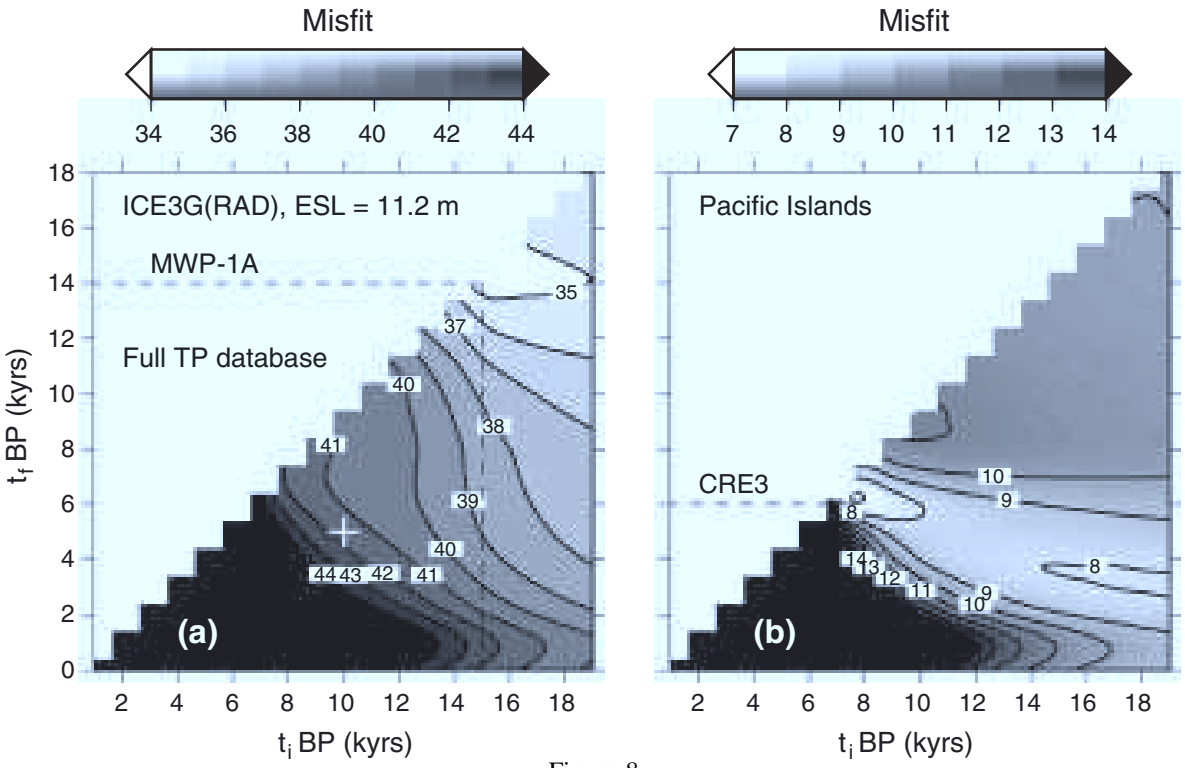

Figure 8

Misfit between predictions and observations on a global scale (a) and for the Pacific Islands (b) for various combinations of the parameters t_i and t_f of ice model RAD. The *ESL* for Antarctica is kept fixed at 11.2 m, as shown in Figure 7. Epochs of possible meltwater pulses (MWP–1A and CRE3) are shown. The misfit obtained using the A3 time parameters is marked by a white cross.

work of BASSETT *et al.* (2005). While these authors have considered a limited set of far–field observations and a significantly different viscosity value for the lower mantle (see model VP2 of Table 1), here the plausibility of MWP–1A is evident even from a global data set. However, since the misfit reduction we obtain with respect to a RAD model with the same temporal parameters of ice sheet A3 (white cross in Fig. 8) is not very large and possibly not statistically significant, estimates of t_i and t_f should be taken cautiously.

Varying the ensemble of RSL observations may significantly affect the values of the best–fitting parameters t_i and t_f. In the case study of Figure 8b, relative to the Pacific Islands, the region of minimum misfit extends diagonally from point ($t_i \sim 18$, $t_f \sim 3$) kyrs to ($t_i \sim 8$, $t_f \sim 7$) kyrs, where the absolute minimum is met. Such an elongated valley in the parameters space indeed provides a very weak constraint on the duration of the melting phase for Antarctica, which may range from ~ 15 to ~ 1 kyrs. We note that the region of plausible parameters contains the Antarctic melting phase of the original A3 model (namely, $t_i = 10$, $t_f = 5$ kyrs). This study shows that a water pulse cannot be rejected from the analysis of the Pacific Islands observations, however its epoch (~ 8 kyrs BP) is shifted forward significantly with respect to MWP–1A (compare with Figure 8a). This meltwater pulse may coincide with the catastrophic rise of event 3

Journal : 24 Dispatch : 1-4-2009 Pages : 23
Article No. : 0488 ☐ LE ☐ TYPESET
MS Code : 0488 ☑ CP ☑ DISK

Figure 9 ▶
Observations and predictions for RSL sites from the revised Mediterranean data set (sites locations are shown in Fig. 1). Here we use ice model ICE3G and four chronologies based on ICE1 and ICE3G, with "$[t_i–t_f]$" indicating the melting interval in kyrs BP.

(CRE3) discussed by BLANCHON and SHAW (1995); the last of a sequence of three episodes starting with MWP–1A (CRE1).

The issue of how the melting scenarios for Antarctica suggested by Figures 6 and 8 may influence the Holocene RSL variations in the Mediterranean basin is addressed in Figure 9. Instead of considering the complete Med data set, as in Figure 8, here we limit our attention to six representative sets of observations (site locations are shown in Fig. 1). These sites are chosen for the overall quality of the observations and their relatively large number of observations in the time span considered. With the sole exception of Djerba, data and error bars are taken from the work of LAMBECK *et al*. (2004). By a trial–and–error approach, we have scrutinized five possible chronologies for the remote ice sheets, suggested by the results of Figure 8 (see inset in Fig. 9a). The first is the ICE3G model (solid curves), which has been employed as a reference scenario since the onset of our discussion. In addition to ICE3G, we deal here with other ice models characterized by various RAD chronologies. Numbers in brackets following the ice sheets' names indicate values of t_i and t_f, in kyrs BP, pertinent to the RAD time history. In particular, a meltwater pulse is accounted for by models ICE3G[15–14] (MWP–1A), ICE3G[8–7](CRE3) and ICE1[8-7](CRE3). We also consider model ICE3G[18–3], characterized by the very long melting phase suggested by the results of Figure 8b. This particular model, in which Antarctica is subject to a delayed melting with respect to A3, is broadly similar to the one termed "ANT 3a" by NAKADA and LAMBECK (1988), characterized by a significant melting ($ESL \sim 3$ m) over the past 6 kyrs. Here we have not analyzed other competing chronologies that support an ice–sheet readvance during the late–Holocene (GOODWIN, 1998). The readvance would cause a global high–stand followed by a sea–level fall, which cannot explain the observations in the northern Mediterranean (STOCCHI and SPADA, 2007). To supplement the computational results of Figure 9, Figure 10 summarizes misfit values for each site and the ice models tested.

Even a cursory inspection of Figure 9 shows that ICE3G cannot explain the Holocene RSL curves across the Mediterranean, which confirms the results of STOCCHI and SPADA (2007). In particular, it fails both in predicting the slow and monotonous trend of sea–level rise observed at the sites of Marseilles and North Adriatic Sea (a, e), and is also inappropriate at Cap Corse (c), where the data suggest a relatively rapid sea–level rise during the last 5 kyrs. While the agreement with the observations is qualitatively acceptable for Versilia Plain (b) and North Sardinia (d), in Djerba (f) ICE3G produces a high–stand of correct amplitude, but significantly delayed (by about 2 kyrs) with respect to that observed by MORHANGE and PIRAZZOLI (2005) (see also Fig. 6). The overall inadequacy of ICE3G is also apparent from Figure 10, where misfits for individual sites are shown by dashed lines, whereas thick solid curves show

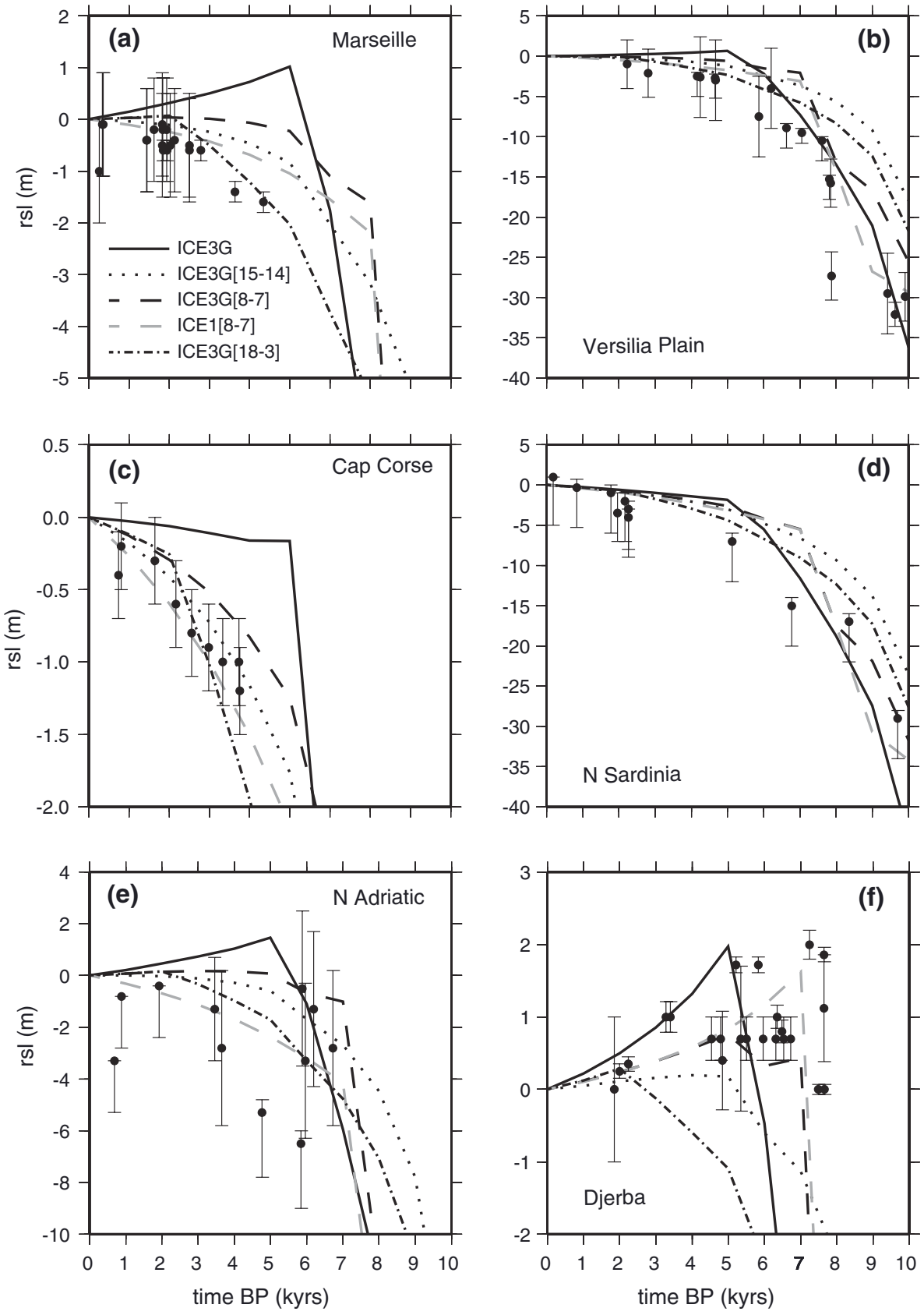

Journal : 24 Dispatch : 1-4-2009 Pages : 23
Article No. : 0488 ☐ LE ☐ TYPESET
MS Code : 0488 ☑ CP ☑ DISK

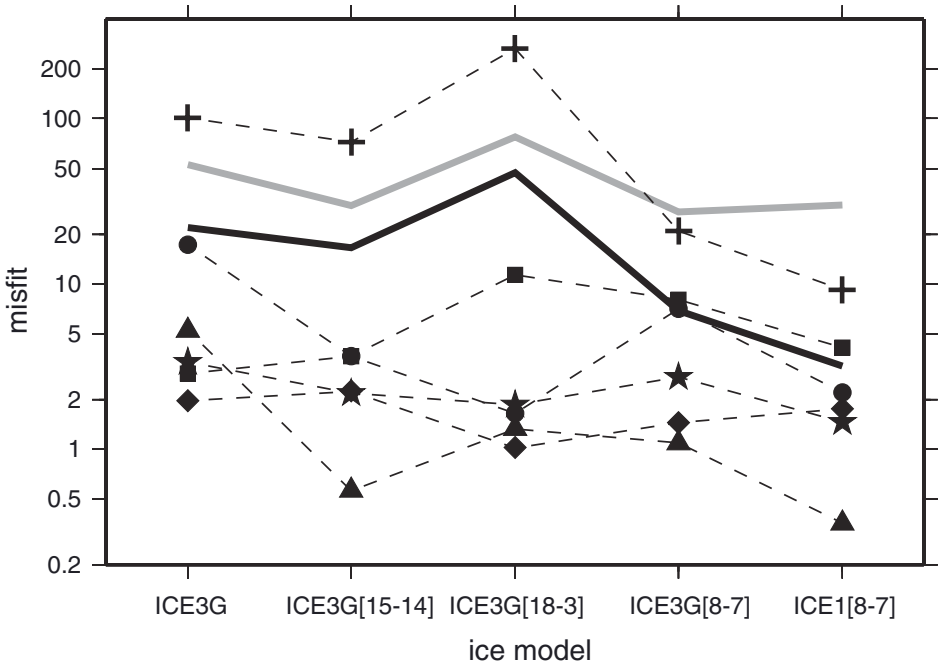

Figure 10
Misfit values computed for each of the ice models considered in Figure 9. Symbols used in Figure 1 are also employed here. Solid curves show average misfit values representative of all the sites considered. A thick grey line shows results obtained using the viscosity profile VP2 of Table 1.

average misfit values for the viscosity profile VP1 and for the viscosity profile of BASSETT *et al*. (2005) (VP2) (see Table 1). Introducing a meltwater pulse that mimics MWP–1A (i.e., model ICE3G[15–14], dotted), greatly improves the match for Marseilles, Cap Corse, and North Adriatic Sea (see also Fig. 10), while for Versilia and North Sardinia the agreement with observations improves for the last $\sim$5 kyrs, but deteriorates prior to this period. In Djerba, ICE3G[15–14] basically reproduces the ICE3G–A3 results of Figure 3a, since an early deglaciation of Antarctica enhances the effects of Northern Hemisphere ice sheets at later times. The late pulse CRE3 implicit in model ICE3G[8–7] deteriorates, with respect to ICE3G[15–14], the agreement with observations at Marseilles, Cap Corse, North Adriatic Sea, and Versilia Plain, as quantitatively confirmed in Figure 10. However, the match is improved for North Sardinia and Djerba. In this latter case, the impulse precedes the transgression, thus providing a better fit to the observed RSL.

Previous investigations on the effects of glacial isostatic movements in northern Italy and southern France (STOCCHI *et al*., 2005) demonstrated the sensitivity of vertical uplift in these regions to the time–history of the former northern Europe ice sheets. To shed light on this issue, in Figure 9 we also show results based on the ICE1 history of deglaciation, which differs from ICE3G for the melting history of Fennoscandia and, most importantly in this context, for an earlier cessation ($\sim$2 kyrs) of the melting phase (PELTIER and ANDREWS, 1976; TUSHINGHAM and PELTIER, 1991) (see Fig. 2). According to

Journal : 24 Dispatch : 1-4-2009 Pages : 23
Article No. : 0488 ☐ LE ☐ TYPESET
MS Code : 0488 ☑ CP ☑ DISK

Figure 9f, this feature of ICE1 has a significant effect at Djerba, where model ICE1[8–7] now reproduces the observed high–stand satisfactorily (grey, dashed). This is also observed for Marseilles (a), Cap Corse (c), and North Adriatic Sea (e), where improvements relative to ICE3G[15–14] are apparent for all observations, as confirmed by Figure 10. A close inspection of the results relative to Versilia Plain in Figure 9b reveals that ICE1[8–7] helps to better explain the kink suggested by the RSL observation at $\sim$8 kyrs BP, which may be interpreted as a signature of CRE3. At the same epoch, ICE1[8–7] is also compatible with the data for North Sardinia. Finally, the dash–dotted curves show the sensitivity of the Mediterranean records to an extended melting phase for Antarctica using model ICE3G[18–3]. As shown, while this model can essentially explain the northern Mediterranean sea–level indicators, it clearly fails along the coasts of SE Tunisia (f), where evidence in support of a late–Holocene high–stand of hydro–isostatic origin is compelling (see Fig. 5). As shown in Figure 10 (thick black), the failure of ICE3G[18–3] in SE Tunisia produces a misfit increase with respect to the meltwater pulse models.

To date, we have studied the sensitivity of RSL to various assumptions regarding the ice–sheets distribution assuming a unique *a priori* viscosity profile for the mantle, characterized by a small viscosity contrast across the upper and lower mantle. To test the robustness of our results to variations of the viscosity profile, we have repeated the analysis of Figure 9 using the viscosity values suggested by Bassett *et al*. (2005), in which the lower mantle viscosity exceeds the sublithospheric upper mantle viscosity by a factor of 80 (see profile VP2 in Table 1). The results, summarized by thick grey curves in Figure 10, confirm that introducing a meltwater pulse improves the agreement with the observations in the Mediterranean with respect to the classical ICE3G model. However, the overall misfit values are increased relative to the reference viscosity model VP1. As we have verified, this is mainly due to the inadequacy of VP2 to reproduce the observed high–stand in Djerba.

5. *Conclusions*

The Holocene sea–level record of SE Tunisia provides a unique opportunity for calibrating competing models for the history of deglaciation of Antarctica. Our conclusions can be summarized as follows.

i) Forward computations based on the SLE confirm previous findings by Stocchi and Spada (2007) that at the sites of SE Tunisia and Gulf of Sirte the RSL variations in the last 8 kyrs are mostly determined by the melting of the remote Antarctic ice sheet, due to the mutual cancellation of the contributions from the Northern Hemisphere. Attempts to identify other sites worldwide sharing this feature with SE Tunisia have been unsuccessful. The RSL curves expected in this region for the deglaciation model ICE3G are characterized by a developed late–Holocene high–stand, which broadly matches a suite of observations and geological indicators.

Journal : 24 Dispatch : 1-4-2009 Pages : 23
Article No. : 0488 ☐ LE ☐ TYPESET
MS Code : 0488 ✔ CP ✔ DISK

ii) In a sensitivity analysis we have established how the choice of the temporal parameter describing the deglaciation of Antarctica affects the high–stand amplitude and timing. Such analysis has shown that a moderately-reduced *ESL* for Antarctica, compatible with recent reassessments of the Holocene mass budget of this ice sheet (see e.g., BENTLEY, 1999; DENTON and HUGHES, 2002), may be compatible with the observed high–stands in the study region. In this latter case, however, a sudden melting model is preferred in which a meltwater pulse from Antarctica occurs between 8 and 6 kyrs BP, possibly coinciding with the CRE3 episode discussed by BLANCHON and SHAW (1995).

iii) To test the reliability of the results obtained for SE Tunisia, we have performed a further analysis aimed at constraining the *ESL* reduction for Antarctica from RSL observations on a global to regional scale. We have found that a $\sim 60\%$*ESL* reduction relative to ICE3G implies a general misfit reduction when observations from Antarctica, Pacific Islands, and the Mediterranean are considered. When we consider the global TP RSL database, the best fit with the observations is obtained assuming a steady–state Antarctic ice sheet during the Holocene. A further misfit reduction is achieved by allowing for modifications of the time–history of Antarctica and particularly by introducing meltwater pulses that have been found to approximately coincide with those suggested by independent investigations (FAIRBANKS, 1989; BLANCHON and SHAW, 1995).

iv) We then have focused our attention on the Mediterranean RSL observations, in an attempt to constrain to the time–history of the late–Holocene ice sheets using an improved data set for this region extracted from the recent literature. A site–to–site study has shown that the Mediterranean RSL observations demand a CRE3 event of Antarctic origin between 8 and 7 kyrs BP. Allowing for such a pulse and assuming a moderate viscosity increase across the mantle, our model reproduces both the SE Tunisia high–stand at 7 kyrs BP and the generally monotonous sea–level rise observed in most parts of the Mediterranean and along its northern coasts.

v) The results obtained from the study of the Mediterranean record indicate that the CRE3 meltwater pulse at ~ 8 kyrs BP may have concluded the last deglaciation. This view contrasts with previous reconstructions of the Antarctic chronology in which the melting of this ice sheet continued throughout the Holocene (NAKADA and LAMBECK, 1988). With the viscosity value adopted here (VP1), such a delayed melting would fit the northern Mediterranean observations reasonably well (STOCCHI and SPADA, 2007), but would contradict the observations in SE Tunisia (MORHANGE and PIRAZZOLI, 2005). As we have verified, the misfit would even be larger in the case of model VP2.

vi) Without evidence from SE Tunisia, the Mediterranean observations would be reasonably reproduced using chronology ICE3G[18–3], which is broadly consistent with the ANT–3a melting history previously introduced by NAKADA and LAMBECK (1988) to explain post–glacial RSL in the Australian region. However, when the data from SE Tunisia are accounted for and assumed to be reliable, the only model that

reconciles northern and southern Mediterranean RSL curves is the meltwater pulse model CRE3.

Acknowledgments

We thank Detlef Wolf for his careful review of this manuscript and for his support. We have greatly benefited from discussions with colleagues during the 2nd IAG Workshop on "Deformation and Gravity change: Indicators of Isostasy, Tectonics, Volcanism and Climate Change" held on Lanzarote (Spain) in March 2007 and by suggestions of two anonymous referees. The figures were prepared using the GMT public domain software (WESSEL and SMITH, 1991).SELEN, the open–source program used to solve the SLE, can be directly requested from GS (email: giorgio.spada@gmail.com). The program is described at the web page http://flocolleoni.free.fr/SELEN.html. This work is partly funded by MIUR (Ministero dell' Università, dell'Istruzione, e della Ricerca) by the PRIN2006 grant "Il ruolo del riaggiustamento isostatico postglaciale nelle variazioni del livello marino globale e mediterraneo: nuovi vincoli geofisici, geologici, ed archeologici".

REFERENCES

ANDERSON, J.B. and THOMAS, M.A. (1991), *Marine ice-sheet decoupling as a mechanism for rapid, episodic sea–level change: the record of such events and their influence on sedimentation*, Sediment. Geol. *70*(2–4), 87–104.

BASSETT, S. E., MILNE, G. A., MITROVICA, J. X., and CLARK, P. U. (2005), *Ice sheet and solid Earth influences on far–field sea–level histories*, Science *309*, 925–928.

BENTLEY, M. J. (1999), *Volume of Antarctic Ice at the Last Glacial Maximum, and its impact on global sea–level change*, Quaternary Sci. Rev. *18*, 1569–1595.

BLANCHON, P. and SHAW, J. (1995), *Reef drowning during the last deglaciation: evidence for catastrophic sea–level rise and ice sheet collapse*, Geology *23*, 1, 4–8.

BOND G.C., HEINRICH, H., BROECKER, W., LABEYRIE, L., MCMANUS, J., ANDREWS, J., HUON, S., JANTSCHIK, R., CLASEN, S., SIMET, C., TEDESCO, K., KLAS, M., BONANI, G., and IVY., S. (1992), *Evidence for massive discharges of icebergs into the North Atlantic Ocean during the last glacial period*, Nature *360*, 245–249.

BOND, G., BROECKER, W., JOHNSEN, S., MCMANUS, J., LABEYRIE, L., JOUZEL, J., and BONANI, G. (1993), *Correlations between climate and records from North Atlantic sediments and Greenland ice*, Nature *365*, 143–147.

CAZENAVE, A. and NEREM, R., S., (2004), *Present day sea level change: observation and causes*, Rev. Geophys. *42*, 1–20.

CHURCH J. A. and WHITE, N., (2006), *A 20th century acceleration in global sea-level rise*, Geoph. Res. Lett. *33*, L01602, doi:10.1029/2005GL024826.

CLARK, J. A. and LINGLE, C. S. (1979), *Predicted relative sea–level changes (18.000 Years B.P. to present) caused by late–glacial retreat of Antarctic ice sheet*, Quaternary Res. *11*, 279–298.

CLARK, P. U., ALLEY, R. A., KEIGWIN, L. D., LICCIARDI, J. M., JOHNSEN, S. J., and WANG, H. (1996), *Origin of the first meltwater pulse following the last glacial maximum*, Palaeoceanography *11*, 563–577.

CLARK, P. U., MITROVICA, J. X., MILNE, G. A., and TAMISIEA, M. E. (2002), *Sea–level finger print as a direct test for the source of global meltwater pulse 1a*, Science *295*, 2438–2441.

DENTON, G. H. and HUGHES, T. H. (2002), *Reconstructing the Antarctic Ice Sheet at the Last Glacial Maximum*, Quaternary Sci. Rev. *21*, 193–202.

Journal : **24** Dispatch : **1-4-2009** Pages : **23**
Article No. : **0488** ☐ LE ☐ TYPESET
MS Code : **0488** ☑ CP ☑ DISK

DENTON, G. H. and HUGHES, T. J., The Last Great Ice Sheets (Wiley, N. Y. 1981).

FAIRBANKS, R. G. (1989), *A 17,000 year glacio–eustatic sea–level record: Influence of glacial melting rates on the Younger Dryas event and deep ocean circulation*, Nature *342*, 637–642.

FAIRBANKS, R. G., CHARLES, C. D., and WRIGHT, J. D., Origin of global meltwater pulses, In Radiocarbon after Four Decades (eds. Long, A., and Kra, R. S.) (Springer, New York 1992) pp. 473–500.

FAIRBANKS, R. G., MORTLOCK, R. A., TZU-CHIEN, C., LI, C., KAPLAN, A., GUILDERSON, T. P., FAIRBANKS, T. W., and BLOOM, A. L. (2005), *Marine radiocarbon calibration curve spanning 0 to 50,000 Years B.P. based on paired 230Th/234U/238U and 14C dates on pristine corals*, Quaternary Sci. Rev. *24*, 1781–1796.

FAIRBRIDGE, R. W. (1961), *Eustatic changes in sea–level*, Phys. Chem. Earth *5*, 99–185.

FARRELL, W. E. and CLARK, J. A. (1976), *On postglacial sea–level*, Geophys. J. Roy. Astr. S. *46*, 647–667.

GOODWIN, I. D. (1998), *Did changes in Antarctic ice volume influence the late Holocene sea–level lowering?*, Quaternary Sci. Rev. *17*, 319–332.

GUIDOBONI, E. and COMASTRI, A., *Catalogue of Ancient Earthquakes and tsunamis in the Mediterranean area from the 11th to the 15th century*, (Istituto Nazionale di Geofisica e Vulcanologia, Rome, 2005).

JEDOUI, Y., KALLEL, N., FUNTUGNE, M., ISMAIL, H. B., M'RABET, A., and MONTACER, M. (1998), *A high relative sea–level stand in the middle Holocene in southeastern Tunisia.*, Mar. Geol. *147*, 123–130.

KANFOUSH, S. L., HODELL, D. A., CHARLES, C. D., GUILDERSON, T. P., MARTYN, P. G., and NINNEMANN, U. S. (2000), *Millennial–scale instability of the Antarctic ice sheet during the last glaciation*, Science *288*, 1815–1819.

KAUFMAN, D. S., MILLER, G. H., STRAVERS, J. A., and ANDREWS, J. T. (1993), *Abrupt early Holocene (9.9–9.6 ka) ice–strean advance at the mouth of the Hudson strait, Arctic Canada*, Geology *21*, 1063–1066.

KIDSON, C. (1982), *Sea–level changes in the Holocene*, Quaternary Sci. Rev. *1*, 121–151.

LAKDAR, R., SOUSSI, M., BEN ISMAIL, M. H., and M'RABET, A. (2006), *A Mediterranean Holocene restricted coastal lagune under arid climate: Case of the sedimentary record of Sabkha Boujmel (SE Tunisia)*, Palaeogeography Paleoclimatology Paleoecology *241*, 177–191.

LAMBECK, K., ANTONIOLI, F., PURCELL, A., and SILENZI, S. (2004), *Sealevel change along the Italian coast from the past 10,000 yr.*, Quaternary Sci. Rev. *23*, 1567–1598.

MEGHRAOUI, M., MAOUCHE, S., CHEMAA, B., CAKIR, Z., AOUDIA, A., HARBI, A., ALASSET, P.-J., AYADI, A., BOUHADAD, Y., and BENHAMOUDA, F., (2004), *Coastal uplift and thrust faulting associated with the* $M_w = 6.8$ *Zemmouri (Algeria) earthquake of 21 May, 2003*, Geophys. Res. Lett. *31*, doi:10.1029/2004GL020466.

MITROVICA, J. X. and MILNE, G. A. (2002), *On the origin of late Holocene sea–level high–stands within equatorial ocean basins*, Quaternary Sci. Rev. *21*, 2179–2190.

MITROVICA, J. X., MILNE, G. A. (2003), *On post-glacial sea–level: I. General theory*, Geophys. J. Int., doi:10.1046/j.1365-246X.2003.01942.x.

MITROVICA, J. X. and PELTIER, W. R. (1991), *On post–glacial geoid subsidence over the equatorial ocean*, J. Geophys. Res. *96*, 20,053–20,071.

MORHANGE, C. and PIRAZZOLI, P. A. (2005), *Mid-Holocene emergence of southern Tunisian coasts*, Mar. Geol. *220*, 205–213.

MORHANGE, C., PIRAZZOLI, P. A., MARRINER N., MONTAGGIONI, L. F., and NAMMOUR, T. (2006), *Late Holocene relative sea–level changes in Lebanon, Eastern Mediterranean*, Mar. Geol. *230*, 99–114.

NAKADA, M., and LAMBECK, K. (1988), *The melting history of the late Pleistocene Antarctic ice sheet*, Nature *333*, 36–40.

PASKOFF, R. and SANLAVILLE, P., *Les côtes de la Tunisie. Variations du niveau marin depuis le Tyrrhénien* (Maison de l'Orient Mediterraneen, Lyon 1983) 192 pp.

PELTIER, W. R. and ANDREWS, J. T. (1976), *Glacial isostatic adjustment, I, The forward problem*, Geophys. J. Roy. Astr. S. *46*, 605–646.

PELTIER, W. R., FARRELL, W. E., and CLARK, J. A. (1978), *Glacial isostasy and relative sea–level: a global finite element model*. Tectonophysics *50*, 81–110.

PELTIER, W. R. (2004), *Global Glacial Isostasy and the Surface of the Ice-Age Earth: The ICE-5G(VM2) model and GRACE*, Annu. Rev. Earth Pl. Sci. *32*, 111-149.

PELTIER, W. R. (2005), *On the hemispheric origins of meltwater pulse 1a*, Quaternary Sci. Rev. *24*, 1655–1671.

RUDDIMAN, W. F., *Synthesis; the ocean ice–sheet record, in North America and adjacent oceans during the last deglaciation* (eds. Ruddiman W. F., and Wright, H. E. Jr.) (Geol. Soc. Am., Boulder, CO 1987) pp. 463–478.

Journal : **24** Dispatch : **1-4-2009** Pages : **23**
Article No. : **0488** ☐ LE ☐ TYPESET
MS Code : **0488** ☑ CP ☑ DISK

SAMMARI, C., KOUTITONSKY, V. G., and MOUSSA, M. (2006), *Sea–level variability and tidal resonance in the Gulf of Gabes, Tunisia*, Cont. Shelf Res. *26*, 338–350.

SHEPARD, F. P., *Thirty-five thousand years of sea level, In Essays in Marine Geology in Honor of K. O. Emery* (ed. Clement T.) (University of South California Press, Los Angeles 1963) pp. 1–10.

SPADA, G. and STOCCHI, P., *The Sea–level Equation, Theory and Numerical Examples* (Aracne, Roma, 2006).

SPADA, G., ANTONIOLI, A., CIANETTI, S., and GIUNCHI, C. (2006), *Glacial isostatic adjustment and relative sea-level changes: the role of lithospheric and upper mantle heterogeneities in a 3-D spherical Earth*, Geophys. J. Int. *165* (2), 692–702.

SPADA, G. and STOCCHI, P. (2007),SELEN: *a Fortran 90 program for solving the "Sea–level Equation,"* Comput. Geosci., doi:10.1016/j.cageo.2006.08.006.

STOCCHI, P., SPADA, G., and CIANETTI, S. (2005), *Isostatic rebound following the Alpine deglaciation: impact on sealevel variations and vertical movements in the Mediterranean region*, Geophys. J. Int. *162*, 137-147, doi:10.1111/j.1365-246X.2005.02653.x.

STOCCHI, P. and SPADA, G. (2007), *Post–glacial sea–level in the Mediterranean Sea: Clark's zones and role of remote ice sheets*, Ann. Geophys. 50 (6).

TUSHINGHAM, A. M. and PELTIER, W. R. (1991), *Ice-3G: A new global model of late Pleistocene deglaciation based upon geophysical prediction of post–glacial sea–level change*, J. Geophys. Res. *96*, 4497–4523.

TUSHINGHAM, A. M. and PELTIER, W. R. (1993), *Relative sea–level Database. IGPB PAGES/World Data Center–A for Paleoclimatology Data Contribution Series # 93–106*, NOAA/NGDC Paleoclimatology Program, Boulder CO, USA.

WEAVER, A. J., SAENKO, O. A., CLARK, P. U., and MITROVICA, J. X. (2003), *Meltwater pulse 1a from Antarctica as a trigger of the Bolling–Allerod warm interval*, Science *299*, 1709–1713.

WESSEL, P., and SMITH, W. H. F. (1991), *Free software helps map and display data*, EOS, Transact. Am. Geophys. Union *72*, 441.

To access this journal online:
www.birkhauser.ch/pageoph

Journal : **24** Dispatch : **1-4-2009** Pages : **23**
Article No. : **0488** ☐ LE ☐ TYPESET
MS Code : **0488** ☑ CP ☑ DISK

Pure appl. geophys. 166 (2009) 1–16
DOI 10.1007/s00024-004-0498-9

© Birkhäuser Verlag, Basel, 2009

Pure and Applied Geophysics

Glacio–isostatic Adjustment in the Po Plain and in the Northern Adriatic Region

G. SPADA,[1*] P. STOCCHI,[1,2] and F. COLLEONI[3]

Abstract—Vertical movements in the Po plain (northern Italy) are controlled by natural and anthropogenic effects. Since Italy is located in the far–field of the former late Pleistocene ice sheets, isostatic deformations are primarily driven by melt water loading and represent a major component of long–term natural movements across the entire Mediterranean. In addition to far–field sources, here we consider the isostatic effects of melting of the nearby Würm Alpine ice–sheet, showing that it is possible to put bounds on its maximum thickness, extent and chronology by Holocene relative sea-level observations from the northern Adriatic. Using various plausible ice models, and adopting a viscosity profile that matches Holocene relative sea-level observations in the Mediterranean, we find that melting of the Alpine ice sheet is always responsible for upward movements in the Po plain, currently at rates of ~ 0.5 mm yr^{-1}. When both far– and near–field sources are considered, the rate of sea-level change in the Venetian Lagoon for the most reasonable mantle rheology and melting chronology is negative, i.e., opposite to that attributed to human activity and recent climatic variations. However, its amplitude (fractions of mm yr^{-1}) is small compared to the secular signal observed by tide gauges (~ 2 mm yr^{-1}), which makes glacial isostasy a second–order mechanism of sea-level variation in this region.

1. Introduction

Geological, geomorphological, and archaeological evidence indicate a slow, but spatially nonuniform sea-level rise across the Italian peninsula during the mid to late Holocene (~ 0.5 mm yr^{-1} in the last 2000 yrs according to ANTONIOLI *et al.*, 2008). In the bulk of the Mediterranean, this has been interpreted as mostly due to the effect of the isostatic disequilibrium induced by melt–water loading, while unloading from the Northern Hemisphere ice sheets may have affected the northern Adriatic region (LAMBECK and PURCELL, 2005; STOCCHI and SPADA, 2007). For the Po plain (northern Italy), it was suggested that approximately one half of the subsidence rates is related to tectonic processes and sediment loading or compaction, while glacio–isostatic adjustment (GIA) may account for the other half (CARMINATI *et al.*, 2003). However, since the effects of GIA are sensitive to assumptions about mantle rheology and the history of ice sheets,

[1] Istituto di Fisica, Università di Urbino "Carlo Bo", Via Santa Chiara n. 27, 61029 Urbino, PU, Italy. E-mail: giorgio.spada@gmail.com
[2] DEOS, Faculty of Aerospace Engineering, Delft University of Technology, The Netherlands.
[3] Laboratoire de Glaciologie et Géophysique de l'Environnement, Grenoble, France.

Journal : 24 | Dispatch : 17-4-2009 | Pages : 16
Article No. : 0498 | ☐ LE | ☐ TYPESET
MS Code : 0498 | ✔ CP | ✔ DISK

providing upper and lower bounds even for a limited number of ice and rheological models may be more useful than giving point estimates as mostly done to date (e.g., CARMINATI and DI DONATO, 1999). This helps to define possible scenarios of the future trend of sea level in key areas such as the Venetian Lagoon, where it is important to separate anthropogenic from natural effects.

In current global models of the late–Pleistocene deglaciation, relatively small ice sheets are generally neglected since they provide only a modest contribution to the eustatic curve (see e.g., PELTIER, 2004). However, on a local to regional scale, these small ice sheets may effectively contribute and perturb the relative sea-level curves associated with the melting of large remote ice sheets. DENTON and HUGHES (1981) accounted for various ice sheets in central and southern Europe, the most important of them was certainly the one that covered the Alps. With a width of $\approx$ 600 km and a length of $\approx$ 200 km, this ice sheet was the largest in southern Europe at the Last Glacial Maximum (LGM, 21 kyrs BP). The last large Alpine ice sheet developed prior to the LGM at $\approx$25 kyrs BP, at the end of the Würm glacial period (corresponding to the Late Weischelian in Eurasia). PREUSSER (2004) proposed that the last advance of the Alpine ice sheet occurred only in the western part, reaching its maximum extent between 24 kyrs BP and 20 kyrs BP, and started retreating before 17.5 kyrs BP. No geomorphological evidence supports an eastern ice advance during the LGM (PREUSSER, 2004; FLORINETH and SCHLÜCHTER, 2000).

Due to its proximity to the Po plain and to the coasts of the northern Adriatic (see Fig. 1), the melting of the Würm ice sheet may have the potential of altering the isostatic equilibrium in these particular areas. This was first proposed by GUDMUNDSSON (1994), who studied the post-glacial rebound process occurring in the Swiss Alps and the surrounding regions by a simplified model. Following GUDMUNDSSON (1994), STOCCHI *et al.* (2005) estimated the effects of melting of the Alpine ice sheet including long–wavelength relative sea-level and geodetic signals. This was done solving the gravitationally self–consistent sea-level equation, accounting for the geometry of the former Alpine ice sheet and for the effects of far–field sources. The same approach was followed by LAMBECK and PURCELL (2005), who were been mainly concerned with the history of sea level during the Holocene on the Mediterranean scale.

Differently from STOCCHI *et al.* (2005), here we focus on the GIA effects in the Po plain and along the coasts of the Adriatic Sea, with attention to past and present sea-level variations at historical sites, such as Ravenna, Trieste, and Venezia (see Fig. 1). This study extends previous results by CARMINATI and DI DONATO (1999) that only accounted for the effects of remote ice sheets and used a viscosity profile which is probably inappropriate for the Mediterranean region (LAMBECK and PURCELL, 2005). Our improved evaluation of the GIA effects in the study area may be useful for the interpretation of the total natural subsidence in the Po plain and for the assessment of the anthropogenic component of sea-level rise during recent decades (CARMINATI *et al.*, 2003).

Journal : 24 Dispatch : 17-4-2009 Pages : 16
Article No. : 0498 ☐ LE ☐ TYPESET
MS Code : 0498 ☑ CP ☑ DISK

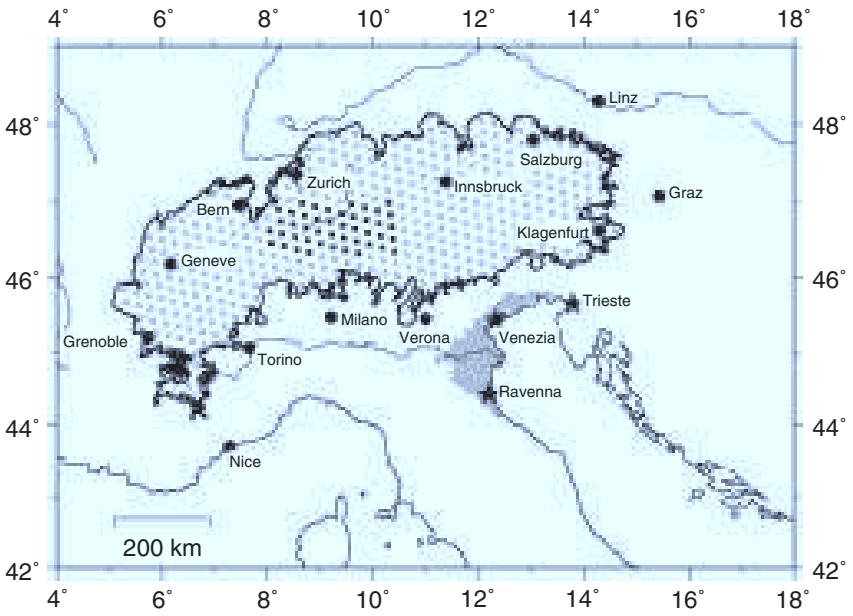

Figure 1

Contours of the Würm Alpine ice sheet at the LGM based on the map of FLORINETH and SCHLÜCHTER (2000). The towns of Ravenna, Venezia and Trieste are marked by stars. The gray shaded area indicates a sea-level rise of 10 m in the eastern portion of the Po plain. The ice sheet is discretized as a set of simple disc elements whose centroids are shown by pixels (the half–amplitude of each disc is $\sim 0.1°$). Black and gray pixels denote ice thicknesses of 1500 and 500 m, respectively, at the LGM for ALPS[H]. All the other ice ALPS models have a spatially uniform thickness (see text).

2. Methods

Sea-level variations are obtained solving the sea-level equation (SLE) (FARRELL and CLARK, 1976) by the pseudo–spectral method (MITROVICA and PELTIER, 1991) assuming a radially stratified, incompressible earth model and a linear Maxwell visco–elastic rheology. The numerical code employed here (SELEN) is freely distributed to facilitate reproducibility of the results (SPADA and STOCCHI, 2007). Horizontal migration of shorelines and effects from Earth rotation will be neglected throughout. Since the spatial resolution of 3-D GIA models (SPADA *et al.*, 2006; DAVIS *et al.*, 2008) is not sufficient to describe observed lateral variations of lithospheric thickness in the Mediterranean region, here we will assume a uniform thickness for the lithosphere, nonetheless we will investigate the effects of varying this parameter.

The SLE reads

$$S = N - U, \tag{1}$$

where S denotes the sea-level change, N is geoid height variation, U is the vertical displacement and dependence upon geographical coordinates and time is dropped to simplify notation. Scalars N and U can be expressed in terms of I (ice sheet thicknes variation) and S to give

Journal : 24 Dispatch : 17-4-2009 Pages : 16
Article No. : 0498 ☐ LE ☐ TYPESET
MS Code : 0498 ☑ CP ☑ DISK

$$S = \frac{\rho_i}{\gamma} G_s *_i I + \frac{\rho_w}{\gamma} G_s *_o S + S^E - \frac{\rho_i}{\gamma} \langle G_s *_i I \rangle - \frac{\rho_w}{\gamma} \langle G_s *_o S \rangle, \quad (2)$$

where the constraint of mass conservation has been imposed, ρ_i and ρ_w are ice and water densities, $*_i$ and $*_o$ are spatiotemporal convolutions over the ice sheets and oceans, respectively, $\langle \ldots \rangle$ denotes an average over the ocean surface, and γ is mean gravity acceleration (FARRELL and CLARK, 1976). In Equation (2), the sea-level Green's function G_s describes mantle visco–elasticity through the load Love numbers for vertical displacement and incremental potential, while $S^E = \langle S \rangle$ represents the spatially uniform (i.e., eustatic) sea-level variation for a rigid, nongravitating Earth. The recursive procedure required for solving the SLE is briefly described by e.g. SPADA and STOCCHI (2007). All following computations are carried out to harmonic degree $l_{\max} = 128$. The ocean function is discretized over a quasi–regular hexagonal icosahedron–based grid (TEGMARK, 1996; SPADA and STOCCHI, 2007) of $\sim 10^5$ elements on the Earth surface, with an average distance between grid points of ~ 70 km. As we have verified, these resolution parameters ensure a satisfactory representation of the solution on the spatial scales of interest here. The rheological profile, kept fixed throughout, is characterized by lower and upper mantle viscosities of 10^{22} and 3×10^{20} Pa s, respectively, while the reference lithospheric thickness is $LT = 65$ km. These rheological parameters were shown by LAMBECK and PURCELL (2005) and ANTONIOLI et al. (2008) to reproduce satisfactorily the Holocene relative sea-level observations in tectonically stable areas of the Mediterranean. The shear modulus and density profiles are obtained by volume-averaged PREM values (DZIEWONSKI and ANDERSON, 1981).

The source term I in Equation (2) stems from two contributions. The first describes the melting of the remote ice sheets in the far–field of the Mediterranean and is based on the ICE–5G model of PELTIER (2004) (here referred to as ICE5G for simplicity), while the second accounts for the melting of the Alpine ice sheet. A sketch of the latter, based on FLORINETH and SCHLÜCHTER (1998, 2000) and EHLERS and GIBBARD (2004), is shown in Figure 1. In this work, we consider four different reconstructions of the Alpine ice sheet at the LGM, namely ALPS[T], ALPS[F], ALPS[H], and ALPS[C] (see Fig. 2). Similarly to LAMBECK and PURCELL (2005), our first conjecture is that its melting occurred in phase with that of the remote ice sheets. The corresponding model, referred to as ALPS[T], assumes a spatially uniform thickness of 750 m at the LGM (here referred to as the global LGM, 21 kyrs BP), which implies an equivalent sea level (ESL) of ~ 0.28 m, comparable to that used in the spatially coarser model of STOCCHI *et al.* ((2005). In model ALPS[F] we account for an inception of melting, in phase with the Eurasian component of ICE5G, without modifying the ESL value at the LGM. Using an ice load of constant thickness certainly represents a poor approximation of the ice sheet, likely characterized by significant heterogeneities (FLORINETH and SCHLUCHTER, 1998). For this reason, in some of our computations we employ model ALPS[H] (see Fig. 2b), characterized by spatially variable thickness (see Fig. 1), a slightly reduced ESL (0.22 m at the LGM) and a comparatively rapid melting ending at 11 kys BP as in STOCCHI *et al.*

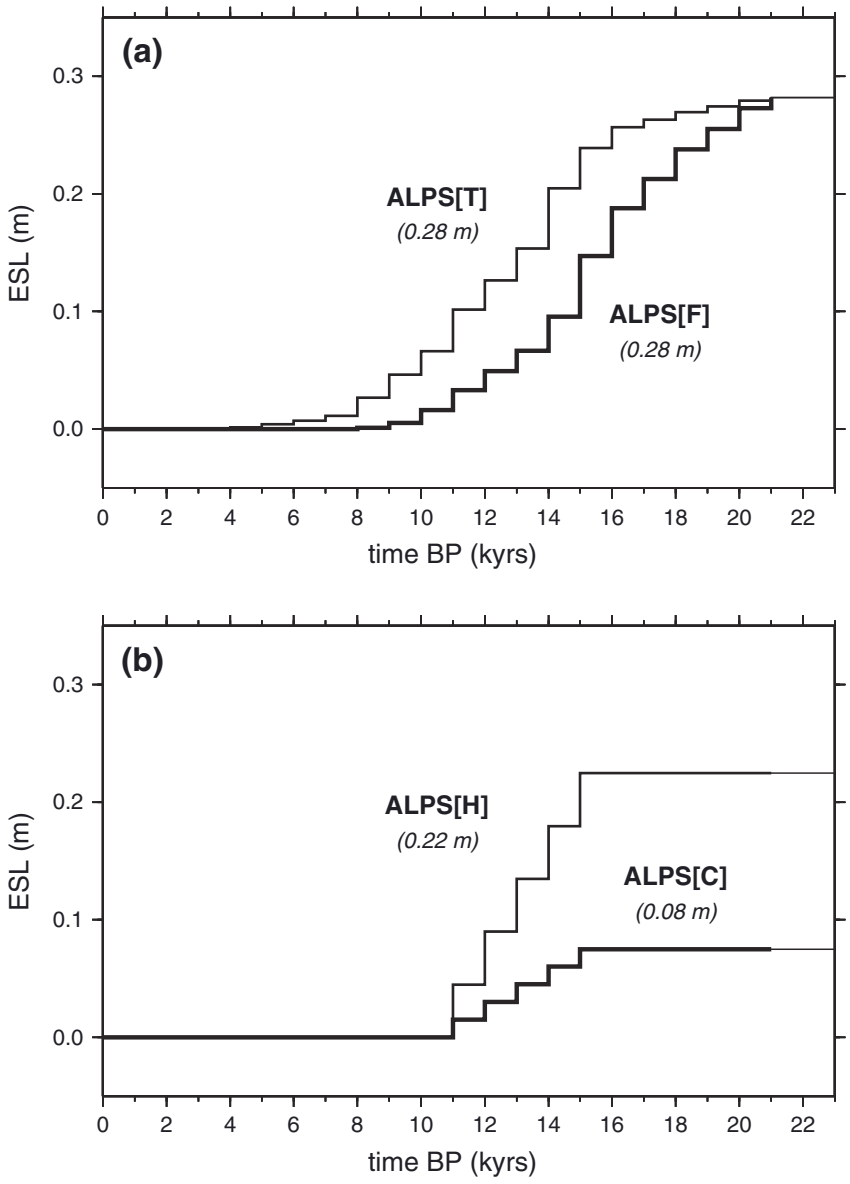

Figure 2

Time–histories of equivalent sea level (ESL) for the four Alpine ice models considered in this study, defined as $\mathrm{ESL} = (\rho_i/\rho_w)(V/A_o)$, where V is ice volume at a given time, ρ_i and ρ_w are ice and water densities, and A_o is the area of the ocean surface at this time. In (a), the ice history is modulated according to complete ICE5G (model ALPS[T]) and to its Eurasian component (ALPS[F]). The two *ad hoc* models considered in (b) share a fast deglaciation between 15 and 11 kyrs BP (Stocchi *et al.*, 2005). Numbers in parentheses show the total ESL variation since the LGM.

((2005). Finally, in model ALPS[C], we assume the same time history as in ALPS[H] and a spatially constant thickness of 200 m (ESL $\sim$0.08 m) that agrees with that used by Carminati *et al.* (2003). We do not account for recent variations of the thickness of the Alpine ice sheet possibly forced by climatic variations and for subsequent vertical movements (Barletta *et al.*, 2006). Since within our approximations the SLE (2) is linear, these can be simply superimposed to those obtained here.

Journal : 24 Dispatch : 17-4-2009 Pages : 16
Article No. : 0498 ☐ LE ☐ TYPESET
MS Code : 0498 ☑ CP ☑ DISK

3. Results

An illustration of the effects of the melting of the Alpine ice sheet upon long–term sea-level variations is displayed in Figure 3, where contour lines show relative sea level (i.e., sea level referred to present datum, abbreviated with RSL) at the epoch $t = 12$ kyrs BP for the three loading scenarios ICE5G, ALPS[T], and ICE5G+ALPS[T]. When only melting of remote ice sheets is accounted for (ICE5G, frame a), RSL is negative across the whole Mediterranean and its spatial pattern reflects the shape of coastlines. As an effect of lithospheric flexure due to melt–water loading, maxima are reached close to the center of the basin. The melting of ALPS[T] (frame b) produces a clear pattern of sea level fall in the bulk of the Alps (by virtue of Equation (1) sea level is defined everywhere, also across the continents) surrounded by a region of sea-level rise across a peripheral bulge that extends through the peninsula in the SW–NE direction. The sea-level changes driven by ALPS[T] extend far beyond the margins of the former ice sheet, as an effect of the flexure of the elastic lithosphere (Stocchi *et al.*, 2005). This possibly indicates that assuming a full isostatic equilibrium for the Alpine ice sheet before melting, thus neglecting plate flexure, may constitute a poor approximation for this ice sheet of relatively small lateral extent, as also pointed out by Carminati *et al.* (2003).

From Figure 3, it appears that the Po plain and the northern Adriatic may be strongly affected by the melting of ALPS[T], due to the proximity to the ice margin. Comparing frame (b) with Figure 1d in Lambeck and Purcell (2005), we observe that ALPS[T] produces a sea-level fall by a factor of ~ 5 in excess of that predicted by these authors. Since we use the same rheological profile as Lambeck and Purcell (i.e., the "nominal E2" model of their Table 1), this effect is to be attributed to the different spatiotemporal distribution of ice volume of remote ice sheets in Lambeck's ice model and ICE5G, to which the Alpine ice sheet APS[T] is locked in phase. Other differences in modeling, including mantle compressibility and time–varying coastlines as in Lambeck and Purcell (2005), are not likely to be a major cause of the discrepancy above. Rigorous benchmarks, which are under way, will be useful to clarify these issues. As shown in Figure 3c, the melting of ALPS[T] counteracts the sea-level rise imposed by ICE5G in northern Italy, resulting in a sea-level fall limited to the bulk of the Alps. This example illustrates how the melting of the small Alpine ice sheet may be important for a correct reconstruction of the history of sea level in this region. Although ALPS[T] alters the sea-level variations driven by ICE5G across the entire Italian peninsula, it is unlikely that the shape of the RSL curves may be sensibly affected south of the $\sim 40°$ parallel. A further issue that may be worthy of investigation of the possible effect of the Alpine ice sheet upon the Holocene sea-level variations along the Atlantic coast of France, where high–quality RSL observations are available (Ters, 1986; Lambeck, 1997). In this region, a possible role may also be played by the small ice cap which covered the Pyrenees (Calvet, 2004).

The RSL variations associated with the melting of the Alpine ice sheet are better analyzed in Figure 4 for model ALPS[F], where we show the RSL contour lines at the

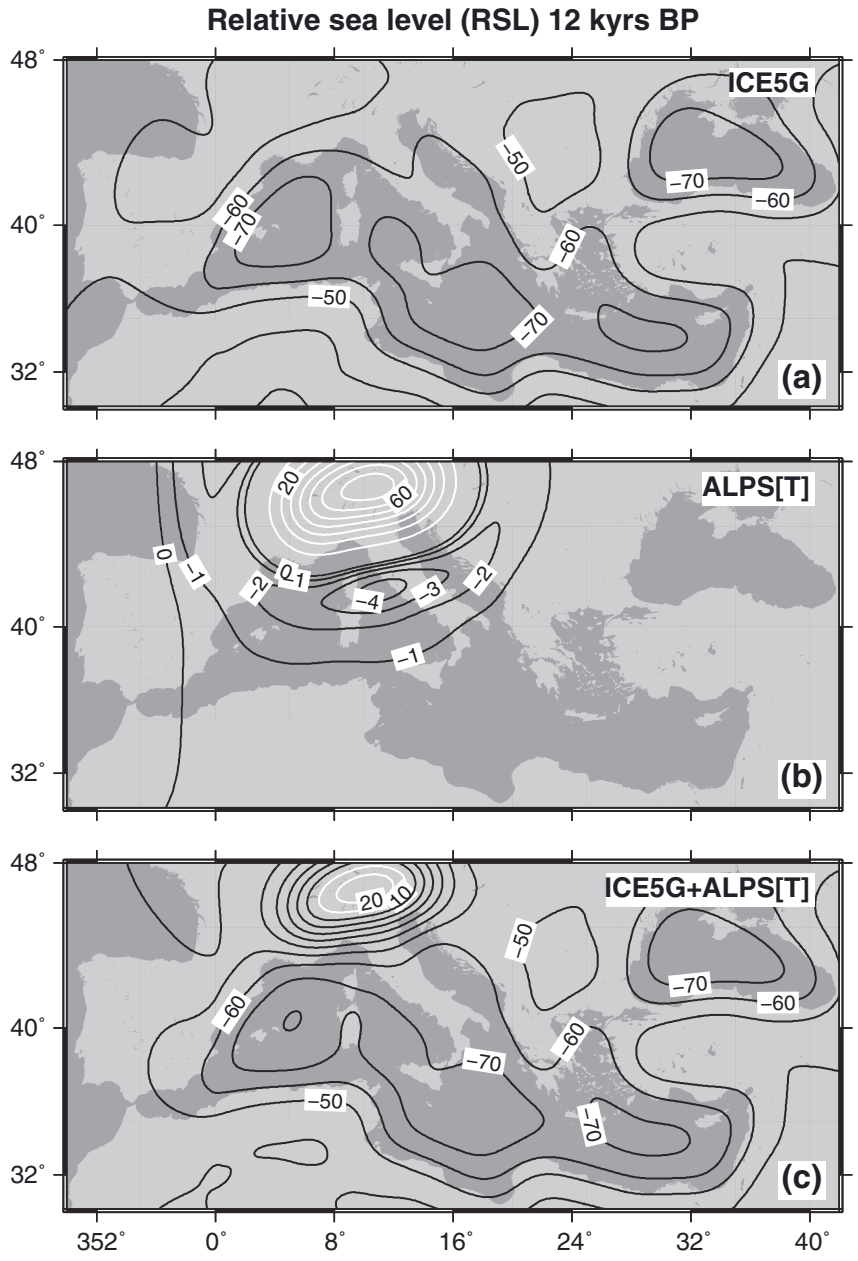

Figure 3
RSL maps for the epoch $t = 12$ kyrs BP, showing how the effects of ALPS[T] (b) interfere with those of ICE5G (a). According to Equation (1), sea-level change is defined also over land, since both N and U are globally meaningful quantities. White and black contours show positive and negative values of RSL, respectively. The RSL contours of ALPS[T] and ICE5G are clearly modulated by the shape of the ice load and of the Mediterranean basin, respectively.

epoch $t = 2$ kyrs BP. Contributions from the remote ice sheets are neglected. While in (a) we compute RSL using the full Equation (1), which accounts for both vertical movements of the Earth crust and of the surface of the geoid, in (b) the geoid term is neglected. Comparison between Figure 4a and b clearly reveals that RSL variations are mainly determined by vertical movements of the crust that strongly prevail over geoid

Journal : 24 Dispatch : 17-4-2009 Pages : 16
Article No. : 0498 ☐ LE ☐ TYPESET
MS Code : 0498 ☑ CP ☑ DISK

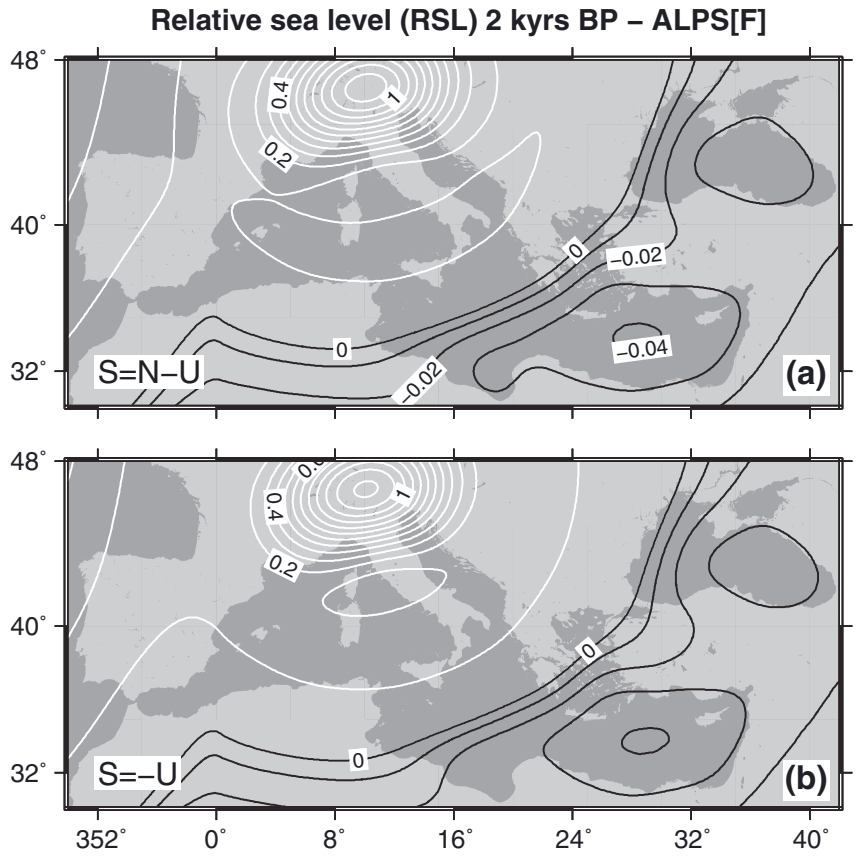

Figure 4
RSL maps for the epoch $t = 2$ kyrs BP using ALPS[F]. In (a), RSL is computed using S as given by Equation (1), whereas in (b) we use the approximation $S = -U$. Differences are negligible, especially close to the center of rebound and in the Po plain region, which may motivate a simplified approach to the sea-level problem for small ice sheets, as discussed in this paper.

height variations, especially the vicinity of the former ice sheet. Qualitatively, this is the consequence of the modest displacement of the Earth surface and of internal boundaries driven by the small ice sheets, which result in small geoid height variations. Furthermore, the shape of the contour lines illustrates that the effect of glacial unloading dominates over the melt–water loading term, only visible in the Eastern Mediterranean and across the Black Sea by smooth contours that follow the coastlines. This result is opposite to that obtained using the remote aggregates alone (see e.g. frames a and c of Fig. 3), which mainly produce sea-level variations by the mechanism of melt–water loading. Small ice sheets, such as ALPS[F], are unable to act effectively through melt–water loading due to their small ESL compared to that of the large ice sheets. The results of Figure 4 indicate that modeling sea-level variations driven by the Alpine ice sheet (and ice sheets of comparable or smaller size, in general) is feasible, to a first approximation, ignoring gravity effects and the shape of the coastlines. It is possible, though we did not verify it, that self–gravitation and the Earth curvature can be neglected when modeling the effects of the melting of the small Alpine ice sheet, which certainly would demand less

Journal : 24 Dispatch : 17-4-2009 Pages : 16
Article No. : 0498 ☐ LE ☐ TYPESET
MS Code : 0498 ☑ CP ☑ DISK

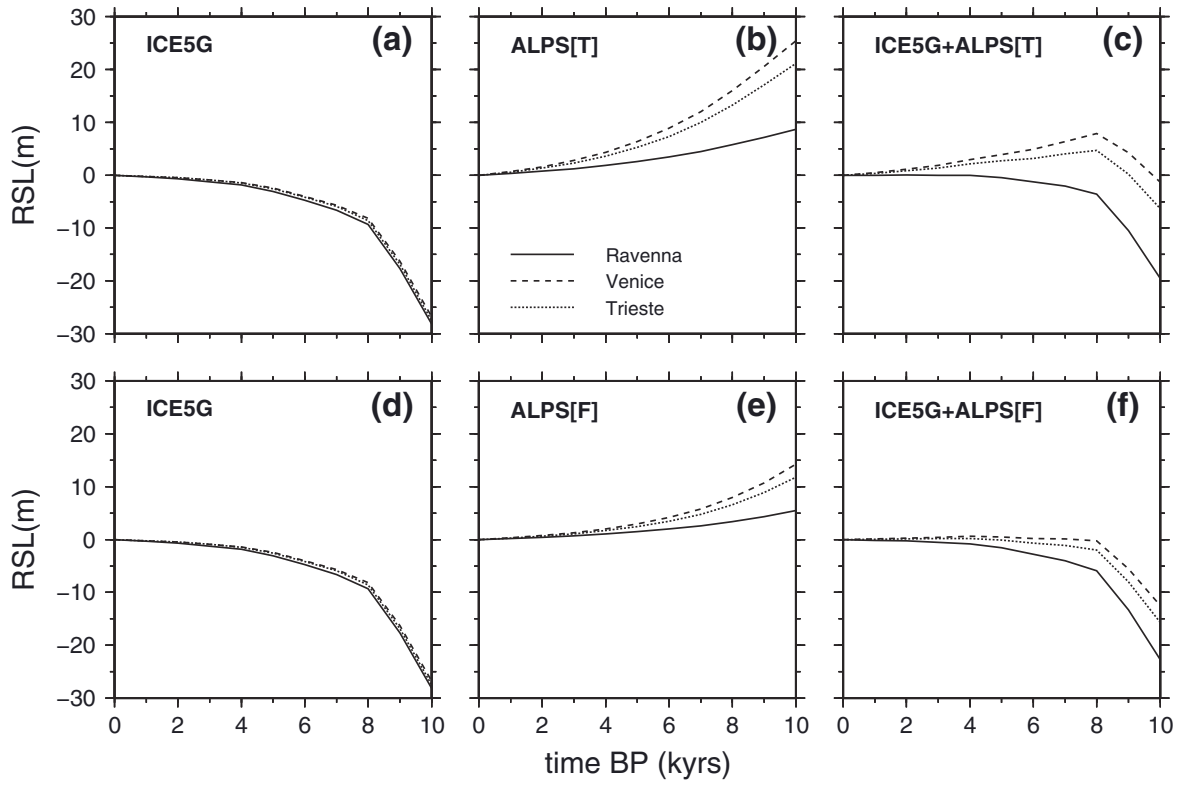

Figure 5
RSL curves for Ravenna (solid), Venezia (dashed) and Trieste (dotted) during the last 10 kyrs, with contributions from both the remote (ICE5G) and the near (Alpine) ice sheet. For both ALPS[T] and ALPS[F], the largest signal is obtained from Venezia (see b and e), which of the sites considered is closest to the center of the former ice sheet (see map of Fig. 1).

computational efforts than solving the full SLE (2), as done in Figure 4. In the following computations, the approximation $S = -U$ will be abandoned.

In Figure 5, the effects of melting of the Alpine ice sheet are shown in terms of RSL curves at the sites of Ravenna (solid), Venezia (dashed), and Trieste (dotted) (the locations of these towns are marked by stars in Fig. 1). Here, we compare the solutions based on ALPS[T] (top) with those obtained with ALPS[F] (bottom). As it appears from frame (a) (or d), ICE5G drives a sea-level rise of comparable amplitude and trend at the three sites, since the wavelength of the melt–water load exceeds the distance between the three sites (of the order of ~ 100 km). The knee of the RSL curves at time $t = 8$ kyrs BP corresponds to the major melting event shown by ICE5G at this epoch (this step is clearly visible in the ALPS[T] ESL curve in Figure 2, which is a scaled version of that of ICE5G). The RSL effects of ALPS[T] (b) and ALPS[F] (e) have opposite trends compared to ICE5G as a consequence of the uplift caused by ice melting. Due to the proximity to the Alpine ice sheet, RSL is different for the three sites, which demonstrates sensitivity to ice thickness. When remote and near–field ice sheets are combined, we note qualitatively opposite trends for ICE5G+ALPS[T] (c) and ICE5G+ALPS[F] (f). The former implies a stationary or nearly falling sea level in the last ~ 8 kyrs, while the latter

Journal : 24 Dispatch : 17-4-2009 Pages : 16
Article No. : 0498 ☐ LE ☐ TYPESET
MS Code : 0498 ☑ CP ☑ DISK

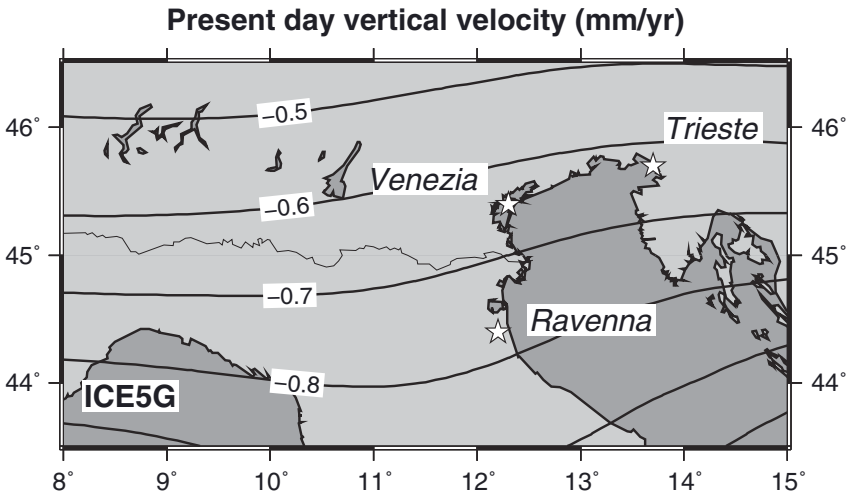

Figure 6
Current rate of uplift $\dot{U}$ in the Po plain and surrounding regions as an effect of melting of ICE5G. The general state of subsidence is in agreement with previous results by CARMINATI and DI DONATO (1999), although values differ significantly.

shows a stationary or rising sea level in the same time span. While a rigorous comparison with available observations and a discussion of possible long–term tectonic contributions to sea level in this area is not our purpose, it appears that the results based upon ALPS[T] are not consistent with the sea-level indicators from the northern Adriatic recently revised by ANTONIOLI *et al*. (2008), which denote a general sea-level rise in this area and no clear high–stands, which is more consistent with results based upon ALPS[F]. This qualitative result indicates that Holocene observations from the northern Adriatic region may usefully constrain the gross features of the melting chronology and ESL of the Alpine ice sheet, or at least set upper bounds on its volume at the LGM. This will be the subject of more refined investigations.

In spite of the extended distance from the centers of late–Pleistocene ice sheets, the Po plain and northern Adriatic region may still be affected by a significant isostatic disequilibrium, which implies vertical motions of the solid surface of the Earth, geoid height variations, and sea-level changes on a secular scale. As first recognized by CARMINATI and DI DONATO (1999), in the aforementioned regions these geodetic signals are characterized by a smooth spatial pattern which contrasts with that associated with long–term geological processes of sediment compaction, sediment loading, and tectonic loading. In Figure 6 we show the predicted present–day vertical velocity according to ICE5G and the rheological model described in Section 2. The pattern of $\dot{U}$ (the dot indicates the time derivative) is broadly similar to that shown by CARMINATI and DI DONATO (1999) (compare with their Fig. 3a, based upon model ICE–3G of TUSHINGHAM and PELTIER (1981)), however here the amplitude of the rate of subsidence is considerably larger (by a factor of ~ 4) due to the different assumptions regarding mantle rheology and ESL of remote ice sheets. It is now recognized that model ICE–3G fails to correctly

reproduce the gross features of the history of sea level in the Mediterranean (STOCCHI and SPADA, 2007) and that the rheological profile assumed by CARMINATI and DI DONATO (1999), representative of a global average, may not be fully adequate in this region (LAMBECK and PURCELL, 2005; ANTONIOLI *et al.*, 2008). Consequently, the results shown in Figure 6 may be useful to obtain a revised estimate of anthropogenic effects upon subsidence in the Po plain, according to the methods outlined by CARMINATI and DI DONATO (1999).

The effects of the melting of ALPS[F] on current sea-level change are considered in Figure 7, where contributions from near– and far–field ice sheets are considered separately. When we only account for ICE5G (frame a), in the study area $\dot{S}$ varies between 0.2 (Trieste and Venezia) to ~ 0.35 mm yr^{-1} (Ravenna), with a spatial trend that closely follows that of $\dot{U}$ in Figure 6. However, it is clear that the approximation $S = -U$ is inappropriate in this area, as geoid subsidence amounts to ~ -0.4 mm yr^{-1} across the entire region (compare frame a with Fig. 6 and recall Equation (1)). The effect of ALPS[F] (frame b) is that of producing a broad sea-level fall across the entire peninsula. According to Figure 4, such sea-level fall stems from vertical movements of equal, but opposite sign with no indication of subsidence in response to melting of ALPS[F]. This finding is at variance with results based on ^{14}C data from peat samples, which suggested to CARMINATI *et al.* (2003) that the southeastern Po plain may behave as a far–field subsiding region relative to the former Alpine ice sheet. It is worth to observe that the total effect of ICE5G+ALPS[F] in frame (c) is very close to zero, which indicates a dominant role of the long–term geological component of vertical deformation upon the isostatic term (CARMINATI and DI DONATO, 1999).

Since GIA induced sea-level variations on the northern Adriatic coasts result from the disruptive interference of two comparable effects, their total amplitude may be particularly sensitive to assumptions regarding mantle rheology and melting history. To address this point, Figures 8 and 9 depiot a sensitivity analysis aimed at establishing how lithospheric thickness *LT* and the time history of the Alpine ice sheet influence the present–day sea-level rise in Venezia. These two parameters are expected to affect the pattern of uplift and subsidence; the role of other key parameters, such as mantle viscosity, will be addressed elsewhere. Since lithospheric thickness and rheology are generally poorly constrained by glacio–isostatic adjustment observations (CIANETTI *et al.*, 2002; SPADA *et al.*, 2006), we assume a relatively broad range of variation for this parameter and a purely elastic rheology for the lithosphere. As shown in Figure 8, present day rate of sea-level change approximately increases monotonously with *LT* for both ICE5G (dashed) and ALPS[F] (gray). We observe no change in the sign of $\dot{S}$ with increasing *LT*, indicating that the mechanisms driving sea-level rise at this site do not change in principle. It is clear that in the range of *LT* values considered, Venezia is never on the fore–bulge of the former Alpine ice sheet, which would imply a sea-level rise. Furthermore, the melting of the Alpine ice sheet always has the effect of reducing the sea-level rise that would be produced by ICE5G alone. The total $\dot{S}$ due to GIA is negative for $LT < 90$ km and positive otherwise, with a maximum value of 0.25 mm yr^{-1} for

Journal : 24 Dispatch : 17-4-2009 Pages : 16
Article No. : 0498 ☐ LE ☐ TYPESET
MS Code : 0498 ✔ CP ✔ DISK

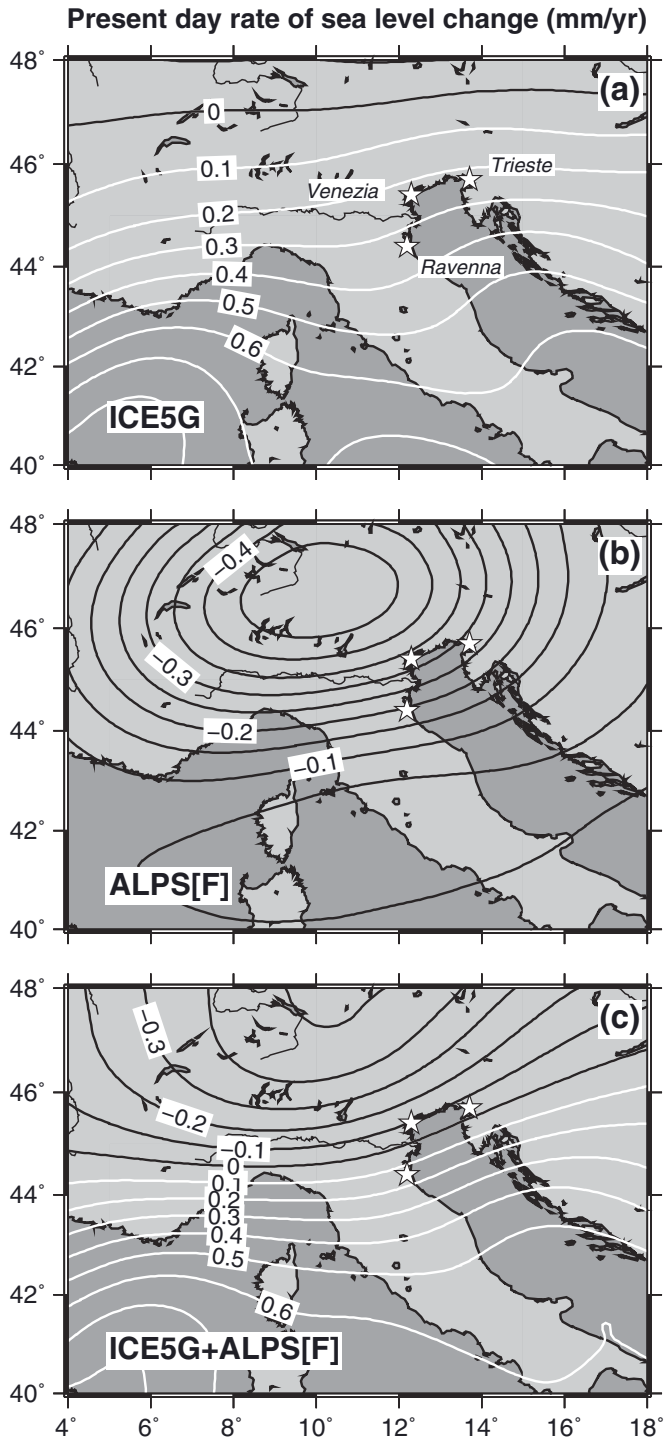

Figure 7
GIA–induced present–day rate of sea-level change in northern and central Italy assuming the melting chronologies ICE5G (a), ALPS[F] (b), and ICE5G+ALPS[F] (c). The melting of the Alpine ice sheet shifts the zero contour line from the bulk of the Alps (a) to the middle of the Po plain (c).

$LT = 145$ km. In Figure 9, we consider the effect of different assumptions pertaining to the melting history of the ice sheets We use the four deglaciation models described in Figure 2, with fixed $LT = 65$ km. This figure clearly shows that, independently from the

Journal : **24** Dispatch : **17-4-2009** Pages : **16**
Article No. : **0498** ☐ LE ☐ TYPESET
MS Code : **0498** ☑ CP ☑ DISK

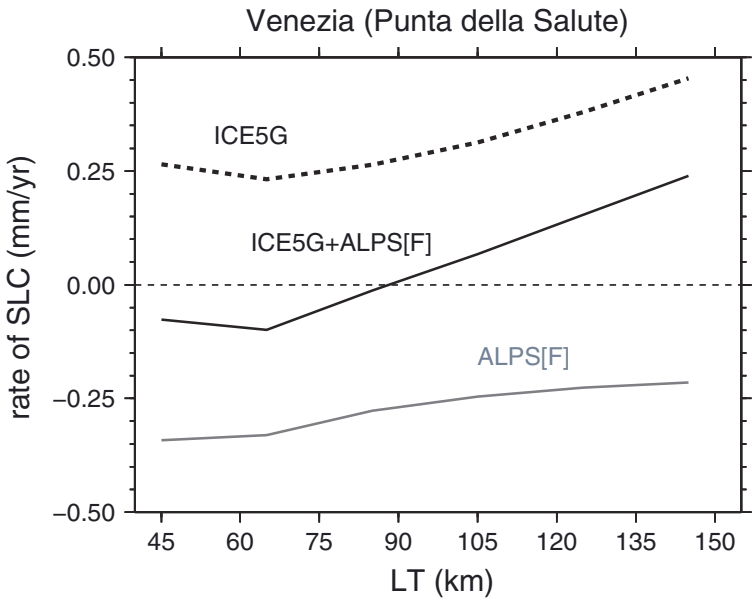

Figure 8
Present–day rate of sea-level change of glacio–isostatic origin predicted at the site of Venezia (Punta della Salute) based on ICE5G (dashed), ALPS[F] (gray), and both ice models (solid) for various values of lithospheric thickness (*LT*). For ICE5G+ALPS, the sign of $\dot{S}$ is sensitive to *LT* and its amplitude does not exceed 0.25 mm yr^{-1}.

ALPS model considered, melting of the Würm ice she*et al*ways has a mitigating effect upon sea-level rise in Venezia, which would amount to $\sim +0.3$ mm/yr if allowing only for the effect of the remote ice sheets (ICE5G, dashed line). The total effect on $\dot{S}$ is negative for all the ALP models excepting ALPS[C], characterized by the smallest ESL at the LGM.

4. Discussion and Conclusions

Glacially–induced sea-level variations and vertical movements in the Po plain and on the northern Adriatic coasts stem from two distinct mechanisms which operate on the millennia time scale. The first, associated with remote ice sheets, is responsible for a sea-level rise that mainly results from the effect of melt–water loading. The second, produced by the decay of the Würm Alpine ice sheet, counterbalances the first since it provides a general sea-level fall directly associated with the glacio-isostatic rebound mechanism.

New and revised indicators of Holocene sea-level variations (ANTONIOLI *et al.*, 2008) indicate a general sea-level rise in the northern Adriatic, which appears to be incompatible with GIA predictions that include the effects of ice model ALPS[T], characterized by an ESL of ~ 0.3 m and a melting history in phase with that of remote ice sheets. Provided that tectonic movements do not exceed GIA movements in this area, a sea-level rise in these areas can only be achieved, if the amount of ice in the ALPS

Journal : 24 Dispatch : 17-4-2009 Pages : 16
Article No. : 0498 ☐ LE ☐ TYPESET
MS Code : 0498 ☑ CP ☑ DISK

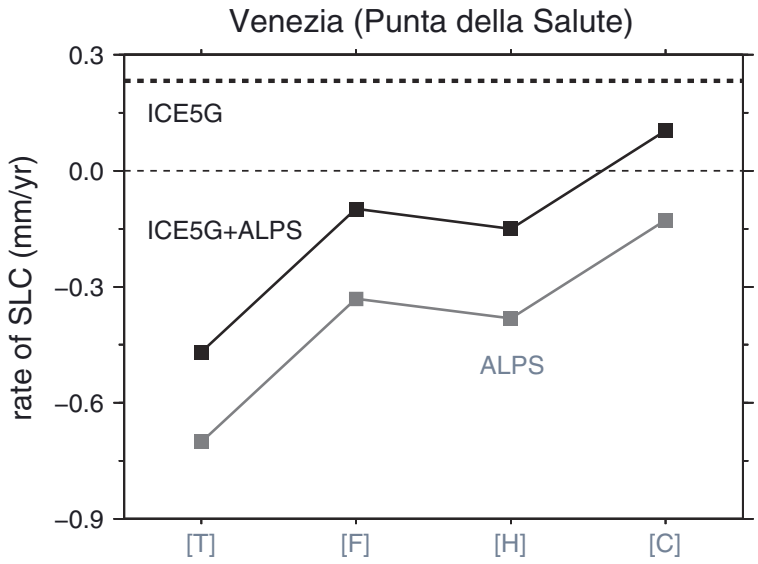

Figure 9
Present–day rate of sea-level change of glacio–isostatic origin at the site of Venezia (Punta della Salute) according to the ALPS models considered in this study, ordered for decreasing ESL (see Fig. 2). At this site, the effects of all ALPS models always counteract those from remote ice sheets (ICE5G, thick dashed line).

models is markedly reduced. This finding, established here on qualitative grounds, indicates that it is possible to establish upper bounds on the ESL of the Alpine ice sheet from RSL observations in the surrounding regions. From our results, it ensues that a melting history in phase with the European ice sheet (ALPS[F]) may be more consistent with Holocene RSL indicators, although other chronologies employed in the literature, such as ALPS[C] (CARMINATI *et al.*, 2003), cannot be completely discounted.

For all the Alpine deglaciation models and the values of lithospheric thickness tested here, the Po plain and the surrounding coasts are subject to a broad uplift which may be locally superimposed to that in response to recent melting episodes of the Alps (BARLETTA *et al.*, 2006). Although we have adopted a limited number of plausible melting histories and have not fully explored the broad parameters space of mantle rheology, we can conclude that melting of the Alps can hardly be responsible for large–scale subsidence across the Po plain, as suggested by CARMINATI *et al.* (2003). Due to the relatively small size, the peripheral fore–bulge of the Alpine ice sheet could not develop in the near-field of the ice sheet during its growth, thus leaving the Po plain in a state of uplift presently.

When the Alpine and the remote ice sheets are simultaneously accounted for, at the site of Venezia the glacially induced rate of sea-level fall is close to ~ -0.2 mm yr^{-1} for models ALPS[F] and ALPS[H]. Larger rates (~ -0.5 mm yr^{-1}) are only obtained for ALPS[T], whose ESL however appears to be unrealistically large according to the considerations above based on the Holocene sea-level rise in the northern Adriatic. Finally, a sea-level rise of $\sim +0.15$ mm yr^{-1} is obtained for ALPS[C], approximately one half of what we would expect if the contribution from the Alpine ice sheet is neglected (see Fig. 9). The amplitude of these rates of secular sea-level change is

Journal : 24 Dispatch : 17-4-2009 Pages : 16
Article No. : 0498 ☐ LE ☐ TYPESET
MS Code : 0498 ☑ CP ☑ DISK

considerably smaller than that determined from tide gauge observations, which ranges between 2 and 3 mm yr^{-1} at the three stations available for Venezia in the PSMSL[1] database when the whole period of observation is considered. Since the characteristic GIA rates are in general smaller or comparable to the uncertainties of the tide gauge's trends, we conclude that at this site the effect of glacio–isostasy is blurred by natural tectonic motions on the time scale of a century. Totally neglecting GIA at this site certainly would be even more appropriate during the last few decades, in view of the recognized recent sea-level acceleration mainly caused by anthropogenic effects (EMERY *et al.*, 1988; CARMINATI and DI DONATO, 1999).

Acknowledgments

We thank Eugenio Carminati and Volker Klemann for very constructive suggestions and Detlef Wolf for his encouragement and for careful review of the manuscript. To facilitate reproducibility of the results, the numerical code employed (SELEN, see http://flocolleoni.free.fr/SELEN.html) is freely available and can be requested from GS (email: giorgio.spada@gmail.com). The figures have been prepared using program GMT of Wessel and Smith (1991). This work is funded by MIUR (Ministero dell' Università, dell'Istruzione, e della Ricerca) by the PRIN2006 grant "Il ruolo del riaggiustamento isostatico postglaciale nelle variazioni del livello marino globale e mediterraneo: nuovi vincoli geofisici, geologici, ed archeologici".

REFERENCES

ANTONIOLI, F., FERRANTI, L., FONTANA, A., AMOROSI, A., M., BONDESAN, A., BRAITENBERG, C., DUTTON, A., FONTOLAN, G., FURLANI, S., LAMBECK, K., MASTRONUZZI, G., MONACO, C., SPADA, G., and STOCCHI, P. (2008), *Holocene relative sea-level changes and vertical movements along the Italian and Istrian coastlines*, Quat. Int., doi:10.1016/j.quaint.2008.11.008.

BARLETTA, V. R., FERRARI, C., DIOLAIUTI, G., CARNIELLI, T., SABADINI, R., and SMIRAGLIA, C. (2006), *Glacier shrinkage and modeled uplift of the Alps*, Geophys. Res. Lett. *33*, L14307, doi:10.1029/2006GL026490.

CALVET, M., *The quaternary glaciation of the Pyrenees*. In *Quaternary Glaciations – Extent and Chronology* (eds. Ehlers J., Gibbard, P. L.) (Elsevier, Rotterdam 2004) pp. 119–128.

CARMINATI, E. and DI DONATO, G. (1999), *Separating natural and anthropogenic vartical movements in fast subsiding areas: the Po plain (N. Italy) case*, Geophys. Res. Lett. *26*, 2291–2294.

CARMINATI, E., MARTINELLI, G., and SEVERI., P. (2003), *Influence of glacial cycles and tectonics on natural subsidence in the Po Plain (Northern Italy): Insights from 14C ages*, Geochem. Geophy. Geosy. *4* (10).

CIANETTI, S., GIUNCHI, C., and SPADA, G. (2002), *Mantle viscosity beneath the Hudson Bay: An inversion based on the Metropolis algorithm*, J. Geophys. Res. *107*, 2352. doi:10.1029/2001JB000585.

DAVIS, J. E., LATYCHEVA, K., MITROVICA, J. X., KENDALL, R., and TAMISIEA, M. E. (2008), *Glacial isostatic adjustment in 3–D earth models: Implications for the analysis of tide gauge records along the U.S. east coast*, J. Geodyn., in press. doi:10.1016/j.jog.2008.04.007.

DENTON, G. H. and HUGHES, T. H., *The last great ice sheets* (John Wiley, New York 1981).

[1] Permanent Service for the Mean Sea Level. Data available on line from http://www.pol.ac.uk/psmsl.

DZIEWONSKI, A. and ANDERSON, D.L. (1981), *Preliminary reference Earth model, Phys. Earth planet*. Int. *25*, 297–356.

EHLERS, J. and GIBBARD, P. L., *Quaternary Glaciations – Extent and Chronology, Part I: Europe* (Elsevier, Amsterdam, 2004).

EMERY, K. O., AUBREY, D. G., and GOLDSMITH, V. (1988), *Coastal neo–tectonics of the Mediterranean from tide–gauge records*, Mar. Geol. *81*, 41–52.

FARRELL, W. E. and CLARK, J. A. (1976), *On postglacial sea level*, Geophys. J. Roy. Astr. S. *46*, 647–667.

FLORINETH, D. and SCHLÜCHTER, C. (1998), *Reconstructing the last glacial maximum (LGM) ice surface geometry and flowlines in the Central Swiss Alps*, Eclogae Geol. Helv. *91*, 341–407.

FLORINETH, D. and SCHLÜCHTER, C. (2000), *Alpine evidence for atmospheric circulation patterns in Europe during the Last Glacial Maximum*, Quat. Res. *54*, 295–308.

GUDMUNDSSON, G. H. (1994), *An order–of–magnitude estimate of the current uplift-rates in Switzerland caused by the Würm Alpine deglaciation*, Eclogae Geol. Helv. *87*, 545–557.

LAMBECK, K. (1997), *Sea–level change along the French Atlantic and Channel coasts since the time of the Last Glacial Maximum*, Palaeog. Palaeoclimatol. Palaeoecol. *129*, 1–22.

LAMBECK, K. and PURCELL, A. (2005), *Sea–level change in the Mediterranean Sea since the LGM: Model predictions for tectonically stable areas*, Quat. Sci. Rev. *24*, 1969–1988.

MITROVICA, J. X. and PELTIER, W. R. (1991), *On post–glacial geoid subsidence over the equatorial ocean*, J. Geophys. Res. *96*, 20,053–20,071.

PELTIER, W. R. (2004), *Global glacial isostasy and the surface of the ice-age earth: The ICE-5G(VM2) model and GRACE*, Annu. Rev. of Earth Pl. Sci. *32*, 111–149.

PREUSSER, F. (2004), *Towards a chronology of the Late Pleistocene in the Northern Alpine Foreland*, Boreas *33*, 195–210.

SPADA, G., ANTONIOLI, A., CIANETTI, S., and GIUNCHI, C. (2006), *Glacial isostatic adjustment and relative sea-level changes: The role of lithospheric and upper mantle heterogeneities in a 3–D spherical Earth*, Geophys. J. Int. 165, doi:10.1111/j.1365-246X.2006.02969.x.

SPADA, G. and STOCCHI, P. (2007), *SELEN: A Fortran 90 program for solving the "Sea Level Equation"*, Comput. Geosci. *33*(4), 538–562. doi:10.1016/j.cageo.2006.08.006.

STOCCHI, P., SPADA, G., and CIANETTI, S. (2005), *Isostatic rebound following the Alpine deglaciation: Impact on the sealevel variations and vertical movements in the Mediterranean region*, Geophys. J. Int. *162*. doi:10.1111/j.1365-246X.2005.02653.x.

STOCCHI, P. and SPADA, G. (2007), *Post–glacial sea–level in the Mediterranean Sea: ClarkÕs zones and role of remote ice sheets*, Ann. Geophys. *50*(6), 741–761.

TEGMARK, M. (1996), *An icosahedron–based method for pixelizing the celestial sphere*, Astrophys. J. *470*, L81–L84.

TERS, M., *Variations in Holocene sea level on the French Atlantic coast and their climatic significance*. In *Climate: History, Periodicity and Predictability* (eds. Rampino *et al.*), (Van Nostrand, Reinhold, New York 1986).

TUSHINGHAM, A. M. and PELTIER, W. R. (1981), *Ice–3G: A new global model of late Pleistocene deglaciation based upon geophysical prediction of post–glacial sea-level change*, J. Geophys. Res. *96*, 4497–4523.

WESSEL, P. and SMITH, W. H. F. (1991), *Free software helps map and display data*, EOS Trans. AGU *72*, 441.

(Received September 19, 2007, revised July 17, 2008, accepted August 14, 2008)

To access this journal online:
www.birkhauser.ch/pageoph

Journal : **24** Dispatch : **17-4-2009** Pages : **16**
Article No. : **0498** ☐ LE ☐ TYPESET
MS Code : **0498** ☑ CP ☑ DISK

Post-glacial readjustment, sea-level variations, subsidence and erosion along Italian coasts

P. Stocchi[1], L. Girometti[2], G. Spada[2], M. Anzidei[3] and F. Colleoni[4]

[1] *DEOS, Faculty of Aerospace Engineering, Delft University of Technology, The Netherlands*
[2] *Istituto di Fisica, Università "Carlo Bo", Urbino, Italy*
[3] *Istituto Nazionale di Geofisica e Vulcanologia, Roma, Italy*
[4] *Laboratoire de Glaciologie et Géophysique de l'Environnement, Grenoble, France*

(Received: March 31, 2008; accepted: July 4, 2008)

ABSTRACT Ongoing sea-level variations and vertical land movements, measured by tide gauges as well as by continuous GPS stations in Italy, stem from several factors acting on different spatiotemporal scales. Contrary to tectonic and anthropogenic effects, characterized by a heterogeneous signal, the melting of the late-Pleistocene ice sheets results in a smooth long-wavelength pattern of sea-level variation and vertical deformation across the Mediterranean, mostly driven by the melt water load. In this work, we define upper and lower bounds of the effects of glacial isostatic adjustment (GIA) on current sea-level variations and vertical movements along the coasts of Italy. For various mantle viscosity profiles, we explore to what extent the spatial variability of the observed rates may be attributed to a delayed isostatic recovery of both solid Earth and geoid. We find that long-wavelength patterns of sea level change are tuned by GIA, and that the coastal retreat in Italy is broadly correlated with the expected present-day rates of sea-level variations.

1. Introduction

The sea level is the offset between the surface of the geoid and that of the solid Earth at a given time (Farrell and Clark, 1976). The melting of ice sheets and glaciers causes a global (but not uniform) redistribution of the ocean mass, thus leading to a new sea level. The offset between the new and the old sea level is referred to as sea level change, which can be described by the sum of three terms. The first (eustatic term) is the globally uniform variation that we would observe for a rigid, non gravitating Earth. The second and the third are due to geoid height variations and ground vertical deformations associated to ice and water loads, respectively. These latter terms have a complex spatiotemporal variability, being also dependent upon the delayed viscoelastic response of the solid Earth [see e. g. Farrell and Clark (1976) and Spada and Stocchi (2006) for a review]. The melting of Pleistocene ice sheets has resulted in a widespread variable sea level change that defines several zones where the geoid has been affected in similar ways, showing sea level curves of equal shape (Farrell and Clark, 1976; Clark and Lingle, 1979). In the Mediterranean, these zones have been recently studied by Stocchi and Spada (2007).

Middle-to-late Holocene geological indicators along the Italian coastlines and coastal archaeological remains of the Roman period (~2500 BP) show that, since the end of the deglaciation, the sea level rose to, and never exceeded, the present- day datum (Pirazzoli, 1991,

© 2009 – OGS

2005; Lambeck *et al.*, 2004a). The general shape of the relative Holocene relative sea-level curves, expected in Italy is peculiar of enclosed basins, where melt-water loading deforms the sea floor thus producing a widespread subsidence (Lambeck and Purcell, 2005; Stocchi and Spada, 2007). The northern and central coasts of Italy are potentially the most affected by the process of isostatic adjustment of the former Alpine and Fennoscandian ice sheets (Stocchi *et al.*, 2005), since ice unloading and the related forebulge collapse shape the overall pattern of land subsidence to a distance of a few thousands kilometres from the ice centers (Lambeck and Johnston, 1995).

Our aim is to compare model predictions with observations at sites where tide gauges and continuous GPS time-series are available and to establish trade offs between various factors currently contributing to sea-level change and subsidence (or uplift) in Italy. Assuming as valid the ICE5G chronology for the former late-Pleistocene ice sheets (Peltier, 2004) and various plausible mantle viscosity profiles, we solve the "Sea Level Equation" (Farrell and Clark, 1976) to estimate current rates of sea-level variations induced by glacial isostatic adjustment (GIA) and vertical deformations in Italy and to discuss their relationship with instrumental observations. In the last part of the paper, we reveal a long-wavelength correlation between the pattern of coastal retreats along the Italian coasts and the current GIA-induced sea-level variations.

2. Methods

In this paper, GIA-induced sea level change (S), vertical displacement (U), and geoid height variation (N) are computed by means of the public-domain program SELEN (Spada and Stocchi, 2007), which solves the "Sea Level Equation" (SLE) in the original form of Farrell and Clark (1976) through the "pseudo-spectral" approach introduced by Mitrovica and Peltier (1991). SELEN assumes a radially stratified, incompressible Earth and a linear Maxwell viscoelastic rheology. Horizontal migration of shorelines and effects from Earth rotation instabilities are not modeled here.

The SLE reads

$$S=\frac{\rho_{\mathrm{i}}}{\gamma}G_s\otimes_i I+\frac{\rho_{\mathrm{w}}}{\gamma}G_s\otimes_o S+S^E-\frac{\rho_i}{\gamma}\overline{G_s\otimes_i I}-\frac{\rho_w}{\gamma}\overline{G_s\otimes_o S}, \qquad (1)$$

where I is the ice sheets thickness variation, ρ_i and ρ_w are densities of ice and water, respectively, $\otimes_i$ and $\otimes_o$ are spatiotemporal convolutions over the ice- and ocean-covered regions, γ is the average gravity at the Earth's surface, and the last two ocean-averaged terms ensure mass conservation. Green's sea level function G_s accounts for mantle viscoelasticity through the load-deformation coefficients for vertical displacement and incremental potential (Farrell and Clark, 1976; Spada and Stocchi, 2006, 2007). The "eustatic term" S^E represents the spatially uniform sea-level change for a rigid, non-gravitating Earth. The integral nature of the SLE [Eq. (1)] demands the recursive procedure outlined in detail by Spada and Stocchi (2007). In this study, the maximum harmonic degree is l_{max} = 96 and the spatial resolution of the icosahedron-based integration grid is R = 28 [this corresponds to a spatial discretization of 30252 pixels on the surface

of the sphere, see Tegmark (1996)].

Once S is obtained from Eq. (1), the vertical displacement and change of geoid elevation are given by

$$U = \rho_i G_u \otimes_i I + \rho_w G_u \otimes_o S, \tag{2}$$

and

$$N = \rho_i G_n \otimes_i I + \rho_w G_n \otimes_o S, \tag{3}$$

where G_u and G_n are appropriate Green functions. Variables S, U, and N obey the fundamental equation

$$S=N-U, \tag{4}$$

which defines sea-level change [see e. g. Spada and Stocchi (2006)].

By adopting the ice chronology ICE5G (Peltier, 2004), we will solve the SLE for an Earth model characterized by a 65-km thick purely elastic lithosphere with PREM-averaged density and shear modulus, and upper- and lower-mantle viscosities (henceafter η_{UM} and η_{LM}) of 3×10^{20} and 1×10^{22} Pa·s, respectively. This viscosity profile (which will be referred to as RVKL) and lithospheric thickness have been constrained by relative Holocene sea level indicators in Italy (Lambeck *et al.*, 2004a; Lambeck and Purcell, 2005; Antonioli *et al.*, 2008). To assess how GIA affects sea-level variations and vertical movements across the Italian region more robustly, we will also consider three rheological models with an increasing contrast between upper and lower mantle viscosities in the following. RVM1 is characterized by a nearly-uniform viscosity profile the with $\eta_{UM} = 10^{21}$ Pa·s and $\eta_{LM} = 2\times10^{21}$ Pa·s (Tushingham and Peltier, 1991), while in RVM2 viscosity increases by one order of magnitude ($\eta_{UM} = 4\times10^{20}$ Pa·s and $\eta_{LM} = 4\times10^{21}$ Pa·s). For RVM3, $\eta_{UM} = 4\times10^{20}$ and $\eta_{LM} = 4\times10^{22}$ Pa·s. In this study we do not consider the effects of varying the thickness of the lithosphere since, from test computations (not shown here), we have verified that this parameter generally plays a minor role compared to mantle viscosity. The role of lateral variations of lithospheric thickness in the region of interest cannot be fully addressed because of the relatively low spatial resolution of current 3D GIA models (Spada *et al.*, 2006).

3. Results

In Figs. 1, 2, and 3, we show expected values of $\dot{S}$, $\dot{U}$, and $\dot{N}$ at the present time (the dot denotes a time-derivative), which obey the fundamental relationship given by Eq. (4). In the bulk of the central Mediterranean, subsidence of the solid surface and of the geoid mainly results from the delayed effect of melt-water loading after the end of melting of the late-Pleistocene ice sheets, which according to model ICE5G occurred 4000 years ago. Rates of subsidence increase

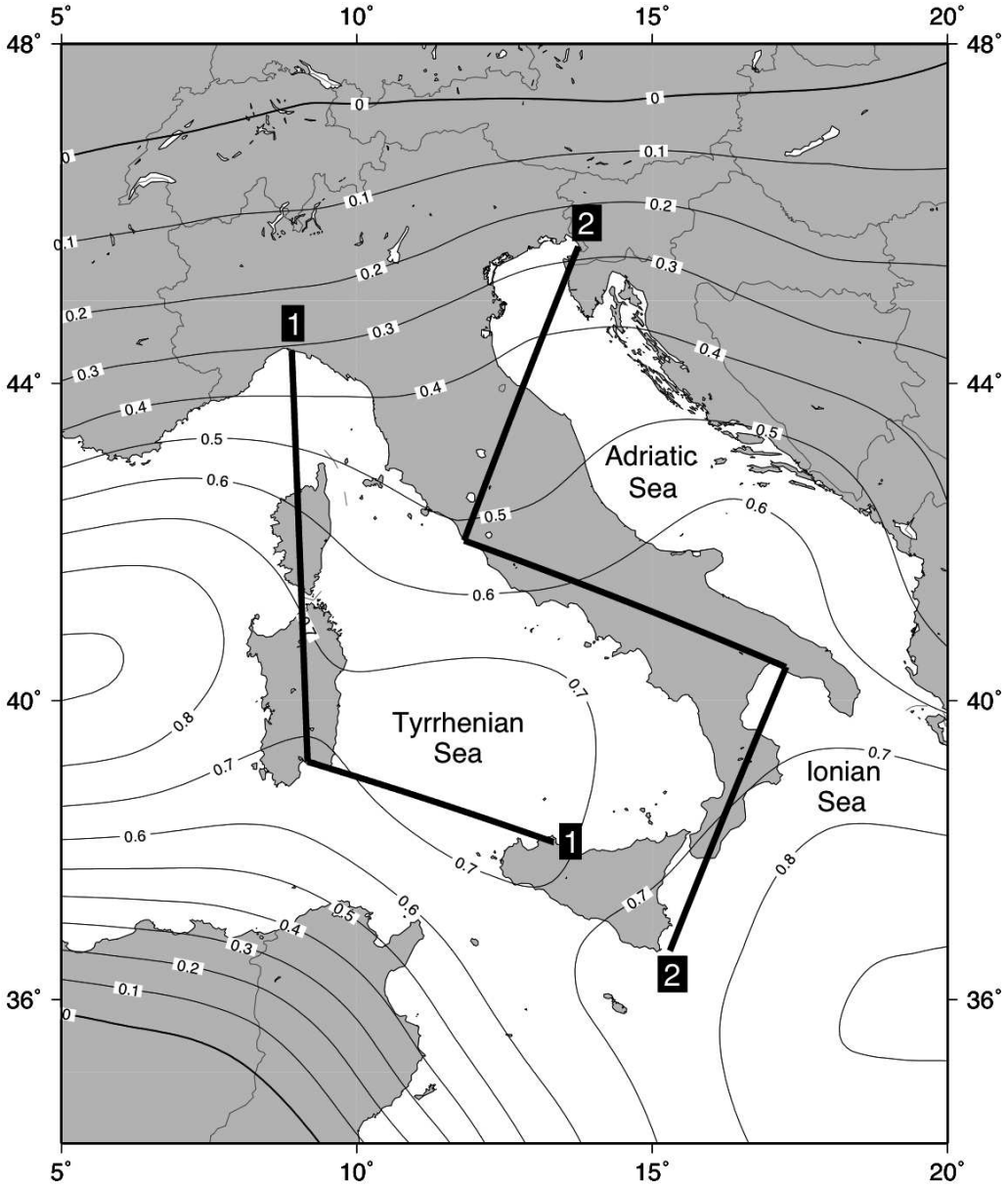

Fig. 1 - Predicted rate of present-day sea-level change $\dot{S}$ (mm yr^{-1}) according to our reference model ICE5G(RVKL). Solid lines show transects "1" and "2" considered in Fig. 7.

southward and $\dot{S}$ reaches maximum values between ~ 0.7 and 0.9 mm yr^{-1} in the bulk of the Tyrrhenian Sea (Sardinia), and between Sicily and Greece (Ionian Sea). The GIA-induced rate of sea level change shown in Fig. 1 represents a significant fraction of the average rate of sea level rise deduced by the global network of tide-gauges during the last century (in the range of 1-2 mm yr^{-1}), mainly associated with the ongoing climatic variations (Douglas, 1991; Cazenave and Nerem, 2004).

The basic data considered in this study are shown in Figs. 4, 5, and 6. The first illustrates sea

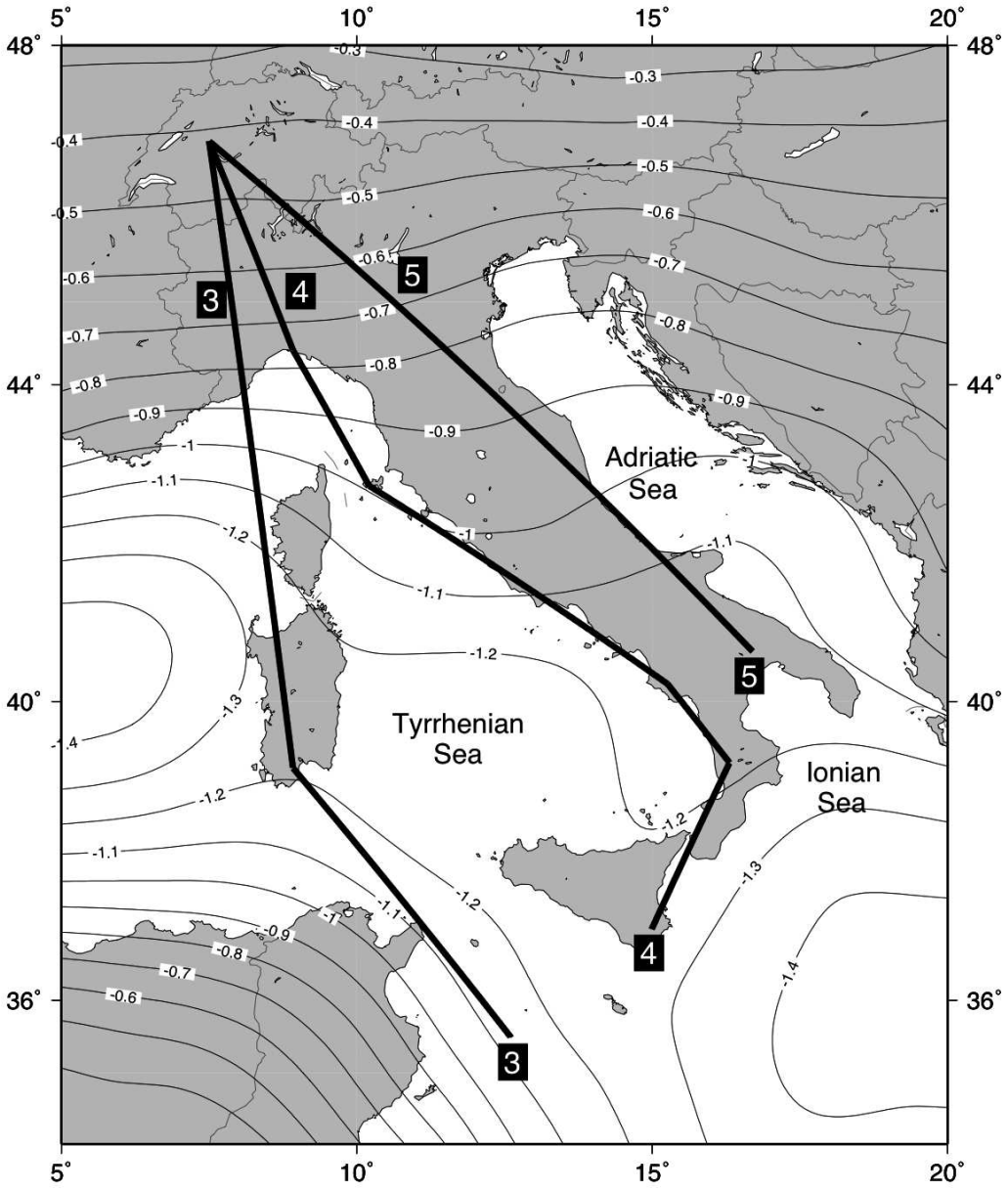

Fig. 2 - Present-day vertical velocity $\dot{U}$(mm y^{-1}), according to the same model of Fig. 1. Solid lines show transects "3", "4", and "5" discussed in the text and considered in Fig. 8.

level trends at the Italian PSMSL tide gauges network (data available from http://www.pol.ac.uk/). The French site of Marseille (Ma) and the Croatian tide gauge of Dubrovnik (Du) are also considered. Whilst Marseille records the longest time series in the Mediterranean, spanning from 1886 to 2004 with a trend of +1.2 ± 0.1 mm yr^{-1}, two other long records of Genova (Ge) and Trieste (Tr) get very close to that, Dubrovnik is of particular interest since it is representative of the southern Adriatic and it is placed close to a continuous GPS station. Fig. 5 displays all the PSMSL observations (a) and those considered in Fig. 4 (b) as

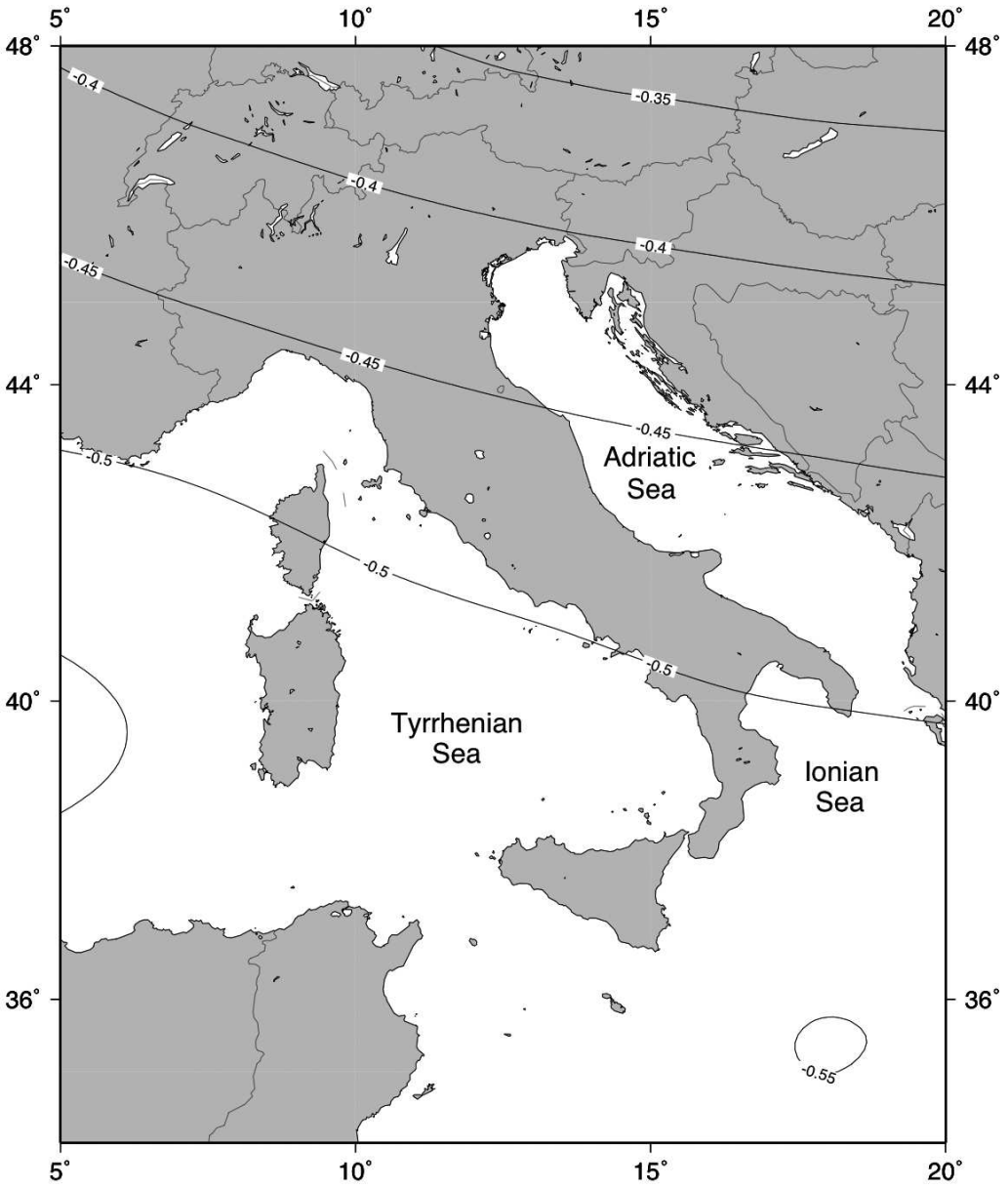

Fig. 3 - Present-day rate of change of geoid height $\dot{N}$ (mm yr^{-1}), according to the same model of Fig. 1. $\dot{N}$ is given by $\dot{S}+\dot{U}$ [see Eq. (4)], where $\dot{S}$ and $\dot{U}$ are shown in Figs. 1 and 2, respectively.

function of record length. For time-series that are shorter or equal to ~15 years, absolute values of observed rates largely exceed those expected from the longest records and show a significant scatter. According to Douglas (1992), tide gauges time series, shorter than 50 years, cannot be considered reliable indicators of sea-level rise or acceleration. The rates shown in Fig. 4 are broadly consistent with those inferred by coastal archaeological observations (Lambeck *et al.*, 2004b; Antonioli *et al.*, 2007). The latter provide relative sea-level rates from historical times (~2000 - 2400 years BP) of 0.8 mm yr^{-1} for the Sardinia, 1.1 mm yr^{-1} for northern Adriatic (but

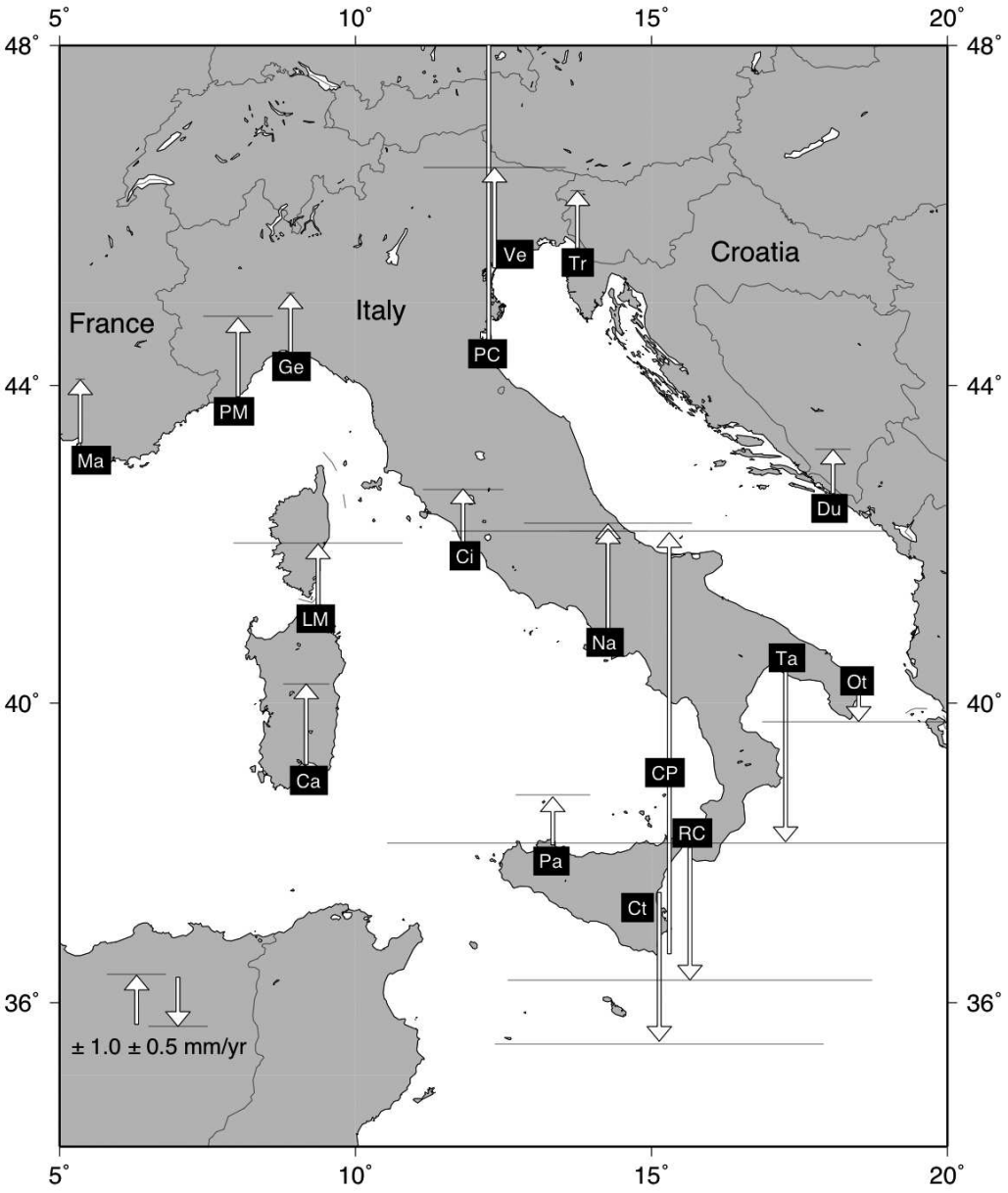

Fig. 4 - Measured rates of sea-level change at tide gauges pertaining to the PSMSL tide gauges network (a). Abbreviations refer to the Italian stations contained in the PSMSL table of mean sea-level trends (see page http://www.pol.ac.uk/psmsl/datainfo/rlr.trends), with the addition of Marseille (Ma) and Dubrovnik (Du).

for this area with an important tectonic contribution of 0.8 mm yr^{-1}) and 0.7 mm yr^{-1} for the peninsular coast of the Tyrrhenian Sea. Rates of GPS vertical velocity, considered in Fig. 6, represent residual, vertical velocities computed by means of a distributed processing approach and refer to the stable Corsica-Sardinia block, and are consistent with Table 4 and Fig. 6b of Serpelloni *et al.* (2006).

To compare the numerical results with the observed rates of Figs. 4 and 6, we now compute $\dot{S}$

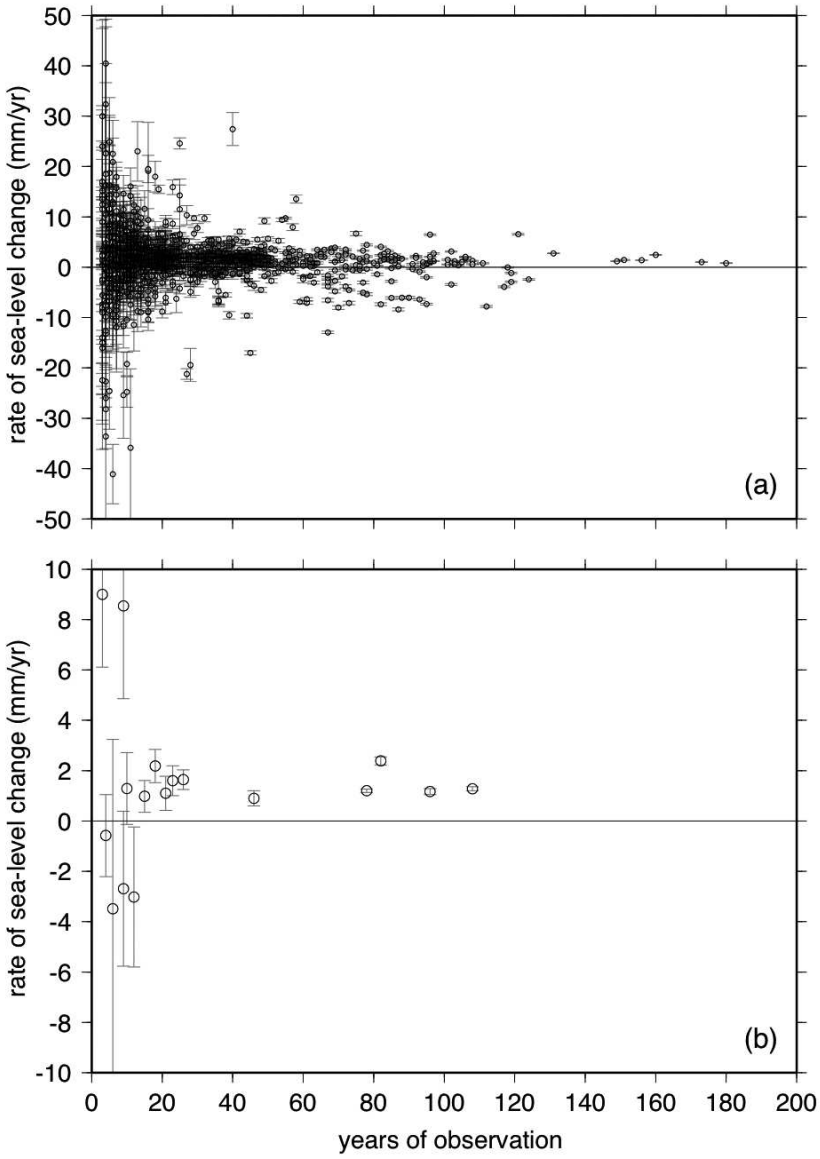

Fig. 5 - Rate of sea-level change according to PSMSL as a function of the period of observation for all tide gages (a), and those considered in this study (b).

and $\dot{U}$ using ICE5G and the viscosity profiles RVM1, RVM2, RVM3 and RVKL. Fig. 7a shows, as a function of latitude, observed $\dot{S}$ values and predictions along transect "1" of Fig. 1, connecting Genova (Ge) to Palermo (Pa), and crossing Sardinia (LM, Ca) (numbers in parentheses indicate the period of observation for each station). Though the 96-year-long time-series of Genova is possibly the only one suitable for a reliable estimate of secular trend (Zerbini *et al.*, 1996), the other Tyrrhenian tide gauges clearly indicate, from the end of nineteenth to the first decades of the twentieth century, positive rates that vary between 1.0 and 1.6 mm yr^{-1},

Fig. 6 - Vertical velocity solutions referred to the stable Corsica-Sardinia block from continuous GPS stations of Table 4 in Serpelloni *et al*. (2006).

consistent with Ge. The observed sea-level rise shows the same trend (grey spline) in the predictions, with a tendency to increase southwards. The lowest values are obtained for the RVM1 model (dotted), with a sea-level fall of -0.2 mm yr^{-1} in Genova. With increasing contrast between η_{UM} and η_{LM}, model results shift progressively towards larger values as a consequence of the increased isostatic disequilibrium. For models RVKL and RVM3, GIA explains a large fraction of observed sea level rise, and leaves a residual of climatic origin that does not exceed 1 mm yr^{-1}, below the estimated average rate during the last century (Douglas, 1991; Douglas *et al.*, 2000;

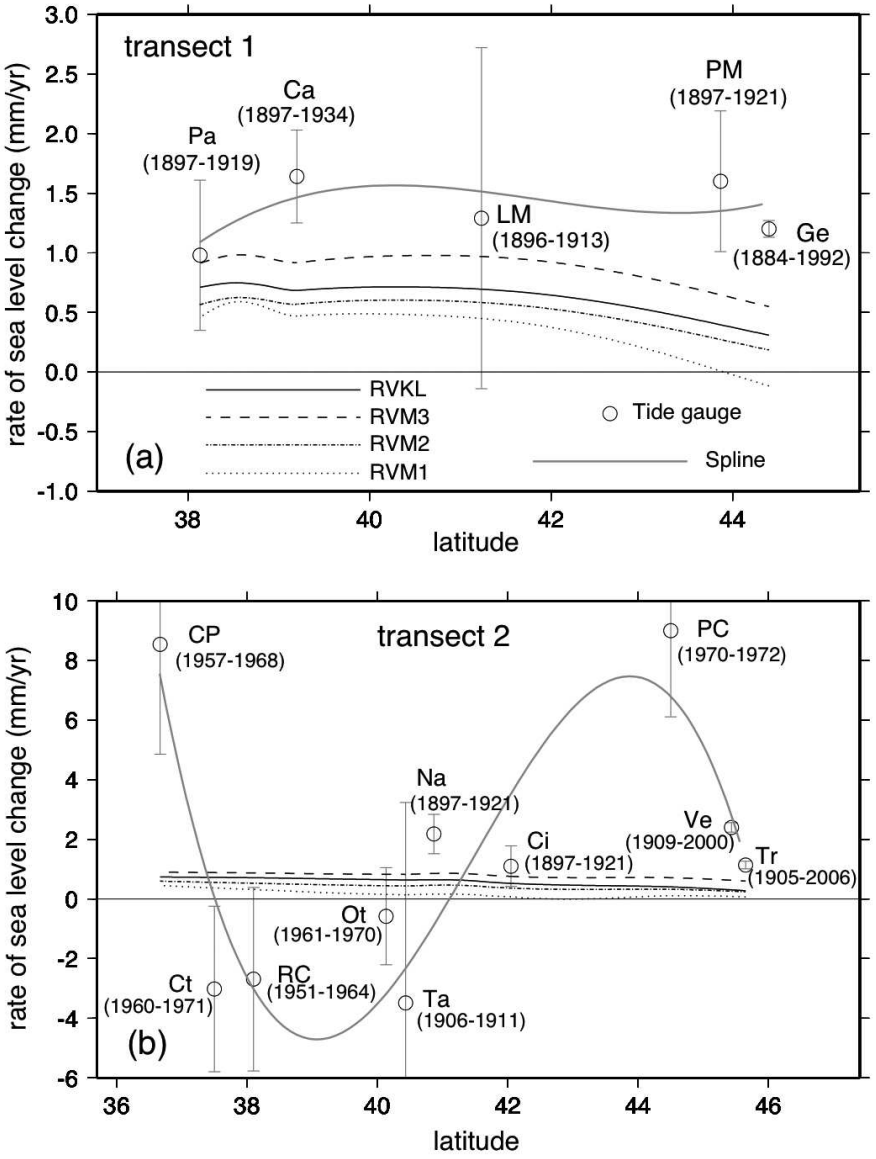

Fig. 7 - Observed (a) and computed (b) $\dot{S}$ along the two transects shown in Fig. 1, respectively. Station abbreviations are as in Fig. 4. Rates and their uncertainties are computed using the PSMSL annual 'RLR' (Revised Local Reference) data-set (see http://www.pol.ac.uk/psmsl/) by straightforward least squares. The time interval used for rate calculation is shown next to each datum. The grey curve is a cubic regression spline of observed $\dot{S}$ values.

Church *et al.*, 2001). This agrees with findings of Tsimplis *et al.* (2005) and Marcos and Tsimplis (2007).

Model calculations and observations along transect "2" of Fig. 1, which connects the northeastern Adriatic (Tr, Ve) to the Ionian sea (Ct) hitting the central the Tyrrhenian coast and crossing the central and southern Apennines, are shown in Fig. 7b. Tide gauges in Napoli (Na) and Venezia (Ve), which are significantly affected by local geological and anthropogenic factors [e.g. Carminati and Di Donato (1999)] record rates in excess of 2 mm yr^{-1}. Disagreement between

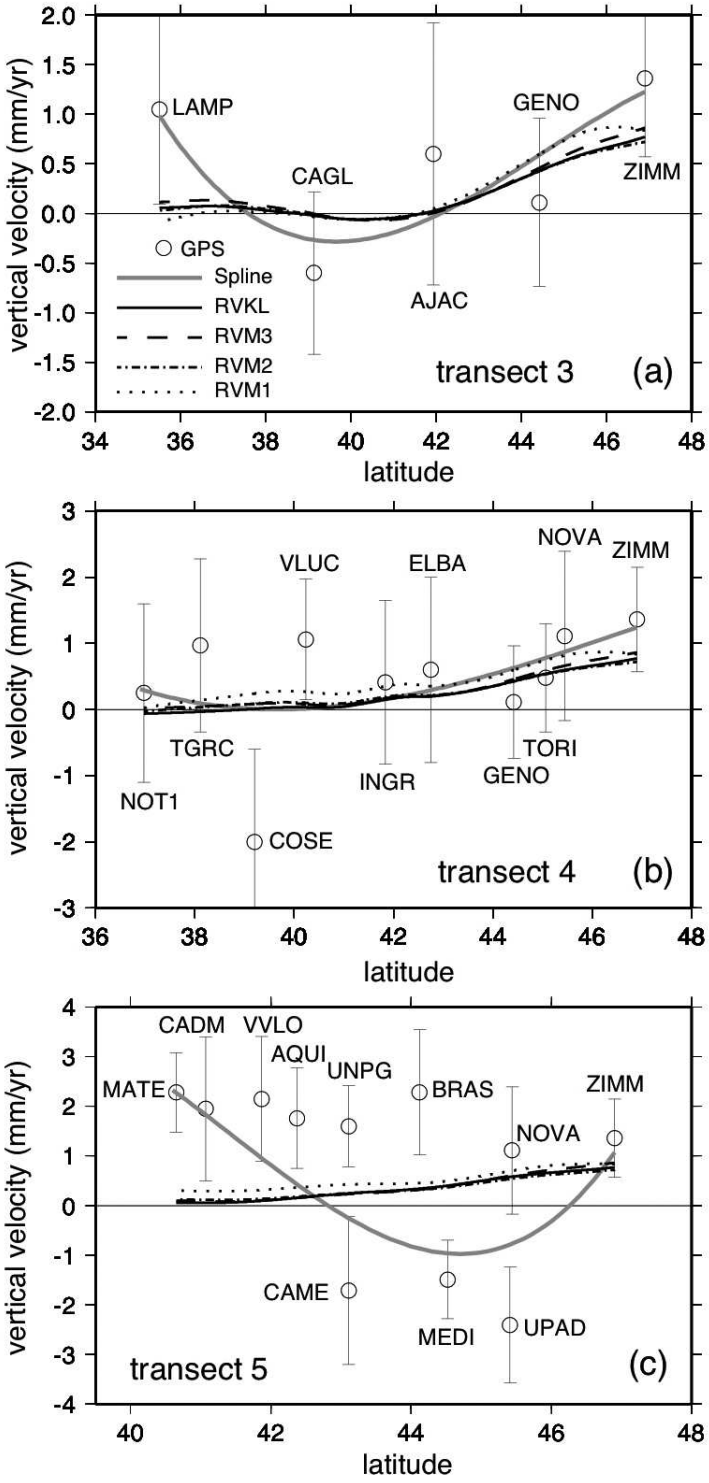

Fig. 8 - Observed and modeled $\dot{U}$ at GPS stations placed along the three transects in Fig. 2. The grey curve is a cubic regression spline of observed $\dot{U}$ values.

predictions and observations from the remaining southern tide gauge stations, which record a sea-level fall, may be attributed to local tectonic effects (Ferranti *et al.*, 2006) and to the short duration of sea-level records (see also Fig. 5).

In Fig. 8, the GPS vertical velocities of Fig. 6 are compared with predictions along the three transects shown in Fig. 2. Observed vertical velocities are residuals computed by removing the average value of CAGL and AJAC (Serpelloni *et al.*, 2006) from each solution. The same correction is applied to the expected $\dot{U}$ values. In Fig. 8a, we consider transect "3", connecting the Swiss station of ZIMM to the central Mediterranean (LAMP). Model calculations define a narrow band whose trend agrees with the cubic regression of data displayed by the grey spline. A satisfactory agreement is also obtained for transect "4" running along the Tyrrenhian coast of Italy, from ZIMM to NOT1, as shown in Fig. 8b. Both Figs. 8a and 8b clearly show that the long-wavelength pattern of vertical displacement, transects "3" and "4", is essentially driven by GIA. When the NW-SE trending path "5" of Fig. 2 is considered (see Fig. 8c), the agreement with GIA predictions is disrupted to indicate that present-day vertical velocities along the Apennines mainly

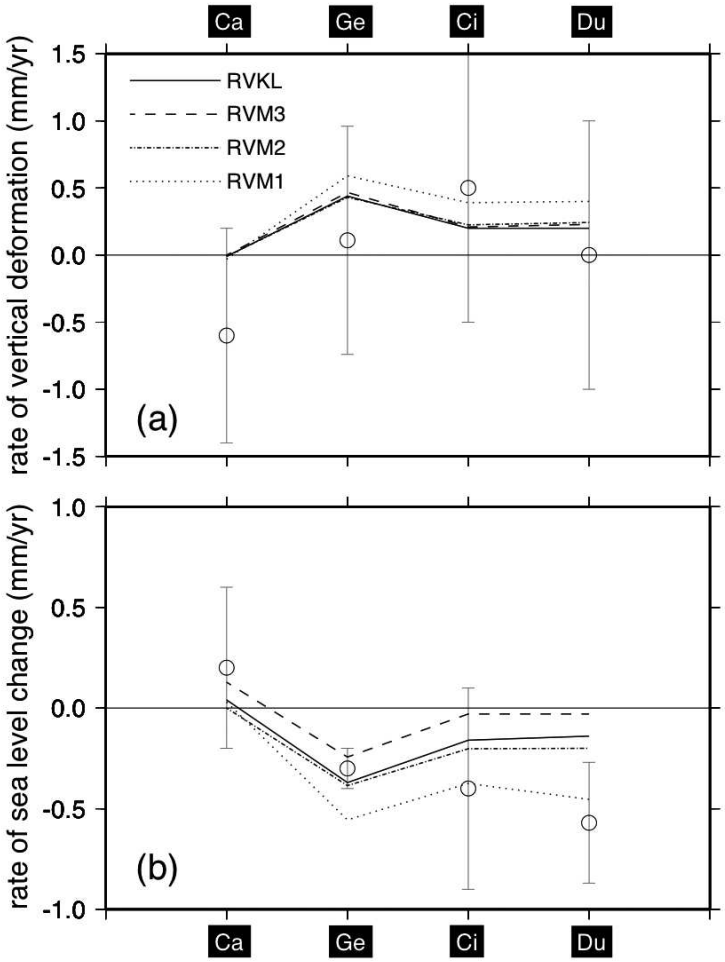

Fig. 9 - Predicted $\dot{U}$ (a) and $\dot{S}$ (b) at the sites of Cagliari (Ca), Genova (Ge), Civitavecchia (Ci), and Dubrovnik (Du), compared to GPS (a) and tide-gauge observations (b) for model RVKL and the other three mantle viscosity profiles discussed in the text.

result from local factors of geological and tectonic origin. Calculated and measured velocities clearly show opposite trends with varying latitude.

To better describe to what extent the spatial variability of current sea level change and vertical movements in Italy is driven by GIA, we consider $\dot{S}$ and $\dot{U}$ at the coastal sites of Cagliari, Genova, Civitavecchia and Dubrovnik (see Fig. 4) in Fig. 9, where both tide gauges and GPS observations are available (for Civitavecchia, we consider the average vertical velocity of nearby stations INGR and ELBA in Fig. 6). Since observed and modeled vertical velocities are referred to the Corsica-Sardinia block (as described above), sea-level trends refer to the average value of Cagliari and La Maddalena. Since $\dot{N}$ shows little variability across the study region (see Fig. 3), if GIA were the major driving process from Eq. (4), we would expect an anticorrelation between $\dot{S}$ and $\dot{U}$, and an agreement between predictions and observations. From the results of Fig. 9, the spatial variability of the referenced instrumental vertical velocities is in fact consistent with the GIA signal for all the viscosity profiles adopted, which define a narrow band within the error

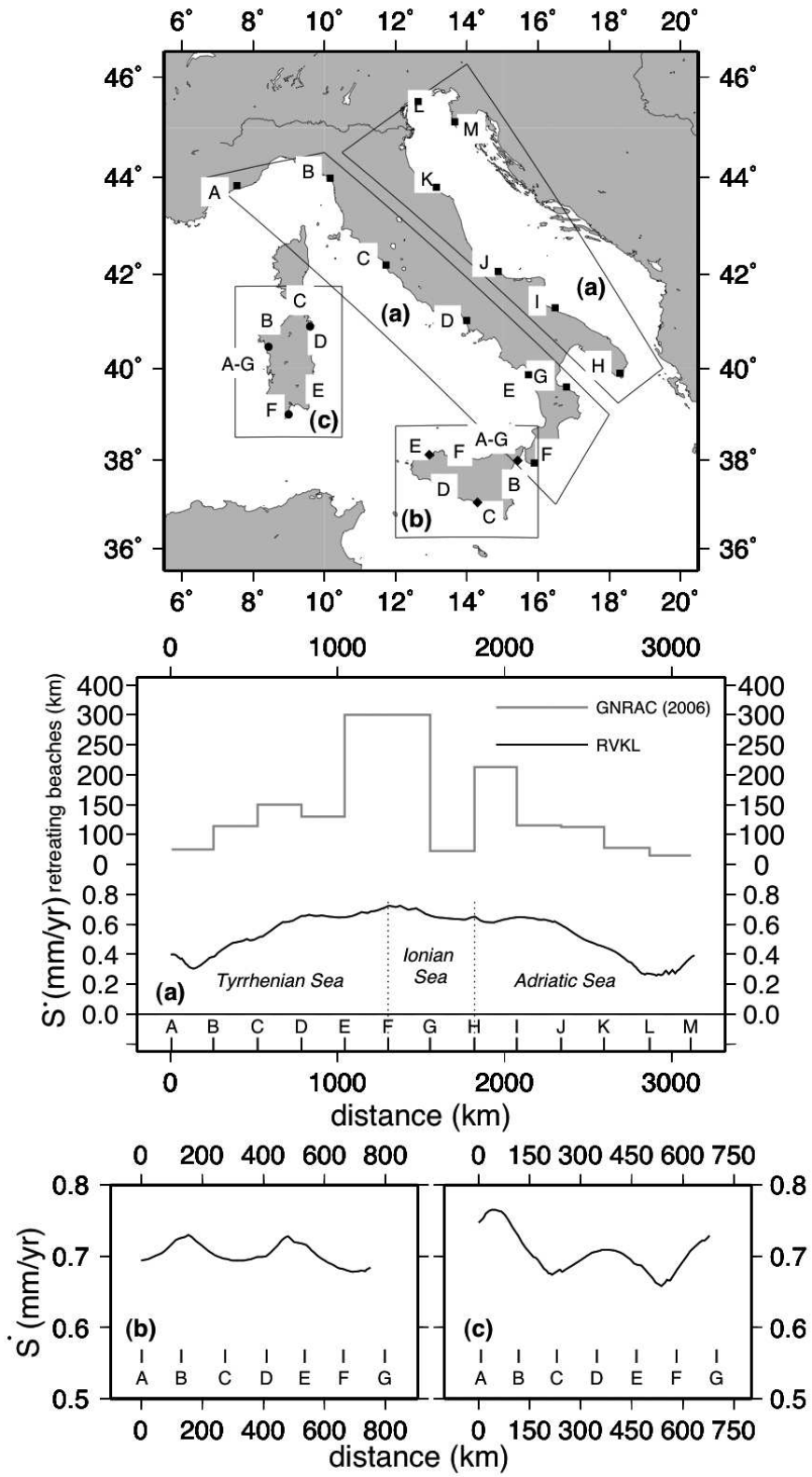

Fig. 10 - Predicted $\dot{S}$ for ICE5G(RVKL) and estimated length of retreating beaches according to GNRAC (2006), relative to the Italian peninsula (a), Sicily (b), and Sardinia (c).

observation, the tide gauge and GPS signals considered here have been significantly affected by the GIA and show broadly consistent rates.

According to recent estimates, at least 70% of the world's beaches are experiencing a permanent retreat in response to extreme phenomena (e.g. storm waves) exacerbated by global sea-level rise (Day, 2004). It is known that quantifying the relationship between sea level rise and beach erosion is not straightforward and that no universally accepted model of shoreline retreat has yet been developed (Cooper and Pilkey, 2004). The sensitivity of erosion to the sea-level rise has been (and can be) tentatively studied using the Bruun rule (e.g. Bruun, 1988), which predicts that the beach profile will shift landwards by an amount $s/\tan\vartheta$, where s is sea level rise and ϑ is the profile slope angle. Although the Bruun rule omits many important variables (Cooper and Pilkey, 2004) and fails in specific areas [see e.g. Dickson *et al.* (2007)], the sea-level rise is recognized as one of the most important factors contributing to beach erosion, mainly operating by the increased destructive power of storms (Day, 2004).

Since the GIA determines a long-wavelength, non-uniform secular sea-level rise that may reach an amplitude close to 1 mm yr^{-1} (see Fig. 1), we wonder whether it may indirectly influence current rates of erosion and beach retreat along the coastlines of Italy. To provide a tentative answer, we assume our reference model ICE5G(RVKL) and compute $\dot{S}$ along the coastlines of the Italian peninsula (see Fig. 10a), Sicily (Fig. 10b) and Sardinia (Fig. 10c). Fig. 10a shows that rates of sea-level variation always exceed 0.3 mm yr^{-1} and increase southwards where rates of ~0.75 mm yr^{-1} are expected in the Calabrian region (Ionian Sea). According to the extensive review of GNRAC (2006), a similar trend is observed for the estimates of coastal erosion, which in Fig. 10a is expressed in terms of length of retreating beaches (km) for an equal-length of coastal traits (grey stepwise curve) based on the regional study shown in the GNRAC Table of page 6.

Though estimates of regional coastal retreat are affected by large uncertainties, due in part to positive and negative feedbacks of man-made structures and human-driven imbalance of sediment supply (GNRAC, 2006), Fig. 10a shows that the trend of the beach retreat broadly follows that of the GIA-induced rate of sea-level change, with a tendency to increase towards the south of the peninsula. Available data do not allow to discern spatial trends in Sicily and Sardinia (Figs. 10b and 10c), where 440 and 170 km of beaches are retreating, respectively, and relatively large rates of GIA-related sea-level rise are expected. The non-linear relationship between sea-level rise and beach erosion is manifest observing that while southern Calabria is presently uplifting in response to tectonic forces (Ferranti *et al.*, 2006), according to GNRAC (2006) the length of retreating beaches reaches its maximum in this region (Fig. 10c).

4. Conclusions

Our analysis provides new estimates of current sea-level variations and vertical land movements along the coasts of Italy in response to GIA, which, since the end of the last deglaciation, resulted in a generalized subsidence of the Italian peninsula. At specific sites, where tide gauges and continuous GPS stations are operating, GIA provides a significant contribution to observed rates, which vary according to assumptions regarding the viscosity contrast across the 670-km depth seismic discontinuity. According to our findings, GIA modulates the long-wavelength pattern of present-day sea-level change and vertical motions along the coasts of the

Tyrrhenian Sea, but cannot explain vertical movements determined by GPS observations across the Apennines.

Present-day GIA-induced sea-level variations are not spatially uniform along the coasts of Italy. Rather, they systematically increase towards low latitudes reaching an amplitude of ~0.8 mm yr^{-1} in the Ionian Sea and are superimposed with regard to the global signal associated with recent climatic forcing (Douglas, 1991), which may be assumed to be constant across the study region. For the first time, we have shown that at long-wavelengths this pattern is correlated with the length of retreating beaches for unit coastal traits (GNRAC, 2006), which supports the existence of a close (but complex) relationship between post-glacial sea-level rise and coastal erosion (Day, 2004).

Acknowledgments. We thank Enzo Mantovani and an anonymous reviewer for their helpful suggestions. Work funded by MIUR (Ministero dell'Istruzione, dell' Università e della Ricerca) by the PRIN2006 grant "Il ruolo del riaggiustamento isostatico post-glaciale nelle variazioni del livello marino globale e mediterraneo: nuovi vincoli geofisici, geologici, ed archeologici". The numerical code employed in this study (SELEN, see http://flocolleoni.free.fr/SELEN.html) is freely available and can be requested from Giorgio Spada (email: giorgio.spada@gmail.com).

REFERENCES

Antonioli F., Anzidei M., Lambeck K., Auriemma R., Gaddi D., Furlani S., Orrù P., Solinas E., Gaspari A., Karinja S., Kovaciè V. and Surace L.; 2007: *Sea-level change during the Holocene in Sardinia and in the northeastern Adriatic (central Mediterranean Sea) from archaeological and geomorphological data*. Quat. Sci. Rev., **26**, 2463-2486.

Antonioli F., Ferranti L., Fontana A., Amorosi A.M., Bondesan A., Braitenberg C., Dutton A., Fontolan G., Furlani S., Lambeck K., Mastronuzzi G., Monaco C., Spada G. and Stocchi P.; 2009: *Holocene relative sea-level changes and vertical movements along the Italian and Istrian coastlines.* Quat. Int., in press.

Bruun P.; 1988: *The Bruun rule of erosion by sea level rise: a discussion of large-scale two- and three-dimensional usages*. J. Coast. Res., **4**, 627-648.

Carminati E. and Di Donato G.; 1999: *Separating natural and anthropogenic vartical movements in fast subsiding areas: the Po plain (N. Italy) case.* Geophys. Res. Lett., **26**, 2291-2294.

Cazenave A. and Nerem R.S.; 2004: *Present-Day sea level change: observations and causes.* Rev. Geophys., **42**, RG3001, doi: 10.1029/2003RG000139.

Church J.A., Gregory J.M., Huybrechts P., Kuhn M., Lambeck K., Nhuan M.T., Qin D. and Woodworth P.L.; 2001: *Changes in sea level.* In: Houghton J.T. *et al*. (eds), Climate Change 2001: The Scientific Basis: Contribution of Working Group I to the Third Assessment Report of the Intergovernmental Panel on Climate Change, Cambridge Univ. Press, New York, pp. 639-694.

Clark J.A. and Lingle C.S.; 1979: *Predicted relative sea-level changes (18.000 Years B.P. to present) caused by late glacial retreat of Antarctic Ice Sheet.* Quat. Res., **11**, 279-298.

Cooper J.A.G. and Pilkey O.H.; 2004: *Sea-level rise and shoreline retreat: time to abandon the Bruun rule.* Global Planet. Change, **43**, 157-171.

Day C.; 2004: *Sea-level rise exacerbates coastal erosion.* Phys. Today, <http://www.physicstoday.org/vol-57/iss-2/p24.html>.

Dickson M.E., Walkden M.J.A. and Hall J.W.; 2007: *Systemic impacts of climate change on an eroding coastal region over the twenty-first century.* Clim. Change, **84**, 141-166.

Douglas B.C.; 1991: *Global sea level rise.* J. Geophys. Res., **96,** 6981-6992.

Douglas B.C.; 1992: *Global sea level acceleration.* J. Geophys. Res., **97**, 12699-12706.

Douglas B.C., Kearney M.S. and Leatherman S.P.; 2000: *Sea Level Rise: History and Consequences.* Academic Press,

232 pp.

Farrell W.E. and Clark J.A.; 1976: *On postglacial sea level.* Geophys. Jour. R. Astron. Soc., **46**, 647-667.

Ferranti L., Antonioli F., Mauz B., Amorosi A., Dai Pra G., Mastronuzzi G., Monaco C., Orrù P., Pappalardo M., Radtke U., Renda P., Romano P., Sansò P. and Verrubbi V.; 2006: *Markers of the last interglacial sea-level high stand along the coast of Italy: Tectonic implications.* Quat. Int., **145-146**, 30-54.

GNRAC (Gruppo Nazionale per la Ricerca sull'Ambiente Costiero); 2006: *Studi Costieri*, **10**, 174 pp.

Lambeck K. and Johnston P.; 1995: *Land subsidence and sealevel change: contributions from the melting of the last great ice sheets and the isostatic adjustment of the Earth.* In: Barends F.B.J. *et al*. (eds), Land Subsidence. Balkema, Rotterdam, pp. 3-18.

Lambeck K. and Purcell A.; 2005: *Sea-level change in the Mediterranean Sea since th LGM: model predictions for tectonically stable areas.* Quat. Sci. Rev., **24**, 1969-1988.

Lambeck K., Antonioli F., Purcell A. and Silenzi S.; 2004a: *Sea level change along the Italian coast from the past 10,000 yr.* Quat. Sci. Rev., **23**, 1567-1598.

Lambeck K., Anzidei M., Antonioli F., Benini A. and Esposito A.; 2004b: *Sea level in Roman time in the Central Mediterranean and implications for recent change.* Earth Planet. Sci. Lett., **224**, 563-575.

Marcos M. and Tsimplis M.N.; 2007: *Forcing of coastal sea level rise patterns in the North Atlantic and the Mediterranean Sea.* Geophys. Res. Lett., **34**, doi:10.1029/2007GL030641.

Mitrovica J.X. and Peltier W.R.; 1991: *On post-glacial geoid subsidence over the equatorial ocean.* J. Geophys. Res., 96, 20,053-20,071.

Peltier W.R.; 2004: *Global glacial isostasy and the surface of the Ice-Age Earth: the ICE-5G(VM2) model and GRACE.* Annu. Rev. Earth Pl. Sc., **32**, 111-149.

Pirazzoli P.A.; 1991: *World atlas of Holocene sea-level changes.* Elsevier, Amsterdam, 300 pp.

Pirazzoli P.A.; 2005: *A review of possible eustatic, isostatic, and tectonic contributions in eight late-Holocene relative sea-level histories from the Mediterranean area.* Quat. Sci. Rev., **24**, 1989-2001.

Serpelloni E., Casula G., Galvani A., Anzidei M. and Baldi P.; 2006: *Data analysis of permanent GPS networks in Italy and surrounding regions: Application of a distributed processing approach.* Ann. Geophys., **49**, 897-928.

Spada G. and Stocchi P.; 2006: *The Sea Level Equation, Theory and Numerical Examples.* Aracne, Roma, 96 pp.

Spada G. and Stocchi P.; 2007: *SELEN: a Fortran 90 program for solving the "Sea Level Equation".* Comput. Geosci., **33**, doi: 10.1016/j.cageo.2006.08.006.

Spada G., Antonioli A., Cianetti S. and Giunchi C.; 2006: *Glacial isostatic adjustment and relative sea-level changes: the role of lithospheric and upper mantle heterogeneities in a 3-D spherical Earth.* Geophys. J. Int., **165**, doi: 10.1111/j.1365- 246X.2006.02969.x

Stocchi P. and Spada G.; 2007: *Glacio and hydro-isostasy in the Mediterranean Sea: Clark's zones and role of remote ice sheets.* Ann. Geophys., **50** (6), 741-761.

Stocchi P., Spada G. and Cianetti S.; 2005: *Isostatic rebound following the Alpine deglaciation: impact on the sealevel variations and vertical movements in the Mediterranean region.* Geophys. J. Int., **162**, doi: 10.1111/j.1365-246X.2005.02653.x.

Tegmark M.; 1996: *An icosahedron-based method for pixelizing the celestialsphere.* ApJ Letters, **470**, L81-L84.

Tsimplis M.N., Alvarez-Fanjul E., Gomis D., Fenoglio-Marc L. and Pérez B.; 2005: *Mediterranean Sea level trends: Atmospheric pressure and wind contribution.* Geophys. Res Lett., **32**, doi:10.1029/2005GL023867.

Tushingham A.M. and Peltier W.R.; 1991: *Ice-3G: a new global model of late Pleistocene deglaciation based upon geophysical prediction of post-glacial sea level change*. J. Geophys. Res., **96**, 4497-4523.

Zerbini S., Plag H.P., Baker T., Becker M., Billiris H., Burki B., Kahle H.G., Marson I., Pezzoli L., Richter B., Romagnoli C., Sztobryn M., Tomasi P., Tsimplis M., Veis G. and Verrone G.; 1996: *Sea level in the Mediterranean: a first step towards separating crustal movements and absolute sea-level variations*. Global Planet. Change, **14**, 1-48.

Corresponding author: Giorgio Spada
Istituto Fisica
Università di Urbino "Carlo Bo"
Via Santa Chiara 27, 61029 Urbino (Italy)
phone: +39 0722 303389; fax: +39 0722 303399; e-mail: giorgio.spada@gmail.com

SELEN 3.0

Last Update:
July 2009

SELEN is a Sea level Equation solver which computes:

- loading Love numbers
- past and present sea level variations
- vertical and horizontal ground deformation
- geoid height variations

in response to evolving surface loads.

SELEN can be distributed and/or modified under the terms of the GNU GPL license.

The current version of SELEN is 2.7 (released March 11, 2009)

Giorgio SPADA*, Florence COLLEONI and Paolo STOCCHI

© 2007 SELEN 3.0